Geology and Genesis of the Mammoth Cu Deposit, Mount Isa Inlier, Australia.

Submitted in fulfilment of the requirements
for the degree of Doctor of Philosophy

Darryl J. Clark
BSc. (Hons)

Darryl James

UNIVERSITY OF TASMANIA

SCHOOL OF EARTH SCIENCES

and

August, 2003

GEOLOGY AND GENESIS OF THE MAMMOTH CU DEPOSIT, MT ISA INLIER, AUSTRALIA

ABSTRACT

Of the numerous structurally-controlled, sediment-hosted Cu deposits throughout the Proterozoic Western Fold Belt of the Mt Isa Inlier, the two most significant are the giant Mt Isa Cu deposit (255 Mt @ 3.3% Cu) and the Mammoth deposit (16.8 Mt @ 3.4% Cu). The deposits are hosted in deformed Proterozoic sediments that range in age from 1740 to 1652 Ma. Copper mineralisation is hosted in breccias and veins, which appear to be fault controlled and is interpreted as occurring approx. 150 Ma after deposition of the host rocks during regional deformation (1590 to 1500 Ma; Isan Orogeny). The Mammoth deposit is located approximately 115 km to the north of Mt Isa, and copper mineralisation is hosted within the Palaeoproterozoic Whitworth Quartzite of the Myally Subgroup. Understanding the local geological and geochemical controls at Mammoth will assist in the development of a genetic model and exploration targeting of similar deposits in ancient, structurally deformed, sedimentary basins in Australia and elsewhere in the world.

Structural studies using orientation and kinematic data from mineralised veins and bounding faults have provided a new understanding of the mechanisms that localised Cu mineralisation at the Mammoth deposit. The Mammoth deposit formed during E-W transpression localised at the intersection of the Mammoth and Portal Faults during periods of high fluid pressure (P_f), subsequent to slip episodes, when the principle stresses were sub-equal ($\sigma_3 \cong \sigma_2 \leq \sigma_1$). Dilation was achieved when fluid pressure (P_f) exceeded the tensile strength (T) of the host rock as indicated: 1) by the irregular development of syn-deformational quartz-Cu sulfide extensional veins; and 2) by the regular development of syn-deformational quartz-Cu sulfide extensional veins along bedding planes when $\sigma_1 \cong \sigma_3$.

The Mammoth deposit has 6 major ore lenses that extend over 1,100 metres vertically and have a strike extent of 100 to 300 m and widths from 10 to 75m. Within these lenses, Cu mineralisation is hosted in veins and breccias adjacent to the intersection of the Mammoth and Portal Faults. A new textural classification scheme, consisting of five categories was used to describe the variations of brecciation and fracturing of the Whitworth Quartzite during hypogene mineralisation. The grade of Cu mineralisation in these units is variable, but is high around zones of intense brittle deformation in the breccia units reflecting zones of enhanced permeability. Wall rock alteration, replacement and cementation of the breccia units by the hypogene mineral assemblage took place after and/or during the fragmentation. Hypogene Cu mineralisation consists of chalcopyrite, bornite and chalcocite. Supergene chalcocite (± covellite) has variably overprinted and enriched the hypogene assemblage. Hypogene and supergene chalcocite within the deposit are texturally and paragenetically distinct. A four stage paragenetic sequence has been defined across the Mammoth ore

zones: Stage I) hypogene pyrite and quartz; Stage II) hypogene chalcopyrite, bornite, chalcocite and carrollite (trace) + chlorite, illite and quartz; Stage III) supergene hematite, chalcocite, covellite and wittichenite, and Stage IV) supergene kaolinite, chalcocite, covellite and wittichenite. Hypogene Cu sulfides are broadly zoned within the Mammoth ore zones from hangingwall to footwall and up dip. This zonation is: 1) Stage II hypogene chalcocite ± bornite; 2) Stage II bornite ± hypogene chalcocite and 3) Stage II chalcopyrite ± bornite.

Microanalytical trace element geochemistry of sulfide minerals from the Mammoth deposit confirmed paragenetic interpretations. These investigations involved the development of a new analytical technique to obtain high quality, sub-ppm, quantitative data from the in situ microanalysis of sulfide minerals using laser ablation (LA) ICP-MS analysis. Pyrite, chalcopyrite, bornite and both supergene and hypogene chalcocite were analysed. Stage III supergene chalcocite is enriched in Bi and depleted in both Ag, Co, Sb, and As compared to Stage II hypogene chalcocite. No differences were detected in trace element composition between disseminated and veined styles of Stage I pyrite. Stage I pyrite has elevated contents of As, Co, Ni, Sb, and Pb compared to chalcopyrite, bornite and chalcocite. Bornite is anomalously enriched in Bi compared to the other sulfides minerals

The processes of meteoric and supergene alteration have led to complex geochemical dispersion patterns overprinting geochemical patterns developed during hypogene mineralisation. Whole-rock geochemistry analysis across the deposit revealed a distinct metal zonation. Elevated Co, Ni, CaO and P_2O_5 contents form a narrow halo (≅ 2 to 5m) around the hypogene ore zones at Mammoth. Along the ore equivalent structural horizon Zn, Co, and Ni are enriched distal (100 to 200m) to the ore zones. In contrast, Cu, Bi, As and Fe, initially at or below detection, all increase with proximity to the ore zones. Mineralised structures that have undergone supergene modification also have a similar suite of trace elements (Cu, Pb, Zn, Ni, Bi, Sb, and As). Their level of enrichment is significantly lower than their un-oxidised equivalent but more enriched than the enclosing host rocks. These suites of trace elements form potential vectors to differentiate mineralised and un-mineralised structures and can be used to identify Mammoth style mineralisation in surface or near surface leached structures.

Sulfur, O - D and Pb isotopic investigations allow characterisation of the ore fluids and identification of potential metal source reservoirs. Lead isotopic ratios from Mammoth ore samples lie along an isochron that originates from the Eastern Creek Volcanics at 1540 Ma, indicating that the Eastern Creek Volcanics were the source of Pb, and by inference Cu, contained in the Mammoth deposit. The $\delta^{34}S$ values of Stage I pyrite (- 15 to - 7 ‰; mean = – 12 ‰) and Stage II Cu and Cu-Fe sulfides (– 19 to – 1 ‰; mean = - 8 ‰) supports the conclusion that the Eastern Creek Volcanics were the source of metals and sulfur as they represent the only probable source of light sulfur in the Western Fold Belt. The calculated $\delta^{18}O$ and δD fluid composition in equilibrium with Stage I quartz and Stage II chlorite yielded a range of – 10 to - 2 ‰ $\delta^{18}O$ and – 2 to + 11 ‰ $\delta^{18}O$ and – 41 to – 56 ‰ δD respectively.

These values suggest the fluid had two end members: 1) dominantly meteoric fluid and 2) fluid originating from metamorphic processes.

Geological, isotopic, paragenetic, geochemical and structural data suggest the Mammoth Cu deposit formed synchronous with regional deformation when channelised flow of hot saline-oxidised Cu-enriched fluid generated by metamorphic devolatilisation, leached Cu and S from the Eastern Creek Volcanics, and was focussed along the Esperanza, Mammoth and Mammoth Extended Faults. Upon reaching the Whitworth Quartzite, a build up of fluid pressure combined with the existing regional stress field, created the appropriate conditions for brittle failure in the quartzite forming dilational sites for sulfide precipitation. The hot metal and sulfur-bearing fluid mixed with a deep circulating methane-bearing hydrothermal fluid originally of meteoric origin. Changes in the physicochemical conditions upon this mixing destabilise the metal chlorine complexes resulting in sulfide precipitation. All of these attributes cumulatively broaden the classification of the metamorphogenic style of Cu deposit. Most notable of which is that the Mammoth deposit provides evidence that metamorphogenic Cu deposits can be hosted in host rocks other than meta-carbonates.

This new model for the genesis of the Mammoth deposit has developed new criteria for the exploration of similar resources in the Western Fold Belt; including the world class Mt Isa Cu deposit. The exploration strategy currently in use throughout the Western Fold Belt of the Mt Isa Inlier has traditionally focussed on sites where structural geometries potentially gave rise to dilatational fault jogs during deformation. This research provides evidence that structural geometries that had the potential to create zones of E-W compression and/or N-S extension should now be included in exploration targeting.

DECLARATION

This Thesis contains no material which has been accepted for the award of any other degree or diploma in any tertiary institution and, to the best of my knowledge and belief, contains no copy or paraphrase of material previously published or written by another person, except where due reference is made in the text of the Thesis.

Darryl Clark

D. J. Clark.

This thesis is not to be made available for loan or copying for two years following the date this statement was signed. Following that time the thesis may be made available for loan and limited copying in accordance with the *Copyright Act 1968.*

Darryl Clark D. J. Clark

Date: 24th July, 2003

ACKNOWLEDGMENTS

Firstly and fore mostly, I wish to express my eternal gratitude to my wife Melanie, who tirelessly gave her love, encouragement, and sacrificed her time in order to support us through *my* decision. To my daughter Maddy, who started her own journey at the same time I started this one, thanks for teaching me patience and brightening my days with your laughter. To my parents James L. and Mary L. Clark: thank you for all your generous support and encouragement.

I wish to thank my supervisor, Assoc. Prof. J. Bruce Gemmell, for his inspirational guidance, patience and tireless enthusiasm throughout the course of this project. My thanks are extended to Dr. Marc Norman for his assistance and leadership in the lab and for his regard of the establishment. I am grateful for Dr. Rob Scott's exceptional educational talent in preforming "corrective surgery" to enhance my concept of structural geology.

Thanks to the past and present staff of the Mt Gordon Copper Mine; with particular gratitude extended for Dr. Gary McArthur, Tony Hespe, Craig Colley, Steve Richardson, Andrew Moy, Craig Irvine, Karin Coppens, Stuart Hall, His Lordship Michael Burnett, Gary Cooper and Jono Lawrence for their individual contributions to both the "mammoth arm waving discussions" and for their unflagging toil in field. This project would not have been possible without the financial, technical and logistical support provided initially from Aberfoyle Ltd and subsequently from Western Metals Copper Ltd.

In addition to my supervisor's corrective comments, this thesis benefited greatly from critical reviews by Dr. Robinia Sharpe, Vanessa Lickfold, Craig Colley and Tony Hespe.

To all of my fellow PhD students at the University of Tasmania, thanks for all the great times and support.

TABLE OF CONTENTS

Figure 3.6. Extensional vein: a) fine grained quartzite host rock; b) euhedral syntaxial quartz growth from the vein margin; c) coarse grained euhedral pyrite; d) chalcopyrite and e) matching irregularities of opposing vein margins. Sample # 768UD184.1. Plane polarised transmitted light combined with reflected light 1X1.25.

Figure 3.7. Schematic reconstruction comparing stratigraphic thickness variations from the Surprise Creek Formation through to the Mt Oxide Chert Member prior to dip-slip movement on the Mammoth and Mammoth Faults. Note: 1) section line A-A1 is north of the Mammoth Extended Fault; 2) section line B-B1 is south of the Mammoth Extended Fault; and 3) section line C-C1 is south of Mammoth Fault. Dips of the Surprise Creek Unconformity and Mount Oxide Chert Member have been averaged from measured dips resulting in an average dip of 57° and 72° respectively. Cross section 'B-B1' has been rotated 11° anti-clockwise in order to re-align stratigraphy. Laterally continuous dips have been assumed for both Mount Oxide Chert Member and Surprise Creek Unconformity. Sections have been stacked to remove the stratigraphic offset mapped on surface. Reconstruction permits the distance of inferred vertical dip-slip displacement to be calculated as indicated on the left margin. Refer to Figure 3.1 for section lines A-A1, B-B1 and C-C1.

Figure 3.8. Sketch illustrating the interpreted movement directions on structures within the Mammoth Mines area during D3. Cu mineralisation occurred in response to EW transpression (s1). A zone of compression is developed at the intersection of the Portal and Mammoth Faults. The Mammoth ore lens formed under conditions of high fluid pressure (Pf), during a transient period, subsequent to dextral-reverse slip failure on the Mammoth Fault and/or reverse slip failure on the Portal Fault. Under these conditions the local stress field was highly perturbed and the least principle stress (s3) and intermediate principle stress (s2) became sub-equal (s3 ~ s2). The orientation of the least and intermediate principle stresses (s3 and s2) is variable as indicated by the irregular distribution of the syn-deformational quartz-Cu sulfide veins around an east-west maxima (Fig. 3.5). SCU = Surprise Creek Unconformity.

Figure 4.1. Three-dimensional view of the Mammoth deposit (from an elevated north-west position), major faults (Mammoth (MF), Portal (PF) and the Mammoth Extended Fault (MEF) and the Surprise Creek Unconformity, with the Mammoth Fault cut away (Note: intersection line of the MF and PF). Solid models of the 2.0 % Cu contour (extracted from resource data base in July 1998) are depicted for No. 1, B, C, D, and 2 Lenes, whilst the approximate position of recently identified E lens ore zone is highlighted by the dashed red ellipse. The distribution of the Mammoth ore lenes is broadly controlled by the intersection of the Mammoth and Portal Fault zones.

Figure 4.2. Surface Geology of the Mammoth Mine modified after Moore et al. (1975). Surface geometry of No. 1 Lens filled with dashed red. Surface exposure of brecciated host rock filled with dashed green.

Figure 4.11.a. Breccia matrix is composed primarily of melnikovite pyrite. Bornite and chalcocite appear to be infilling vug space. Note; a) clast supported breccia with subangular to rounded clasts. Clasts are devoid of disseminated sulfides. Dashed lines highlight bedding within clasts. UD773-204m, 2 Lens.

Figure 4.11.b. Clast to matrix supported breccia with matrix composed primarily of chalcocite and bornite. UD255-1051m, E Lens.

Figure 4.11.c. Clast to matrix supported breccia with matrix composed of pyrite. Diameter of coin is 2cm. UD611-50.5m, B Lens.

Figure 4.11.d. Matrix to clast supported breccia. The breccia matrix is composed primarily of pyrite, chlorite and rock flour. Diameter of coin is 2cm. UD710-102.5m, B Lens.

Figure 4.11.e. Clast to matrix supported breccia. Host rock is altered to chlorite and hematite. Vein/breccia matrix composed of pyrite and/or bornite. Diameter of coin is 2cm. UD611-170.5m, B Lens.

Figure 4.11.f. Angular to subangular sandstone fragments altered to pyrite, chlorite and hematite. Matrix composed of pyrite. Diameter of coin is 2cm. UD717-50.6m, D Lens.

Figure 4.12.a. Matrix supported breccia with bornite, chalcocite and pyrite as matrix components. Pyrite also occurs as breccia fragments. Some breccia fragments are replaced by pyrite and chalcocite, relict clast is highlighted by dashed line. UD774-208.1m, 2 Lens.

Figure 4.12.b. Brecciated Host Rock (B2). Matrix supported breccia. Matrix is composed of pyrite (20%) and chalcocite (80%). Breccia fragments are well rounded to angular. UD774-200.9m, 2 Lens.

Figure 4.12.c. Close up of fragment from Fig. 4.12.b. The margin of this well rounded fragment grades into the fine grained sulfide matrix. This is due to the replacement of the fragment by fine grained pyrite (dashed lines outline relict breccia clasts). The lighter coloured rim of the clast is due to kaolinite alteration. UD774-200.9m, 2 Lens.

Figure 4.12.d. Matrix supported breccia with very fine grained sand to clay sized matrix variably altered to chlorite and rare disseminated pyrite and bornite. Breccia fragments range in composition from siltstone to sandstone. Surface grab sample from No. 1 ore zone GP014.

Figure 4.12.e. Subangular clast to matrix supported breccia. Coarse grained sandstone fragments clearly fractured and infilled with bornite. Fragments are coated in crustiform euhedral pyrite. Diameter of coin is 2cm. UD611-59.5m, B Lens.

Figure 4.12.f. Matrix supported breccia. Subangular fragments composed of siltstone and sandstone, with the siltstone fragment preferentially altered to

chlorite. Matrix comprised of bornite and pyrite. Diameter of coin is 2cm. UD710-106m, B Lens.

Figure 4.12.g. Matrix supported breccia. Breccia fragments consist of euhedral pyrite; well-rounded silicified sandstone and chlorite altered fine-grained clasts. Matrix is comprised of bornite and pyrite Diameter of coin is 2cm.. UD700-59.6m, D Lens.

Figure 4.13.a. Matrix to clast supported breccia. Matrix is chlorite partially replaced by hematite. SD255-1081.6m, E Lens.

Figure 4.13.b. Matrix supported breccia. In general the specimen is similar to Fig. 4.13.a, however the degree of hematite alteration of the chlorite matrix has increased. SD255-1081.6m, E Lens.

Figure 4.13.c. Rare example of zoned euhedral quartz crystals hosted in a dominantly pyrite matrix. SD255E-1156.9m, E Lens.

Figure 4.13.d. Angular to well-rounded sandstone fragments in a dominantly coarse grained pyrite matrix. UD708-123.5m, B Lens.

Figure 4.13.e. Matrix supported breccia with very fine grained sand to clay sized matrix material either silicified or replaced by very fined grained pyrite. Breccia fragments composed of sandstone. Diameter of coin is 2cm. UD710-88.1m, B lens.

Figure 4.13.f. Chalcopyrite-pyrite vein overprinting fractured sandstone host rock. Veins propagating into the host rock are predominantly composed of bornite with minor pyrite and chalcopyrite. Diameter of coin is 2cm. UD735-71m, C Lens.

Figure 4.14. Mammoth Mine. Geological interpretation plan 4720 level.

Figure 5.1.a. Detrital feldspar partially replaced by hematite (red-brown). Fine grained hematite (red-brown) coat detrital quartz grains. Pore space is filled by silica cement. UD768-184.1m, transmitted light, X40.

Figure 5.1.b. Detrital quartz grains coated with fine grained hematite (hm). Pore space is filled by quartz cement. UD768-184.1m, transmitted light, X40.

Figure 5.1.c. Disseminated fine grained stage I pyrite (py) hosted in quartzite. UD746-215.1m, reflected light, X62.5.

Figure 5.1.d. Disseminated fine grained stage I pyrite (py) hosted in quartzite. UD746-263.4m, reflected light, X5.

Figure 5.1.e. Vein-hosted stage I euhedral pyrite (py) and euhedral quartz (qz) overprinted by stage II bornite (bn) and chlorite (ch). Note inclusions of chalcopyrite (cpy) and rutile (rt) in euhedral quartz (qz) (see inset). UD746-136.2m, reflected light, X5.

Figure 5.1.f. Vein-hosted stage I melnikovite pyrite (py) and stage II bornite (bn) and chalcopyrite (cpy). UD746-207.0m, reflected light, X50.

Figure 5.1.g. Brecciated zoned stage I pyrite (py) overprinted by a myrmekitic intergrowth of stage II hypogene chalcocite (hcc) and bornite (bn). Void space is filled with quartz (qz) and chlorite (ch). UD746-145.5m, reflected light, X5.

Figure 5.1.h. Stage I colloform pyrite (py) fractured and replaced by stage II chalcopyrite (cpy) and bornite (bn). UD746-207.1m, reflected light, X25.

Figure 5.2.a. Vein hosted stage I euhedral pyrite (py) crosscut and replaced by stage II chalcopyrite (cpy). UD768-184.1m, reflected light, X1.25.

Figure 5.2.b. Fractured stage I pyrite (py) infilled by stage II chalcopyrite (cpy). UD746-212.9m, reflected light, X10.

Figure 5.2.c. Basket weave exsolutions and exsolution laminae (flames) of stage I chalcopyrite (cpy) in stage I bornite (bn). UD744-28.9m, reflected light, X200.

Figure 5.2.d. Disseminated stage II chalcopyrite (cpy) and bornite (bn) fills vug space in quartzite host rock. UD710-106.0m, reflected light, X50.

Figure 5.2.e. Vein hosted stage II bornite (bn) and chalcopyrite (cpy) crosscutting and replacing stage I pyrite (py). Note irregular bornite (bn)-chalcopyrite (cpy) grain boundaries. UD710-106.0m, reflected light, X5.

Figure 5.2.f. Stage II chalcopyrite (cpy) and bornite (bn) as breccia matrix infill. Note chalcopyrite (cpy) "flames" penetrating into bornite (bn). Stage II carrollite (cr) is hosted within chalcopyrite. UD746-207.0m, reflected light, X40.

Figure 5.2.g. Veined hosted stage I pyrite (py) overprinted and replaced by stage II chalcopyrite (cpy) and bornite (bn). UD710-106.0m, reflected light, X1.25.

Figure 5.2.h. Vein hosted stage II bornite (bn) infilling vug space around stage I euhedral quartz (qz). Note stage II chalcopyrite (cpy) replacing stage I pyrite (py) vein. SD255-1009.9m, reflected light, X1.25.

Figure 5.3.a. Stage II bornite (bn) replacing stage I zoned pyrite (py). UD768-124.4m, reflected light, X20.

Figure 5.3.b. Stage II myrmekitic hypogene chalcocite (hcc)-bornite (bn) intergrowths replacing stage I zoned pyrite (py). UD746-159.8m, reflected light, X20.

Figure 5.3.c. Stage II myrmekitic hypogene chalcocite (hcc)-bornite (bn) intergrowths replacing stage I pyrite (py) along fractures. UD746-159.8m, reflected light, X20.

Figure 5.3.d. Stage II myrmekitic hypogene chalcocite (hcc)-bornite (bn) intergrowths. SD255-1051.1m, reflected light, X40.

Figure 5.3.e. Vein hosted stage I euhedral quartz (qz) overprinted by stage II myrmekitic hypogene chalcocite (hcc)-bornite (bn) intergrowths. UD611-59.8m, reflected light, X5.

Figure 5.3.f. Stage III supergene chalcocite (scc) replacing stage I bornite (bn). Stage III hematite (hm) replacing stage II chlorite (ch)/illite intergrowth. UD746-145.5m, reflected light, X10.

Figure 5.3.g. Vermiform exsolutions of stage II digenite in stage II bornite (bn). UD710-88.0m, reflected light ,X125.

Figure 5.3.h. Stage II bornite (bn) replacing stage I pyrite (py). Stage III covellite (cv) replacing stage I bornite (bn). Stage III hematite (hm) replacing stage II chlorite (ch)/illite intergrowth. UD746-171.7m, reflected light, X20.

Figure 5.4.a. Stage III covellite (cv) replacing stage II bornite (bn). Stage I disseminated pyrite around stage I veined pyrite (py). UD768-162.5m, reflected light, X5.

Figure 5.4.b. Anhedral grains of stage II carrollite (cr) within stage II chalcopyrite (cpy). Stage I euhedral pyrite (py). UD746-223.9m, reflected light, X40.

Figure 5.4.c. A rare anhedral grain of stage II linnaeite (ln) hosted in stage II bornite (bn) infilling vug space around stage I euhedral pyrite (py). UD717-59.3m, reflected light, X40.

Figure 5.4.d. Anhedral grains of stage III wittichenite (wt) intergrown with stage III supergene chalcocite (scc), stage II bornite (bn) and stage III hematite (hm). UD746-116.8m, reflected light, X20.

Figure 5.4.e. Vein-hosted stage I euhedral pyrite (py) and quartz (qz) overprinted by stage II chlorite (ch)/illite (ill) intergrowths and traces of chalcopyrite (cpy). UD746-225.4m, reflected light, X1.25.

Figure 5.4.f. Vein-hosted stage I euhedral pyrite (py) and quartz (qz) overprinted by stage II chlorite (ch)/illite (ill) intergrowths and traces of chalcopyrite (cpy). Note occurrence of chlorite (ch)/illite (ill) intergrowth. UD746-225.4m, transmitted light, X1.25.

Figure 5.4.g. Stage II hypogene chalcocite (hcc) intergrown with stage II chlorite (ch). Note absence of stage III hematite and/or stage IV kaolinite. UD611-59.8m, reflected light, X40.

Figure 5.4.h. Stage II hypogene chalcocite (hcc) intergrown with stage II chlorite (ch). Note absence of stage III hematite and/or stage IV kaolinite. UD611-59.8m, transmitted light, X40.

Figure 5.5.a. Stage II hypogene chalcocite (hcc) intergrown with stage II chlorite (ch) and stage I quartz (qz) in the absence of stage III hematite and/or stage IV kaolinite. UD708-123.5m, reflected light, X50.

Figure 5.5.b. Stage II hypogene chalcocite (hcc) intergrown with stage II chlorite (ch) and stage I quartz (qz) in the absence of stage III hematite and/or stage III kaolinite. Note radial habit of chlorite (ch) UD708-123.5m, transmitted light, X50.

Figure 5.5.c. Stage III supergene chalcocite (scc) replacing stage II bornite (bn). Stage III hematite (hm) replacing stage II chlorite (ch). UD746-145.5m, reflected light, X40.

Figure 5.5.d. Stage III supergene chalcocite (scc) replacing stage II bornite (bn). Stage III hematite (hm) replacing stage II chlorite (ch). UD746-145.5m, transmitted light, X40.

Figure 5.5.e. Stage I quartz and stage II illite-chlorite (ill-ch) intergrowth with stage II chalcopyrite (cpy) infilling breccia vug space. UD746-207.1m, reflected light, X10.

Figure 5.5.f. Stage I quartz (qz) and stage II illite-chlorite (ill-ch) intergrowth with stage II chalcopyrite (cpy) infilling breccia vug space. UD746-207.1m, transmitted light with crossed polars, X10.

Figure 5.5.g. Stage II hematite (hm) replacing stage I bornite (bn) and stage II chlorite (ch). UD744-128.9m, reflected light, X10

Figure 5.5.h. Stage II hematite (hm) replacing stage I bornite (bn). Stage IV kaolinite replacing stage II chlorite (ch). UD744-128.9m, transmitted light with crossed polars, X10.

Figure 5.6.a. Stage III hematite (hm) developed along stage II bornite (bn)-stage IV kaolinite (ka) grain boundaries and preferentially replacing bornite (bn) along cleavage planes. Stage III covellite (cv) replaces bornite (bn) on the edge of the hematite-(hm) bornite (bn) grain boundary. UD746-171.7m, reflected light, X10.

Figure 5.6.b. Stage II chlorite-(ch) illite (ill) intergrowths preferentially replaced by stage III hematite (hm). Note stage II chalcopyrite (cpy) and bornite (bn) not replaced by stage III hematite (III). UD746-207.1m, reflected light, X40.

Figure 5.6.c. Stage III hematite (hm) replacing stage II chlorite (ch) and chalcopyrite (cpy). Stage II chalcopyrite (cpy) is only preserved within stage II chlorite (ch). UD746-112.5m, reflected light, X20.

Figure 5.6.d. Relic hexagonal fabric developed in hematite (hm) after bornite (bn). Chlorite (ch) is partially replaced by hematite (hm). UD746-112.5m, reflected light, X8.

Figure 5.6.e. Disseminated chlorite (ch)-illite (ill) intergrowth partially replaced by hematite (hm). UD767-181.6m, transmitted light, X40.

Figure 5.6.f. Disseminated pyrite (py) in host quartzite proximal to pyrite (py)-supergene chalcocite (scc) filled vein. UD746-136.2m, reflected light, X1.25.

Figure 5.7. Schematic east-west cross section illustrating the variable distribution of alteration and sulphide minerals within D Lens B2 breccia units (Fig. 4.5). Note: chalcocite that occurs with the Stage III and IV haematite and kaolinite mineralogy is interpreted to be of supergene origin and chalcocite occurring with the Stage II chlorite-illite intergrowths is interpreted to be of hypogene in origin. Refer to text for details.

Figure 6.1.1. STDGL-1 analysed in spot mode versus line san mode. Refer to text for details.

Figure 6.1.2. Correlation between the major and trace elements contained in the STDGL-1 calibration standard (outlined in Table 6.1) analysed via independent methods (XRF vs. solution ICPMS).

Figure 6.1.3. Box and whisker plots help summarize large amounts of data into an easy-to-read diagram. Related to the median, which separates the data into half, quartiles divide a data set into quarters. Q2 is the median of the data set, Q1 is the median of the lower half of the data and Q3 is the median of the upper half. The difference between the upper quartile and the lower quartile, Q3 – Q1, is called the interquartile range, or IQR. Data values less than Q1 – 1.5(IQR) or larger than Q3 +1.5(IQR) are called outliers. They are data values that are widely separated from the rest of the group of data. Outliers have not been plotted. Whiskers are drawn to the extreme points that are not outliers.

Figure 6.1.4. Box and whisker plots (refer Fig 6.1.3) summarising the trace element geochemistry of the major Cu sulphide minerals. Abbreviations: bn = bornite; cpy = chalcopyrite; hcc = hypogene chalcocite; scc = supergene chalcocite.

Figure 6.1.5. E Lens. Oblique cross-section looking south-west.

Figure 6.2.1. Electron micro-probe geochemical data from Stage II chlorites (Fe and Mg chlorite), illite and kaolinite plotted as wt% on a Al2O3-K2O-MgO ternary diagram.

Figure 7.1.a. E Lens hole SD255B down hole plots Cu, Ag, Bi, As, Sb and Fe.

Figure 7.1.b. E Lens hole SD255B down hole plots As, Pb, Ni, Co and Zn

Figure 7.1.c. E Lens hole SD255A down hole plots Cu, Ag, Bi, As, Sb and Fe.

Figure 7.1.d. E Lens hole SD255A down hole plots As, Pb, Ni, Co and Zn.

Figure 7.4.b. 2 Lens and MFM hole UD768 down hole plots Ni, Co, Zn, MgO, S, Y, V, and Ba.

Figure 7.4.c. 2 Lens and MFM hole UD768 down hole plots SiO_2, TiO_2, Al_2O_3, Fe_2O_3, MnO, MgO, CaO K_2O and P_2O_5.

Figure 7.4.d. 2 Lens and MFM hole UD767 down hole plots Cu, Bi, Sb, Mo, As, Pb, Tl and Ni.

Figure 7.4.e. 2 Lens and MFM hole UD767 down hole plots Ni, Co, Zn, MgO, S, Y, V, and Ba.

Figure 7.4.f. 2 Lens and MFM hole UD767 down hole plots SiO_2, TiO_2, Al_2O_3, Fe_2O_3, MnO, MgO, CaO K_2O and P_2O_5.

Figure 7.4.g. 2 Lens surface traverse plots Cu, Bi, Sb, Mo, As, Pb, Tl and Ni.

Figure 7.4.i. 2 Lens surface traverse plots SiO_2, TiO_2, Al_2O_3, Fe_2O_3, MnO, MgO, CaO K_2O and P_2O_5.

Figure 7.6.a-h. Box and whisker plots summarising the distribution of the major and trace elements classified by textural style: S0 = Unfractured Host Rock; S1 & S2 = Fractured Host Rock and B1 & B2 = Brecciated Host Rock.

Figure 7.7.a-h. Box and whisker plots summarising the distribution of the major and trace elements classified by textural style: S0 = Unfractured Host Rock; S1 & S2 = Fractured Host Rock and B1 & B2 = Brecciated Host Rock.

Figure 7.8.a-h. Box and whisker plots summarising the distribution of major and trace elements classified by textural style: S0 = Unfractured Host Rock; S1 & S2 = Fractured Host Rock and B1 & B2 = Brecciated Host Rock.

Figure 7.9. Whole-rock geochemical data plotted on wt% Al_2O_3-K_20-MgO ternary diagrams. This data illustrates the distribution of chlorite, illite and kaolinite alteration mineralogy associated with the Mammoth ore zones: Mineralised and barren breccia units (B1-B2); hangingwall and footwall units (S0, S1-S2).

Figure 7.10.a-f. XY plots summarising the correlations of: a) SiO_2 vs Fe_2O_3; b) SiO_2 vs Al_2O_3; c) Al_2O_3 vs K_2O; d) CaO vs P_2O_5; e) CaO vs Y & f) SiO_2 vs Cu. Data categorised by textural classification scheme: S0 = unfractured Host Rock; S1 & S2 = Fractured Host Rock and B1 & B2 Brecciated Host Rock.

Figure 7.11.a-f. XY plots summarising the correlations of: a) Cu vs Bi; b) Cu vs As; c) Pb vs As; d) Tl vs As; e) Sb vs As & f) Ni vs As. Data categorised by textural classification scheme: S0 = unfractured Host Rock; S1 & S2 = Fractured Host Rock and B1 & B2 Brecciated Host Rock.

Figure 7.12.a-f. XY plots summarising the correlations of: a) Co vs As; b) Zn vs As; c) Fe_2O_3 vs MgO; d) Al_2O_3 vs MgO; e) SiO_2 vs MgO & f) Zn vs MgO. Data categorised by textural classification scheme: S0 = unfractured Host Rock; S1 & S2 = Fractured Host Rock and B1 & B2 Brecciated Host Rock.

Figure 7.13. Schematic representation of idealized mineralogical domains and corresponding element abundances in a: a) typical un-oxidised ore Mammoth ore lens; and b) Mammoth ore lens with a significant supergene overprint. Distribution of the dominant alteration mineral assemblage as noted. Data in ppm except *Fe in wt%. Not to scale. Data compiled from Figures, 7.1-7.4.

Figure 8.1. A comparison of fluid compositions calculated from Mammoth hypogene stage II chlorite, supergene Stage III hematite. Water compositions in equilibrium with chlorite were calculated using fraction factors of: $\delta^{18}O_{chlorite\text{-}water} = 1.56 \times 10^6/(T^2) - 4.7$; $\delta D_{chlorite\text{-}water} = -4.38 \times 10^6/(T^2) - 24.6$; $\delta^{18}O_{hematite\text{-}water} = 1.63 \times 10^6/(T^2) - 12.3$. Refer to text for details.

Figure 8.2. Sulphur isotope distributions for stage I pyrite, stage II chalcopyrite, stage II bornite and chalcocite and stage II and stage III chalcocite. Note no distinction is made between stage II and stage III chalcocite (refer to text for details).

Figure 8.3. Sulphur isotope distributions for Mammoth Cu ore bodies categorised by sulfide type (refer to text for details).

Figure 8.4. A comparison of sulfur isotopic ranges of representative deposit styles and possible sulfur sources (Eastern Creek Volcanics and disseminated/digenetic sediment hosted pyrite) within the Western Fold Belt of the Mount Isa Inlier and Mid-Proterozoic seawater (20 ‰) and those of this study from the Mammoth Cu Deposit (modified after Davidson and Dixon, 1990; Taylor and Scott, 1976; Andrew et al., 1989).

Figure 8.5. This figure models the relationship between the Pb isotopic composition of the Eastern Creek Volcanics and the Mammoth ore system using the double spike method. Note differences in analytical precision between the DS and conventional methods (modified from Carr et al., 2001). The fields for Mt Isa Pb-Zn, HYC (McArthur River), Lady Loretta and Century (conventional) are included for comparison (modified after Carr, 2000).

Figure 9.1. Simplified diagrammatic model illustrating geological relationships between the Lawn Hill Platform, Mount Gordon Fault Zone and the Leichhardt River Fault Trough during east-west transpression (D3) synchronous with metamorphic fluid flow. Metamorphic water fluid reservoirs are within D2 (and D3?) anticlinal structures of the Eastern Creek Volcanics. Channelised fluid flow (red arrows) is initiated during D3, when the fluid reservoirs are broach by highly permeable structures, and focussed into

dilatant fault jogs, where it mixes with deep circulating waters (blue arrows) of meteoric origin. Refer to text for details.

Figure 9.2. Schematic model of the Mammoth (M) and Esperanza (E) Cu deposits during east-west transpression (D3) and synchronous with metamorphic fluid flow. Metamorphic water (red arrows), generated by devolatilisation, driven out of Eastern Creek Volcanics and focussed into dilatant fault jogs during periods of high fluid pressure, where it mixes with deep circulating hydrothermal waters (blue arrows) of meteoric origin. Refer to text for details.

Figure 9.3. A comparison of fluid compositions calculated from Mammoth hypogene stage II chlorite, and Mt Isa copper ore body fluid inclusions (Heinrich et al., 1989). Water compositions in equilibrium with chlorite were calculated using fraction factors of: $\Delta^{18}O_{\text{chlorite-water}} = 1.56 \times 106/T^2 - 4.7$; $\Delta D_{\text{chlorite-water}} = -4.38 \times 106/T^2 - 24.6$; $\Delta^{18}O_{\text{quartz-water}} = 3.34 \times 106/T^2 - 3.31$ (Taylor, 1979).

CHAPTER 1

INTRODUCTION

1.1 PREAMBLE

The Mammoth deposit is a sediment-hosted, structurally-controlled, Proterozoic Cu deposit located in the Western Fold Belt of the Proterozoic Mt Isa Inlier, western Queensland, Australia. The pre-mining resource contained 16.8 Mt grading 3.4 % Cu (≅ 384, 500 t of Cu metal). The mine is situated 4 km north of the Gunpowder Township in northwest Queensland, Australia (latitude = 19°20'S, and longitude = 139°22'E) (Fig 1.1). Access to Mt Isa is by road.

Copper was first discovered in the area by Ernest Henry in 1882 at Mt Oxide, 23 km to the north of Gunpowder (Blainey, 1965). The discovery of Cu mineralisation at the Mammoth deposit was made in 1923 by two Afghan cameleers, the Shaw brothers (Richardson and Moy, 1998). The Shaw brothers operated a small open cut mine from 1927 through to 1948. Production from the mine was intermittent between 1948 and 1989. Mechanised underground mining and heap leach extraction of Cu ore commenced following the acquisition of the mine by Adelaide Brighton in 1989 (Richardson and Moy, 1998). Exploration drilling 1 km west of the Mammoth mine led to the discovery of the Esperanza deposit in 1969. Aberfoyle acquired the operation in 1996 and implemented mill expansions and upgrades following a successful exploration/resource development program that proved up the Esperanza deposit. Copper ore production from the Esperanza deposit commenced late 1998. Production from the Mammoth mine was suspended in March of 1997. Western Metals Ltd acquired the mine and surrounding leases in 1998 which they renamed the operation (previously know as Gunpowder) to the Mt Gordon Mine. The Mammoth deposit is currently in a pre-feasibility stage and underground mining is planned to resume during 2002 (A. Hespe pers. comm. 2001).

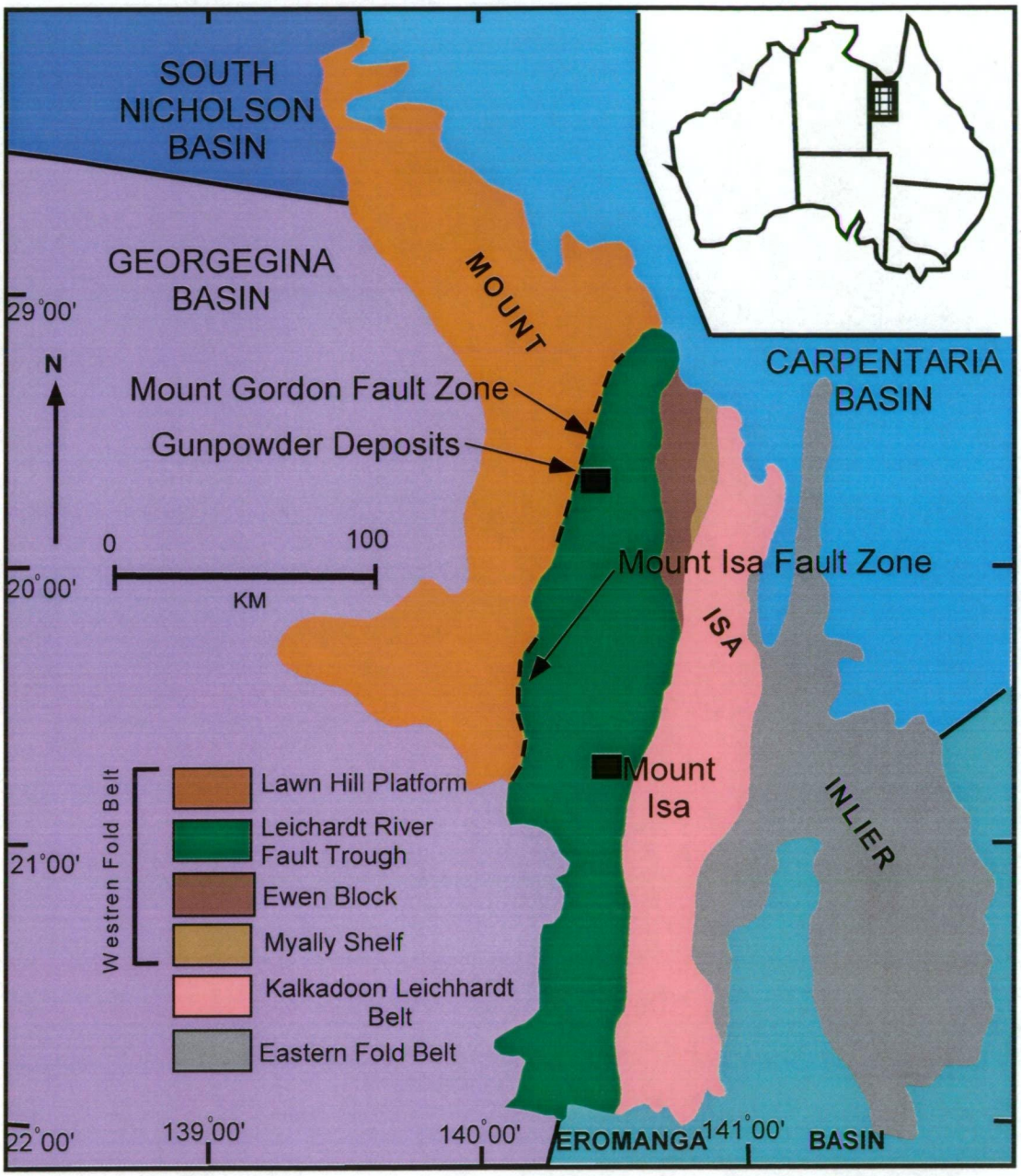

Figure 1.1: The Proterozoic Mount Isa Inlier showing location of the Gunpowder deposits and Mt Isa. Tectonic units after Blake et al. (1987).

The Mt Gordon Mine (Mammoth and Esperanza deposits) represents a significant Cu resource (total of ≅ 22.2 Mt @ 4.5 % Cu) (A. Hespe, pers. comm., 2000). The ore bodies exhibit similarities to other known Cu occurrences hosted in the Western Succession (eg Mt Isa) and yet obvious contrasts exist. Following the characterisation of the Mammoth deposit these comparisons and contrasts will be examined.

1.2 PREVIOUS WORK

C. Sydney Honman (1938) initially inspected the surface open cut of the Mammoth deposit and described the mineralisation:

> "The lode consists of a replacement of a brecciated zone in quartzite and red sandstone.....The ore occurs principally in the fractures of the breccia, and is associated with a fault or fissure of veined quartzite...."

Subsequent geological appraisals were conducted on the near surface workings of Mammoth by Government Survey Geologists (Shepherd, 1946; Brooks, 1957 and Brooks, 1962). Brooks (1962) commented on the occurrence of kaolinite, native Cu and cuprite associated with massive and disseminated supergene chalcocite. Mitchell and Moore (1975) documented geology and mineralisation of the Mammoth deposits near surface ore zone (No. 1 lens) and concluded that the distribution of the breccias hosting Cu mineralisation appeared to be controlled by the intersection of strike-slip faults with competent sandstone units. The strike-slip movement was interpreted as syn-sedimentary and therefore Mitchell and More (1975) proposed a diagenetic model for the genesis Mammoth copper deposit

Scott and Taylor (1977), Scott et al. (1985) and Scott (1986) made significant contributions to the characterisation of the geochemistry of the deposit. Limited sulfur and lead isotope measurements (Scott et al., 1985 and Vaasjoki, 1980) were conducted. Cursory paragenetic studies were undertaken by van Dijk (1991). Scott and Taylor (1982) and van Dijk (1991)

classified Mammoth as a structurally-controlled, sediment-hosted copper deposit.

1.3 AIMS OF THIS STUDY

Van Dijk (1991) classified the Mammoth Cu deposit as a structurally controlled metamorphic Cu deposit. The aim of this project is to understand the geology and genesis of metamorphogenic, structurally-controlled, sediment-hosted copper deposits via a detailed study of the Mammoth deposit. Detailed investigations include:

- determining the primary sulfide, sulfosalt and oxide mineralogy, textures and paragenesis of primary copper deposits and their relationship to the supergene deposits
- documenting the metal zoning throughout the vertical and horizontal extent of the deposits
- identifying the hydrothermal alteration assemblages and determine if a zonation is developed
- investigating the geochemical characteristics of the alteration and copper deposits using mineral geochemistry, and stable and radiogenic isotopes
- using the information generated above to propose a genetic model which will incorporate structural and lithological controls, mineralogical aspects and geochemical conditions related to the mechanism of primary copper ore deposition
- developing useful criteria for further exploration in the Western Succession of the Mount Isa Block and elsewhere in Australian and world wide sedimentary basins

1.4 METHODS

The goals of this research project have been accomplished via the following investigations:

- detailed logging and sampling of both exploration and production diamond drill holes throughout the Mammoth deposit (50 diamond drill holes; refer appendix 1 for details). Access to the underground mine was restricted during the course of this project.
- detailed petrographic and textural studies on the sulfide, alteration and host rocks mineralogy using polished thin sections and thin sections.
- development of a new technique to obtain sub-ppm quantitative data on the concentration of trace elements in sulfide minerals via laser ablation ICPMS
- electron micro-probe analysis to determine the mineral chemistry of gangue phases within the alteration assemblages
- comprehensive whole-rock geochemical analyses of ore and alteration assemblages
- measurement of the sulfur isotopic composition of sulfides within the ore lenes and alteration halo
- measurement of the Pb isotopic ratios within the ore zone.

CHAPTER 2

REGIONAL GEOLOGY

2.1 REGIONAL GEOLOGICAL SETTING

Major Cu ore bodies (Mt Isa, Mt Oxide, Mammoth, Esperanza, & Mt Kelly Table 2.1), located throughout the Western Fold Belt of the Mt Isa Inlier northwest Queensland, are structurally controlled, sediment-hosted ore bodies (van Dijk, 1991; Bell et al., 1988). The Mt Isa Inlier, covers approximately 50,000 km^2 (Fig. 1.1) and is comprised of early to middle Proterozoic rocks and is surrounded by younger sequences. To the south and south-east, the Mesozoic Eromanga Basin borders the Inlier. The Paleozoic Georgina Basin delineates the western and southern margins. The northern extents of the Inlier are bounded by the Proterozoic South Nicholson Basin in the northwest, and the Mesozoic Carpenteria Basin to the north-east (Blake, 1987).

The Mt Isa Inlier has been subdivided into three dominant N-S trending structural belts: 1) the Western Fold belt 2) the central Kalkadoon-Leichhardt Block and 3) the Eastern Fold Belt (Fig. 1.1). These belts are separated by transcurrent faulting and each has its own distinctive stratigraphy (Blake and Stewart, 1992).

The central belt, the Kalkadoon-Leichhardt Block, consists of deformed and metamorphosed crystalline basement rocks. This block separates a thick succession of intensely deformed and metamorphosed sedimentary and volcanic rocks in the Eastern Fold Belt from a much less deformed and metamorphosed succession in the Western Fold Belt (Blake, 1987).

The geodynamic evolution of the Proterozoic Mt Isa terrain has been the focus of much research and is best summarised by O'Dea et al. (1997). A period of tectonic activity lasting from 1900 to 1500 Ma resulted in the formation of a complex array of bimodal volcanics, intra-plate rift structures and associated sedimentary packages. The effects of metamorphism and

deformation events recorded during the long period of tectonic history overprint the lithologies.

The stratigraphy of the Mt Isa Inlier has been divided into a basement sequence and three younger cover sequences (Fig. 2.1). The basement consists of early Proterozoic sediments, volcanics and intrusives that were deformed and regionally metamorphosed prior to 1875 Ma (Blake, 1987). The emplacement of granitic intrusions and felsic magmatism followed this deformation of the basement and resulted in the extrusion of 1870 to 1850 Ma felsic volcanics known as the Leichhardt Volcanics, which represent Cover Sequence 1. Cover Sequence 2 ranges in age from 1790 to 1760 Ma and is comprised of bimodal volcanics and coarse grained conglomerates that grade conformably into two sandstone units separated by a basaltic unit. Cover Sequence 2 unconformably overlays Cover Sequence 1. Cover Sequence 3 consists of sedimentary and volcanic rocks, deposited between 1680 and 1670 Ma, that crop out extensively in the Western Fold Belt. Cover Sequence 3 both concordantly and discordantly overlies Cover sequence 2 (Blake, et al. 1990).

The successions in the Mt Isa Inlier have been interpreted to have formed in response to periods of intra-continental rifting that occurred between 1870-1600 Ma (Etheridge et al., 1987). Tectonism began with onset of the Barramundi Orogeny (1870-1840 Ma), which has associated felsic magmatism and plutonism. These rocks form the crystalline basement of the Mt Isa Inlier (Etheridge et al., 1987). Subsequent to the Barramundi Orogeny the Mt Isa terrain underwent a complex history of intermittent rifting and deposition between 1800 and 1600 Ma (Etheridge et al., 1994). The size of this extensional rift system is comparable to the modern day rift environments of the Baikal Rift and the East African Rift (O'Dea et al., 1996). This rift structure is known as the Leichhardt River Fault Trough (LRFT) and represents episodes of regional uplift and subsequent infilling from which the cover sequences were derived.

Within the Western Fold Belt (WFB) of the Mount Isa Inlier the Barramundi Basement is the oldest unit and consists of highly metamorphosed rocks of

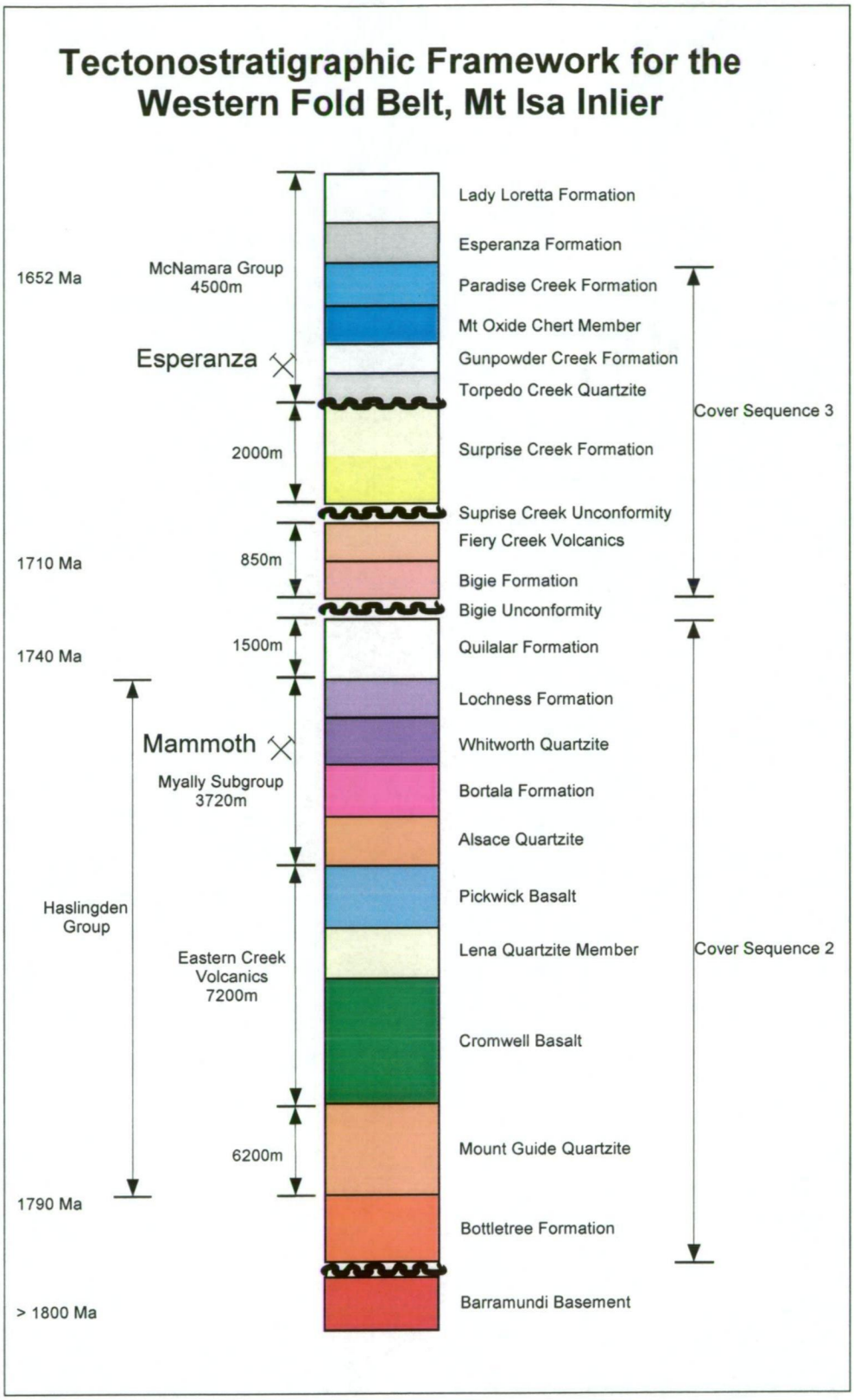

Figure 2.1. Tectonostratigraphic Framework for the Western Fold Belt, Mt Isa Inlier. After Odea et al.(1997).

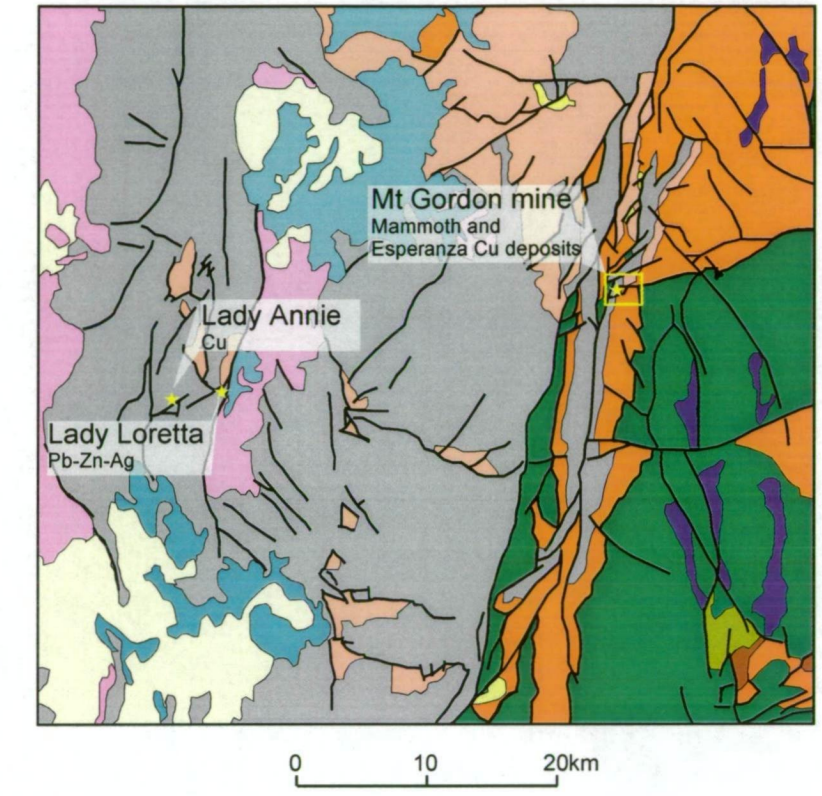

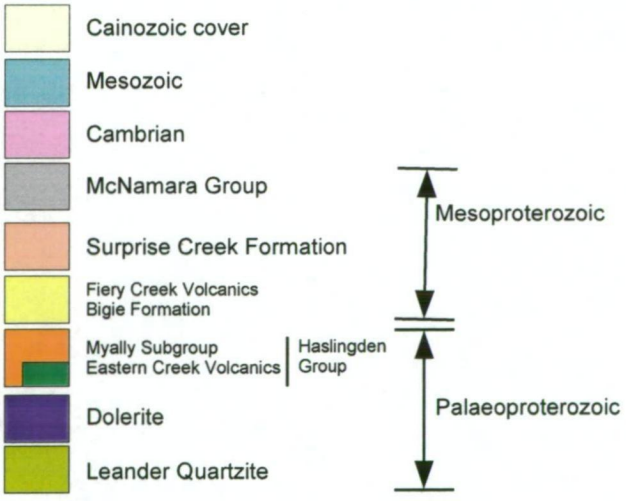

Figure 2.2. Geology of the Mammoth Mines 1:100,000 map sheet region, modified after Hutton and Wilson (1985). Refer to text and Table 2.1 for detailed description of units. Boxed area is that depicted in Figure 3.1.

igneous origin (Blake 1987). The Bottletree Formation unconformably overlies the Barramundi Basement and consists of continental sediments (Blake 1987). The Haslingden Group are the oldest rocks exposed within the Mammoth Mines area (Figs 2.1 and 2.2, Table 2.1) and consists of arenaceous rocks (Leander Quartzite, Lena Quartzite Member, Myally Subgroup, Alsace Quartzite), flood basalt (Cromwell Metabasalt Member, Pickwick Metabasalt Member), and minor argillaceous rocks (Bortala Formation) (Hutton and Wilson, 1985). Both volcanic members have compositions similar to continental tholeiites (Wilson et. al., 1985). The Haslingden Group was deposited, between 1790 ± 10 Ma and 1737 ± 15 Ma (Page, 1983), in a rift basin during initially east-west extension and subsequent north-south extension. Numerous dolerite dykes and sills of undetermined age intrude the Haslingden Group.

The deposition of the Bidgie Formation, a redbed conglomerate and sandstone sequence, marks the onset of a second stage of rifting. The Bidgie Formation is unconformably overlain by the bimodal Fiery Creek Volcanics. The fining-upward sequence of the Surprise Creek Formation were deposit during post rift sedimentation unconformably on the either the Fiery Creek Volcanics or the Myally Formation. Within the vicinity of the Mammoth deposit both the Fiery Creek Volcanics and the Bidgie Creek Formation are not preserved in the stratigraphy and hence the Surprise Creek Formation unconformably overlies the Myally Subgroup (Hutton and Wilson, 1985).

The Torpedo Creek Quartzite unconformably overlies the Surprise Creek Formation and represents the lower member of the McNamara Group. Within the vicinity of the Mammoth deposit the McNamara Group comprises the following formations from base to top: Torpedo Creek Quartzite, Gunpowder Creek Formation, Mount Oxide Chert Marker, Paradise Creek Formation, Esperanza Formation, Lady Loretta Formation. The McNamara Group is made up of coarse clastics grading upwards into fine clastics and then into carbonates (Hutton and Wilson, 1985) (Table 2.1). The deposition of the McNamara Group is constrained by ages established for the Paradise Creek Formation of 1653 Ma (Page et. al., 1994; Page and Sweet, 1998).

Table 2.1. Descriptions of stratigraphic units within the Mammoth Mines 1:100,000 map sheet region (modified after Hutton and Wilson, 1985)

Phanerozoic (Cenozoic, Mesozoic, Cambrian)	Siltstone, conglomerate, sandstone, limestone, phosphorite, colluvium, black soil, duricrust
Mesoproterozoic McNamara Group	
Riversleigh Siltstone	Fine siltstone, shale; thin coarse siltstone interbeds
Shady Bore Quartzite	Orthoquartzite; fine sandstone and siltstone interbeds
Lady Loretta Formation	Dolomite, dolomitic siltstone, limestone, carbonaceous and sulfidic shale
Esperanza Formation	Chert, dolomite, siliceous and dolomitic siltstone
Paradise Creek Formation	Dolomite, dolomitic siltstone, minor tuff
Mount Oxide Chert Member	Grey laminated chert
Gunpowder Creek Formation	Siltstone, dolomitic and carbonaceous siltstone, sandstone, feldspathic quartzite
Torpedo Creek Quartzite	Orthoquartzite, conglomerate
Surprise Creek Formation	Siltstone, feldspathic sandstone, quartzite
Fiery Creek Volcanics	Rhyolite, agglomerate, basalt and trachybasalt
Bidgie Formation	Feldspathic and lithic sandstone, pebbly sandstone
Palaeoproterozoic Haslingden Group	
Myally Subgroup	Feldspathic and lithic sandstone, dolomitic siltstone - *Includes the Whitworth Quartzite, host to the Mammoth Cu Deposit
Eastern Creek Volcanics (Pickwick metabasalt, Lena Quartzite Member, Cromwell metabasalt)	Metabasalt, feldspathic quartzite, orthoquartzite
Leander Quartzite	Orthoquartzite, feldspathic quartzite

The extensional history was terminated with the onset of the Isan Orogeny (1590 to 1500 Ma). This orogeny is characterised by a period of compressional deformation and metamorphism from 1590 to 1500 Ma (Blake et al., 1990).

2.2 REGIONAL STRUCTURAL HISTORY

The deposits at Gunpowder (Mammoth and Esperanza) are hosted within the Leichhardt River Fault Trough (Figs 2.1, 2.2 and 2.3). The fault architecture

of the Mt Isa Inlier was originally created during early (1870-1600 Ma) extensional processes (O'Dea and Lister, 1996). Subsequent reactivation of these extension faults, within the Leichhardt River Fault Trough, occurred during the Isan Orogeny (1590-1500 Ma). During the Isan Orogeny four deformation events are recognized within the terrain (D1-D4) (Bell et al, 1998).

Early north-south shortening (D1) resulted in the formation of east-west trending folds with a north-south trending mineral elongation. Subsequent east-west (D2) shortening formed both north-south trending upright folds and a penetrative north-south orientated foliation. A third deformation event (D3) resulted in further production of north-south striking folds and the development of brittle faults. During D3 the compression vector shifted slightly to east-north-east to west-south-west from east-west (D2) (Bell et al, 1998). Page and Bell (1986) using Pb isotopic measurements, placed age constraints of 1544 Ma for the D2 and 1510 Ma for the D3 deformation events.

Large-scale north south striking faults are a prominent feature within the Leichhardt River Fault Trough (LRFT) (Fig. 1.1). These fault zones (Mt Gordon Fault & Mt Isa Fault) are thought to have initially formed as growth faults during the early (1800-1650 Ma) extensional phases. Subsequent compression, during the Isan Orogeny, has reactivated these into strike slip faults. It is considered that the main copper-mineralising event in the Western Fold Belt occurred during D3 time (van Dijk, 1991; O'Dea et al., 1997; Bell et al, 1998)

2.3 REGIONAL METAMORPHISM

Early regional metamorphism (1870-1840 Ma) occurred during the Barramundi Orogeny. Subsequent mid-Proterozoic metamorphic overprinting has rendered the recognition and distribution of this early metamorphism difficult. No known major mineral deposits have been associated with this early event (Oliver et al, 1998).

Regional metamorphism began with the onset of the Isan Orogeny (1590-1500 Ma). Connors and Page (1995) concluded that the terrain had been metamorphosed, multiply deformed and metasomatised at approx. 1532 Ma. The metamorphic grade ranges from sub-green schist to amphibolite facies with anticlockwise P-T-t paths (Connors and Page, 1995; Rubenach and Barker, 1998). Metamorphic isograd mapping of this regional assemblage indicate granite emplacement and associated tectonic processes have contributed to this regional metamorphic event (Oliver, 1995; Rubenach and Barker, 1998). In the Leichhardt River Fault Trough peak temperatures ranged from 350 to 400°C during metamorphism.

This regional metamorphic event (Isan Orogeny: 1590-1500 Ma) was terrain wide and is interpreted to be responsible for the formation of the structurally controlled mineral deposits (Mt Isa Cu, Ernest Henry Cu-Au, Mary Kathleen U-REE, Stara Cu-Au & Osborne Cu-Au) found through the Mt Isa Inlier (Laing 1998, Williams and Hienemann, 1993; Valenta 1994, Oliver 1995, Heinrich et al. 1995).

2.4 METALLOGENY OF MT ISA TERRAIN

The Mt Isa Terrain has been the focus of various exploration and mining efforts for over a century. This is reflected in the numerous styles of mineral deposits that have been identified within the terrain (Fig. 2.3): 1) Pb-Zn-Ag: Mt Isa (Pb-Zn-Ag), Hilton, George Fisher, Lady Loretta, Mc Arthur River, Century, Walford Creek and Cannington; 2) Fe Oxide Cu-Au: Ernest Henry, Starra, Eloise and Osbourne; 3) U-REE: Mary Kathleen; 4) Au: Tick Hill and 5) Cu: Mt Isa, Mammoth, Esperanza, Mt Oxide, Mt Kelly and Lady Annie. A summary of deposit styles and host rocks is given in Table 2.2.

The Mt Isa Inlier has recorded throughout its long-lived orogenic history, multiple periods of metamorphic fluid flow and deformation. Significant stratiform Pb-Zn-Ag mineralisation (eg McArthur River, Lady Loretta, Century) is thought to have occurred, syn- to post-deposition of Cover sequence 3 (1680-1620 Ma), prior to regional metamorphism (Fig. 2.1 and 2.3). These deposits are largely hosted in the carbonaceous, dolomitic-siltstone-shale units of Cover sequence 3. In general, the ore and alteration

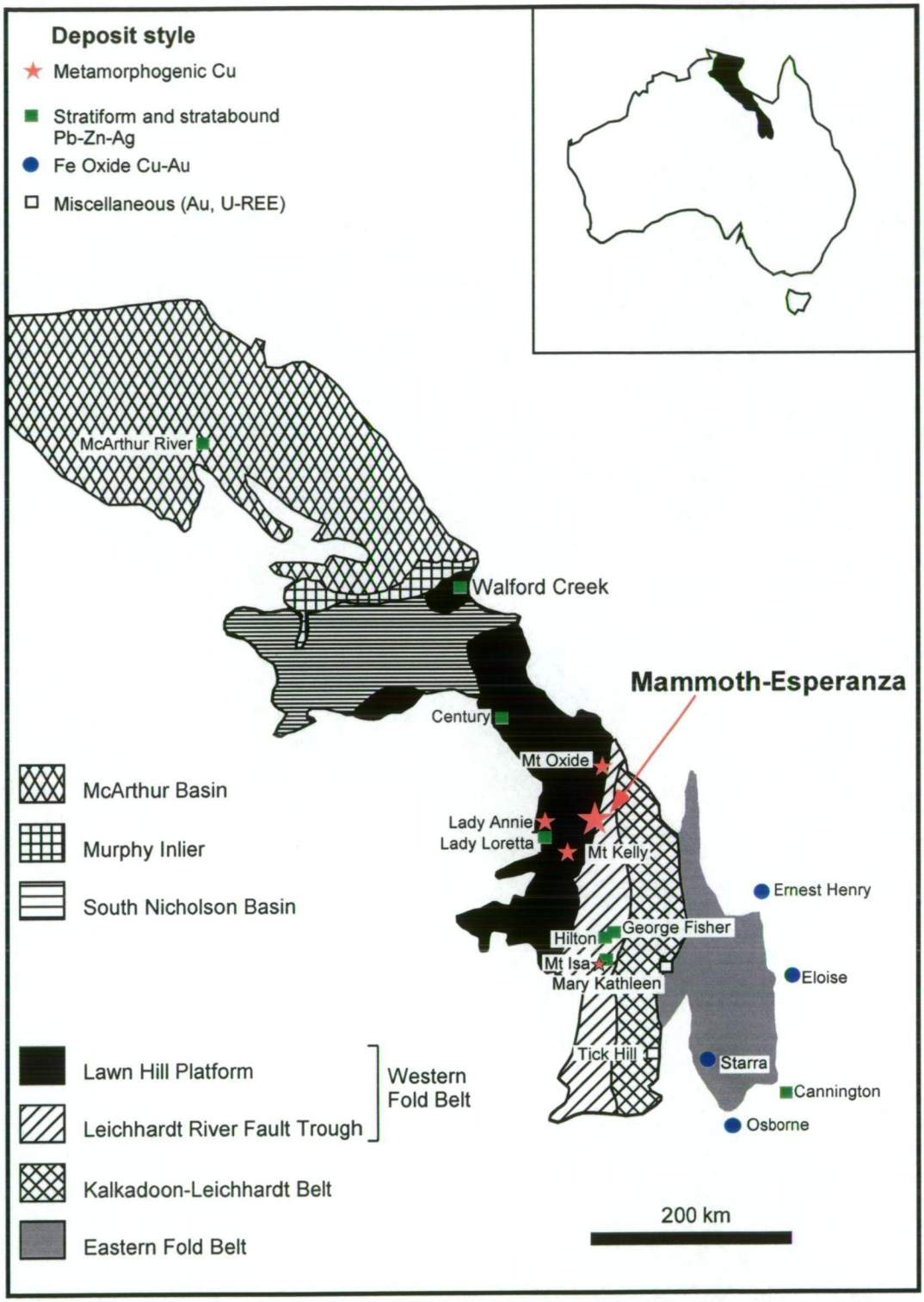

Figure 2.3. Major tectonic units of the McArthur-Mt Isa-Cloncurry region and representative styles of the major mineral deposits. Refer to Table 2.1 for details. (modified after Williams (1998); originally adapted from Plumb et al. (1990) and Blake and Stewart (1992)).

Deposit					Tectonic Unit	Age of Host Rock (Ma)	Style
Metamorphogenic Cu	**Mt**		**Cu (%)**				
Mt Isa (Cu)	255		3.3		Leichhardt River Trough	1652 ± 7	Quartz-carbonate-sulphide replacement bodies
Mammoth[1]	16.8		3.4		Leichhardt River Trough	> 1740	Sulfide chlorite breccias and replacement
Esperanza[2]	8.4		7.9		Leichhardt River Trough	~ 1652	Quartz-carbonate-sulphide replacement bodies
Mt Kelly[3]	2.6		2.3		Lawn Hill Platform	~ 1652	Quartz-carbonate-sulphide replacement bodies
Mt Oxide[3]	28		0.5		Leichhardt River Trough	~ 1652	Quartz-carbonate-sulphide replacement bodies
Lady Annie[3]	6		1.4		Lawn Hill Platform	> 1625	Quartz-carbonate-sulphide replacement bodies
Stratiform Pb-Zn-Ag	**Mt**	**Pb (%)**	**Zn (%)**	**Ag (g/t)**			
Mt Isa (Pb)	≥150	7	6	160	Leichhardt River Trough	1652 ± 7	Carbonaceous pyritic shale-hosted
Mc Arthur River	237	4.1	9.2	41	McArthur Basin	1640 ± 3	Carbonaceous pyritic shale-hosted
Lady Loretta	8.3	8.5	18.4	125	Lawn Hill Platform	> 1625	Carbonaceous pyritic shale-hosted
Hilton	49	6.5	9.3	151	Leichhardt River Trough	1654 ± 5	Carbonaceous pyritic shale-hosted
George Fisher	107	5.4	11.1	93	Leichhardt River Trough	1654 ± 5	Carbonaceous pyritic shale-hosted
Walford Creek	n/a	-	-	-	Lawn Hill Platform	1640 ± 7	Carbonaceous pyritic shale-hosted
Century	118	1.5	10.2	36	Lawn Hill Platform	1595 ± 6	Pyrobituminous sideritic shale-hosted
Cannington	47.3	10.9	4.3	490	Eastern fold Belt	< 1676 ± 5	Iron-rich Broken Hill-type
Fe Oxide Cu-Au	**Mt**	**Cu (%)**		**Au (g/t)**			
Ernest Henry	167	1.1		0.54	Eastern fold Belt	≈ 1745?	Tectonic breccia with magnetite-sulfide matrix
Starra	7.4	1.9		3.8	Eastern fold Belt	≈ 1750	Magnetite-hematite ironstone hosted
Eloise	3.1	5.5		1.4	Eastern fold Belt	< 1676 ± 5	Shear controlled biotite-hornblende replacement
Osborne	36	2		1	Eastern fold Belt	< 1676 ± 5	Quartz-magnetite-sulfide replacement
Miscellaneous	**Mt**	**U_3O_8 (%)**					
Mary Kathleen	9.5	0.13			Kalkadoon Leichhardt Belt	≈ 1750 ?	Skarn in calcareous metasediments
Tick Hill	0.5			27	Kalkadoon Leichhardt Belt	≈ 1750?	Shear controlled

Table 2.2. Summary of selected deposits and major styles of mineralisation hosted in the Mt Isa Inlier (modified after Williams, 1998; van Dijk, 1991). Unless stated resource figures from Williams (1998). [1] Estimated pre-mining resource calculated during this study. [2] In situ resource at end of 1998 (A. Moy, pers. comm., 1998). [3] From van Dijk (1991).

mineralogy is dominated by galena, sphalerite and Fe-rich carbonates. Most accepted genetic models invoke a syn-sedimentary exhalative process where hot oxidised metal-rich saline brines are: 1) expelled directly onto the sea floor under reduced conditions (eg McArthur River; Large et al., 1998); or 2) percolated into unconsolidated sediment just below the sediment water interface into reduced pyritic shales (eg Mc Arthur River, Hinman, 1996); or 3) introduced into the reduced conditions present in a hydrocarbon trap during basin inversion (eg Century, Broadbent, et al., 1998).

The Eastern Succession is dominated by Fe oxides Cu-Au deposits (Fig 2.3). These deposits occur in a variety of host rocks and structural settings. Paragenetic and structural criteria suggest that this style of deposit was emplaced synchronous with hydrothermal activity subsequent to the peak of the Isan Orogeny (Williams, 1998). Collectively these deposits all display a strongly oxidised alteration and ore mineralogy consisting of K feldspar, magnetite, hematite, pyrite, chalcopyrite, carbonates ± native Au (Davidson and Large, 1998). Two genetic models are presently accepted for this style of deposit: 1) magmatic; or 2) amagmatic. Williams (1998) suggests that the ore fluid chemistry, consisting of a hot CO_2-bearing, highly saline, complex brine, in conjunction with observed sulphide δ^{34} sulphur isotope values of $\cong 0$ ‰ indicate the source was principally magmatic. However, Williams (1998) acknowledges a direct links to magmatic sources remains to be demonstrated. Davidson and Large (1998) and Davidson et al. (1989) suggest that the Fe oxide host rocks were formed during syntectonic hydrothermal events early in the basin history. Mineralisation resulted from a hot highly oxidised saline brine convectively driven by granitoid intrusions and focussed during deformation.

The Kalkadoon-Leichhardt Belt hosts two small but spectacular deposits: Mary Kathleen (U-REE) and Tick Hill (Au). Mary Kathleen is hosted in metamorphosed carbonate units of the Corrella Formation (Solomon and Groves, 1994). The ore genesis is interpreted to be the result of the formation of a high temperature exsoskarn in contact with an oxidised U-rich, fractionated granite (Oliver, et al., 1998; Williams, 1998; Solomon and Groves, 1994). Tick Hill is a gold rich (~ 470,000 t @ 27 g/t Au) sediment-

hosted deposit. After several years of research the origin of this deposit still remains enigmatic with proposed genetic models ranging from syn-sedimentary to syn-prograde metamorphism D2 to late D3, synchronous with granite emplacement (Forrestal, et al., 1998).

Numerous Cu occurrences are located throughout the Western Fold Belt of the Mt Isa Inlier (van Dijk, 1991, Hutton and Wilson, 1985). The largest of which include: Mt Isa (Cu), Mammoth, Esperanza, Lady Annie, Mt Kelly and Mt Oxide (Table 2.2). Controversy has previously existed as to the genesis of these Cu deposits with proposed models oscillating between three end members: 1) syngenetic; 2) diagenetic and 3) epigenetic. An epigenetic model is now widely accepted and this style of deposit is presently known as a metamorphogenic Cu deposit (Heinrich et al., 2000; Warring et al., 1998; Oliver et al., 1998; Heinrich et al., 1995; Valenta, 1994; Bell et al., 1988; Perkins, 1984). The term metamorphogenic is first used by Hunt (1873) to describe the formation of ore deposits by hydrothermal fluids generated by metamorphic processes. In the case of these Cu deposits the genetic model is based around processes where initially highly oxidised saline fluids, mobilised during metamorphism, pass through and react with tholeiitic basalts (Eastern Creek Volcanics). This reaction is interpreted to buffer the oxidation state of the fluid towards a more reduced state ($\Sigma SO_4 \cong \Sigma H_2S$) and leach Cu in the process. This fluid reacts, after focusing into a favourable structural and chemical trap site, with meta-sedimentary rocks and their *in situ* metamorphic fluid as represented by the following schematic equation (Heinrich et al., 2000).

Cu^+ + SO_4^{2-} + H^+	+	$CaMg(CO_3)_2$ + $H_2S \pm FeS_2$ + CH_4	⇒	$CuFeS_2$	+	$Ca^{2+} + Mg^{2+}$	(Eq. 2.1)
NaCl-rich ore fluid from meta-basalts		meta-sedimentary rocks and their local metamorphic fluid		copper ore		cations in spent ore fluid	

This widely accepted syn-deformation model is largely based on a structural framework developed during the Isan Orogeny (1590-1500 Ma) (Swager, 1983; Bell, 1983; Perkins, 1984; Bell et al., 1988). The Cu mineralisation

event is interpreted to have occurred in a structural trap during D3, that resulted from earlier D1 thrusting and folding during D2 and D3.

van Dijk (1991) conducted regional studies focussed on assessing the validity of the metamorphogenic Cu model when applied to the other significant Cu deposits located in the Western Fold Belt. He concluded that all the hypogene Cu mineralisation is temporally associated with syn D3 alteration and veining. Another major contribution of van Dijk's (1991) work includes the recognition of two dominant alteration styles within this deposit class. Overall it was observed that a variation in the style of alteration between deposits is dependent on host rock lithologies. Copper mineralisation hosted in dolomitic rocks is associated with a silica and carbonate alteration assemblage and mineralisation hosted in arenaceous rocks is associated with a sulfide and chlorite alteration assemblage.

2.5 CONCLUSIONS

- The Proterozoic Mt Isa Inlier has experienced a complex extensional history and basin infill followed by prolong periods of metamorphic fluid flow and structural deformation and basin inversion during the Proterozoic.

- The Mt Isa terrain is host to significant mineral resources including Cu, Cu-Au-Fe oxide, Pb-Zn-Ag, Au and U-REE deposits. The Cu deposits located in the Western Fold Belt of the Mt Isa Inlier have been classified as metamorphogenic Cu deposits. There is a lack of comprehensive studies on these deposits.

CHAPTER 3

GEOLOGY AND STRUCTURE OF THE MAMMOTH MINE

3.1 INTRODUCTION

It is generally accepted that the main sediment-hosted Cu ore bodies in the Western Fold Belt (WFB) of the Mt Isa Inlier (Mt Isa, Mt Oxide, Mammoth, Esperanza, Mt Kelly & Lady Annie) (Fig. 2.2 and Table 2.2), are structurally controlled (Bell, 1983; Bell et al., 1988; van Dijk, 1991). There have been four previous unpublished reports on the structural setting of the Mammoth deposit (Askew, 1992; ERA MAPTEC 1994; Connors, 1997; Williams, 1999) All of these studies (Askew, 1992; ERA MAPTEC 1994; Connors, 1997; Williams, 1999) agree on the positions of the major ore bodies with respect to the local structures (Mammoth, Portal and Mammoth Extended Faults), and on the apparent control of these faults on the location mineralisation by virtue of the spatial association. However the previous workers do not agree in their interpretations of the age and kinematics of many of the major structures, and propose very different models for the stress/deformation regime in which mineralisation occurred. All of these studies inferred the local stress regime during Cu mineralisation from the geometry and interpreted kinematics of the local- and regional-scale faults. Inferences about fault displacement were principally based on stratigraphic offsets in plan. Limited kinematic data was obtained in some cases (Williams, 1999; Askew, 1992) but given the complicated deformation history Askew (1992) suggested it may not be possible to confidently couple real or inferred fault movements to the Cu mineralisation event. As a result the kinematics of the structures during Cu mineralisation is poorly constrained.

In this study inferences about the stress regime during Cu mineralisation are based on the orientation and kinematics of the mineralised quartz-Cu sulfide veins and sulfide matrix breccias. From a geometric analysis of syn-Cu-mineralisation extensional veins, within Mammoth, the orientation of the stress regime during Cu mineralisation can be deduced. This data was coupled with both new and existing constraints on the geometry and

kinematics of the bounding faults to provide more rigorous constraints on the mechanisms responsible for localisation of Cu mineralisation at Mammoth. The present exploration strategy in use throughout the Mt Gordon area (Honman, 1938; Warring et al., 1998; A.M. Hespe pers. comm., 1999) is reliant upon contributions from the previous structural model/models invoked for the formation of the Mt Gordon Cu deposits (Mammoth & Esperanza). Accordingly it is critical to evaluate and, where necessary, revise these models based the new constraints on the local stress regime under which Cu mineralisation occurred at the Mammoth Mine.

This chapter has two primary aims: 1) document the geometry, relative age and kinematics of the host structures in relation to movement on the bounding structures of the Mammoth deposit; and hence 2) determine the local deformation regime under which Cu mineralisation occurred. A revised structural model is proposed based on new data collected during this project.

3.2 STRATIGRAPHY

The Mammoth deposit is hosted by the Proterozoic Whitworth Quartzite of the Myally Subgroup (Table 2.1), which strikes north and dips west at 65-85° in the study area (Fig. 3.1, see map pocket). Within the mine environs the lower most exposed unit of the Whitworth Quartzite is a ~60m thick pink massive to poorly stratified quartzite which abuts the Portal Fault. Stratigraphically overlying the massive quartzite unit is an interbedded sequence of cross-bedded to thinly laminated quartz-rich and arkosic sandstone, siltstone and minor quartzite (~60m thick) (Richardson and Moy, 1998). Hutton and Wilson (1985) interpret the Whitworth Quartzite to have been deposited in a moderately high-energy palaeoenvironment such as a mature fluvial, or near-shore lacustrine or marine setting.

The Proterozoic Surprise Creek Formation unconformably overlies the Whitworth Quartzite. Within the mine environs, the Surprise Creek Formation consists of conglomerate, sandstone and siltstone. The unit strikes north and dips between 50-55° to the west. The lower dip of the Surprise Creek Formation reflects an angular discordance of 20-30° between the Whitworth Quartzite and the Surprise Creek Formation. Hutton and Wilson (1985)

interpret the Surprise Creek Formation to have been deposited after a minor phase of regional deformation and erosion during the late Palaeoproterozoic.

3.3 STRUCTURE

On a regional scale the 1:100 000 Mammoth Mines geology sheet illustrates the close spatial association between Cu mineralisation and the intersection of regional NNE trending fault zones with EW to ENE trending short en echelon faults. At Mammoth, mineralisation is hosted within broadly pipe-like breccia bodies that plunge SW parallel to the intersection of the Mammoth and Portal Faults (Fig. 3.1).

3.3.a Previous Work

Previous workers (Askew 1992; ERA MAPTEC 1994; Connors 1997; Williams, 1999) have conducted field and air photo investigations into the structure of the area. However, there is little consensus, between the various studies.

The main conclusions of the three major structural studies (Askew 1992; ERA MAPTEC 1994; Connors 1997) are summarised in Table 3.1. The ERA MAPTEC report favoured Cu mineralisation during N-S directed extension. In contrast, Askew (1992) and Connors (1997) considered that Cu mineralisation was synchronous with NE-SW compressional deformation. The main point of contention between Askew (1992) and Connors (1997) is the degree to which interpreted early extensional events (refer Chapter 2) contributed to the development of the structural framework. In general all of these studies assume Cu mineralisation was focussed into zones of dilation associated with the intersection of major N to NE trending faults and the ENE to EW trending faults. The following assessment of the proposed models centres on the different interpretations for the movement history of the major faults and both the age and origin of spatially associated folds.

Table 3.1. Summary of structural models.

Investigation	Structural Setting During Cu Mineralisation	D1	D2	D3	D4
Askew (1992)	Faulting and fault related deformation characteristic of regional strike slip deformation.	Ductile deformation, producing an E-W trending lineation.	E-W shortening, resulting in the production of upright N-S folds	Brittle deformation resulting in the development of a NNE-SSW trending fault zone. **Formation of Cu deposits.**	Development of mutually overprinting conjugate fracture sets, at a high angle to fault trends
ERA MAPTEC (1994)	N-S extension.	Extensional deformation.	E-W shortening creating N-S trending folds and pinched synclines	N-S extension creating NE trending dextral fault zones and extensional E-W fault zones. **Formation of Cu deposits.**	N/A
Connors (1997)	Formation of a structural framework during earlier (pre-1600 Ma) syn-depositional extensional deformation. Later reactivation of this framework during compressional deformation resulted in a complex fault array.	Extensional deformation (pre-1740 Ma) creating NNE transfer faults & WNW normal faults.	Extensional deformation (post-1740 Ma) creating NNW transfer faults & ENE normal faults.	E-W shortening resulting in N-S trending folds.	NE-SW transpression resulting in the development of NNE trending dextral reverse faults and ENE to E trending sinistral reverse faults. **Formation of Cu deposits.**
Williams (1990)	As above	As above	As above	As above	ENE-WSW to E-W transpression resulting in the development of NNE trending sinistral reverse faults. **Formation of Cu deposits.**

Mt Gordon Fault

The NE striking Mt Gordon Fault forms the western margin of the Mt Gordon Fault Zone (MGFZ) and defines the boundary between the Lawn Hill Platform to the west and the Mt Isa Inlier to the east (Figs 1.1 and 3.2). The Mt Gordon Fault Zone has a strike extent in excess of 150 km and is a major tectonic feature of the Mt Isa Inlier. Stratigraphic thickness changes and facies variations within the McNamara Group (post-1740 Ma sediments) occur across this structure. Askew (1992) suggests the Mt Gordon Fault (Fig. 3.2) was initially a syn-sedimentary fault and interprets stratigraphic thickness variations within the McNamara Group as evidence in support of this hypothesis. Subsequent re-activation of the Mt Gordon Fault as a dextral strike-slip fault occurred during D3 (Askew, 1992) (Table 3.1). ERA MAPTEC (1994) interpret the Mt Gordon Fault as a dextral strike-slip fault formed during N-S orientated extension (D3) (Table 3.1).

Connors (1997) interprets the Mt Gordon Fault as an east dipping dextral reverse fault that was either re-activated or initiated during D4. Prior to D4, it may have been an extensional fault related to the pre-1740 Ma extensional event, but thickness changes in the pre-1740 Ma stratigraphy (Eastern Creek Volcanics and Myally Subgroup sediments) across the fault have not been verified (Connors, 1997). However, thickness variations in the post-1740 Ma sediments (McNamara Group) across the fault are consistent with re-activation during post-1740 Ma extension (Connors, 1997).

Esperanza Fault

The Esperanza Fault is a westerly dipping N- to NE-trending fault that delineates the eastern margin of the Mt Gordon Fault Zone within the Mammoth Mine area (Figs 3.1 and 3.2). In the vicinity of the Mammoth Mine the fault is developed in the Esperanza Formation. The fault gouge consists of carbonaceous cataclasite derived from shale and siltstone units within the Esperanza Formation. Connors (1997) identified changes in stratigraphic thicknesses of pre-1740 Ma stratigraphy across the fault. Williams (1999), identified footwall folds and ENE to EW orientated striations on the fault surface. The fault hosts anomalous concentrations of Cu and was therefore

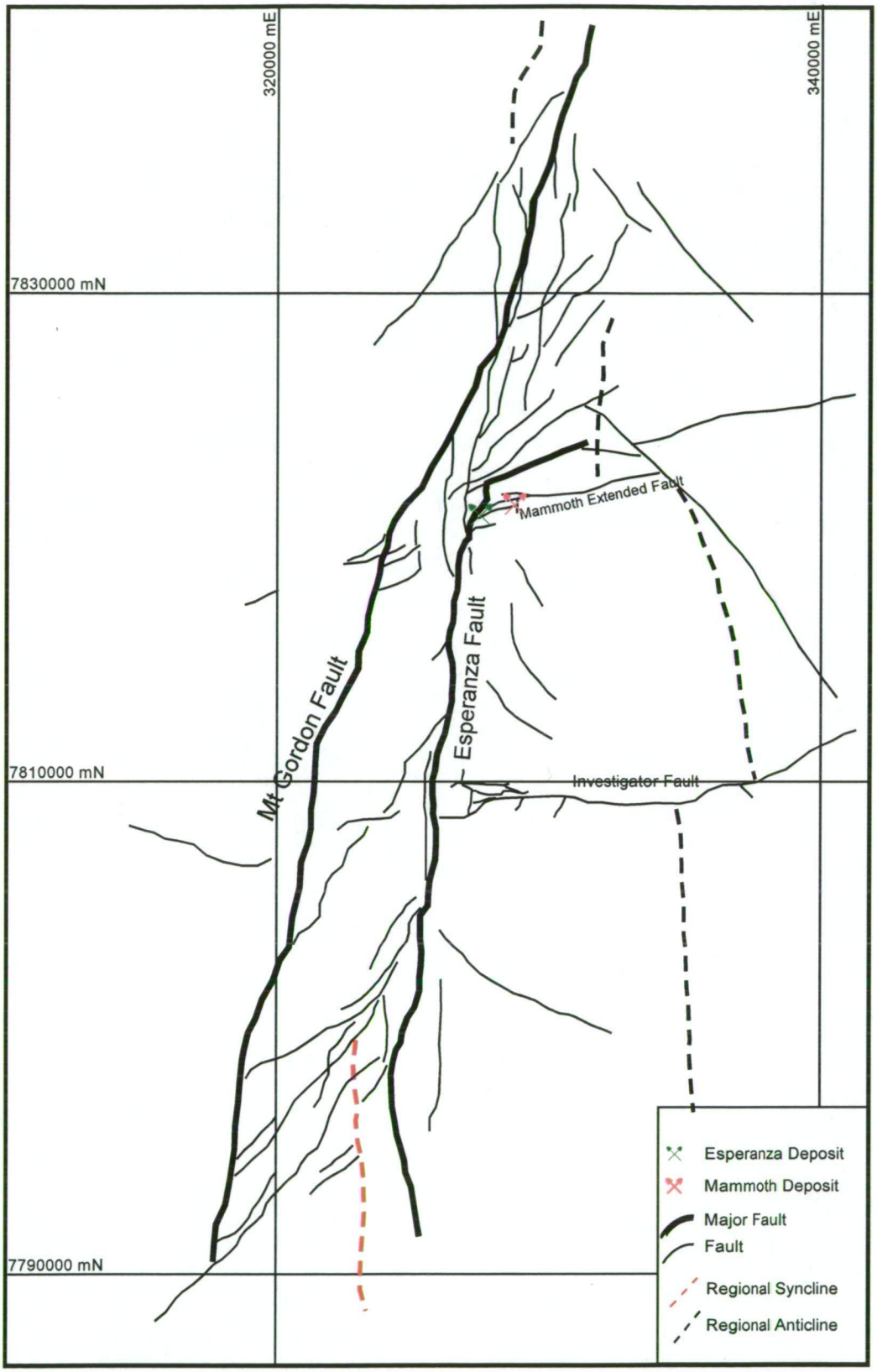

Figure 3.2. Regional fault summary of the Mammoth Mines 1:100,000 map sheet area. (after ERA MAPTEC, 1994). Grid coordinates in AMG.

was likely to have been active during Cu mineralisation (C. Colley pers. comm., 1999; Williams, 1999).

Askew (1992) notes N-S trending folds, formed during D2, appear to be preferentially developed in a NNE-SSW zone, along which later faulting is also preferentially developed. This observation is supported by the following: 1) the geometry and distribution of the D2 folds suggests they represent an en echelon array prior to faulting; and 2) the hinge zones are commonly faulted out leaving a change in younging direction as the only evidence of an earlier fold. Askew (1992) interpreted to the Esperanza Fault (Figs 3.1 and 3.2) to be a dextral reverse fault that originated during D3 time. Variations in bedding orientation localised along D2 fold hinge zones are interpreted to have controlled the propagation of late (D3) faults thereby constraining the origin of the fault to D3 (Askew, 1992).

The ERA MAPTEC (1994) report states that the Esperanza Fault was originally a reverse fault formed during D2, EW orientated compression (Table 3.1). They (ERA MAPTEC, 1994) suggest that during D2 broad NS trending anticlines and pinched synclines were developed. Subsequent EW compression caused reverse faults (Esperanza Fault) to propagate through the pinched synclines resulting in the cores of the synclines being faulted out Experimental studies indicate folding of a competent unit overlain by a less competent unit can result in the formation of broad anticlines and pinched synclines (Ramsay et al., 1985). In the Mammoth Mine area this process may have been favoured (during D2) by the likely competency contrast between the Eastern Creek Volcanics and the Leander Quartzite or the Myally Sub-Group. The Esperanza Fault is interpreted by ERA MAPTEC (1994) to have been re-activated as a dextral strike-slip fault during D3 NS extension.

Connors (1997) considers the Esperanza Fault to have originated as a transfer fault associated with pre-1740 Ma extension (D1) that was re-activated as a dextral reverse fault during D4. Evidence cited in support of this interpretation is: 1) changes in stratigraphic thicknesses of pre-1740 Ma stratigraphy across the fault and 2) the strike of the fault is sub-parallel to the

interpreted pre-1740 Ma extensional direction (Connors, 1997). Subsequent reactivation after the post-1740 extensional deformation is supported by the truncation of normal faults, related to the post-1740 extensional event, against it.

Williams (1999) interpreted the Esperanza Fault as a thrust, due to the development of footwall folds and oblique to down-dip lineations trending between 270° and 240° on the fault surface. Williams (1999) suggests the lineations indicate the last movement on the fault (during Cu mineralisation) was in response to E–W to NNE-SSW compression, with the compression direction rotating anticlockwise later in the deformation.

ENE to EW trending faults

There are three major EW to ENE faults within the vicinity of the Mammoth deposit, namely the Mammoth, Mammoth Extended Faults, and NE extents of the Esperanza Fault (Fig. 3.2). The Mammoth and Mammoth Extended Faults all have steep southerly dips (Richardson and Moy, 1998) and at surface fault-fill varies in composition from carbonaceous fault gouge, brecciated host rock, massive quartz veins with coatings of Fe-oxide and lesser secondary Cu-oxide minerals (A.M. Hespe & C. Colley pers. com., 1999). At depth, in the Mammoth Extended Fault, chalcopyrite is hosted in massive quartz veins. Within the Mammoth deposit significant primary and secondary mineralisation is hosted in breccias associated with the Mammoth Fault (Mammoth Fault Mineralisation; Chapter 4).

Despite abrupt changes in the thickness of units across the faults, uniform bed thicknesses and the absence of scree horizons adjacent to the faults have been interpreted to be inconsistent with syn-sedimentary faulting (Connors, 1997). The absence of scree horizons or significant facies changes within the Surprise Creek Formation adjacent to the faults does not rule out syn-sedimentary faulting, but indicates these faults were unlikely to have been scarp-forming features during sedimentation. However, it is reasonable to expect thickness changes in the vicinity of a syn-sedimentary fault even if it does not breach the surface, in response to differential subsidence. Thickness variations should also be reflected in deflection of

layering across the fault zone. The uniform thickness and consistent strike of bedding either side of the ENE-EW trending faults does not support a syn-sedimentary origin.

Askew (1992) considers the ENE-EW faults to be splays off the major NNE-SSW trending Mt Gordon Fault Zone (Fig. 3.2), as they appear to link and terminate against these major faults rather than be offset by them. The Mammoth Fault is interpreted to postdate early deformation (D1 and D2) because it truncates D2 faults and folds (Askew, 1992). Therefore, the apparent thinning of stratigraphy across the faults was interpreted to reflect the juxtaposition of different parts of an originally wedge-shaped unit within the Surprise Creek Formation due to (N–S directed) dip-slip (reverse) movement on the faults (Fig 3.1).

The ERA MAPTEC report (1994) notes opposite senses of apparent displacement occur at surface between beds on opposite limbs of an upright N-S trending anticline truncated by the EW and ENE faults (Fig. 3.2). Such a geometry is difficult to explain purely by strike-slip displacement, and is interpreted to reflect a component of reverse movement on the EW and ENE trending faults during D3. The opposing sense of apparent offset of the Surprise Creek Formation is interpreted to reflect the different geometry of bedding on either side of the fold.

Connors (1997) interprets the E and ENE trending faults as normal faults developed in response to post-1740 Ma extension (D2). These faults were inferred to have been reactivated, with oblique-dextral movement, during E-W shortening (D3) and sinistral-reverse movement during NE-SW transpressional deformation (D4). Folding during D3 EW compression did not affect the faults because they acted as transfers enabling material on either side to shorten at different rates (Connors 1997).

Dilational zones within proposed models and timing of Cu emplacement

The structural models proposed by Askew (1992) (Fig. 3.3.a), ERA MAPTEC (1994) (Fig. 3.3.b) and Connors (1997) (Fig. 3.3.c) all suggest emplacement of Cu mineralisation occurred at dilation sites formed during late deformation,

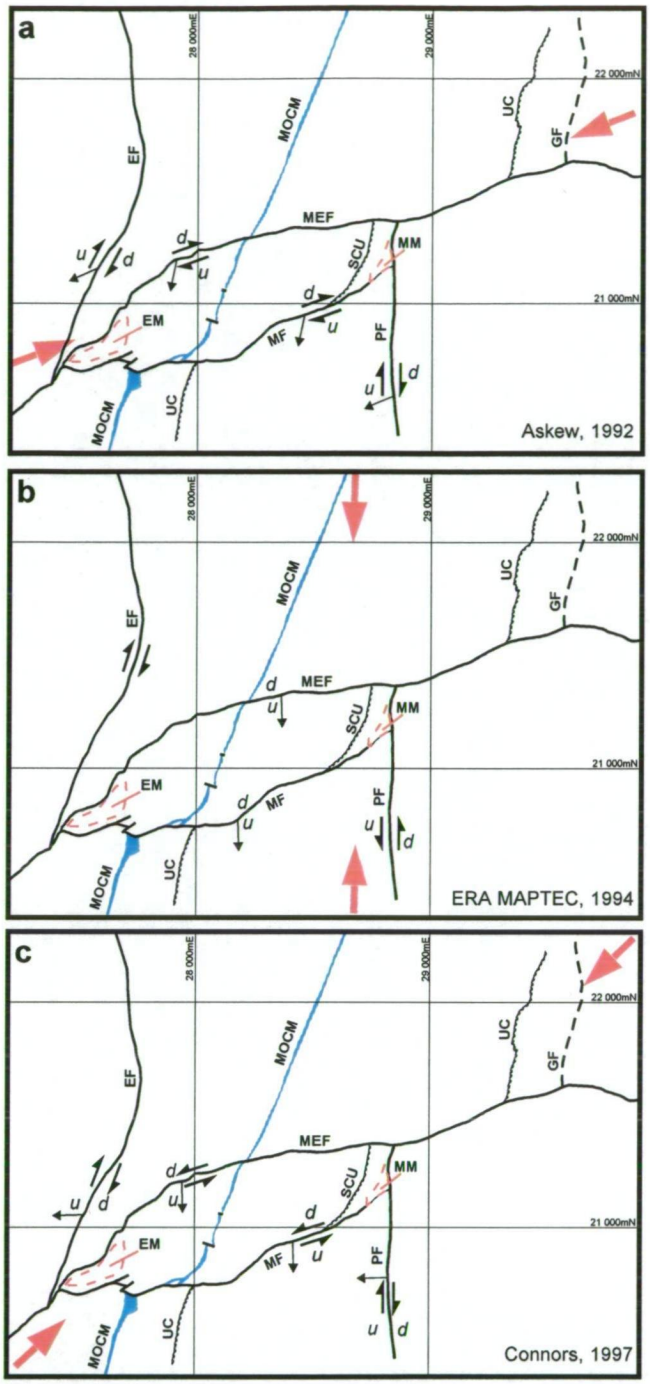

Figure 3.3. Structural models during the Cu mineralisation event. A. Askew (1992), The overall kinematics of the mine area during D3 are transpressional with maximum principle compressive stress orientated ENE-WSW. B. ERA MAPTEC (1994), Cu mineralisation occurred during a steeply inclined NS compression event resulting in NS extension. C. Connors (1997), Cu mineralisation occurred during NE-SW tranpression. Abreviations: MF = Mammoth Fault, MEF = Mammoth Extended Fault, SCU = Surprise Creek Unconformity, PF = Portal Fault, MOCM = Mt Oxide Chert Member, EF = Esperanza Fault, GF = Green Stone Fault, MM = Surface expression of Mammoth mineralisation, EM = Esperanza Ore Zone.

however, no evidence to support this conclusion is presented. The main points of contention between the various structural models are the relative age and sense of movement on the faults bounding the mineral deposits and the mechanism by which the dilational zones formed.

Askew (1992) interpreted dextral reverse movement on the Mammoth and Mammoth Extended Faults during Cu emplacement resulting from overall ENE-WSW compression during D3. Askew's (1992) structural model invokes zones of extension between left-stepping NS trending dextral faults (ie. Mt Gordon and Esperanza Faults) within a broad zone of dextral shear. This zone formed an extensional bridge (Fig. 3.1) linking the two faults. Faults discordant to bedding were developed within the extensional bridge (Mammoth Extended, Mammoth Faults and NE extents of the Esperanza Fault). Extension within zones of overlap is interpreted to have been further accommodated by local brecciation, such as that along the Portal Fault, between the Mammoth and Mammoth Extended Faults.

ERA MAPTEC (1994) propose Cu mineralisation occurred along the Mammoth and Mammoth Extended Faults during late N-S extension (D3) prior to late movements on the Portal Fault. In order to account for the reverse movement on the Mammoth and Mammoth Extended Faults, during N-S extension, $\sigma 3$ is inferred to plunge ~30° towards the north and $\sigma 1$ plunges steeply to the south (~60°). The location of dilational breccia bodies is interpreted to be primarily controlled by changes in the dip of the Mammoth Extended Fault and Mammoth Faults rather than changes in strike.

Connors (1997) interprets Cu emplacement at Mammoth during D4 sinistral-reverse movement on the Mammoth and Mammoth Extended Faults in response to NE-SW transpression D4.

In order to further evaluate the various models, evidence for the relative age and movement history of all major faults in the area needs to be examined. Both Connors (1997) and ERA MAPTEC (1994) interpret major faults within the map area as reactivated transfer faults and normal faults related to early (syn-depositional) extension in an intra-continental setting. This

interpretation is primarily based upon stratigraphic thickness changes in post-1740 sediments across the faults. In contrast Askew (1992) cites the absence of facies or bedding thickness changes across the EW to NE trending faults as evidence precluding a growth fault origin.

3.4 FIELD AND DRILL CORE INVESTIGATIONS

A key aim of the field investigation is to constrain the stress regime in and around the Cu ore bodies at the time of mineralisation and re-evaluate the movement history of the bounding faults. A subsequent goal is to propose a mechanism for Cu emplacement, by linking the kinematics during Cu emplacement to a phase of movement on the bounding faults. This is possible through the recognition of consistent structural features via geometric analysis of syn-Cu-mineralisation extensional veins implied to have formed in response to the same stress field.

To explain the apparent stratigraphic thickness variations (from the Mt Oxide Chert Member through to the Surprise Creek Formation) N and S of the Mammoth and Mammoth Extended Faults (Fig. 3.1) previous workers inferred that the faults originated either as: 1) normal faults generated during D3 extension (in conjunction with Cu mineralisation) (ERA MAPTEC, 1994); 2) growth faults developed in response to pre-1740 D1 extension (prior to Cu mineralisation) (Connors, 1997); or 3) dextral-normal faults formed during NE-SW transpression (D3) (Askew, 1992). The dips of the Surprise Creek Formation and Mount Oxide Chert Member were investigated both N and S of the Mammoth Extended Fault in order to clarify the possible origins of the Mammoth Extended Fault and the Mammoth Fault. A change in dip between the Mount Oxide Chert Member and the Surprise Creek Formation will result in an apparent surface offset of the stratigraphy N and S of the faults subsequent to any dip-slip movement along the either or both of the faults (Mammoth and Mammoth Extended). In addition the surface outcrops of the Mammoth, Mammoth Extended and Esperanza Faults were inspected for sense of movement structures (Fig. 3.4 & 3.5.a).

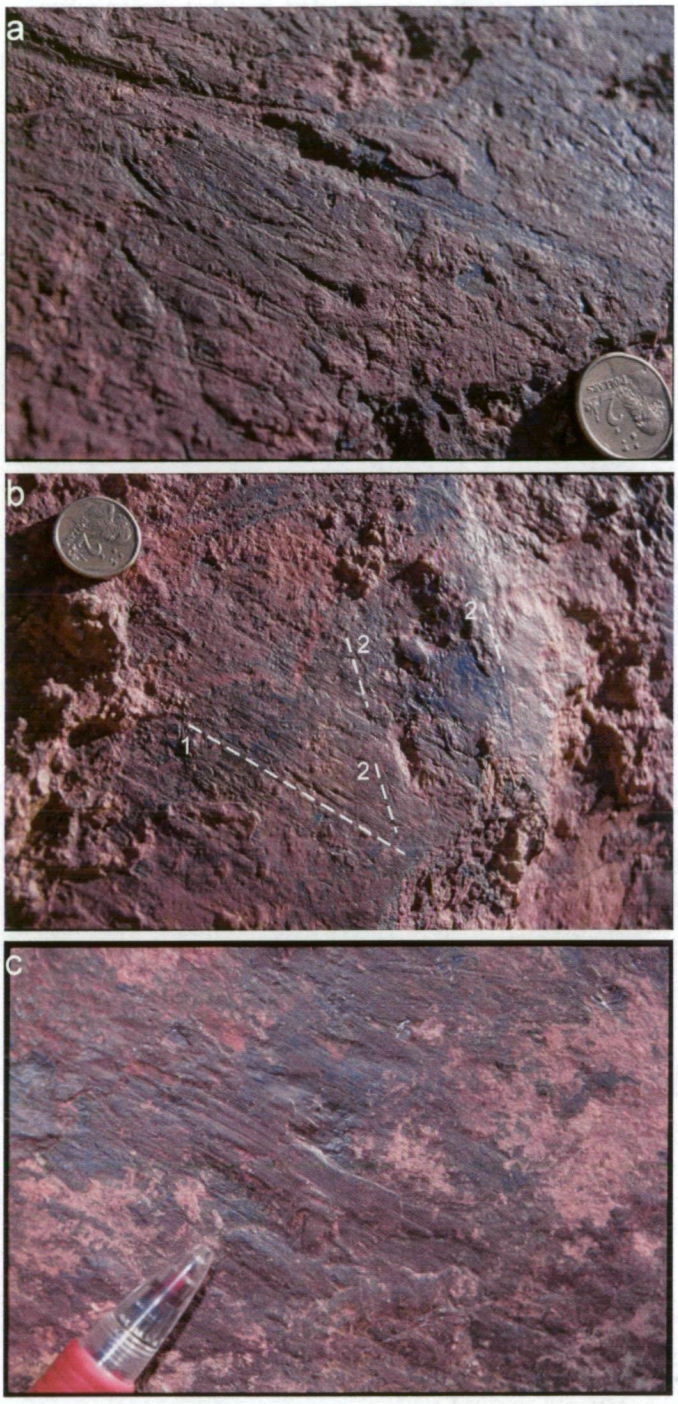

Figure 3.4. Examples of striations measured on the Mammoth Extended Fault. Fault surface trending NE-SW dipping SE (looking towards NW): a) Groove gouged into fault shallows from left to right plane suggesting dextral movement; b) two generations of striations: 1) steep plunge to the east and 2) gentle plunge to the east. The striation (1) plunging steeply to the east appears to be overprinted by the striation (2) plunging to the east at a shallower angle; and c) fibre growth, sense of movement unclear.

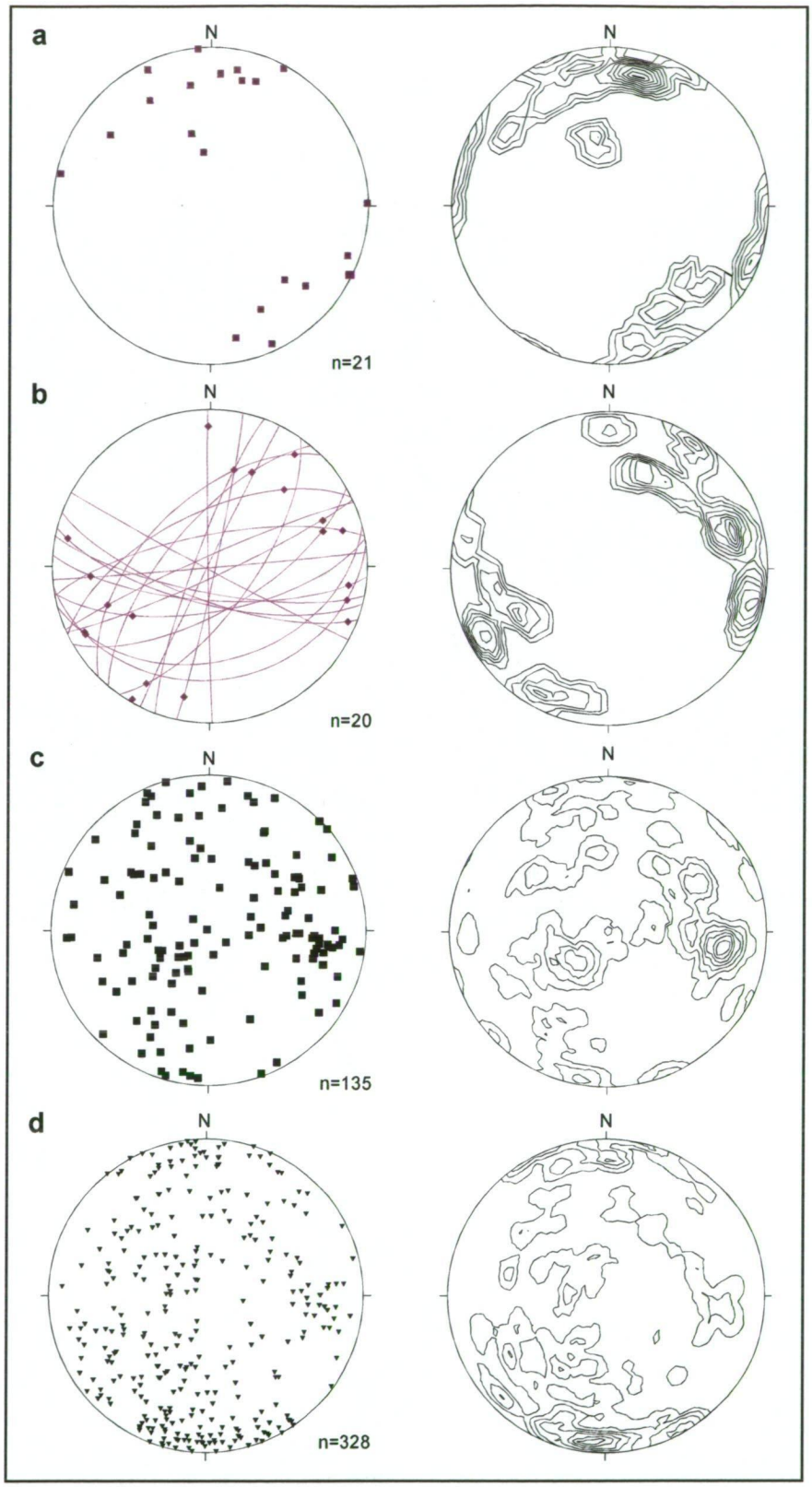

Figure 3.5. Structural measurements representing major faults located within the Mt Gordon Mine and extensional vein arrays from the Mammoth deposit: a) Poles to Faults within the Mt Gordon Mine area (MF & MEF) (this study); b) Striations measured on Fault surfaces (this study); Note low angle strike slip orientation; c) Poles to pyrite and/or Cu sulfide (+/- quartz, chlorite, hematite and illite) filled extensional veins representing B, C upper D and Mammoth Fault ore zones from the 4720 (+/- 25m) mRL (this study). d) Poles to pyrite and/or Cu sulphide (+/- quartz, chlorite, hematite and illite) filled extensional veins representing the E Lens ore zone modified after Richardson (2000).

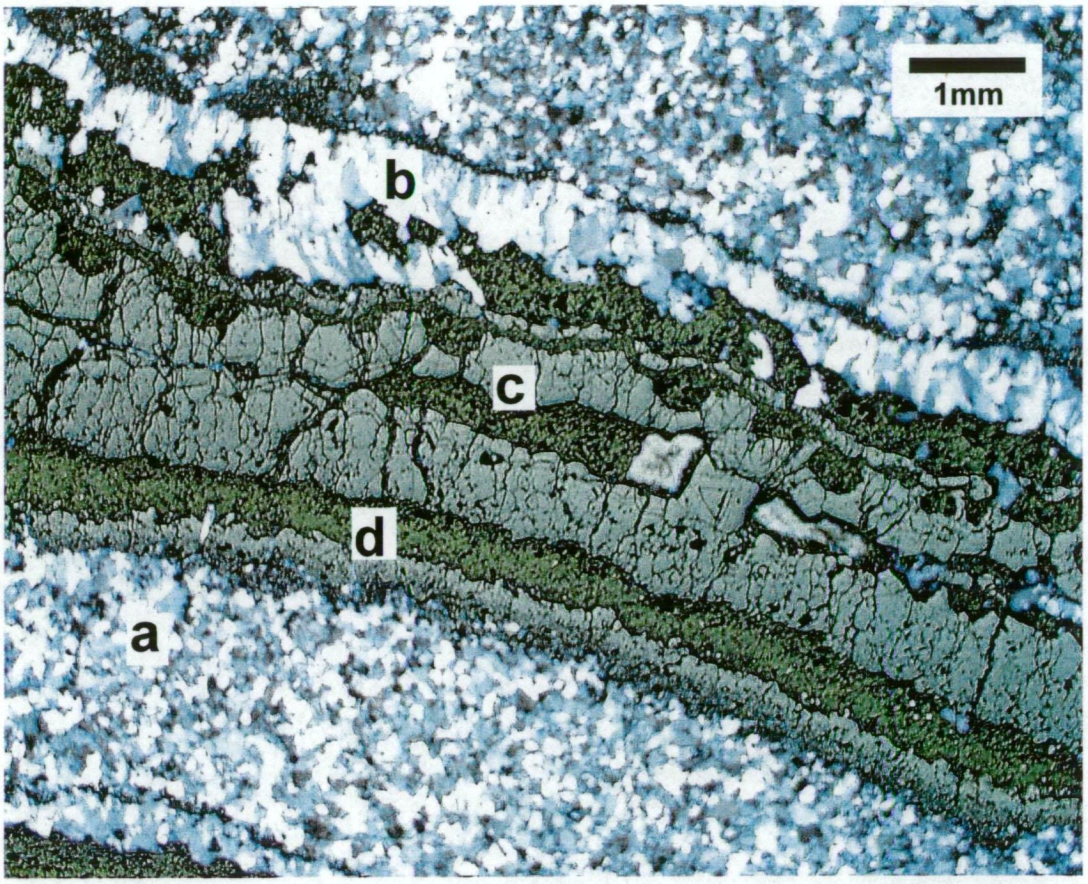

Figure. 3.6. Extensional vein: a) fine grained quartzite host rock; b) euhedral syntaxial quartz growth from the vein margin; c) coarse grained euhedral pyrite; d) chalcopyrite and e) matching irregularities of opposing vein margins. Sample # 768UD184.1. Plane polarised transmitted light combined with reflected light 1X1.25.

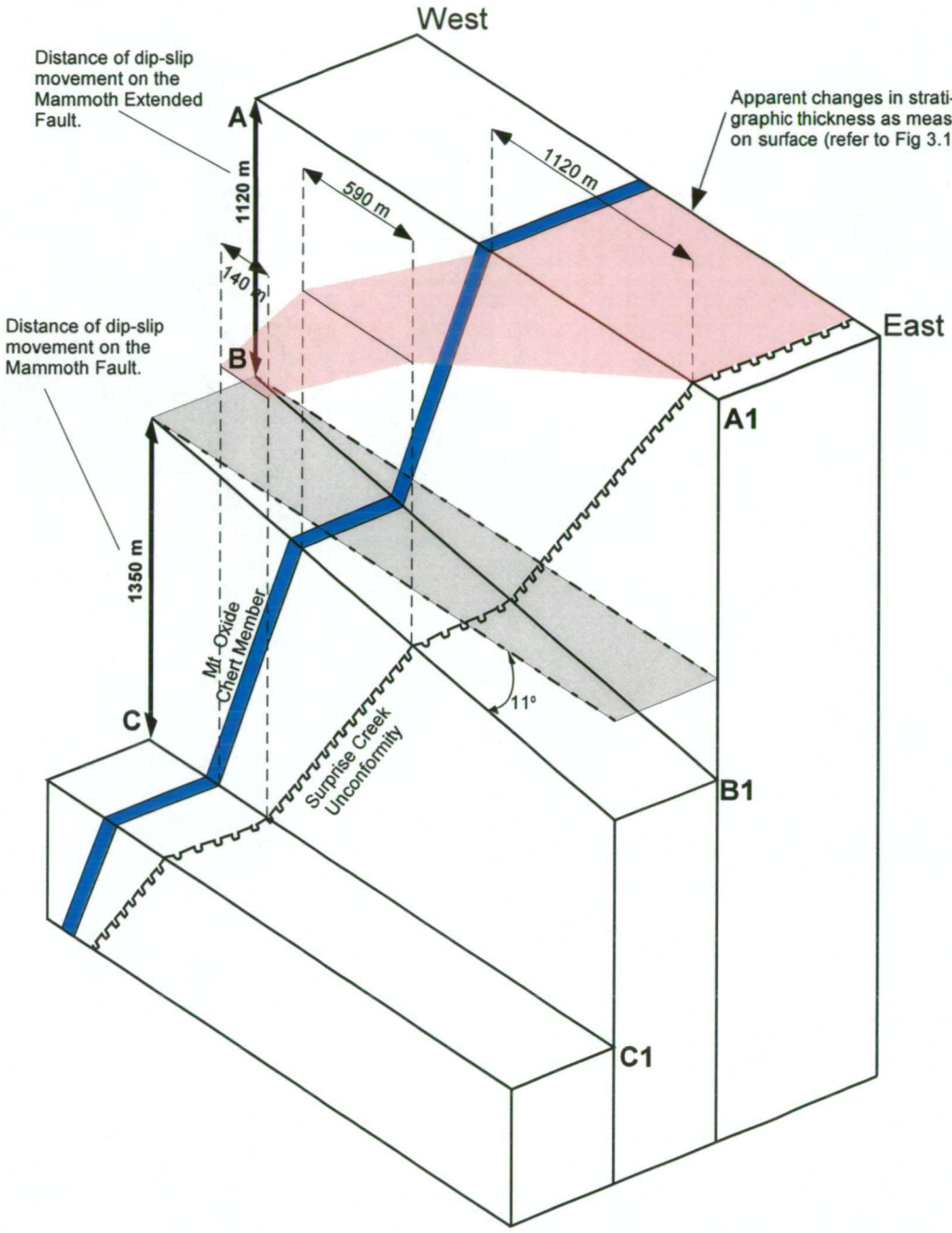

Figure 3.7. Schematic reconstruction comparing stratigraphic thickness variations from the Surprise Creek Formation through to the Mt Oxide Chert Member prior to dip-slip movement on the Mammoth and Mammoth Faults. Note: 1) section line A-A1 is north of the Mammoth Extended Fault; 2) section line B-B1 is south of the Mammoth Extended Fault; and 3) section line C-C1 is south of Mammoth Fault. Dips of the Surprise Creek Unconformity and Mount Oxide Chert Member have been averaged from measured dips resulting in an average dip of 57° and 72° respectively. Cross section 'B-B1' has been rotated 11° anti-clockwise in order to re-align stratigraphy. Laterally continuous dips have been assumed for both Mount Oxide Chert Member and Surprise Creek Unconformity. Sections have been stacked to remove the stratigraphic offset mapped on surface. Reconstruction permits the distance of inferred vertical dip-slip displacement to be calculated as indicated on the left margin. Refer to Figure 3.1 for section lines A-A1, B-B1 and C-C1.

3.4.a Results

Field Data

North of the Mammoth Extended Fault and south of the Mammoth Fault the dips of the Mount Oxide Chert Member and the Surprise Creek Formation are similar (Fig. 3.1). North of the Mammoth Extended Fault the Mount Oxide Chert Member dips at 71° towards 291° and the Surprise Creek Formation, 56° towards 282°; south of the Mammoth Fault, Mount Oxide Chert Member = 66° towards 278 and Surprise Creek Formation = 61° towards 282° (Fig. 3.1). To the south of the Mammoth Extended Fault and north of the Mammoth Fault the Mount Oxide Chert Member and Surprise Creek Formation dip, 80° towards 283° and 72° towards 278° respectively, to the west (Fig. 3.7). Allowing for some minor rotation of the fault-bounded blocks the data supports a dip-slip sense of movement on the Mammoth Extended Fault with a throw of approximately 1120m south block up (Fig 3.7).

In contrast, the numerous striations identified on the Mammoth, Mammoth Extended and Esperanza Fault surfaces (Fig. 3.4 & 3.5.b) all pitch at low angles supporting strike-slip movement on the E-W to NE-SW oriented faults. The sense of movement, however, could not be confidently determined.

Drill Core Survey

The orientation of the stress field during Cu mineralisation was deduced from a study of (Cu-) mineralised vein orientations within the Mammoth deposit. Data was collected from surveyed but non-oriented drill core. However, the consistent bedding orientation provides a suitable reference fabric with which to predict the most likely position of the core (Scott and Berry, in review). The core is re-oriented by comparing the dip and strike of a known constant planar fabric (bedding, in this case) to the same fabric intersected in the core. The core is rotated about its axis until the angle between bedding and its reference orientation is at minimum. The orientation of bedding within Whitworth Quartzite appears relatively constant throughout the Mammoth deposit (Richardson, 2000). Selected drill holes both a) intersected B, C and upper D ore lenses and Mammoth Fault Mineralisation and b) penetrate the 4720 (± 25m) mRL level (Table 3.2, Fig. 4.14). Direct constraints of bedding

orientation were obtained from underground mapping by company geologists on multiple levels through out the Mammoth deposit (Richardson, 2000).

The E Lens ore zone is represented by data collected by company geologists (Richardson, 2000) from drill holes SD255D and SD255E. Orientated core was obtained through the use of a down hole spear.

Table 3.2. Drill holes used for structural study of extensional vein arrays

Drill Hole	^Northing	^Easting	^mRL	Azim	Dip	EoH	Ore Zone
UD700	20744	28424	4719	245.5	5	166.6	B, D & MFM
UD708	20742	28506	4764	270.0	-18.8	177.6	B & MFM
UD651	20742	28506	4764	270.0	-25	192.5	B & MFM
UD710	20802	28516	4756	262.5	-10	191.2	B
UD571	20802	28571	4756	280.0	-15	206.5	B
UD642	20880	28532	4745	256.0	-15	247.4	B
UD732	21039	28519	4719	270.4	-3	130.0	C
UD734	21039	28519	4718	270.9	-37.9	186.2	C

Abbreviations: EoH = end of hole in metres; MF = Mammoth Fault Mineralisation; Azim = azimuth of drill hole. ^Mammoth mine grid coordinates.

Core-based determinations of the attitudes of sulfide (± quartz and/or chlorite) filled extensional veins (Fig. 3.6) from the Mammoth ore zones are divided into three main groups: 1) bedding parallel veins dipping (72°/270°); 2) gently E-dipping veins and subvertical E-W striking veins; and 3) more irregularly oriented veins, largely scattered along a broad girdle that spreads between the E-W maxima. The broad girdle of data defined by the poles to the veins indicates the veins range in orientation from an E-W strike through to an irregular vein array (Fig. 3.5.c-d). Both data sets show considerable scatter in the orientation of the extensional veins from the Mammoth ore zones but similar patterns can be recognised in both. The major difference is the predominance of sub-vertical east-west orientated veins within E Lens.

3.5 DISCUSSION

Interpretation of extensional vein sets

Extensional veins form when fluid pressures (P_f) exceed the minimum confining pressure (σ_3) and tensile strength (T) of the host rock; $P_f \geq \sigma_3 + T$. Extensional fractures propagate perpendicular to the minimum principal stress (σ_3) and parallel to the maximum principal stress (σ_1) (Cox, 1995).

This may occur either by increasing the P_f in the rock or by decreasing σ_3 until the sum of P_f - σ_3 > T. Therefore, by documenting the geometries of extensional veins present it is possible to determine the orientation of the minimum principal stress (σ_3), and by extrapolation the orientation of the specific planes containing the maximum (σ_1) and intermediate (σ_2) principal stresses, at the time of extensional vein formation. Extensional veins can also form along pre-existing planes of weakness (foliation or bedding), rather than perpendicular to far-field σ_3 indicate that vein orientations can also be influenced by anisotropies in the tensile strength of the host rock.

The Mammoth extensional vein array (Figs 3.5.C and D) can be divided into three main groups: 1) veins sub-parallel to bedding (72°/270°); 2) a conjugate set comprised of gently E-dipping veins and steeply dipping E-W veins and 3) more irregularly oriented veins, largely scattered along two broad girdles that spread between the E-W maxima. The set of steeply dipping E-W veins, implies σ_3 was horizontal N-S, consistent with either N-S extension or E-W transpression locally focussed on the bend in the Mammoth Fault (Fig. 3.8). Veins sub-parallel to bedding (72°/270°), are interpreted to represent extensional veins opening along pre-existing planes of weakness in the host rock at times of high $P_f \pm$ negligible differential stress (σ_1-σ_3). The remaining much more variably oriented veins have poles are mostly scattered between two broad girdles that link the E-W maxima (Fig. 3.5). This suggests that either: 1) the principal stresses were at least transiently sub-equal such that there was no preferred orientation of extensional veins; or 2) fracturing was highly dynamic and occurred in response to a highly perturbed stress field (ie the σ_3 direction changed irregularly with time). Both these possible stress states can be envisaged as occurring close to rupture terminations, fault jogs or fault intersections, where abrupt strain gradients on the major structures are in part accommodated by deformation of the adjacent wall rocks (e.g. Cox, 1995). Both the extensional origin of the veins, and the wide variation in their orientation, suggests the mineralised rock underwent net dilation. This dilation may have been in response to either: 1) dextral-reverse movement, interpreted to have occurred, along the Mammoth Fault as suggested by Askew (1995); or 2) reverse movement on the Mammoth and Mammoth

Extended Faults as suggested by ERA MAPTEC (1994). During either of these scenarios σ_3 would have had to be locally oriented NS horizontal as suggested by the extensional vein array.

The gross geometry of the Mammoth ore lenses reflects the two dominant orientations observed in the measured extension vein arrays. E and 2 ore lenses have an overall E-W geometry and B and C ore lenses are sub-parallel to bedding (refer Chapter 4).

The data and interpretations presented above do not collaborate the structural model of Connors (1997) in which it is suggested that Cu emplacement occurred at Mammoth during D4 sinistral-reverse movement on the Mammoth and Mammoth Extended Faults in response to NE-SW transpression.

The interpreted geometry of the proposed structural models of ERA MAPTEC (1994) and Connors (1997) require the development of hard-linkage strike-slip transfer structures (eg Mammoth and Mammoth Extended Faults) and border fault segments (eg Mt Gordon and Esperanza Faults) in excess of 150km to have formed during an intra-continental rifting. The geometry and styles of fault linkage structures found both in experimental and well exposed intra-continental rift settings do not support the development of transfer faults and/or the development of border faults in excess of 70km (Machette et al., 1991; McClay, 2000). Therefore, structural models (ERA MAPTEC, 1994; Connors, 1997) that invoke the reactivation of early extensional strike slip transfer faults and long border faults (> 70km) are not supported by either modern analogies or laboratory studies conducted on fault formation under extension. In summary, the geometries that exist between the major faults located in the Mammoth Mines Area are most consistent with a brittle strike-slip model as proposed by Askew (1992) (Table 3.1).

The apparent stratigraphic offset and abrupt thickness variations N and S of the Mammoth Extended Fault and S of the Mammoth Fault between the Mount Oxide Chert Member and the Surprise Creek Formation can best be explained by early reverse dip-slip and later dextral-reverse movement (Figs

3.3 and 3.7). Both the lack of a thickening of beds adjacent to the faults and the absence of scree horizons (synsedimentary breccias) near the fault (Askew, 1992) may support the interpretation of post D1 movement on these faults. However, the absence of linear synsedimentary breccias (scree horizons) near faults does not preclude the possibility of synsedimentary fault movement. Synsedimentary faults may not breach the surface, but may result in sagging of the sedimentary pile resulting the subsiding block. Thickness changes across synsedimentary faults in these circumstances may be relatively gentle and maximum subsidence and thickest accumulations of sedimentary fill may not necessarily develop immediately adjacent to the faults. The thickness changes observed N and S of the Mammoth Extended Fault and S of the Mammoth Fault between the Mount Oxide Chert Member and the Surprise Creek Formation are interpreted here as being too abrupt to be related to synsedimentary movement on these faults. The late strike-slip movement that is indicated by the low angle striations (Figs 3.4 and 3.5.b) is consistent with movement during an E-W transpression event, however no direct link has been established between the timing of these striations and Cu mineralisation. This interpretation of E-W oriented transpression and resultant dextral strike-slip movement along E-W trending faults is consistent with the late-stage subhorizontal striations locally preserved on the fault surfaces. Therefore, the Mammoth deposit is interpreted to have formed during E-W oriented transpression that locally produced NS orientated dilatation at minor restraining bends and deviations in dip and strike of the Mammoth Fault and at the intersection of the Portal and Mammoth Faults (Figs 3.1,3.8 and 4.4) where the E-W strike-slip movement was transferred to reverse movement(?) on the Portal Fault. The suggested transfer of EW shortening from the Mammoth to the Portal Faults, is interpreted to have led to the formation of the brecciated ore zones within the accommodation/damage zone at the intersection of these faults. Fracturing in the accommodation/damage zone at the intersection of the faults would have acted to focus fluid into this zone (by virtue of the higher permeability).

The new data constraining σ_3 to be horizontal N-S, are consistent with formation of the Mammoth deposit occurring during either an E-W

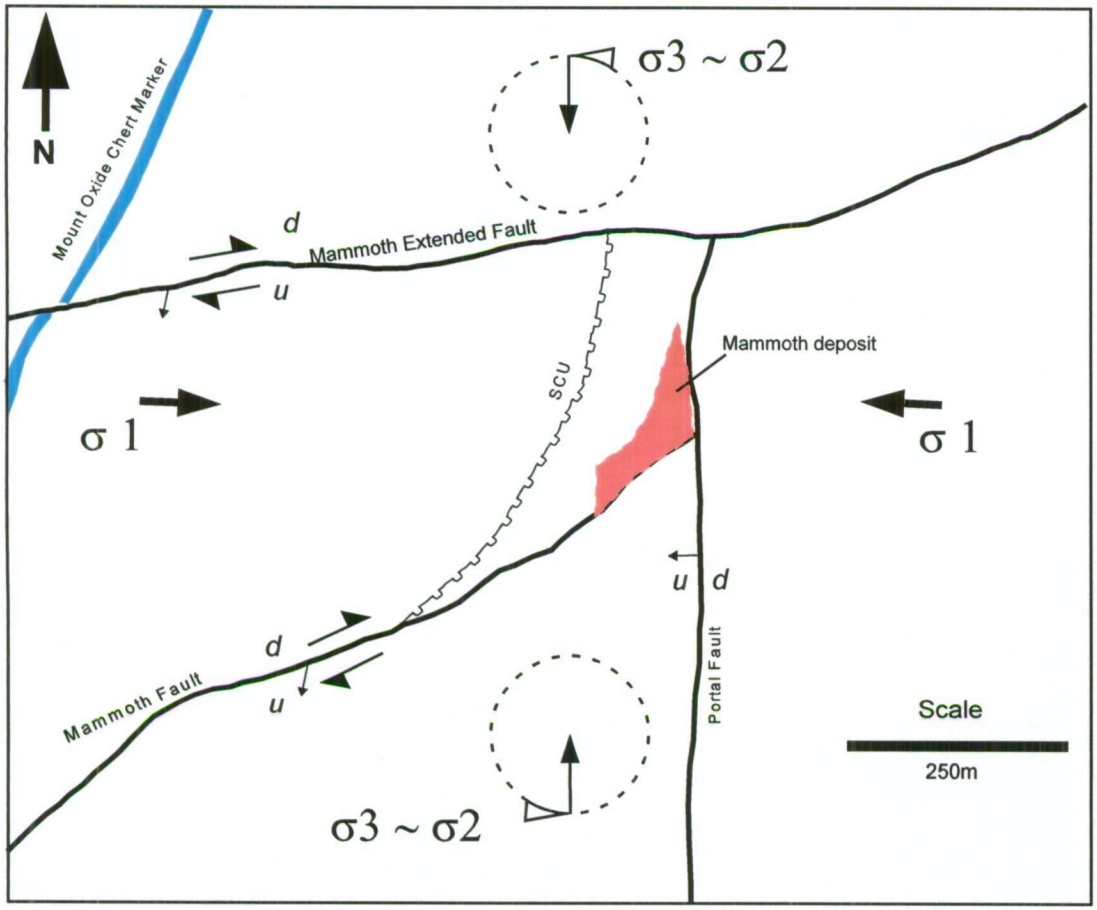

Figure 3.8. Interpreted movement directions on structures within the Mammoth deposit area during D3. Cu mineralisation occurred in response to EW transpression (σ1). A zone of compression is developed at the intersection of the Portal and Mammoth Faults. The Mammoth ore lenes formed under conditions of high fluid pressure (P_f), during a transient period, subsequent to dextral-reverse slip failure on the Mammoth Fault and/or reverse slip failure on the Portal Fault. Under these conditions the local stress field was highly perturbed and the least principle stress (σ3) and intermediate principle stress (σ2) became subequal (σ3 ~ σ2). The orientation of the least and intermediate principle stresses (σ3 and σ2) is variable as indicated by the irregular distribution of the syn-deformational quartz-Cu sulfide veins around an east-west maxima (Fig. 3.5). SCU = Surprise Creek Unconformity.

transpression (localised at the intersection of the Mammoth and Portal Faults); or N-S extension. ERA MAPTEC (1994) proposed mineralisation during N-S extension and hence their model predicts $\sigma 3$ plunging ~30° towards the north. The ERA MAPTEC (1994) model doesn't account for the dominant extensional vein orientations (the set of steeply dipping E-W veins; Fig 3.5), and therefore it is likely that $\sigma 3$ was not steeply inclined as they suggest.

Mineralisation is interpreted to have occurred during periods of high fluid pressure (P_f), following slip events, when the principal stresses may have been sub-equal ($\sigma_3 \cong \sigma_2 \leq \sigma_1$). Dilation and subsequent Cu mineralisation was achieved when fluid pressure (Pf) exceeded the tensile strength of the intact host rock or across bedding interfaces.

3.6 CONCLUSIONS

The Mammoth and Mammoth Extended Faults during brittle strike-slip deformation associated with the formation of the major NNE-SSW trending Mt Gordon Fault Zone during ENE-WSW oriented compression. The Mammoth deposit formed during E-W transpression (localised at the intersection of the Mammoth and Portal Faults) during periods of high fluid pressure (P_f), subsequent to slip episodes, when the principal stresses were sub-equal ($\sigma_1 \geq \sigma_3 \cong \sigma_2$). Dilation and subsequent Cu mineralisation was achieved when fluid pressure (P_f) exceeded the tensile strength (T) of the host rock or resulted in dilational opening at bedding interfaces.

Stratigraphic thickness changes evident across the Mammoth and the Mammoth Extended Faults, in the stratigraphy from the Surprise Creek Formation to the Mt Oxide Chert Member, can be explained by an earlier phase of reverse dip-slip movement prior to dextral strike-slip movement. No evidence was identified to support a model in which Mammoth and the Mammoth Extended Faults developed initially as growth faults in response to crustal extension.

Previous structural models proposed for formation of the Mammoth deposit suggested that late sinistral reverse movement on the Mammoth Fault

created a dilational jog, localised at the intersection of the Mammoth and Portal Faults, in which Cu mineralisation occurred. This work demonstrates that the Mammoth Cu deposit is hosted in an overall zone of transpression where high fluid pressures induced dilation in discrete zones localised at the intersection of the Mammoth and Portal Faults. The resultant fracturing in the accommodation/damage zone at the intersection of these faults would have increased permeability and therefore focussed fluid flow into this zone.

The exploration strategy currently in use through out the Mt Gordon Fault Zone has traditionally focussed on sites were structural geometries gave rise to dilational fault jogs created during deformation. The results of this investigation have significant implications for the exploration targeting of structurally controlled Cu mineralisation within the Western Fold Belt of the Mt Isa Inlier. Structural geometries where zones of N-S extension occurred during in response to ENE-WSW oriented compression have the potential to host significant Cu resources.

CHAPTER 4

DESCRIPTION OF MINERALISATION

4.1 INTRODUCTION

The Mammoth deposit consists of multiple lenses of Cu ore (> 2.0 % Cu) (Fig. 4.1). In order to investigate the mineralised system an understanding of the spatial distribution of the ore zones needs to be established. It is the primary aim of this chapter is to characterise the geometry of the ore zones and macro textures of Cu mineralisation within the Mammoth ore system. This will be achieved by:

- documenting the distribution and geometry of Mammoth Cu ore bodies.
- describing macro ore textures and classifying the mineralisation based on these textural categories.

Throughout the long history of intermittent production and various research efforts at the Mammoth deposit there is little consensus on the nomenclature used to define individual ore zones. To date company geologists have used Cu grade considerations to define the limits and geometry of the ore lenses. Therefore, a secondary aim of this chapter is to define the nomenclature applied to these ore lenses.

4.2 DISTRIBUTION AND GEOMETRY OF ORE ZONES

Mineralisation is hosted within vein and breccia units that plunge SW; a trend parallel to the intersection of the two major faults (Mammoth and Portal Faults) (Fig. 4.1). Six ore lenses form the Mammoth deposit (No.1 B, C, D, E, 2 Lens and Mammoth Fault Mineralisation (MFM)). The naming convention used during this research project is outlined as follows:

4.2.a No. 1 Lens

The No.1 ore zone cropped out at surface and is now mined out (Fig. 4.2). At surface the ore zone consisted of four main shoots which coalesced to

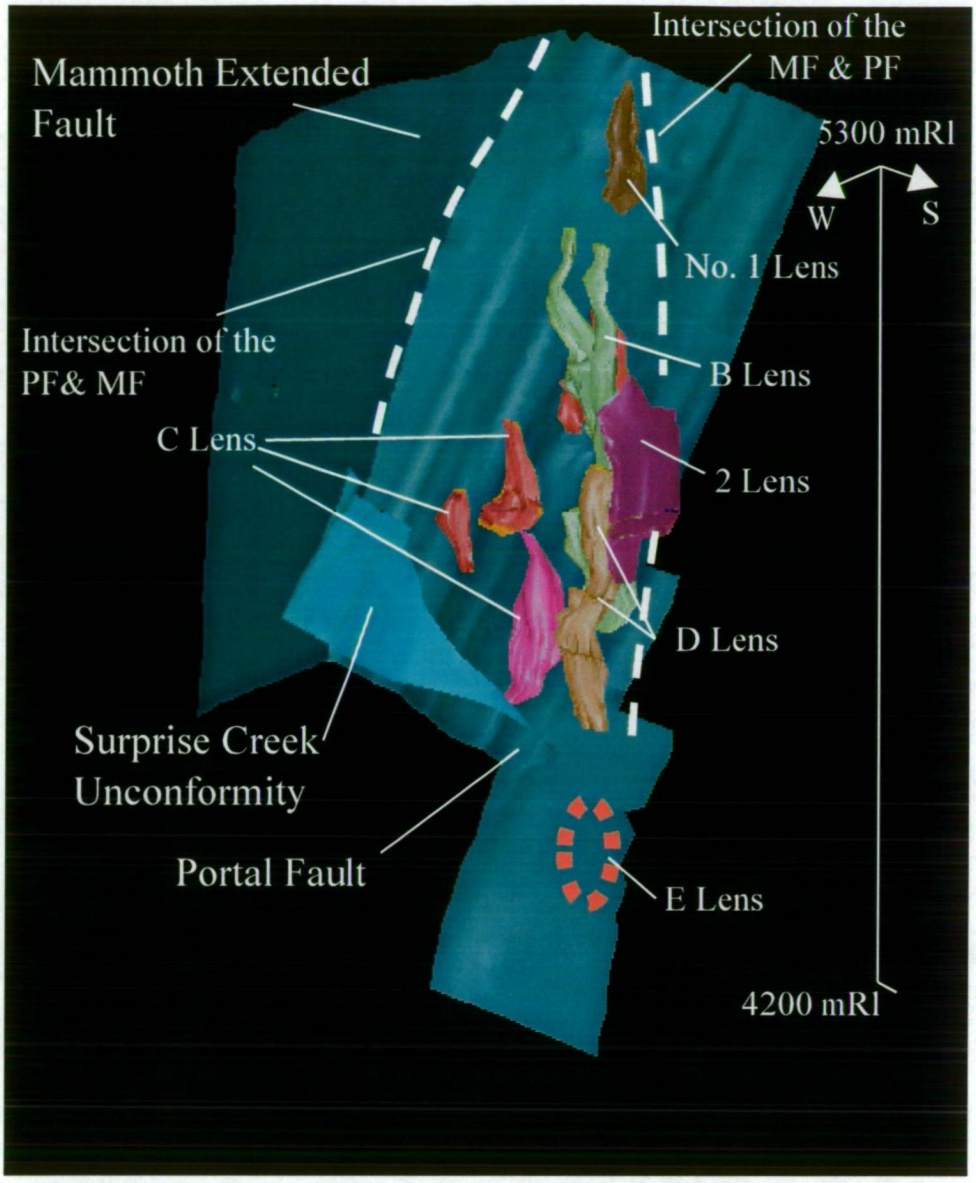

Figure 4.1. Three-dimensional view of the Mammoth deposit (from an elevated north westerly position), major faults (Mammoth (MF), Portal (PF) and the Mammoth Extended Fault (MEF) and the Surprise Creek Unconformity, with the Mammoth Fault cut away (Note: intersection line of the MF and PF). Solid models of the 2.0 % Cu contour (extracted from resource data base in July 1998) are depicted for No. 1, B, C, D, and 2 Lenes, whilst the approximate position of recently identified E lens ore zone is highlighted by the dashed red ellipse. The distribution of the Mammoth ore lenes is broadly controlled by the intersection of the Mammoth and Portal Fault zones.

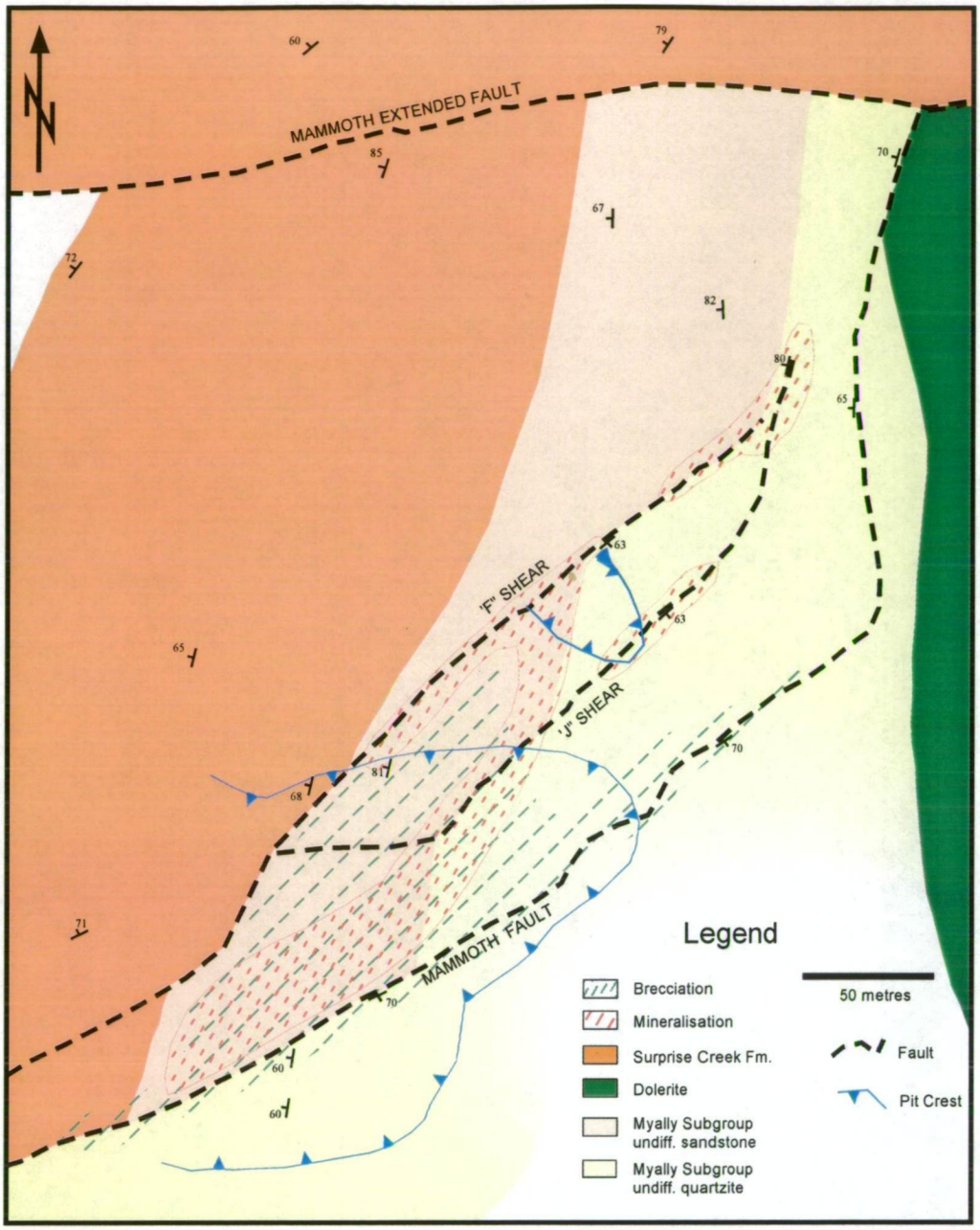

Figure 4.2. Surface geology of the Mammoth deposit (modified after Mitchell and Moore, 1975). Surface geometry of No. 1 Lens filled with dashed red. Surface exposure of brecciated host rock filled with dashed green.

from one ore zone at depth (Richardson and Moy, 1998). In general, the ore zone has a subvertical dip to the south and a NE-SW strike. The ore zone has been interpreted as extending down to 5050mRL and has a strike extent of 350 metres, a down dip extension of 220 metres and ranges from 10 to 75 metres in width.

4.2.b B Lens

The geometry of B ore lens is well constrained through development drilling and previous production exposures. The ore zone occurs down plunge from No. 1 Lens and significant mineralisation begins at 5100mRL (approximately 200 metres below surface) (Figs 4.1 and 4.3). The lode strikes NS and dips 65° to the west. The mineralised zone has a strike extent that ranges from 35 m to ~ 300 metres and varies in width from 30-100 with both length and width increasing with depth. The B Lens ore body has been interpreted as terminating against the Portal Fault.

4.2.c C Lens

C Lens is interpreted to be the faulted extension of B Lens (Figs 4.1 and 4.3). C Lens strikes NS and dips west at 65°. The bulk of the ore is contained beneath 4950mRL, above 4700mRL, and between 20,880mN and 21,100mE. Known dimensions of the lens are approximately 140 metres long and 50 metres wide.

4.2.d D Lens

D lens mineralisation is located between 28200-28450mE and 20600-20750mN and the bulk of the mineralisation is contained beneath 4850mRL and above 4500 mRL (Figs. 4.1 and 4.4). The mineralised zone is confined to the south by the Mammoth Fault and to the east by the Portal Fault. Previous workers (G. McArthur pers. comm., 1998) have suggested that the gross geometry of D lens is a cylindrical body that had its long axis plunge defined by the intersection of the Portal and Mammoth Faults.

4.2.e E Lens

E lens is located between 20450 to 20550mN and 28000 to 28200mE between 4000mRL and 4500mRL(Figs. 4.1 and 4.5). The geometry of E lens

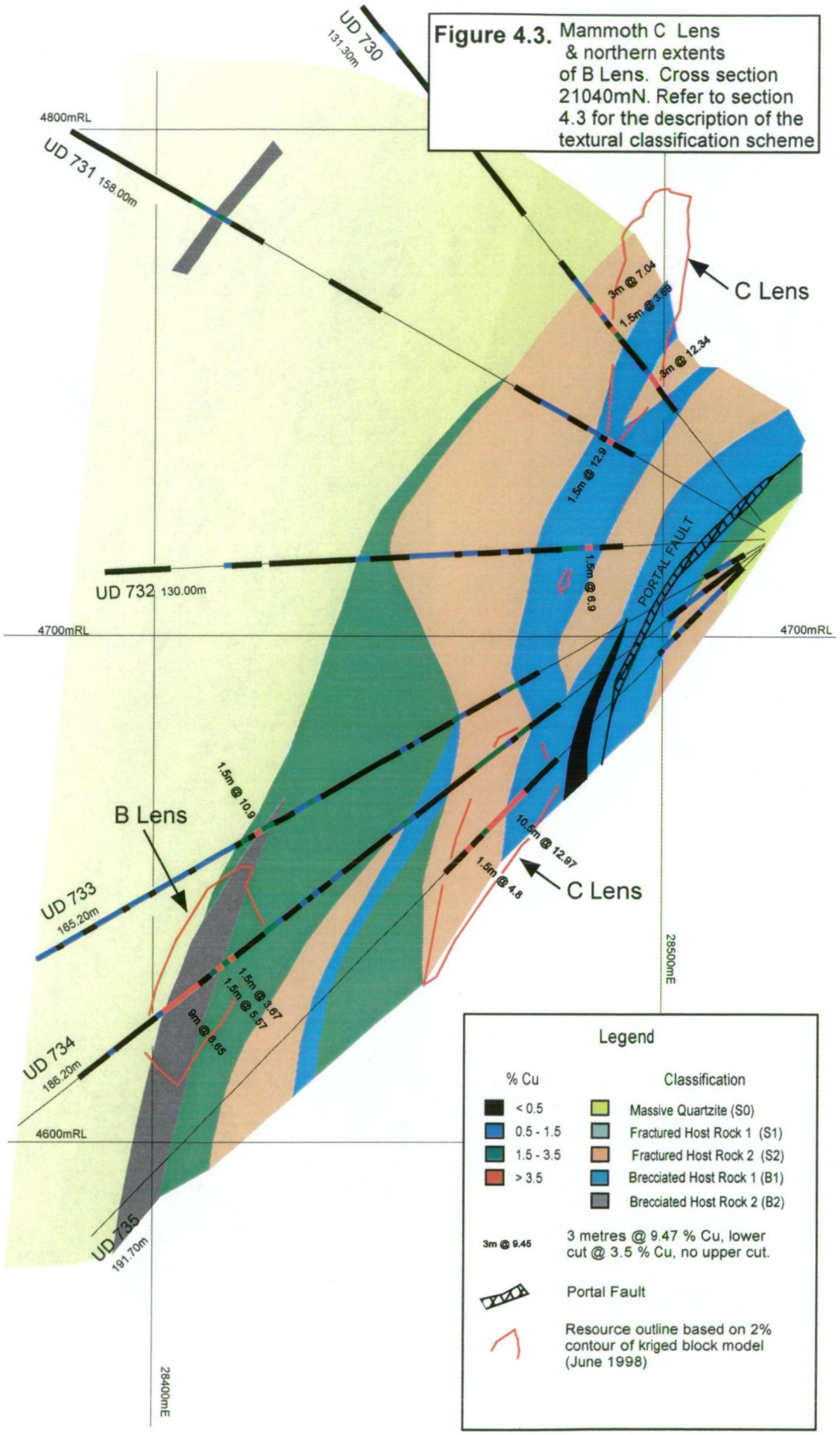

Figure 4.3. Mammoth C Lens & northern extents of B Lens. Cross section 21040mN. Refer to section 4.3 for the description of the textural classification scheme

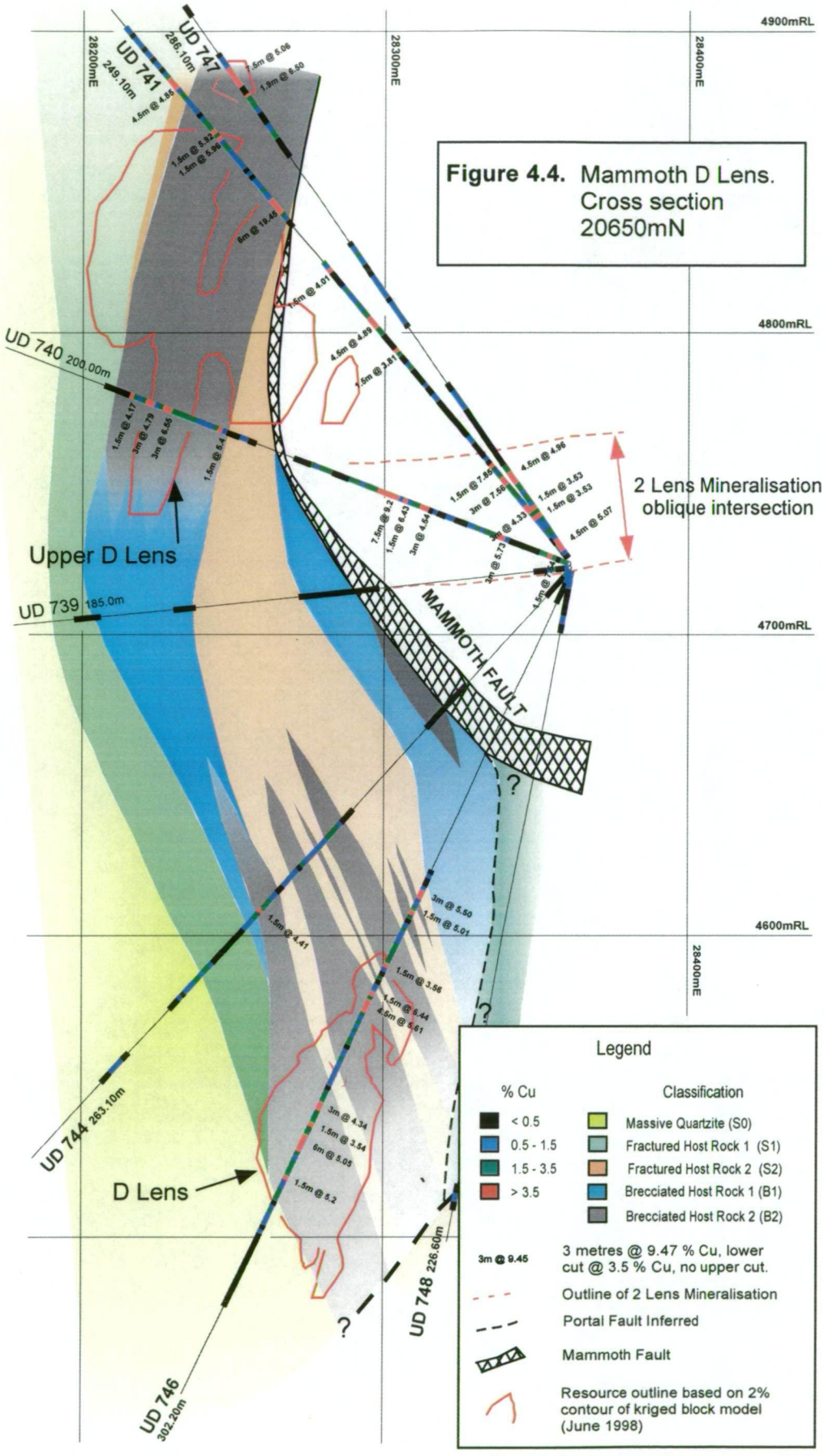
4900mRL
4800mRL
4700mRL
4600mRL
28200mE
28300mE
28400mE
UD 747 286.10m
UD 741 249.10m
UD 740 200.00m
UD 739 185.0m
UD 744 263.10m
UD 746 302.20m
UD 748 226.60m
Upper D Lens
D Lens
MAMMOTH FAULT
2 Lens Mineralisation oblique intersection
Figure 4.4. Mammoth D Lens. Cross section 20650mN
Legend
% Cu
< 0.5
0.5 - 1.5
1.5 - 3.5
> 3.5
Classification
Massive Quartzite (S0)
Fractured Host Rock 1 (S1)
Fractured Host Rock 2 (S2)
Brecciated Host Rock 1 (B1)
Brecciated Host Rock 2 (B2)
3m @ 9.45
3 metres @ 9.47 % Cu, lower cut @ 3.5 % Cu, no upper cut.
Outline of 2 Lens Mineralisation
Portal Fault Inferred
Mammoth Fault
Resource outline based on 2% contour of kriged block model (June 1998)

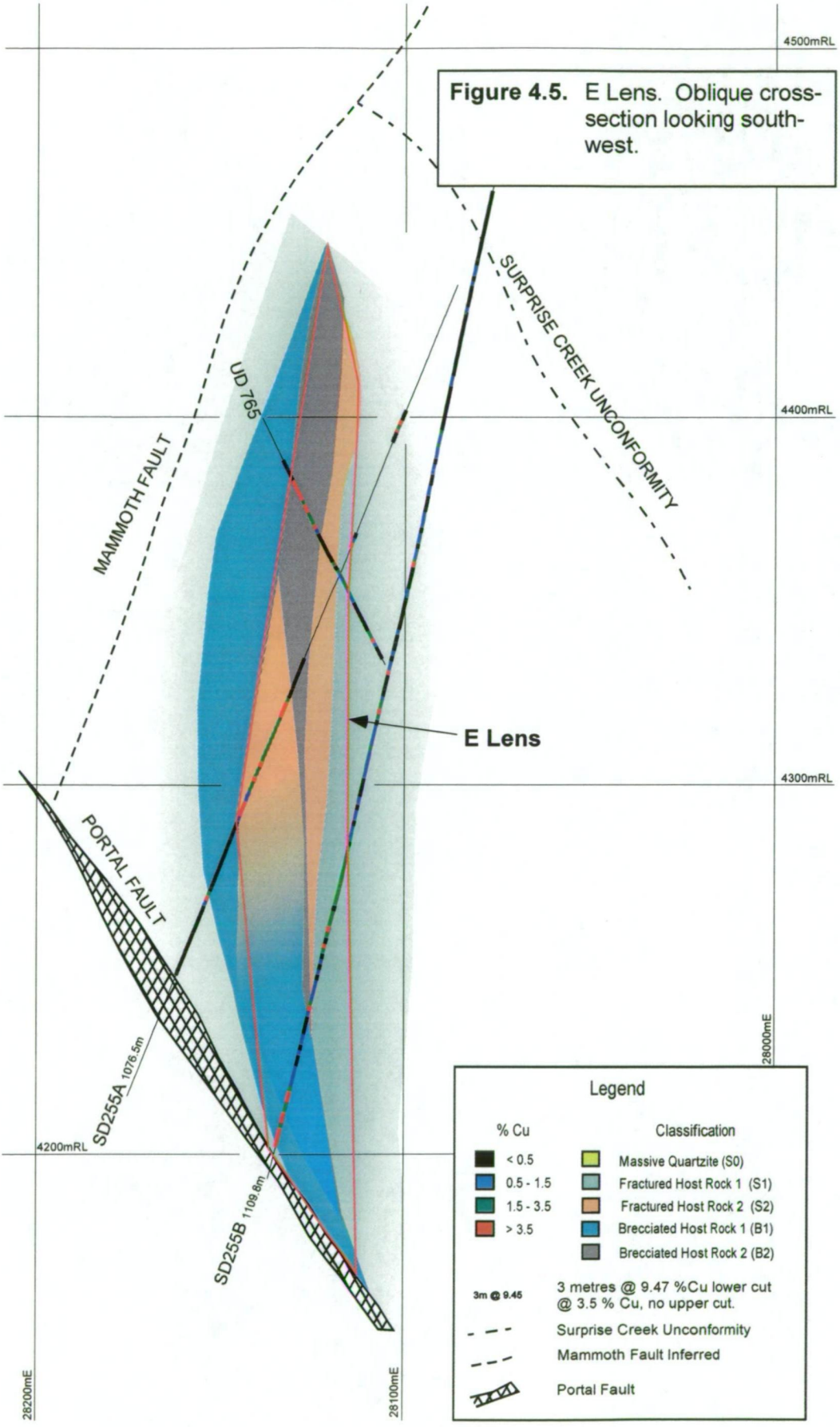

Figure 4.5. E Lens. Oblique cross-section looking south-west.

is not well constrained as only 7 drill holes have intersected mineralisation. The ore zone has been interpreted to strike EW, parallel to the Mammoth Fault with a subvertical to steep south dip. The mineralised zone occurs over a 250m vertical extent and 150m-strike extent with a true width of 10 to 20m. The ore zone is bounded to the east by the Portal Fault and to the south-east by the Mammoth Fault (Richardson, 2000).

4.2.f 2 Lens and Mammoth Fault Mineralisation (MFM)

2 lens strikes east-west at 80° with a steep to subvertical dip to the south and is located between its known limits of 28250-28475mE and 20650-20720mN and the bulk of the mineralisation is contained beneath 5000mRL and above 4700mRL (Figs 4.1, 4.6 and 4.7). The mineralised zone is well defined and is confined to the east by the Portal Fault and to the east by the Mammoth Fault. The ore zone ranges in thickness from 2 to 28 metres and has a contained resource of 1,100,000 t @ 5.8% Cu. The Mammoth Fault Mineralisation (MFM) is a poorly defined ore zone that is located in the hanging wall of the Mammoth Fault adjacent to the 2 Lens ore zone. The MFM ore zone appears to be sub-parallel to the 2 Lens ore zone and has a known strike length of ≅ 50 metres centred on ≅ 28315mE (Richardson, pers. comm., 1998). The structure that hosts the 2 Lens ore zones crops out at surface (Fig. 4.7.b). This structure is 1 to 3 metres wide and strikes EW for ≅ 75 m. The mineralogy of the veins and breccia cement consists of Fe-oxides.

4.3 TEXTURAL CLASSIFICATION SCHEME

As summarised by Richardson and Moy (1998), much of the underground development and drill core from the Mammoth Mine was either inaccessible or unavailable for the purposes of this research project. Therefore, the focus of this project was limited by availability of drill core and historic underground mapping.

The majority of the known Mammoth mineralisation is hosted within the Whitworth Quartzite unit. Within the mine environs company geologists have noted that the basal section of the Whitworth Quartzite is represented by a poorly-sorted, pink, massive-bedded quartzite. Interbedded laminated

Figure 4.6. 2 Lens and Mammoth Fault Mineralisation. Cross section 28315mE.

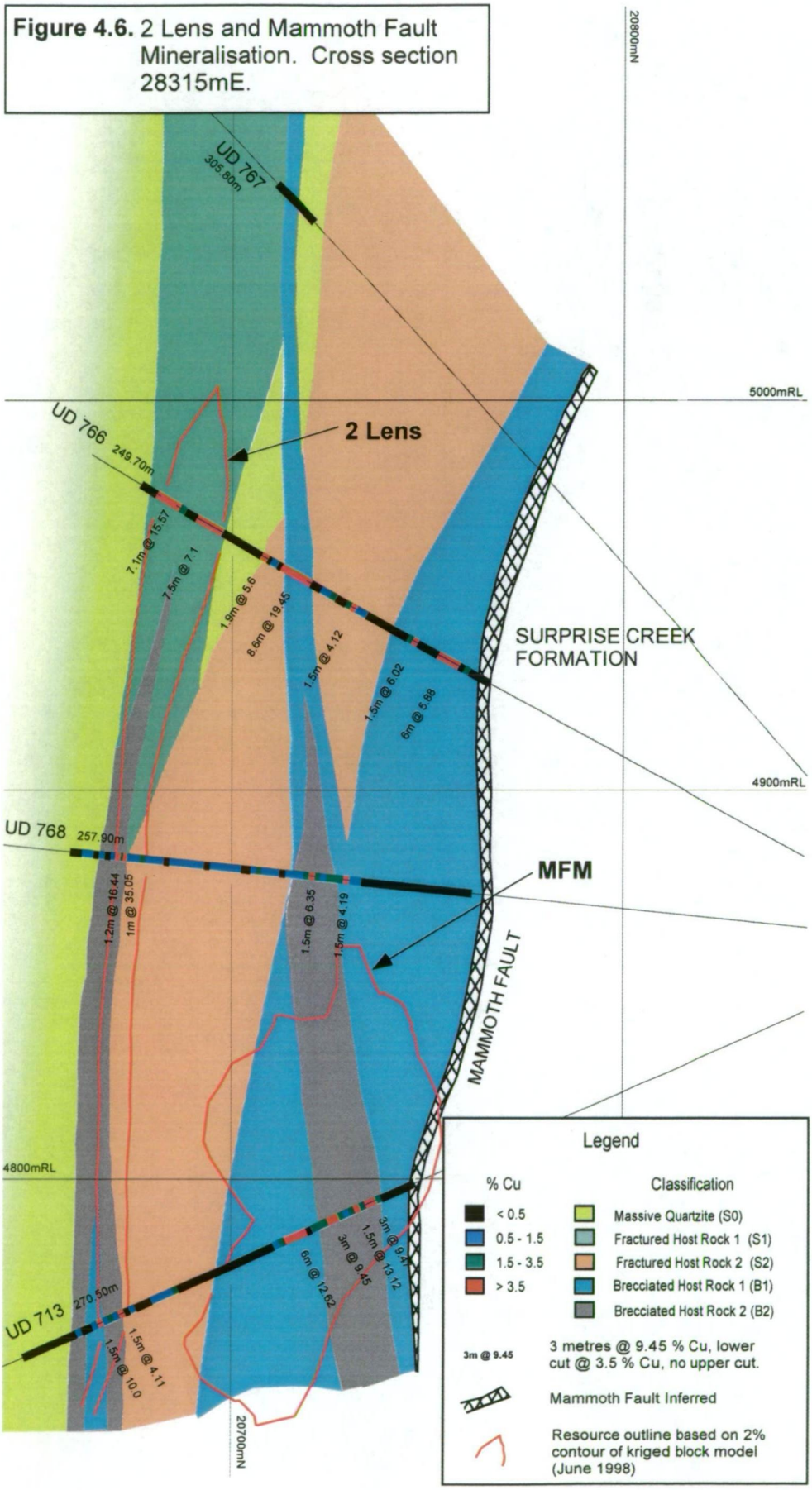

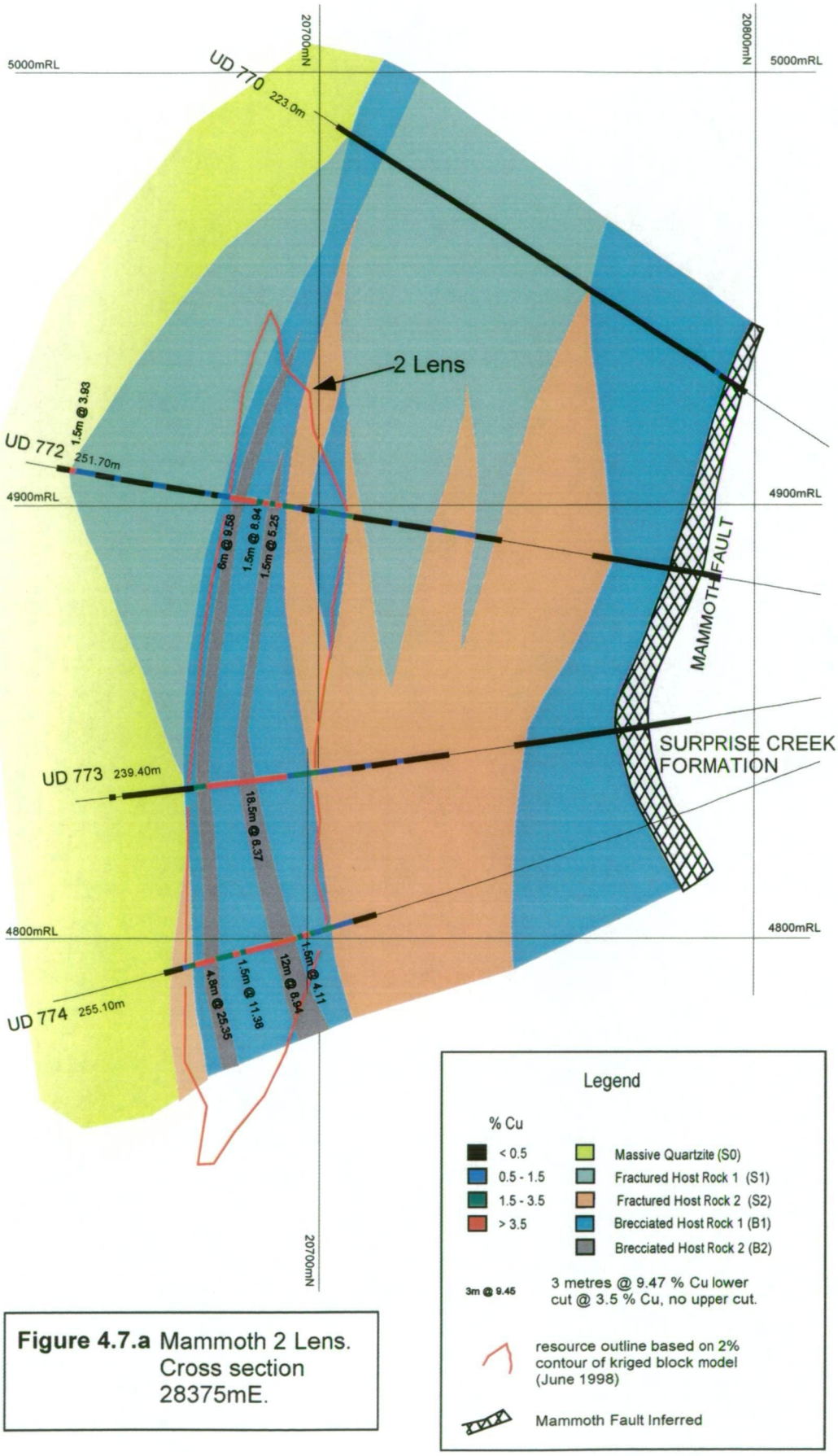

Figure 4.7.a Mammoth 2 Lens. Cross section 28375mE.

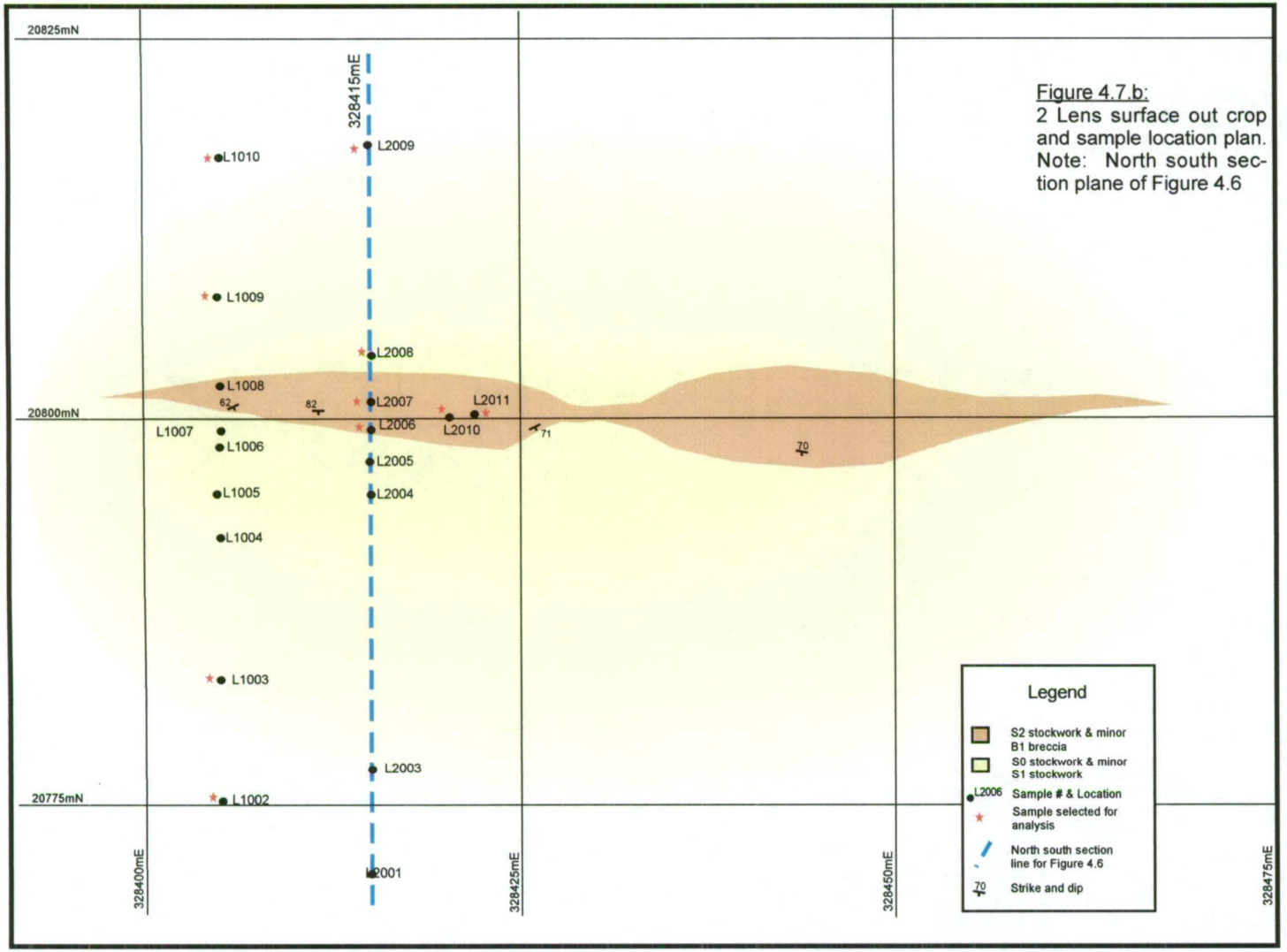

Figure 4.7.b:
2 Lens surface out crop and sample location plan. Note: North south section plane of Figure 4.6

sandstones, arkoses, siltstones, arenites and quartzites stratigraphically overlie the pink, massive-bedded quartzite (Richardson et al. 1998). The brittle nature of the host rock influences the over all character of the macro ore textures developed.

Mineralisation at Mammoth is texturally and mineralogically variable. Previous work has linked textural differences with distance from controlling fault zones (Mammoth, Mammoth Extended and Portal Faults) (Richardson and Moy, 1998). In order to characterise and document the textural variation through out the deposit a classification scheme based on textures has been developed. This system categorises the fracturing that the Whitworth Quartzite has undergone during the mineralising event from unfractured through, with increasing fracture intensity, to brecciation.

The scheme consists of 3 major divisions: Unfractured Host Rock (S0), Fractured Host Rock and Brecciated Host Rock. Subdivisions are given to further clarify the internal variations. Subdivisions are used in the Fractured and Brecciated Host Rock divisions as follows; Fractured Host Rock, Stockwork 1 (S1), Stockwork 2 (S2); Brecciated Host Rock, Breccia 1 (B1) and Breccia 2 (B2). Table 4.1 outlines the main criteria used to distinguish the major and sub divisions.

Table 4.1. Summary of textural criteria for the textural classification scheme.

Unit	Characteristics	
Unfractured Host Rock	**S0** ▪ No significant veins, fracture patterns, or brecciation developed ▪ Figure 4.8.	
Fractured Host Rock	**S1** ▪ < 100 veins over 1 metre ▪ Individual veins are typically < 4mm thick ▪ Veins consistently cross cut at a high angle to each other ▪ No significant wall rock bleaching at the hand specimen scale ▪ Figure 4.9.	**S2** ▪ > 100 veins over 1 metre ▪ Localised in situ brecciation ▪ Replacement of host rock components by sulfides along vein edges ▪ Veins consistently cross cut at a high angle to each other ▪ Significant wall rock alteration is often visible at the hand specimen scale ▪ Figures 4.10.a-f.
Brecciated Host Rock	**B1** ▪ Clast supported breccia ▪ Subangular to rounded clasts ▪ Clasts **rarely** contain disseminated sulfides ▪ Figures 4.11.a-f.	**B2** ▪ Matrix supported breccia ▪ Rounded clasts dominate ▪ **Common** replacement of breccia clasts by sulfides ▪ Figures 4.12.a-g and 4.13.a-f

4.3.a Unfractured Host Rock (S0)

The first major division of the textural classification scheme is distinguished by the absence of significant veins, fracture patterns, or brecciation overprinting the Whitworth Quartzite. The Whitworth Quartzite ranges from a massive to poorly stratified quartzite to an interbedded sequence of cross-bedded to thinly laminated quartz-rich and, siltstone and minor quartzite (Fig. 4.8). The quartzites consist of detrital quartz and feldspar (± relict mafic rock fragments). Detrital quartz grains are overgrown by a fine dusting of hematite that renders the quartzite orange-red in colour.

4.3.b Fractured Host Rock (S1 and S2)

The occurrence of stockwork vein sets distinguish the second major division of the Textural classification scheme. The Fractured Host Rock division contains two internal sub-divisions (S1 and S2). The criteria that distinguish

HOST ROCK (S0)

Figure 4.8.a. Example of massive quartz-rich arenite host rock displaying relatively little stockwork-brecciation development. Note; a) rare veins and cavities filled with chlorite which has subsequently oxidised, in part, to Fe hydroxides. Bleached front around veins and cavities due the presence of clay minerals. UD733-93.8m.

Figure 4.8.b. Laminated to thinly bedded quartz-feldspar sandstone with no stockwork developed. UD766-246.3m.

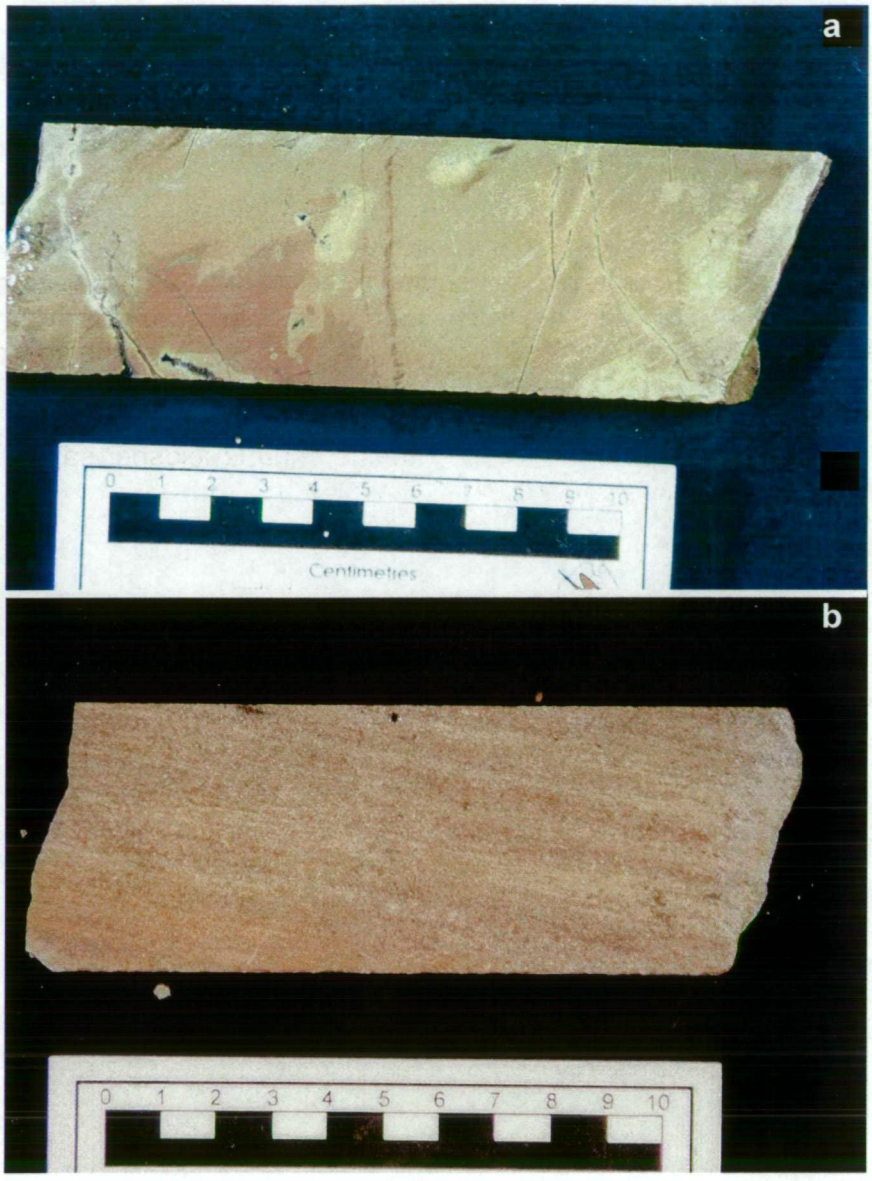
a
0 1 2 3 4 5 6 7 8 9 10
Centimetres
b
0 1 2 3 4 5 6 7 8 9 10

FRACTURED HOST ROCK
S1 Stockwork Subdivision

Figure 4.9.a. Veins composed of pyrite and chalcocite hosted in massive quatzite. Weakly disseminated chalcocite and pyrite occur zoned around veins. Dashed lines highlight angle of intersection of vein sets. UD773-175.2m, 2 Lens.

Figure 4.9.b.. Sulfide veins (chalcocite & pyrite), hosted in a bedded quartzite, clearly cross cut bedding. Bedding defined by dashed lines. UD733-170.5m, 2 Lens.

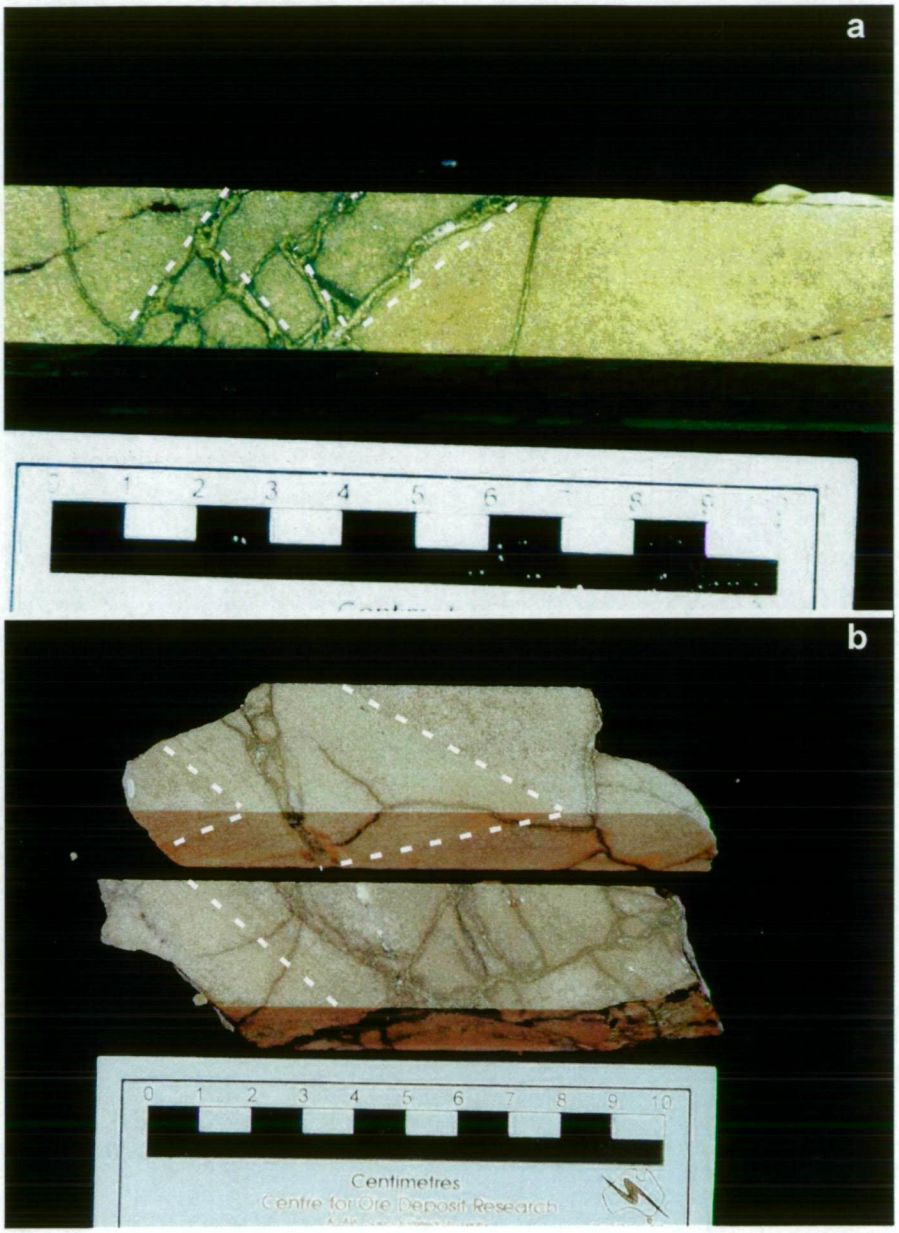
a
b
0 1 2 3 4 5 6 7 8 9 10
Centimetres
Centre for Ore Deposit Research

FRACTURED HOST ROCK
S2 Stockwork Subdivision

Figure 4.10.a. Veins contain pyrite, bornite and chalcocite. Note; a) localised in situ brecciation, b) infilling kaolinite and c) hematite. UD774-194.9m, 2 Lens.

Figure 4.10.b. Veins consist of pyrite and chalcocite. Note: a) chalcocite infilling at the intersection of vein sets, b) consistent high angle of intersection of vein sets and c) replacement of wall rock by pyrite and chalcocite. Dashed lines highlight trend of vein sets. UD773-178.9m, 2 Lens.

Figure 4.10.c. Laminated sandstone overprinted by pyrite and bornite vein. Diameter of coin is 2cm. UD710-136.6m, B Lens.

Figure 4.10.d. Laminated sandstone overprinted by pyrite and quartz vein. Minor replacement of host rock by fine grained pyrite along vein margin. Diameter of coin is 2cm. SD254-1042.5m, E Lens.

Figure 4.10.e. A good example of this style of S2 stockwork in massive sandstone. Veins composed of chalcocite, hematite and minor chlorite. Underground development 4850mRL, B Lens.

Figure 4.10.f. Massive sandstone overprinted by bornite, chalcocite, hematite and minor chlorite. Underground development 4850mRL, B Lens.

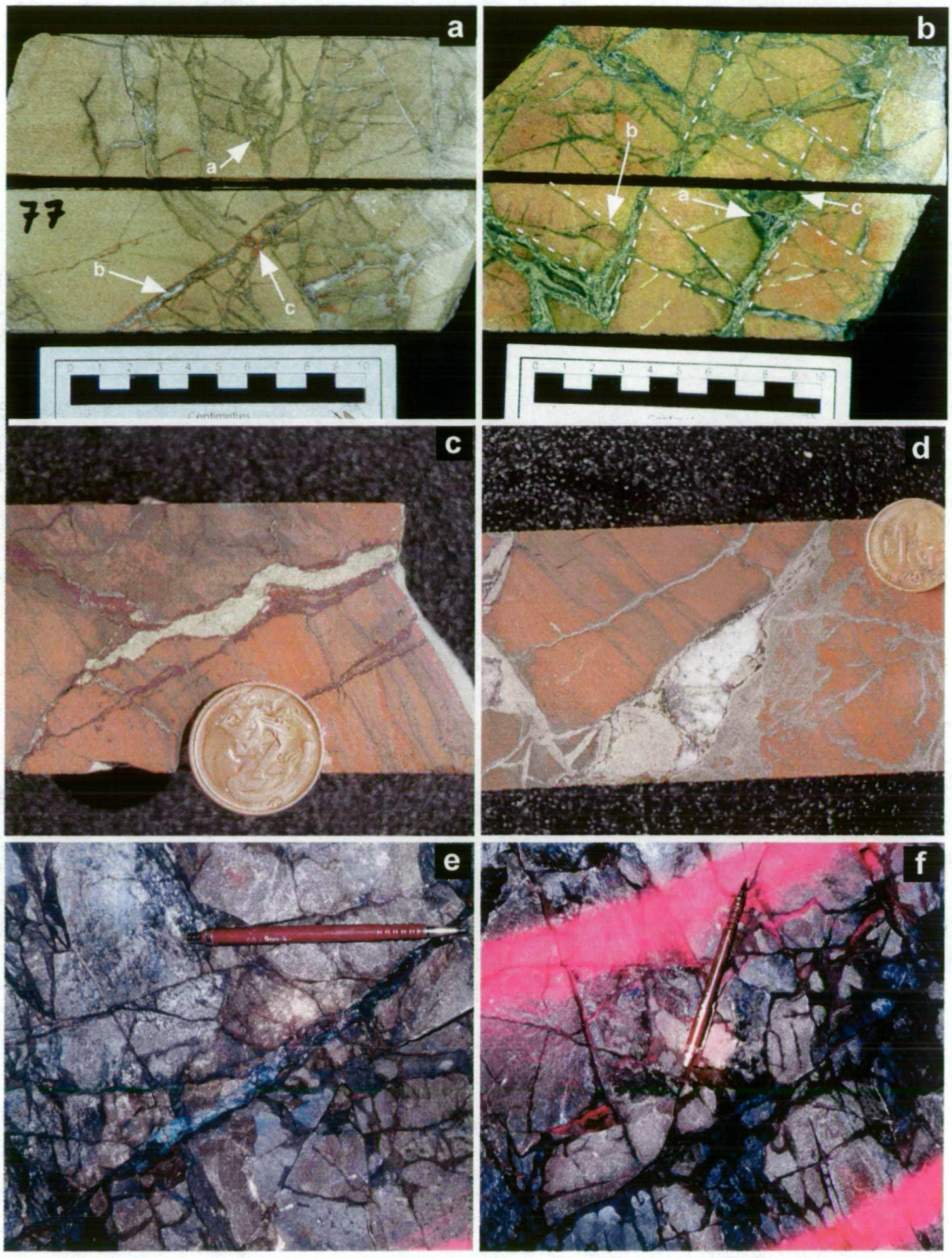
a
77
a
b
c
b
b
a
c
c
d
e
f

BRECCIATED HOST ROCK
B1 Breccia Subdivision

Figure 4.11.a. Breccia cement is composed primarily of melnikovite pyrite. Bornite and chalcocite appear to be infilling vug space. Note; a) clast supported breccia with subangular to rounded clasts. Clasts are devoid of disseminated sulfides. Dashed lines highlight bedding within clasts. UD773-204m, 2 Lens.

Figure 4.11.b. Clast to matrix supported breccia with matrix composed primarily of chalcocite and bornite. UD255-1051m, E Lens.

Figure 4.11.c. Clast to matrix supported breccia with matrix composed of pyrite. Diameter of coin is 2cm. UD611-50.5m, B Lens.

Figure 4.11.d. Matrix to clast supported breccia. Breccia matrix is composed primarily of pyrite, chlorite and rock flour. Diameter of coin is 2cm. UD710-102.5m, B Lens.

Figure 4.11.e. Clast to matrix supported breccia. Host rock is altered to chlorite and hematite. Vein/breccia matrix composed of pyrite and/or bornite. Diameter of coin is 2cm. UD611-170.5m, B Lens.

Figure 4.11.f. Angular to subangular sandstone fragments altered to pyrite, chlorite and hematite. Matrix composed of pyrite. Diameter of coin is 2cm. UD717-50.6m, D Lens.

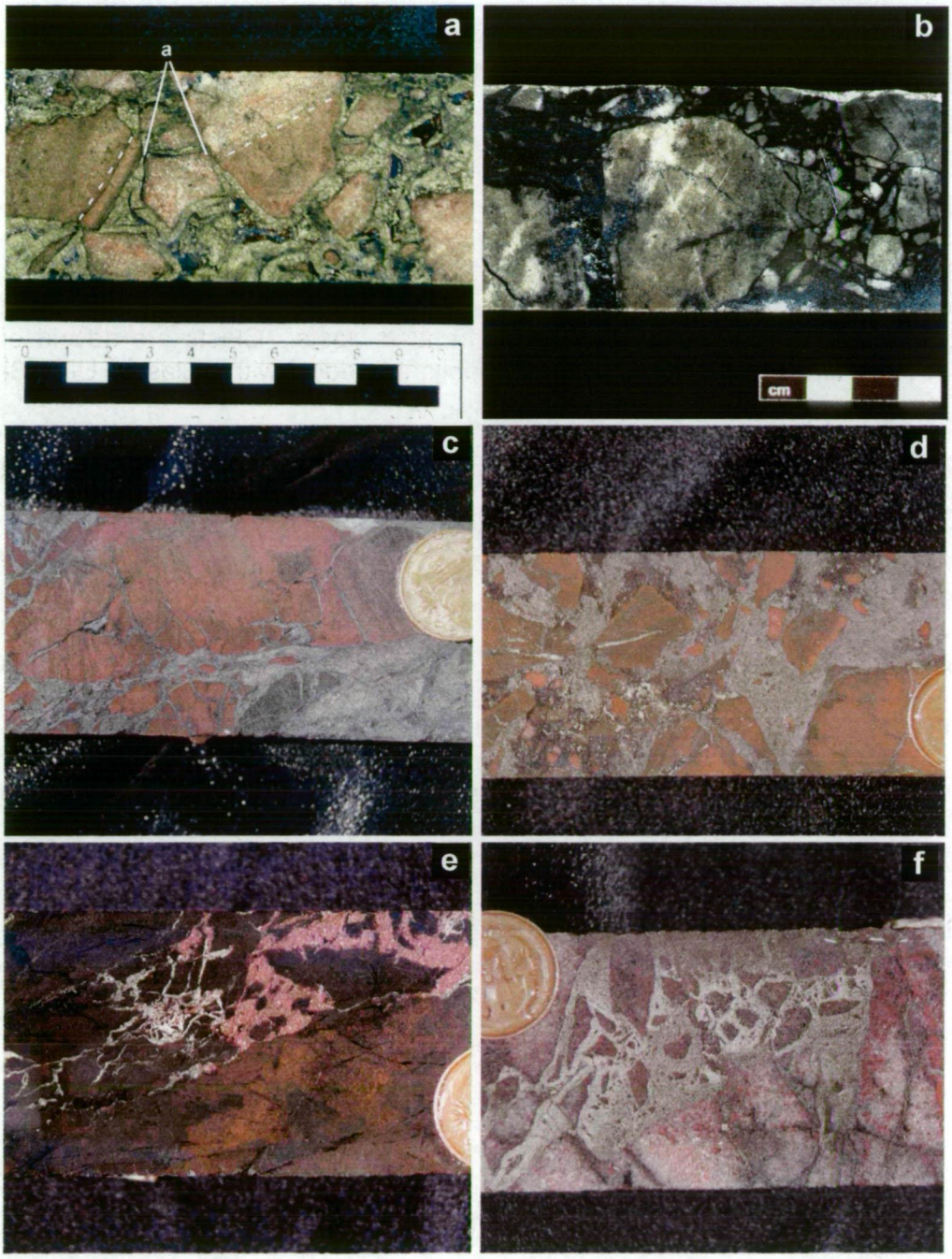
a
a
b
cm
c
d
e
f

BRECCIATED HOST ROCK
B2 Breccia Subdivision

Figure 4.12.a. Matrix supported breccia with bornite, chalcocite and pyrite as matrix components. Pyrite also occurs as breccia fragments. Some breccia fragments are replaced by pyrite and chalcocite, relict clast is highlighted by dashed line. UD774-208.1m, 2 Lens.

Figure 4.12.b. Brecciated Host Rock (B2). Matrix supported breccia. Matrix is composed of pyrite (20%) and chalcocite (80%). Breccia fragments are well rounded to angular. UD774-200.9m, 2 Lens.

Figure 4.12.c. Close up of fragment from Fig. 4.12.b. The margin of this well rounded fragment is replaced by pyrite and chalcocite. This is due to the replacement of the fragment by fine grained pyrite (dashed lines outline relict breccia clasts). The lighter coloured rim of the clast is due to kaolinite alteration. UD774-200.9m, 2 Lens.

Figure 4.12.d. Matrix supported breccia with very fine grained sand to clay sized matrix variably altered to chlorite and rare disseminated pyrite and bornite. Breccia fragments range in composition from siltstone to sandstone. Surface grab sample from No. 1 ore zone GP014.

Figure 4.12.e. Subangular clast to matrix supported breccia. Coarse grained sandstone fragments clearly fractured and infilled with bornite. Fragments are coated in crustiform euhedral pyrite. Diameter of coin is 2cm. UD611-59.5m, B Lens.

Figure 4.12.f. Matrix supported breccia. Subangular fragments composed of siltstone and sandstone, with the siltstone fragment preferentially altered to chlorite. Matrix comprised of bornite and pyrite. Diameter of coin is 2cm. UD710-106m, B Lens.

Figure 4.12.g. Matrix supported breccia. Breccia fragments consist of euhedral pyrite; well-rounded silicified sandstone and chlorite altered fine-grained clasts. Matrix is comprised of bornite and pyrite Diameter of coin is 2cm.. UD700-59.6m, D Lens.

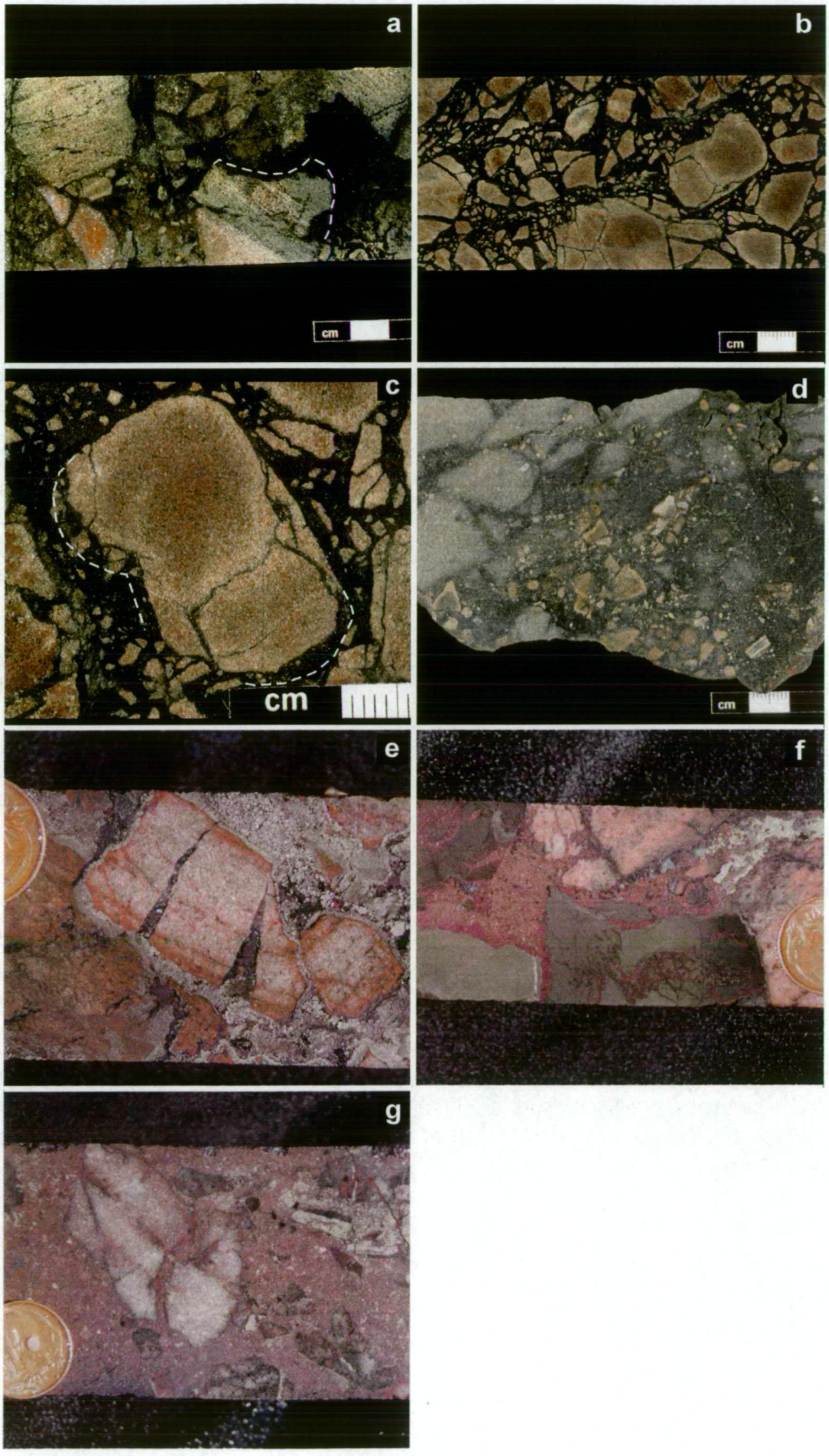
a
cm
b
cm
c
cm
d
cm
e
f
g

BRECCIATED HOST ROCK
B2 Breccia Subdivision (continued)

Figure 4.13.a. Matrix to clast supported breccia. Matrix is chlorite partially replaced by hematite. SD255-1081.6m, E Lens.

Figure 4.13.b. Matrix supported breccia. In general the specimen is similar to Fig. 4.13.a, however the degree of hematite alteration of the chlorite matrix has increased. SD255-1081.6m, E Lens.

Figure 4.13.c. Rare example of zoned euhedral quartz crystals hosted in a dominantly pyrite matrix. SD255E-1156.9m, E Lens.

Figure 4.13.d. Angular to well-rounded sandstone fragments in a dominantly coarse grained pyrite matrix. UD708-123.5m, B Lens.

Figure 4.13.e. Matrix supported breccia with very fine grained sand to clay sized matrix material either silicified or replaced by very fined grained pyrite. Breccia fragments composed of sandstone. Diameter of coin is 2cm. UD710-88.1m, B lens.

Figure 4.13.f. Chalcopyrite-pyrite vein overprinting fractured sandstone host rock. Veins propagating into the host rock are predominantly composed of bornite with minor pyrite and chalcopyrite. Diameter of coin is 2cm. UD735-71m, C Lens.

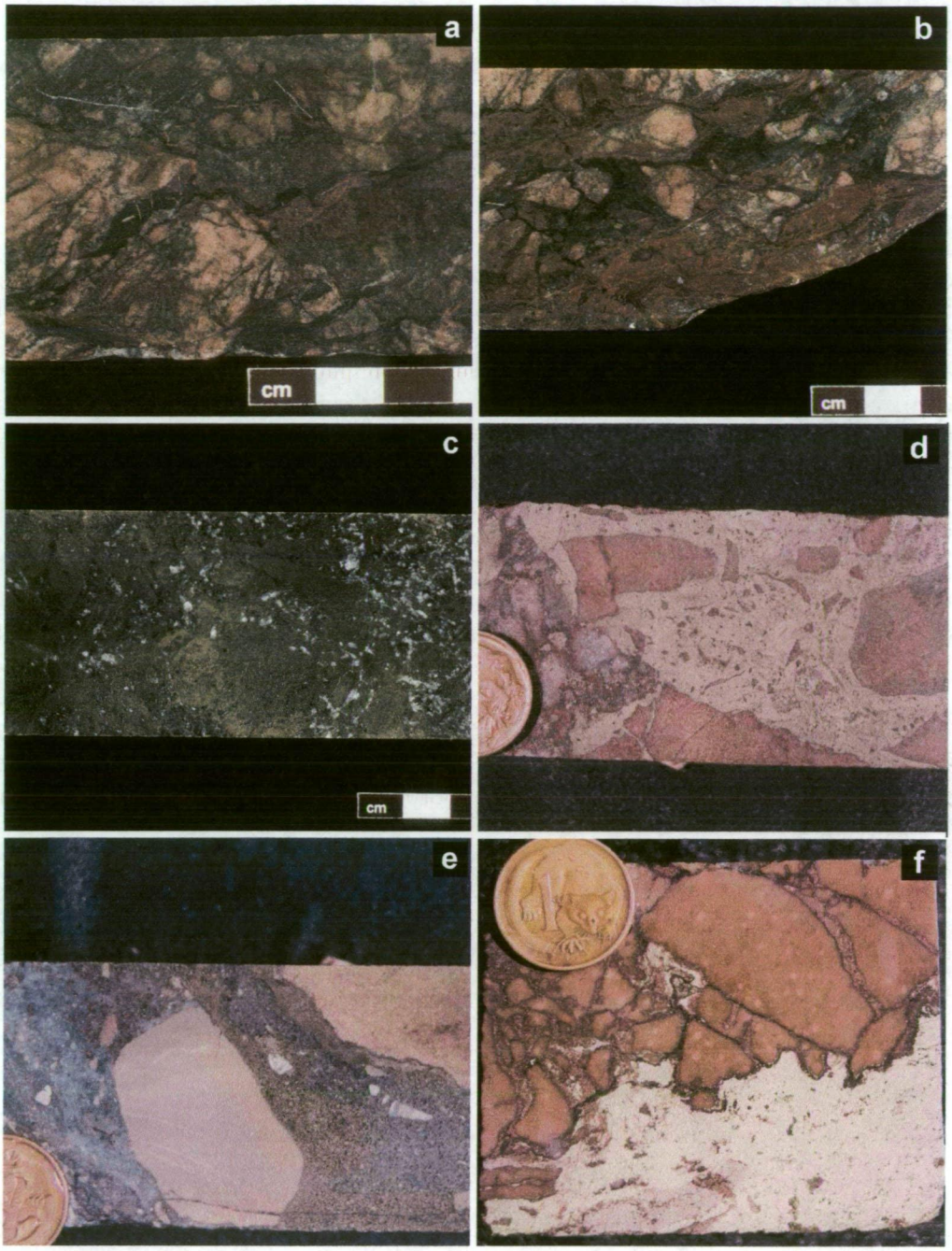
a
cm
b
cm
c
cm
d
e
f

the sub-division is empirical and is based on the number of veins occurring over a metre interval: S1) < 100 veins per metre; and S2) ≥ 100 veins per metre. The veins predominantly occur as conjugate pairs that are at a high angle to each other (Figs 4.9, and 4.10). Some veins occur sub-parallel to bedding but are always associated with a conjugate vein that crosscuts bedding (Fig. 4.9). The widths of the veins range in size from sub-millimetre to centimetres and vary in length for centimetres to metres (Figs 4.9 and 4.10). Commonly, irregularities in the vein walls can be matched with no significant apparent offset. Vein fill consists of coarse grained euhedral pyrite (± euhedral quartz) and anhedral chalcopyrite, bornite and/or chalcocite (±chlorite and/or hematite (± kaolinite)). A thin selvedge (<5mm) of host rock is pervasively altered with to chlorite and disseminated sulfides or kaolinite and/or hematite.

4.3.c Brecciated Host Rock

This classification has two sub-divisions (B1 and B2). The criteria that define the subdivisions are based on the whether the breccia is clast to matrix supported with little cement (B1; Figs 4.11.a-f), or well cemented and matrix supported (B2; Figs, 4.12 and 4.13). In general, the degree of alteration, of clasts and wall rock, and cementing, by sulfides, chlorite and/or hematite, of the breccias increases with the transition from the B1 sub-division to the B2 sub-division (Table 4.1). Contacts between breccia units (B1 and B2) and the wall rocks are commonly abrupt, or alternatively they can grade into a stockwork of S2 or S1 veins over a few metres. A zone of cataclasite consisting of chlorite or hematite and clay pug with relatively littlie sulfides (≤ 2%) marks the contacts between the Portal Fault and the Breccia units. The within the Whitworth Quartzite the Mammoth Fault occurs as a member of the either the B1 or B2 breccia units.

B1 subdivision

These breccias are normally characterised by angular to sub-angular clasts ranging in size from a few a centimetres to tens of centimetres. The breccia clasts are separated by 5 to ≤ 20 of sulfide cement (± chlorite and/or hematite) with no void space remaining (Fig. 4.11). The lithology of the clasts closely matches the adjacent wall rocks and hence brecciation resulted

in essentially monolithic breccias. Commonly the clasts can be rotated or fit back into position ("jigsaw fit") (Figs 4.11.c-f). The matrix consists of rock flour (sand to silt –size clastic material) variably altered to chlorite (± sulfides) and/or hematite (± kaolinite and relict sulfides) (Fig. 4.11.c-f). Typically the outer rim (≤ 1cm) of the clasts are pervasively altered to either: 1) chlorite and disseminated sulfides; or 2) kaolinite and/or hematite. This alteration (replacement) can result in an increase in the apparent rounding of the clasts as the rims are completely replaced by sulfides.

B2 subdivision

In general, the spatial distribution and variations of the alteration and sulfide mineralogy of the B2 sub-division are identical to the B1 sub-division. Marked differences include: 1) the breccias are matrix to clast supported; 2) clasts are sub-angular to sub-rounded and are well-cemented (20 to ≤ 50%) by sulfides (pyrite, chalcopyrite, bornite, or chalcocite) and chlorite and/or hematite (± relict sulfides and chlorite) and 3) an increase in the degree of alteration (replacement) of the clasts by sulfides. Sub-rounded clasts are typically associated with matrix supported breccias the matrix consists of rock flour (sand to silt –size clastic material) (Figs. 4.12.d and 4.13.a,b,d-e).

4.4 DISTRIBUTION OF MINERALISATION AND TEXTURES

The primary aim of this field investigation was focused on recording the textural variation, distribution and geometry of Cu mineralisation within the Mammoth deposit. Using the textural classification scheme (Table 4.1) representative sections were relogged through the main major ore lenses (B, C, D, E, 2 and MFM,). The geometry and distribution of the brecciated and stockworked units, hosting Cu mineralisation, have been reinterpreted and drafted in accordance with this textural classification scheme (Figs 4.3-4.7).

In general, within the Whitworth Quartzite, there is a good correlation of fractured and brecciated units between drill holes. Cross section 28315mE, through 2 Lens, is a typical example of Mammoth style mineralisation (Fig 4.7) and illustrates the relationship of host rock fracture/breccia intensity and

Cu grades associated with both the 2 Lens and Mammoth Fault ore bodies. Features of note include:

a) Strong correlation between drill holes of the Fractured (S1 and S2) and Brecciated Rock (B1 and B2) units.
b) Discordant apparent dips of the Mammoth Fault zone and the Mammoth Fault ore body are distinguished by the distribution of B1 & B2 units.

Previous workers, (A. Moy, pers com., 1998) have suggested that the gross geometry of D lens, as illustrated in Figure 4.1 was a cylindrical body that had its long axis plunge defined by the intersection of the Portal and Mammoth Faults. This model was generated by 2 %Cu grade contours extracted from a relatively unconstrained block model. The geometry of D lens has been re-interpreted subsequent to the re-logging of the drill holes on the drill section 20650 mN (Fig. 4.5). The drill holes (UD747, UD746, UD744, UD741, UD740 & UD739) within the section were re-logged using the textural classification scheme (Table 4.1). The geometry of D lens is presently interpreted as a series of variably mineralised, stacked brecciated lens. The lenses are interpreted to strike north-east and dip steeply south east (Figs 4.5 and 4.14).

The geological model of the 4720mRL (Fig. 4.14, refer map pocket), developed during the course of this project, is based upon interpretations from vertical drill sections that intersect this level. Mapping of the Mammoth mine underground development has been prevented due to the lack of access. The 4720 level was selected because it had previously been mapped (Moy, pers. com., 1998) and representative drill core was accessible. Representative drill core is not accessible for other mapped levels. Drill holes were selected that intersected the 4720mRL within a +/-25 metre window from 20600mN to 21200mN and from 28100mE to 28600mE. These holes were re-logged using the textural classification scheme (Table 4.1). The geology was then transposed into plan view (Fig. 4.14, refer map pocket). Good correlation of logged units exists between drill holes. Major Fault (Portal and Mammoth Fault) positions were taken from the development mapping where possible.

This combined interpretation (Fig. 4.14) of the re-logged drill core and mapped faults through the 4720mRL illustrates the typical geometry and distribution between the B, C and D Lenses and the Mammoth and Portal Faults. The D Lens ore breccias and associated stockwork units (S2, B1 and B2) initiate from the junction of the Mammoth and Portal Faults and strike at 145° for approx. 200 metres. The B Lens ore zone is, at this level (4720mRL) is hosted predominantly in Fractured Host rock (S2) unit and strike predominantly north south at 10°. The C Lens ore zone is hosted with a Brecciated Host Rock (B1) unit and has a strike length of 200m and occurs along strike from B Lens.

Company geologists have distinguished the ore bodies based on only on Cu grade considerations. Ore body outlines based on a 2 % Cu contour taken from an unconstrained spherical Kriged resource block model (June, 1998) are noted on Figure 4.14. Significant overlap occurs between the breccia (B1 and B2) and stockwork (S2) units and the ore body outlines defined on the modelled Cu grade. This work illustrates that the geometry of the variably mineralised breccia and stockwork units hosting the Mammoth mineralisation can be defined through mapping in accordance with the textural classification scheme (Table 4.1).

4.5 CONCLUSIONS

The major ore lenses (No. 1, B, C, D, E, 2 and MFM) of the Mammoth deposit are hosted in a variety of stockworked and breccia units. A classification scheme based on textural variations has been developed. This scheme categorises the fracturing that the Whitworth Quartzite has undergone during the mineralising event from un-fractured (S0) through, with increasing fracture intensity (S1 and S2), to brecciation (B1 and B2). The Cu mineralisation is developed within these units is highly variable, however, it appears to centred around zones of intense brittle deformation.

Copper grade is variably developed throughout the breccia units and probably reflected enhanced permeability resulting form more original open

space between fragments. The alteration (replacement) stage in the breccia units took place during fragmentation of the host rock. It was followed by a period of open space filling as indicated by the occurrence of coarse grained and crystalline pyrite followed by Cu and C-Fe sulfides (± chlorite). All the breccia units and stockwork vein units under went some degree of hydrothermal alteration (replacement) and open space filling stages indicating that the alteration and mineralisation were linked to the breccia and stockwork processes.

CHAPTER 5

MINERALOGY, ALTERATION AND PARAGENESIS

5.1 INTRODUCTION AND AIMS

The aim of this chapter is to determine the sulfide, sulfosalt, oxide and alteration mineralogy, textures and paragenesis of the primary copper mineralisation and their relationship to the supergene mineralisation. In order to achieve these aims ore microscopy investigation was conducted on 162 polished thin section representing the major ore zones of the Mammoth deposit (B, C, D, E and No. 2). In this chapter, detailed petrography is used to; 1) establish the variable mineralogy of the ore zones; 2) document the mineral textures; and 3) construct a paragenetic sequence of brecciation, veining and mineral deposition. This work allows comparison of the ore textures and alteration assemblages both within the Mammoth deposit and with other sediment-hosted, structurally-controlled Cu ore deposits. Furthermore, this approach will provide valuable information concerning the physicochemical conditions of the mineralising fluid during the formation of the deposit, which will contribute to the understanding of the genesis of the Mammoth deposit.

Copper mineralisation in the Mammoth deposit consists of chalcopyrite, bornite, chalcocite, covellite and rare occurrences of carrollite, wittichenite and linnaeite. The major ore minerals are hosted within veins and breccia matrixes and is weakly disseminated proximal to these vein and breccias. In general, the distribution of the sulfides are zoned from chalcopyrite and pyrite at depth to chalcocite up dip. This zoning has been a point of contention as to whether it is hypogene zoning or supergene zoning. This study has resolved the contentious issues regarding the origin of the chalcocite mineralisation. Clarification of this contentious issue has also led to a better understanding of the ore fluid condition during the formation of the deposit.

5.2 PREVIOUS WORK

Early workers Mitchell and More (1975) summarise the mineralogy of the No. 1 ore body as composed of chalcocite, bornite (± chalcopyrite, digenite covellite) and abundant pyrite. Two phases of mineralisation were recognised with an early pyritic phase and a late chalcocite-bornite phase. Chalcocite predominantly occurred as a zoned replacement of the pyrite. Bornite and chalcocite were noted to display an eutectic intergrowth interpreted to result from precipitation under hypogene conditions. Chalcocite and bornite mineralisation was regarded as primary with only the sooty chalcocite mineralisation the result of secondary enrichment. Sooty chalcocite mineralisation was reported at No 1 ore body and extending from surface down to 70 metres.

Scott and Taylor (1977), Scott et al. (1985) and Scott (1986) investigated the mineralogy of the No. 1, B and C ore lens. Hypogene alteration of the wall rock is interpreted to consist of sericite, chlorite and hematite replacing detrital feldspars. In the upper levels of No. 1 ore zone (> 5000mRl) kaolinite and/or dickite were identified in abundance. To a lesser extent Sr-Ca rare earth sulfate-phosphates were identified intergrown with kaolinite. In each of the three ore bodies (No.1, B and C) Cu mineralisation has been interpreted to consist of chalcocite, bornite, chalcopyrite and pyrite occurring in veins and breccia bodies. A paragenetic sequence based on isotopic and geochemical evidence was proposed: 1) early syngenetic, disseminated pyrite (± copper sulfides) 2) moderate As-rich pyrite 3) copper sulfides and 4) high As-rich pyrite (Scott, 1986).

In contrast, van Dijk (1991) proposed a two stage paragenetic sequence. The first stage is characterised by the formation veins and breccias consisting of pyrite (± chlorite, quartz and copper sulfides). Coeval pyrite replacement of the wall rocks, resulting in the formation of disseminated pyrite, occurs during this first stage. The disseminated pyrite was

demonstrated to form adjacent to the vein and breccia margins grading from massive to disseminated replacement of the host rock. Copper sulfides (± quartz and chlorite) are introduced during the second stage. van Dijk (1991) refutes the paragenetic sequence proposed by Scott and Taylor (1977) and Scott (1985). The lack of microstructural distinction between the two styles of pyrite (vein/breccia hosted *versus* disseminated) is cited in support of a contemporaneous origin for both styles.

Sillitoe (1997) commented briefly on the origin of the chalcocite mineralisation in the Mammoth deposit. A supergene origin was interpreted due to: 1) the occurrence of the hematite with chalcocite and 2) the development of chalcocite proximal to the Mammoth and Portal faults. However, a hypogene origin for the deep seated steely chalcocite mineralisation was not ruled out.

Richardson and Moy (1998) reviewed previous research conducted on the Mammoth deposit and hence their conclusions parallel the above summary. They concluded that the chalcocite mineralisation was the result of supergene enrichment of a dominantly pyrite-chalcopyrite mineralogy. Similar to the conclusions reached by Sillitoe (1997), the possibility for a hypogene origin to the bornite and chalcocite mineralogy was not discounted.

A consultant's investigation of the D Lens ore mineralogy identified different Cu sulfide zones (Gary McArthur, pers. com., 1999). Within the brecciated D lens ore zone it was demonstrated that the sulfides are zoned from chalcopyrite at depth to bornite and chalcocite up dip.

5.3 DESCRIPTION OF ORE AND ALTERATION MINERALOGY AND TEXTURES

The sulfide and sulfosalt mineralogy of the major ore bodies (B, C, D, E and No. 2) in the Mammoth deposit consists predominantly of pyrite, chalcopyrite, bornite, and chalcocite group minerals ($Cu_{1.7-2.0}S$) and covellite; with linnaeite, carrollite and wittichenite observed in trace amounts. The textural and mineralogical associations of the Fe-sulfide, Cu-Fe-sulfide, Cu-sulfide and sulfosalt mineralogy varies throughout the Mammoth deposit. The silicate and oxide alteration mineralogy of the host rock and gangue mineral assemblage includes quartz, illite, chlorite, kaolinite, hematite with trace amounts of rutile and apatite (Fig. 5.1.a and b).

5.3.a Sulfides and sulfosalt mineralogy

Pyrite

Iron sulfides occur both as disseminated (Figs 5.1.c, d and 5.6.f) and veined pyrites (Figs 5.1.e, f and g). Vein-hosted pyrite typically occurs in the form of euhedral crystals (Fig. 5.1.e) or melnikovite-pyrite (Fig. 5.1.f). The pyrites are firstly overprinted by veined quartz and secondly infilled and replaced Cu- and Cu-Fe sulfides and chlorite/illite (Figs 5.1.e-h, 5.2.a and b).

Chalcopyrite

Chalcopyrite (CuFeS) occurs: 1) predominantly as a replacement of compositionally zoned pyrites and/or as vein/fracture infill in pyrite (Figs 5.1.h, 5.2.a and b); 2) within bornite as classic basket weave exsolutions (Fig. 5.2.c) and 3) disseminated throughout the host rock proximal to vein/breccia margins (Fig. 5.2.d). Anhedral forms of vein-fill chalcopyrite are often rimmed by bornite with irregularly shaped chalcopyrite-bornite grain boundaries (Fig. 5.2.e). Chalcopyrite exsolution textures ("flames") penetrate into anhedral vein-fill bornite (Fig. 5.2.f). Chalcopyrite filled veins commonly grade into bornite (Figs 5.2.g and h). Rare inclusions of

chalcopyrite have been observed hosted with euhedral veined quartz (Fig. 5.1.e).

Bornite

Bornite (Cu_5FeS_4) occurs: 1) predominantly as vein/void fill and as a replacement of both disseminated and veined pyrite (Figs 5.1.e, 5.2.e and 5.3.a); 2) as a rim along chalcopyrite grain boundaries (Figs 5.2.f); and 3) as a myrmekitic intergrowth with hypogene chalcocite (Figs 5.3.b, c and d).

Cu-sulfide minerals

The Cu-sulfide mineral phases at in Mammoth are varied. They include chalcocite (Cu_2S), djurleite ($Cu_{1.93-1.97}S$), digenite (Cu_9S_5) and covellite (CuS). Differentiating chalcocite optically from djurleite is difficult as both minerals have similar properties. Optical differentiation is only possible within hours of polishing, as these particular sulfides rapidly tarnish to a similar reflectivity and colour. Therefore, during the course of this petrographic study the occurrence of either chalcocite or djurleite has been reported as "chalcocite".

"Chalcocite" occurs: 1) predominantly as vein/void fill and as a replacement of both disseminated and veined pyrite (Figs 5.3.b, c and e); 2) as a replacement of bornite (Figs 5.3.f) and 3) as a myrmekitic intergrowth with bornite (Figs 5.3.b, c and d). Digenite occurs as vermiform exsolution laminae in bornite (Fig. 5.3.g). Covellite occurs as a replacement of bornite (Figs 5.3.h and 5.4.a).

Trace sulfides and sulfosalts

Carrollite ($CuCo_2S_4$), linnaeite (Co_3S_4) and wittichenite (Cu_3BiS_3) occur in trace amounts in the Mammoth deposit. Carrollite occurs as anhedral inclusions in chalcopyrite (Fig. 5.4.b). Linnaeite occurs as anhedral inclusions in bornite (Fig. 5.4.c). Wittichenite commonly occurs as anhedral clots closely associated with grain boundaries between hematite, bornite and chalcocite (Fig. 5.4.d).

5.3.b Gangue mineralogy

Chlorite-illite intergrowths

Chlorite has been reported by previous workers to be associated with the wall rocks and ore throughout the Mammoth deposit (Scott and Taylor, 1977; Scott, 1986; and van Dijk, 1991). Chlorite, variably intergrown with illite, occurs as a vug space fill within veins and breccia matrixes (Figs 5.4.e-h, 5.5.a-f).

Kaolinite

Kaolinite occurs a vug space fill within veins and breccia matrixes (Figs 5.5.g-h and 5.6.a). There is a noticeable lack of chlorite in the kaolinite-rich areas.

Hematite

Specular hematite occurs throughout in various textural and mineralogical associations. Its occurrence ranges from partial through to complete replacement of chlorite and Cu-Fe sulfides (Figs 5.3.f, 5.4.d, 5.5.c-d, g-h and 5.6.a-e)

Apatite

Small (1-2μm) crystals of apatite are hosted within chlorite.

Rutile

Rare inclusions of rutile are hosted in chalcopyrite and in euhedral vein quartz (Figs 5.1.d. and 5.2.b).

Alteration of host rock

Host rock for the Mammoth deposit ranges from laminated siltstone to massive sub-arkose to a coarse to medium grained felspathic quartzite. The dominant minerals in the felspathic quartzite are detrital quartz, feldspar (microcline) and chert (Figs 5.1.a and b). Minor components of the host rock include zircon, tourmaline, mica, apatite, relict mafic rock

fragments and rare disseminated sulfides (Fe, Cu and Cu-Fe sulfides). The host rocks are well cemented by quartz with little pore space remaining.

Detrital quartz grains are, to varying degrees, overgrown by a mixture of hematite or limonite/goethite. Relict feldspar grains display partial to complete replacement by fine-grained iron oxides (fig. 5.1.a) interpreted to have occurred during digenesis (Taylor and Scott, 1976). Alteration of relict feldspars, to an intergrowth of illite and chlorite, occurs proximal to mineralisation. Intergrowths of prismatic hematite occur with the illite/chlorite. Pervasive alteration/replacement of host rock by quartz is observed immediately adjacent (1-2 cm) to quartz-chlorite veins and/or breccias. Disseminated pyrite, chalcopyrite, chalcopyrite-bornite and chalcocite-bornite intergrowths replace both the quartz cement and relict feldspars (Figs 5.2.d and 5.6.f) within 5 -10 centimetres of vein or breccia margins.

5.4 PARAGENESIS

5.4.a Discussion of Hypogene versus Supergene

The origin of Cu and Cu-Fe sulfide zonation at Mammoth, which ranges from chalcopyrite to bornite through to the chalcocite group minerals ($Cu_{(1.7\ -2.0)}S$), has been a continuous issue. Either hypogene or acidic supergene processes have been proposed to account for this observed sulfide zonation (Richardson and Moy, 1998; Sillitoe, 1997; Mitchell and Moore, 1975) A definitive answer has not been reached, however, a modified version of the supergene model is the presently accepted model (Richardson and Moy, 1998).

Mechanisms of oxidation of Cu, Cu-Fe and Fe sulfides

In order to differentiate supergene Cu and Cu-Fe sulfides from hypogene Cu and Cu-Fe sulfides it is necessary to have a thorough understanding of supergene alteration processes and products. Sulfide occurrences

Figure 5.1.a. Detrital feldspar partially replaced by hematite (red-brown). Fine grained hematite (red-brown) coat detrital quartz grains. Pore space is filled by silica cement. UD768-184.1m, transmitted light, X40.

Figure 5.1.b. Detrital quartz grains coated with fine grained hematite (red-brown). Pore space is filled by quartz cement. UD768-184.1m, transmitted light, X40.

Figure 5.1.c. Disseminated fine grained stage I pyrite (py) hosted between detrital quartz grains (dtq) in quartzite. UD746-215.1m, reflected light, X62.5.

Figure 5.1.d. Disseminated fine grained stage I pyrite (py) hosted in quartzite. Note pyrite is preferentially aligned along fractures UD746-263.4m, reflected light, X5.

Figure 5.1.e. Vein-hosted stage I euhedral pyrite (py) and euhedral quartz (qz) overprinted by stage II bornite (bn) and chlorite (ch). Note inclusions of chalcopyrite (cpy) and rutile (rt) in euhedral quartz (qz) (see inset). UD746-136.2m, reflected light, X5.

Figure 5.1.f. Vein-hosted stage I melnikovite pyrite (py) and stage II bornite (bn) and chalcopyrite (cpy). UD746-207.0m, reflected light, X50.

Figure 5.1.g. Brecciated zoned stage I pyrite (py) overprinted by a myrmekitic intergrowth of stage II hypogene chalcocite (hcc) and bornite (bn). Void space is filled with quartz (qz) and chlorite (ch). UD746-145.5m, reflected light, X5.

Figure 5.1.h. Stage I colloform pyrite (py) fractured and replaced by stage II chalcopyrite (cpy) and bornite (bn). UD746-207.1m, reflected light, X25.

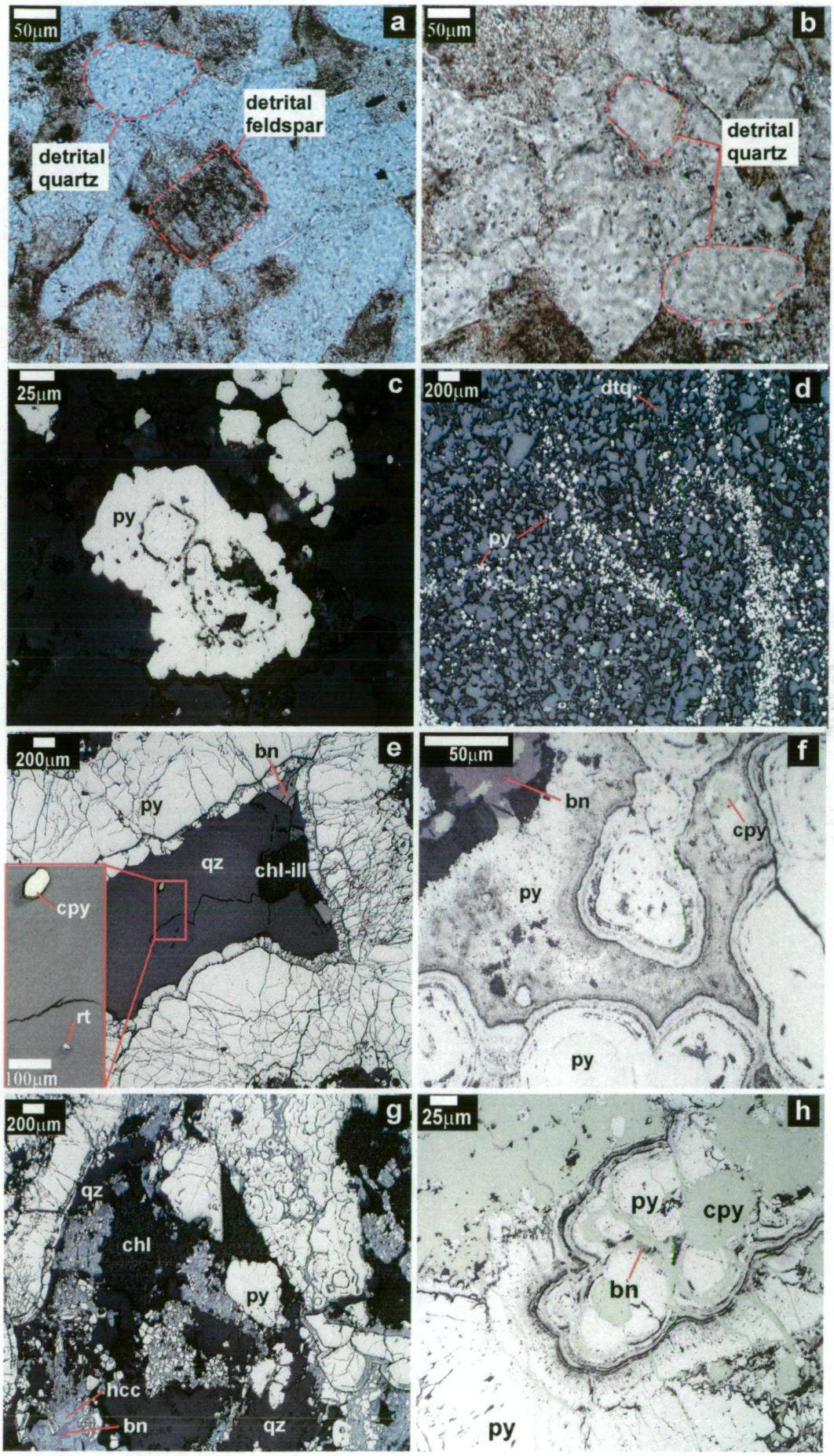
50μm
a
detrital feldspar
detrital quartz
50μm
b
detrital quartz
25μm
c
py
200μm
dtq
d
py
200μm
bn
e
py
qz
chl-ill
cpy
rt
100μm
50μm
f
bn
cpy
py
py
200μm
g
qz
chl
py
hcc
bn
qz
25μm
h
py
cpy
bn
py

Figure 5.2.a. Vein hosted stage I euhedral pyrite (py) crosscut and replaced by stage II chalcopyrite (cpy). UD768-184.1m, reflected light, X1.25.

Figure 5.2.b. Fractured stage I pyrite (py) infilled by stage II chalcopyrite (cpy). UD746-212.9m, reflected light, X10.

Figure 5.2.c. Basket weave exsolutions and exsolution laminae (flames) of stage I chalcopyrite (cpy) in stage I bornite (bn). UD744-28.9m, reflected light, X200.

Figure 5.2.d. Disseminated stage II chalcopyrite (cpy) and bornite (bn) fills vug space in quartzite host rock. UD710-106.0m, reflected light, X50.

Figure 5.2.e. Vein hosted stage II bornite (bn) and chalcopyrite (cpy) crosscutting and replacing stage I pyrite (py). Note irregular bornite (bn)-chalcopyrite (cpy) grain boundaries. UD710-106.0m, reflected light, X5.

Figure 5.2.f. Stage II chalcopyrite (cpy) and bornite (bn) as breccia matrix infill. Note chalcopyrite (cpy) "flames" penetrating into bornite (bn). Stage II carrollite (cr) is hosted within chalcopyrite. UD746-207.0m, reflected light, X40.

Figure 5.2.g. Veined hosted stage I pyrite (py) overprinted and replaced by stage II chalcopyrite (cpy) and bornite (bn). UD710-106.0m, reflected light, X1.25.

Figure 5.2.h. Vein hosted stage II bornite (bn) infilling vug space around stage I euhedral quartz (qz). Note stage II chalcopyrite (cpy) replacing stage I pyrite (py) vein. SD255-1009.9m, reflected light, X1.25.

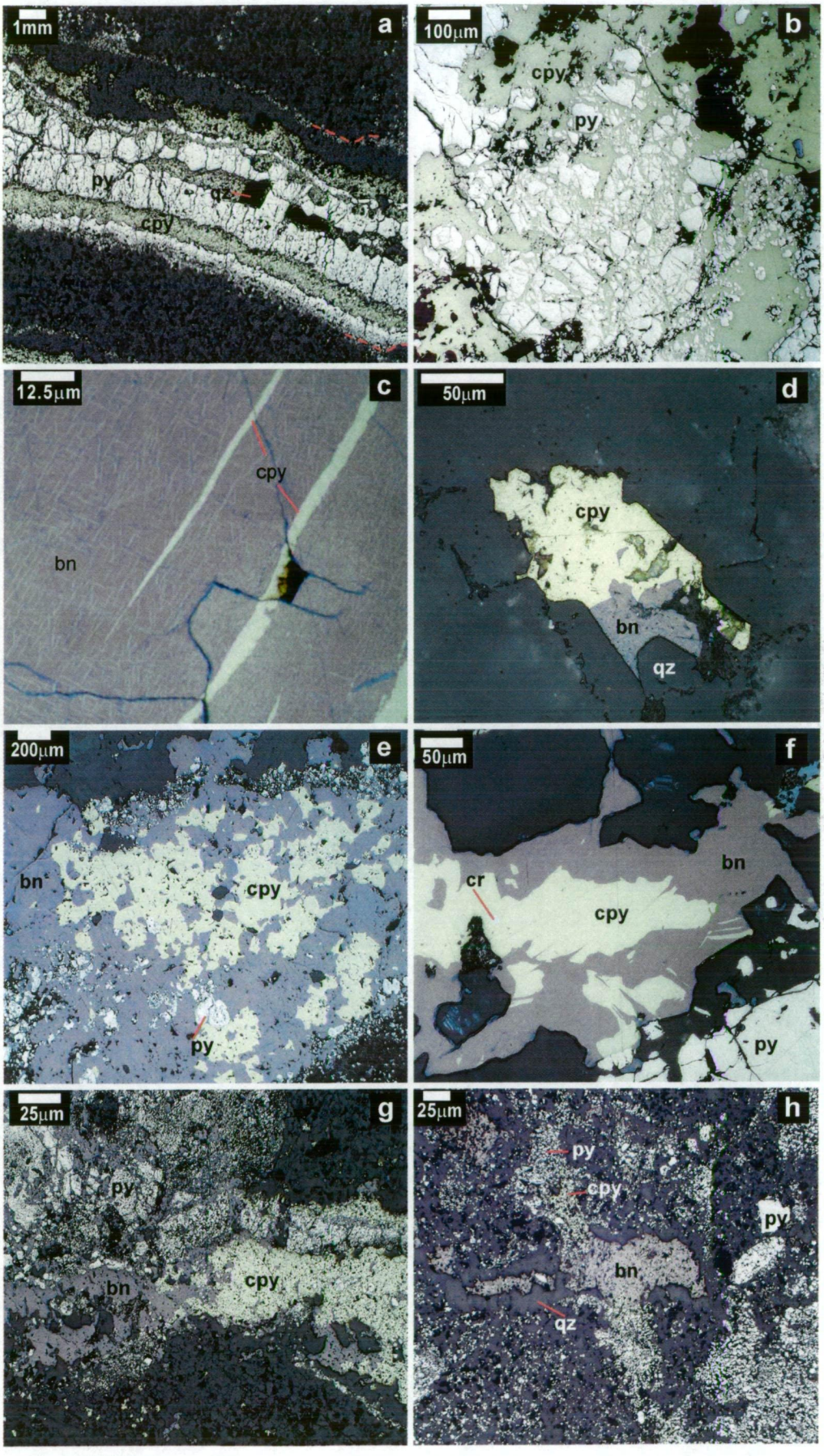
1mm
a
py
qz
cpy
100μm
b
cpy
py
12.5μm
c
cpy
bn
50μm
d
cpy
bn
qz
200μm
e
bn
cpy
py
50μm
f
bn
cr
cpy
py
25μm
g
py
bn
cpy
25μm
h
py
cpy
py
bn
qz

Figure 5.3.a. Stage II bornite (bn) replacing stage I zoned pyrite (py). UD768-124.4m, reflected light, X20.

Figure 5.3.b. Stage II myrmekitic hypogene chalcocite (hcc)-bornite (bn) intergrowths replacing stage I zoned pyrite (py). UD746-159.8m, reflected light, X20.

Figure 5.3.c. Stage II myrmekitic hypogene chalcocite (hcc)-bornite (bn) intergrowths replacing stage I pyrite (py) along fractures. UD746-159.8m, reflected light, X20.

Figure 5.3.d. Stage II myrmekitic hypogene chalcocite (hcc)-bornite (bn) intergrowths. SD255-1051.1m, reflected light, X40.

Figure 5.3.e. Vein hosted stage I euhedral quartz (qz) overprinted by stage II myrmekitic hypogene chalcocite (hcc)-bornite (bn) intergrowths. UD611-59.8m, reflected light, X5.

Figure 5.3.f. Stage III supergene chalcocite (scc) replacing stage I bornite (bn). Stage III hematite (hm) replacing stage II chlorite (ch)/illite intergrowth. UD746-145.5m, reflected light, X10.

Figure 5.3.g. Vermiform exsolutions of stage II digenite (dg) in stage II bornite (bn). UD710-88.0m, reflected light ,X125.

Figure 5.3.h. Stage II bornite (bn) replacing stage I pyrite (py). Stage III covellite (cv) replacing stage I bornite (bn). Stage III hematite (hm) replacing stage II chlorite/illite (black) intergrowth. UD746-171.7m, reflected light, X20.

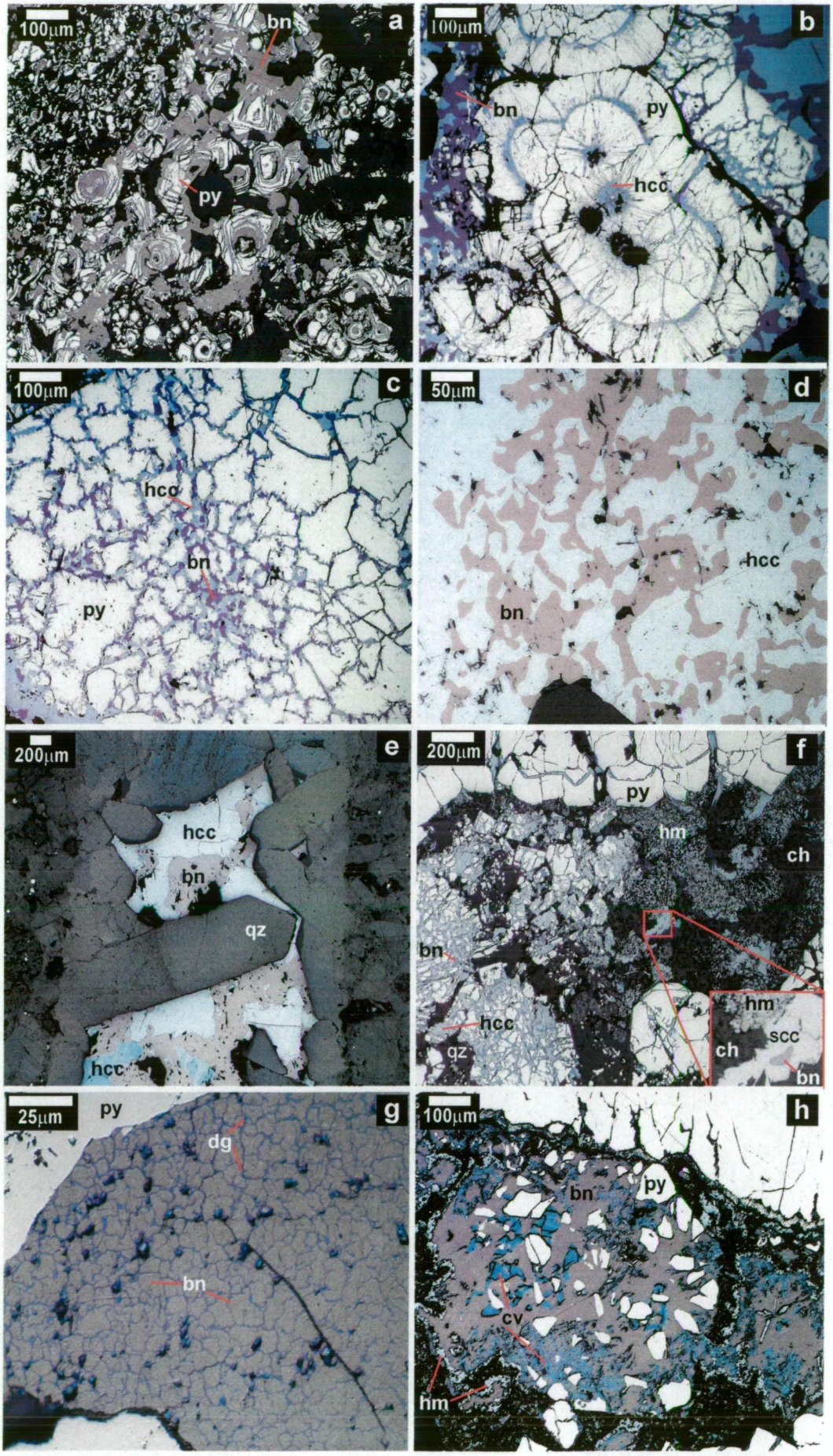
100µm
bn
a
py
100µm
b
bn
py
hcc
100µm
c
hcc
bn
py
50µm
d
hcc
bn
200µm
e
hcc
bn
qz
hcc
200µm
f
py
hm
ch
bn
hcc
qz
hm
scc
ch
bn
25µm
py
g
dg
bn
100µm
h
bn
py
cv
hm

Figure 5.4.a. Stage III covellite (cv) replacing stage II bornite (bn). Stage I disseminated pyrite around stage I veined pyrite (py). UD768-162.5m, reflected light, X5.

Figure 5.4.b. Anhedral grains of stage II carrollite (cr) within stage II chalcopyrite (cpy). Stage I euhedral pyrite (py). UD746-223.9m, reflected light, X40.

Figure 5.4.c. A rare anhedral grain of stage II linnaeite (ln) hosted in stage II bornite (bn) infilling vug space around stage I euhedral pyrite (py). UD717-59.3m, reflected light, X40.

Figure 5.4.d. Anhedral grains of stage III wittichenite (wt) intergrown with stage III supergene chalcocite (scc), stage II bornite (bn) and stage III hematite (hm). UD746-116.8m, reflected light, X20.

Figure 5.4.e. Vein-hosted stage I euhedral pyrite (py) and quartz (qz) overprinted by stage II chlorite/illite (ch-ill) intergrowths and traces of chalcopyrite (cpy). UD746-225.4m, reflected light, X1.25.

Figure 5.4.f. Vein-hosted stage I euhedral pyrite (py) and quartz (qz) overprinted by stage II chlorite/illite (ch-ill) intergrowths and traces of chalcopyrite (cpy). Note occurrence of chlorite/illite (ch-ill) intergrowth. UD746-225.4m, transmitted light, X1.25.

Figure 5.4.g. Stage II hypogene chalcocite (hcc) intergrown with stage II chlorite (ch). Note absence of stage III hematite and/or stage IV kaolinite. UD611-59.8m, reflected light, X40.

Figure 5.4.h. Stage II hypogene chalcocite (hcc) intergrown with stage II chlorite (ch). Note absence of stage III hematite and/or stage IV kaolinite. UD611-59.8m, transmitted light, X40.

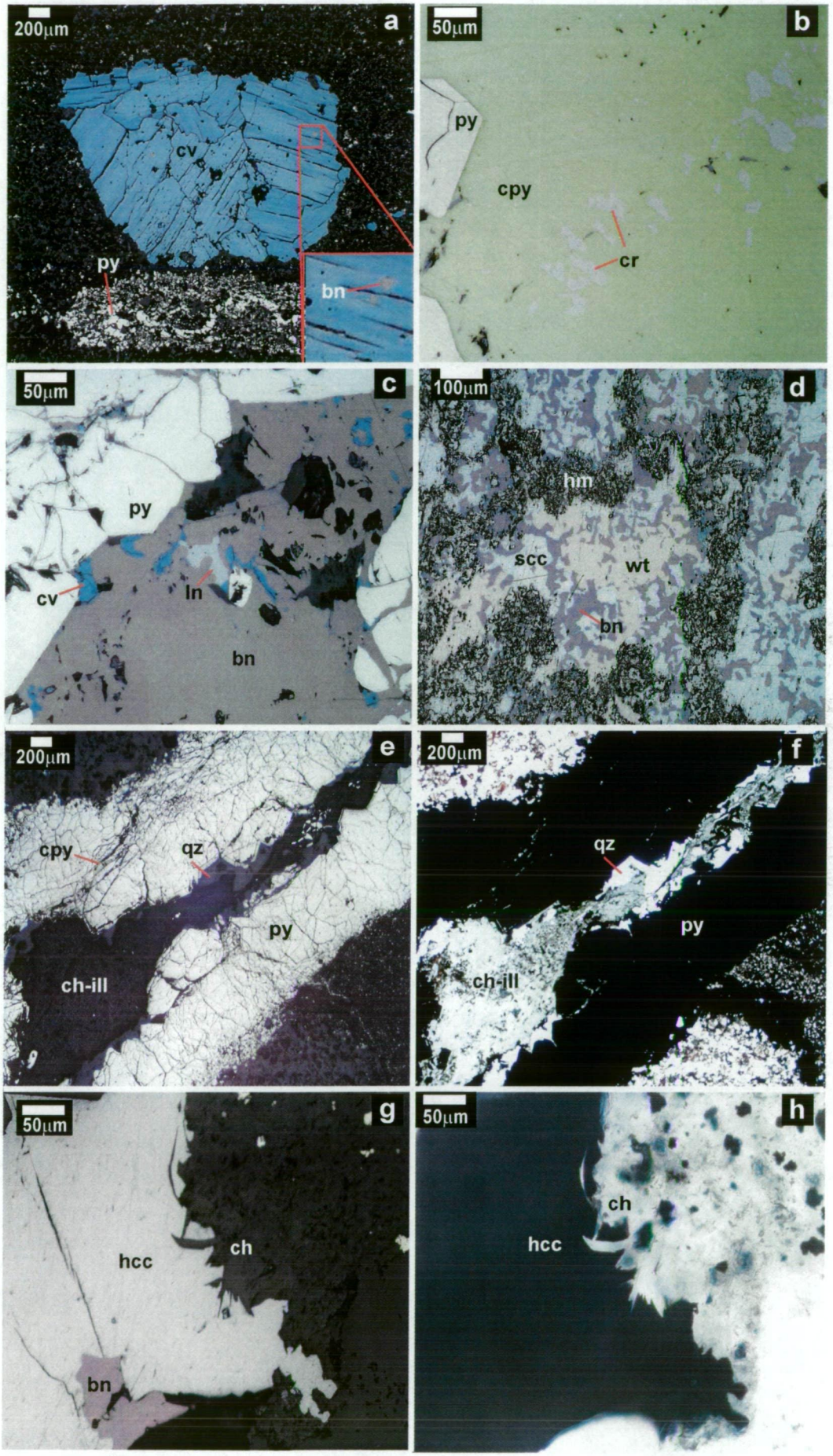
200μm
a
cv
py
bn
50μm
b
py
cpy
cr
50μm
c
py
cv
ln
bn
100μm
d
hm
scc
wt
bn
200μm
e
cpy
qz
py
ch-ill
200μm
f
qz
py
ch-ill
50μm
g
hcc
ch
bn
50μm
h
ch
hcc

Figure 5.5.a. Stage II hypogene chalcocite (hcc) intergrown with stage II chlorite (ch) and stage I quartz (qz) in the absence of stage III hematite and/or stage IV kaolinite. UD708-123.5m, reflected light, X50.

Figure 5.5.b. Stage II hypogene chalcocite (hcc) intergrown with stage II chlorite (ch) and stage I quartz (qz) in the absence of stage III hematite and/or stage III kaolinite. Note radial habit of chlorite (ch) UD708-123.5m, transmitted light, X50.

Figure 5.5.c. Stage III supergene chalcocite (scc) replacing stage II bornite (bn). Stage III hematite (hm) replacing stage II chlorite (ch). UD746-145.5m, reflected light, X40.

Figure 5.5.d. Stage III supergene chalcocite (scc) replacing stage II bornite (bn). Stage III hematite (hm) replacing stage II chlorite (ch). UD746-145.5m, transmitted light, X40.

Figure 5.5.e. Stage I quartz and stage II illite-chlorite (ill-ch) intergrowth with stage II chalcopyrite (cpy) infilling breccia vug space. UD746-207.1m, reflected light, X10.

Figure 5.5.f. Stage I quartz (qz) and stage II illite-chlorite (ill-ch) intergrowth with stage II chalcopyrite (cpy) infilling breccia vug space. UD746-207.1m, transmitted light with crossed polars, X10.

Figure 5.5.g. Stage II hematite (hm) replacing stage I bornite (bn) and stage II chlorite (ch). UD744-128.9m, reflected light, X10

Figure 5.5.h. Stage IV kaolinite replacing stage II chlorite (ch). UD744-128.9m, transmitted light with crossed polars, X10.

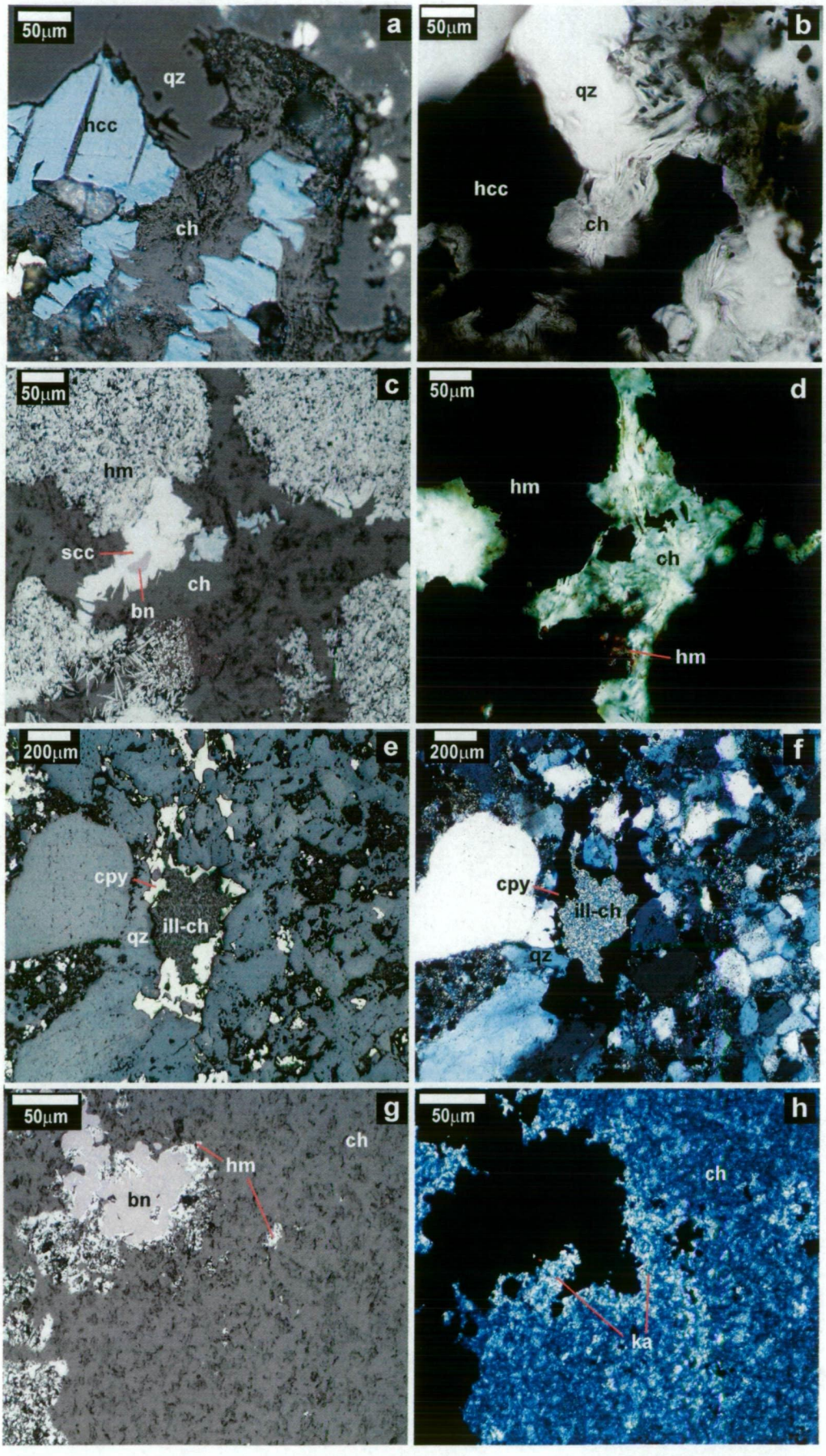
50μm
a
qz
hcc
ch
50μm
b
qz
hcc
ch
50μm
c
hm
scc
ch
bn
50μm
d
hm
ch
hm
200μm
e
cpy
ill-ch
qz
200μm
f
cpy
ill-ch
qz
50μm
g
ch
hm
bn
50μm
h
ch
ka

Figure 5.6.a. Stage III hematite (hm) developed along stage II bornite (bn)-stage IV kaolinite (ka) grain boundaries and preferentially replacing bornite (bn) along cleavage planes. Stage III covellite (cv) replaces bornite (bn) on the edge of the hematite-(hm) bornite (bn) grain boundary. UD746-171.7m, reflected light, X10.

Figure 5.6.b. Stage II chlorite-(ch) illite (ill) intergrowths preferentially replaced by stage III hematite (hm). Note stage II chalcopyrite (cpy) and bornite (bn) not replaced by stage III hematite (III). UD746-207.1m, reflected light, X40.

Figure 5.6.c. Stage III hematite (hm) replacing stage II chlorite (ch) and chalcopyrite (cpy). Stage II chalcopyrite (cpy) is only preserved within stage II chlorite (ch). UD746-112.5m, reflected light, X20.

Figure 5.6.d. Relic hexagonal fabric developed in hematite (hm) after bornite (bn). Chlorite (ch) is partially replaced by hematite (hm). UD746-112.5m, reflected light, X8.

Figure 5.6.e. Disseminated chlorite-illite (ch-ill) intergrowth partially replaced by hematite (hm). UD767-181.6m, transmitted light, X40.

Figure 5.6.f. Disseminated pyrite (py) in host quartzite proximal to pyrite (py)-supergene chalcocite (scc) filled vein. UD746-136.2m, reflected light, X1.25.

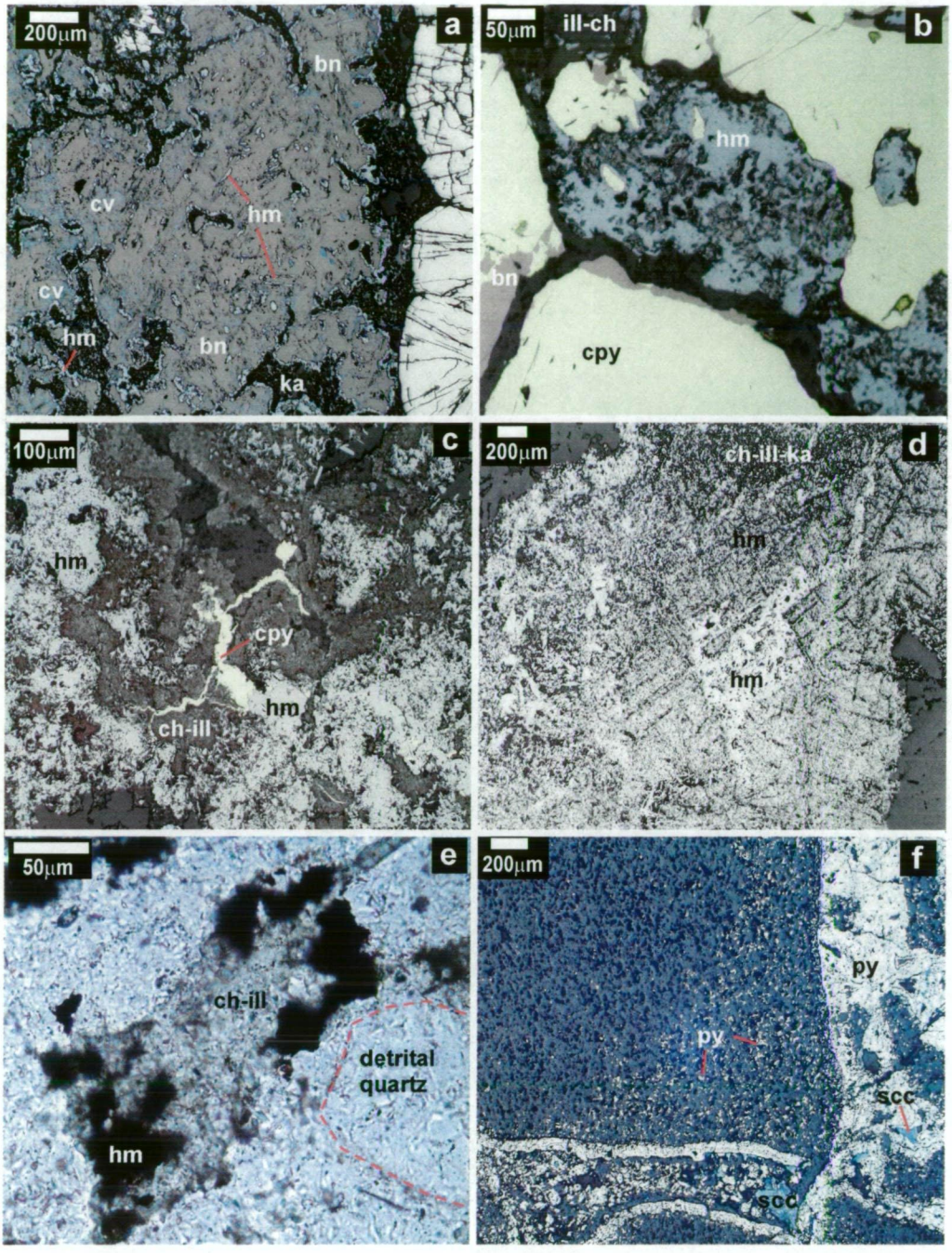
200μm
a
bn
cv
hm
cv
hm
bn
ka
50μm
ill-ch
b
hm
bn
cpy
100μm
c
hm
cpy
hm
ch-ill
200μm
ch-ill-ka
d
hm
hm
50μm
e
ch-ill
detrital
quartz
hm
200μm
f
py
py
scc
scc

located within the weathered zone are subject to oxidation through interaction with air and groundwaters. The mechanisms for the oxidation of such sulfides has been the focus of numerous studies into the formation of supergene deposits and leached out crops (e.g. Blanchard, 1968, Anderson, 1982). The following is largely a review and summary of the processes as presented by these authors.

The processes and end products of sulfide oxidation vary significantly. Oxidation takes place above and below the water table in the presence of acidic and/or neutral solutions. The most significant oxidation process occurs just above and below the water table, where groundwater has access to sulfides through fractures, joint planes and grain boundaries for long periods of time. The rate and extent of oxidation is ultimately governed by the process's ability to generate an acid. Sulfuric acid is primarily generated by the oxidation of pyrite by the following equation:

$$4FeS_2 + 15O_2 + 2H_2O = 2Fe_2(SO_4)_3 + 2H_2SO_4 \text{ (eq. 1)}$$

The above reaction generates ferric sulfate and sulfuric acid. Similar reactions occur when Cu and Cu-Fe sulfides are exposed to oxidised groundwaters, generating additional acid and cupric sulfate. However, the oxidation of pyrite is the more efficient mechanism for the production of acid.

As the groundwater becomes more acidic its capacity to take metals into solution is increased, thereby allowing the metals to be transported away from the site (leached). A groundwater with a near neutral ph will take metals into solution but will not transport them very far. The deposition of metals from these neutral waters occurs, as the ferric sulfate is hydrolysed to form hematite and/or Fe oxides in the following equation:

$$Fe_2(SO_4)_3 + 3H_2O = Fe_2O_3 + 3H_2SO_4 \text{ (eq. 2)}$$

Iron is far more insoluble than Cu in such solutions and is therefore readily hydrolysed to form Fe oxides. Some researchers have reported that traces of Cu co-precipitate with Fe oxides during hydrolysis (Anderson, 1982). Cu is more soluble than Fe and therefore can be partially exported from the site of oxidation.

Groundwaters can remain neutral while the oxidation of sulfides continues, if the acid produced is neutralised or buffered. This may occur as the solution reacts with gangue minerals such as silicates, carbonates and or organics.

In summary, the mechanisms for oxidation of Cu and Cu-Fe sulfides hinges upon the generation of an acid. The ability of the solution to retain its acidity will govern the extent to which the fluid can transport the dissolved metals away from the site of oxidation. If the ph of the solution remains near neutral metals will only undergo local transport.

Effects of supergene alteration on silicate mineralogy

Supergene fluids, through the oxidation of sulfides and the production of sulfuric acid, have the potential to interact with the chlorite-illite intergrowths of the Mammoth deposit. Chlorite, at low temperatures and pressures, is only stable under neutral to alkaline conditions. It will alter to kaolinite upon contact with an acidic fluid via the following reaction:

$$(Mg_3Fe_2Al)(Si_3Al)O10(OH)_8 + 8H_2O + 4H = Al_2Si_2O_5(OH)_4 + 3Mg + 2Fe(OH)_3 + 7H_2O + H_4SiO_4 + 2O_2 \quad \text{(eq. 3)}$$

Therefore, the presence of chlorite can be used as an indicator as to whether a package of rocks has undergone alteration by an acidic supergene fluid (Anderson, 1982). The interaction of chlorite with the acidic supergene fluid (equation 3) has the net effect of buffering the pH to near neutral. A weakly acidic to near neutral fluid may not be able to remove all of the Fe, which may result in the alteration of chlorite to hematite. This can be represented by the following reactions:

$$(Mg_3Fe_2Al)(Si_3Al)O_{10}(OH)_8 + 2Cu + SO_4 + 10H = Fe_2O_3 + Cu_2S + 0.5O + 3H_4SiO_4 + 2Al(OH)_3 + 3Mg \quad \text{(eq. 4)}$$

*Note: cupric sulfite and the sulfuric acid are generated from the oxidation of the Fe and Cu sulfides.

Therefore, chlorite altering to hematite acts as a buffer to keep the fluid at near neutral pH. When the pH of fluid locally decreases (through the process of further sulfide oxidation during the generation of a supergene fluid) chlorite directly alters to kaolinite as per equation.

Anderson (1982) suggests that the presence of hematite in the oxidised, low temperature (<125°C), sulfur-rich systems (that are associated with the oxidation of largely chalcocite-rich ore zones) is widespread. Experimental data does not support the precipitation of hematite from Fe-S systems at temperatures below 125°C. Therefore the occurrence of hematite in these systems does not fit with experimental evidence. This may indicate that the processes associated with oxidation of chalcocite may stabilise hematite in these environments.

In summary, the occurrence of chlorite as an alteration and vein fill phase, indicates that the hypogene mineralogy has not been modified via interaction with an acidic supergene fluid. The replacement of chlorite by hematite occurs at a stage during the generation of a supergene fluid, when the solubility of Fe is not high.

5.4.b D Lens Case Study

D lens, a typical example of the Mammoth ore lenses, represents a significant portion of the total in situ Mammoth resource. The availability of drilling information coupled with the observed zoning of Cu sulfides (Fig. 5.7) renders the ore zone well suited for a petrological study focused on detailing their distribution and genesis. This study focussed on a set of samples that represent the chalcopyrite, bornite, hypogene chalcocite and supergene chalcocite zones of D lens: A total of 42 polished thin sections

taken from diamond drill holes UD746 and UD744 were examined (Fig. 5.7 4.5 and).

D lens mineralisation is located between its known limits of 28200-28450mE and 20600-20750mN and the bulk of the mineralisation is contained beneath 4850mRl and above 4500 mRl. The mineralised zone is confined to the south by the Mammoth Fault and to the east by the Portal Fault. Previous workers have suggested that the gross geometry of D lens, as illustrated in Figure 4.1 was a cylindrical body that had its long axis plunge defined by the intersection of the Portal and Mammoth Faults. This model was generated by 2 %Cu grade contours extracted from a relatively unconstrained block model.

The geometry of D lens has been re-interpreted subsequent to the re-logging of the drill holes on the drill section 20650 mN (Fig. 4.5). The drill holes (UD747, UD746, UD744, UD741, UD740 and UD739) within the section were re-logged using the textural classification scheme (refer Chapter 4). The geometry of D lens is presently interpreted as a series of variably mineralised, stacked brecciated lens. The lenses are interpreted to strike north-east and dip steeply south-east.

A previous investigation of the sample set representing hole UD746, by Gary McArthur (pers. comm., 1998) identified 3 different Cu sulfide zones:

1. chalcocite plus bornite, from 105-116 metres
2. bornite plus chalcocite, from 116-180 metres
3. chalcopyrite plus bornite, from 180-230 metres

A subsequent ore microscopy investigation, on samples from hole UD746 has been further expanded upon during this study. The re-interpretation of the geometry of D Lens together with the observations made from the polished thin section set representing UD746, have resulted in the recognition a more complex mineralogical and textural zonation than was previously reported.

The present study has attempted to subdivide the mineralised zones, representing the stacked breccia bodies that define the geometry of D lens, on the basis of the presence of hematite replacing chlorite and/or Cu sulfides mineralogical and textural variations. Specular hematite occurs with sulfides and chlorite/illite intergrowths and as the major component of breccia matrix and vein fill (Figs 5.3.f, 5.4.d, 5.5.c-d and 5.6. a-d). Textural evidence suggests the specular hematite has replaced, to varying degrees, chlorite and Cu sulfides throughout the sample set.

In sample UD746-112.5m, late chalcopyrite stringers overprint a chlorite vein. Both of which have been replaced by specular hematite (Fig. 5.6.c.). Relict chalcopyrite stringers occur predominantly in residual clots of chlorite. The massive specular hematite variably displays a hexagonal habit (Fig. 5.6.d). This may be the result of the specular hematite pseudomorphing an orthorhombic crystal structure of a mineral previously intergrown within the chlorite-illite filled vein. In sample UD746-171.7m, pyrite and bornite dominate the opaque mineralogy. A pyrite, bornite and chlorite-filled vein has been partially replaced by specular hematite and covellite (Fig. 5.6.a). Specular hematite primarily occurs along the chlorite-bornite grain boundaries and appears to rim the bornite. Within the bornite mass specular hematite has partially replaced the Cu sulfide along its orthorhombic cleavage planes. Covellite occurs as a replacement of bornite and its distribution within the bornite crystal is spatially related to specular hematite. In sample UD746-207.1m, specular hematite has preferentially replaced the chlorite/illite intergrowth of the predominantly pyrite, chalcopyrite and bornite breccia matrix (Fig. 5.6.b). Sample UD746-145.5m consists of pyrite veins that have been brecciated and infilled with bornite, "chalcocite", chlorite and euhedral quartz. Specular hematite has largely replaced the chlorite component of the matrix (Fig. 5.3.f).

In summary, specular hematite occurs throughout D lens in various textural and mineralogical associations. Its occurrence ranges from partial

and preferential replacement through to almost complete replacement of either chlorite (± illite), Fe, Cu and Cu-Fe sulfides.

Distribution of mineralogical associations in D Lens

In order to clarify the distribution of the supergene alteration styles, the variety of mineralogical associations needs to be documented. The key factors are; a) the Cu sulfide species present and b) their spatial association with chlorite, kaolinite and specular hematite.

The distribution of Cu, Cu-Fe and Fe sulfide, hematite and silicate minerals have been plotted onto the D lens section (Fig. 5.7). The textural and mineralogical associations represented within the sample set are complex. A classification scheme was developed in order to simplify these associations. The scheme classifies the samples by the:

1. dominant Cu sulfide phase observed
2. presence or absence of chlorite vs kaolinite
3. the abundance of pyrite

The distribution of the mineralogical phases varies between drill holes and within the brecciated ore zones. Chlorite is present with chalcopyrite, bornite, "chalcocite" and hematite to varying degrees. The kaolinite zones have a decreased abundance of hematite, which corresponds to an increase in the amount of observed pyrite.

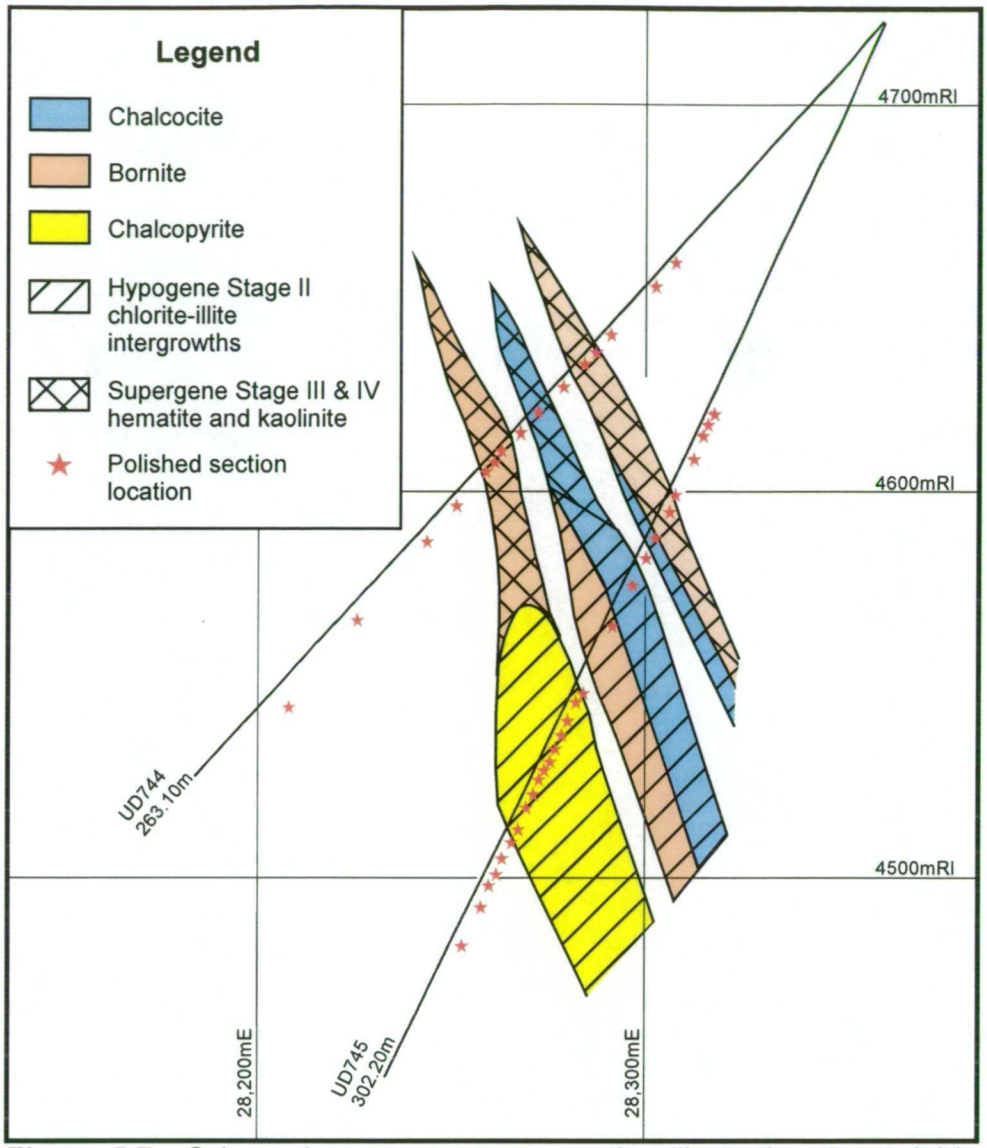

Figure 5.7. Schematic east-west cross section illustrating the variable distribution of alteration and sulfide minerals within D Lens B2 breccia units (Fig. 4.5). Note: chalcocite that occurs with the Stage III and IV hematite and kaolinite mineralogy is interpreted to be of supergene origin and chalcocite occurring with the Stage II chlorite-illite intergrowths is interpreted to be of hypogene in origin. Refer to text for details.

Interpretation of the observed mineralogical and textural zonation in D lens

This study has focussed on D Lens mineralisation and not the entire ore system, so as to reduce the number of variables. It is possible to hypothesise on the genesis of the observed D lens mineralogy by taking into consideration the following:

a) the geometry of D lens mineralisation
b) textural and mineralogical observations
c) mechanisms of sulfide oxidation
d) the effects of supergene alteration on silicate mineralogy
e) the distribution of mineralogical assemblages throughout D Lens

At Mammoth the presence of kaolinite, as opposed to chlorite and illite, is interpreted as an indication that acidic supergene fluids have modified pre-existing mineralogy. The coincidence of bornite being replaced by covellite and the absence of significant specular hematite within the kaolinite dominated zones, further supports the supergene origin for this mineral assemblage.

The absence of chlorite has been widely used as an indicator of alteration via supergene fluids (Anderson, 1982). Within the Mammoth ore system, chlorite commonly occurs intimately associated with the Cu and Fe sulfides. This association suggests that acidic supergene fluids have not interacted and modified the ore mineral assemblage.

The development of specular hematite in these low temperature, oxidised, high sulfur systems, has been reported as anomalous with regard to experimental data. However, the occurrence is reported to be common in environments where "chalcocite" ore bodies are oxidising (Anderson, 1982). The replacement of chlorite and Cu and Cu-Fe sulfides by specular hematite may mark a stage in the transition of a neutral groundwater to an acidic supergene fluid, where Fe has not yet attained solubility.

Therefore, where "chalcocite" occurs in close spatial association with chlorite, "chalcocite" can be interpreted to be of hypogene origin. The presence of kaolinite within an oxidising sulfide body may suggest supergene fluids have modified the silicate and sulfides. The occurrence of specular hematite replacing the chlorite and sulfides suggests the oxidation of sulfides has occurred and any spatially associated "chalcocite", may be the result of supergene alteration.

In summary, the combined interpretation of mineralogy, mineralogical textures and the geometry of D lens has revealed a complex superposition of supergene Cu sulfide and alteration mineral zonation on top of a hypogene Cu sulfide and silicate mineralogical zonation. This petrographic study of the D Lens mineralogy has documented clear evidence supporting the hypothesis that the "chalcocite" mineralogy has both a supergene and hypogene origin. Furthermore, evidence that supergene processes have modified the mineralogy of D lens is documented.

5.4.c Paragenetic Sequence

Within the major ore bodies (B, C, D, E, No. 2 and MFM) the sequence of mineral formation has been established using crystal morphology coupled with replacement and crosscutting relationships. These textural relationships define a four stage paragenetic sequence with Stage 1 and 2 representing mineral precipitation via hypogene processes and Stages 3 and 4 representing mineral precipitation/replacement via supergene processes (Table 5.1).

Table 5.1. Paragenesis for Mammoth ore lenses (B, C, D, E, 2 and MFM)

	Stage I	Stage II	Stage III	Stage IV
Pyrite (disseminated and veined)	----------			
Chalcopyrite		----------		
Carrollite		----------		
Bornite		----------		
Linnaeite		----------		
Hypogene Chalcocite		----------		
Euhedral Quartz	----------			
Chlorite-illite intergrowth		----------		
Hematite			----------	
Supergene Chalcocite and covellite			----------	----------
Wittichenite			----------	
Kaolinite				----------
	Hypogene		**Supergene**	

Stage I

The formation of both veined (euhedral and colloform) and disseminated pyrite within the host rock define the first stage. As outlined above (section 5.3.2) both forms of pyrite are texturally similar (Figs 5.1.b-h, 5.2a-b, 5.2.e-h and 5.6.f). Euhedral quartz crystals often infill void space nucleating from the surface of the vein hosted pyrite (Figs 5.1.e and 5.4.e-f).

Stage II

The major Cu and Cu-Fe sulfides overprint and replace the Stage 1 pyrite and quartz. Chalcopyrite, bornite and hypogene chalcocite often replace and overprint both euhedral and colloform form varieties of veined pyrite (Figs 5.1.e-h, 5.2.a-h, and 5.3.a-g). A coeval origin is proposed for the hypogene chalcocite, bornite and chalcopyrite. The absence of crosscutting textural relationships between the hypogene Cu and Cu-Fe

sulfides supports this proposition. The common occurrence of exsolution textures (Figs 5.2.c, e-d and 5.3.b-d) further support this conclusion. Rare vermiform exsolutions of digenite in bornite have been observed and are included within this paragenetic stage (Fig. 5.3.g).

Chlorite and illite, variably intergrown with each other, infill vug space both within veins and the host rock overprinting the Stage 1 pyrite and euhedral quartz (Figs 5.1.e, g, 5.4.e-f, 5.5.a-f and 5.6.e). The ubiquitous occurrence of the Cu and Cu-Fe sulfides with chlorite-illite intergrowths in conjunction with the absence of any crosscutting relationships between them implying that they formed largely contemporaneously. Rare overprinting textures between hypogene chalcocite and chlorite (Fig. 5.4.g-h) suggest that the hypogene chalcocite, and by inference chalcopyrite and bornite, may have precipitated after the chlorite.

Stage III

Stage 3 is first stage of the supergene modification of the Mammoth ore and gangue mineralogy. This stage is marked by hematite replacing both the Fe and Cu-Fe sulfides and the chlorite-illite intergrowths (Figs 5.3.f, 5.5.c-d and 5.6.a-e). Covellite and supergene chalcocite commonly replace both pyrite, bornite and chalcopyrite (Figs 5.3.h, 5.4.a, and d). Wittichenite only occurs in close spatial association where hematite and supergene chalcocite appear to have replaced bornite and therefore it is interpreted as having formed during Stage 3.

Stage IV

The presence of kaolinite replacing the chlorite-illite gangue characterises the fourth and final paragenetic stage (Figs 5.5.g-h and 5.6.a). The model of supergene process, as outlined above, suggests that the formation of supergene chalcocite and covellite replacing the Fe and Cu-Fe sulfides is also likely during this stage, however no textural relationships supporting this hypothesis have been identified within the Mammoth ore zones during this study.

Relationship between the paragenetic sequence and textural classification scheme

The relationship between the paragenetic sequence derived from microscopic observations and the textural classification scheme derived from core logging is as follows: 1) the hypogene stages I and II are found in all textural classes (S0, S1, S2, B1 and B2); and 2) supergene stages III and IV also occur in all textural styles. The major difference is that hypogene mineralisation is dominated by fracture infill and replacement, where as the supergene overprint is almost entirely replacement.

5.5 CONCLUSIONS

Both hypogene and supergene processes are responsible for the observed mineral zoning in D Lens and by inference the entire Mammoth deposit. The ore and alteration minerals can now be divided into hypogene and supergene assemblages:

- Hypogene assemblage consists of pyrite, chalcopyrite, bornite, hypogene chalcocite, chlorite-illite intergrowths and traces of rutile, carrollite ($CuCo_2S_4$) and linnaeite (Co_3S_4).
- Supergene assemblage consists of hematite, kaolinite, supergene chalcocite, covellite and wittichenite (Cu_3BiS_3)

Textural relationships define a four stage paragenetic sequence: Stage I) hypogene pyrite and quartz; Stage II) hypogene chalcopyrite, bornite, chalcocite and carrollite (trace) + chlorite, illite and quartz; Stage III) supergene hematite, chalcocite, covellite and wittichenite, and Stage IV) supergene kaolinite, chalcocite, covellite and wittichenite.

This work has know made it possible to clearly distinguish the genesis of chalcocite mineralisation using mineralogical and textural criteria: 1) hypogene chalcocite occurs intergrown with chlorite in the absence of kaolinite and/or hematite; 2) supergene chalcocite occurs intergrown with kaolinite and/or hematite in the absence of chlorite.

Hypogene and supergene paragenetic sequences occur in all categories of macroscopic textures of the Mammoth deposit.

CHAPTER 6

MINERAL GEOCHEMISTRY

6.1 SULFIDE GEOCHEMISTRY

This section presents the results of geochemical investigations on major sulfide minerals of the Mammoth ore zones. An understanding of the predictable behaviour of trace elements in many geological environments has contributed to the generation of geological models (Loftus-Hills and Solomon 1967). Major and trace element compositions of ore, alteration and gangue minerals to a large part reflect the physiochemical conditions during their formation (Huston et al., 1995). Because the major element composition of a mineral is controlled by stoichiometry, trace elements may provide additional information about the conditions of alteration and ore formation.

Sulfides can contain high levels of trace elements either as inclusions or within the crystal lattice (Loftus-Hills and Solomon 1967; Huston et al., 1995). Studies of the trace element content of sulfides have the potential to: 1) determine conditions of ore formation; 2) discriminate different classes of ore deposits; and 3) provide vectors in mineral exploration. Using a relatively new analytical technique, laser ablation ICPMS, a trace element geochemistry investigation of the sulfides in the Mammoth ore system was undertaken with two principle aims: 1) distinguish hypogene chalcocite from supergene chalcocite; and 2) identify the trace element geochemistry of the major sulfides within the Mammoth ore system.

6.1.a Previous Work

The trace element geochemistry of the major sulfides pyrite, chalcopyrite, bornite and chalcocite was investigated by Scott and Taylor (1977) and Scott (1986). Individual sulfide mineral separates were obtained from hand specimens with a dentist drill or by using gravity separation methods. Samples were analysed for As, Ba, Rb, Sr, Y, and Zr via XRF; Na, Li, Cu, Pb, and Zn via AAS; and Ag, Bi, Co, Mo, Ni, Sb, Sn and Tl via optical emission

spectrometry (OES). Sulphur and C were determined using a Leco thermal/gravimetric/titrimetric analyser. Chlorite, carbonate and K-feldspar identification was achieved by X-ray diffraction (XRD) analysis on diamond drill core samples, approximately 5 cm in length. The authors note that due to the lack of a suitable calibration standard the data derived from OES, for samples with a high sulfide content, are only semi-quantitative.

Scott and Taylor (1977) and Scott (1986) suggest that both the syngenetic/diagenetic (disseminated) and epigenetic (veined) sulfides can be distinguished via their trace element geochemistry: 1) syngenetic/diagenetic pyrite has higher Co and Ni and lower As, Mo, Sb, and Tl contents relative to epigenetic pyrite, and 2) chalcopyrite associated with syngenetic/diagenetic pyrite is characterised by low Ag, Bi, Mo, Ni and Tl contents relative to epigenetic chalcopyrite. van Dijk (1991) refutes the paragenetic sequence proposed by Scott and Taylor (1977) and Scott (1985) and uses the lack of microstructural distinction between the two styles of pyrite (vein *versus* disseminated) as support for a contemporaneous origin for both styles. The differing trace element and isotopic signature observed between the two styles of pyrite (Scott, 1985) is interpreted to be the result of interaction between the host rock and mineralising fluid (van Dijk, 1991). This chapter will demonstrate that no significant geochemical difference exists between styles of pyrite mineralisation (disseminated or veined).

6.1.b Analytical Procedures

In this study Laser Ablation (LA) ICPMS was used to measure the trace element composition of sulfide minerals. During this program the trace elements Co, Ni, Zn, As, Ag, Sb, Pb, Cu and Bi and major elements S and Fe were analysed.

Sulfide samples were selected from the Mammoth Fault Mineralisation (MFM), 2 and E lens ore zones. Samples chosen included Stage I disseminated and veined pyrite, Stage II chalcopyrite, bornite and hypogene chalcocite and Stage III supergene chalcocite. Individual minerals, optically free of any inclusions, were selected for analysis. The individual sulfide

analyses were screened for sub-surface inclusions using time-resolved data acquisition and data reduction software. All analyses presented here represent homogenous volumes of ablated material at the scale sampled by the laser. Analysis where sub-surface mineral inclusions were encountered have been discarded from the data set.

Methods

Using laser ablation (LA) ICPMS to provide quantitative analysis of geological material is a relatively new technique. Ridley and Lichte (1998) summarise the research studies that have applied this method. LA ICPMS analyses have previously been used to demonstrate that different paragenetic stages of sulfide mineralisation have unique trace element signatures (Viets et al., 1996). However, the study conducted by Viets et al. (1996) only produced qualitative data on the concentration of trace elements in sulfide minerals due to the lack of a suitable calibration material. The present study provides quantitative data on the concentration of trace elements in sulfide minerals.

Procedures by which quantitative results were obtained from the *in situ* microanalysis via LA ICPMS of silicate minerals have been outlined by several authors including Jackson et al. (1992), Longerich et al. (1992) and Norman et al. (1996). Relative element sensitivities of the silicate mineral are calibrated against an external well-calibrated standard. Because different materials ablate at different rates, variations in the volume of ablated material between the external standard and the silicate mineral are corrected for by normalising each analysis to an independently known element, usually a major element determined by emission mass spectrometry (EMP) or assumed from stoichiometry (i.e., an internal standard such as Ca, Mg, Al or Si).

Laser and ICPMS operating conditions

The laser used for this study, was a Merchantek LUV 266 frequency quadrupled Nd:YAG producing a 266 nm wavelength laser beam. Laser repetition rate was set at 5hz (hz = pulses per second) with 60% power setting (0.10mJ/pulse), and a 50μm beam diameter. Power was adjusted to give good ablation without producing significant condensate deposits around

the ablation site. All ablation was done under a He atmosphere with the ablated material mixed with Ar prior to introduction to the ICPMS. The ICPMS used in this study was an Arglent HP 4500, operated in time resolved mode, with one peak per mass and dwell times of 50 msec per mass (Table 6.1.1). Backgrounds were collected for 30 seconds on gas prior to each analysis.

Calibration and standards

To date the limiting factor in the application of LA ICPMS to the quantitative analysis of sulfide minerals has been the lack of suitable calibration materials. Sulfide minerals are known to host a wide range of trace elements and therefore materials with the potential to be external calibration standards must have measurable quantities of these same trace elements. In addition the calibration material should have a matrix that is at least broadly comparable to those of common sulfides in order to assure similar ablation characteristics and provide suitable internal standard elements for normalisation of the analysis. In practice this means a bulk composition with percent levels of Fe, Cu, S, Zn and Pb.

To overcome this problem an in-house calibration standard was synthesized from certified high sulfide rock standards (RTS-4 and CZN-1 CANMET, 1994) with known trace element concentrations. The calibration standard was made via a method used to produce fusion disks of high sulfide material at the University of Tasmania's XRF Laboratory (P. Robinson pers. comm. 2000). For many of the analyses the external calibration standard was analysed in line scan mode by rastering the stage beneath the laser, whereas unknowns were analysed primarily as spots. The benefit of this was better stability of the calibration signal. Analysis of the calibration standard in both spot and line mode shows no difference in results (Fig. 6.1.1)

The rock standards RTS-4 (pyrrhotite) and CZN-1 (Zn-Pb concentrate) are certified standards obtained from CANMET Energy Technology Centre (Table 6.1.2). The standards RTS-4 and CZN-1 were combined in a 3 to 1 ratio and mixed with 12/22 Flux and lithium nitrate in the following proportions:

- 12/22 Flux 4.1210 g
- RTS-4 and CZN-1 composite 0.4000 g
- Lithium nitrate 1ml of 60.6% $LiNO_3$ solution (0.6060g $LiNO_3$)

The composite rock powder and 12/22 Flux require thorough mixing prior to the addition of the lithium nitrate solution. Lithium nitrate ($LiNO_3$) is added to retain S during heating. The materials are combined in a platinum/gold (5%Au/95%Pt) crucible and preheated to 700°C for ten minutes after first mixing well with a platinum wire. Following this the sample is fused at 1000-1100°C, while undergoing gentle agitation, and cast in a platinum-gold mould. The fusion process ensures sample homogeneity and fused products are checked for optical clarity.

The resultant fused wafer was analysed via XRF at the University of Tasmania's Laboratory for major and trace element concentrations (Table 6.1.1). The results of this XRF analysis have been adopted as the reference values (RV) for STDGL-1. Further independent analysis of the wafer was undertaken via ICPMS solution analysis at the University of Tasmania's Central Science Laboratory (CSL) using a Finnegan element high resolution ICPMS. 0.1 g of ground wafer was digested into 100 ml of dilute HNO_3 for solution ICPMS. Both independent major and trace element analysis are in agreement (Table 6.1.1 and Fig. 6.1.2). A total of 51 LA-ICPMS analyses of STDGL-1 were obtained during this study, using the Fe concentration as the internal standard, where STDGL-1 was used as a calibration standard using these reference values (Table 6.1.1). The multiple analyses of the STDGL-1 calibration standard demonstrate both the internal homogeneity of the sample and the long-term analytical precision of this calibration method (Table 6.1.1). An acceptable level of analytical precession (1-6%rsd, Table 6.1.1) has been achieved for the elements S, Co, Ni, Cu, Zn, Ag, Sb, Pb and Bi. Conversely a poor level of precision (≅ 27% rsd) has been achieved for the trace elements As and Mo related to low concentrations and resultant low count rates. Fe is used as the internal standard during the analysis of pyrite, chalcopyrite and bornite and S is used for chalcocite.

In addition the certified rock standards RTS-4 and CZN-1 were prepped, via the method outlined above, and analysed by LA-ICPMS as unknowns calibrated against STDGL-1 (Table 6.1.2). Good agreement is achieved between the LA-ICPMS analysis and the certified reference values for the rock standards. This work provides new data on the concentration of trace elements within the certified rock standards and demonstrates the usefulness of this technique for the analysis of ore materials and the relative lack of a matrix effect.

Table 6.1.1. Relative sensitivities for each mass established by multiple (51) analyses of STDGL-1 analysed as a calibration standard by LA ICPMS, using Fe as an internal standard. Independent analyses of STDGL-1 via XRF and ICPMS solution methods. DL = typical detection limits in ppm for individual analysis under the operating conditions detailed in the text.

	mass	DL	Reference Values for STDGL-1 (XRF) (n=1)	ICPMS Solution (n=1)	LA ICPMS (n=51)	1σ	%rsd
S	34	1429.66	245,700	209,508.11	245,427.50	11,468.6	4.7
Fe	57	69.98	415,700	392,872.67	415,700	0.0	0.0
Co	59	0.11	133	140.92	133.03	1.7	1.2
Ni	60	0.39	5,626	5,669.30	5,625.79	86.1	1.5
Cu	65	0.81	543	514.31	543.26	32.8	6.0
Zn	66	2.01	101,800	82,431.97	101,000.47	2,628.1	2.6
As	75	0.78	253	263.25	257.31	68.7	27.2
Mo	95	1.08	10.43	10.55	10.31	2.9	27.8
Ag	107	0.14	28.22	22.31	28.23	1.4	5.0
Sb	121	0.17	188.59	135.78	188.62	3.8	2.0
Pb	208	0.15	17,000	19,305.10	17,005.12	495.8	2.9
Bi	209	0.05	6.64	9.56	6.63	0.4	6.3

Table 6.1.2. Continuation of Table 6.1.1: Certified values (CANMET) for RTS-4 and CZN-1 compared to LA ICPMS analyses of RTS-4 and CZN-1 analysed as unknowns, via the method detailed in the text, and calibrated against the standard STDGL-1 using Fe as an internal standard. STDGL-1 analysed as an unknown and compared to its reference values.

	RTS-4 Certified Data	RTS-4 LA ICPMS (n=4)	1σ	CZN-1 Certified Data	CZN-1 LA ICPMS (n=4)	1σ	Reference Values STDGL-1 (XRF)	STDGL-1 analysed as an unknown (n=2)
S	359,000.0	320,693.9	10,233.9	302,000.0	228,947.3	9,285.6	245,700.00	262,261.4
Fe	567,000.0	567,000.0	0.0	109,300.0	109,300.0	0.0	415,700.00	415,700.0
Co	186.0	185.6	3.1	-	9.5	0.7	133.00	134.1
Ni	7,940.0	7,876.4	117.7	-	63.9	10.6	5,626.00	5,512.1
Cu	280.0	275.2	15.9	1,440.0	1,449.5	131.0	543.00	521.0
Zn	158.0	202.7	22.8	447,400.0	427,953.4	84,110.5	101,800.00	94,535.8
As	207.0	211.1	59.0	260.0	328.0	33.6	253.00	238.2
Mo	-	8.4	0.7	-	21.6	7.7	10.43	10.3
Ag	-	2.0	0.2	93.0	120.8	23.0	28.22	26.5
Sb	-	0.7	0.1	520.0	853.6	241.0	188.59	166.6
Pb	60.0	72.3	8.4	74,500.0	77,797.1	20,493.7	17,000.00	15,159.8
Bi	3.3	2.6	0.3	27.0	27.4	10.2	6.64	6.0

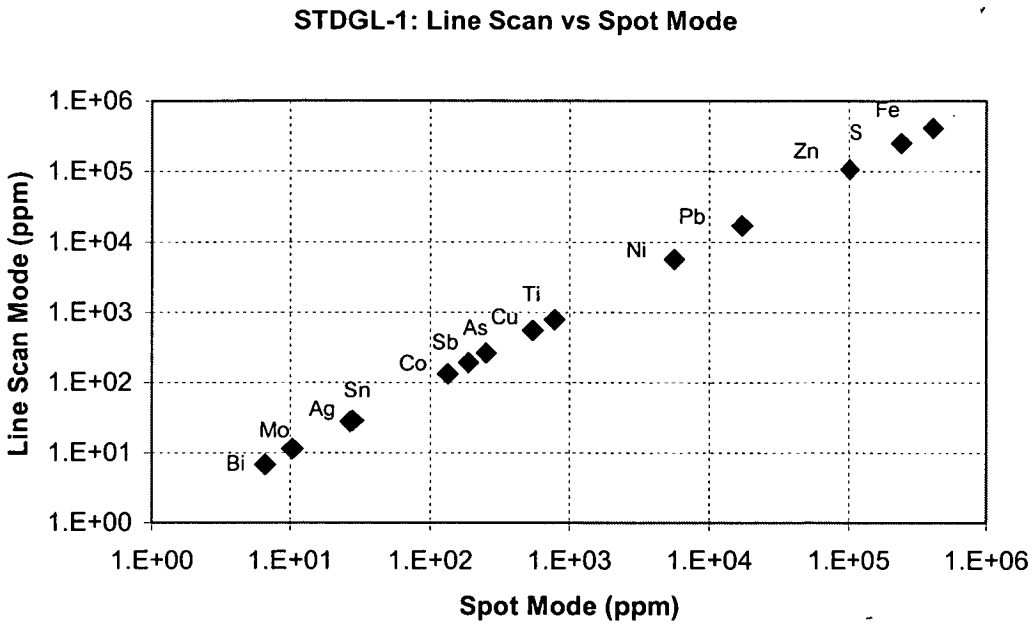

Figure 6.1.1. STDGL-1 analysed in spot mode versus line scan mode.

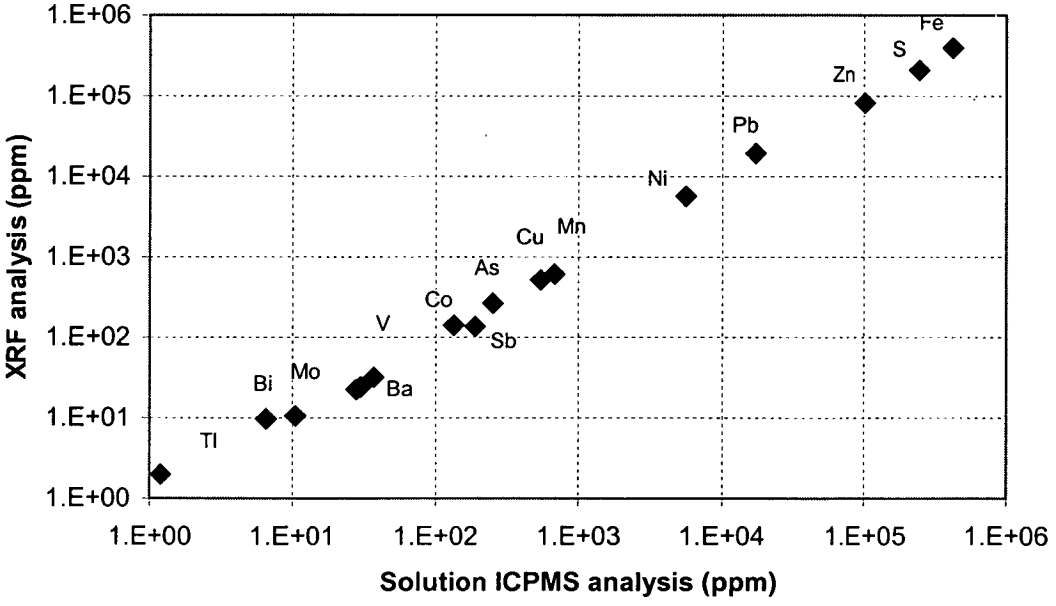

Figure 6.1.2. Correlation between the major and trace elements contained in the STDGL-1 calibration standard (outlined in Table 6.1) analysed via independent methods (XRF vs. solution ICPMS).

6.1.c Results

Sulfides from the Mammoth ore bodies representing both hypogene and supergene styles of mineralisation were analysed. The mean, maximum and minimum trace element concentrations of all analysed sulfides (stage I pyrite

and stage II chalcopyrite, bornite, hypogene chalcocite and stage III supergene chalcocite) are summarised in Tables 6.1.3, 6.1.4, 6.1.5 and Figure 6.1.4 .

Table 6.1.3. Mean, minimum and maximum trace element concentrations of sulfide minerals via Laser Ablation ICP-MS analysis. Sub-ppm detection limits refer table 6.1.4.

Element	Vein Pyrite			Chalcopyrite			Bornite		
	mean	min.	max.	mean	min.	max.	mean	min.	max.
Co ppm	77	0	867	46	0	459	2	0	18
Ni ppm	43	1	399	46	1	171	2	0	5
Pb ppm	955	3	6482	58	0	276	6	0	19
Zn ppm	8	2	57	6	2	7	12	2	70
As ppm	25934	91	66232	219	0	988	9	1	55
Ag ppm	9	0	79	13	0	59	34	3	110
Sb ppm	325	1	1237	142	1	792	1	0	2
Bi ppm	45	0	290	17	2	45	647	139	1262
No. of Analysis		65			18			41	

Element	Disseminated Pyrite			Hypogene Chalcocite			Supergene Chalcocite		
	mean	min.	max.	mean	min.	max.	mean	min.	max.
Co ppm	214	20	881	7	0	21	1	0	8
Ni ppm	152	1	542	1	1	3	2	0	10
Pb ppm	879	238	1748	4	1	12	13	0	87
Zn ppm	7	3	18	16	3	44	8	3	15
As ppm	19620	5136	47776	45	4	261	7	1	29
Ag ppm	10	2	40	302	137	473	23	7	40
Sb ppm	439	104	1290	11	2	31	1	0	4
Bi ppm	74	13	254	26	15	40	83	8	555
No. of Analysis		24			16			33	

Table 6.1.4. Mean, median, minimum and maximum trace element concentrations of Stage I veined pyrite via Laser Ablation ICP-MS analysis categorized by ore zone.

Sulfide		Element								
	Veined Pyrite	Co ppm	Ni ppm	Pb ppm	Zn ppm	As ppm	Ag ppm	Sb ppm	Bi ppm	Cu ppm
E Lens	mean	26	16	1198	8	20523	5	376	24	3947
	median	11	8	596	5	13965	3	257	13	1340
	min.	0	2	5	2	3175	0	0.98	0	8
	max.	137	51	6482	57	51475	19	1130	85	15241
	No. of Analysis	18	20	20	19	20	19	20	18	20
MFM	mean	142	75	865	8	31665	13	432	67	7715
	median	86	48	608	5	28295	6	415	38	2039
	min.	2	1	3	2	91	1	1	0	3
	max.	867	399	3142	48	66232	79	1237	290	76965
	No. of Analysis	24	26	27	21	27	24	26	26	27
2 Lens	mean	38	27	821	8	23350	7	113	35	3913
	median	26	16	745	7	20951	3	61	20	2788
	min.	0	1	23	3	3638	0	3	0	6
	max.	93	95	3141	21	49526	41	363	109	18125
	No. of Analysis	16	18	18	17	18	18	18	17	18
	Detection limit	0.11	0.39	0.15	2.01	0.78	0.14	0.17	0.05	0.81

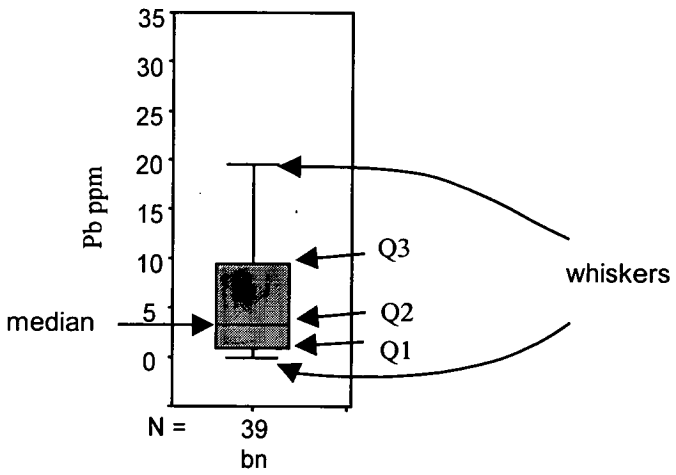

Figure 6.1.3. Box and whisker plots help summarize large amounts of data into an easy-to-read diagram. Related to the median, which separates the data into half, quartiles divide a data set into quarters. Q2 is the median of the data set, Q1 is the median of the lower half of the data and Q3 is the median of the upper half. The difference between the upper quartile and the lower quartile, Q3 – Q1, is called the interquartile range, or IQR. Data values less than Q1 – 1.5(IQR) or larger than Q3 +1.5(IQR) are called outliers. They are data values that are widely separated from the rest of the group of data. Outliers have not been plotted. Whiskers are drawn to the extreme points that are not outliers.

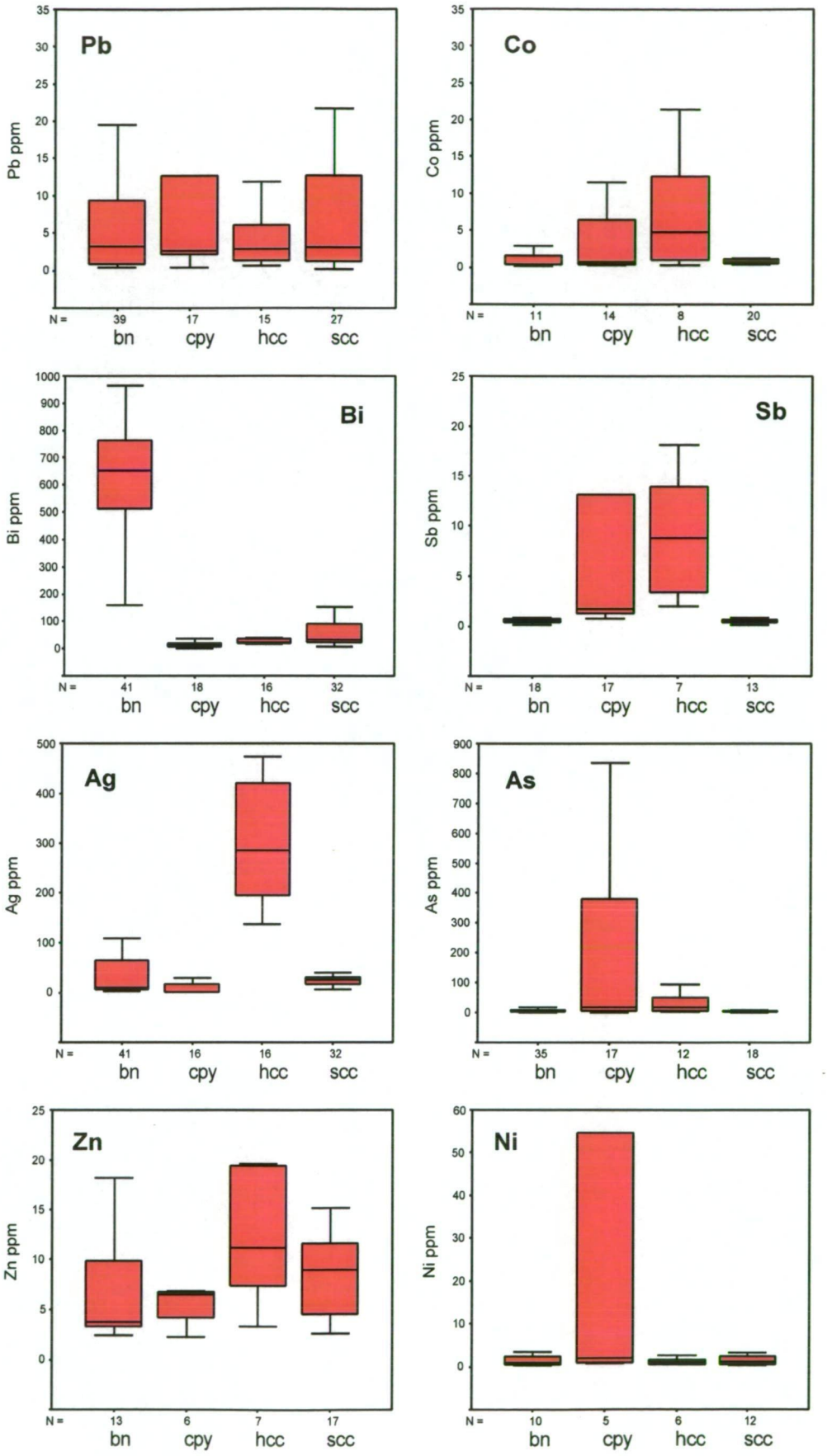
Pb
Pb ppm
N = 39 17 15 27
bn cpy hcc scc
Co
Co ppm
N = 11 14 8 20
bn cpy hcc scc
Bi
Bi ppm
N = 41 18 16 32
bn cpy hcc scc
Sb
Sb ppm
N = 18 17 7 13
bn cpy hcc scc
Ag
Ag ppm
N = 41 16 16 32
bn cpy hcc scc
As
As ppm
N = 35 17 12 18
bn cpy hcc scc
Zn
Zn ppm
N = 13 6 7 17
bn cpy hcc scc
Ni
Ni ppm
N = 10 5 6 12
bn cpy hcc scc

Table 6.1.5. Mean, median, minimum and maximum trace element concentrations of Stage II chalcopyrite and bornite and via Laser Ablation ICP-MS analysis categorized by ore zone.

Sulfide		Element							
Chalcopyrite		Co ppm	Ni ppm	Pb ppm	Zn ppm	As ppm	Ag ppm	Sb ppm	Bi ppm
E Lens	mean	155	75	6	4	228	2	5	13
	median	80	55	3	4	5	2	1	11
	min.	0	1	1	2	0	1	1	2
	max.	459	171	13	7	988	6	13	34
	No. of Analysis	4	3	8	2	7	8	7	8
MFM	mean	2	2	2	7	10	1	1	10
	median	1	2	2		6	1	1	8
	min.	0	1	0		4	0	1	4
	max.	6	2	3		21	1	2	22
	No. of Analysis	6	2	5	1	6	4	6	6
2 Lens	mean	4		219	6	633	54	747	42
	median	1		220	7	681	54	740	45
	min.	1		211	4	380	49	708	38
	max.	12		226	7	836	59	792	45
	No. of Analysis	3	N/A	3	3	3	3	3	3
Bornite		Co ppm	Ni ppm	Pb ppm	Zn ppm	As ppm	Ag ppm	Sb ppm	Bi ppm
E Lens	mean	2	3	7	8	7	72	2	709
	median	2	1	6	5	3	77	1	667
	min.	0	1	1	2	1	28	0	348
	max.	4	7	20	18	33	110	7	1473
	No. of Analysis	5	5	20	4	13	24	10	24
MFM	mean	0	1	5	16	9	19	1	689
	median	0	0	2	7	6	7	1	615
	min.	0	0	0	3	2	3	0	435
	max.	0	2	17	70	30	79	2	1262
	No. of Analysis	5	5	15	7	13	15	6	15
2 Lens	mean	10	3	4	3	11	6	0	579
	median	10	3	3	3	3	5	0	686
	min.	3	1	1	3	2	3	0	139
	max.	18	5	9	3	55	12	1	962
	No. of Analysis	2	2	11	2	10	12	4	12
Detection limit		0.11	0.39	0.15	2.01	0.78	0.14	0.17	0.05

6.1.d Discussion

Loftus-Hills and Solomon (1967) reviewed mechanisms by which trace elements are incorporated into a mineral from a fluid phase. They concluded

that the trace elements are integrated within the crystallising mineral by solid solution, by adsorption or as independent mineral phases. Once incorporated within a crystallising mineral the trace elements are retained either: as exsolved mineral inclusions; in diadochic substitution in lattice defects, in growth zones or in interstitial sites. Griffin et al. (1991) present further discussions into the mechanisms by which trace elements are incorporated into pyrite. They suggest that the trace elements are present as sub-microscopic occluded sulfide and or sulphosalt phases deposited on the growing surfaces of the sulfide. Regardless of the mechanism invoked, to account for trace element incorporation into a crystallising mineral, the researchers (Loftus-Hills and Solomon, 1967; Griffin et al., 1991) conclude that the trace element concentration of a sulfide mineral is contingent upon the physicochemical conditions of the fluid at the time of deposition in addition to the rate of crystal growth. The physicochemical conditions of the fluid phase include the variables: element concentration; pH; oxygen fugacity; pressure; and temperature, all of which in combination control element solubility in the fluid phase. Therefore, the trace element signature for any given paragenetic stage of sulfide style may be used as a diagnostic tool to clarify different generations of mineralising events.

Variation of sulfide trace element geochemistry between ore zones (E, 2 & MFM)

Samples of Stage I veined pyrite and Stage II bornite and chalcopyrite from the MFM, 2 and E lens ore zones were analysed. This suite of samples was chosen to ensure that any potential variation of trace element geochemistry between ore zones would be illuminated.

E Lens vein hosted pyrite is depleted in Co, Ni and Bi (average values: 26 ppm Co, 16 ppm Ni and 24 ppm Bi) relative to MFM (average values: 142 ppm Co, 75 ppm Ni and 67 ppm Bi) and 2 Lens (average values: 38 ppm Co, 27 ppm Ni and 35 ppm Bi) (Table 6.1.4). Veined pyrite from 2 Lens is depleted in Sb (112 ppm) relative to MFM and E lens (Table 6.1.4). Despite these difference the concentrations of Pb, Zn, As and Ag in vein pyrite are

similar between all three ore zones (820-1197 ppm Pb; 8.2-8.4 ppm Zn; 20, 523-31; 664 ppm As; and 5-13 ppm Ag).

The average As, Bi, Co, Ni, Pb, Sb and Zn trace element content of bornite is consistent between the individual ore zones (E and 2 Lens and MFM) (Table 6.1.5). The average concentration of Ag (71 ppm) in the E Lens bornite is elevated relative to MFM (19 ppm Ag) and 2 lens (6 ppm Ag) ore zones (Table 6.1.5).

Spatial variation within individual ore zones

The distribution of trace element concentrations of Co, Ni, Zn, As, Ag, Sb, Pb and Bi within chalcocite, bornite, chalcopyrite and veined pyrite were investigated for spatial variation across individual ore zones (E and 2 lens and MFM). No significant spatial variations in the concentration of these trace elements, in chalcocite, chalcopyrite and veined pyrite were identified. However, the Bi content of bornite, within the E lens ore zone increases with depth and from hangingwall to footwall (Fig. 6.1.5). This variation in the concentration of Bi in bornite with respect to depth is illustrated in Figure 6.1.5, where the Bi concentration increases from 477 ppm at 4110 mRL to 1074 ppm at 4220 mRL. Within drill hole SD255A (Fig. 6.1.5) the Bi content of the bornite increases from 427 ppm, in the footwall, to 674 ppm in the hangingwall. This demonstrated variation in the Bi content may have direct implications to exploration programs targeting near mine extensions to known mineral resources.

Hypogene versus supergene chalcocite

A major focus of this investigation was to document the primary sulfide mineralogy and its relationship to the supergene mineralogy. Despite previous contentions regarding the origin of the chalcocite mineralisation at the Mammoth deposit, work presented here clearly demonstrates that both supergene and hypogene chalcocite mineralisation have distinct geochemical signatures (Table 6.1.3 and Fig. 6.1.4). Stage III supergene chalcocite is enriched in Bi (83 ppm) and depleted in both Ag (23 ppm) and As (7 ppm), compared to hypogene chalcocite (Fig. 6.1.4). These results provide

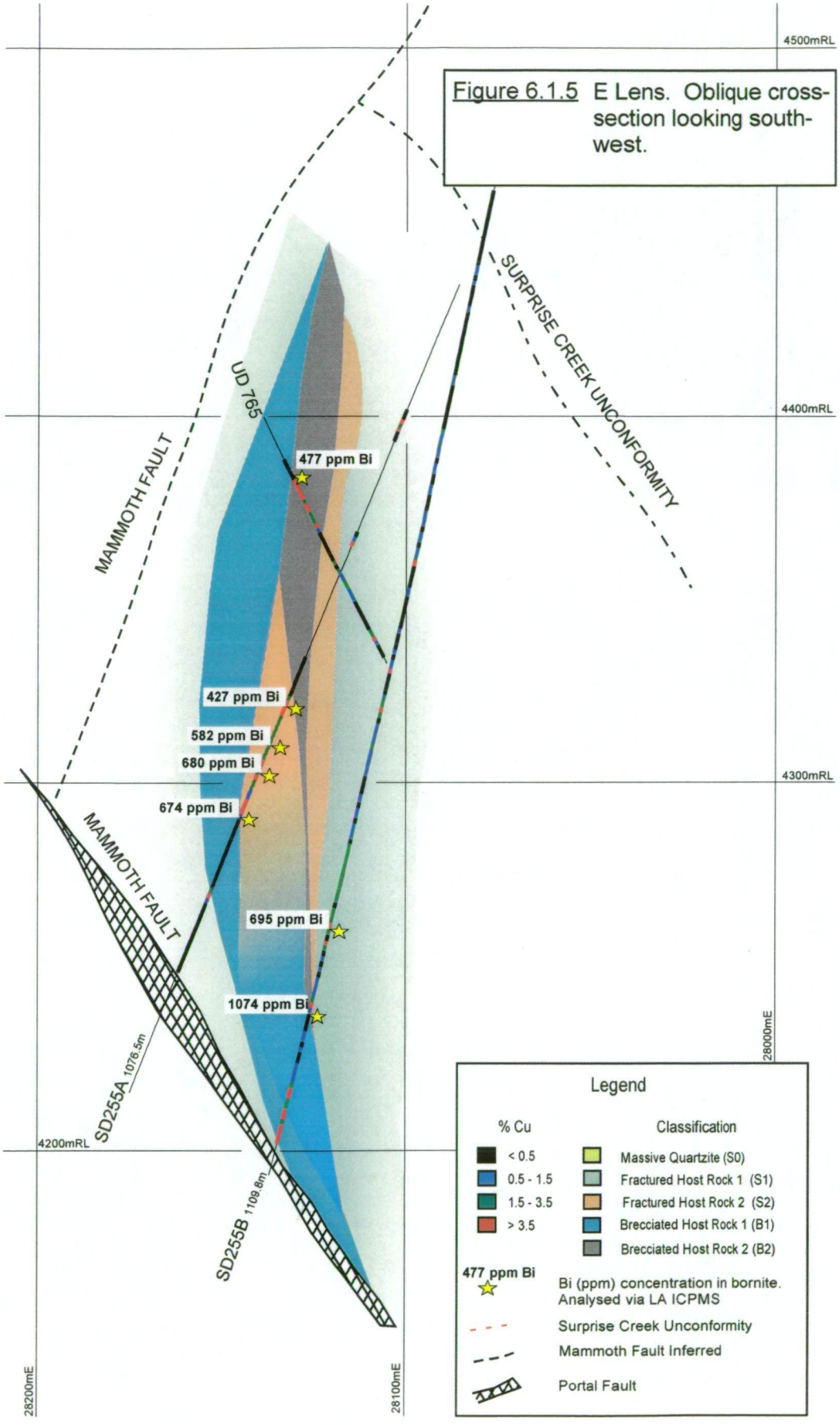

Figure 6.1.5 E Lens. Oblique cross-section looking south-west.

additional evidence to support the proposed paragenetic sequence of Stage II hypogene chalcocite and Stage III supergene chalcocite (Chapter 5).

Veined pyrite versus disseminated pyrite

Both veined and disseminated pyrite occurs throughout the Mammoth deposit. Previous workers did not reach a consensus regarding the genesis of this pyrite mineralisation (Scott and Taylor, 1977; Scott, 1985; and van Dijk, 1991). Geochemical data presented here suggests that the average Co, Ni, As and Sb compositions for both disseminated and veined pyrite overlap, with the minimum and maximum ranges identified for each element broadly similar (Table 6.1.3 and 6.1.4). These data (Tables 6.1.3 and 6.1.4) are interpreted to indicate that no clear geochemical distinction can be made between texturally different styles of pyrite at Mammoth. However, disseminated pyrite is weakly elevated in Ni (152 ppm) and Co (214 ppm) relative to the veined pyrite (43 ppm Ni and 77 ppm Co). However as stated previously the maximum values for both types are similar (Table 6.1.3) and therefore the mean values are not statistically valid. This is interpreted to be a sampling effect due to the width of the laser beam where the width finegrained disseminated pyrite approaches the width of the laser beam. This results in the homogenisation growth ring effects of the data collected.

6.1.e Conclusions

- The ability to obtain quantitative analyses of trace elements in sulfides by LA ICPMS has been demonstrated.

- The trace element geochemistry of the major sulfide minerals associated with Mammoth ore zones clearly indicate that the different paragenetic stages of the sulfides have systematic differences in the abundance of Pb, Zn, As, Co, Ni, Bi, Ag and Sb. Hypogene chalcocite is distinguished by an average abundance of Ag (302 ppm), As (45 ppm), Sb (11 ppm), Co (7 ppm) and Bi (26 ppm) from supergene chalcocite. Supergene chalcocite is enriched in Bi (83 ppm) and depleted in both Ag (23 ppm) and As (7 ppm), when compared to hypogene chalcocite. Both veined

and disseminated styles of pyrite have elevated contents of As, Co, Ni, Sb, and Pb compared to chalcopyrite, bornite and chalcocite. Disseminated pyrite is weakly elevated in Ni (152 ppm) and Co (214 ppm) relative to the veined pyrite (43 ppm Ni and 77 ppm Co). Chalcopyrite has elevated levels of As (219 ppm) and Sb (142 ppm) compared to the other Cu sulfides. Bornite is characterised by an enrichment in Bi (647 ppm) relative to the other sulfides.

6.2 ALTERATION MINERAL GEOCHEMISTRY

The electron microprobe was used to determine the composition and mineral chemistry of chlorite, illite, and kaolinite.

6.2.a Methods

Representative samples of illite, chlorite and kaolinite from the D lens ore zone were chosen and analysed using the Cameca SX50 electron microprobe under the guidance of Dr D. Steele at the CSL, University of Tasmania. Instrument settings were:

Beam Current: 15 nA
Accelerator Voltage: 15 kV
Nominal beam diameter: 5um

Acquisition parameters are detailed in Table 6.2.1. X-ray lines were calibrated using a combination of simple synthetic oxides, pure metals, and natural minerals of 'known' composition. The results have been calculated using XmasPlus quantitative analysis software. Matrix corrections were computed via the PAP procedure. The XmasPlus software calculates detection limits and detection thresholds using the statistical methods outlined in Ancey et al. (1979).

Table 6.2.1. Electron microprobe acquisition parameters

Element		Spectrometer	Xtal	Peak time (sec)	Background time (sec)	Detection Threshold Wt %	Detection Limit Wt %
F	Ka	1	PC0	30	30	0.25	0.20
Na	Ka	4	TAP	20	10	0.06	0.04
Mg	Ka	4	TAP	10	5	0.05	0.03
Al	Ka	4	TAP	10	5	0.06	0.04
Si	Ka	4	TAP	10	5	0.06	0.04

Table 6.2.1. Electron microprobe acquisition parameters

Cl	Ka	2	PET	20	10	0.05	0.03
K	Ka	2	PET	10	5	0.06	0.04
Ca	Ka	2	PET	10	5	0.05	0.03
Ti	Ka	2	PET	10	5	0.06	0.04
V	Ka	3	LiF	30	15	0.08	0.05
Cr	Ka	3	LIF	15	8	0.13	0.07
Mn	Ka	3	LiF	10	5	0.14	0.08
Fe	Ka	3	LiF	10	5	0.16	0.09
Ni	Ka	3	LiF	10	5	0.19	0.11
Zn	Ka	3	LiF	10	5	0.31	0.18
Sr	La	2	PET	30	15	0.28	0.17
Ba	Lb	2	PET	20	10	0.31	0.20

6.2.b Results

The mineral chemistry of chlorite, illite, and kaolinite from D Lens were determined using the electron microprobe generating a total of 30 micro-probe analyses. These analyses are summarised in Tables 6.2.2, 6.2.3 and 6.2.4 and Figure 6.2.1.

6.2.c Discussion

Stage II chlorites from the D Lens bornite-chalcocite zones (samples UD746-111.8mand UD746-112.5m) and the D Lens chalcopyrite-bornite zone (samples UD746-145.5mand UD746-159.2m) were analysed. Only FeO and MgO have significant differences between analyses (Table 6.6.2 and Figs. 6.2.1 and 6.2.2), other elements such as MnO, CaO and Na_2O have only minor variations. Using the classification of Bayliss (1975) compositions from the samples UD746-111.8m and UD746-112.5m indicate these Stage II chlorites are ferro-clinochlore (Fe-rich Mg-chlorites). In contrast, the compositions of the Stage II chlorites in samples UD746-145.5m and UD746-159.2m indicate they are magnesio-chamosite (Mg-rich Fe-chlorite). Ferro-clinochlore occurs in the high Fe-Cu sulfides (chalcopyrite plus bornite) zone of D Lens. In contrast the magnesio-chamosite (Fe-rich Mg-chlorite) occur in the low Fe-Cu sulfide zone (chalcocite plus bornite) of D Lens.

Illite is the dominant alteration mineral in the chalcopyrite zones (Table 6.6.3). The K_2O concentration of the Stage II illite increases down hole (UD746) from 5.4 wt % K_2O at 116.8m to 9.79 wt % K_2O at 223.1m. This

increase in the K_2O the content is consistent with the transition from bornite-chalcocite assemblage at 116.8m to a chalcopyrite dominated assemblage at 159.1m. This observed increase in the K_2O content of illite corresponding with the sulfide transition (from a bornite-chalcocite assembalge to a chalcopyrite assemblage) may be due to either: 1) a slight change in the stabilty field of illite; or 2) a decrease in the solubility of K due to changing pressure, temperature and/or pH conditions of the mineralising fluid. In both cases the illite sampled was representative of direct precipattion (void space fill) as opposed to replacement of variable Potassium rich minerals (eg. Feldspar)

Compositions of two occurrences of supergene Stage IV kaolinite from samples UD746-124.2m and UD746-136.2m were investigated. No significant variation in the composition of kaolinite was observed, however, the possibility that some of the kaolinite is dickite has not been ruled out PIMA analyses of clay mineralogy identified kaolinite only. No XRD analyses were undertaken.

These spatial variations in ore and alteration mineralogy result in an over all hypogene mineral zonation from Stage II chalcopyrite-illite (± ferro-clinochlore), to Stage II bornite (± chalcopyrite) –ferro-clinochlore (± illite) to Stage II chalcocite (± bornite) -magnesio-chamosite (± illite) up dip. Supergene Stages III and IV variably overprint this assemblage to kaolinite as discussed in Chapter 5.

The compositions of alteration minerals at Mammoth are plotted on an Al_2O_3-K_2O-MgO ternary diagram (Fig. 6.2.1). Illite and kaolinite have near perfect stoichiometry. Chlorite has two distinct populations one being Fe-rich and the other Mg-rich. There is no spread in composition between the two-chlorite populations. These data will aid in the interpretation of the whole-rock geochemistry (Chapter 7).

The compositions of chlorite, illite and kaolinite are plotted on. Mineral stability tie lines have been constructed between: 1) the stoichiometric

composition of detrital K-feldspar (microcline) and Mg-rich chlorite (magnesio-chamosite); 2) illite and Mg-rich chlorite (magnesio-chamosite); 3) illite and Fe-rich chlorite (ferro-clinochlore) for use as a template in interpreting the style of alteration present, in the major Mammoth ore lens (B, C, D, E, 2 and Mammoth Fault Mineralisation), from the whole rock geochemical data set (Fig. 7.9).

Table 6.2.2. Electron microprobe analyses of stage II chlorites from D Lens (drill hole UD746).

	UD746 111.8m	UD746 111.8m	UD746 111.8m	UD746 112.5m	UD746 112.5m	UD746 145.5m	UD746 145.5m	UD746 145.5m	UD746 145.5m	UD746 145.5m	UD746 145.5m	UD746 159.2m	UD746 159.2m
SiO_2	33.65	33.95	32.81	31.02	29.39	22.93	23.87	23.79	23.46	23.30	23.56	24.38	24.32
TiO_2	0.00	0.00	0.02	0.03	0.02	0.04	0.03	0.02	0.04	0.00	0.01	0.03	0.02
Al_2O_3	19.69	19.70	20.10	19.32	19.94	21.01	22.12	22.45	22.46	22.62	22.75	22.80	23.54
FeO	8.22	9.41	9.18	11.73	15.40	38.39	36.57	37.22	37.35	39.06	37.07	36.18	37.57
MnO	0.27	0.18	0.22	0.37	0.29	0.10	0.13	0.15	0.19	0.12	0.15	0.10	0.08
MgO	24.97	22.97	24.41	23.21	22.75	4.11	4.23	4.21	4.12	4.37	4.21	4.92	4.93
CaO	0.14	0.10	0.11	0.09	0.07	0.03	0.00	0.00	0.00	0.06	0.04	0.04	0.02
Na_2O	0.06	0.16	0.04	0.09	0.03	0.00	0.03	0.00	0.04	0.03	0.08	0.01	0.01
K_2O	0.00	0.25	0.00	0.01	0.03	0.02	0.29	0.14	0.04	0.03	0.01	0.34	0.07
$H_2O(c)$	12.57	12.46	12.48	12.09	12.10	10.40	10.63	10.70	10.65	10.80	10.70	10.89	11.07
Sum Ox%	99.60	99.23	99.40	97.99	100.01	97.03	97.92	98.69	98.34	100.44	98.59	99.70	101.69
Si	6.42	6.54	6.31	6.15	5.83	5.29	5.39	5.33	5.29	5.18	5.28	5.37	5.27
Al/Al IV	1.58	1.46	1.69	1.85	2.17	2.71	2.62	2.67	2.72	2.82	2.72	2.63	2.73
Al VI	2.85	3.01	2.86	2.67	2.49	3.00	3.27	3.26	3.25	3.10	3.29	3.29	3.28
Fe^{2+}	1.31	1.52	1.48	1.95	2.55	7.40	6.90	6.98	7.04	7.26	6.95	6.67	6.81
Mg	7.11	6.59	7.00	6.86	6.72	1.41	1.42	1.41	1.38	1.45	1.41	1.61	1.59
Ca	0.03	0.02	0.02	0.02	0.01	0.01	0.00	0.00	0.00	0.01	0.01	0.01	0.01
Na	0.01	0.03	0.01	0.04	0.03	0.00	0.02	0.04	0.01	0.00	0.04	0.08	0.01
K	0.01	0.00	0.09	0.01	0.01	0.04	0.01	0.00	0.01	0.01	0.27	0.29	0.03
OH	16.00	16.00	16.00	16.00	16.00	16.00	16.00	16.00	16.00	16.00	16.00	16.00	16.00
Sum Cat#	35.32	35.17	35.46	35.54	35.81	35.86	35.62	35.69	35.68	35.83	35.97	35.96	35.72
Fe/(Fe+Mg)	0.25	0.29	0.27	0.34	0.40	0.90	0.90	0.90	0.90	0.90	0.90	0.88	0.88

Table 6.2.3. Electron microprobe analyses of stage II illite from D Lens (drill hole UD746).

	UD746 116.8m	UD746 124.2m	UD746 124.2m	UD746 145.5m	UD746 145.5m	UD746 159.1m	UD746 193.2m	UD746 193.1m	UD746 193.2m	UD746 193.1m	UD746 223.1m
SiO_2	48.22	48.36	52.26	49.96	49.23	49.48	52.75	51.53	52.19	50.87	50.57
TiO_2	0.01	0.00	0.06	0.01	0.02	0.06	0.11	0.17	0.16	0.07	0.08
Al_2O_3	32.44	33.29	33.83	35.33	32.69	33.48	30.04	33.33	31.25	30.32	31.80
FeO	6.04	3.16	3.04	1.34	1.57	3.31	2.99	1.11	2.72	3.79	4.30
MnO	0.00	0.02	0.00	0.02	0.00	0.00	0.00	0.03	0.04	0.00	0.00
MgO	4.61	0.99	1.24	0.61	1.26	1.69	1.27	1.68	1.46	1.16	1.39
CaO	0.15	0.12	0.11	0.08	0.05	0.14	0.10	0.02	0.11	0.10	0.01
Na_2O	0.14	0.11	0.16	0.49	0.49	0.27	0.09	0.41	0.07	0.07	0.08
K_2O	5.40	8.03	9.36	9.63	8.62	8.40	10.38	10.36	10.07	10.38	9.79
$H_2O(c)$	4.60	4.50	4.77	4.62	4.45	4.61	4.59	4.59	4.62	4.52	4.58
Sum Ox%	101.69	98.63	104.90	102.22	98.59	101.52	102.39	103.41	102.78	101.38	102.71

Table 6.2.4. Electron microprobe analyses of stage IV kaolinite from D Lens (drill hole UD746).

	UD746 124.2m	UD746 124.2m	UD746 124.2m	UD746 136.2m	UD746 136.2m
SiO_2	50.88	49.65	48.76	50.95	51.05
TiO_2	0.00	0.00	0.02	0.04	0.00
Al_2O_3	39.77	40.27	39.78	41.46	40.64
FeO	0.82	0.45	1.75	0.36	0.12
MnO	0.01	0.00	0.00	0.00	0.00
MgO	0.26	0.20	0.17	0.08	0.00
CaO	0.09	0.06	0.02	0.08	0.01
Na_2O	0.09	0.01	0.05	0.02	0.01
K_2O	2.80	0.77	0.51	0.15	0.01
$H_2O(c)$	4.77	4.68	14.56	4.79	14.92
Sum Ox%	99.49	96.09	105.63	97.96	106.80

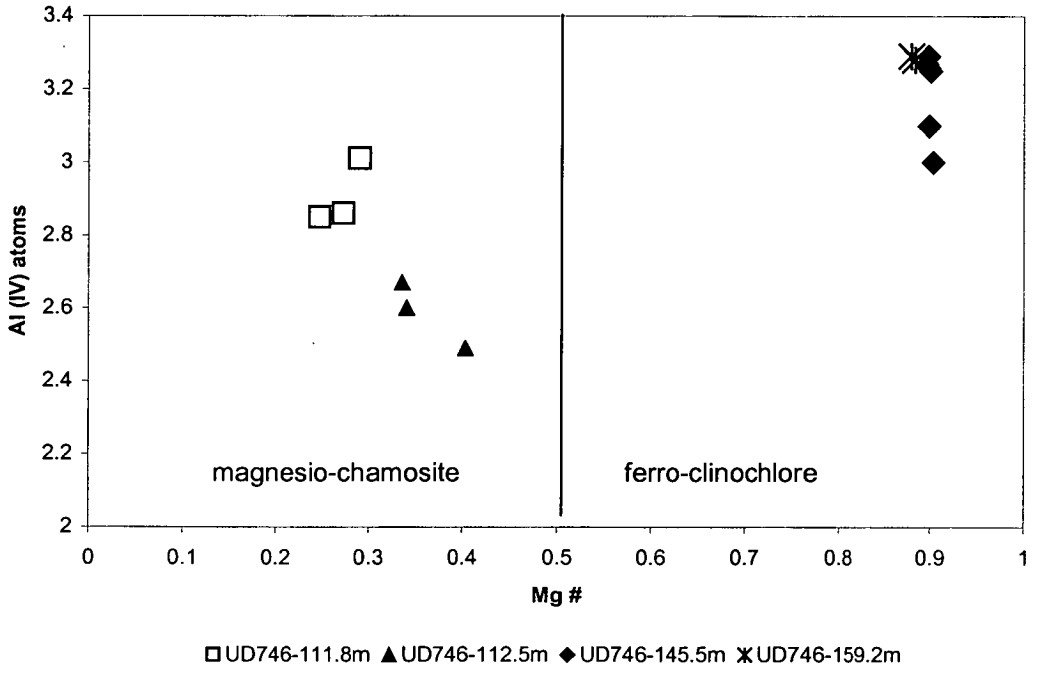

Figure 6.2.1. Compositions of Stage II chlorite for the chalcocite-bornite and the bornite-chalcopyrite dominated zones based on the classification of Bayliss (1975). Chlorites from the chalcocite-bornite dominated zones (UD746-111.8m and UD746-112.5m) are magnesio-chamosite. Chlorites from the bornite-chalcopyrite dominated zones (UD746-145.5m and UD746-159.2m) are ferro- clinochlore. Data from Table 6.2.2.

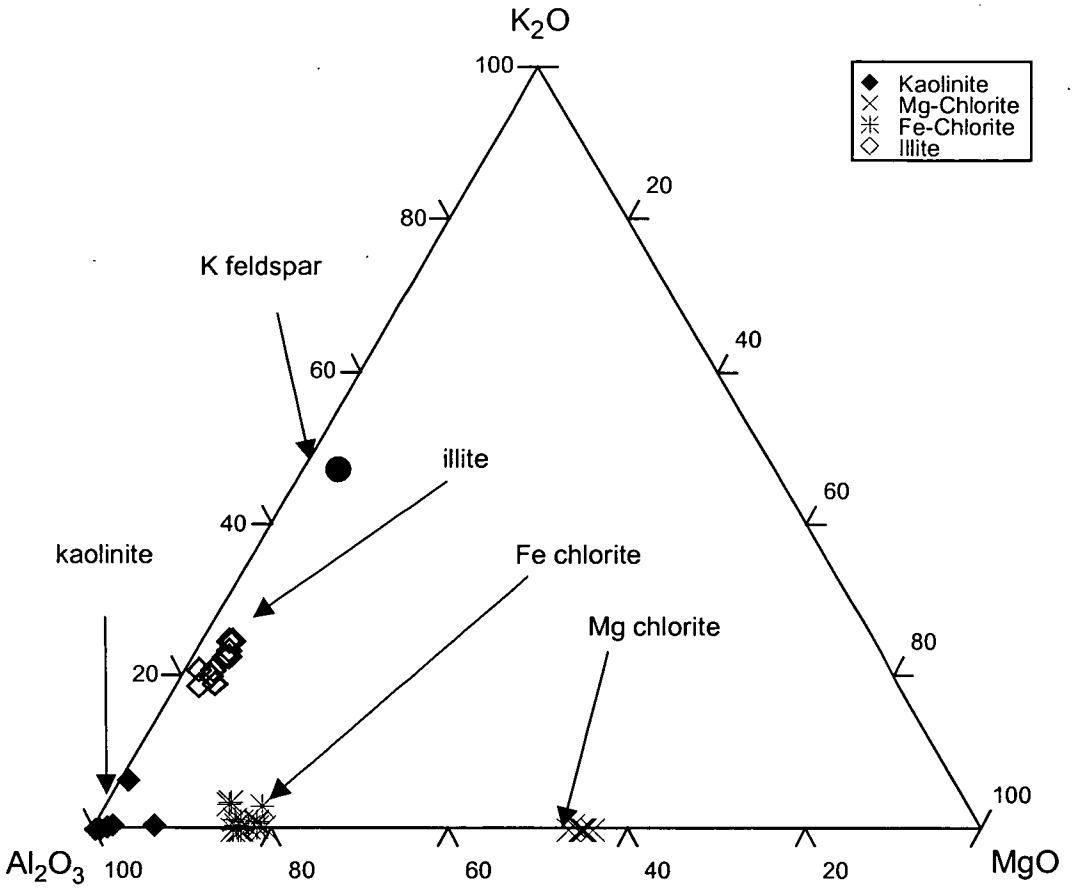

Figure 6.2.2. Electron micro-probe geochemical data from Stage II chlorites (Fe and Mg chlorite), illite and kaolinite plotted as wt% on a Al_2O_3-K_2O-MgO ternary diagram.

6.2.d Conclusions

- Chlorite compositions include magnesio-chamosite and ferro-clinochlore. The bornite-chalcopyrite dominated ore zones are associated with ferro-clinochlore compared to the chalcocite-bornite dominated ore zones where magnesio-chamosite occurs.
- The K_2O concentration of illite is elevated in the chalcopyrite dominated zones in contrast to the bornite-chalcocite dominated zones
- The occurrence of kaolinite has been confirmed as occurring in the Mammoth gangue mineralogy.

CHAPTER 7

WHOLE-ROCK GEOCHEMISTRY AND METAL ZONATION OF THE MAMMOTH ORE SYSTEM

7.1 INTRODUCTION

The major goals of this chapter are to: 1) investigate the geochemical characteristics of the ore and alteration and 2) document the metal zoning throughout the deposit. These goals will be achieved by:

- Documenting the geochemistry of the alteration and gangue minerals.
- Characterising the geochemical signatures of the categories of the textural classification system.
- Documenting the geochemical signature of both the Mammoth ore zones and spatially associated alteration halos.

Documenting the metal zonation and geochemistry of the deposit will be achieved by a comparison between the spatial distributions of the major and trace element geochemistry and the ore and alteration mineralogy. It is anticipated that an investigation of the alteration mineral and metal zonation associated with the Mammoth deposit will lead to an understanding of primary controls responsible for the formation of both the hypogene and supergene ore and alteration minerals.

The data set used in this chapter has either been generated during the course of this project or sourced from the company's archive. Conclusions and assumptions reached in this chapter are based on and supported by conclusions reached in Chapter 5 Mineralogy, Alteration and Paragenesis.

7.2 PREVIOUS WORK

Scott and Taylor (1977) and Scott (1986) describe the style of mineralisation, sulfide geochemistry and wall rock alteration in and about No. 1, B and C orebodies and sub-economic mineralisation hosted within the Surprise Creek

Formation immediately adjacent to the Mammoth deposit. The zone occurring between the ore body and the most proximal major fault (Mammoth or Portal Faults) has been referred to as the footwall, relative to the ore zone (Scott and Taylor, 1977). In this chapter this zone will be referred to as the hangingwall as it predominantly occurs structurally above the ore body (refer Chapter 3).

Scott and Taylor (1977), Scott et al. (1985) and Scott (1986) reported that the wall rock alteration associated with the major orebodies (No. 1, B and C) is characterised by alkali depletion and Fe-enrichment in the hangingwall. The footwall is enriched in K, Na and Ba relative to the hangingwall. Variations of the Ca, P, Sr and Y were considered to be primarily associated with the distribution of detrital apatite and therefore their distributions were not considered relevant to the mineralising system. Within the upper levels of B and C orebodies the occurrence of kaolinite mixed with rare sulphates and phosphates was noted. Their geochemical study concludes that within the ore zones the primary detrital feldspars were altered to sericite and chlorite. The ore zones are noted to have an observed enrichment in the trace elements Ag, As, Bi, Co, Cu, Mo, Ni, Pb, Sb and Tl. These previous studies identified the anomalous concentrations of Ag, Bi, Mo, Pb, and Sb to be associated with Cu sulfide mineralisation. In contrast As, Co, Ni and Tl were found to be associated with pyrite mineralisation (Scott, 1986).

In order to account for the observed geochemical variations the conclusions reached by Scott and Taylor (1977), Scott et al. (1985) and Scott (1986) are based upon a genetic model that included both syngenetic and epigenetic styles of mineralisation. A lack of recognition of the meteoric and supergene oxidation processes weakens their conclusions. The processes of meteoric and supergene alteration have led to complex geochemical dispersion patterns overprinting geochemical patterns developed during hypogene mineralisation.

7.3 METHODOLOGY

7.3.a Whole-Rock Geochemistry (XRF) & Trace Element Geochemistry (ICP-OES)

After an investigation of previous literature (Scott and Taylor, 1977; Scott et al., 1985; Scott 1986), combined with hand sample and thin section observations, the following element suite was chosen for analysis to provide valuable information on the geochemical signature for the host rocks alteration and mineralisation. This suite included the major oxides and the following trace elements Ag, As, Ba, Bi, Co, Cu, Ga, Mo, Ni, Pb, Rb, Sb, Sc, Se, Sn, Sr, Tl, V, Y, Zn, and Zr. It was anticipated that V, Zr and Y may reflect variations in the composition of the host rock. In addition to the elements previously found to be associated with Cu and pyrite mineralisation (Ba, Ga, Rb, Sc, Se, Sn, Sr and Zn) are likely to be associated with mineralisation.

The sample set available for geochemical analysis consists of composite sample pulps and hand samples collected from drill core and surface outcrop. The sample pulps are typically averaged over composite lengths of 1.5 metres. The distribution of the composite sample pulps is limited to the intervals that were routinely analysed for either Cu or Cu, Fe and As or Cu, Fe, Co, Ni, Pb, Zn and As by company geologists. Typically only the known ore horizons and significantly altered intervals were analysed. Therefore potential distal alteration and/or weakly mineralised zones are not represented in the company sample set. The suite of elements analysed by company geologists changed through time resulting in an inconsistent data set. Furthermore detection limits provided by the routine analyses of composite samples were high (Zn>25ppm, Pb>50ppm, Co>25ppm & As>50ppm). Early on during the course of this study the method of routine analyses of drill core by company geologists changed to include the trace elements Ag, As, Mo, Ni, Co, Cu, Bi, Sb, Zn, Fe, MnO and Pb, analysed via multi-acid digest with analysis by ICPOES at the Analabs Laboratory in Townsville; thereby standardizing the analytical methods for data collection.

Drill holes included in this study, that were analysed via this method, are from the E Lens ore zone and include SD255A, SD255B and UD765 (Table 7.1).

Table 7.1. Summary of analytical methods and data sets used during this geochemical investigation.

Ore Zone	Sample Set ID	Method of Analysis
B	UD611, UD642 UD651, UD676 UD708, UD717	XRF majors and trace elements.
C	UD732, UD734	XRF majors and trace elements
D	UD739,UD744 UD746	XRF majors and trace elements. Subset for Au and Ag via Fire Assay/ Flame Atomic Absorption Spectrometry for Au and Multi-acid digest/ICPMS for Ag.
E	SD254^* SD255^* SD255A^{+} SD255B^{+} UD765^{+}	^XRF majors and trace elements. $^{+}$Total digest/ICPOES for trace elements. *Subset for Au and Ag via Fire Assay/ Flame Atomic Absorption Spectrometry for Au and Multi-acid digest/ICPMS for Ag
2 Lens	UD767 UD768 Surface Outcrop^	XRF majors and trace elements.
Mammoth Fault Mineralisation	UD768	XRF majors and trace elements

Individual drill core, surface rock chip and pulped drill core composite samples were collected. The sampling strategy ensured that a comprehensive mineralogical and textural sample suite was collected. One hundred and seventy four samples, both pulps and individual hand samples, were analysed by XRF. Samples were crushed, pulverised (tungsten-carbide mill) and made into pressed powder pills and disks, by the author. They were then analysed for major and trace elements by XRF at the University of Tasmania. XRF analyses were conducted by Phil Robinson on a Phillips, PW1480, X-ray florescence spectrometer. This sample set consisted of samples from the drill holes that intersect E, D, C, B, 2 lens ore zones and the Mammoth Fault Mineralisation (MFM) and the surface out crop of 2 lens. Barren hangingwall and footwall lithologies spatially associated with the ore zones were represented. The samples were classified in accordance with the textural classification scheme, (refer Chapter 4) as either: 1) Unfractured Host Rock (S0); 2) Fractured Host Rock (S1-S2) and 3) Brecciated Host Rock (B1-B2).

7.4 RESULTS

The results of geochemical program have been plotted against down hole depth for the drill holes that intersect E, D, C, 2 and MFM ore zones (Figs 7.1.a-f, 7.2.a-i, 7.3.a-f, 7.4a-i). Geology, logged using the textural classification scheme (Chapter 4) and ore zones or ore zone equivalent horizons are shown on the down hole plots. In addition the distribution of non-sulfide alteration and/or vein and breccia matrix fill minerals either, as logged during the project (E Lens) or as represented in the company drilling database are also plotted against down hole depth. The varying intensity of alteration mineralogy has been recorded in the company database in a numerical form, ranging from 1 to 5 which corresponds to weak (1) to extreme (5) for either chlorite, quartz, illite, hematite and/or kaolinite. In general, the intensity of only chlorite, quartz and hematite have been recorded in the company database. The occurrence of kaolinite in drill holes intersecting the 2 Lens and MFM ore zones was recorded in the company database. The occurrence of chlorite is interpreted here to include illite as was demonstrated in Chapter 5. The percent and type of sulfides occurrence, logged by hand specimen investigation, are also plotted against down hole depth.

7.4.a E Lens

The geochemical characterisation of the hangingwall, footwall and ore of the E lens ore body is based on assay data from drill holes SD255A, SD255B and UD765 (Fig. 4.6) (Appendix 3). This data set was assayed for the major and trace elements Fe, MnO, Cu, Pb, Zn, Ni, Co, Mo, Ag, As, Bi, and Sb via multi acid digest and ICPOES analysis (Table 7.1). The lack of a comprehensive suite of major element concentrations (SiO_2, TiO_2, K_2O, CaO, P_2O_5, Na_2O and Al_2O_3) precludes a discussion on the distribution and zoning of the alteration mineral chemistry.

SD255B intersects the E lens ore zone from 1081-1098m at ~ 4200mRL where it is interpreted to abut the Portal Fault. SD255A intersects the ore zone from 955-991m at ~ 4320mRL, 125m up dip from the ore intersection in

SD255B. UD765 intersects the ore zone from 381-397m at ~ 4390mRL, 70m up dip from the ore intersection in SD255A.

Samples from hole SD255b represent the barren brecciated footwall (B1) of the E lens ore zone, the high-grade brecciated ore zone (B1) from 1081-1098m, the barren hangingwall (B1) from 1098-1101m and the Portal Fault from 1101-1109.8m. Samples from hole SD255A represent the barren brecciated footwall (B1) of the E lens ore zone from 950-955m, high grade brecciated ore zone (B1) from 955-963m, mineralised S2 unit from 963-991m, and barren hangingwall S2 unit from 991-1000m and the barren hangingwall B1 unit from 1000-1010m. Samples from hole UD765 represent the barren hangingwall B1 unit of the E lens ore zone from 375-381m, high-grade B2 ore zone from 381-397m, barren footwall B2 unit from 397-403m and barren S2 unit from 403-405m.

The intensity of the alteration mineralogy of the footwall ranges from quartz ± hematite and very weak chlorite in hole SD255B to hematite ± quartz in hole SD255A to quartz and weak hematite and chlorite in hole UD765. Alteration mineral intensity in the hangingwall units is dominated by chlorite with exception that the occurrence of hematite increases relative to and at the expense of the chlorite content up dip.

The sulfide mineralogy of E lens ore zone as represented by the drill holes UD765, SD255A and SD255B consists of pyrite (FeS_2), chalcopyrite ($CuFeS_2$), bornite ($Cu_5 FeS_4$) and chalcocite (Cu_2S). Bornite is the dominant Cu-Fe sulfide mineral present in all three E lens drill holes. Chalcocite occurs within the hangingwall contact of the ore zone in hole SD255A. Chalcopyrite occurs throughout the ore zone in trace amounts, with the exception of holes UD765 and SD255B where it occurs with bornite and pyrite above the footwall contact of the ore zone. Pyrite is ubiquitously distributed throughout the ore zone, reaching concentrations of > 60% in hole UD765 and > 80% in hole SD255A. In general the Cu sulfides appear to be zoned from hypogene chalcocite and bornite in the hangingwall through to bornite and chalcopyrite in the footwall.

Element distributions are summarised in Table 7.2. In general, Pb, Ni, Co, Sb and Bi concentrations are elevated in the footwall barren B1 unit relative to the barren hangingwall units in 255A and 255B. Arsenic, Sb, Bi and Pb are elevated within the barren footwall B2 unit, relative to the hangingwall B1 unit intersected in UD765. In contrast, the concentration of Zn is higher (> 85 ppm) in the barren hangingwall S2, B2 and Portal Fault zones, relative the barren footwall units, and in general Zn correlates with the occurrence of chlorite. The distribution of Cu, Ag and Bi within the E lens ore zone corresponds to the primarily bornite content and to a lesser extent the chalcopyrite and hypogene chalcocite content. The Ag content of hole SD255A notably increases with a corresponding high hypogene chalcocite content.

Table 7.2. Element distributions in E lens drill holes SD255A, SD255B and UD765.

Drill Hole	Element	Comment on distribution
SD255B	Cu	Low in footwall and hangingwall, highs correspond to elevated bornite and to a lesser extent the chalcopyrite content in the ore zone
SD255B	As	Broadly similar to Cu, however peaks with increase in pyrite content
SD255B	Pb	Similar to As
SD255B	Ni	Elevated in footwall and hangingwall relative to ore zone, however peaks with increase in pyrite content as for As
SD255B	Co	Similar to Ni
SD255B	Sb	Similar to As, peaks with corresponding increase in pyrite content, elevated footwall, relative to hangingwall, where it corresponds to an increase in hematite content
SD255B	Zn	Weakly elevated in footwall, depleted in ore zone, peaks in hangingwall with corresponding increase in chlorite content
SD255B	Ag	Similar to Cu
SD255B	Bi	Weakly elevated in the hangingwall and footwall units, highs correspond to bornite increased bornite content
SD255B	Fe	Depleted in hangingwall to ore zone, erratic throughout ore zone
SD255A	Cu	Elevated in ore zone, peaks in footwall and hangingwall correspond to elevated bornite content in footwall and hangingwall and chalcocite content in hangingwall
SD255A	As	Flat background in hangingwall and footwall, peaks correspond to pyrite content in ore zone
SD255A	Pb	Weakly elevated in footwall, similar to As in ore zone
SD255A	Ni	Elevated in footwall, variable throughout but peaks predominantly correspond to high pyrite contents
SD255A	Co	Similar to Ni
SD255A	Sb	Similar to As, with the exception that it is elevated in hangingwall with a corresponding increase in hematite
SD255A	Zn	Elevated in footwall (~ 80 ppm), low through ore zone, significantly elevated in hangingwall units corresponding to an increase in chlorite content
SD255A	Ag	Similar to Cu and Bi, significant peak corresponds to occurrence

Table 7.2. Element distributions in E lens drill holes SD255A, SD255B and UD765.

Drill Hole	Element	Comment on distribution
		of chalcocite in the hangingwall contact of the ore zone
SD255A	Bi	Similar to Cu and Ag, distribution in ore zone correlates to bornite content
SD255A	Fe	High in footwall to ore zone, erratic throughout ore zone
UD765	Cu	Elevated in ore zone, broad high corresponds to bornite content in hangingwall ore zone
UD765	As	Weakly elevated in footwall, broad high corresponds primarily to pyrite content and secondly to chalcopyrite content
UD765	Pb	Similar to Pb
UD765	Ni	Elevated in hangingwall and footwall units and depleted in the ore zone relative to hangingwall and footwall units
UD765	Co	Similar to Ni
UD765	Sb	Broad plateau in ore zone and footwall (> ~ 80 ppm) from ~ 30 ppm in the hangingwall
UD765	Zn	Similar to Ni and Co
UD765	Ag	Similar to Cu, corresponds to bornite content
UD765	Bi	High in hangingwall of ore zone, weakly elevated in footwall concurrent with hematite front
UD765	Fe	Elevated in ore zone

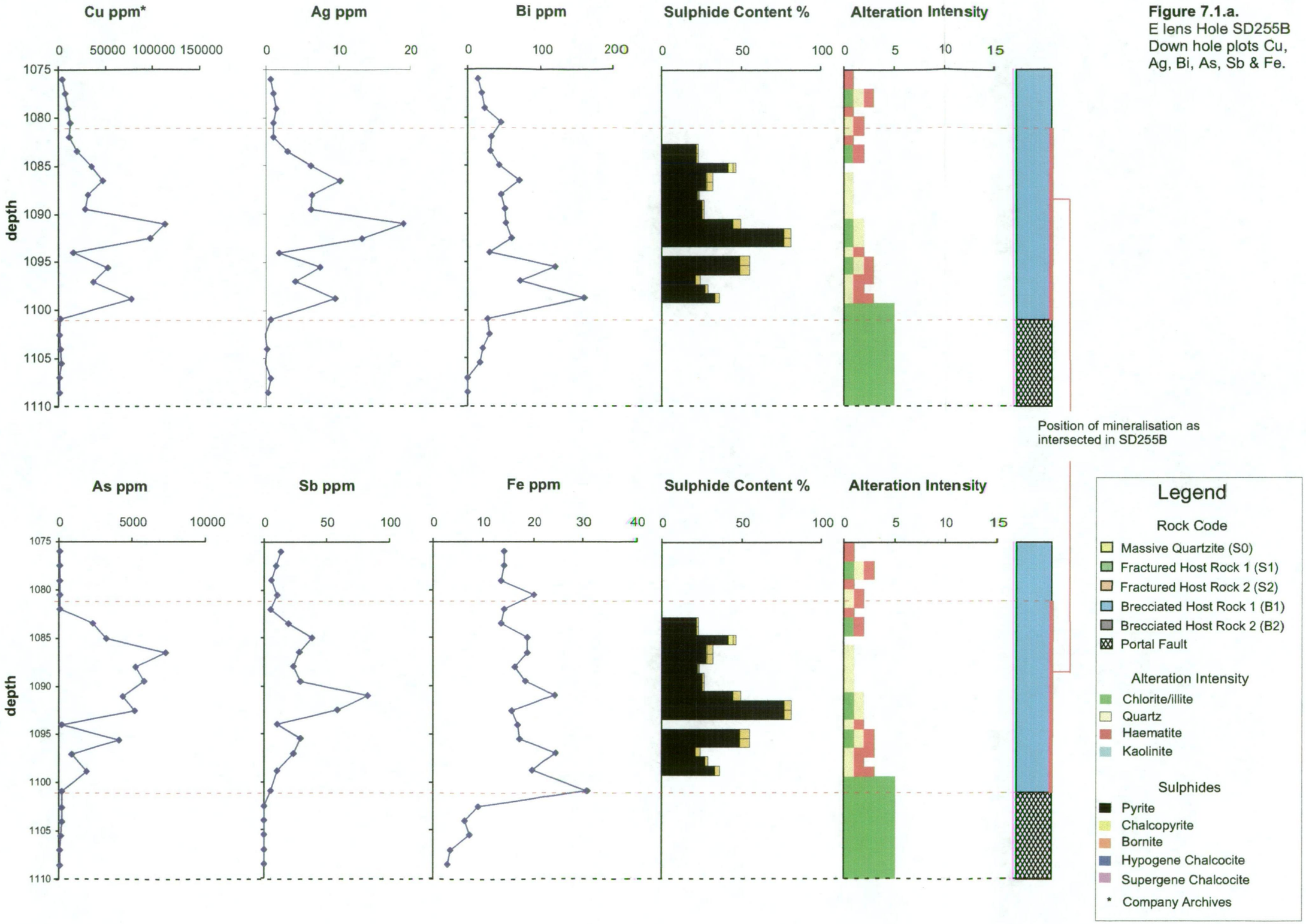

Figure 7.1.a.
E lens Hole SD255B
Down hole plots Cu, Ag, Bi, As, Sb & Fe.

Figure 7.1.b
Elens Hole SD255B
Down hole plots As, Pb, Ni, Co & Zn.

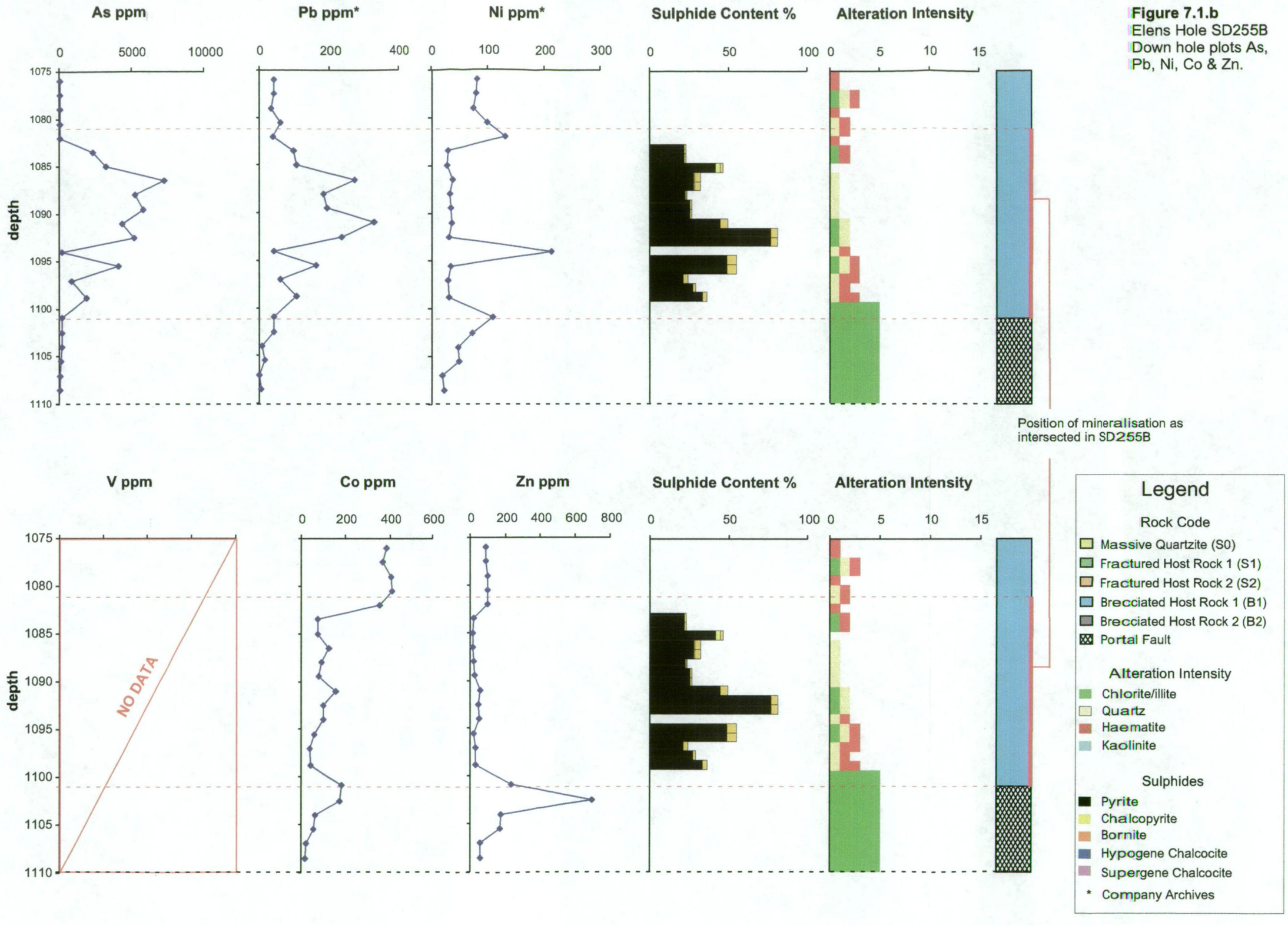

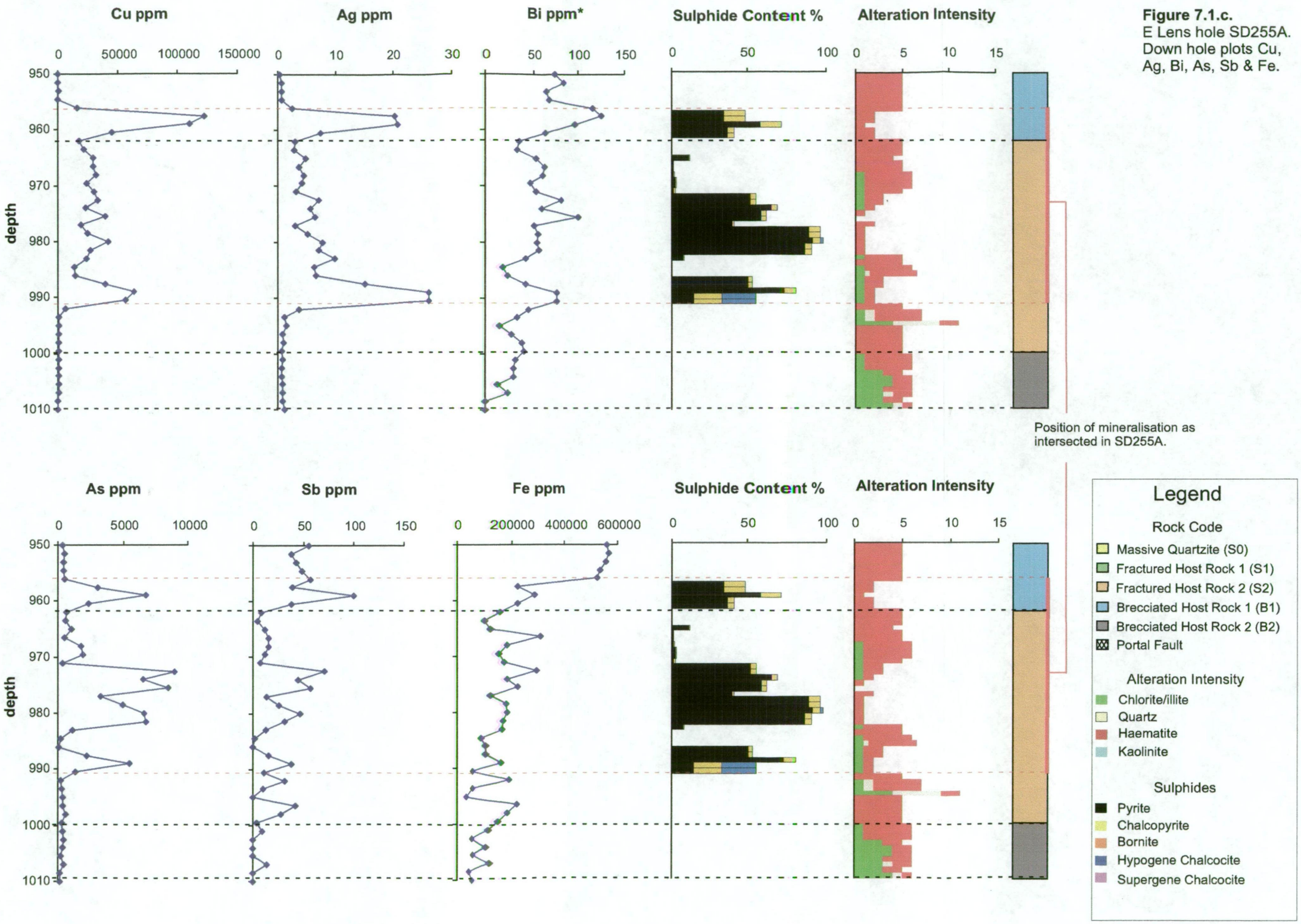

Figure 7.1.c.
E Lens hole SD255A.
Down hole plots Cu, Ag, Bi, As, Sb & Fe.

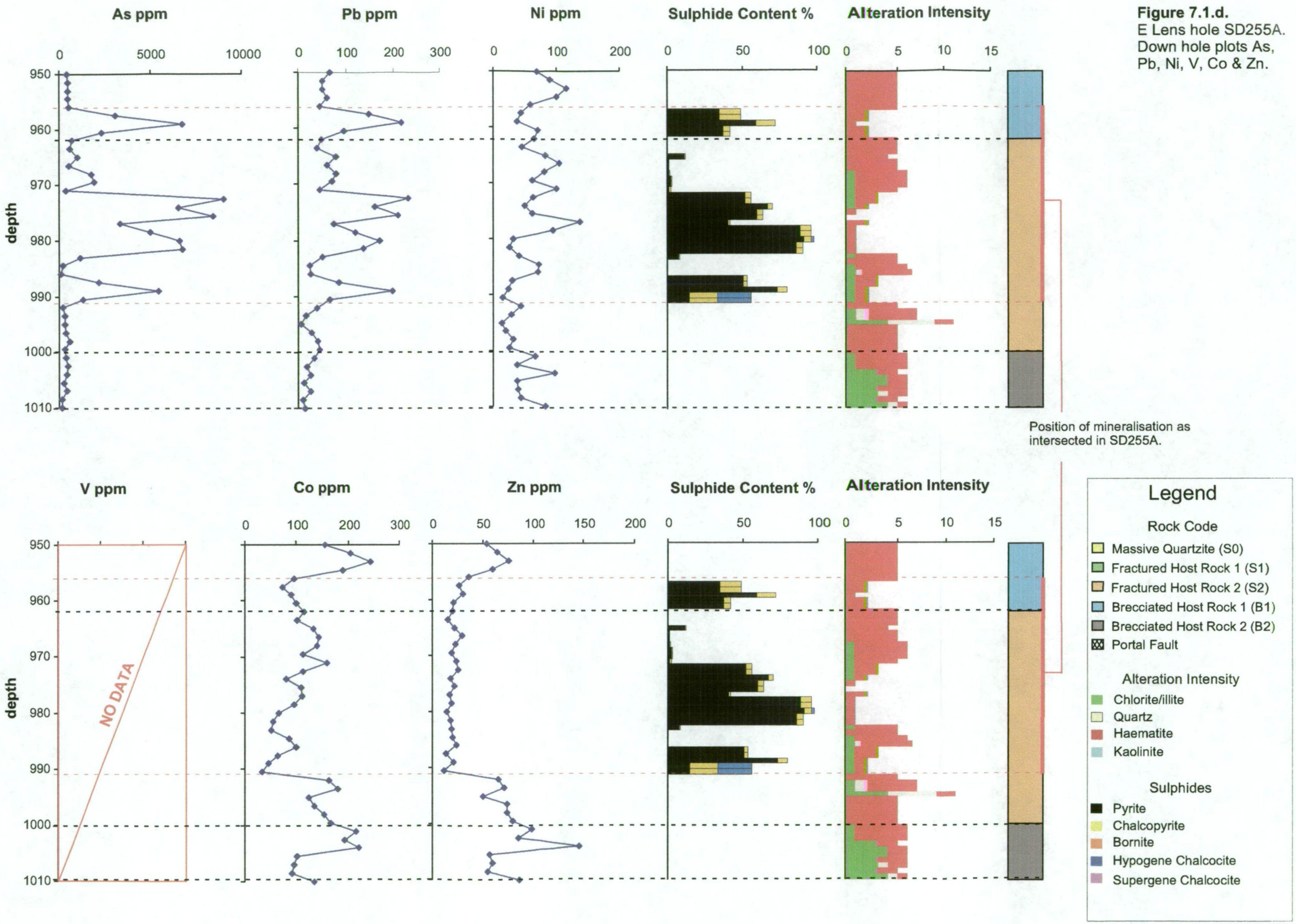

Figure 7.1.d.
E Lens hole SD255A.
Down hole plots As, Pb, Ni, V, Co & Zn.

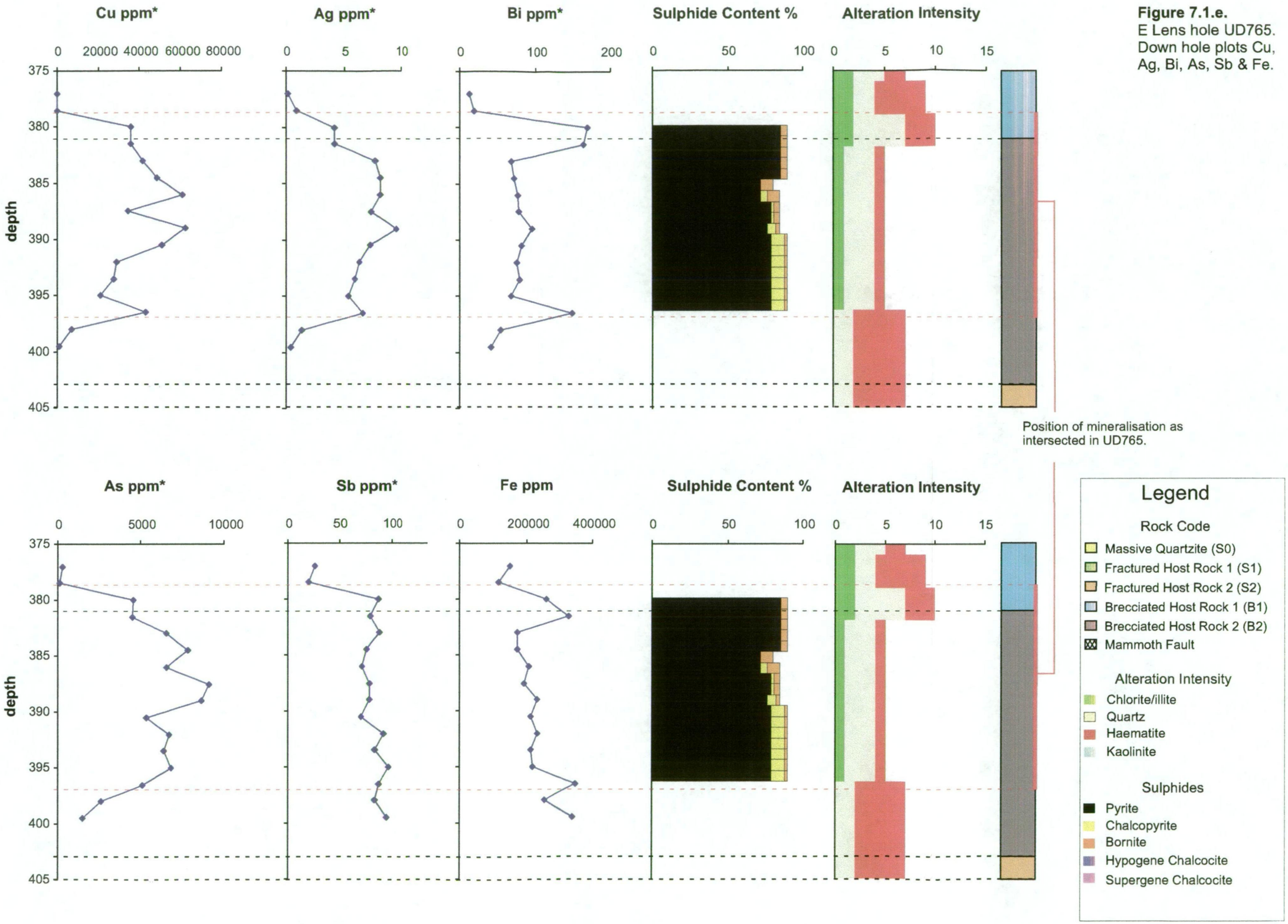

Figure 7.1.e.
E Lens hole UD765.
Down hole plots Cu, Ag, Bi, As, Sb & Fe.

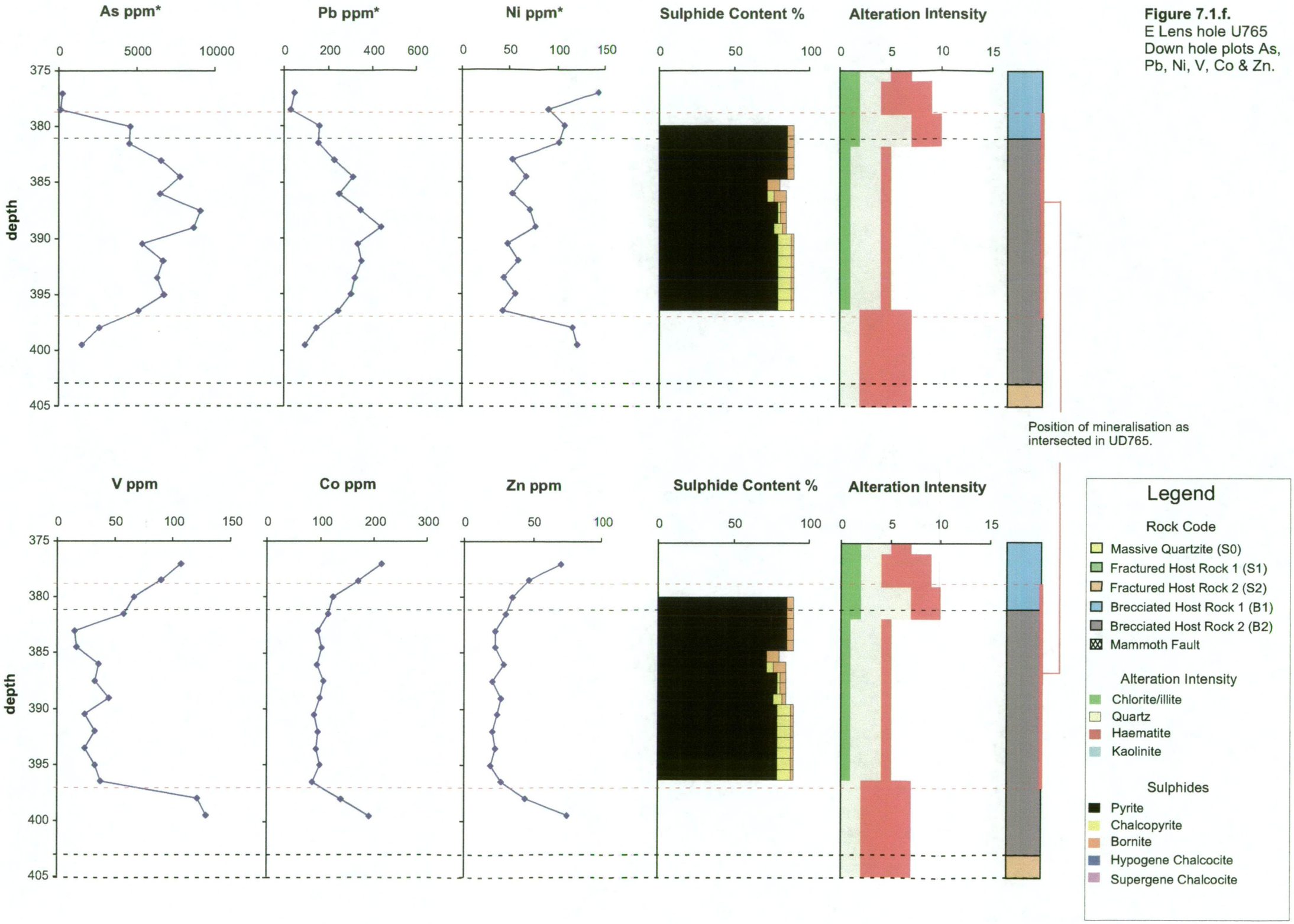

Figure 7.1.f.
E Lens hole U765
Down hole plots As, Pb, Ni, V, Co & Zn.

7.4.b D Lens

The geochemical characterisation of the hangingwall, footwall and ore of the D lens ore zones is based on assay data generated from drill holes UD746, UD744 and UD739 (Fig. 4.5) (Appendix A, Table A1.1). This data set was assayed for the major and trace elements SiO_2, TiO_2, Al_2O_3, K_2O, Fe, MgO, MnO, CaO, Na_2O, P_2O_5, Cu, Pb, Zn, Ni, Co, Mo, Ag, As, Bi, Sb, Tl, Ga, Sr, Rb, Ba, Y, V and Zr via whole-rock XRF analysis. Additional data on the concentration of Cu and As from the company database is included to complement the data set (Figs 7.2.a-j). The D lens ore zone consists of a number of stacked brecciated B2 lenses that dip steeply south and strike north east. These lenses vary in thickness from UD746 to UD744 and lessen in intensity of brecciation and Cu grade from UD744 to UD739 as they have been interpreted on the D lens section (Fig. 4.5).

Drill hole UD746 intersects the D lens ore zones from 110-238m at ~ 4500mRL to 4610mRL. Hole UD744 intersects the D lens ore zones from 110-155m at ~ 4600mRL to 4640mRL, 40-80m up dip from the ore intersection in hole UD746. Hole UD739 intersects the non-mineralised (< 2000 ppm Cu) ore zone equivalent zone from 125-165m at ~ 4705mRL, 85-110 metres up dip from the ore intersection in hole UD744.

Samples from hole UD746 represent the weakly mineralised to ore grade (> 15000 ppm Cu) hangingwall S2 and B2 units of the upper middle and lower D lens ore zones (Figs 7.2.a-c). Samples from UD744 represent the barren hangingwall S2 unit of the D lens ore zone from 100-110m, high grade brecciated and stockworked ore zones (B1 and S2) from 110-155m and barren footwall B1 and S1 units from 155-190m (Figs 7.2.d-f). Samples from UD739 represent the barren ore zone equivalent B1 unit distal to the D lens ore zones from 134-131m and 156-164m (Figs 7.2.h-j).

The distribution of chlorite, quartz and hematite is erratic throughout the D lens hangingwall, ore zone and footwall units with the exception that hematite displays an antithetic relationship with chlorite in all three drill holes and the intensity of hematite increases, relative to chlorite, up dip.

The distribution of the sulfides in D lens is illustrated in drill holes UD746, UD744 and UD739 and consists of pyrite, chalcopyrite, bornite, hypogene chalcocite and supergene chalcocite (Figs 7.2.a-j). In general, sulfides display a complex zoning that ranges from pyrite-chalcopyrite at depth to pyrite-bornite-chalcocite (hypogene and supergene) up dip (refer Chapter 5). Within the stacked ore zone breccias (B2) and stockworked units (S2) the sulfides are zoned from pyrite-chalcopyrite in the footwall to pyrite-bornite-chalcocite (hypogene and supergene) in the hangingwall as shown in hole UD746 (Figs 7.2.a-c). Pyrite and bornite are the dominant sulfides in hole UD744 with both supergene and hypogene chalcocite, chalcopyrite and covellite occurring in trace amounts erratically throughout the ore and wall rock units. No sulfides were observed in hole UD739 within the ore equivalent horizon.

The major and trace element distributions are summarised in Table 7.3. In general, Cu, Pb, Zn, Co, Ni, Mo and As concentrations decrease up dip between UD746 and UD744. In contrast, the concentration of Bi increases up dip corresponding with the change of the dominant Cu sulfide from chalcopyrite to bornite. No significant change occurs in the concentration of Sb and Tl between UD746 and UD744. Zn is elevated in both the footwall units of UD746 and UD744 and the hangingwall S2 unit of UD744. The trace element concentrations of Zn, Ni and Co are elevated within the ore equivalent horizon intersected in UD739, relative to UD744, in contrast to the other trace elements which demonstrate a decrease in concentration, corresponding to the low sulfide content.

The concentrations of the major elements vary in accordance with the occurrence of the non-sulfide alteration and gangue mineralogy. The distribution of SiO_2, in all three drill holes has an antithetic relationship reflecting the dilatant infill style of the mineralisation. Concentrations of MgO and MnO have been interpreted to correlate with the abundance of chlorite and are noticeably increased in the hangingwall and footwall units relative to the main ore zones. Al_2O_3, TiO_2, K_2O, CaO and P_2O_5 are enriched with the pyrite-chalcopyrite rich footwall ore zone of hole UD746, relative to the pyrite-bornite-chalcocite hangingwall ore zones. The enrichment in Al_2O_3 and K_2O,

relative to the host rock, corresponds to occurrence of illite associated chalcopyrite. Variations in the concentration of Fe_2O_3, within the D ore zones, correspond to the variable occurrence of chlorite, hematite, pyrite and other Cu-Fe sulfides. MgO, MnO, CaO and P_2O_5 display a significant increase in concentration from the ore zone units in hole UD744 to the un-mineralised ore equivalent zone in hole UD739.

Table 7.3. Element distributions in D lens drill holes UD746, UD744 and UD739.

Drill Hole	Element	Comment on distribution
UD746	SiO_2	Decreased in ore zones
UD746	TiO_2	Similar to Al_2O_3
UD746	Al_2O_3	Elevated in chalcopyrite ore zones
UD746	Fe_2O_3	Elevated in ore zones
UD746	MnO	Weakly elevated in hangingwall and footwall units, decreased in ore zones
UD746	MgO	Similar to MnO
UD746	CaO	Significantly elevated in chalcopyrite ore zone, weakly elevated in bornite chalcocite ore zone
UD746	Na_2O	Erratic, with no consistent correlations
UD746	K_2O	Elevated in chalcopyrite ore zone
UD746	P_2O_5	Similar to CaO
UD746	Y	Erratic
UD746	Rb	Similar to K_2O
UD746	Tl	Peaks correspond to high pyrite content in ore zones
UD746	Pb	Similar to Tl in ore zones, weakly elevated in hangingwall relative to footwall
UD746	Zn	Erratic but elevated in ore zones, peaks in footwall unit
UD746	Cu	High in ore zones, corresponds well to style and distribution of Cu mineral, similar to As, Tl and Pb in chalcopyrite footwall ore zone
UD746	Bi	Elevated in bornite-chalcocite hangingwall ore zones relative to footwall chalcopyrite ore zones
UD746	As	Peaks correspond well to variable pyrite content in hangingwall ore zones and both pyrite and chalcopyrite in footwall ore zones
UD746	Ni	Similar to As
UD746	Co	Similar to As
UD746	Mo	Erratic in hangingwall ore zones, elevated in footwall chalcopyrite dominated ore zones
UD746	Ga	Similar to Al
UD746	S	Similar to Cu and to a lesser extent Fe
UD746	Sb	Similar to As
UD746	Zr	erratic
UD746	Sr	Similar to K_2O
UD746	Ba	Similar to K_2O
UD746	V	Erratic
UD744	SiO_2	Decreased in ore zones
UD744	TiO_2	Similar to Al_2O_3
UD744	Al_2O_3	Decreased in ore zone relative to hangingwall and footwall units
UD744	Fe_2O_3	Elevated in ore zones
UD744	MnO	Similar to Al_2O_3
UD744	MgO	Similar to Al_2O_3
UD744	CaO	Similar to Al_2O_3

Table 7.3. Element distributions in D lens drill holes UD746, UD744 and UD739.

Drill Hole	Element	Comment on distribution
UD744	Na_2O	Similar to Al_2O_3
UD744	K_2O	Weakly elevated in ore zone, peaks in footwall units
UD744	P_2O_5	Similar to Al_2O_3
UD744	Y	Erratic
UD744	Rb	Similar to K_2O
UD744	Tl	Similar to As
UD744	Pb	Similar to As
UD744	Zn	Decreased in ore zones, elevated in hangingwall and footwall units
UD744	Cu	Elevated in ore zones
UD744	Bi	Primary peak corresponds to high chalcocite content
UD744	As	Elevated in ore zones, demonstrates an antithetic relationship with the distribution of Cu (refer 100-125m)
UD744	Ni	Similar to As
UD744	Co	Similar to As
UD744	Ga	Similar to Al_2O_3
UD744	S	Similar to As and Cu
UD744	Sb	Weakly elevated in hangingwall unit immediately above ore breccia (B2) contact
UD744	Zr	Erratic
UD744	Sr	Similar to K_2O
UD744	Ba	Similar to K_2O
UD744	V	Erratic in ore zone
UD739	SiO_2	Decreased in ore equivalent horizon
UD739	TiO_2	Similar to Al_2O_3
UD739	Al_2O_3	Elevated in ore equivalent horizon
UD739	Fe_2O_3	Elevated in ore equivalent horizon
UD739	MnO	Elevated in ore equivalent horizon
UD739	MgO	Elevated in ore equivalent horizon
UD739	CaO	Elevated in ore equivalent horizon
UD739	Na_2O	Similar to Al_2O_3
UD739	K_2O	Similar to Al_2O_3
UD739	P_2O_5	Elevated in ore equivalent horizon
UD739	Y	Similar to Al_2O_3
UD739	Rb	Similar to Al_2O_3
UD739	Tl	Near detection limits
UD739	Pb	Elevated in ore equivalent horizon
UD739	Zn	Elevated in ore equivalent horizon
UD739	Cu	Elevated in ore equivalent horizon
UD739	Bi	Elevated in ore equivalent horizon
UD739	As	Elevated in ore equivalent horizon
UD739	Ni	Elevated in ore equivalent horizon
UD739	Co	Elevated in ore equivalent horizon
UD739	Ga	Similar to Al_2O_3
UD739	S	Weakly elevated in ore zone
UD739	Sb	Elevated in ore equivalent horizon
UD739	Zr	Erratic
UD739	Sr	Elevated in ore equivalent horizon
UD739	Ba	Elevated in ore equivalent horizon
UD739	V	Erratic

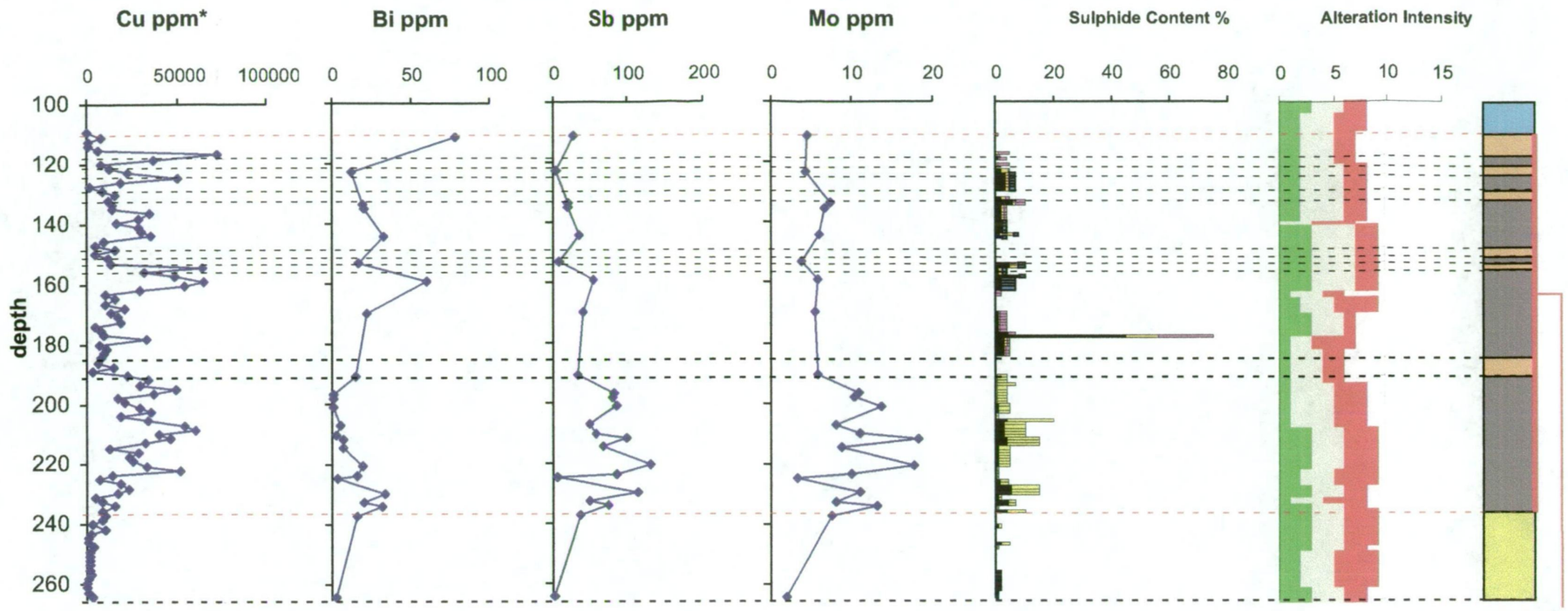

Figure 7.2.a.
D Lens hole UD746. Down hole plots Cu, Bi, Sb, Mo, As, Pb, Tl & Ni.

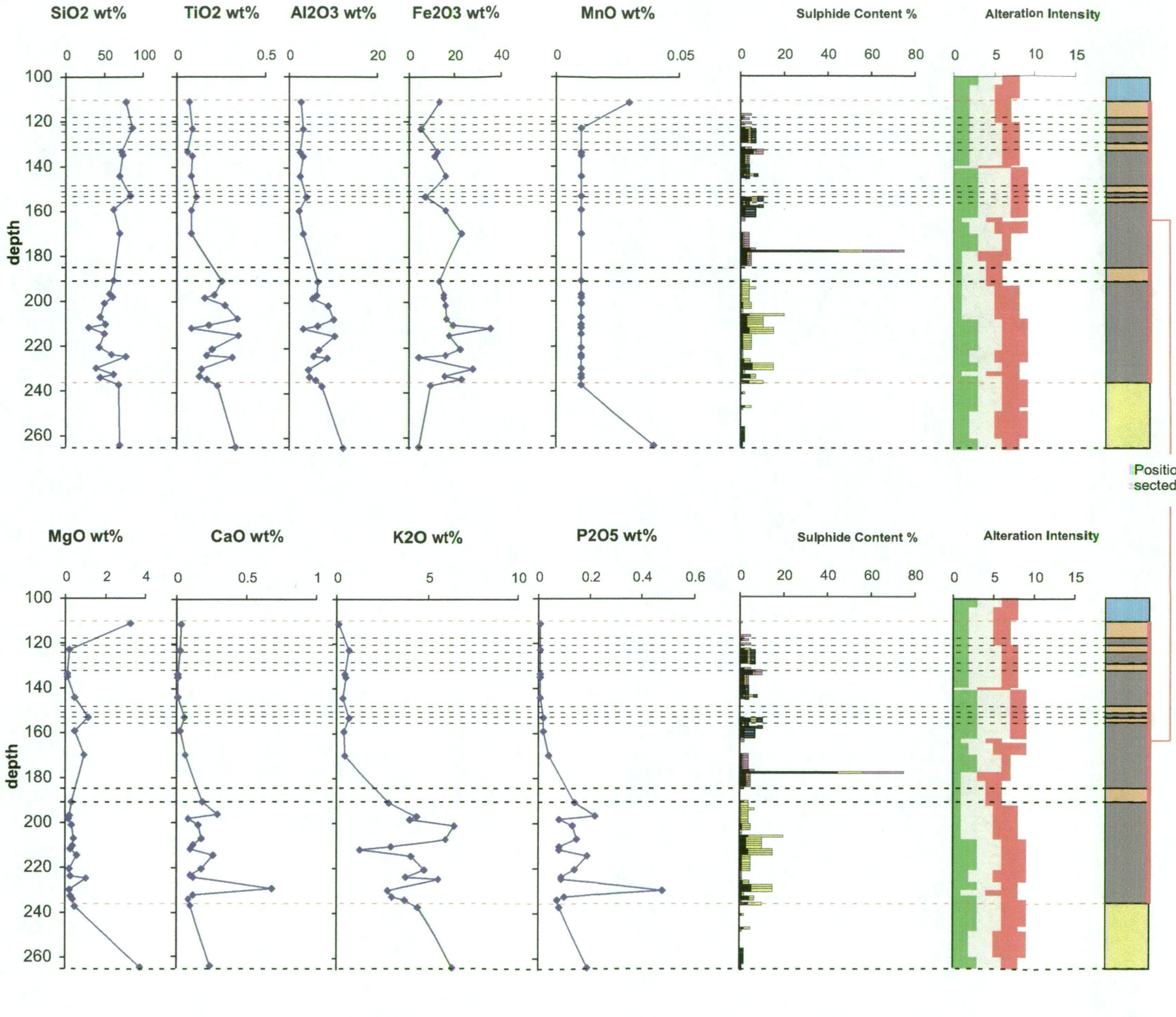

Figure 7.2.c.
D Lens hole UD746.
Down hole plots
SiO2, TiO2, Al2O3,
Fe2O3, MnO, MgO,
CaO, K2O & P2O5.

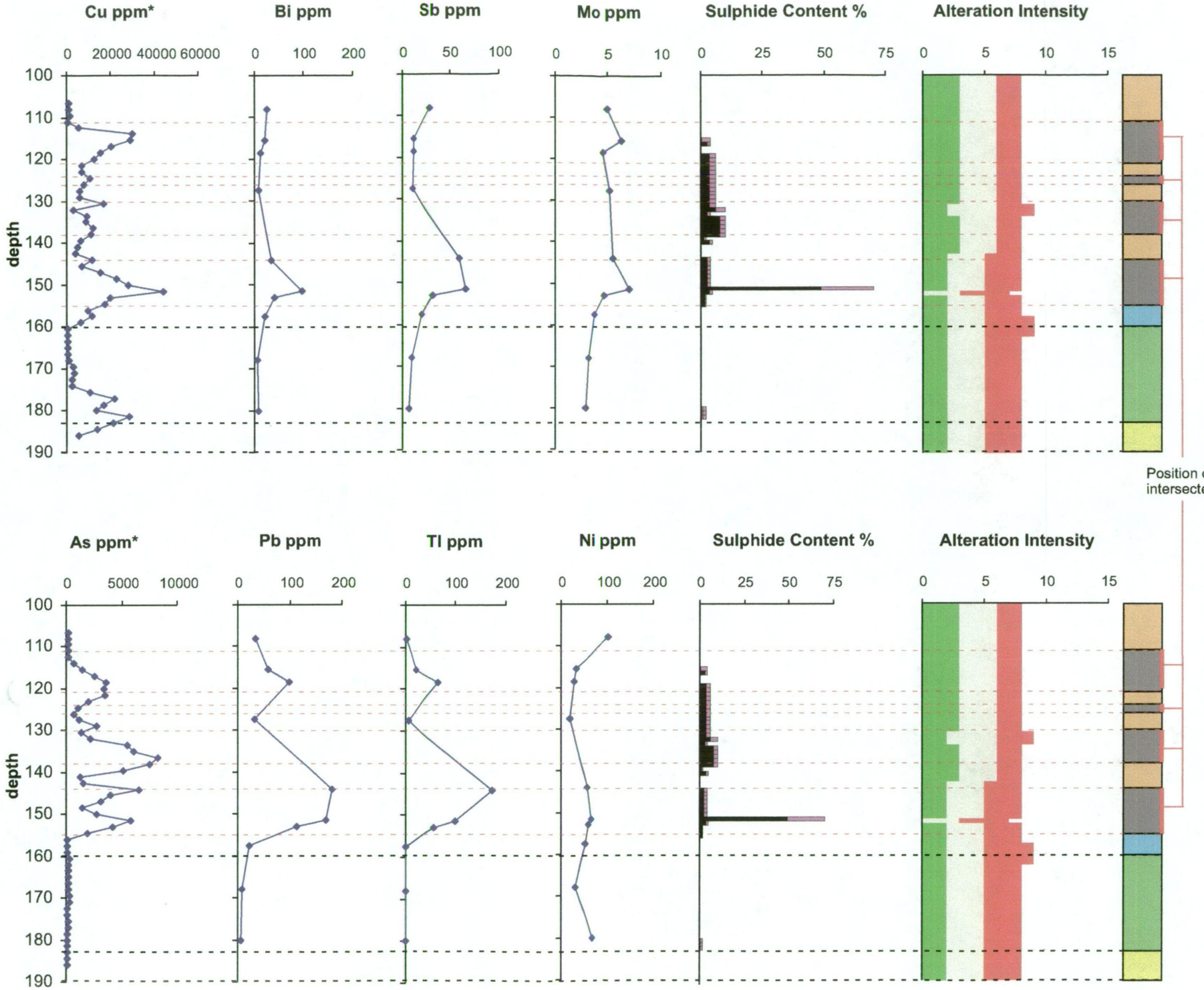

Figure 7.2.d.
D Lens hole UD744.
Down hole plots Cu, Bi, Sb, Mo, As, Pb, Tl & Ni.

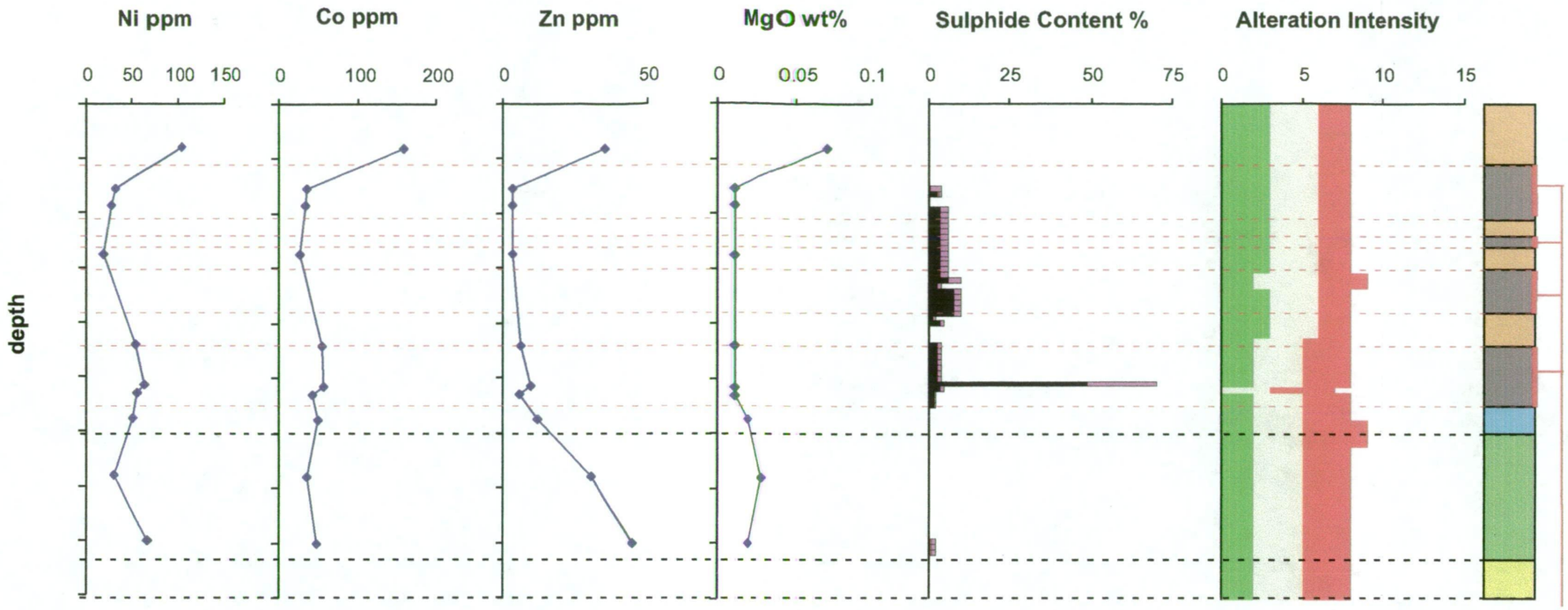

Figure 7.2.e.
D Lens hole UD744.
Down hole plots Ni, Co, Zn, Mgo, S, Y, V & Ba.

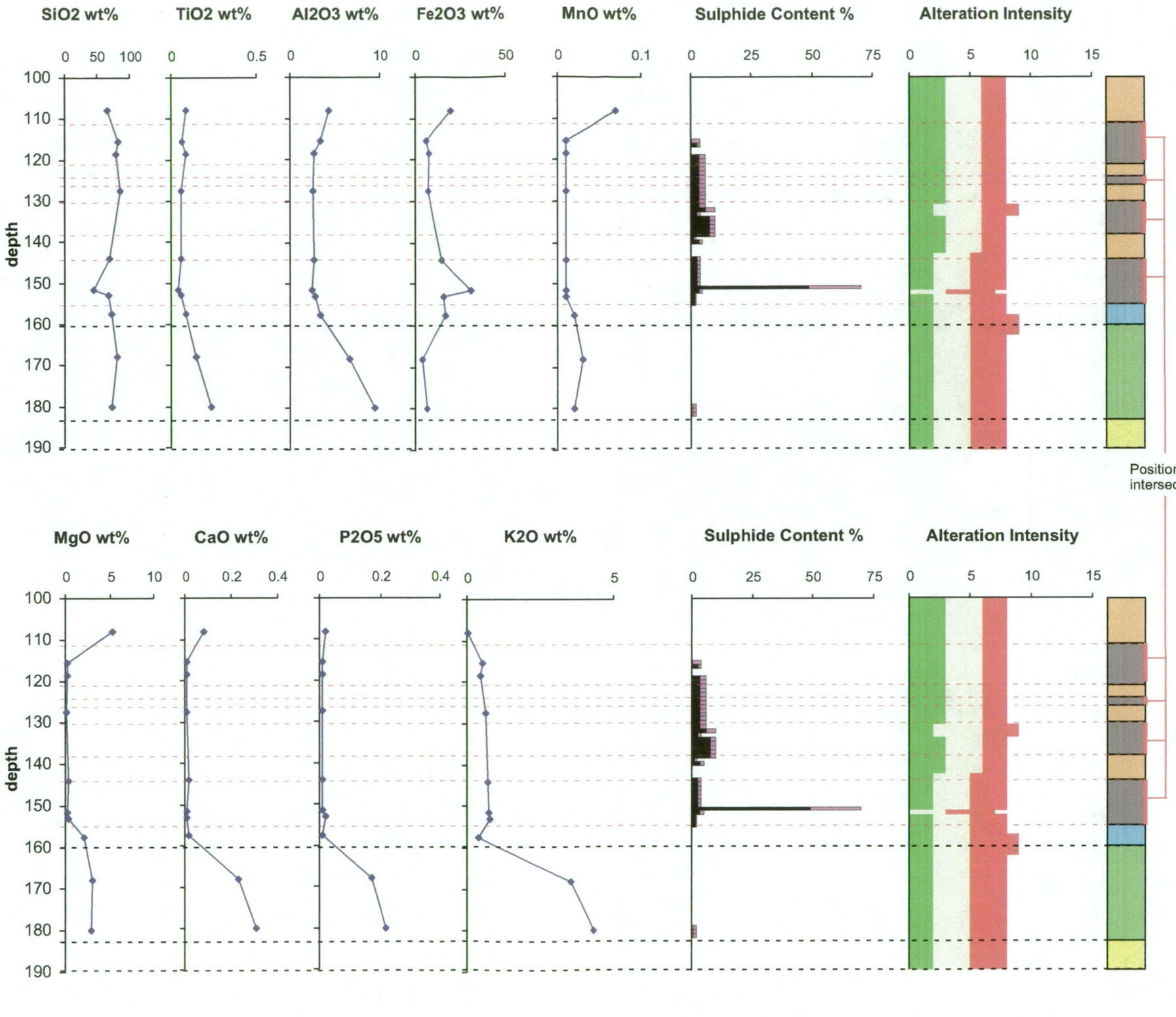

Figure 7.2.f.
D Lens hole UD744.
Down hole plots
SiO2, TiO2, Al2O3,
Fe2O3, MnO, MgO,
CaO, P2O5 & K2O.

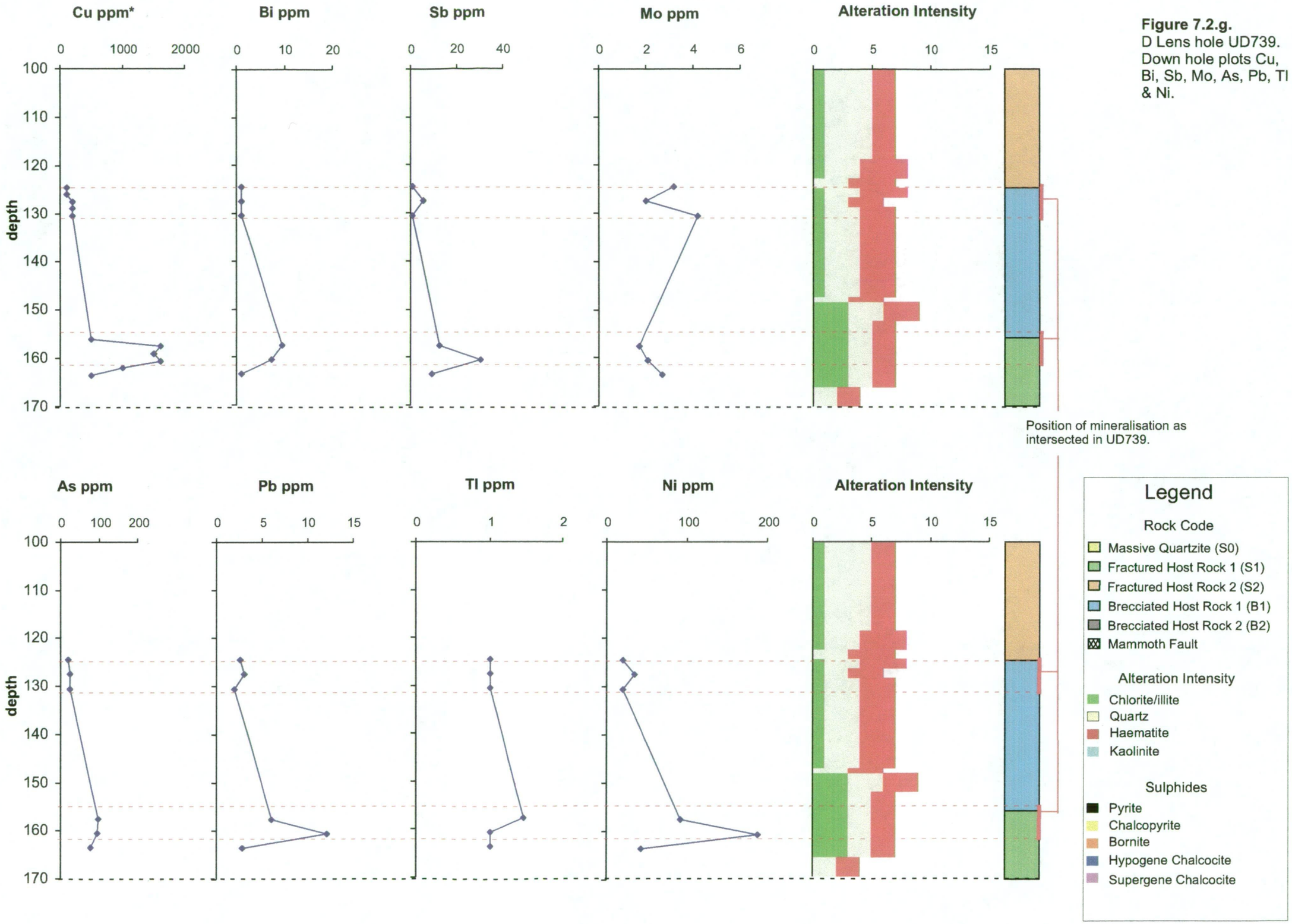

Figure 7.2.g.
D Lens hole UD739.
Down hole plots Cu, Bi, Sb, Mo, As, Pb, Tl & Ni.

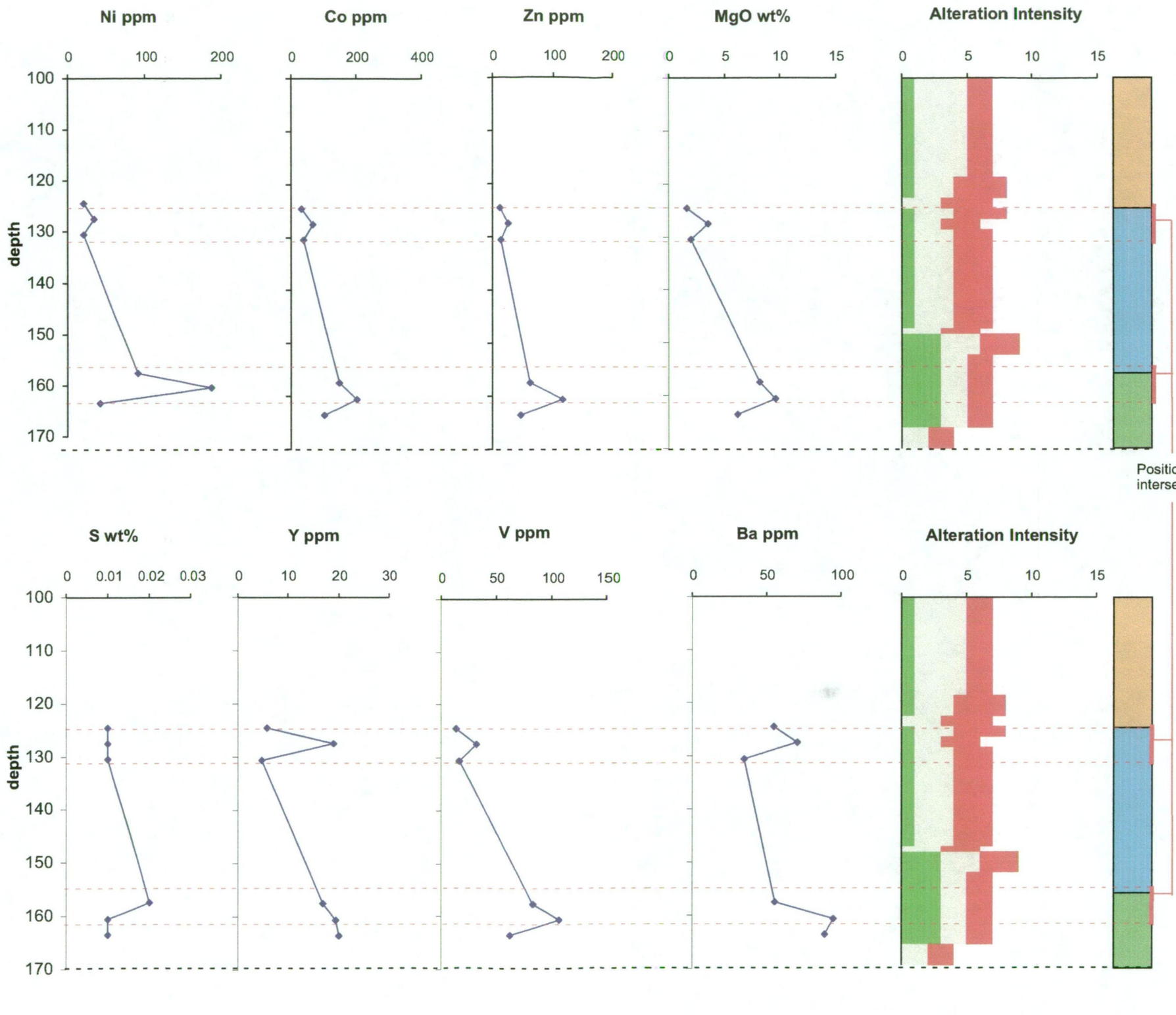

Figure 7.2.h.
D Lens hole UD739. Down hole plots Ni, Co, Zn, MgO, S, Y, V& Ba.

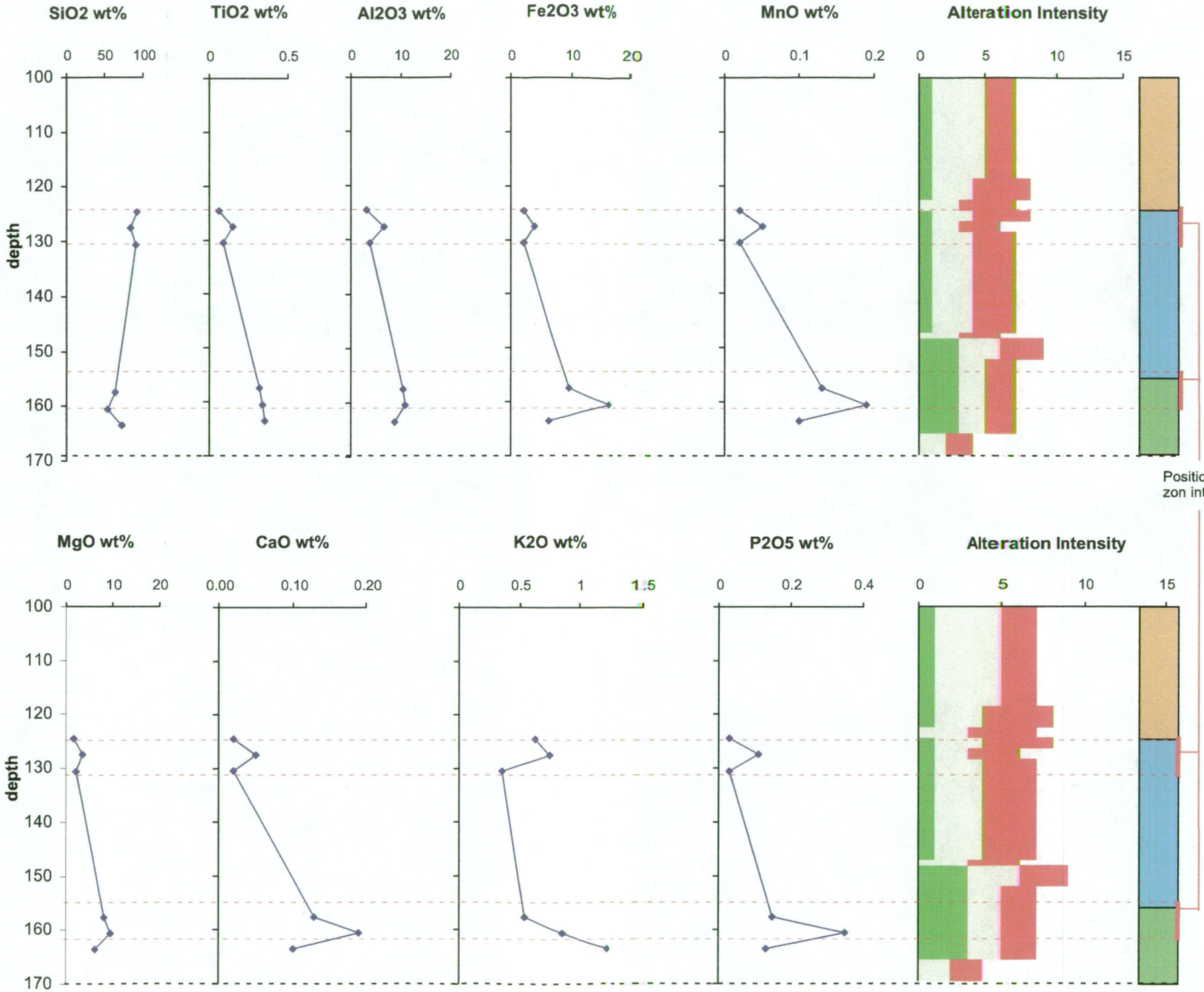

Figure 7.2.i.
D Lens hole UD739.
Down hole plots
SiO2, TiO2, Al2O3,
Fe2O3, MnO, MgO,
CaO, K2O & P2O5

7.4.c C Lens

The geochemical characterisation of the hangingwall, footwall and ore of the C lens ore zones is based on assay data generated from drill holes UD734 and UD732 (Figs 4.4, Appendix 1, Table A1.1). This data set was assayed for the major and trace elements SiO_2, TiO_2, Al_2O_3, K_2O, Fe_2O_3, MgO, MnO, CaO, Na_2O, P_2O_5, Cu, Pb, Zn, Ni, Co, Mo, Ag, As, Bi, Sb, Tl, Ga, Sr, Rb, Ba, Y, V and Zr via whole-rock XRF analysis (Table 7.1). The C lens ore zone consists of a brecciated B2 lens and a stockworked S2 unit that dip ~ 55° west and strike north south. These units vary in thickness and lessen in intensity of brecciation and Cu grade from holes UD734 to UD732 as they have been interpreted on the C lens section (Fig. 4.4).

Hole UD734 intersects the C lens ore zone from 132-149m at ~ 4625mRL to 4645mRL. Drill hole UD732 intersects the mineralised to non-mineralised (< 2000 ppm Cu) ore zone equivalent zone from 45-81m at ~ 47105mRL, 90-100m up dip from the ore intersection in hole UD734.

Samples from hole UD734 represent the weakly mineralised to ore grade (> 15000 ppm Cu) hangingwall S1 and B2 units of the C lens ore zones (Figs 7.4.a-f). Samples from hole UD732 represent the barren S1, S2 and B1 units of the C lens ore zone from 16-120m, including the Cu rich brecciated and stockworked C lens ore zones (B1 and S2) from 30-81m and the barren footwall S0 unit from 155-190m.

The distribution of chlorite, quartz and hematite is varied throughout the C lens hangingwall, ore zone and footwall units. Chlorite is absent in hangingwall S1 unit intersected in hole UD734. In general, chlorite displays an antithetic relationship with hematite.

The sulfide mineral assemblage in holes UD734 and UD732 consists of pyrite, bornite and chalcocite. Within the C lens ore zone as intersected in hole UD734, the sulfide content increase from footwall to hangingwall from ~ 5% to ~ 80% with a relative increase in pyrite, bornite and hypogene chalcocite. The sulfide assemblage in hole UD732 intersected in the

interpreted ore equivalent horizon consists only of pyrite and minor hypogene chalcocite. The chalcocite (2-4%) intersected in UD732 occurs in the unit located in the hangingwall of the interpreted ore horizon as projected up dip from UD734 (Fig. 4.4).

Element distributions are summarised in Table 7.4. Cu and Bi are elevated in the ore zone and correspond to high bornite and hypogene chalcocite contents. Arsenic, Pb, Sb, Tl and Mo concentrations are elevated within the C lens ore zone and peak with corresponding high pyrite contents. MgO and MnO are generally decreased in the ore zone, relative to the hangingwall and footwall units, with the exception that they are weakly elevated with in the ore zone corresponding with an increases in bornite, hypogene chalcocite and the first occurrence of chlorite. Al_2O_3, K_2O, CaO, P_2O_5 and TiO_2 are elevated in the hangingwall and appear to correspond to the distribution of MgO and MnO within the ore zone.

The C Lens ore equivalent horizon as intersected in hole UD732 (100 metres up dip from the intersection in UD734) in general illustrates a decrease in the concentration Cu, S, Sb, Bi, As, Sr, Tl, Ni, Co, Fe and Pb, reflecting the low sulfide content.

Table 7.4. Element distributions in C lens drill holes UD732 and UD734.

Drill Hole	Element	Comment on distribution
UD732	SiO_2	Weakly decreased in ore equivalent horizon
UD732	TiO_2	Similar to Al_2O_3
UD732	Al_2O_3	Elevated in footwall and weakly elevated in hangingwall immediately adjacent to ore zone
UD732	Fe_2O_3	Increased in ore zone
UD732	MnO	Elevated in hangingwall immediately adjacent to ore zone
UD732	MgO	Elevated in footwall and elevated in hangingwall immediately adjacent to ore zone
UD732	CaO	Elevated in footwall and elevated in hangingwall immediately adjacent to ore zone
UD732	Na_2O	Similar to Al_2O_3
UD732	K_2O	Elevated in footwall
UD732	P_2O_5	Elevated in footwall and elevated in hangingwall immediately adjacent to ore zone
UD732	Y	Erratic
UD732	Rb	Similar to K_2O
UD732	Tl	Similar to As
UD732	Pb	Similar to As
UD732	Zn	Similar to Ni and Co
UD732	Cu	Elevated in ore equivalent horizon

Table 7.4. Element distributions in C lens drill holes UD732 and UD734.

Drill Hole	Element	Comment on distribution
UD732	Bi	Similar to As and weakly elevated corresponding to hangingwall chalcocite ore body
UD732	As	Elevated in ore equivalent horizon
UD732	Ni	Weakly elevated in ore equivalent horizon, and elevated in hangingwall and footwall
UD732	Co	Weakly elevated in ore equivalent horizon, and elevated in hangingwall and footwall
UD732	Ga	Similar to Al_2O_3
UD732	S	Similar to Cu
UD732	Sb	Similar to As
UD732	Zr	Erratic
UD732	Sr	Similar to K_2O
UD732	Ba	Similar to K_2O
UD732	V	Erratic
UD734	SiO_2	Decreased in ore zone
UD734	TiO_2	Similar to Al_2O_3
UD734	Al_2O_3	Elevated in hangingwall, decreased in hangingwall of ore zone and weakly elevated in ore zone
UD734	Fe_2O_3	Elevated in ore zone
UD734	MnO	Elevated in hangingwall immediately adjacent to ore zone
UD734	MgO	Elevated in hangingwall immediately adjacent to ore zone and elevated in ore zone
UD734	CaO	Similar to K_2O
UD734	Na_2O	Similar to Al_2O_3
UD734	K_2O	Elevated in hangingwall decreased in hangingwall immediately adjacent to ore zone and weakly elevated in ore zone.
UD734	P_2O_5	Similar to K_2O
UD734	Y	Erratic
UD734	Rb	Similar to K_2O
UD734	Tl	Similar to As
UD734	Pb	Similar to As
UD734	Zn	Similar to Ni
UD734	Cu	Elevated in ore zone
UD734	Bi	Similar to Cu
UD734	As	Elevated in ore zone
UD734	Ni	Elevated in ore zone and elevated in hangingwall immediately above ore zone
UD734	Co	Similar to Ni
UD734	Ga	Similar to Al_2O_3
UD734	S	Similar to Cu and As
UD734	Sb	Similar to As
UD734	Zr	Erratic
UD734	Sr	Similar to K_2O
UD734	Ba	Similar to K_2O
UD734	V	Erratic

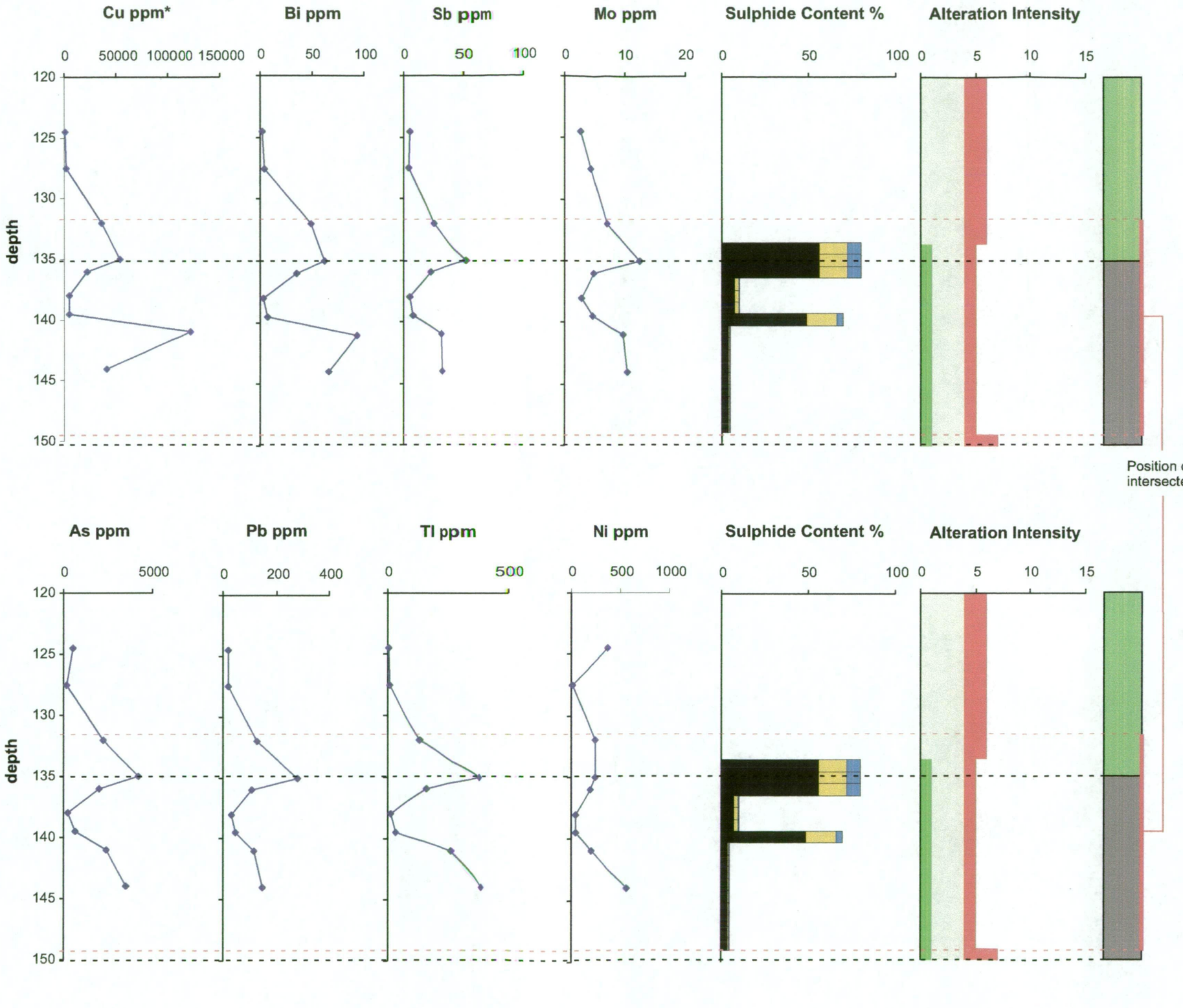

Figure 7.3.a.
C Lens hole UD734.
Down hole plots Cu, Bi, Sb, Mo, As, Pb, Tl & Ni

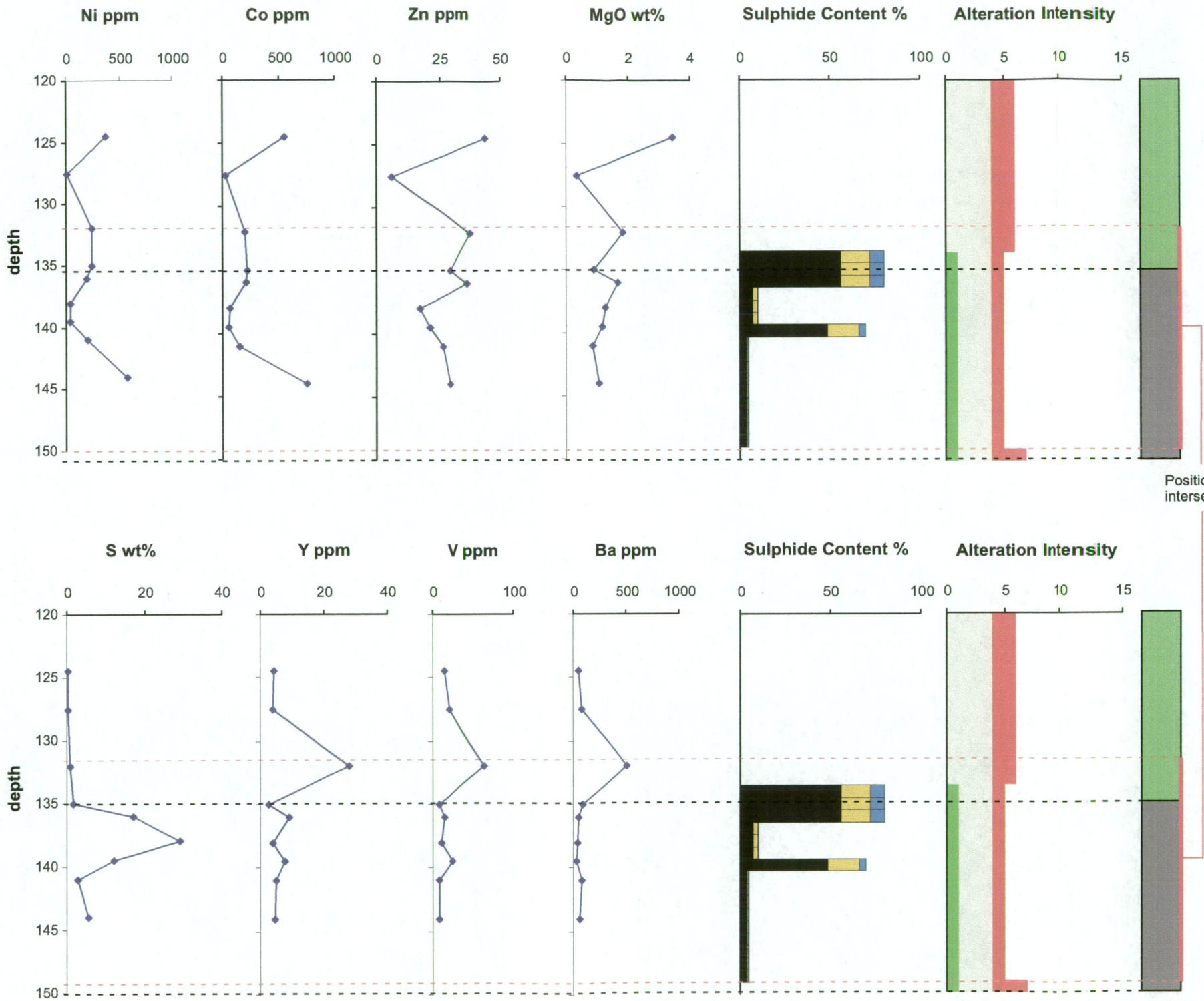

Figure 7.3.b.
C Lens hole UD734.
Down hole plots Ni, Co, Zn, MgO, S, Y, V & Ba.

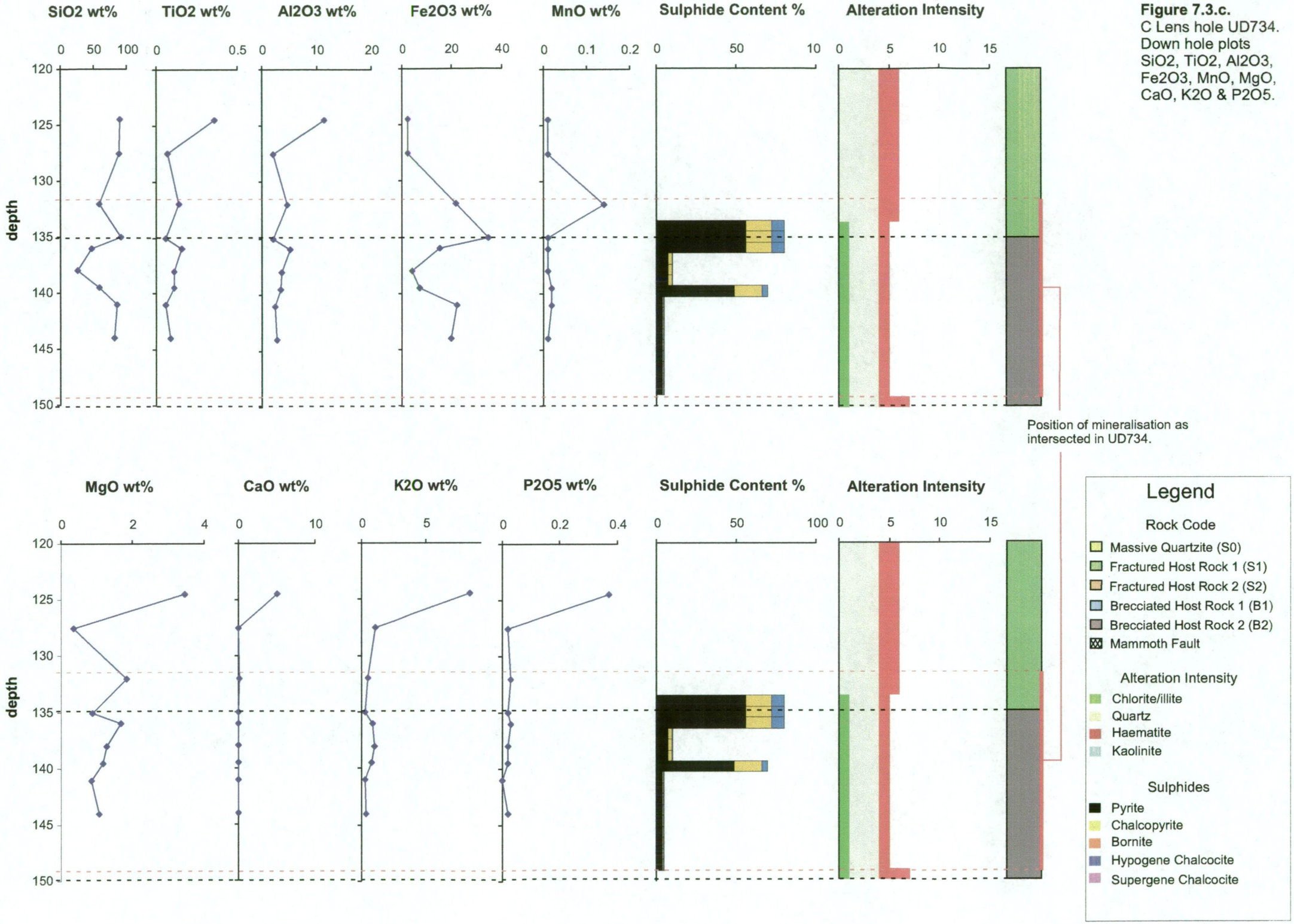

Figure 7.3.c.
C Lens hole UD734.
Down hole plots
SiO2, TiO2, Al2O3,
Fe2O3, MnO, MgO,
CaO, K2O & P2O5.

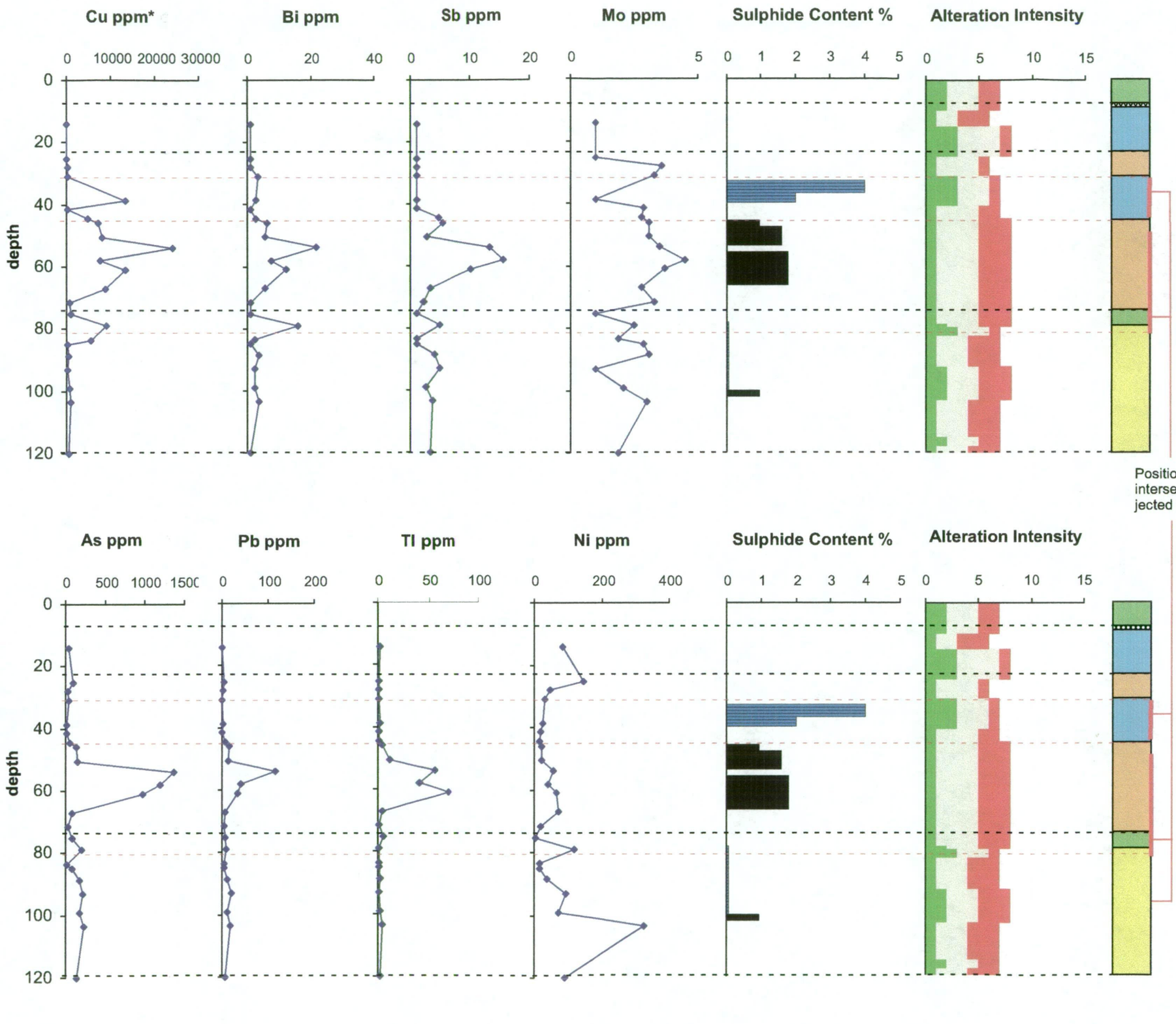

Figure 7.3.d.
C Lens hole UD732. Down hole plots Cu, Bi, Sb, Mo, As, Pb, Tl & Ni.

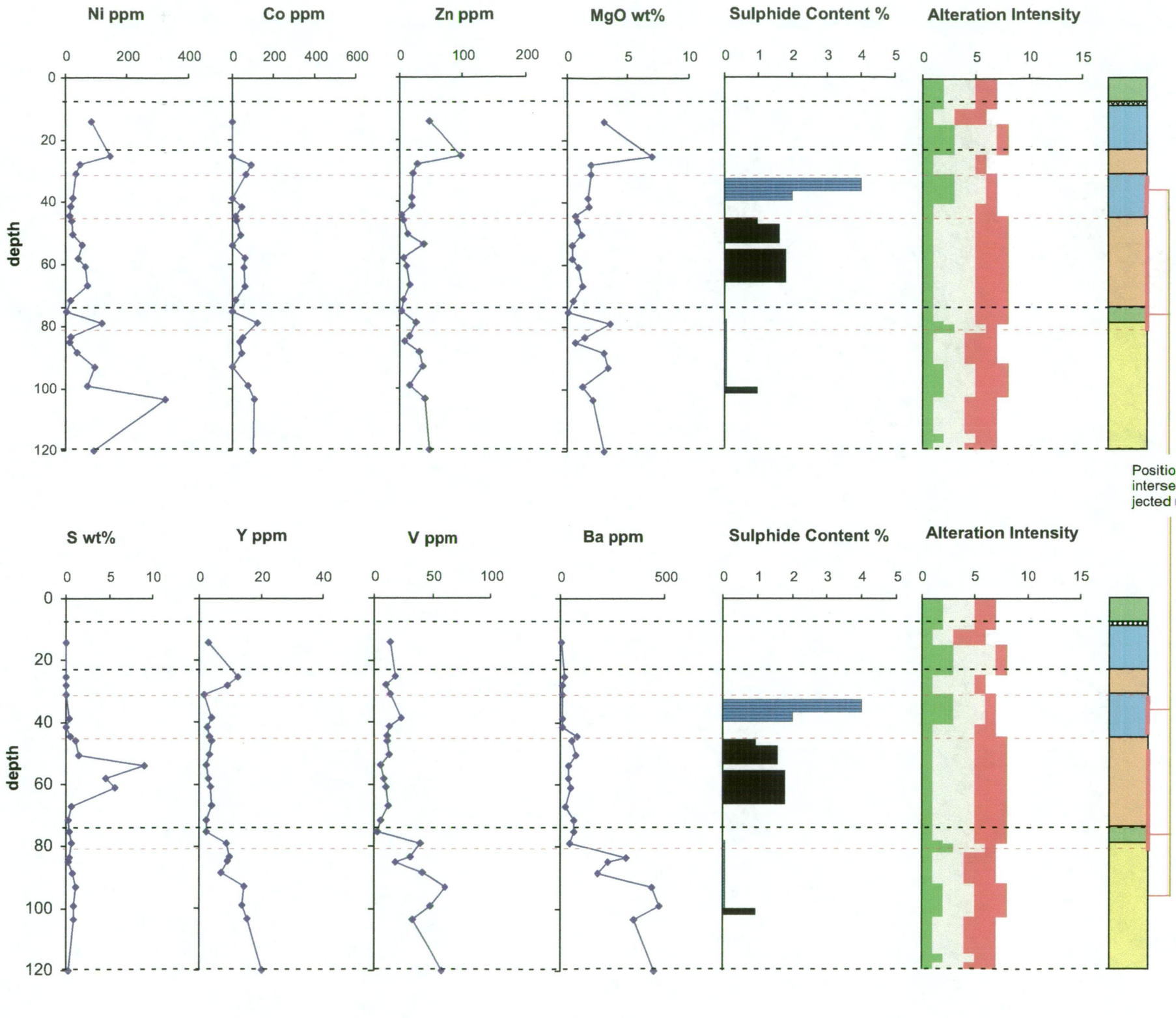

Figure 7.3.e.
C Lens hole UD732. Down hole plots Ni, Co, Zn, MgO, S, Y, V & Ba

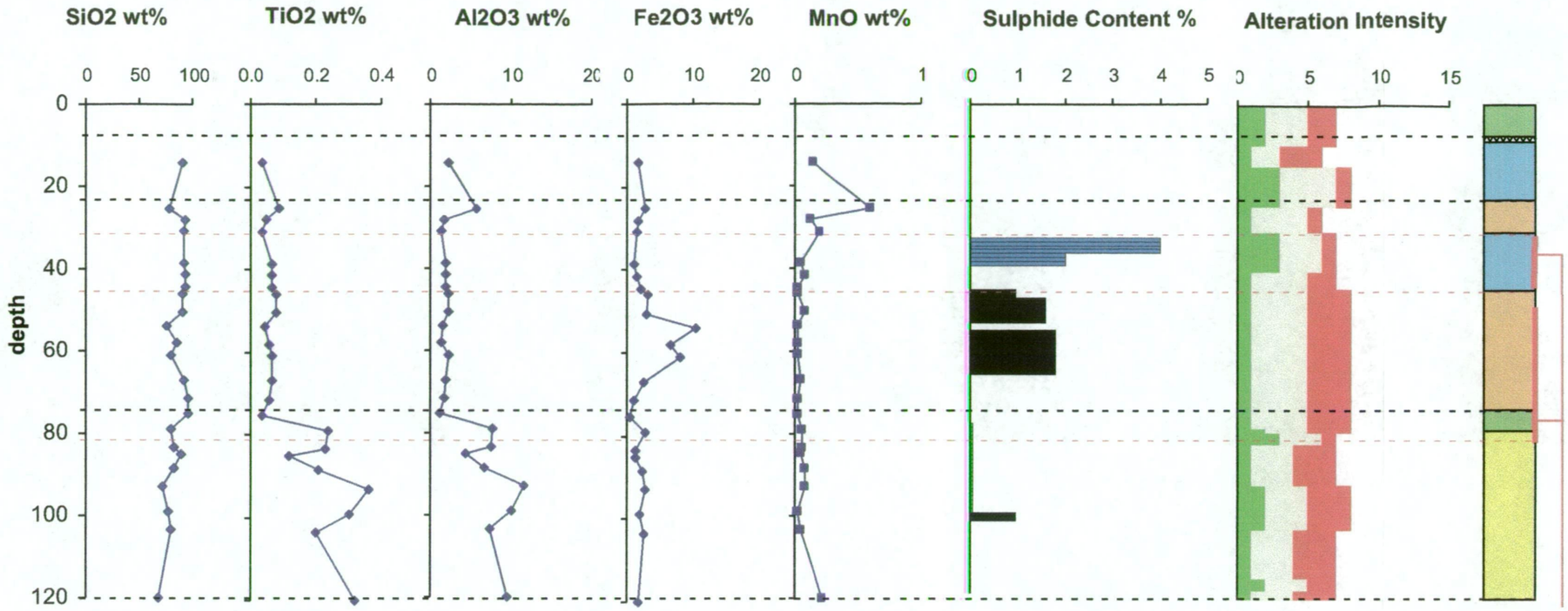

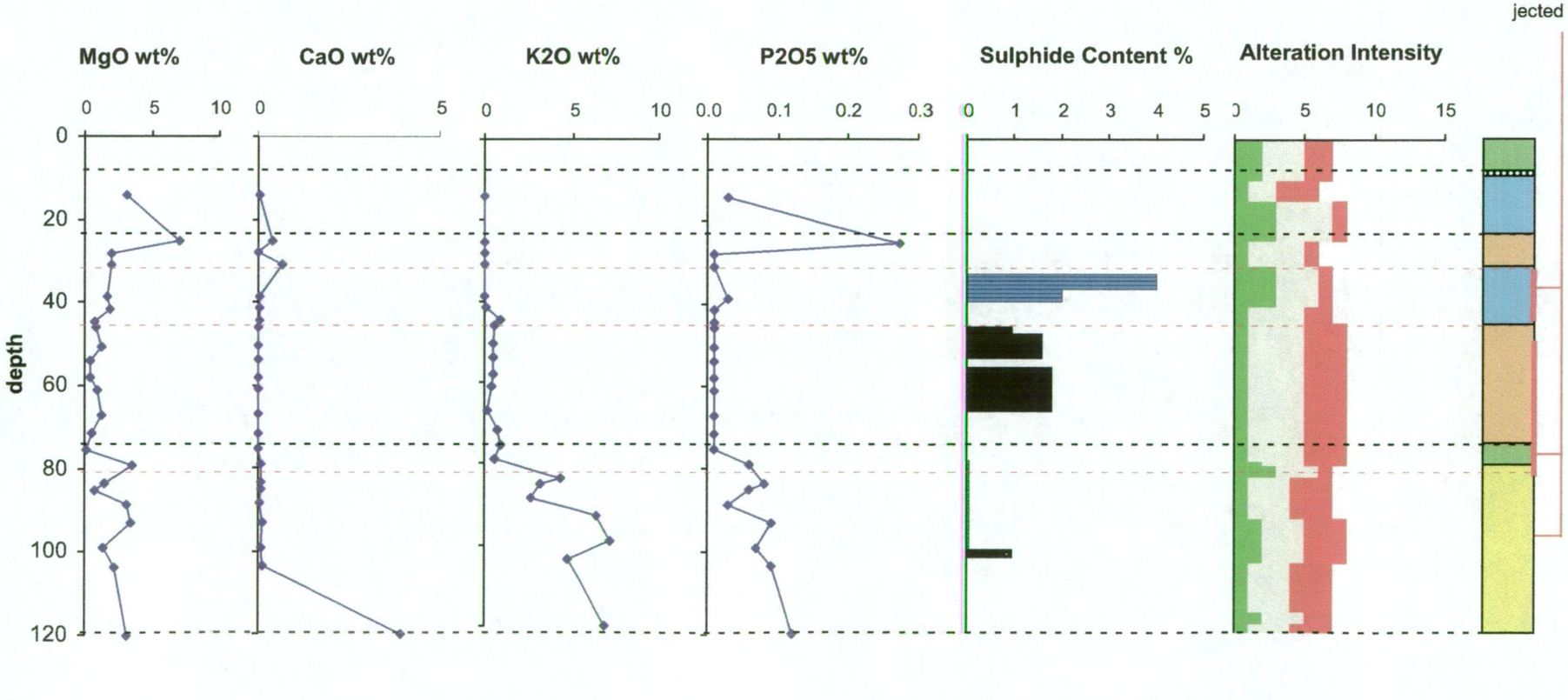

Figure 7.3.f.
C Lens hole UD732.
Down hole plots
SiO2, TiO2, Al2O3,
Fe2O3, MnO, MgO,
CaO, K2O & P2O5.

7.4.d 2 lens and Mammoth Fault Mineralisation (MFM)

Two drill holes, UD768 and UD767 were selected to represent the MFM and the 2 lens ore zones. Hole UD768 intersects the Mammoth Fault and both the Mammoth Fault and 2 lens ore zones. Hole UD767 intersects the Mammoth Fault and the un-mineralised up dip extensions of the ore structures intersected in hole UD768 (Fig. 4.6).

Samples from UD768 were selected to represent the brecciated hangingwall (B1) of the Mammoth Fault zone, the high-grade ore zone from 150-162m (B2), stockwork hosted ore from 162-205m and the Unfractured Host Rock distal to the ore zone (239m). Samples selected from UD767 represent the brecciated hangingwall (B1) of the Mammoth Fault zone, the Fractured Host Rock unit (S2) from 172-239m, the Unfractured Host Rock unit (S0) from 239-249m, the Brecciated Host Rock unit (B1) from 249-255m, the Fractured Host Rock unit from 249m-298m and the Unfractured Host Rock from 298-305m. No significant mineralisation was intersected in the hole. Only 13.5m from 243-256.5m were cut and assayed by company geologists. This zone contains the Brecciated Host Rock unit (B2), which correlates with the known ore zones, projected up dip from holes UD768 and UD766 (Fig. 4.6).

The 2 Lens mineralised structure crops out at surface and is located at 20800mN and 328430mE (Fig. 4.7.a). This position is the up dip projection (approx 250 meters) of the 2 Lens structure as intersected by UD767. The structure strikes east-west (between 64° and 100°) and dips south from 62° to 82°. It has a known strike length of 60 metres and ranges from 2-8 metres in width. The zone consists of a vein stockwork, containing quartz and Fe oxides, hosted in a quartzite (S1-S2). The surrounding host rock ranges from a massive to a well bedded quartzite (S0-S1). Rock chip samples were collected along two north south traverses: 1) 32405mE and 2) 32415mE. A further two grab samples were collected from within the outcrop (L2-010 and L2-011) (Fig. 4.7.a).

The distribution of chlorite, quartz, hematite and kaolinite is relatively consistent throughout the hangingwall, ore zone and footwall units

associated with the 2 lens and Mammoth Fault Mineralisation. Chlorite is present in hangingwall B1 unit intersected in hole UD768 and in all of the hangingwall units above the interpreted 2 Lens ore equivalent horizon position intersected in hole UD767. In general, chlorite displays an antithetic relationship with hematite. Kaolinite occurs in the footwall units of the 2 lens ore zone intersected in hole UD768 and in the footwall units of the interpreted 2 Lens ore equivalent horizon intersected in hole UD767. A notable exception to the above is the occurrence of chlorite with hypogene chalcocite in the footwall of the 2 lens ore zone.

The sulfide mineral assemblage as represented in hole UD768 consists of pyrite, chalcopyrite, bornite and hypogene and supergene chalcocite. Within the 2 Lens ore zone and MFM as intersected in hole UD768, the sulfide content appears erratic. No sulfides were observed in hole UD767. Pyrite, bornite and both hypogene and supergene styles of chalcocite occur in the 2 Lens ore zone with the total sulfide content increasing towards the footwall. Pyrite, and to a lesser extent bornite and supergene chalcocite characterise the MFM B2 unit. The chalcopyrite mineralisation intersected in hole UD768 occurs in the S2 pillar located between the MFM B2 unit and the 2 Lens B2 unit.

When comparing the elemental distributions between the mineralised intersections in hole UD768 and the barren intersection, interpreted to represent the ore structure in hole UD767, several distinctive associations are evident (Table 7.5). In hole UD767 Cu, Pb, Zn, Ni, Co, As, Sb, V, Bi and Mo in the interpreted barren ore structure are enriched above background values. Lead, Zn, Ni, Co, As, Sb, and Mo are all elevated within the known ore zones in hole UD768 and all have a positive correlation with Cu. Potassium (K_2O) in the hangingwall breccia to the Mammoth Fault adjacent to the known ore horizons in hole UD768 is significantly enriched in K_2O when compared to the equivalent unit in hole UD767.

The concentration of the major and trace elements (SiO_2, TiO_2, Al_2O_3, Fe_2O_3, MnO, MgO, CaO, K2O, P_2O_5, Cu, Sb, Pb, As, Mo, Bi, Tl and Ni), geology, (mapped using the textural classification scheme), and the position of the 2

Lens structure have been plotted against their relative out crop position (Figs 7.4.g-i). Within the 2 Lens surface outcrop the trace elements Cu, Pb, As, Bi, Zn, Ni, Co, Ti, Mo, & Sb and the major element Fe_2O_3 are enriched above background values. This element suite is also enriched in the 2 Lens ore zone (as intersected by UD768) and its up dip mineralised structure (intersected by UD767). The surface outcrop of the 2 Lens ore zone is enriched in Cu, Pb, As, Sb, Mo and Bi but depleted in Zn, Ni and Co relative to the 2 Lens intersection in hole UD767.

Table 7.5. Element distributions in 2 lens and MFM drill holes UD767 and UD768.

Drill Hole	Element	Comment on distribution
UD767	SiO_2	Similar behaviour in both footwall and hangingwall but depleted in projected mineralised zone
UD767	TiO_2	Erratic, with no consistent variations
UD767	Al_2O_3	Substantially increased in the hangingwall B1 unit of the Mammoth Fault and constant elsewhere
UD767	Fe_2O_3	Constant throughout with a substantial increase in the projected ore zone
UD767	MnO	Constant throughout with a substantial increase in the projected ore zone. Similar to Fe_2O_3
UD767	MgO	Erratic, slight decrease in projected ore zone
UD767	CaO	Low values, significantly increased immediately above and below projected ore zone. Similar to P_2O_5
UD767	K_2O	Slight decrease through footwall into projected ore zone.
UD767	P_2O_5	Low values, significantly increased immediately above and below projected ore zone. Similar to CaO
UD767	Cu	Low values in footwall and hangingwall, increased in projected ore zone
UD767	Pb	Similar pattern to Cu
UD767	Zn	Similar pattern to Cu
UD767	Ni	Similar pattern to Cu
UD767	Co	Similar pattern to Cu
UD767	As	Similar pattern to Cu
UD767	Sb	Similar pattern to Cu
UD767	V	Similar pattern to Cu
UD767	Ga	Erratic, with no consistent variations
UD767	Bi	Similar pattern to Cu
UD767	Y	Similar pattern to CaO and P_2O_5
UD767	Zr	Lowest in projected ore zone.
UD767	Rb	Erratic, with no consistent variations.
UD767	Sr	Lowest in projected ore zone, significantly increased immediately above and below projected ore zone.
UD767	Ba	Erratic with no consistent variations.
UD767	Mo	Similar pattern to Cu
UD768	SiO_2	Decreased in ore zones
UD768	TiO_2	Erratic with a slight increase in ore zones
UD768	Al_2O_3	Erratic with a slight increase in the hangingwall B1 unit of the Mammoth Fault (similar to UD767)
UD768	Fe_2O_3	Erratic, increased in ore zones and chlorite alteration zone
UD768	MnO	Low throughout hole with an increase in the chlorite alteration zone

Table 7.5. Element distributions in 2 lens and MFM drill holes UD767 and UD768.

Drill Hole	Element	Comment on distribution
UD768	MgO	Low throughout hole with an increase in the chlorite alteration zone
UD768	CaO	Low values throughout hole, significantly increased in chlorite alteration zone
UD768	K_2O	General decrease through footwall to ore zones and increases away from ore zone in hangingwall
UD768	P_2O_5	Erratic through footwall and ore zones, steady increase in hangingwall away from ore zones, similar to CaO
UD768	Cu	Low values in footwall and hangingwall, increased in ore zones.
UD768	Pb	Similar pattern to Cu
UD768	Zn	Erratic, with no consistent variations
UD768	Ni	Similar pattern to Cu
UD768	Co	Similar pattern to Cu
UD768	As	Similar pattern to Cu
UD768	Sb	Similar pattern to Cu
UD768	V	Very erratic in ore zone
UD768	Ga	Erratic, high in ore zones
UD768	Bi	Similar pattern to Cu
UD768	Tl	Similar pattern to Cu
UD768	Sn	Similar pattern to Cu
UD768	Mo	Similar pattern to Cu
UD768	Y	Similar pattern to CaO and P_2O_5
UD768	Zr	Erratic, with no consistent variations
UD768	Rb	Erratic, with no consistent variations
UD768	Sr	Erratic, with no consistent variations
UD768	Ba	Erratic, with no consistent variations
UD768	S	Similar pattern to Cu
UD768	Mo	Similar pattern to Cu

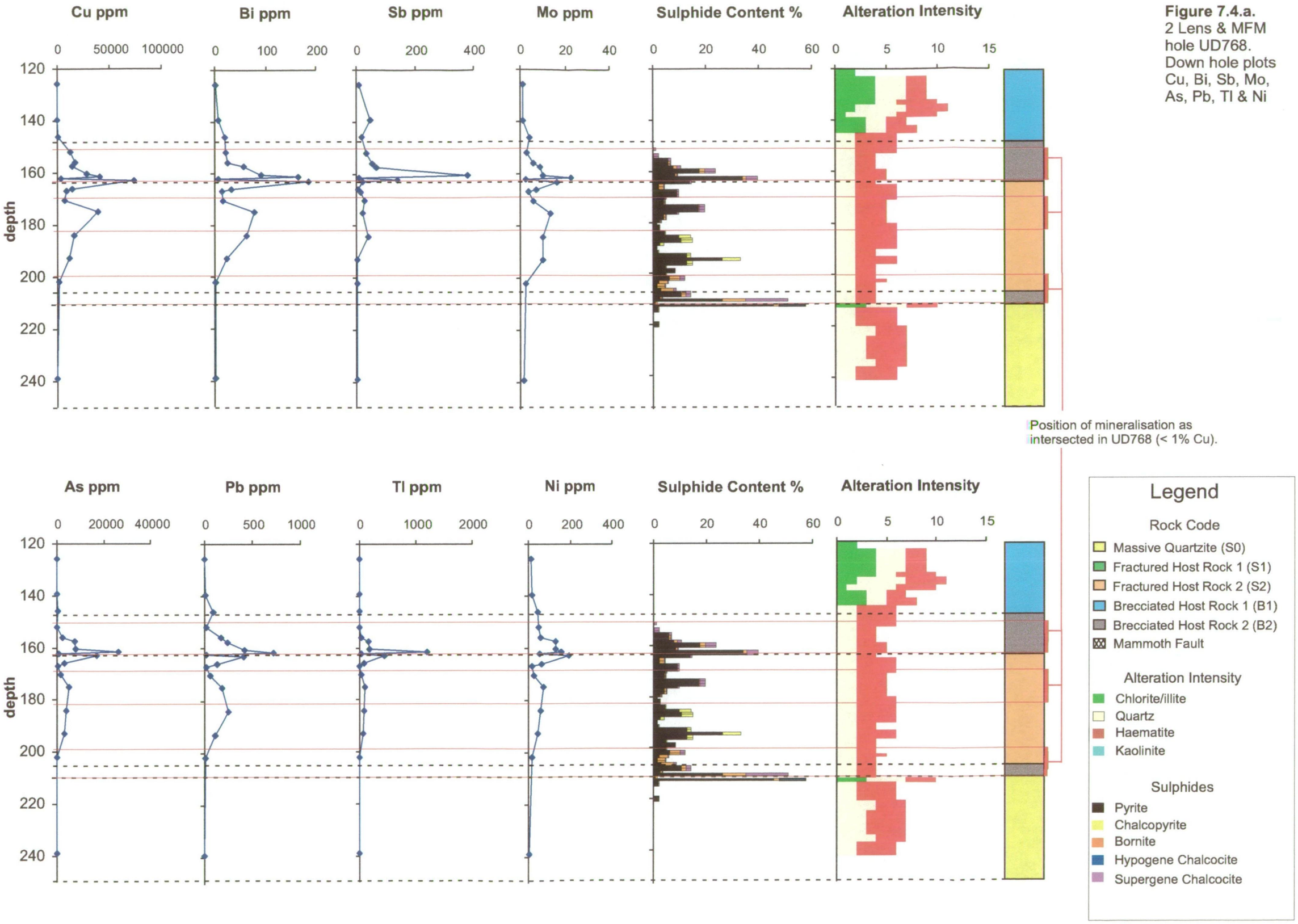

Figure 7.4.a.
2 Lens & MFM hole UD768. Down hole plots Cu, Bi, Sb, Mo, As, Pb, Tl & Ni

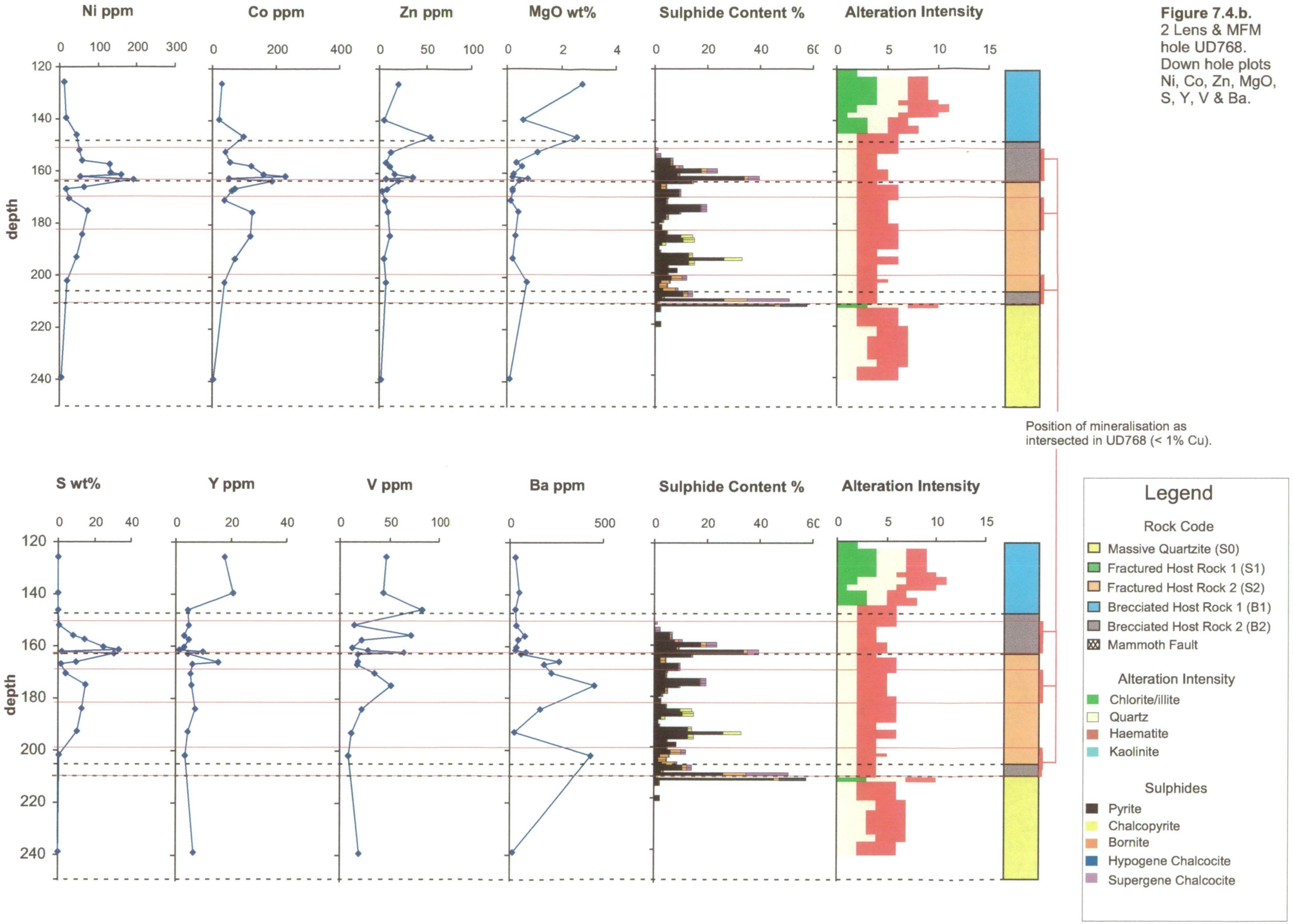

Figure 7.4.b.
2 Lens & MFM hole UD768. Down hole plots Ni, Co, Zn, MgO, S, Y, V & Ba.

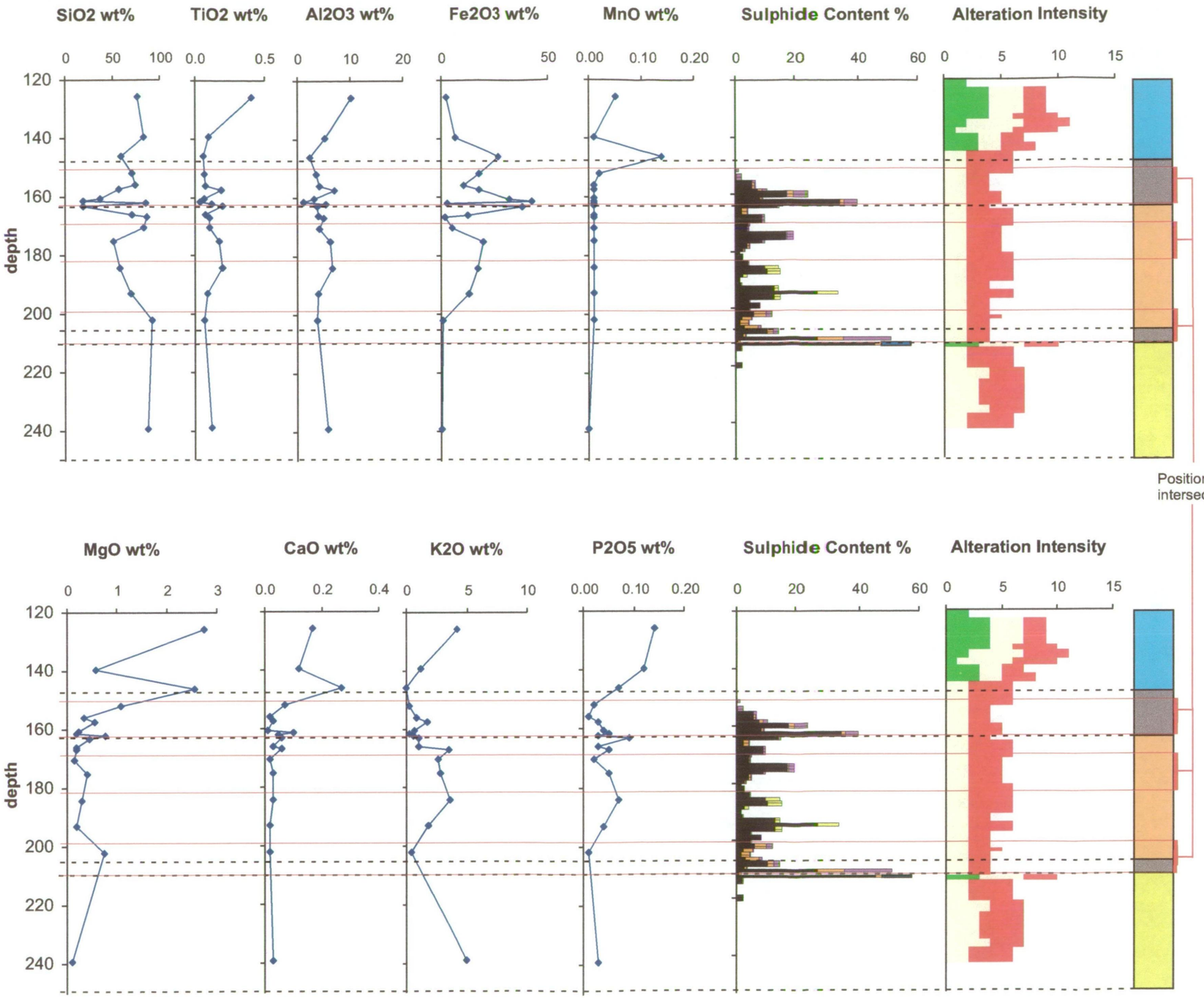

Figure 7.4.c.
2 Lens & MFM hole UD768. Down hole plots SiO2, TiO2, Al2O3, Fe2O3, MnO, MgO, CaO, K2O & P2O5.

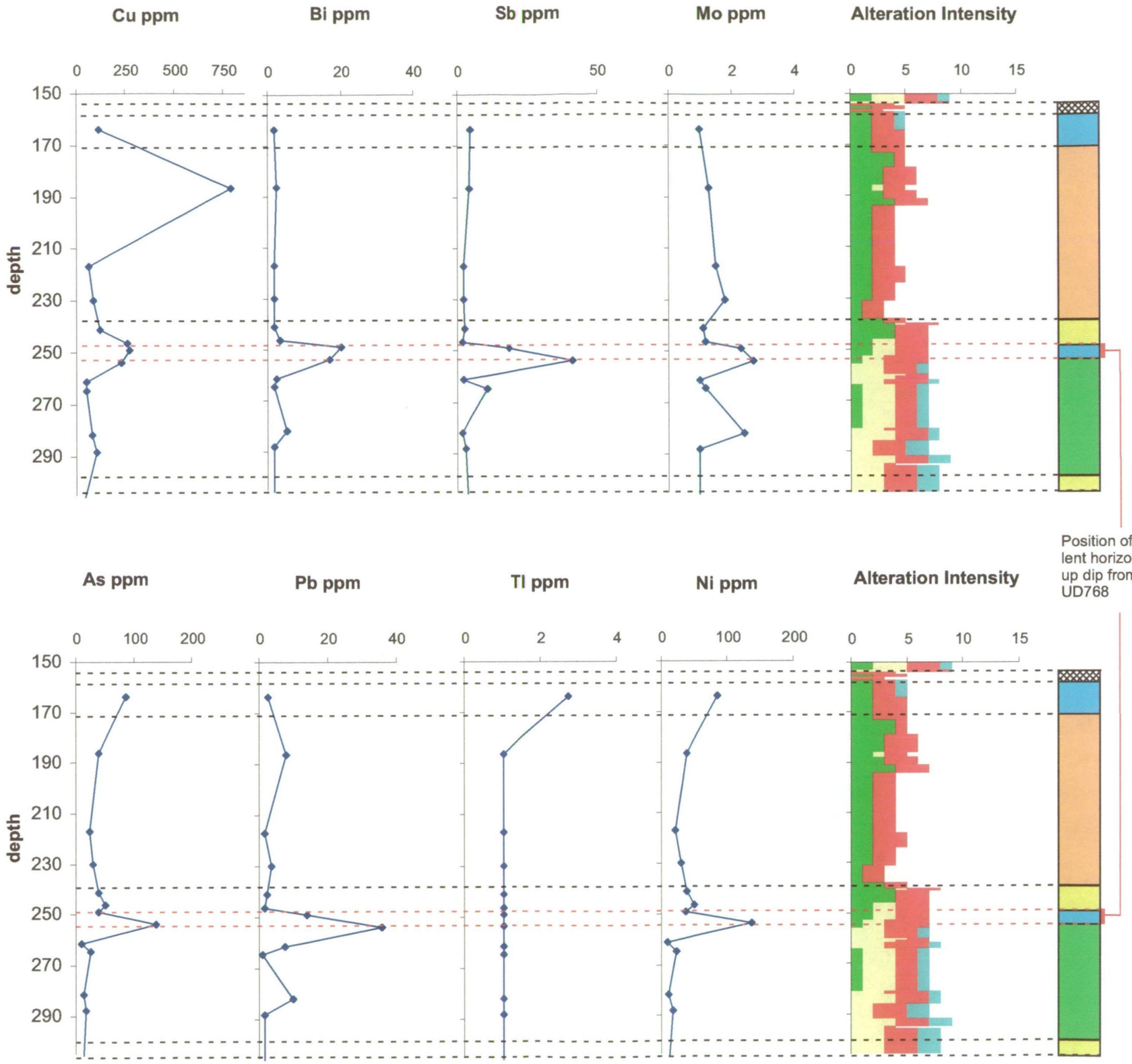

Figure 7.4.d.
2 Lens & MFM hole UD767. Down hole plots Cu, Bi, Sb, Mo, As, Pb, Tl & Ni.

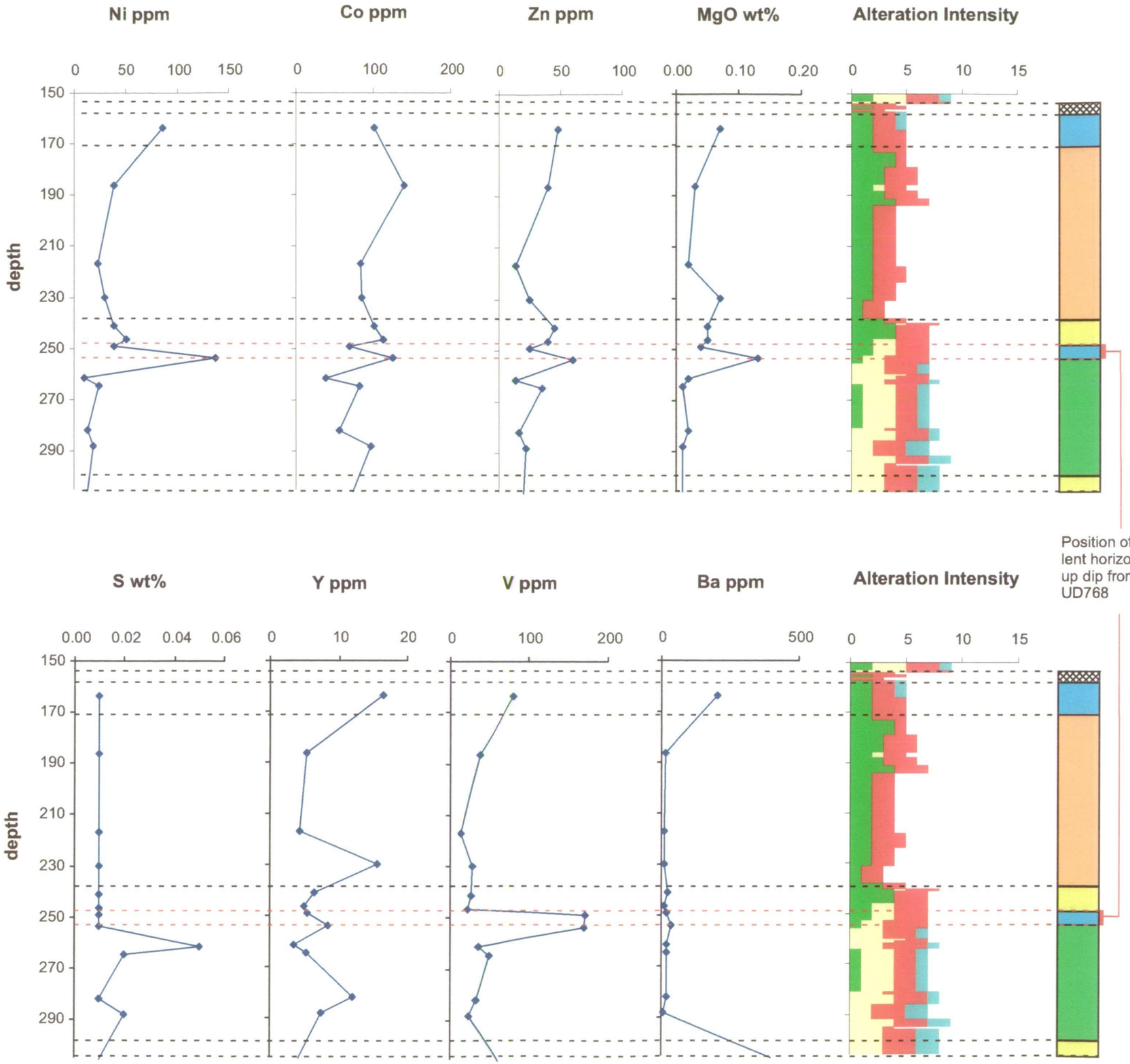

Figure 7.4.e.
2 Lens & MFM hole UD767. Down hole plots Ni, Co, Zn, MgO, S, Y & Ba.

Figure 7.4.f.
2 Lens & MFM hole UD767. Down hole plots SiO2, TiO2, Al2O3, Fe2O3, MnO, MgO, CaO, K2O & P2O5.

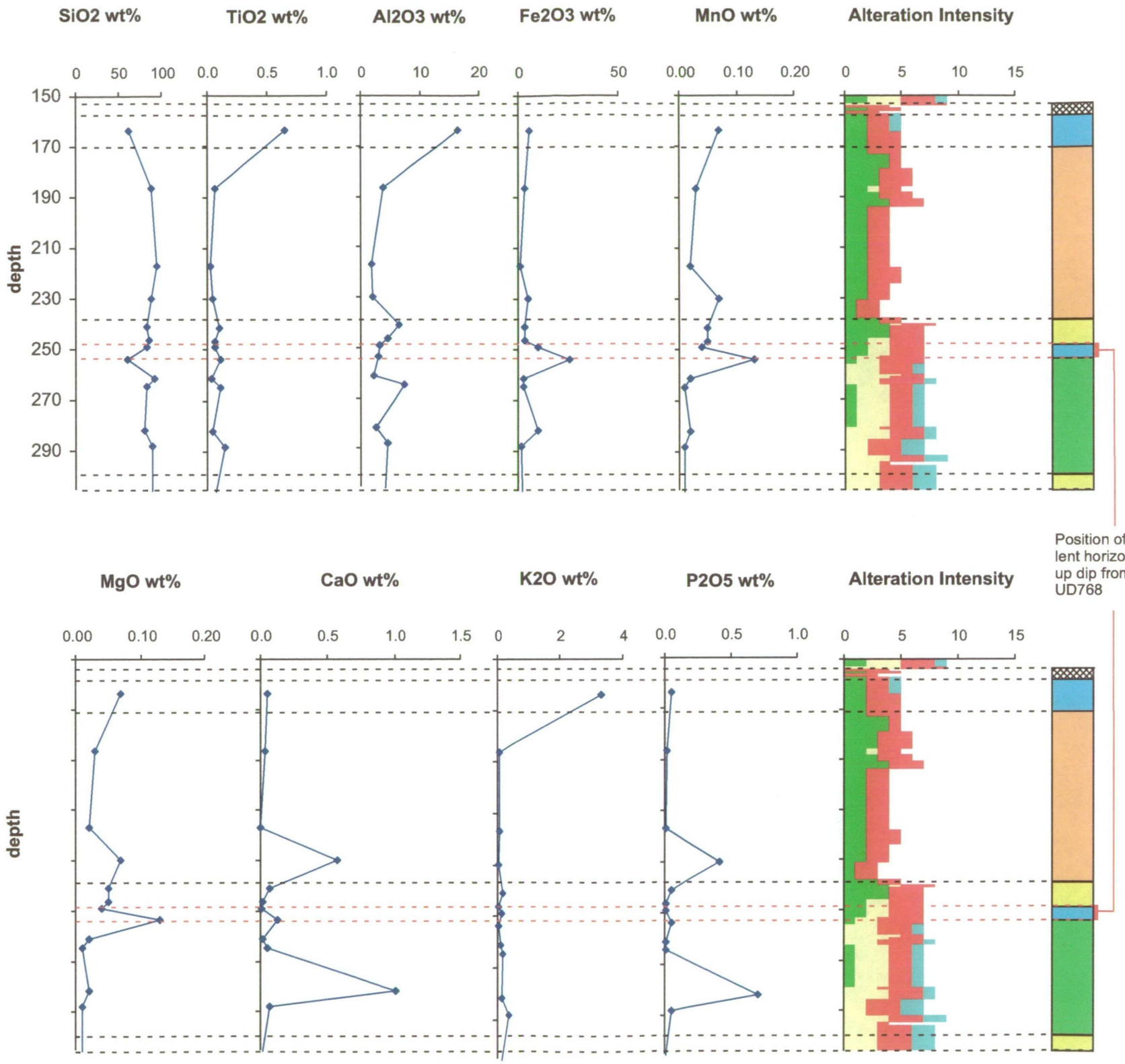

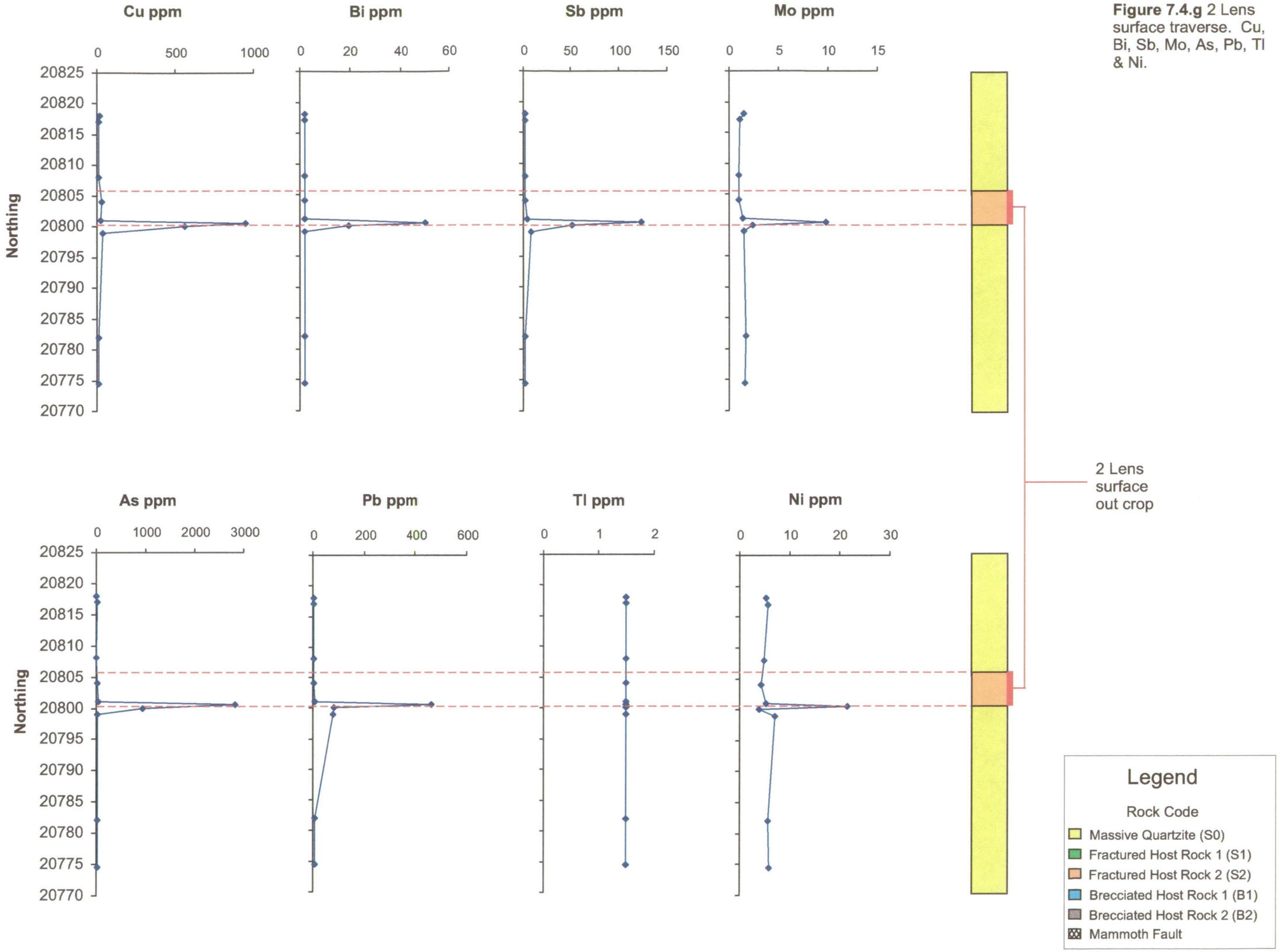

Figure 7.4.g 2 Lens surface traverse. Cu, Bi, Sb, Mo, As, Pb, Tl & Ni.

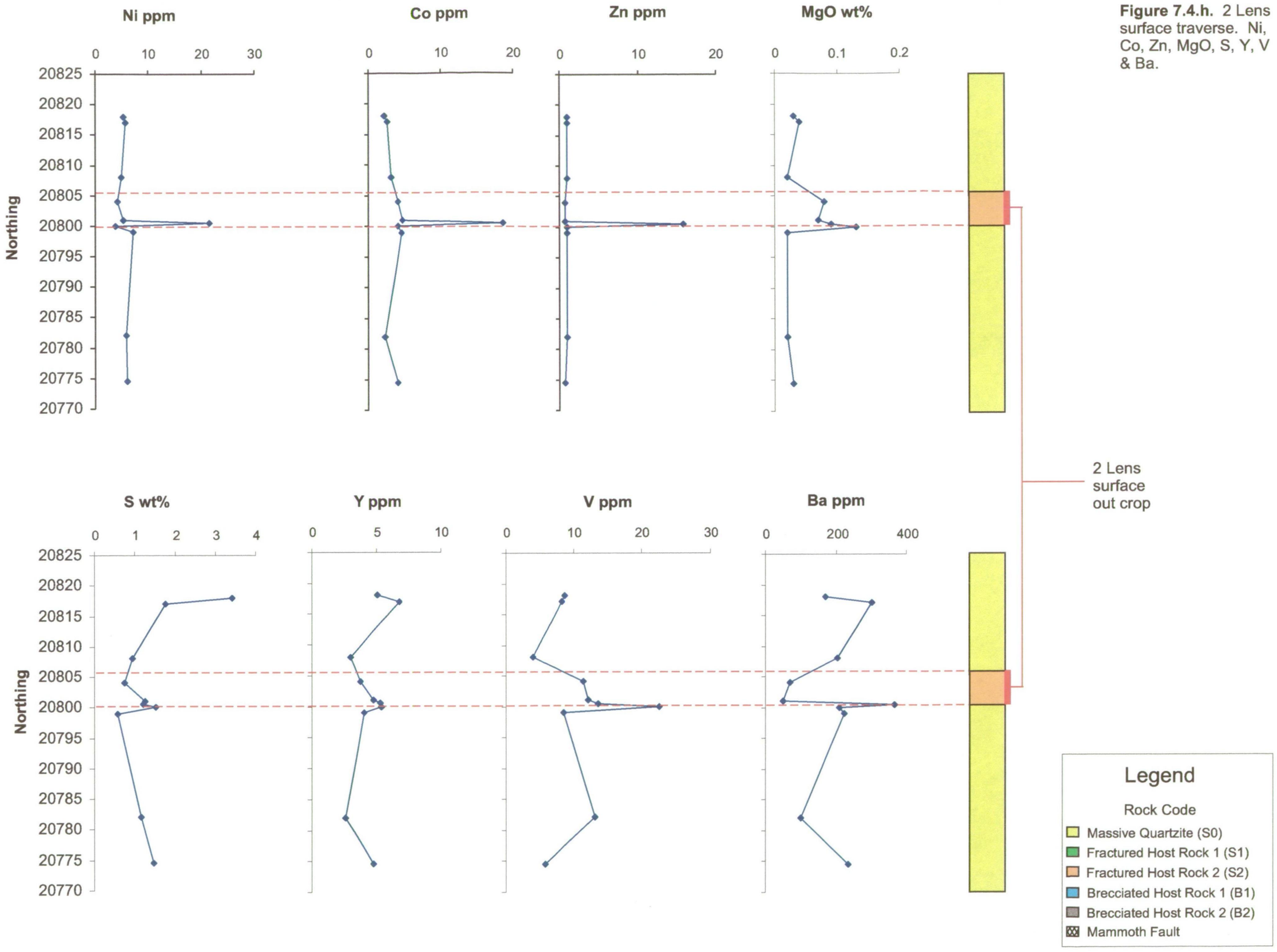

Figure 7.4.h. 2 Lens surface traverse. Ni, Co, Zn, MgO, S, Y, V & Ba.

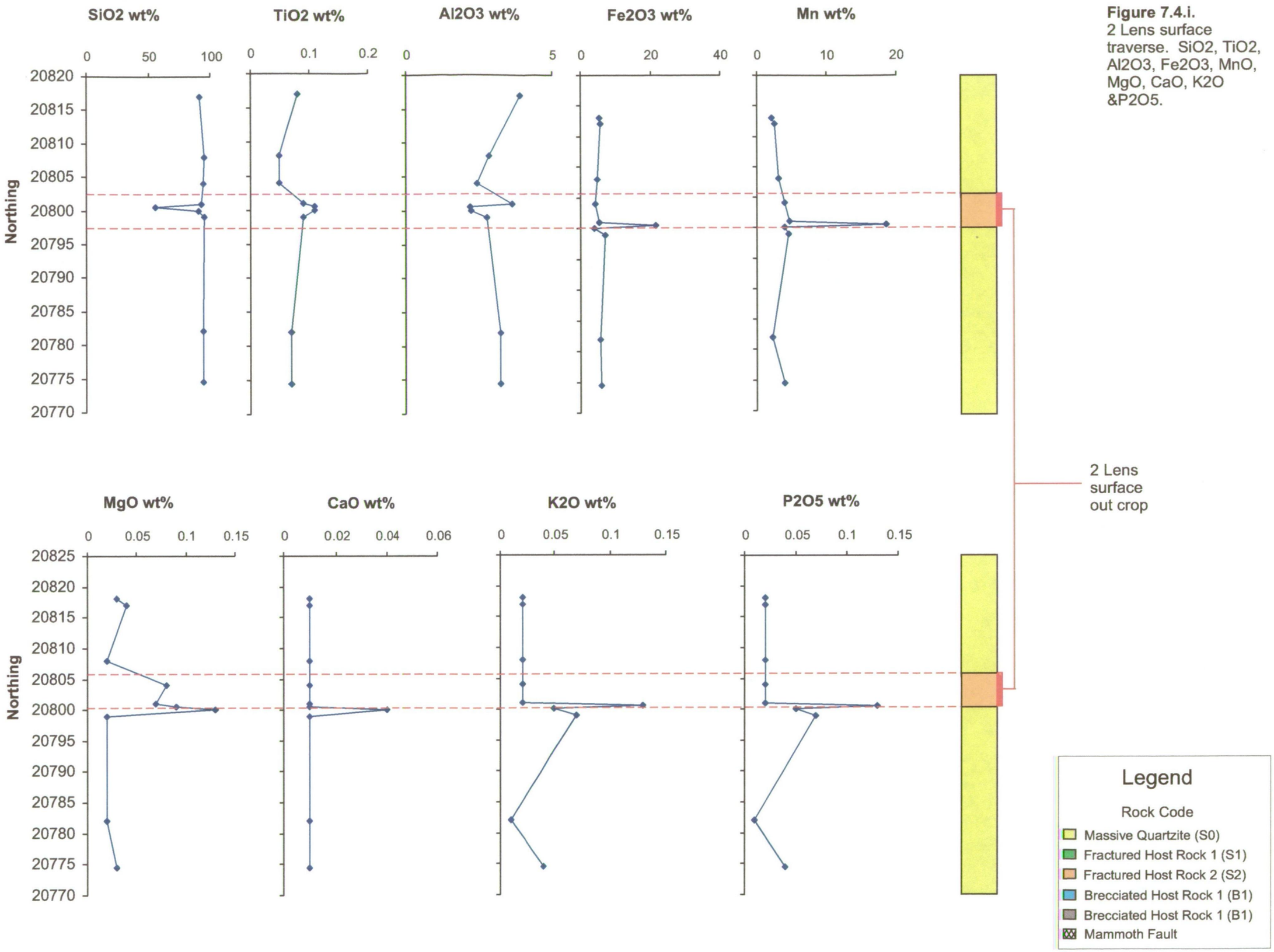

Figure 7.4.i.
2 Lens surface traverse. SiO2, TiO2, Al2O3, Fe2O3, MnO, MgO, CaO, K2O &P2O5.

7.5 DISCUSSION

7.5.a Elements by Textural Classification

The textural classification scheme developed during the course of this project categorises the ore and host rocks into three primary divisions based on the degree of dilation undergone during formation of the Mammoth deposit. These broad primary divisions are: 1) Unfractured Host Rock (S0); 2) Fractured Host Rock (S1 & S2) and 3) Brecciated Host Rock (B1 & B2). The results of this geochemical program when divided into these categories clearly demonstrate the individual geochemical signatures of the units (S0, S1-S2 and B1-B2) (Figs 7.6.-7.8). Overall the median values of the elements S, Sb, Bi, As, S, Sr, Tl, Ni, Co, Fe_2O_3, and Pb, known to be associated with Cu mineralisation, increase as the degree veining/brecciation increases.

Elements not directly associated with Cu and Fe sulfides are divisible into three groups:

1) Al_2O_3, CaO, Na_2O, TiO_2, K_2O, P_2O_5, Zn, Ga, Sr, Ba, Rb, & V decrease from Unfractured Host Rock (S0) through to Fractured Host Rock (S1-S2). However, these elements display an increase in the Brecciated Host Rock (B1-B2) units relative to the Fractured Host Rock (S1 & S2).
2) SiO_2, initially increases from Unfractured Host Rock (S0) through to Fractured Host Rock (S1-S2), then displays a decrease in the Brecciated Host Rock (B1-B2) units relative to the Fractured Host Rock (S1 & S2).
3) Zr, MgO & MnO have a uniform decrease from Unfractured Host Rock (S0), Fractured Host Rock (S1 & S2) through to Brecciated Host Rock (B1 & B2).

The geochemical signatures are related to the, variably developed, ore and alteration mineralogy. Sulphur, Sb, Bi, As, Sr, Tl, Ni, Co, Fe and Pb are associated with Cu mineralisation and increase as the degree veining/brecciation increases. Aluminium (Al_2O_3), CaO, Na_2O, TiO_2, K_2O, P_2O_5, Zn, Ga, Sr, Ba, Rb, & V display an increase in the B1 and B2 units relative to S1 & S2 units, suggesting that these elements may be leached/depleted during alteration of wallrock. The SiO_2 content is highest in the S1 and S2 units reflecting the precipitation of SiO_2 as quartz during the

vein emplacement and alteration of wall rock by the mineralising fluid. The observed uniform decrease in the concentration MgO and MnO from S0, S1 & S2 through to B1 & B2 is interpreted as being associated with the occurrence of chlorite. The decrease of both MgO and MnO may reflect a change in chlorite composition that ranges from Mg-chlorite distal to Fe-chlorite proximal to, and within, the brecciated ore zones (B1 & B2). Zirconium is present as the detrital mineral zircon and the uniform decrease occurs in response to the dilution of the host rock by the dilatant infilling nature of the mineralising system.

The categories outlined in the textural classification scheme have, in general, geochemical signatures that are directly related to the ore and alteration mineralogy associated with each textural division (S0, S1, S2, B1 & B2).

7.5.b Alteration Mineral Zonation

Hypogene alteration at Mammoth is typified by intergrowths of illite and both Fe and Mg chlorite, with variations in the degree of alteration reflected by the relative abundances of these minerals. This alteration primary replaces detrital microcline and is zoned from illite to chlorite with the illite corresponding to chalcopyrite-dominated zones and chlorite corresponding to bornite and hypogene chalcocite zones. Within the chlorite alteration, chlorite chemistry changes from Fe chlorite to Mg chlorite (Chapter 6, section 6.2). Within the stacked D lens ore zones the distribution of Fe chlorite corresponds to the bornite-dominated ore zones and the Mg chlorite corresponds to the chalcocite-dominated zones. Therefore, as can be demonstrated by the distributions of ore and alteration minerals in D lens, an overall zoned pattern occurs from pyrite-chalcopyrite, illite with minor chlorite at depth to pyrite-bornite, Fe chlorite with minor illite in the middle, to pyrite-hypogene chalcocite, Mg chlorite with minor illite at the upper extents of the ore zones. Subsequent supergene alteration principally illite and chlorite of the hypogene alteration mineralogy results in the production of kaolinite.

Rutile ($FeTiO_3$) has been identified as an inclusion within chalcopyrite, euhedral quartz and as a common accessory detrital mineral in the host rock. Elevated TiO_2 values associated with the chalcopyrite zone are interpreted to

correlate with the presence of rutile as an inclusion in the ore mineral assemblage. The strong positive correlation of CaO to P_2O_5 within the data set implies that these elements in the ore zone altered wall rock and barren host rock occur in the form of apatite. Apatite has been identified as an accessory detrital mineral in the host rock and as a product of alteration. Chlorite and hematite display an antithetic relationship supporting the hypothesis that hematite formed via supergene alteration of chlorite. Significant occurrences of supergene chalcocite have been identified within the D, 2 and MFM ore zones where corresponding occurrences of hematite are in greater abundance relative to chlorite or where chlorite is entirely absent.

The extent and style of alteration can be characterised geochemically by plotting the major elements Al_2O_3, K_2O and MgO on a ternary diagram. Ternary diagrams, demonstrating the style and distribution of the hypogene alteration phases and supergene kaolinite are presented for the E, D, B, C, 2 and the Mammoth Fault Mineralisation (MFM) ore zones (Figure 7.9).

The alteration mineralogy of E, D, C, B, 2 and MFM ore zones is divisible in two broad categories: 1) chlorite dominated or 2) illite and chlorite dominated. The ore zones E, D, 2 and MF are included in the illite and chlorite-dominated category. Alteration in the B and C ore zones is dominated by chlorite. The supergene alteration product, kaolinite has only been observed within the D Lens data set. Kaolinite also occurs in the footwall to the 2 Lens ore zone as identified via hand specimen investigation and noted in Figure 7.4.

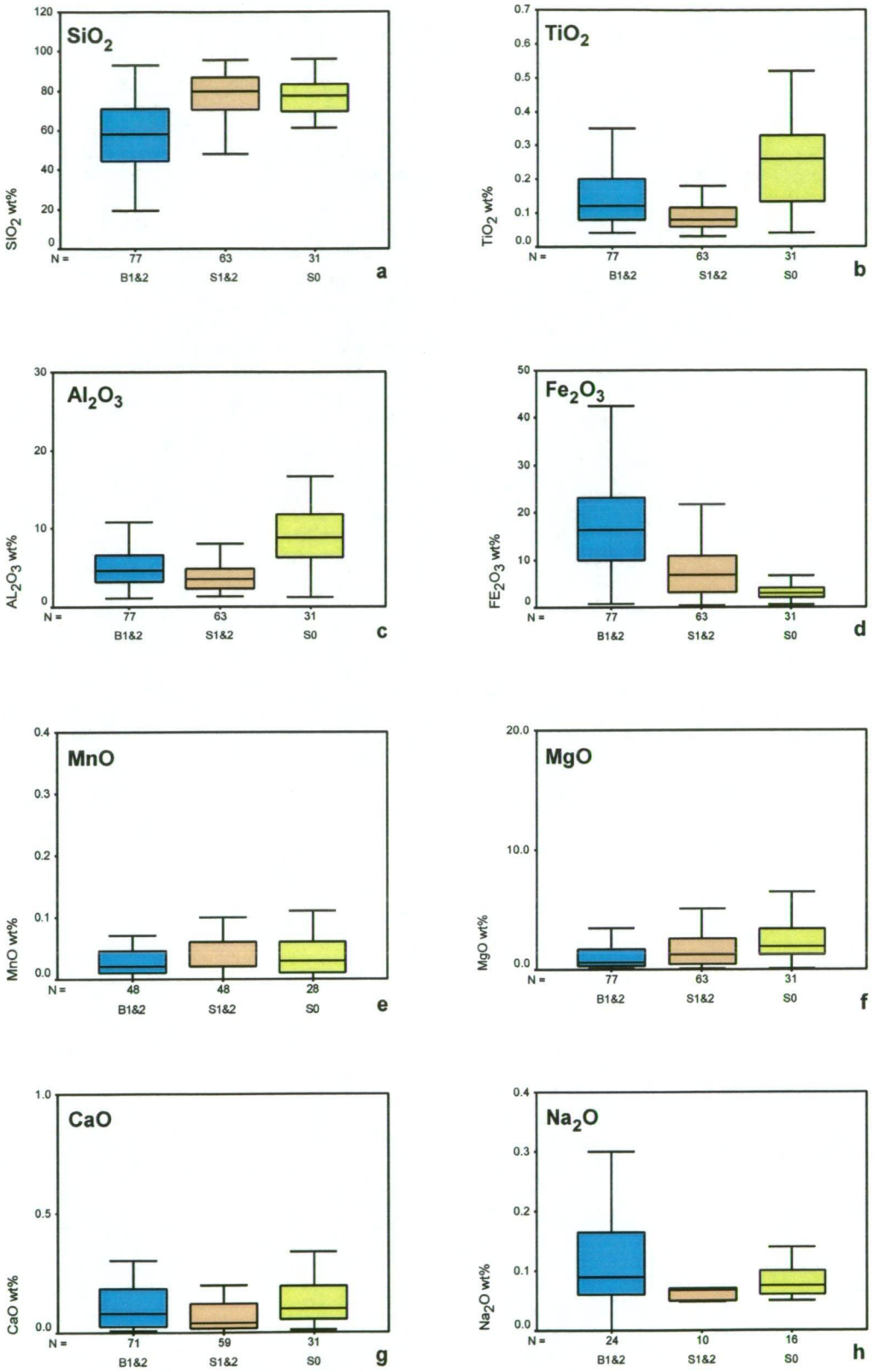

Figure 7.6.a-h. Box and whisker plots summarising the distribution of the major and trace elements classified by textural style: S0 = Unfractured Host Rock; S1 & S2 = Fractured Host Rock and B1 & B2 = Brecciated Host Rock.

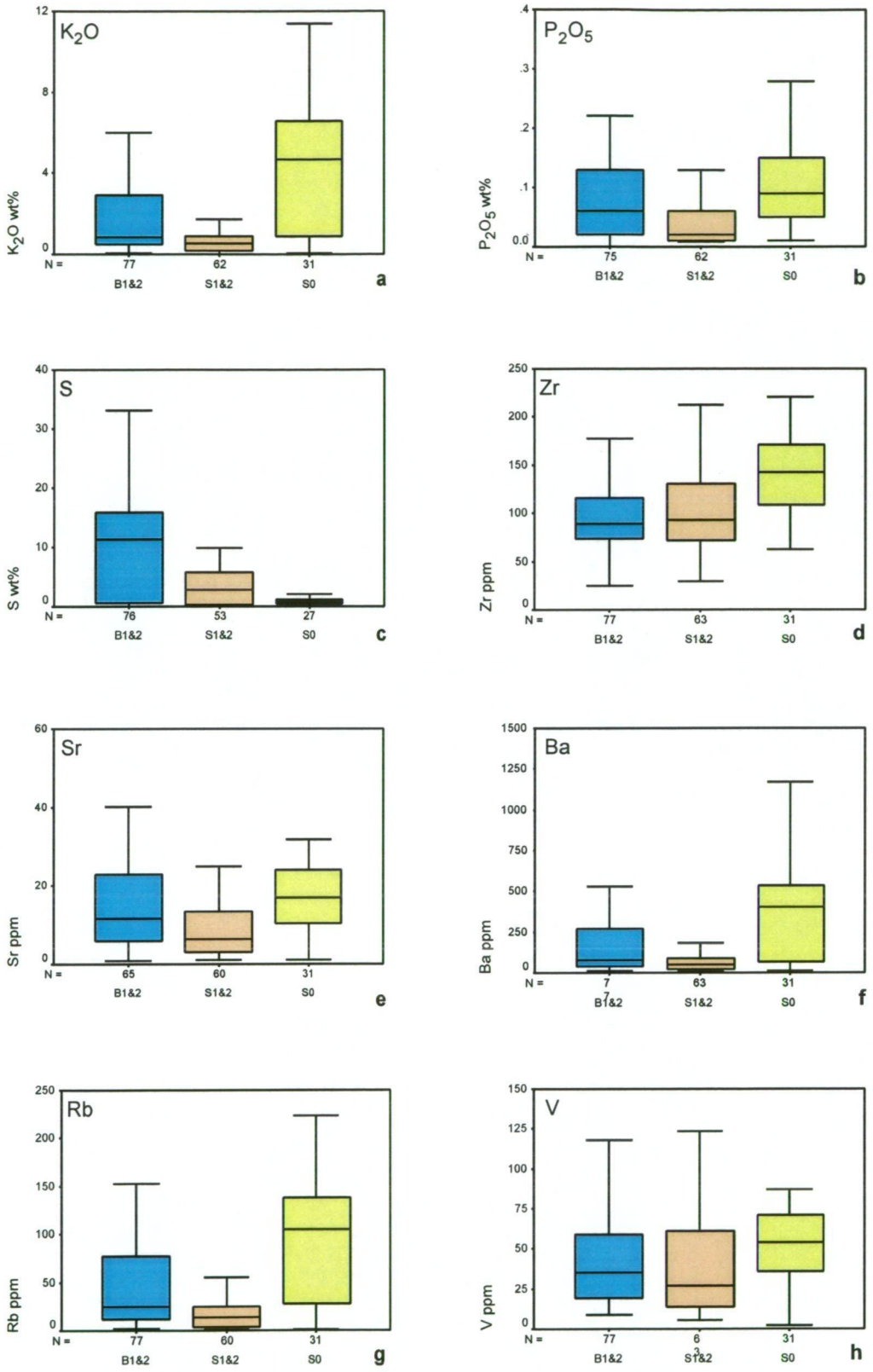

Figure 7.7.a-h. Box and whisker plots summarising the distribution of the major and trace elements classified by textural style: S0 = Unfractured Host Rock; S1 & S2 = Fractured Host Rock and B1 & B2 = Brecciated Host Rock.

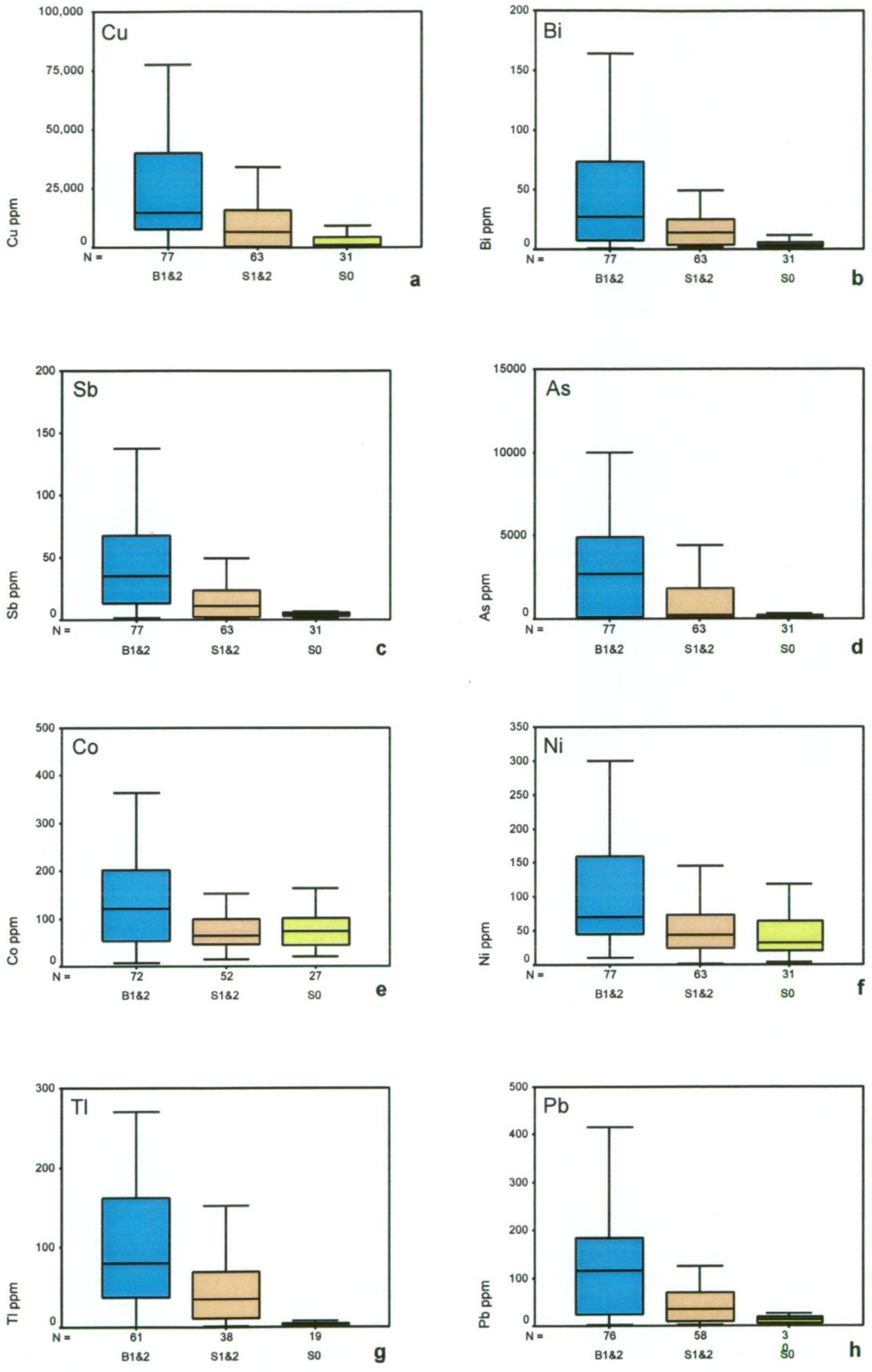

Figure 7.8.a-h. Box and whisker plots summarising the distribution of major and trace elements classified by textural style: S0 = Unfractured Host Rock; S1 & S2 = Fractured Host Rock and B1 & B2 = Brecciated Host Rock.

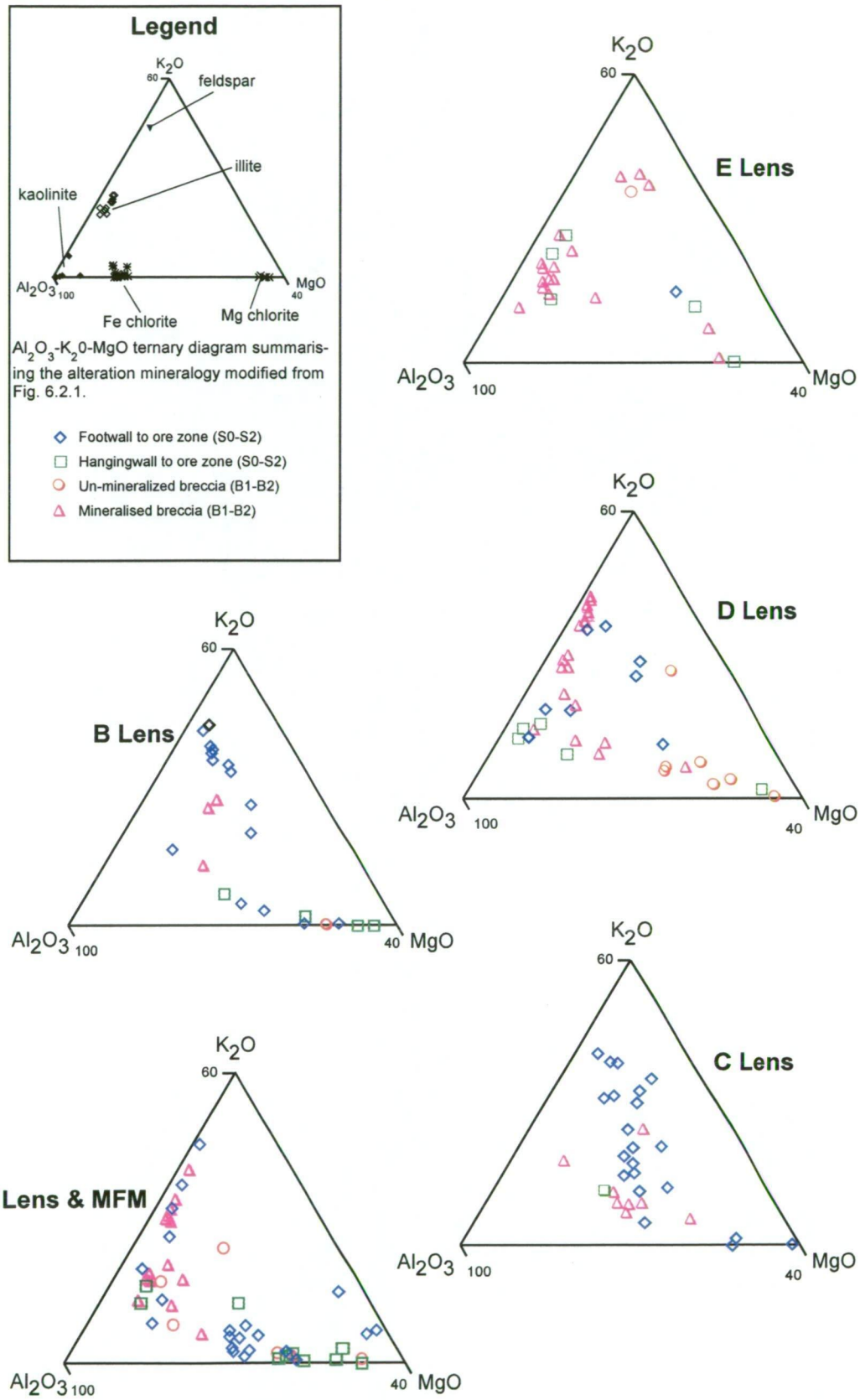

Figure 7.9. Whole-rock geochemical data plotted on wt% Al_2O_3-K_20-MgO ternary diagrams. This data illustrates the distribution of chlorite, illite and kaolinite alteration mineralogy associated with the Mammoth ore zones: Mineralised and barren breccia units (B1-B2); hangingwall and footwall units (S0, S1-S2).

7.5.c Element Correlation

Correlations between elements were investigated using XY scatter plots for all elements analysed via XRF whole-rock for major and trace elements (Figure 7.10-7.12). The results have been divided based the textural classification of the sample either as Unfractured Host Rock (S0); Fractured Host Rock (S1-S2) and Brecciated Host Rock (B1-B2) and are summarised in Table 7.6.

In general, Cu has a strong positive correlation with S, Fe, Pb, Ni, Bi & As, and a strong negative correlation with SiO_2. However correlations between the major and trace elements obtained for individual textural types vary significantly, as follows:

- Unfractured Host Rock (S0); Cu demonstrates a weak positive correlation with Zn and does not correlate positively or negatively with any other major or trace element in the data set. SiO_2 has a negative correlation with TiO_2, Al_2O_3, MgO, CaO, K_2O, P_2O_5, Fe, Y, V, Ga, Zr, Sr, Rb, Ba, and Zn. Al_2O_3 demonstrates a positive correlation with TiO_2, CaO, K_2O, P_2O_5, Fe_2O_3, Y, Rb, Ga and Sr. Potassium (K2O) has a positive correlation with TiO_2, Al_2O_3 CaO, P_2O_5, Rb, Sr, and Ba. Iron (Fe_2O_3) demonstrates a positive correlation with TiO_2, Al_2O_3, MnO, MgO, CaO, Na_2O, P_2O_5, Y, Ga, V, Zn, Sb and S (at > 2000 ppm S; Table 7.6).
- Fractured Host Rock (S1 & S2); Cu has a broad negative correlation with SiO_2 and weak to strong positive correlations with the major and trace elements Fe, Pb, Bi, As, Ni, S, and Mo, above noted element concentrations (Table 7.6). SiO_2 demonstrates a broad to strong negative correlation with Pb, Cu, Bi, As, Sb, Ni, Co, Tl, S and Mo. Al_2O_3 demonstrates a broad to strong positive correlation with TiO_2, K_2O, Y, Rb, Ga and Sr. Fe_2O_3 demonstrates a weak to strong positive correlation with Pb, Cu, Bi, As, Sb, Ni, Co, Tl and Mo, above noted element concentrations (Table 7.6).
- Brecciated Host Rock (B1 & B2); In general the correlation's between major and trace elements within this category are the same as for S1 & S2.

In addition to the above, Figures 7.10-7.12 illustrates the positive correlation between Fe_2O_3, Al_2O_3, and Zn with MgO, within a subset of barren (>0.25% S) samples.

The variable correlation that Cu displays with other trace and major elements between textural types ultimately reflects the dominant mineralogy of the respective textural classifications. The negative correlation between SiO_2 and Cu, Fe, Pb, S, Sb, Bi, Mo, Co, Ni and Tl (Table 7.6), as seen in the Fractured (S1 and S2) and Brecciated Host Rock (B1 and B2) units, reflects the dilatant infilling style of the mineralisation process. The consistent positive correlation observed between Al_2O_3, CaO, MgO, P_2O_5, K_2O, Rb, Sr, Ba, TiO_2, Y and Ga within the Unfractured Host Rock (S0) category is related to the ubiquitous distribution of the primary detrital minerals microcline ($KalSi_3O_8$), apatite ($Ca_5(PO_4)_3(OH,F,Cl)$), accessory ferro-magnesious minerals and rare mafic lithic clasts. The occurrence of the hypogene alteration mineral illite ($K_{1.5\text{-}1.0}Al_4[Si_{6.5\text{-}7.0}Al_{1.5\text{-}1.0}O_{20}](OH)_4$) within and adjacent to stock work veins and breccia matrixes of S1, S2 B1, and B2 units is demonstrated by the weak to broad positive correlation between Al_2O_3, Ga, K_2O, Sr and Rb (Fig. 7.10.c and Table 7.6). The occurrence of chlorite (Mg, Fe, MnO, $Al)_{12}[(Si, Al)_8O_{20}](OH)_{16}$ within and adjacent to stockwork veins and breccia matrixes of S1, S2 B1, and B2 and partially in S0 units is demonstrated by the broad positive correlation between Fe_2O_3 and MgO (<5000 ppm S) (Fig. 7.12.c). The strong negative correlation demonstrated between SiO_2 and MgO (<5000 ppm S) confirm this association, which again reflects the dilatant infilling style of the mineralisation process (Fig. 7.12.e). The observed positive correlation of Zn with MgO suggests the distribution of Zn is linked to the occurrence of chlorite (Fig. 7.12.f)

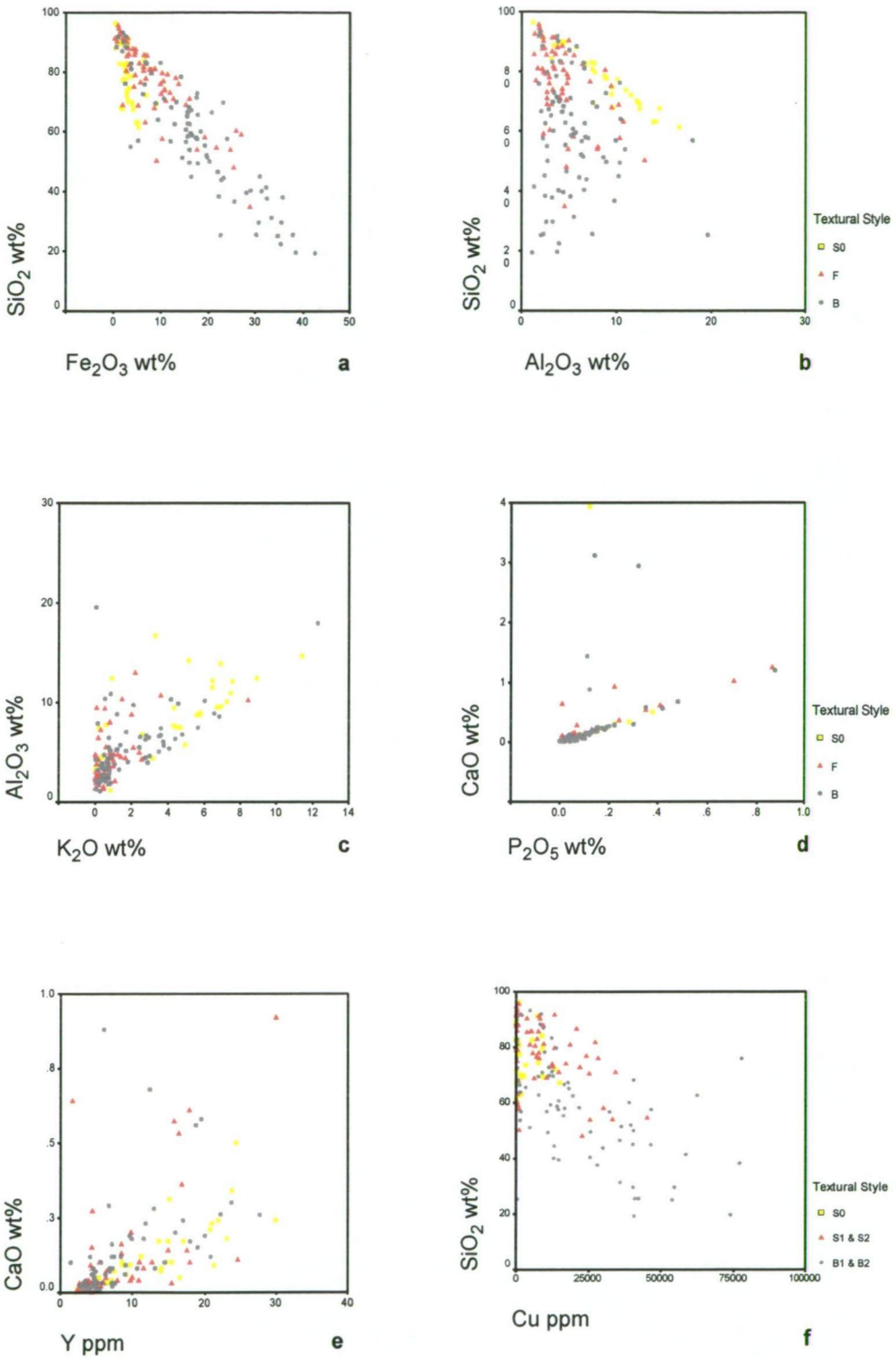

Figure 7.10.a-f. XY plots summarising the correlations of a) SiO_2 vs Fe_2O_3; b) SiO_2 vs Al_2O_3; c) Al_2O_3 vs K_2O; d) CaO vs P_2O_5; e) CaO vs Y & f) SiO_2 vs Cu. Data categorised by textural classification scheme: S0 = Unfractured Host Rock; S1 & S2 = Fractured Host Rock and B1 & B2 = Brecciated Host Rock.

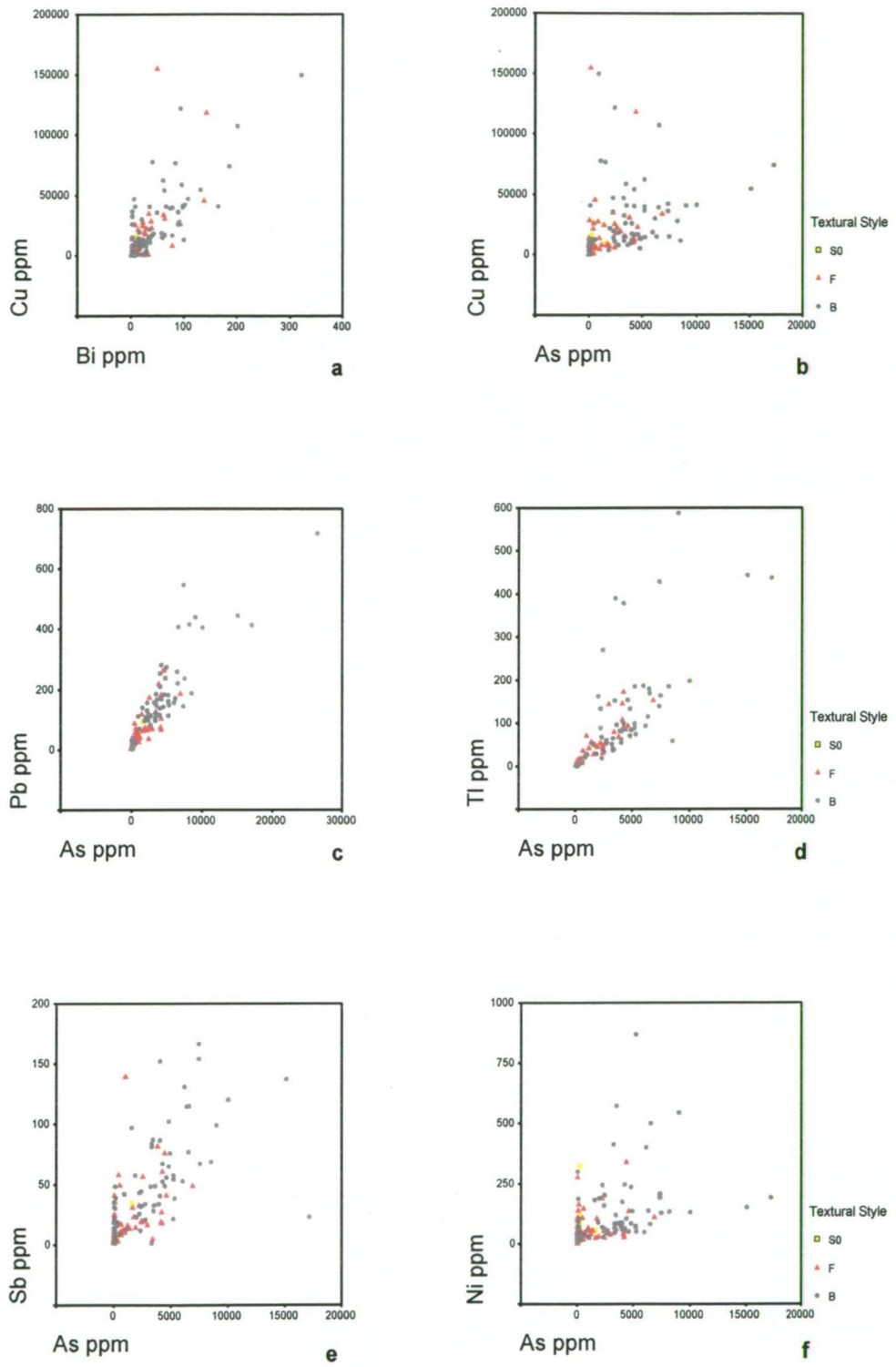

Figure 7.11.a-f. XY plots summarising the correlations of a) Cu vs Bi; b) Cu vs As; c) Pb vs As; d) Tl vs As; e) Sb vs As & f) Ni vs As. Data catagorised by textural classification scheme: S0 = unfractured Host Rock; S1 & S2 = Fractured Host Rock and B1 & B2 Brecciated Host Rock.

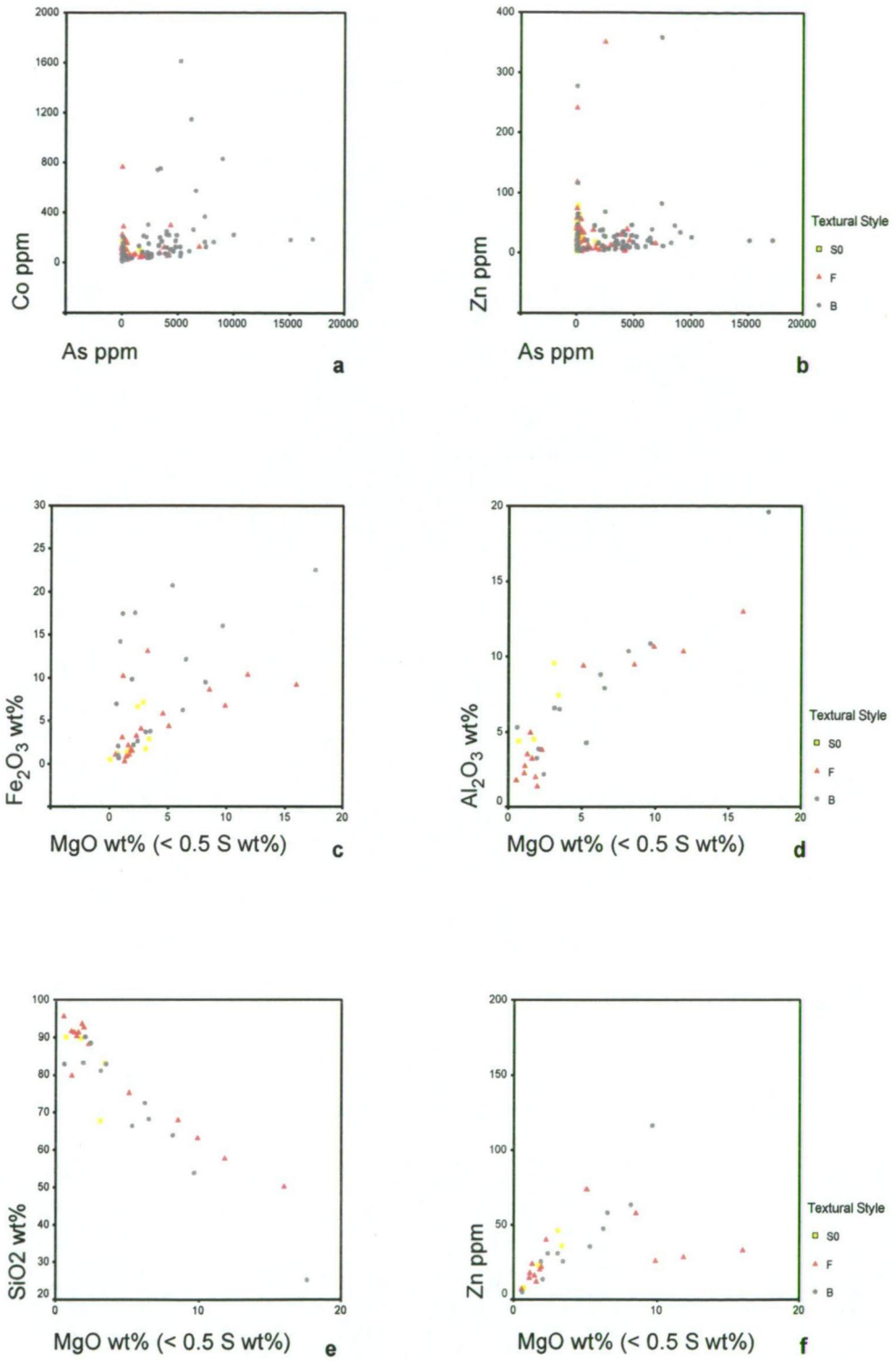

Figure 7.12.a-f. XY plots summarising the correlations of a) Co vs As; b) Zn vs As; c) Fe_2O_3 vs MgO; d) Al_2O_3 vs MgO; e) SiO_2 vs MgO & f) Zn vs MgO . Data catagorised by textural classification scheme: S0 = unfractured Host Rock; S1 & S2 = Fractured Host Rock and B1 & B2 Brecciated Host Rock.

Table 7.6. Summary of correlations in the major and trace element data set (examples given in Figures 7.10-7.12). Data have been classified into categories as per the textural classification scheme: Unfractured Host Rock (S0), Fractured Host Rock (S1 & S2) and Brecciated Host Rock (B1 & B2). Note: lower limit of concentration are noted where correlations are evident above this concentration, for example there is a broad positive correlation (b+) between Fe & Pb above 40 ppm Pb. Abbreviations: + = strong positive correlation; - = strong negative correlation; b+ = broad positive correlation; b- = broad negative; wk+ = weak positive; wk- = weak negative correlation; and a "*blank*"= no correlation. Major and trace element data in Appendix 2

	categories	SiO2	TiO2	Al2O3	MnO	MgO	CaO	Na2O	K2O	P2O5	Fe	Y	Rb	Ga	Zr	Sr	Ba	V
	S0	N/A	-	-		wk-	wk-		b-	b-	-	b-	wk-	-	b-	b-	b-	-
SiO2	S1&2	N/A									-							
	B1&2	N/A									-							
	S0	-	+	N/A			wk+		b+	wk+	wk+	+	+	+		+		
Al2O3	S1&2		+	N/A					wk+			b+	wk+	+		wk+		
	B1&2		+	N/A					b+			b+	b+	+		b+		
	S0	wk-	+	b+			wk+		N/A	wk+			+			+	+	
K2O	S1&2			b+					N/A				+			+	+	
	B1&2		b+	b+					N/A				+			+	+	
	S0	-	b+	wk+	wk+	+	wk+	wk+		b+	N/A	wk+		b+				wk+
Fe	S1&2	-									N/A							
	B1&2	-									N/A							
	S0																	
Cu	S1&2	b-									+							
	B1&2	b-									+							

		Pb	Zn	Cu	Bi	As	Sb	Ni	Co	Tl	S	Mo
	S0		wk-	>5000 ppm b-								
SiO2	S1&2	>40 ppm -		>5000 ppm b-	>15 ppm -	>500 ppm -	>10 ppm -	-	>100 ppm -	>10 ppm -	> 5000 ppm -	> 4 ppm -
	B1&2	>40 ppm -		>5000 ppm b-	>15 ppm -	>500 ppm -	>10 ppm -	-	>100 ppm -	>10 ppm -	> 5000 ppm -	> 4 ppm -
	S0											
Al2O3	S1&2											
	B1&2											
	S0											
K2O	S1&2											
	B1&2											
	S0		b+				b+				>2000 ppm +	
Fe	S1&2	>180 ppm b+		>5000 ppm +	wk+	>500 ppm b+	b+	>25 ppm b+	>20 ppm b+	>10 ppm b+	>2000 ppm +	>2 ppm b+
	B1&2	>180 ppm b+		>5000 ppm +	wk+	>500 ppm b+	b+	>25 ppm b+	>20 ppm b+	>10 ppm b+	>2000 ppm +	>2 ppm b+
	S0		wk+	N/A								
Cu	S1&2	wk+		N/A	+	wk+		wk+			b+	
	B1&2	wk+		N/A	b+	b+	b+	wk+			b+	

7.5.d Sulfide Mineral Zonation

In general, hypogene Cu sulfides are zoned from hangingwall to footwall and up dip, within the major Mammoth ore zones. This zonation is broadly categorised as: 1) chalcocite ± bornite; 2) bornite ± chalcocite and 3) chalcopyrite ± bornite. The chalcopyrite ± bornite zone occurs in the footwall and deeper positions within individual ore zones and the chalcocite ± bornite occurring in the hangingwall and up dip positions. 2 lens, an exception to the above, is zoned from chalcocite ± bornite in the footwall to bornite in the hangingwall. The supergene modification of the hypogene mineralogy results in supergene chalcocite (± covellite) overprinting the hypogene Cu sulfide zonation as clearly demonstrated in the D lens and Mammoth Fault ore zones (Fig. 7.13).

7.5.e Comparison of Sulfide Geochemistry to Whole-Rock Geochemistry: Implications for Geochemical Halos and Vectors to Mammoth Ore Zones.

The spatial distribution of the major and trace element geochemistry reflects the occurrence and distribution of the sulfide and alteration mineralogy. The identification of geochemical halos and potential vectors to the Mammoth ore zones is reliant upon documenting the specific correlations between the variations in the whole-rock geochemistry and mineral assemblages (sulfide and/or alteration minerals).

Investigations into the pyrite geochemistry (Chapter 6) demonstrated that Stage I pyrite (disseminated and veined) is significantly enriched in As (average value ≅ 2 wt% As, Table 6.1.3) and moderately enriched in Co, Pb, Ni and Sb relative to the Stage II Cu and Cu-Fe sulfides. Within the whole-rock geochemical data set As has a strong positive correlation with Tl, Pb, Co and Ni, and a moderately positive correlation with Cu, Fe and Sb. Therefore, the observed co-variation of the trace elements As, Tl, Pb, Co and Ni, within the Mammoth ore zones as identified by whole-rock geochemistry is interpreted to correspond to the occurrence of Stage I pyrite.

The trace element signatures of Stage II chalcopyrite, bornite and hypogene chalcocite, identified via LA ICPMS, (Table 6.3.1 and Fig. 6.1.4) all broadly

overlap with the exceptions of Bi (elevated in bornite; average value = 647 ppm Bi) and Ag (elevated in hypogene chalcocite; average value = 302 ppm Ag). Within the whole-rock geochemical data set (Table 7.6 and Figs 7.10-12) Cu has a positive correlation with Fe and Bi. The occurrence of hypogene chalcocite intersected in drill hole SD255A (Fig. 7.1.c) corresponds with a significant elevation of the Ag content (≅ 30 ppm Ag, above a background of ≅ 8 ppm). The occurrence of bornite within the same drill hole (SD255A, Fig. 7.1.c) corresponds with increases in the Bi content. These observations, coupled with the known trace element signatures of the Stage I and II sulfides (Table 6.1.3), suggest that bornite and hypogene chalcocite are associated with elevated concentrations of Bi and Ag in contrast to Stage I pyrite and Stage II chalcopyrite.

Stage III supergene chalcocite is enriched in Bi (83 ppm) and depleted in both Ag (23 ppm) when compared to Stage II hypogene chalcocite (Table 6.1.3 and Fig. 6.1.4). However due to the common occurrence of Stage II bornite (and its elevated Bi content, ≅ 647 ppm) with both supergene and hypogene styles of chalcocite (Figs 5.3 and 5.4) the applicability of using Bi as an indicator for the specific occurrence of Stage III hypogene chalcocite from whole-rock geochemical data is limited.

As demonstrated in sections 7.5.b and 7.5.c the spatial distribution of alteration mineralogy is reflected in variations in the whole-rock geochemistry and is summarised as follows. The elevated concentrations of Zn occur with corresponding increases in the chlorite content. Cobalt and Ni are weakly elevated, relative to host rock, in the hangingwall and footwall units immediately adjacent to the ore zones. CaO and P_2O_5 are variably enriched in the hangingwall and footwall units adjacent to the ore zones and weakly elevated within the chalcopyrite ore zones. Aluminium (Al_2O_3), TiO_2, K_2O, MnO, MgO, Sr, Rb, Ba and Ga are weakly elevated in the ore zones reflecting the occurrence of chlorite and illite alteration phases. MnO and MgO are enriched in the hangingwall and footwall units adjacent to the bornite and ore chalcocite dominated ore zones and to a lesser extent the chalcopyrite dominated ore zones

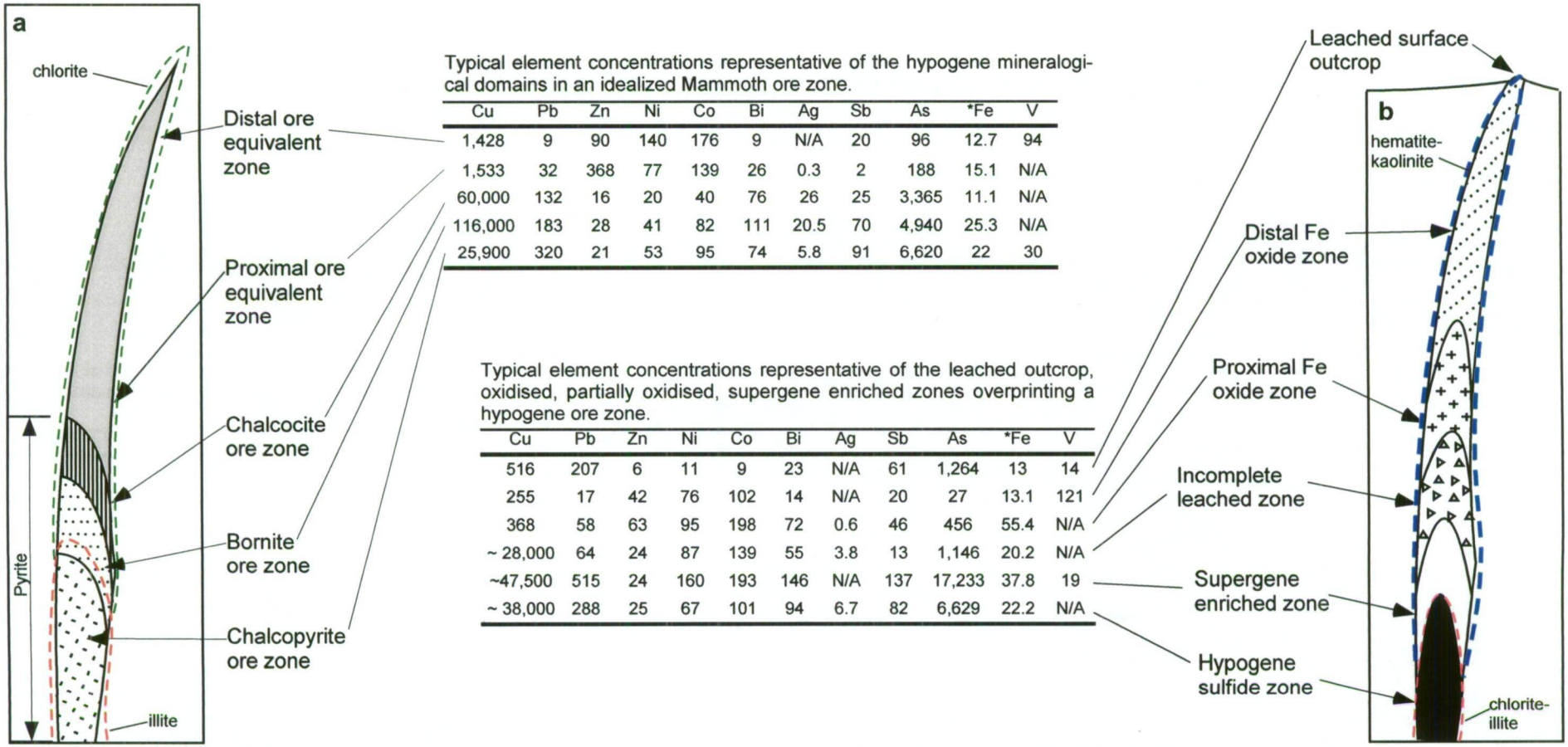

Typical element concentrations representative of the hypogene mineralogical domains in an idealized Mammoth ore zone.

Cu	Pb	Zn	Ni	Co	Bi	Ag	Sb	As	*Fe	V
1,428	9	90	140	176	9	N/A	20	96	12.7	94
1,533	32	368	77	139	26	0.3	2	188	15.1	N/A
60,000	132	16	20	40	76	26	25	3,365	11.1	N/A
116,000	183	28	41	82	111	20.5	70	4,940	25.3	N/A
25,900	320	21	53	95	74	5.8	91	6,620	22	30

Typical element concentrations representative of the leached outcrop, oxidised, partially oxidised, supergene enriched zones overprinting a hypogene ore zone.

Cu	Pb	Zn	Ni	Co	Bi	Ag	Sb	As	*Fe	V
516	207	6	11	9	23	N/A	61	1,264	13	14
255	17	42	76	102	14	N/A	20	27	13.1	121
368	58	63	95	198	72	0.6	46	456	55.4	N/A
~ 28,000	64	24	87	139	55	3.8	13	1,146	20.2	N/A
~47,500	515	24	160	193	146	N/A	137	17,233	37.8	19
~ 38,000	288	25	67	101	94	6.7	82	6,629	22.2	N/A

Figure 7.13. Schematic representation of idealized mineralogical domains and corresponding element abundances in a: a) typical un-oxidised ore Mammoth ore lens; and b) Mammoth ore lens with a significant supergene overprint. Distribution of the dominant alteration mineral assemblage as noted. Data in ppm except *Fe in wt%. Not to scale. Data compiled from Figures, 7.1-7.4.

Geochemical halos and vectors to mineralisation can be deduced from these observed variations in the geochemistry when related to the spatial distribution of the sulfide and alteration mineralogy associated within and distal to Mammoth ore zones. Figure 7.13, a schematic representation of idealized mineralogical domains and corresponding element abundances in representative styles of Mammoth ore zones, summarises the main conclusions from this chapter.

The geochemistry of <1500 ppm Cu chlorite/illite, hematite and quartz filled S1, S2, B1, B2 filled structures, interpreted as distal ore equivalent horizons, were investigated from C, D and 2 lens ore zones. The trace elements Zn, Ni, Co are elevated relative to the wall rock and the ore zones within these distal ore equivalent horizons (Fig. 7.13). Significant variations within the hypogene sulfide ore zones include: 1) hypogene chalcocite zone enriched in Ag (26 ppm) compared to the bornite (21 ppm Ag) and chalcopyrite zones (6 ppm Ag); 2) bornite ore zone is enriched in Bi (111 ppm) relative to either the hypogene chalcocite (76 ppm Bi) or the chalcopyrite (74 ppm Bi) ore zones; and 3) chalcopyrite ore zone is comparatively enriched in Co, Pb, Ni, Sb and As (Fig. 7.13).

Distal ore equivalent horizons dominated by the meteoric oxidation products of hematite and other Fe-oxides demonstrate an increase in the concentrations of the major and trace elements MgO, MnO, Fe, Cu, Bi, Sb, Mo, As, Pb, Tl, Ni, Co and Zn relative to the host rock. Hematite dominated B1-B2 and S1-S2 units, adjacent to sulfide ore zones, are variably enriched and depleted in trace elements but in general, demonstrate and enrichment in Zn, Ni, Co, Bi, Sb, and Fe relative to the proximal ore zone (Fig. 7.13).

7.6 CONCLUSIONS

The three primary categories of the textural classification scheme (Chapter 4) are geochemically distinct. The concentrations of Cu, Fe and S uniformly increase from S1 through to B2 reflecting the degree of stockwork vein and breccia development under gone during the mineralisation event. Cu has a

strong positive correlation with Fe_2O_3, Pb, Bi, As, Ni, S, and Mo within in the Fractured and Brecciated rock units (S1, S2, B1 and B2).

The alteration mineralogy of E, D, C, B, 2 and MF ore zones is can be divisible in two broad categories: 1) chlorite dominated or 2) illite and chlorite dominated. The ore zones E, D, 2 and MF are included in the illite and chlorite-dominated category. Alteration in the B and C ore zones is dominated by chlorite.

The hypogene Cu sulfides are zoned both, from hangingwall to footwall and up dip, within the major Mammoth ore zones. This zoned distribution is broadly categorised as follows: 1) Stage II hypogene chalcocite ± bornite; 2) Stage II bornite ± hypogene chalcocite and 3) Stage II chalcopyrite ± bornite. The chalcopyrite ± bornite zone occurs in the footwall and deeper positions within individual ore zones and the hypogene chalcocite ± bornite occurring in the hangingwall and up dip positions. The supergene modification of the hypogene mineralogy results in supergene chalcocite (±covellite) overprinting the hypogene Cu sulfide zonation. The processes of meteoric and supergene alteration have led to complex geochemical dispersion patterns overprinting geochemical patterns developed during hypogene mineralisation

Cobalt and Ni and to a lesser extent CaO and P_2O_5 appear to halo the hypogene ore zones at Mammoth. Within distal ore equivalent structures that have not been modified by meteoric and/or supergene processes the trace elements Zn, Ni and Co are significantly enriched relative to the ore zone. The concentrations of Cu, Bi, Pb, As and Fe increases towards mineralisation and therefore can be used as a geochemical vector for Mammoth style mineralisation. Within ore equivalent horizons leached through supergene and/or meteoric (near surface or at surface) processes the trace elements Cu, Pb, Zn, Ni, Bi, Sb, and As remain enriched relative to host rocks. This suit of trace elements can be used to identify Mammoth style mineralisation in surface or near surface leached structures.

CHAPTER 8

ISOTOPE GEOCHEMISTRY

8.1 INTRODUCTION

Numerous research efforts have focused on the stable isotope systematics of structurally controlled sediment hosted Proterozoic Cu deposits in the Western Fold Belt (WFB) of the Mt Isa Inlier (Andrews et al., 1989; Heinrich et al., 1993; Heinrich et al., 1989; Heinrich et al., 1995; Warring et al., 1998). The widely accepted model for this style of deposit is primarily founded on those studies that are directly focussed on the Mt Isa Cu deposit. Collectively these researchers have detailed the S, O-D and Pb isotopic systematics of the Mt Isa Cu deposit. This work will detail the S, O-D, and Pb isotopic systematics of the Mammoth Cu deposit interpreted within the geological frame work established previously in Chapters 3, 4, 5 and 7.

Stable and radiogenic isotope studies, an integral part of an ore deposit study, provide means to address issues of source, transport and mechanisms of deposition of minerals from a hydrothermal fluid (Taylor, 1979). As H_2O is a major component of hydrothermal fluids an analysis of the O and H isotopes ($\delta^{18}O$ and δD) may provide indications to the original source as either magmatic, metamorphic or meteoric H_2O or a combination of all three (Taylor, 1979). Another principle component of this ore forming fluid is sulfur, however the source of this sulfur may not be the same as the H_2O (Ohmoto, 1986).

At Mammoth Stage I pyrite and Stage II chalcopyrite, bornite, and hypogene chalcocite and Stage III supergene chalcocite are the major sulfide assemblage in the deposit and therefore an analysis of the S isotopic systematics will constrain the possible source of this sulfur. The radiogenic isotope system of Pb can and has been used in ore deposit studies both as a method of tracing the source metals and as a geochromometer (Sun et al., 1994). In this study on the Mammoth Cu ore system the application of Pb isotopic systematics will be used to address the source of Pb and by inference other chemically similar elements, principally Cu.

8.2 OXYGEN AND HYDROGEN

The investigation of oxygen and hydrogen isotopic systematics undertaken during this study were conducted on Stage II chlorite and quartz, and Stage III hematite. It is anticipated that this work will identify the source or sources of the H_2O that contributed to the fluid from which theses minerals precipitated. The interpretation of these results within a sound paragenetic framework will further contribute to an understanding of their respective mechanisms of precipitation.

8.2.a Methods

Samples of hypogene Stage II chlorite (5) and quartz (2) and supergene Stage III hematite (7) were analysed from cutoff blocks from which thin sections were taken for petrographic studies (Table 8.1). Deuterium-Hydrogen analyses were done using a modified method published by Bigeleisen (1952).

Samples of the Stage II chlorite were loaded into small Mo envelopes and placed in Pt buckets suspended in 19mm od quartz glass vessels. The vessels were attached to a vacuum line and evacuated overnight while heating at 150°C. The samples were heated to >1400°C using a RF generator furnace. H_2 produced was converted to H_2O by contact with CuO_2 at 600°C. All water was collected cryogenically and stored in sealed 6mm od borosilicate glass tubes. The water was released from the sealed tubes into a vacuum line and circulated using a pump through depleted uranium at 800°C. When conversion was complete the H_2 was pumped into the mass spectrometer via a stainless steal line and analysed immediately. Samples were analysed relative to an internal water standard prepared using the same circulating system. Standards were calibrated daily using laboratory and international standards. Replicate analyses of the standard waters are generally better than +/-1 although this does not indicate errors in the H_2O extraction from mineral separates. Analyses are reported in per mil relative to the SMOW standard.

Samples of quartz and hematite were analysed in Ni bombs with BrF_5 at 550°C overnight using the method first described by Clayton and Mayeda (1963). The oxygen was converted to CO_2 using an internally heated graphite rod and quantitatively collected. The CO_2 was analysed automatically on a Finnigan 252 mass spectrometer against an internal standard. Two quartz standards were run with every 10 samples. Replicate analyses of the standard quartz is generally better than +/-0.2. Analyses are reported in per mil relative to the SMOW standard.

8.2.b Results

Results of the oxygen and hydrogen analyses are given in Table 8.1 and the data for each mineral phase are discussed as follows. Stage II chlorite were analysed and the $\delta^{18}O$ and δD values range from 0.75 to 10.51 ‰ and –84.8 to –88.5 ‰ respectively. $\delta^{18}O$ values from stage I quartz range from 13.66 to 15.18 ‰. $\delta^{18}O$ values form stage III supergene hematite range from –10.75 to 12.61‰.

Table 8.1. Oxygen and hydrogen isotope analysis of minerals from the Mammoth Cu deposit. Analyses are reported in permil relative to the SMOW standard

Sample Id	Location	Mineral	δD (‰)	$\delta^{18}O$ (‰)
DC1	UD711-59.4m	chlorite	-84.8	4.51
DC2	SD255-1043.1m	chlorite	-88.0	10.51
DC3	UD715-96.4m	chlorite	-92.5	0.75
DC4	UD717-39.1m	chlorite	-92.0	1.18
DC7	UD715-98.3m	chlorite	-88.5	1.72
DC5	SD255-985.1m	quartz	-	15.18
DC6	SD255-984.1m	quartz	-	13.66
DC10	UD713-212.1m	hematite	-	-10.44
DC11	UD768-146.1m	hematite	-	7.90
DC12	UD770-103.0m	hematite	-	2.47
DC13	SD255-1053.0m	hematite	-	-10.69
DC14	UD711-57.9m	hematite	-	12.61
DC15	UD718-38.1m	hematite	-	-1.83
DC16	SD255-1043.1m	hematite	-	-10.75

8.2.c Discussion

Methods of estimating the isotopic composition of D and O from ore forming fluids are classified into direct and indirect methods. Direct methods involve the sampling of the fluid extracted from host minerals. Indirect methods rely upon the measurement of $\delta^{18}O$ and δD of minerals assumed to be in

equilibrium with the mineralising fluid in conjunction with an estimated temperature at the time of mineralisation (Ohmoto, 1986). Due to the lack of suitable material (fluid inclusions ect.) the indirect method was used during this study.

The isotopic composition of the mineralisation fluid was calculated by applying using the following fraction factors (Taylor, 1979; and Yapp, 1990) to stage I quartz, stage II chlorite and stage III hematite:

$$\Delta^{18}O_{\text{chlorite-water}} = 1.56 \times 10^6/(T^2) - 4.7$$

(eq. 1. Taylor, 1979)

$$\Delta D_{\text{chlorite-water}} = -4.38 \times 10^6/(T^2) - 24.6$$

(eq. 2. Taylor, 1979)

$$\Delta^{18}O_{\text{quartz-water}} = 3.34 \times 10^6/(T^2) - 3.31$$

(eq. 3. Taylor, 1979)

$$\Delta^{18}O_{\text{hematite-water}} = 1.63 \times 10^6/(T^2) - 12.3$$

(eq. 4. Yapp, 1990)

Correct estimation of temperature is an important step in the calculation of the fluid compositions as these fraction factors are partially dependant on temperature. The host rocks to the Mammoth deposit have largely undergone low-grade metamorphism (lower greenschist), with the exception of the Pickwick Metabasalt that attained greenschist grade metamorphic grade (Hutton and Wilson, 1985). The Mammoth ore zone has previously been classified as a syn-deformational deposit (van Dijk, 1991; this study chapter 2) and therefore the temperatures during precipitation of the hypogene stages of mineralisation (Stage I and II) can be estimated from alteration mineral assemblages and local metamorphic grade. These lines of evidence suggest mineralisation occurred between temperatures of 200 to 350°C assuming a temperature range that concurrent with lower greenschist metamorphism and the stability field of chlorite (Hedenquist et al., 1996; Yardley, 1989). Therefore, a range of possible temperatures are used and

the fluid composition has been calculated within this range. A range of temperatures were applied to the fraction factor, at 50°C intervals, from 200 to 350°C (Table. 8.2). Temperatures during oxidation of sulfide ore bodies in the weathering zone can range from 50-60°C (Sheppard et al., 1969) and therefore a temperature of 55°C has been used in the calculation of the $\delta^{18}O$ and δD of the fluid interpreted to be in equilibrium with Stage III hematite.

Table 8.2. Temperatures and calculated fluid compositions for oxygen and hydrogen isotope data. Analyses are reported in permil relative to the SMOW standard.

Sample Id	Mineral	Temperature	Calculated water $\delta^{18}O$(‰)	Calculated water δD (‰)	Fraction Factor
DC1	chlorite	200	2.24	-40.62	Eq # 1 & 2
		250	3.51	-44.19	
		300	4.46	-46.86	
		350	5.19	-48.92	
DC2	chlorite	200	8.24	-43.82	Eq # 1 & 2
		250	9.51	-47.39	
		300	10.46	-50.06	
		350	11.19	-52.12	
DC3	chlorite	200	-1.52	-48.32	Eq # 1 & 2
		250	-0.25	-51.89	
		300	0.70	-54.56	
		350	1.43	-56.62	
DC4	chlorite	200	-1.10	-47.82	Eq # 1 & 2
		250	0.17	-51.39	
		300	1.12	-54.06	
		350	1.86	-56.12	
DC7	chlorite	200	-0.56	-44.32	Eq # 1 & 2
		250	0.71	-47.89	
		300	1.66	-50.56	
		350	2.40	-52.62	
DC5	quartz	200	-3.56		Eq. # 3
		250	-6.28		
		300	-8.32		
		350	-9.88		
DC6	quartz	200	-2.04		Eq. # 3
		250	-4.76		
		300	-6.80		
		350	-8.36		
DC10	hematite	55	-7.11		Eq. # 4
DC11	hematite	55	11.22		
DC12	hematite	55	5.79		
DC13	hematite	55	-7.37		
DC14	hematite	55	15.93		
DC15	hematite	55	1.50		
DC16	hematite	55	-7.42		

The isotopic composition of the hydrothermal fluid that precipitated the stage I quartz and stage II chlorite is shown in Figure 8.1. The calculated fluid composition occurs in relatively constrained area of moderate δD values (-57

to -40 δD‰) and broad range of $\delta^{18}O$ values (-1.5 to 11.2 $\delta^{18}O$‰). The majority of the data plot in a linear array to the left of the metamorphic water box, with only one value plotting within the metamorphic water box. The large shift in $\delta^{18}O$ and relatively minor shift in δD suggests a mixing of dominantly meteoric fluid and minor metamorphic fluid. The calculated $\delta^{18}O$ fluid composition form which the stage III supergene hematite precipitated from ranges from –7.11 to 15.93 ‰ (Fig. 8.1). Such a fluid variably enriched in $\delta^{18}O$ (+/- 23 ‰) precludes the involvement of a fluid with a relatively homogeneous $\delta^{18}O$ isotopic content. Near surface meteoric water is variably enriched in $\delta^{18}O$ (Taylor, 1997) and therefore the calculated fluid values from the stage III hematite are considered to be representative of such a fluid. This observation further confirms the conclusion of the paragenetic study (Chapter 5) in which the hematite is considered to have formed during the late oxidation of the Mammoth ore deposit.

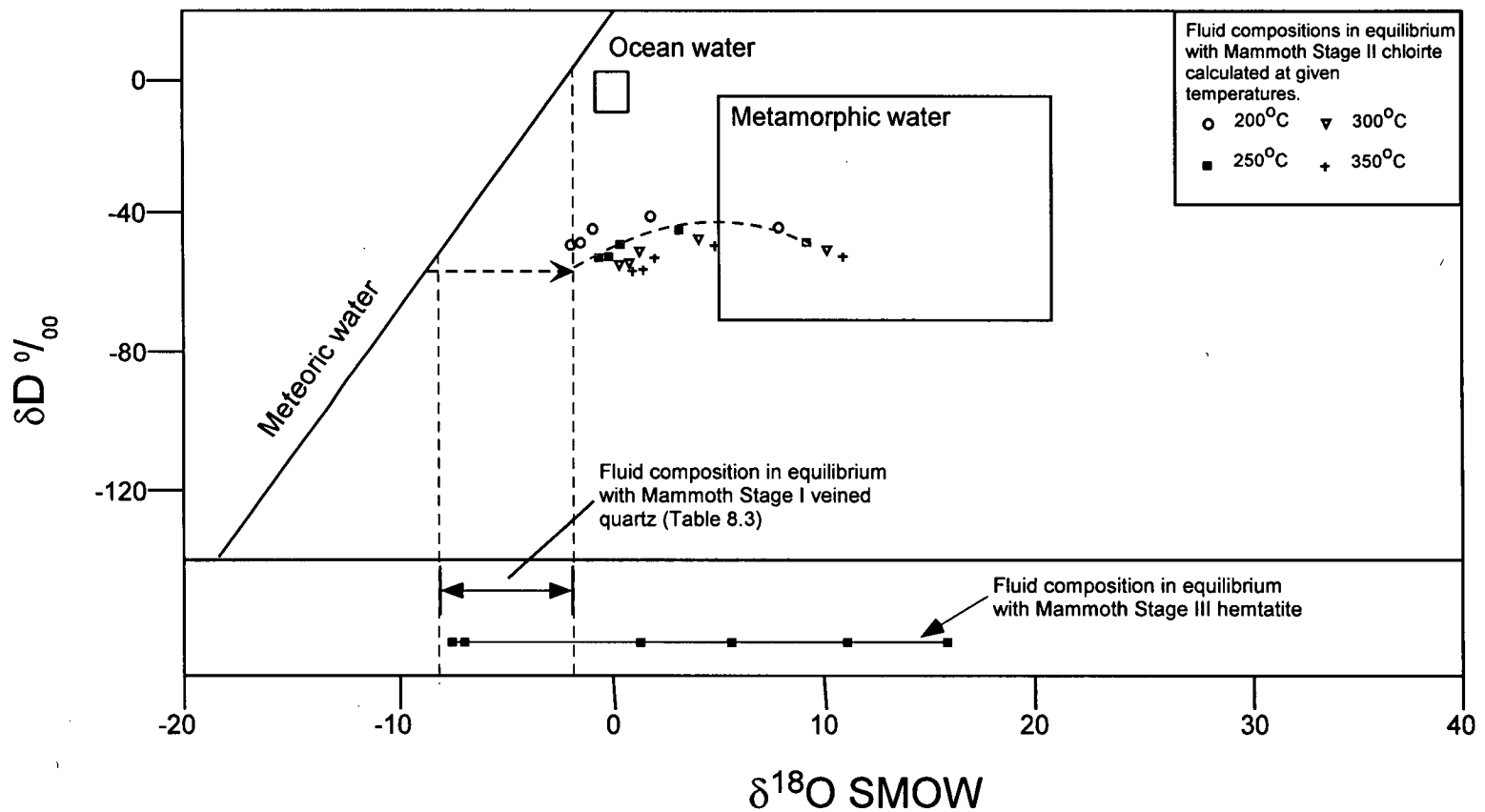

Figure 8.1. A comparison of fluid compositions calculated from Mammoth hypogene stage II chlorite, supergene Stage III hematite. Water compositions in equilibrium with chlorite were calculated using fraction factors of: $\Delta^{18}O_{chlorite\text{-}water} = 1.56 \times 10^6/T^2 - 4.7$; $\Delta D_{chlorite\text{-}water} = -4.38 \times 10^6/T^2 - 24.6$; $\Delta^{18}O_{hematite\text{-}water} = 1.63 \times 10^6/(T^2) - 12.3$. Refer to text for details.

8.3 SULFUR

Sulfur isotope studies were under taken to:

- Document $\delta^{34}S$ variations between paragenetic stage and ore zones in the Mammoth deposit
- Identify the possible sources of sulfur
- Estimate physicochemical conditions of the ore-forming processes, in conjunction with other geochemical studies (mineral phase equilibria) and sulfide paragenesis

8.3.a Previous Work

The majority of sulfur isotope research conducted on structurally controlled sediment hosted Cu ore deposits in the West Fold Belt of the Mt Isa inlier has been conducted on the giant Mt Isa Cu ore zone studies and therefore it is prudent to this study to briefly outline and review these studies and their conclusions.

Andrew et al. (1989) documented the sulfur isotopic systematics of the Mt Isa Cu system and concluded that the $\delta^{34}S$ signature of the Cu ore body implied that the mineralising fluid largely was enriched in ^{34}S and the resultant observed $\delta^{34}S$ signature was the result of progressive interaction of the ore fluid with pre-existing earlier pyrite. Subsequent studies by Warring et al. (1990) and Heinrich et al. (1995) suggested that the incoming ore fluid was reduced and concurred with conclusion reached by Andrew et al. (1989) that ore fluid was indeed enriched with respect to ^{34}S. In addition, Warring (1990) demonstrated via mass balance calculations that the Cu bearing fluid was accompanied by a significant amount of sulfur, therefore lessening the need for chalcopyrite deposition to rely upon a pre-existing *in situ* source of sulfur.

In addition, Andrew et al. (1989) identified another source of S. Unaltered Eastern Creek Volcanics distal to mineralisation host disseminated pyrite, chalcopyrite and bornite that range in $\delta^{34}S$ values from –7 to +3 ‰ $\delta^{34}S$. Painter et al. (1999) undertook petrographic, sedimentological and sulfur isotopic investigations to examine the relationship between the fine-grained pyrite and the Cu mineralisation at Mt Isa. They concluded that the ore fluid,

responsible for the Cu mineralisation, was dominated by reduced aqueous sulfur and the most likely sulfur source was a deep seated Proterozoic marine sulfur reservoir. Therefore, the source of sulfur in the Cu ore bodies at Mt Isa remains a controversial issue. Evidence supports the role of early fine grained pyrite as in integral component for the trap mechanism (Andrew et al. (1989); Heinrich et al. (1988). Warring (1990) suggested that this early pyrite is not critical in the formation of the Mt Isa chalcopyrite ore bodies and the ore fluid may in fact carry its own reduced sulfur. The question remains as to the initial source of this reduced sulfur.

At Mammoth the complexity of having significant early/digenetic pyrite as a source for sulfur is removed. With an understanding of the sulfur isotope systematics of the Mammoth deposit it is possible to identify potential sources for the sulfur in the mineralising fluid.

Scott et al. (1985) conducted isotopic studies on the Mammoth Cu sulfides; chalcopyrite & bornite/chalcocite, and veined and disseminated pyrite. The researchers analysed at total of 60 samples from No. 1, B and C ore zones (Table 8.3). The sulfide samples were converted to SO_2 gas at 900°C under a vacuum using Cu_2O as an oxidising agent (Kaplan et al., 1970). The resultant SO_2 gas sample was analysed using a Micromass 6 isotopic ratio mass-spectrometer and presented $\delta^{34}S‰$ values relative to Canyon Diablo Troilite (CDT).

Scott et al (1985) found that within the Mammoth ore zones (No.1, B and C) the disseminated pyrite ranged from -5.7 to -1.7 $\delta^{34}S‰$; veined pyrite ranged from -17.9 to -7.1 $\delta^{34}S‰$; disseminated Cu sulfides ranged from –15.9 to –11.6 $\delta^{34}S‰$; and veined Cu sulfides ranged from –15.9 to –0.2 $\delta^{34}S‰$ (Table 8.3, Figs 8.2 and 8.3). The relatively light isotopic signature identified for the disseminated pyrite was proposed to be the result of preferential reduction of seawater sulphate trapped in pore space through microbial process. Subsequent epigenetic Cu sulfide mineralisation was interpreted to have partially or completely replaced the existing disseminated pyrite. Therefore, inheriting the light isotopic signature of the disseminated pyrite. Their study suggested that the observed isotopic disequilibrium between associated

Table 8.3. Sulfur isotopic data for samples from the Mammoth ore bodies: E, D, 2 Lenses (this study) and that of Scott et al. (1985): No. 1, B and C Lenses. * mixed bornite and chalcocite. Abbreviations: Py = pyrite, Cpy = chalcopyrite, Bn = bornite, Cc = chalcocite.

Ore Zone	Drill Hole	Depth (m)	Py	Cpy	Bn	Cc	Method
E LENS	UD754	251.8	-13.3	-1.0			Laser Ablation
E LENS	SD254	1012.5	-13.3	-8.3			Laser Ablation
E LENS	SD254	1155.8		-7.3	-1.0		Laser Ablation
E LENS	SD254	1155.8		-4.6			Laser Ablation
E LENS	SD255	1009.9	-6.6	-9.2	-5.6		Laser Ablation
E LENS	SD255	1009.9	-5.17(DISS)		-1.3		Laser Ablation
E LENS	SD255	1034.6	-15.0		-10.3		Laser Ablation
E LENS	SD255	1051.0				-0.8	Laser Ablation
E LENS	SD255	981.2	-14.4		-12.3		Laser Ablation
2 LENS	UD768	211.6			-5.1		Conventional (UTAS)
2 LENS	UD768	162.2			-10.5		Conventional (UTAS)
2 LENS	UD768	208.9a			-7.7		Conventional (UTAS)
2 LENS	UD768	202.7A				-10.3	Conventional (UTAS)
2 LENS	UD766	217.5				-8.1	Conventional (UTAS)
2 LENS	UD766	214.2				-12.1	Conventional (UTAS)
2 LENS	UD766	191.8				-12.4	Conventional (UTAS)
2 LENS	UD766	186.5				-10.3	Conventional (UTAS)
2 LENS	UD766	226.4				-2.9	Conventional (UTAS)
2 LENS	UD766	189.5				-10.9	Conventional (UTAS)
2 LENS	UD768	184		-9.0			Conventional (UTAS)
2 LENS	UD768	189.8		-4.0			Conventional (UTAS)
2 LENS	UD766	230.1		-18.7			Conventional (UTAS)
2 LENS	UD760	133.5		-7.9			Conventional (UTAS)
2 LENS	UD768	184	-12.8				Conventional (UTAS)
2 LENS	UD768	211.6a	-8.3				Conventional (UTAS)
2 LENS	UD768	211.6b	-9.2				Conventional (UTAS)
2 LENS	UD768	211.6c	-9.2				Conventional (UTAS)
2 LENS	UD768	211.6d	-7.9				Conventional (UTAS)
2 LENS	UD768	211.6e	-12.2				Conventional (UTAS)
2 LENS	UD768	206.5	-14.9				Conventional (UTAS)
2 LENS	UD768	189.8	-12.5				Conventional (UTAS)
2 LENS	UD768	202	-14.1				Conventional (UTAS)
2 LENS	UD768	175.1	-12.7				Conventional (UTAS)
2 LENS	UD768	170.1	-11.4				Conventional (UTAS)
2 LENS	UD768	163.1	-11.4				Conventional (UTAS)
2 LENS	UD768	162.1	-12.3				Conventional (UTAS)
2 LENS	UD768	116.5	-12.3				Conventional (UTAS)
2 LENS	UD713	158.4	-13.2				Conventional (UTAS)
2 LENS	UD713	178.6	-10.0				Conventional (UTAS)
2 LENS	UD713	231.9	-8.2				Conventional (UTAS)
2 LENS	UD713	226.3	-10.0				Conventional (UTAS)
DLENS	UD746	195.5		-7.5			Conventional (UTAS)
DLENS	UD746	191.4		-11.4			Conventional (UTAS)
DLENS	UD746	230		-7.0			Conventional (UTAS)
DLENS	UD746	210.1		-12.3			Conventional (UTAS)
DLENS	UD746	195.5	-11.0				Conventional (UTAS)
DLENS	UD746	191.4	-10.8				Conventional (UTAS)
DLENS	UD746	160.6	-13.6				Conventional (UTAS)
DLENS	UD746	133.4	-14.6				Conventional (UTAS)
DLENS	UD746	230	-14.6				Conventional (UTAS)
DLENS	UD746	210.1	-15.0				Conventional (UTAS)
DLENS	UD744	144.5	-13.6				Conventional (UTAS)
DLENS	UD744	152.8	-14.0				Conventional (UTAS)
DLENS	UD744	119.5	-14.1				Conventional (UTAS)
DLENS	UD744	154.4	-14.2				Conventional (UTAS)
DLENS	UD744	115.6	-15.0				Conventional (UTAS)
No. 1 Lens	grab				-7.0*		Conventional (Scott et al, 1985)
No. 1 Lens	U125	30.1	-11.5	-3.9			Conventional (Scott et al, 1985)

Table 8.3. Sulfur isotopic data for samples from the Mammoth ore bodies: E, D, 2 Lenses (this study) and that of Scott et al. (1985): No. 1, B and C Lenses. * mixed bornite and chalcocite. Abbreviations: Py = pyrite, Cpy = chalcopyrite, Bn = bornite, Cc = chalcocite.

Ore Zone	Drill Hole	Depth (m)	Py	Cpy	Bn	Cc	Method
No. 1 Lens	U125	35.1	-11.0	-4.2			Conventional (Scott et al, 1985)
No. 1 Lens	U125	45.1	-10.5	-5.3			Conventional (Scott et al, 1985)
No. 1 Lens	U125	54.4	-11.9				Conventional (Scott et al, 1985)
No. 1 Lens	grab				-5.7*		Conventional (Scott et al, 1985)
No. 1 Lens	grab		-8.6	-1.6			Conventional (Scott et al, 1985)
No. 1 Lens	grab				-3.1*		Conventional (Scott et al, 1985)
No. 1 Lens	grab		-11.2	-7.7			Conventional (Scott et al, 1985)
No. 1 Lens	grab		-9.0		-5.1*		Conventional (Scott et al, 1985)
No. 1 Lens	U237	0.8	-10.5		-5.1*		Conventional (Scott et al, 1985)
No. 1 Lens	U237	1.2	-10.0				Conventional (Scott et al, 1985)
No. 1 Lens	U237	10.1			-6.9*		Conventional (Scott et al, 1985)
No. 1 Lens	U237	14.1	-8.1	-6.1			Conventional (Scott et al, 1985)
No. 1 Lens	U237	15.9		-5.2	-6.2*		Conventional (Scott et al, 1985)
No. 1 Lens	U237	16.6	-7.1	-4.5			Conventional (Scott et al, 1985)
No. 1 Lens	U237	18.2			-4.3*		Conventional (Scott et al, 1985)
No. 1 Lens	U237	23.1	-10.6				Conventional (Scott et al, 1985)
No. 1 Lens	U237	27.1	-10.7		-6.2*		Conventional (Scott et al, 1985)
No. 1 Lens	U237	31.2	-10.8	-5.1			Conventional (Scott et al, 1985)
No. 1 Lens	U237	39.5	-12.3	-5.0			Conventional (Scott et al, 1985)
No. 1 Lens	U201	72.0	-10.7		-6.6*		Conventional (Scott et al, 1985)
No. 1 Lens	U201	73.0	-14.2		-5.3*		Conventional (Scott et al, 1985)
No. 1 Lens	U201	74.0			-12.7*		Conventional (Scott et al, 1985)
B Lens	U217	43.0	-13.8		-6.6*		Conventional (Scott et al, 1985)
B Lens	U226	51.0					Conventional (Scott et al, 1985)
B Lens	U226	60.0					Conventional (Scott et al, 1985)
B Lens	U343	81.2					Conventional (Scott et al, 1985)
B Lens	U343	88.3	-14.5				Conventional (Scott et al, 1985)
B Lens	U343	89.8	-17.9				Conventional (Scott et al, 1985)
B Lens	U343	98.1	-15.6				Conventional (Scott et al, 1985)
B Lens	S175	486.7	-17.8				Conventional (Scott et al, 1985)
B Lens	S175	490.2	-13.7				Conventional (Scott et al, 1985)
B Lens	S175	493.4	-4.0(DISS)				Conventional (Scott et al, 1985)
B Lens	S175	497.6	-16.4				Conventional (Scott et al, 1985)
B Lens	S175	502.4	-11.0				Conventional (Scott et al, 1985)
B Lens	S175	502.6	-9.7				Conventional (Scott et al, 1985)
B Lens	S175	508.1					Conventional (Scott et al, 1985)
B Lens	S175	511.7	-12.5				Conventional (Scott et al, 1985)
B Lens	S175	512.6					Conventional (Scott et al, 1985)
B Lens	S175	513.4	-5.7(DISS)				Conventional (Scott et al, 1985)
B Lens	S175	515.4					Conventional (Scott et al, 1985)
B Lens	S175	515.8	-16.0				Conventional (Scott et al, 1985)
B Lens	S175	515.9					Conventional (Scott et al, 1985)
B Lens	S175	521.1	-11.1				Conventional (Scott et al, 1985)
B Lens	S175	521.6					Conventional (Scott et al, 1985)
B Lens	S175	522.8	-12.1				Conventional (Scott et al, 1985)
B Lens	S175	525.1		-11.6			Conventional (Scott et al, 1985)
B Lens	S175	528.1					Conventional (Scott et al, 1985)
B Lens	S175	532.1		-6.6			Conventional (Scott et al, 1985)
B Lens	S175	570.7		-15.9			Conventional (Scott et al, 1985)
B Lens	U363	284.7	-16.5				Conventional (Scott et al, 1985)
B Lens	U363	302.6	-16.2				Conventional (Scott et al, 1985)
B Lens	U363	329.4	-12.7				Conventional (Scott et al, 1985)
B Lens	U363	366.4	-10.1				Conventional (Scott et al, 1985)
C Lens	U343	3.5					Conventional (Scott et al, 1985)
C Lens	U343	45.1					Conventional (Scott et al, 1985)
C Lens	U343	60.6	-14.5				Conventional (Scott et al, 1985)
C Lens	U343	67.4	-13.8				Conventional (Scott et al, 1985)

pyrite and Cu sulfides was due to isotopic disequilibrium and the formation of the veined pyrite subsequent to Cu sulfides (Scott et al, 1985). The paragenetic sequence adopted by these workers appears to have been based solely on geochemical evidence as no textural evidence was presented in support (refer Chapters 5 and 6).

8.3.b Methods

Fifty-nine sulfur isotope analyses were obtained in this study from: Stage I pyrite, Stage III chalcopyrite, bornite, and chalcocite, Stage IV chalcocite. Two analytical methods were used; 47 analyses were obtained using convention (hand-drilling) techniques; the remainder (12) were obtained by laser ablation.

Conventional analyses were conducted at the University of Tasmania Central Science Laboratory on samples that could be separated with a dentist drill using the techniques of Robinson and Kusakabe (1975). Analytical uncertainty is estimated at ± 0.2‰. Internal standards homogenous galena from Broken Hill ($\delta^{34}S$ = 3.2‰), Rosebery ($\delta^{34}S$ = 12.4‰) and Tullah ($\delta^{34}S$ = 15.2‰), were run with an SO_2 reference gas ($\delta^{34}S$ = 1.83‰) and NBS 123 ($\delta^{34}S$ = 4.34‰), and isotope measurements were performed on a VG Micromass 602d mass spectrometer.

Laser ablation analyses were conducted at the University of Tasmania Central Science Laboratory. Samples containing sulfides were mounted on a 200mm thick polished wafer, and ablated with currents of 22-35mA for up to two seconds in an oxygen-rich atmosphere. SO_2 gas was then passed via a liquid nitrogen trap into a VG Sira 10 mass spectrometer. The fractionation factor and analytical uncertainty for pyrite when using this method is 6.75 ± 0.15‰ (Huston et al. 1995). Fractionation factors for chalcopyrite and chalcocite when using this method are 4.45‰ and 15.36‰ respectively. Only homogenous coarse grained (<100mm) sulfides were selected for either the laser ablation or conventional analytical techniques.

Huston et al. (1995) tested for internal consistency between the to methods (conventional versus laser ablation). The maximum difference between the two methods was 0.2‰, which is within the analytical errors of the mass-spectrometer.

8.3.c Results

Stage I veined pyrite

Thirty-four analyses of veined pyrite (5 ablations and 29 conventional) have $\delta^{34}S$ values from -15.1 to -6.6‰ (Table 8.3). The distribution is positively skewed, with median and mean values of -12.8 and -12.2‰ respectively.

Stage I disseminated pyrite

One analysis (ablation) of disseminated pyrite has a $\delta^{34}S$ value of -5.2‰ (Table 8.3).

Stage II chalcopyrite

Thirteen analyses (5 ablations and 8 conventional) of chalcopyrite (vein and matrix fill) have $\delta^{34}S$ values from -18.7 to -1.0‰ (Table 8.3). The distribution is negatively skewed, with median and mean values of -7.9 and -8.3‰ respectively.

Stage II bornite/chalcocite (mixed)

Three analyses (conventional) of intergrown bornite and chalcocite (vein and matrix fill) have $\delta^{34}S$ values from -10.5 to -5.1 with median and mean values of -7.7 and -7.8‰ respectively (Table 8.3).

Stage II hypogene chalcocite

One analysis (ablation) of hypogene chalcocite has a $\delta^{34}S$ value of –0.8 ‰ (Table 8.3).

Stage III supergene chalcocite

Seven analyses (conventional) of supergene chalcocite (vein and matrix fill) have $\delta^{34}S$ values from -12.4 to –2.9‰ (Table 8.3). The distribution is

positively skewed, with median and mean values of –10.3 and –8.5‰ respectively.

8.3.d Discussion

The analytical method, used by Scott et al. (1985), determined the $\delta^{34}S$ values of the samples relative to Canyon Diablo Troilite (CDT) with an analytical uncertainty of 0.2‰. There is consistency between methods of $\delta^{34}S$ determination used by Scott et al. (1985) and this study; therefore the two data sets have been combined for interpretation. This has resulted in a $\delta^{34}S$ data set compiled from samples of Stage I pyrite and Stage III and IV Cu-Fe and Cu sulfides collected from the main ore zones within the Mammoth system (No1, 2, B, C, D and E Lenses) (Table 8.3; Figs 8.2 and 8.3).

Isotopic characteristics of ore zones (No. 1, 2, B, C, D and E Lenes)

Figure 8.3 illustrates the sulfur isotope distributions for the major ore zones categorised by sulfide. In general, no significant variations between the ore zones set are apparent in the sample set. However, the relatively narrow plateau of $\delta^{34}S$ values (3.9 ‰) for No. 1 Lens bornite indicates the spread of $\delta^{34}S$ is significantly more constrained than range identified (~ 11.6 ‰) for the other ore Lenes (2, B, C, D and E). The $\delta^{34}S$ data set representing No. 1 Lens was collected and analysed by Scott et al. (1985). Scott et al. (1985) noted that the bornite samples contained significant contamination with chalcocite and therefore the $\delta^{34}S$ values represented an unquantified mixture of chalcocite and bornite. Without replicating the collection and analysis of No. 1 lens sulfides for $\delta^{34}S$ it is impossible to speculate with accuracy on possible mechanism for this observed difference in $\delta^{34}S$ values obtained for bornite.

Isotopic characteristics of individual paragenetic stages

The $\delta^{34}S$ values of stage I pyrite are characterised by a wide spread of data from –4 to –17.9‰, with a mean of –12.0‰ and a standard deviation of 2.9. This results in the bulk of the data displaying a broad plateau of values that range form –9.1 to –14.9 (Fig 8.2). The stage II $\delta^{34}S$ values for chalcopyrite

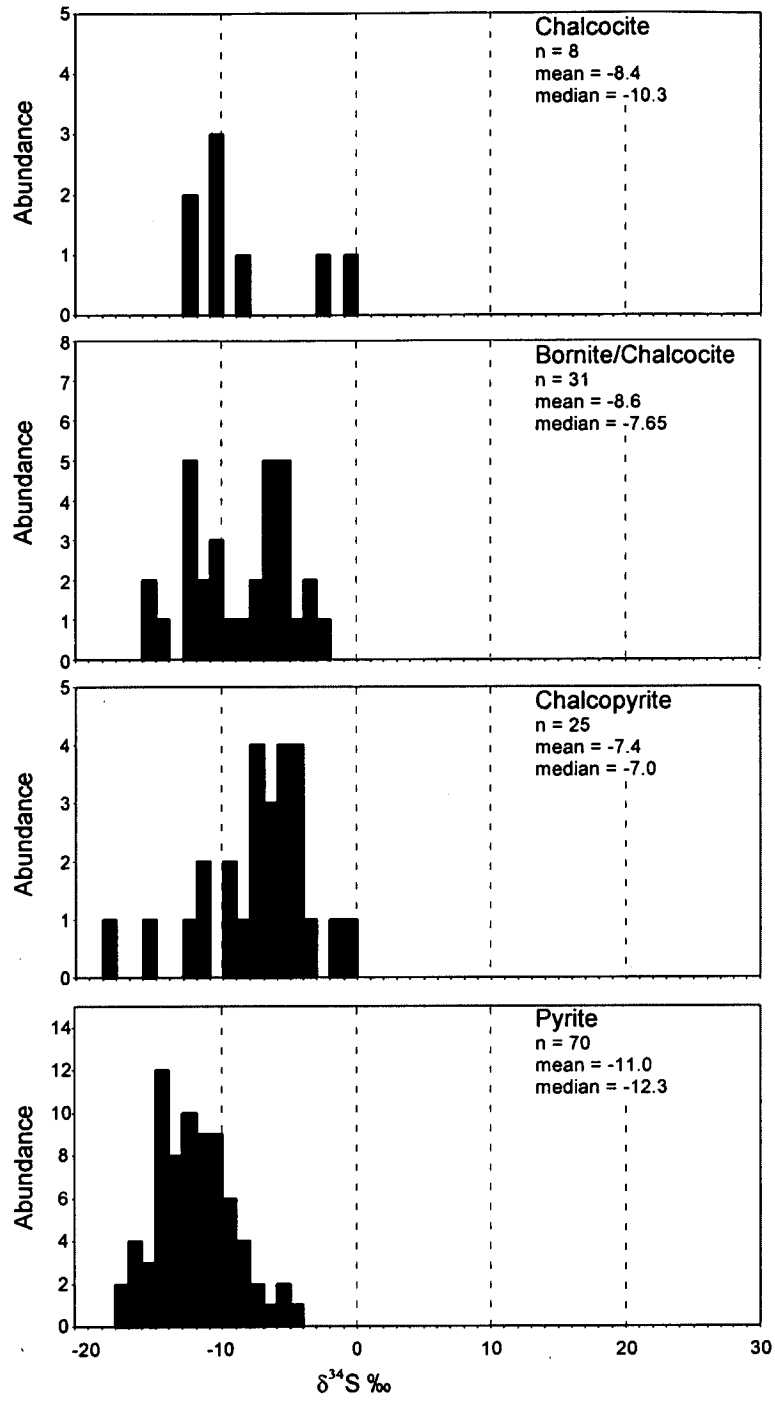

Figure 8.2. Sulphur isotope distributions for stage I pyrite, stage II chalcopyrite, stage II bornite and chalcocite and stage II and stage III chalcocite. Note no distinction is made between stage II and stage III chalcocite (refer to text for details).

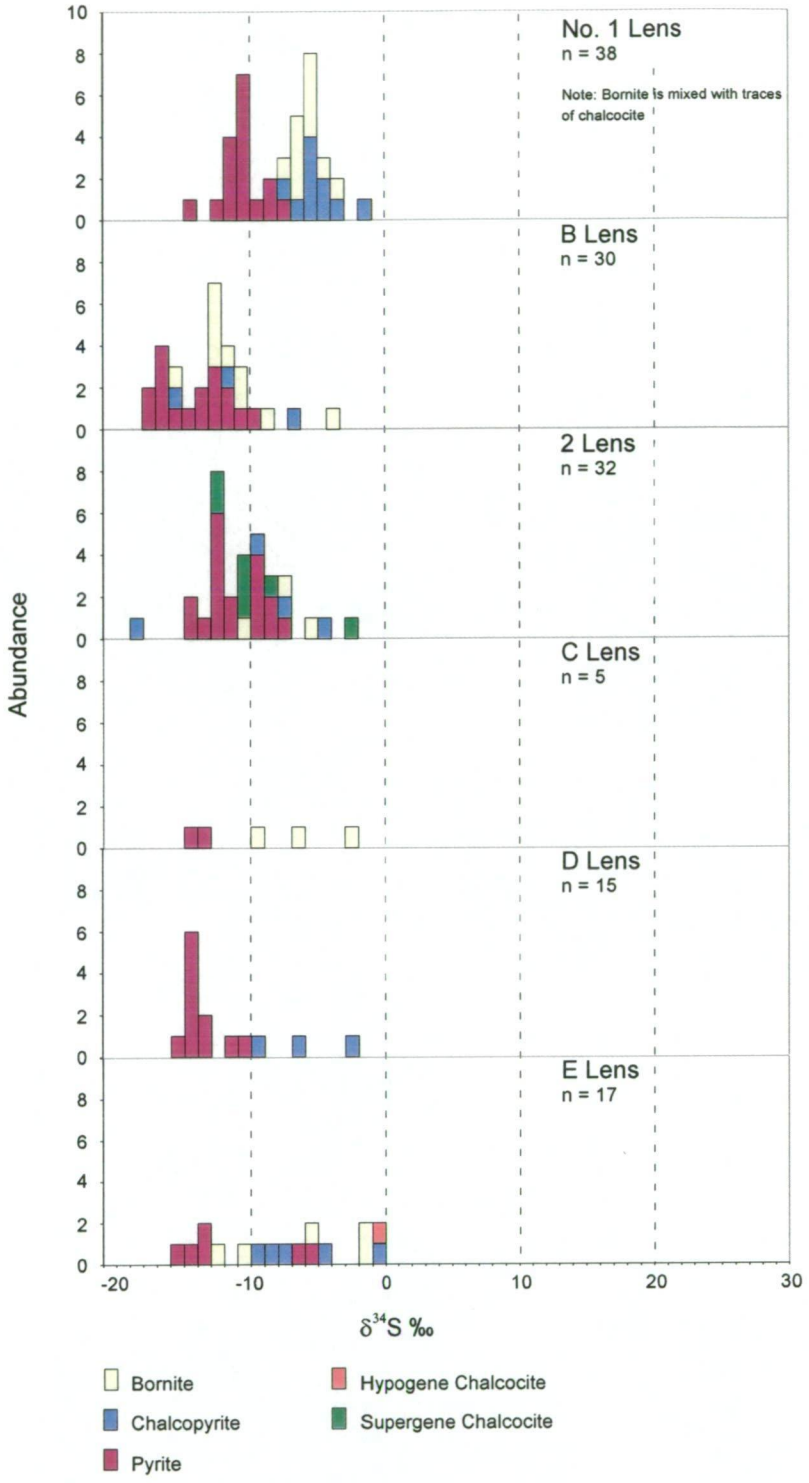

Figure 8.3. Sulphur isotope distributions for Mammoth Cu ore bodies catagorised by sulfide type (refer to text for details).

have a wide spread of $\delta^{34}S$ values ranging from –1 to –17.7‰ with a mean of –7.4‰ and a standard deviation of 4.1‰. This chalcopyrite data set is negatively skewed with the bulk of the values occurring between –4 and –8‰. In general, the stage II bornite $\delta^{34}S$ values have a similar spread as the chalcopyrite values. The data ranges form –2.9 to –15.9 ‰ with the bulk of the values occurring between –4 to -7‰. Only one $\delta^{34}S$ value (-0.8‰) of hypogene chalcocite was obtained due to its fine grain size and its myrmekitic intergrown nature with bornite. There is a limited number (7) of $\delta^{34}S$ values obtained for the Stage III supergene chalcocite, however the bulk of the data occurs between –10 to –11‰ within an overall range from –2.9 to –12.4‰. It is worthy of note that the this bulk range of $\delta^{34}S$ (–10 to –11‰) is similar to the average of the bulk $\delta^{34}S$ values obtained form the stage I pyrite (12.2‰) confirming the oxidation of pyrite was significant supply of sulfur during the formation of the supergene chalcocite.

The $\delta^{34}S$ signature of both the Stage I and II sulfides has a wide range of values (~-0‰ to ~-18‰). This distribution is consistent with sulfide precipitation from a fluid that is closed with respect to sulphate (SO_4^-) and that the fluid does not have enough resonance time to obtain equilibrium (Ohmoto and Rye, 1979). These observed large variations of $\delta^{34}S$ values suggest that the fluid was at or above the oxidation/reduced boundary with respect to the SO_4^{2-}/H_2S ratio (Ohmoto and Goldhaber, 1997). Reduction of sulphate under disequilibrium conditions, due to varying mineral fraction factors produces $\delta^{34}S$ distributions with broad plateaus. During the precipitation of sulfides at Mammoth the variance in the fraction factors may be the result of rapid precipitation. Textural evidence for rapid precipitation is documented in Chapter 5. Melnikovite and colloform pyrite textures suggest rapid precipitation from the hydrothermal fluid (Rimstidt, 1997). Furthermore, as documented in Chapter 6 the varied and high trace element content of all Stage I and II sulfides can be interpreted to suggest with rapid precipitation of sulfide (Griffin et al., 1991). The mechanisms for rapid sulfide precipitation from hydrothermal fluids include: a) the cooling of a fluid through mixing of a hot metal carrying with a cooler fluid during which dilution and H^+ consuming

reactions occur, or b) the un-mixing of a fluid through the processes of boiling or condensation (Ohmoto and Goldhaber,. 1997).

The absence of textural evidence for widespread coprecipitation of sulfide minerals within an individual paragenetic stage at Mammoth provides complementary evidence that the system did not attain isotopic equilibrium with respect to $\delta^{34}S$ (Ohmoto and Goldhaber, 1997). If the total metal content of the fluid was the same as the proportion of reduced sulfur (H_2S), precipitation of the first sulfide mineral phase consumes the majority of reduced sulfur, and therefore significantly depletes the reduced sulfur reservoir. These conditions typically lead to monomineralic ores, the result of only one mineral phase being saturated and consuming all the fluid H_2S during precipitation.

Comparison with other deposits

The sulfur isotope signature of the Mammoth Cu ore system (Stages I, II and III) is significantly different from other documented syn-deformational sediment hosted Cu deposits within the Western Fold Belt of the Mt Isa inlier (Scott et al., 1985; Davidson and Dixon, 1992). Sulfur isotope data from Cu and Pb-Zn mineralisation at Mt Isa, Lady Loretta and Esperanza generally have a positive $\delta^{34}S$ signatures from >0‰ to 30‰ (Fig. 8.4). This observed difference between the Mammoth Cu ore bodies and other Cu systems may reflect either a) different sulfur source, b) different trap mechanism or a combination of both. It is interesting to note that the majority other documented examples of diagenetic pyrite in the Western Fold Belt of the Mt Isa Inlier are positive (Fig. 8.4). With the notable exception of the fine grained disseminated sulfides within the Eastern Creek Volcanics. This lends further evidence to suggest that the origin of the diagenetic pyrite at Mammoth is not the result of diagenetic processes as suggested by previous researchers (Scott et al., 1985). In deposits were the occurance of diagenetic pyrite is well documented (eg. Esperanza and Mt Isa Cu deposits) the signature of the ore sulfur isotope signature ore the mineralising system is similar to range of the values identified for the diagenetic pyrite (Fig. 8.4). At Esperanza there is cleary a local source of diagenetic pyrite, the Esperanza Shale. The Esperanza shale is a pyritic shale and therefore a

different trap mechanism is responsible for the reduction of Cu to form the Esperanza Cu-sulfide deposit. This different mechanism of precipitation is further compared and contrasted in the following chapter.

Following on from the above examination of the $\delta^{34}S$ isotopic systematics of the sulfides in the Mammoth hydrothermal system it is now possible to speculate on the potential sources of sulfur. The obvious sulfur source is the Eastern Creek Volcanics that host disseminated pyrite, chalcopyrite and bornite distal to known mineralisation with documented $\delta^{34}S$ values ranging from –7 to +3% (Andrews et al.,1989). This hypothesis is further strengthened by the absence of textural evidence supporting bacterial reduced sulfur (pyrite framboids). Further more if bacterial reduction of sulphate did occur the Sulphur isoptoe signature of the sulphide phases would be wide spread between the range of $\delta^{34}S$ +/- 45%.

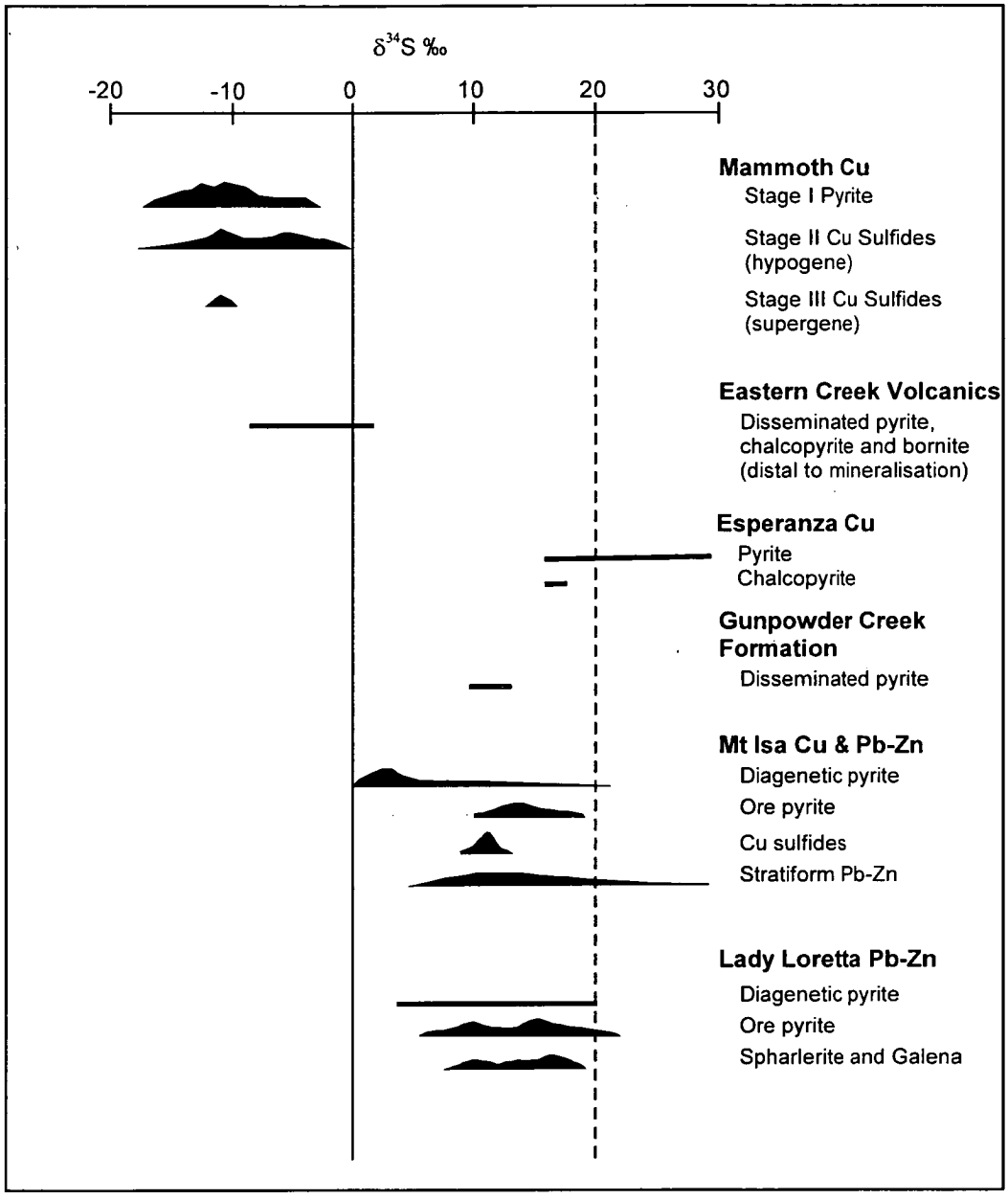

Figure 8.4. A comparison of sulfur isotopic ranges of representative deposit styles and possible sulfur sources (Eastern Creek Volcanics and disseminated/digenetic sediment hosted pyrite) within the Western Fold Belt of the Mount Isa Inlier and Mid-Proterozoic seawater (20 ‰) and those of this study from the Mammoth Cu Deposit (modified after Davidson and Dixon, 1992 Taylor and Scott, 1976; Andrew et al., 1989).

8.4 LEAD

8.4.a Previous Work

Vaasjoki (1980) conducted lead isotope analyses on samples from the Mammoth deposit. These samples were selected from No.1 and B ore zone and both mineralised wall rocks and high-grade ore samples were included. In addition, samples were collected from the No. 1 ore body surface gossan and the Eastern Creek Volcanics. Vaasjoki (1980) concluded that the similarity of the lead isotopic trends of the Mammoth copper ores and the Eastern Creek Volcanics suggests a common origin for the source of the Pb. However, due to analytical uncertainties no clear distinction could be made between the source of Pb for the Mt Isa Pb-Zn and the source of Pb for the Cu system.

8.4.b Collaborative Work

Carr et al. (2001), in collaboration with the author, conducted lead isotope analyses on high lead (250-750 ppm Pb) samples from the Mammoth deposit using the high precision double spike method of Woodhead et al. (1995). The samples were selected by the author from the 2 Lens ore zone and are representative of the paragenetic Stage II hypogene Cu mineralisation at Mammoth. Results are presented in Table 8.4. The work conducted by Carr et al. (2001) was a part of a industry-funded, confidential study focussed on using Pb isotope technologies in mineral exploration to identify sources of metals within the Mt Isa Inlier.

Table 8.4. Double spike (DS) Pb isotope data (207/204 and 206/204) from whole rock samples representing Mammoth Stage I and Stage II ore samples (hand specimens ≅ 15cm in length)

Sample Id	206/204	207/204	Pb ppm
UD768-163.1m	16.375	15.460	413.1
UD768-160.5m	16.284	15.453	415.6
UD768-163.1m	16.339	15.434	413.1
UD768-161.5m	16.275	15.435	717.7
UD768-160.5m	16.265	15.440	415.6

208/204 ratios not reported in Carr et Al. (2001).

8.4.b Interpretation

Gulson et al (1983) and Sun et al (1994) report the Pb isotope values for the major Australian early Proterozoic sediment-hosted Pb-Zn deposits (Fig. 8.5) and conclude that consistency between Pb model ages and stratigraphic ages supports a syn- to diagenetic origin for these deposits. A further conclusion of these Pb isotope data is a model where is Pb is derived from the host-meta-sediments (crustal source) (Gulson et al., 1983, Sun et al., 1994, Carr et al., 2001).

The Pb isotope ratios for the Mammoth hypogene ore samples plot at lower 207Pb/204Pb ratios (less radiogenic) than the sediment-hosted Pb-Zn mineralisation in the Western Fold Belt of the Mt Isa Inlier (Fig. 8.5). These data indicate a different Pb source for Mammoth deposit compared to the sediment-hosted Pb-Zn deposits. Gulson et al. (1983) suggested that there were only minor amounts of Pb from the diagenetic Pb-Zn ore incorporated into the younger metamorphic Cu ores in the Mt Isa district.

Excluding the host sediments, the potential source(s) of Pb for the Mammoth Cu system are the basement lithologies, principally the mafic units of the Eastern Creek Volcanics (Fig. 2.1 and Table 2.1). Carr et al. (2001) measured the initial Pb isotopic ratios for the unaltered Eastern Creek Volcanics and the results plot in a tight field as shown on Figure 8.5. Carr et al. (2001) concluded that the range of Pb isotope ratios from the Mammoth deposit are in agreement with the expected range for the Eastern Creek Volcanics at 1540 Ma (Fig. 8.5). Therefore, it is interpreted that the Mammoth hydrothermal system derived its Pb (and by extrapolation Cu) from Eastern Creek Volcanics, a less radiogenic mantle source as compared to the host meta-sediments (Carr et al., 2001).

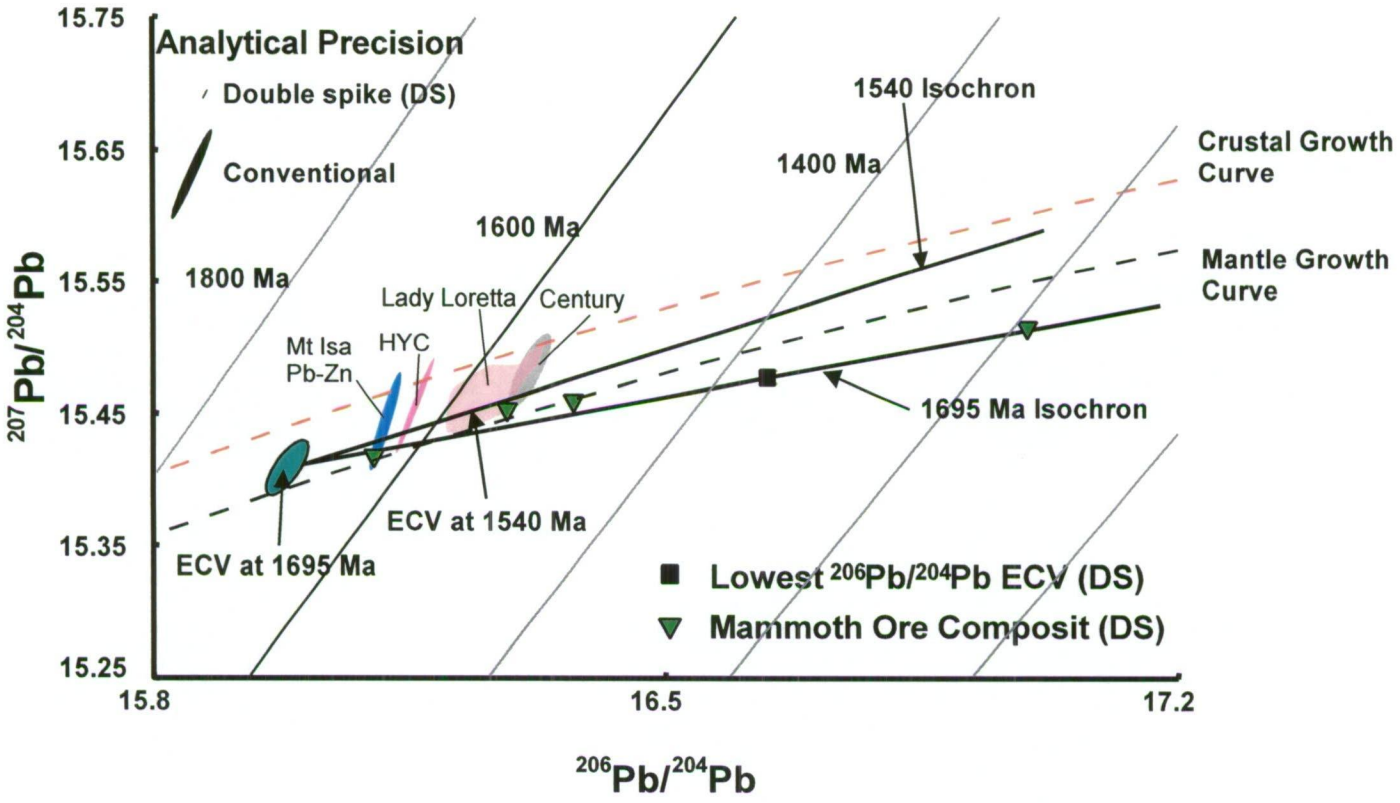

Figure 8.5. Relationship between the Pb isotopic composition of the Eastern Creek Volcanics and the Mammoth ore system. Note differences in analytical precision between the DS and conventional methods (modified from Carr et al., 2001). The fields for Mt Isa Pb-Zn, HYC (McArthur River), Lady Loretta and Century (conventional) are included for comparison (modified after Carr, 2001 and Sun et al. 19).

8.5 CONCLUSIONS

- Oxygen and deuterium isotope investigations conducted on the hypogene mineral phases suggest the H_2O was derived from two end members: 1) a dominantly meteoric fluid and 2) a fluid originating from metamorphic processes. This interpretation supports the mechanisms for the precipitation of the Mammoth sulfides from the mixing of a hot, metal and sulfur carrying metamorphic fluid with a moderately cooler, meteoric fluid.

- The broadly negative $\delta^{34}S$ values identified for the hypogene Stage I and II paragenetic stages at Mammoth suggest that the Eastern Creek Volcanics are the only source of light sulfur in the Western Fold Belt of the Mt Isa Inlier.

- The sulfide textures, mineralogy, distribution and systematics of $\delta^{34}S$ within the individual paragenetic phases at Mammoth suggest sulfide precipitation occurred rapidly from a fluid that was closed with respect to sulfur, under disequilibrium conditions with a metal content that was less than or equal to the contained reduced sulfur content. The mechanism required to initiate the rapid precipitation of sulfides from such hydrothermal fluid is most likely to involve a moderate temperature decrease in conjunction with dilution and H^+ consuming reactions.

- Pb isotope data from the Mammoth Cu deposit are less radiogenic than the sediment-hosted Pb-Zn deposit in the Western Fold Belt of the Mt Isa Inlier. Interpretation of the potential source rocks indicates that the mafic Eastern Creek Volcanics are the source for the Pb (and by extrapolation Cu) in the Mammoth deposit.

CHAPTER 9

GENETIC MODEL AND IMPLICATIONS FOR EXPLORATION

9.1 INTRODUCTION

The aim of this study was to understand the geology, geochemistry and genesis of structurally-controlled, sediment-hosted copper deposits via a detailed study of the Mammoth Cu deposit, Queensland, Australia. The Mammoth deposit is a structurally controlled, brecciated, sediment hosted ore deposit located in the Western Fold Belt of the Proterozoic Mt Isa Inlier. The pre-mining resource at Mammoth was 16.8 Mt grading 3.4% Cu, and potential for further discovery of similar resources is within the region is high.

This chapter will review the key geological and geochemical criteria of the Mammoth deposit and then propose a genetic model for its formation. An understanding of the geochemical and structural controls of the deposit has contributed to improved exploration strategies for this style of Cu deposit within the region and may be extrapolated to similar structurally deformed ancient basins elsewhere.

9.2 GEOLOGY, GEOCHEMISTRY AND STRUCTURE OF THE MAMMOTH MINE

The following geologic and geochemical characteristics of the Mammoth deposit are reviewed as constraints for the proposed genetic model.

9.2.a Geology of the Mammoth Mine

The Mammoth deposit is hosted within dilational veins and breccias bounded by faults in the Palaeoproterozoic Whitworth Quartzite that strikes north and dips west (65-85°) near the deposit. The lowermost exposed unit of the Whitworth Quartzite is a ~60 meter thick, pink, massive to poorly stratified quartzite that abuts the Portal Fault. Stratigraphically overlying this quartzite unit is an interbedded sequence of cross-bedded to thinly laminated quartz-rich and arkosic sandstone, siltstone and minor quartzite (up to 60 meters

thick) (Richardson and Moy 1998). The Palaeoproterozoic Surprise Creek Formation unconformably overlies the Whitworth Quartzite to the east and consists of conglomerate, sandstone and siltstone. The Surprise Creek Formation strikes north and dips west (50-55°) with an angular discordance of 20 to 30° existing between the Whitworth Quartzite and the overlying Surprise Creek Formation.

9.2.b Structural Controls On Cu Mineralisation at the Mammoth Deposit

Detailed structural field investigations were undertaken to constrain the geometry of the local stress regime under which Cu mineralisation occurred at the Mammoth deposit. It was found that the geometry and temporal relationships that exist between the major faults located in the Mammoth mine area are consistent with a brittle strike slip model similar to that proposed by Askew (1992). Late strike-slip movement, on the Mammoth and Mammoth Extended Faults, indicated by the low angle striations is consistent with movement during an east-west compression event. This interpretation of east-west compression and resultant dextral strike-slip movement along east-west oriented faults agrees with the compression regime suggested by the orientation of syn-mineralisation extensional vein arrays. Therefore, it is concluded that the Mammoth deposit formed during east-west transpression that locally produced dilatational sites along the major restraining bends in the Mammoth Fault during periods of high fluid pressure (Pf) as indicated by the development of syn-deformational quartz-Cu sulfide extensional veins.

9.2.c Description of Mineralisation

The Mammoth deposit consists of multiple lenes of Cu ore (No.1, B, C, D, E, 2 and Mammoth Fault Mineralisation). This mineralisation is hosted in stockworked and breccia units that plunge south-west paralleling the intersection of the Mammoth and Portal Faults. A classification scheme based on textural variations observed between these stockworked and breccia units has been developed. This scheme categorises the fracturing that the Whitworth Quartzite has undergone during the mineralising event from un-fractured (S0) through, with increasing fracture intensity (S1 and S2),

to brecciation (B1 and B2). Copper grade is variably developed throughout the breccia units and probably reflected enhanced permeability resulting form more original open space between fragments. The alteration (replacement) stage in the breccia units took place immediately after or during fragmentation of the host rock. The breccia and stockwork vein units under went hydrothermal alteration (replacement) and open space filling stages indicating that the alteration and mineralisation were linked to the breccia and stockwork processes.

9.2.d Mineralogy, Paragenesis, Alteration and Sulfide Mineral Chemistry

At the Mammoth deposit, Cu & Cu-Fe sulfides grade from chalcopyrite to bornite at depth, to chalcocite group minerals ($Cu_{(1.7-2.0)}S$) near surface. Controversy exists as to the origin of these different Cu sulfide phases. Richardson and Moy (1998) attributed sulfide mineral zonation to acidic supergene processes that modified a largely chalcopyrite-pyrite mineralogy. In contrast, early workers regarded chalcocite and bornite to be primary, with the sooty chalcocite, which extends from surface to depths of 70 metres, the product of supergene enrichment (Mitchell & Moore 1975).

Both hypogene and supergene processes are responsible for the observed mineral zonation across D Lens and by inference, the entire Mammoth deposit. The ore and alteration minerals have been divided into hypogene and supergene assemblages based on textural criteria. These are:

- Hypogene assemblage of pyrite, chalcopyrite, bornite, hypogene chalcocite, chlorite-illite intergrowths and traces of rutile, carrollite ($CuCo_2S_4$) and linnaeite (Co_3S_4).
- Supergene assemblage of hematite, kaolinite, supergene chalcocite, covellite and wittichenite (Cu_3BiS_3)

Textural relationships define a four stage paragenetic sequence that involves an early hypogene phase (Stages I & II) and a later supergene phase (Stages III & IV):

- Stage I) hypogene pyrite and quartz;

- Stage II) hypogene chalcopyrite, bornite, chalcocite and carrollite (trace) + chlorite, illite and quartz;
- Stage III) supergene hematite, chalcocite, covellite and wittichenite;
- Stage IV) supergene kaolinite, chalcocite, covellite and wittichenite.

Mineralogical associations and trace element compositions support this paragenetic sequence as: 1) hypogene chalcocite is intergrown with chlorite in the absence of kaolinite and/or hematite; 2) supergene chalcocite is widely intergrown with kaolinite and/or hematite in the absence of chlorite; 3) supergene chalcocite enriched in Bi and depleted in both Ag, Co, Sb and As compared to hypogene chalcocite.

In contrast to the chalcocite mineralisation, different styles of pyrite (disseminated versus veined) do not show distinctive differences in trace element composition. In general, the pyrite has elevated contents of As, Co, Ni, Sb, and Pb compared to chalcopyrite, bornite and chalcocite. Chalcopyrite has elevated levels of As and Sb compared to the other sulfides. Bornite is enriched in Bi.

9.2.e Metal Zonation and Major and Trace Element Correlation within the Mammoth Ore System

In general, Cu has a strong positive correlation with Fe_2O_3, Pb, Bi, As, Ni, S, and Mo within in the fractured and brecciated rock units (S1, S2, B1 and B2). The alteration mineralogy of E, D, C, B, 2 and Mammoth Fault (MF) ore zones is divisible in two broad categories: 1) chlorite dominated or 2) illite and chlorite dominated. The E, D, 2 and MF ore zones are included in the illite and chlorite-dominated category. Alteration in the B and C ore zones is dominated by chlorite. The hypogene Cu sulfides are zoned both, from hangingwall to footwall and up dip, within the major Mammoth ore zones. This zonation is broadly categorised as follows: 1) hypogene chalcocite ± bornite; 2) bornite ± hypogene chalcocite and 3) chalcopyrite ± bornite. The chalcopyrite ± bornite zone occurs in the footwall and deeper positions within individual ore zones and the hypogene chalcocite ± bornite occurring in the hangingwall and up dip positions. The supergene modification of the hypogene mineralogy results in supergene chalcocite (±covellite) overprinting

the hypogene Cu sulfide zonation. The processes of meteoric and supergene alteration have led to complex geochemical dispersion patterns overprinting geochemical patterns developed during hypogene mineralisation. Within S1, S2, B1 and B2 structures, interpreted as distal ore equivalent horizons, the trace elements Zn, Ni and Co are elevated relative to the wall rock and the ore zones. Distal ore equivalent horizons dominated by the meteoric oxidation products of hematite and other Fe-oxides demonstrate an increase in the concentrations of trace elements Ni, Co and Zn (Fig. 7.5).

9.2.f Isotope Geochemistry

The use of isotope geochemistry in the Mammoth system has determined sources for Pb, S, and H_2O. The Pb isotope data clearly indicate that the Eastern Creek Volcanics (ECV's) is the source for the Pb (and by inference Cu) contained in the Mammoth deposit. The broadly negative $\delta^{34}S$ values identified for the Stage I and II suggest that the Eastern Creek Volcanics are the only likely source of light sulfur in the Western Fold Belt of the Mt Isa Inlier.

The sulfide textures, mineralogy, distribution and systematics of $\delta^{34}S$ within the individual paragenetic phases at Mammoth suggest sulfide precipitation occurred rapidly from a fluid that was closed with respect to sulfur, under disequilibrium conditions, with a metal content that was less than or equal to the contained reduced sulfur content. The mechanism required to initiate the rapid precipitation of sulfides from such hydrothermal fluid most likely involved a moderate temperature decrease in conjunction with dilution.

Conclusions of the oxygen and deuterium isotope investigation conducted on the hypogene mineral phases suggest the H_2O was derived from two end members: 1) a dominantly meteoric fluid and 2) a fluid originating from metamorphic processes. These observations support and further substantiate the mechanisms, inferred from the sulfur isotopic data, for the precipitation of the Mammoth sulfides via the mixing of a hot metal and sulfur carrying metamorphic fluid with a moderately cooler relatively dilute meteoric fluid.

9.3 EVALUATION OF THE EASTERN CREEK VOLCANICS AS A SOURCE FOR MINERALISING FLUIDS

The Eastern Creek Volcanics consist of three members (Derrick et al., 1976). The basal unit is the Cromwell Metabasalt Member that ranges in thickness from 1750 to 5430 metres. The Lena Quartzite member stratigraphically overlies this member and ranges in thickness from 200 to 1000 metres. The upper most member is the Pickwick Metabasalt, which ranges in thickness from 50 to 700 metres. Geochemical investigations (Wilson et al., 1985) have shown them to be continental tholeiites. These Volcanics consist of metabasalt flows, typically 20 to 50 metres thick, with amygdaloidal rich bases and tops. Flow top breccias are well developed in some flows. No evidence of hyaloclastites, fluid banding or pillow structures have been identified (Wilson et al., 1985). Weakly disseminated chalcopyrite, bornite and pyrite have been observed throughout the unaltered metabasalts distal to know mineralisation (Andrews et al., 1989). These sulfides, interpreted to the result of the generation of an immiscible sulfide phase during fractional crystallisation, predominantly occur as intergranular blebs or in vesicles (Wilson et al., 1985).

The Eastern Creek Volcanics (Figs 2.1 and 9.2) have long been proposed as a source of metal for the metamorphogenic Cu deposits hosted in the Western Fold Belt of the Mt Isa Inlier (Scott and Taylor, 1982; Wilson et al., 1985; Wyborn, 1987; Warring, 1990;; Hannan et al., 1993; Heinrich et al., 1993,1995). Wilson et al., (1985) investigated the geochemistry of the Volcanics and concluded that they contained an uncommonly high Cu content (> 200 ppm) and recognised five styles of alteration distinguished by a variable enrichment in K_2O, MgO, CO_2, CaO and/or Na_2O. The alteration styles dominated by K_2O, MgO or CO_2 enrichment are associated with a significant depletion in the Cu content. Subsequent studies (Heinrich et al., 1995 and references therein) summarised the alteration style into two broad categories: 1) district scale epidote-sphene alteration coincident with the peak of greenschist metamorphism; and 2) kilometre scale fractures associated with carbonate – Fe-oxide alteration and Cu mobility, concurrent with the widely accepted syntectonic (D3) model proposed for these metamorphogenic Cu deposits (Warring et al., 1998).

Therefore, conclusions drawn from the isotopic investigations conducted in this study (and in collaboration with Carr et al., 2001) combined with the alteration styles, and associated Cu depletion, of the Eastern Creek Volcanics suggests they are the source of Cu and S required to form the mineralisation at the Mammoth deposit.

9.3.a Mechanisms for Formation and Flow of a Saline Metal Carrying Metamorphic Fluid

Yardley (1997) summarises the mechanisms for metamorphic fluid formation via the modification of pore water through the processes of compaction, dewatering and devolatilisation of hydrous mineral phases during metamorphism. The key assumption made is that the original pore waters are not abruptly lost and subsequently replaced by a new metamorphic fluid. The resultant salinity of the metamorphic fluid will likely be higher than the original seawater entrained in its pore space, as the solute content increases via leaching chloride from minerals, as long as it is hydrologically decoupled from the sea floor (for example a highly porous, impermeable, basaltic unit; or a highly porous quartzite capped above and below by relatively impermeable basaltic units). In addition to increasing the salinity of the proto-metamorphic fluid these processes will facilitate the oxidation, and leaching into solution, of the sulfides thereby contributing metals and sulfate to the fluid. However, if the strata undergoing metamorphism has a high degree of permeability then the solute content (salinity) of the pore fluid will not significantly increase (Yardley, 1997; Giggenbach et al., 1993). In consideration of the above, the metamorphism of the Eastern Creek Volcanics could potentially have generated a metamorphic fluid with a salinity > than seawater (~ 3.5 wt % equiv. NaCl) that contained metals and sulfate sourced from oxidation during metamorphism of disseminated chalcopyrite, bornite and pyrite.

During deformation the permeability of the deforming rock mass is relatively low (Yardley, 1997). In order for the metamorphic fluid generation processes to become an efficient mechanism to generate large scale channelised fluid

flow (necessary to create a mineral deposit) an increase in the permeability of the rock mass must be created. High rates of fluid flow are only achieved when highly permeable pathways are created, in the deforming rock mass, which access areas of lower hydraulic head. Extensive fluid flow will occur along these pathways until: permeability decreases; or it is no longer connected to an area of lower hydraulic head (Yardley, 1997). However, channelised flow is not an efficient means to leach metals form the source rocks.

The most efficient mechanism of leaching metals from a rock mass during deformation, as previously mentioned, is by pervasive fluid flow (Oliver et al., 1998). Large reservoirs of metamorphic fluid may accumulate as the result of the pervasive migration of fluids through the rock mass during deformation. These reservoirs may form in various structural and lithological settings were highly permeable units abut aquitards that retard fluid flow (Thompson, 1997). Metamorphic fluids are stored within these reservoirs until either 1) over pressured from subsequent fluid flow or 2) tapped by a highly permeable pathway form above that connects with a zone of lower hydraulic head. Pre-existing heterogeneities such as anitforms and synforms will vary the direction and extent to which metamorphic fluid flow may be focussed. Anitforms will focus upwards-migrating fluids whereas a synforms will disperse upwards-migrating fluids and only focus downwards fluid migration. Following fluid generation and migration under low permeability conditions, such that exist during deformation, fluids are stored in reservoir at high fluid pressures. If these reservoirs are tapped by a highly preamble structure channelised fluid flow will occur and fluid will be drawn in to the structure from the surrounding rock mass (Yardley, 1997; Thompson, 1997).

The geochemical, structural and isotopic constraints that form the basis of the conceptual model proposed for the Mammoth deposit requires that mineralisation occurred in response to the mixing of two fluids: 1) a metamorphic fluid and 2) a meteoric fluid. The metamorphic fluid originated from the Eastern Creek Volcanics during the metamorphic processes (refer above). Highly channelised flow of this fluid occurred when the metamorphic fluid reservoir(s) was tapped by crustal scale fault zones active during D3 (Mt

Gordon Fault zone). Fluid flow was focussed along these highly permeable structures to zones of lower hydraulic head where they subsequently formed mineral deposits along 2nd and 3rd order faults (Mammoth Fault) through a combination chemical and structural controls.

9.4 ORIGIN OF THE METEORIC FLUID

Based on metamorphic and geothermal gradient considerations for unstable cratons (Philpots, A.R., 1990) the depth of emplacement of the Mammoth mineralisation is likely to be at 5 to 10 Km's (Briese, 1998 and references therein). The proposed model for the Mammoth mineralisation requires a mechanism to enable the meteoric fluids to penetrate to these depths. Major meteoric-hydrothermal systems are an ubiquitous feature of both continental and oceanic rift zones (Wickham et al., 1993). Conclusions reached by Wickham et al., (1993), McCaig (1988), Koons and Craw (1991), Sturichio et al. (1996), Oliver (1986) and Powell et al. (1999) provide ample evidence for the existence of deeply (≥ 7 - 8 km's) circulating meteoric fluids into a metamorphic core complex during orogenesis. Their work demonstrates that meteoric water present in hydrostatically pressured fractures, in the upper plate can be drawn down into the lower plate region via seismic pumping in active fault zones. Powell et al. (1999) propose a model for the genesis of the giant Hamersley iron oxide deposit in which deep circulating meteoric waters play a major role.

The chemical composition of deeply penetrating meteoric waters is relatively unknown. These waters will equilibrate with the aquifer in which they are transported. The migration of surface waters through hydrocarbon traps is a well-studied process (Simoneit, 2000). Thus the migrating meteoric water entrains the hydrocarbon phases and results in the flushing of these hydrocarbon phases from the reservoir. Sturchio et al. (1996) conducted a comprehensive chemical and isotopic study of thermal waters being discharged into springs and shallow artesian wells in the Gulf of Suez area, Egypt. They concluded that the waters represented paleometeoric waters that had been heated by percolation to a depth of several kilometres within crustal scale structures. Gas effervescence analysis of this water indicated that it contained ~ 4% methane (CH_4) and had an over all CO_2:CH_4 ratio of ≅

3. Carbon isotope analysis suggested that the methane was most likely of thermogenic origin. Sturchio et al. (1996) also note the O_2 content was depleted relative to the N_2 and Ar contents and suggest that it was probably consumed by reactions in the aquifer. In summary, originally oxidised cool meteoric waters may be chemically buffered to a more reduced state via interactions within the aquifers providing the host rocks are reduced or contain hydrocarbons.

9.5 GENETIC MODEL

Conceptual models proposed for the formation of metamorphogenic mineral deposits are dependant on two phases: 1) pervasive leaching of metals and 2) a channelised deposition of leached metals at a trap site under a structural, lithological and/or chemical control (Oliver et al., 1998). The genetic model proposed here for the mineralisation at the Mammoth deposit is a new interpretation, based on field and laboratory investigations, of the metamorphogenic Cu model proposed by Heinrich et al. (1995) and Warring et al. (1998) for the Mt Isa Cu deposit. Heinrich et al. (1995) and Warring et al. (1998) propose a model that describes a class of Cu deposits that form from fluid mixing during regional deformation. These deposits are inferred to have formed during high fluid flow synchronous with the waning stages of metamorphism associated with the Isan Orogeny, 1540 to 1510 Ma (Perkins, et al., 1999). Characteristically mineralisation occurs as brecciated to stockworked vein systems along zones of significant competency contrast. Copper is commonly present as either chalcopyrite or bornite with rare occurrences of other base and precious metals. Cobalt is a notable exception with abundances commonly > 150 ppm Co corresponding to elevated Cu occurrences. Within the metamorphogenic class of mineral deposits significant occurrences of hypogene chalcocite appear to be particular to the Mammoth deposit. Deposits cited by Warring et al. (1998) as examples of metamorphogenic Cu deposits include Mt Isa, and Nifty. The inclusion of the Mammoth deposit represents an addition to the known deposit styles and in so doing broadens the classification criteria by highlighting new styles of host rock, alteration, ore mineral assemblage and trap mechanisms.

A conceptual model for development of Cu mineralisation at Mammoth is shown in Figures 9.1 and 9.2. Cu mineralisation occurred during the later

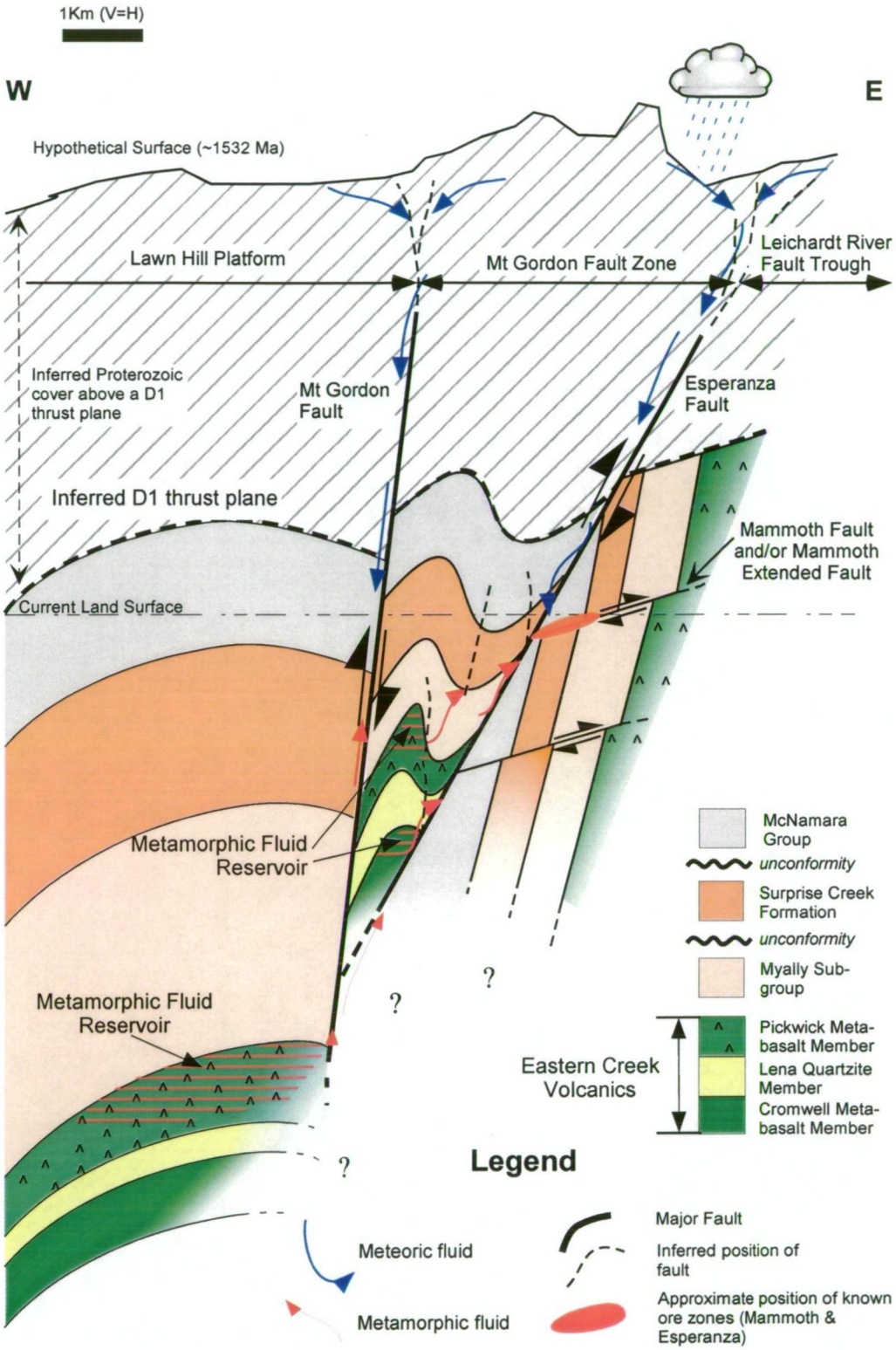

Figure 9.1. Simplified diagrammatic model illustrating geological relationships between the Lawn Hill Platform, Mount Gordon Fault Zone and the Leichardt River Fault Trough during east-west transpression (D3) synchronous with metamorphic fluid flow. Metamorphic water fluid reservoirs are within D2 (and D3?) anticlinal structures of the Eastern Creek Volcanics. Channelised fluid flow (red arrows) is initiated during D3, when the fluid reservoirs are broach by highly permeable structures, and focussed into dilatant fault zones , where it mixes with deep circulating waters (blue arrows) of meteoric origin. Refer to text for details.

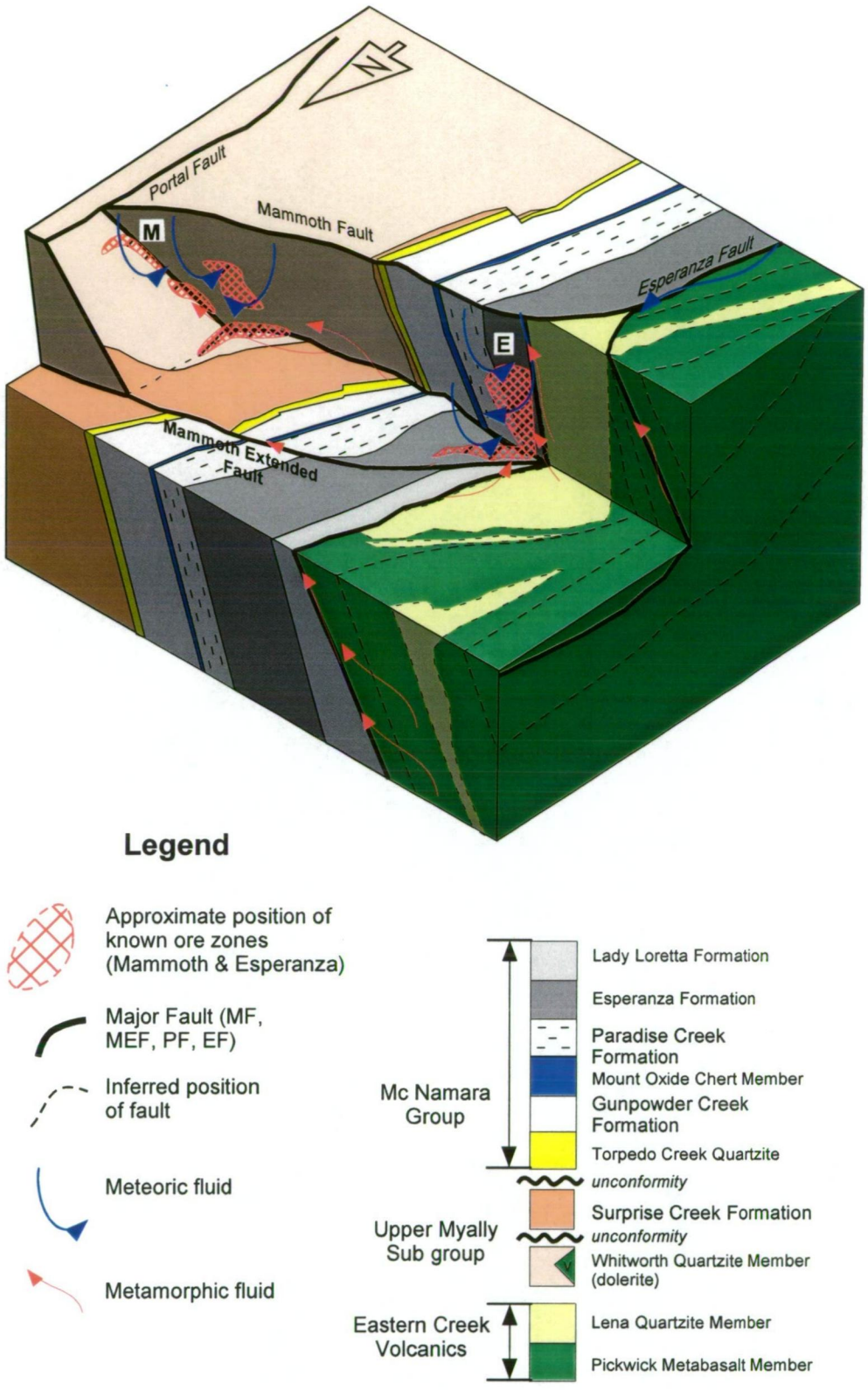

Figure 9.2. Schematic model of the Mammoth (M) and Esperanza (E) Cu deposits during east-west transpression (D3) and synchronous with metamorphic fluid flow. Metamorphic water (red arrows), generated by devolatilisation, driven out of Eastern Creek Volcanics and focussed into dilatant fault zones during periods of high fluid pressure, where it mixes with deep circulating crustal waters (blue arrows) of meteoric origin. Refer to text for details.

stages of the Isan Orogeny (1590-1500 Ma). This orogeny, superimposed on an extension rift basin, resulted in formation of upright north south trending folds bounded by large scale, north-south striking faults and caused regional metamorphism to upper greenschist facies (Mt Gordon Fault). These fault zones are interpreted to have initially formed as growth faults during early (1800-1650 Ma) extensional phases. Movement on the Mt Gordon Fault and on faults (Esperanza Fault) within Mt Gordon Fault zone has resulted in the complicated juxtaposition of McNamara Group and Myally Subgroup sediments against the Eastern Creek Volcanics.

A metamorphic fluid generated by devolatilisation leaches Cu and S from the Eastern Creek Volcanics. This metamorphically derived fluid upwells, either along stratigraphy, and/or was focussed into actively deforming faults. Fluid flow was possibly driven by convection and/or seismic pumping associated with faults that were hydrological connected to the surface. Upon reaching the Whitworth Quartzite, a build up of fluid pressure combined with the existing regional stress field, create the appropriate conditions for brittle failure in the quartzite. Subsequently the hot metal and sulfur-bearing fluid mixes with a deep circulating hydrothermal fluid originally of meteoric origin. Changes in the physicochemical conditions (pressure, temperature and oxidation state) upon this mixing destabilise the metal chlorine complexes resulting in sulfide precipitation as detailed below.

Hydrothermal transport of metals (Cu, Zn, Pb, Au) is dependant on their respective aqueous solubility. The solubility of these metals is controlled by the physiochemical conditions (pH, oxidation state, temperature, pressure and salinity) of the hydrothermal fluid (Huston, 1998). The transport of Pb and Zn in the hydrothermal environment is well understood due to the availability of quality hydrothermal data on the behaviour of their aqueous species (Huston, 1998). In contrast, the behaviour of Cu is poorly constrained due to the lack of thermodynamic data. However, Cu transport is generally believed to occur as a chloride complex, in similar fashion to Pb and Zn (Huston, 1998; Ohmoto and Goldhaber, 1997).

To achieve ore grade mineralisation precipitation of metals, as sulfides, must occur in a localised area generally know as the trap site. Mechanisms to facilitate this precipitation rely on changes in the physiochemical conditions of the metal laden fluid, brought about by either: 1) dilution and salinity decrease; 2) changes in the redox state; 3) cooling or 4) phase separation (Huston, 1998; Seaward and Barnes, 1997). At Mammoth the lack of textures commonly associated with phase separation (banded quartz veins and highly acidic alteration assemblages) precludes this as a mechanism for sulfide precipitation. Therefore, it is proposed that sulfide precipitation occurred in response to dilution and changes in the redox state of the fluid via fluid mixing.

The physiochemical condition of the metamorphically derived metal laden fluid at the trap site remains unclear due to the lack of suitable material for a comprehensive fluid inclusion study. However, based on considerations from the sulfur, oxygen, hydrogen and lead isotopic investigations, in conjunction with the deposits mineral assemblage and textural relationships, these conditions can be estimated: $\cong$ 250 to 300°C (based on illite and chlorite stability fields); moderate salinity ($\geq$ 3.5 wt % equiv. NaCl); weakly acidic (illite stable) to neutral (chlorite stable) (pH = 5 to 7); weakly oxidised with respect to its SO_4/H_2S ratio so that $SO_4^{2-} \geq H_2S$ (absence of a hypogene Fe oxide assemblage); $\sum$ Cu $\cong$ $\sum$ S (suggested by the mono-mineralic nature of the ore assemblage (Ohmoto and Goldhaber, 1997)).

The physiochemical characteristics of the deeply circulating hydrothermal fluid originally of meteoric origin are poorly understood. In general, there is a lack of data available on the chemical composition of these types of crustal fluids. As previously mentioned Sturichio et al. (1996) demonstrated these originally highly oxidised fluids could be buffered to a more reduced state by interactions with the host rocks in the aquifer. Therefore, the physicochemical conditions inferred for this meteorically derived fluid are considered: $\cong$ 200 to 250°C (based on the crustal geothermal gradient); $CO_2 \geq CH_4$ (oxidised but still carrying a significant component of methane) and; H_2O dominated and therefore of a neutral pH.

9.5.a Formation Reactions

In order for the precipitation of sulfides to commence the reduction of sulfate has to occur. This is likely to occur via two processes: 1) moderate to weak cooling and/or salinity decrease via dilution (eq. 9.1); and 2) production of H_2S at the trap site via the reduction of sulfate by methane (eqs 9.2 and 9.3). Both of these processes will occur upon fluid and may be represented by the following series of reactions. The precipitation of pyrite from hydrothermal solutions involves the initial formation of a Fe monosulfide that is subsequently modified to pyrite:

$$FeCl_2 + SO_4^{2-} + 4H_2 = FeS + 4H_2O + 2Cl^- \text{ (eq.9.1)}$$

$$CH_4 + SO_4^{2-} = H_2S + HCO_3^- + OH^- \text{ (eq. 9.2)}$$

$$FeCl_2 + H_2S = FeS + 2H^+ + 2Cl^2 \text{ (eq. 9.3)}$$

Equations 9.1 and 9.3 illustrate the reactions that result in the nucleation of an iron monosulfide. As outlined in Ohmoto and Goldhaber (1997) the precipitation of pyrite and subsequent growth of pyrite crystals is dependant on the formation of this initial Fe monosulfide. Pyrite nuclei is then formed from these Fe monosulfides via sulfidization and Fe loss from the precursor monosulfide:

$$Fe^+ + H_2S_2 = FeS_2 + 2H^+ \text{ (eq. 9.4)}$$

Murowchick and Barnes (1986) suggest that the production of the polysulfide (H_2S_2) must be generated continuously at the trap site in order to facilitate pyrite formation. Polysulfides can be generated by various pathways: 1) from the reduction of sulfate; or 2) from the further sulfidization of H_2S. Polysulfide generation via pathway 2 to will result in isotopic ($\delta^{34}S$) equilibrium conditions existing between pyrites and other sulfides formed. However, polysulfide generation via the reduction of sulfate (pathway 1) will result in isotopic ($\delta^{34}S$) disequilibrium conditions existing between pyrites and other sulfide phases. The results of the $\delta^{34}S$ isotopic investigation conducted on hypogene stage I

pyrite have been interpreted to indicate sulfide precipitation did not occur under equilibrium conditions (Fig. 8.3). This interpretation confirms that polysulfide generation and subsequent pyrite precipitation occurred via the reduction of sulfate (pathway 1). A reaction that may control polysulfide generation via pathway 1 is:

$$7H_2S + 2H^+ + SO_4^{2-} = 4H_2S_2 + 4H_2O \text{ (eq. 9.5)}$$

Reaction 9.6, operating in conjunction with reaction 9.4, further drives the alteration of the Fe monosulfide to pyrite by consuming H^+ the produced during pyrite precipitation (eq. 9.4):

$$2FeS + 2H^+ = FeS_2 + Fe^{2+} + H_2 \text{ (eq. 9.6)}$$

The extent to which methane is responsible driving the reduction of sulfate via reaction 9.2 has been interpreted as being significant. This interpretation is founded upon the absence of any obvious mechanism to drive the reaction: 1) insignificant wall rock interaction (quartzite host rock); 2) no significant quartz co-precipitation in hypogene Stage II; 3) evidence for increased SiO_2 solubility; and 4) no evidence for the interaction of any other obvious reductant (shales or pyrite). However, the amount of methane introduced at the trap site via the influx of the hydrothermal fluid (originally of meteoric origin) is limited. Based on the physiochemical conditions of this fluid, the content of methane (CH_4), ultimately unknown, has been inferred to be low ($\cong$ 4% CH_4). Therefore, a mechanism is required to abiogenically produce methane at the trap site to enable enough methane to be present to kinetically drive sulfate reduction to from sulfide.

Berndt et al. (1996) demonstrated experimentally the reduction of CO_2 (Fisher Tropsch synthesis, eq. 9.7) during the serpentinization of olivine. Fisher-Tropsch synthesis is a well known industrial processes were methane is produced by the reaction of CO_2 with H_2. There is a lack of understanding on how this process may occur in a hydrothermal fluid where H_2O is predicably the dominant medium and H_2 is scarce. During the precipitation of the stage I pyrite H_2 may not be scarce. The production of H_2 via reaction 9.6

during the production of pyrite can be inferred to be an significant source of H_2 and therefore a catalyst for the reduction of CO_2 to form methane:

$$CO2 + 4H_2 = CH_4 + 2H_2O \text{ (eq. 9.7)}$$

The precipitation of hypogene stage II chalcopyrite, bornite and chalcocite is inferred to occur via two mechanisms 1) addition of H_2S at the trap site and 2) the replacement of stage I pyrite. Textural evidence supports both mechanisms (Chapter 5); with the sulfide phases more commonly occurring in void space and to a lesser extent as a replacement of pyrite. Sulfur isotope data also suggest that the majority of the Cu and Cu-Fe sulfides did not utilise the sulfur from the pre-existing stage I pyrite (Fig. 8.3). The precipitation of hypogene stage II chalcopyrite, bornite and chalcocite by the addition of H_2S at the trap site as can be expressed by the following reactions:

$$CuCl_2^- + FeCl_2 + 2H_2S + 0.25O_2 = CuFeS_2 + 3H^+ + 0.5H_2O + 4Cl^- \text{ (eq. 9.8)}$$

$$5CuCl_2^- + FeCl_2 + 4H_2S + 0.5O_2 = Cu_5FeS_4 + 4H^+ + 2H_2O + 12Cl^- \text{ (eq. 9.9)}$$

$$2CuCl_2 + H_2S + 0.5O_2 = Cu_2S + H_2O \text{ (eq. 9.10)}$$

The reduction of sulfate to sulfide by methane (eq. 9.2) will generate elevated concentrations HCO_3^- in the mineralising fluid. In ore deposits where the reduction by methane is inferred to have been the dominant process driving sulfide precipitation the co-precipitation of carbonate minerals is common (Rimstidt, 1997). As demonstrated by this reaction (Me^{2+} represents by Ca, Mg and or Fe):

$$HCO_3^- + Me^{2+} = MeCO_3^- + H^+ \text{ (eq. 9.11)}$$

No carbonate phases have been observed in thin sections from the major ore lenses (B, C, D, E, 2 and Mammoth Fault Mineralisation) at Mammoth. This may be interpreted to suggest that reduction via the interaction of methane was not a significant process. If this were the case then the pH of the

mineralising fluid would decrease in response to the acid production during stage I pyrite and Stage II chalcopyrite and bornite precipitation (eqs 9.2, 4, 8 and 9). However, the pH of the fluid is interpreted to have remained weakly acidic to near neutral as indicated by the presence of illite and chlorite in the ore assemblage. Therefore, it is proposed that methane was an active agent of sulfate reduction and the pH was buffered by the production of carbonate HCO_3^- (eq. 9.11), as indicated by this reaction:

$$2H^+ + 2HCO_3^- = 4H_2O + CO_2 \text{ (eq. 9.12)}$$

Further evidence for the abiotic production of methane from CO_2 via Fischer-Tropsch synthesis (eq. 9.7) and subsequent reduction of sulfate to sulfide via interaction with methane (eq. 9.2) can be deduced by the absence of significant SiO_2 precipitation. The solubility SiO_2, in the presence of OH^-, generated as a result of the direct reduction of sulfate by methane (eq. 9.2), is considerably increased via the process outlined by Dove and Rimstidt (1994):

$$SiO_2 + OH^- + H_2O = H_3SiO_4^- \text{ (eq. 9.13)}$$

9.5.b Supergene Modification of the Mammoth Deposit

Sulfide occurrences located within the weathered zone are subject to oxidation through interaction with air and groundwater. The mechanisms for sulfide oxidation has been the focus of numerous studies into the formation of supergene deposits and leached outcrops (Blanchard 1968, Anderson 1982). The mechanisms for oxidation of Cu and Cu-Fe sulfides hinge upon the generation of an acid. The ability of the solution to retain its acidity will govern the extent to which the fluid can transport the dissolved metals away from the site of oxidation. If the pH of the solution remains near neutral, metals will only undergo local transport. Chlorite, at low temperatures and pressures, is only stable under neutral to alkaline conditions and will alter to kaolinite upon contact with an acidic fluid. Therefore, the presence of chlorite is an indicator as to whether a package of rocks has undergone alteration by an acidic supergene fluid.

The interaction of chlorite with an acidic supergene fluid will buffer the pH to near neutral. A weakly acidic to near neutral fluid (meteoric groundwater) will not remove all of the Fe resulting in the alteration of chlorite to hematite. The occurrence of chlorite as an alteration and vein fill phase, indicates that the hypogene mineralogy has not been modified from interaction with an acidic supergene fluid.

At Mammoth, faults (Fig. 9.2) provide conduits for the penetration of meteoric water to depths in excess of 1000 metres. Oxidation with and without supergene effects is overprinted on hypogene sulfide zonation. The resultant complex mineralogical and textural relationships has caused the previous conflicting interpretations regarding the origin of chalcocite and the overall sulfide zoning pattern in the deposit.

Briese (1998) conducted geochronological investigations into the timing of the supergene modification of the Esperanza ore body (Figs. 3.1, 9.2). Ar^{40}/Ar^{39} dating techniques were applied to the supergene gangue mineral assemblages. It was concluded that the major supergene enrichment of the Esperanza deposit and by inference the Mammoth deposit occurred during two events: 1) at 23 Ma to 15 Ma during the Miocene; and 2) a $\cong$ 3 Ma in the Pliocene. In addition, Briese (1998) identified numerous dates ranging from 620 Ma to 1194 Ma that were interpreted to represent hypogene mineral contamination of the samples. These dates were discounted based on the methodology of the technique. However, in light of the genetic model proposed here for the Mammoth deposit it is quite possible that supergene modification of the ore zone may have commenced immediately after the cessation of hypogene event; when the thermal perturbations associated with the ingress of the metamorphic fluid abated.

9.6 COMPARISON WITH OTHER METAMORPHOGENIC CU DEPOSITS

Following the initial proposal of a syntectonic emplacement model (metamorphogenic) for the structurally controlled, sediment hosted, Cu deposits in the Western Fold Belt of the Mt Isa Inlier (Swager, 1983; Bell,

1983; Perkins, 1984; Bell et al., 1988) relatively few comparative studies have been undertaken. This lack is in part due to both the limited number of large deposits of this style and the relatively recent proposal of the model. van Dijk (1991) conducted a reconnaissance study assessing the styles of other significant Cu deposits (Table 2.1), interpreted to belong to the metamorphogenic Cu style, located in the Western Fold Belt. Two dominant alteration styles were recognized within this deposit class: 1) Cu mineralisation hosted in dolomitic rocks is associated a silica and carbonate alteration assemblage; and 2) Cu mineralisation hosted arenaceous rocks is associated with a sulfide and chlorite alteration assemblage.

Esperanza is the only other significant Cu deposit, located in the immediate vicinity of the Mammoth Cu deposit (Fig. 3.1, Table 2.1). The Esperanza deposit contained a pre-mining resource of 8.4 Mt @ 7.9 % Cu (including 0.9 Mt @ 0.19% Co) and hosted within the dolomitic-carbonaceous-pyritic shales of the Esperanza Formation (Richardson and Moy, 1998). The ore zone is located near the convergence of the Mammoth and Mammoth Extended Faults and Cu emplacement appears to be fault controlled. Hypogene mineralisation consists of pyrite-chalcopyrite (± enargite, cobaltite and linnaeite) filled veins, disseminations and massive sulfide (pyrite only) (Sillitoe, 1997; Richardson and Moy, 1998). Supergene alteration of the ore body resulted in the significant enhancement of grade through the formation of secondary Cu sulfides which envelope the hypogene mineralisation (Briese, 1998; Richardson and Moy, 1998; Sillitoe, 1997). Paragenetic relationships define a four stage mineralisation sequence, for the Esperanza deposit, as follows: Stage I syngenetic fine-grained pyrite; Stage II colloform pyrite; Stage III chalcopyrite-pyrite-quartz ± chlorite; Stage IV supergene Cu sulfides, chert, Fe-oxides and smectite (Briese, 1998; Richardson and Moy, 1998). A significant zone of silicification is developed above the ore body that overlaps with the leached weathering profile. Briese (1998) demonstrated that this silicified zone originated during hypogene stage II pyrite and stage III chalcopyrite-pyrite-quartz deposition and was overprinted by chert during supergene modification (Stage IV).

The genetic model for the Esperanza deposit proposes that mineralisation occurred in two specific stages in one hydrothermal event (Richardson and Moy, 1998; Sillitoe, 1997). Oxidised hydrothermal fluids were focused into favourable structure sites during D3 of the Isan Orogeny. Stage II colloform pyrite was precipitated when the oxidised fluid was introduced to the dolomitic-carbonaceous-pyritic shales of the Esperanza Formation. Subsequent fault movement extensively shattered the colloform pyrite and allowed the influx of oxidised Cu-rich fluids. Precipitation of Stage III chalcopyrite-pyrite-quartz ± chlorite occurred via the reduction of this fluid.

Previous workers (Sillitoe, 1997; Richardson and Moy, 1998; Briese, 1998; and Bruce Gemmell, pers. com., 1998) compared the physical characteristics of the Mammoth deposit to the Esperanza deposit. The deposits share several significant features (Table 9.1). The most obvious differences include the: 1) style of host rock; 2) development of massive pyrite as a precursor to Cu mineralisation at Esperanza (accompanied by intense SiO_2 alteration immediately above this massive pyrite); and 3) the low Co content of typical Mammoth ore relative to Esperanza ore.

Table 9.1. Deposit Characteristics: Esperanza and Mammoth

Characteristics	Esperanza	Mammoth
[1]Resource	8.4 Mt @ 7.9 % Cu (including 0.9 Mt @ 0.19% Co)	16.8 Mt @ 3.4 % Cu
Host rock	Esperanza Formation. Dolomitic-carbonaceous-pyritic shales and siltstones	Whitworth Quartzite. Massive to poorly stratified quartzite.
Sulfide Assemblage	[3]pyrite marcasite, chalcopyrite, ± enargite, cobaltite and linnaeite	pyrite, chalcopyrite, bornite, chalcocite, carrollite, chalcocite, covellite and wittichenite
Alteration Assemblage	[3]quartz, chlorite, rutile, dolomite, pyrobitumen, massive silicification	illite, chlorite, hematite
Primary Hypogene Sulfide Texture	[3] replacement dominant (massive pyrite), open space infill (chalcopyrite)	open space infill dominant (pyrite, Cu and Cu-Fe sulfides)
Paragenesis	[3]Stage I - diagenetic/syngenetic pyrite	Stage I - pyrite and quartz
	[3]Stage II - colloform pyrite (massive), marcasite + extensive silicification	Stage II - chalcopyrite, bornite, chalcocite and carrollite (trace) + chlorite, illite and quartz
	[3]Stage III - pyrite, chalcopyrite, quartz ± enargite, cobaltite and linnaeite	Stage III - supergene hematite, chalcocite, covellite and wittichenite
	[3]Stage IV - supergene Cu sulfides, chert, Fe-oxides and smectite	Stage IV - supergene kaolinite, chalcocite, covellite and wittichenite
Sulfur Isotopes	[2]pyrite - ≥ 16.9 to 31.1 ‰ $\delta^{34}S$	[4]stage I pyrite average value - –11‰ $\delta^{34}S$
	[2]chalcopyrite - 16.8 ‰ $\delta^{34}S$	[4]stage II Cu and Cu-Fe sulfides - –8.1 ‰ $\delta^{34}S$

[1] Resource figures from Table 2.1; [2] Limited data, sourced from Scott et. al., (1985);
[3] Paragenesis sourced from Sillitoe (1997), Richardson and Moy (1998) and Briese (1998);
[4] Average value this study refer to Chapter 8 for details

The different host rock between the deposits has the potential to vary the trap mechanism and hence the style of ore and alteration assemblages. Sillitoe (1997) suggested that the formation of the massive pyrite lens at Esperanza probably occurred via replacement processes. The silicification of the host sequence immediately above the massive pyrite lens was a product of this replacement processes. The absence of a comparable silicification event associated with Mammoth deposit is most likely due to the brittle and

chemical inert nature of the Whitworth Quartzite. At Mammoth the first stage of pyrite mineralisation (Stage I, this study) dominantly occurs as open space fill and not replacement. In contrast, the ductile nature and higher chemical potential of host rock for Esperanza may it render more prone to deformation and replacement.

The distribution of Co in the Mammoth deposit has been demonstrated to be hosted principally in hypogene stage I pyrite (≤ 881 ppm Co) and to a lesser degree hypogene stage II chalcopyrite (≤ 459 ppm Co), and rare occurrences of carrollite and/or linnaeite hosted in stage II chalcopyrite (Chapters 5 and 6). To date an estimation of any potential cobalt resource at Mammoth has not been conducted although in the absence of significant occurrences of Co sulfides it is not likely to be a significant figure (< 0.04 % Co, based on whole rock geochemical investigations of Mammoth ore breccias, Chapter 7). A definitive explanation for the absence of ore grade Co mineralisation (≅ > 0.15 % Co) in the Mammoth deposit remains unclear however it may be linked to differences in the physiochemical conditions during sulfide precipitation.

The paucity of comprehensive ore deposit studies on the other known deposits similar in style to Mammoth, with the exception of the Mt Isa Cu system, precludes an in depth comparison between the deposits. However, a comparison between conclusions drawn from the research conducted on the Mt Isa deposit and the Mammoth deposit is now possible. The Mt Isa deposit is unique in the respect that it appears to be emplaced 150 m.y. after the formation of a major Pb-Zn-Ag, which it is adjacent to. Not withstanding this major difference between the Mt Isa and Mammoth deposits the controls on deposition Cu and the generation of the ore fluid may be similar in many respects.

The conceptual model proposed for the Mt Isa deposit (Heinrich et al., 2000; Oliver et al., 1998; Heinrich et al., 1993 and 1995; Valenta, 1994; Bell et al., 1988; Perkins, 1984) requires that Cu is sourced from the Eastern Creek Volcanics via leaching by a highly saline (8-15 wt% NaCl) oxidised fluid during regional greenschist facies metamorphism. The origin of this highly

saline fluid is interpreted to be via the introduction of basin brines infiltrating the terrain during the waning stages of regional metamorphism (Heinrich et. al., 1993). This is in contrast to mechanism proposed at Mammoth for the generation of the entirely metamorphically derived saline brine (> 3.5 wt% NaCl).

The Mt Isa Cu deposit is hosted within dolomitic shales of the Mt Isa Group, and located within the Western Fold Belt of the Mt Isa Inlier approximately 120 km to the south of the Mammoth deposit (Fig. 2.2). The deposit contained a pre-mining resource estimated at 255 Mt @ 3.3 % Cu (Table 2.1). Warring et al. (1998) and Heinrich et al. (2000) provide thorough reviews and summaries of the geology and the widely accepted genetic model for the Mt Isa Cu deposit. Copper ore deposition is considered not due to the simple up welling of metamorphically derived oxidised brines along deep-seated structures where it reacts with the reduced pyritic dolomitic shales. Instead, a model based around the mixing of two chemically different fluids was derived based on mass-balance and isotopic constraints. The metamorphically derived fluid reacts, after focusing into a favourable structural and chemical trap site, with meta-sedimentary rocks and their *in situ* metamorphic fluid that is weakly reduced ($CH_4 \pm H_2S$) (Heinrich et al., 2000). Chalcopyrite precipitation follows via a mixing of this CH_4 ($\pm H_2S$) fluid with the Cu^+ and SO_4^{2-} bearing brine (Heinrich et al., 2000).

Warring et al. (1998) and Heinrich et al. (2000) acknowledged that the proposed origin of the methane (Heinrich et. al., 1995), critical for the formation of chalcopyrite, was not supported by mass balance calculations (Warring, 1990) or by petrological investigations. Heinrich et al. (1995) suggested that methane (CH_4) was produced via metamorphic reactions of the reduced carbon, hosted in the dolomitic shale, during synchronous with the ore forming event. Warring (1990) demonstrated by mass balance equations that the in situ reduction of C was insufficient to account for the total amount of chalcopyrite precipitation and subsequently proposed that chalcopyrite precipitation resulted from pH neutralisation via host rock reactions.

At Mammoth due to the lack of other obvious mechanisms, as outlined above, the precipitation of the Cu and Cu-Fe sulfides is interpreted to largely controlled via the reduction sulfate by methane (CH_4) (eq. 6.2). It is further proposed that the abiotic reduction of methane (eq. 9.7) may be a significant mechanism controlling the precipitation of chalcopyrite in the Mt Isa Cu system. Heinrich et al. (1989) conducted oxygen and hydrogen isotopic analysis on fluids sourced fluid inclusions interpreted to be in equilibrium with the main phase Cu mineralisation. The results from this investigation (Chapter 8) overlap with the calculated fluid composition for the Mt Isa Cu mineralisation (Fig. 9.3) providing further evidence of a genetic link between the deposits.

In summary, the Mammoth deposit is similar to the Mt Isa Cu deposit and other metamorphogenic Cu deposits hosted in the Western Fold Belt of the Mt Isa inlier. The deposits are hosted in deformed Proterozoic sediments that range in age from 1740 to 1652Ma and the Cu mineralisation is interpreted as occurring 260 to 150Ma after deposition of the host rocks during regional deformation. Copper mineralisation in these deposits is hosted in breccias and veins, which appears to be fault controlled. As outlined in Table 2.1, variations in styles of alteration are related to differences in host rock.

9.7 IMPLICATIONS FOR EXPLORATION

This section outlines the major implications of this study for exploration in the Western Fold Belt of the Mt Isa Inlier. The Mt Isa Inlier is structurally complex and the Western Fold Belt is a relatively well-explored area and yet only a few significant metamorphogenic Cu deposits have been identified to date (Table 2.1). The present regional exploration strategy, for this style of deposit, in use through out the Western Fold Belt is dominantly reliant upon contributions from structural models. Accordingly any revision of these models may impact of the success of future exploration programs. Prospect scale exploration strategies are driven by a combination of geochemical and geophysical programs. The characterisation of the geochemical signature from the Mammoth deposits leached gossan, hypogene and supergene

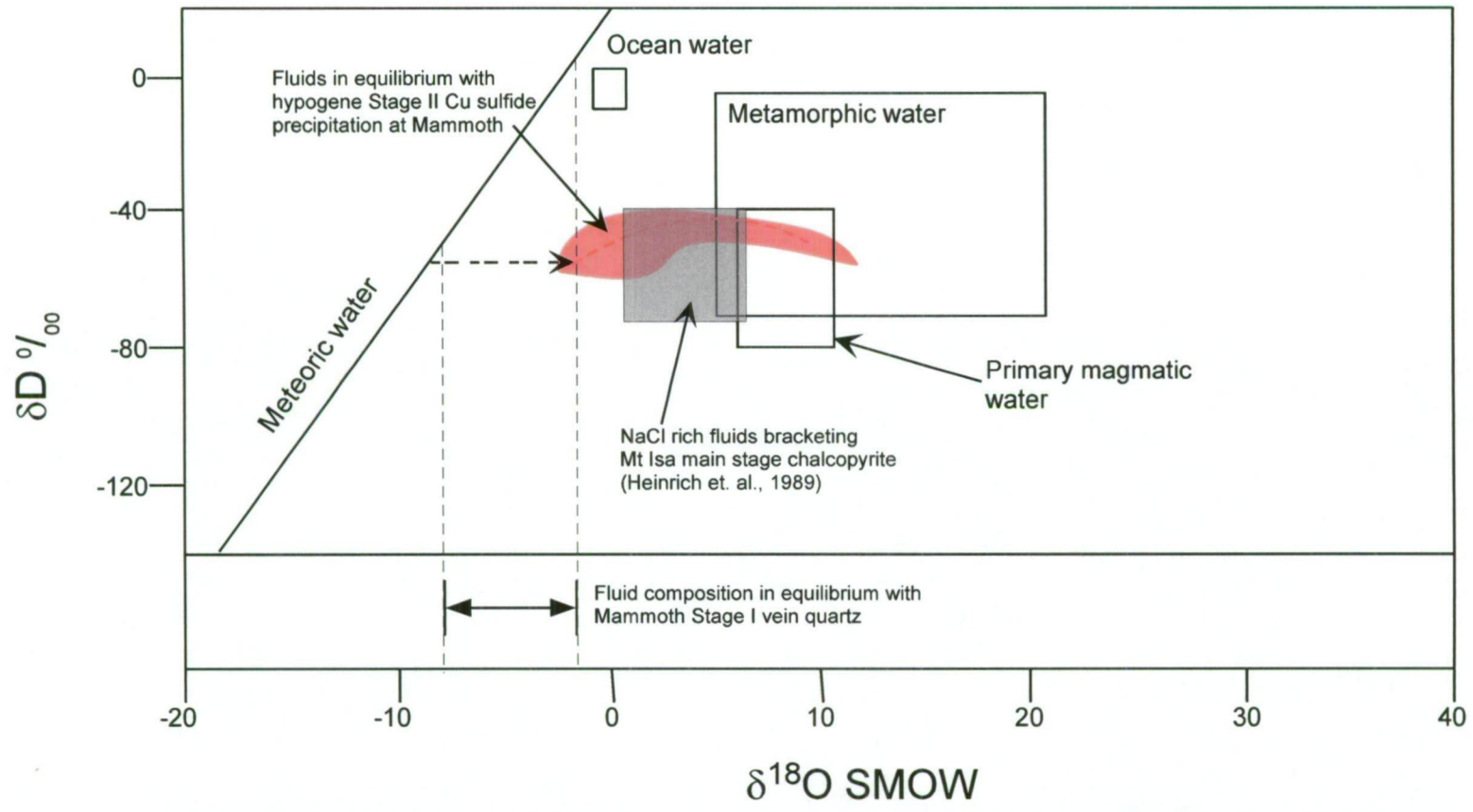

Figure 9.3. A comparison of fluid compositions calculated from Mammoth hypogene stage II chlorite, and Mt Isa copper ore body fluid inclusions (Heinrich et al., 1989). Water compositions in equilibrium with chlorite were calculated using fraction factors of: $\Delta^{18}O_{chlorite\text{-}water} = 1.56 \times 10^6/T^2 - 4.7$; $\Delta D_{chlorite\text{-}water} = -4.38 \times 10^6/T^2 - 24.6$; $\Delta^{18}O_{quartz\text{-}water} = 3.34 \times 10^6/T^2 - 3.31$ (Taylor, 1979).

styles of mineralisation has led to the identification of potential vectors towards mineralisation that can be applied in the exploration for similar deposits.

9.7.a Regional Scale Targeting

The major criteria in targeting regional exploration for metamorphogenic Cu in the Western Fold Belt of the Mt Isa Inlier is based on structural considerations (Warring et al., 1998; A.M. Hespe pers. comm., 1999). C. Sidney Honman (1938) first summarised the importance of structural controls to mineralisation hosted in the Mt Gordon Fault Zone:

> "The results of the geological survey indicate that large portions of the area contain no major structural features and may therefore be unfavourable for the occurrence of mineral deposits. The results also indicate that future prospecting can be directed to fairly narrow well-defined zones along the major structural features. These zones are —
>
> (i) The Mount Oxide fault north-east and south-west of the Mount Oxide Mine.
>
> (ii) The Mount Gordon fault and its extension northwards.
>
> (iii) The central zone of shearing and faulting representing the southern continuation of the Mt Gordon fault plane. This zone is about 2 miles wide and has parallel faults and shears striking through it in a general north-south direction."

The results of this investigation at Mammoth have significant implications for the exploration targeting of structurally controlled metamorphogenic Cu mineralisation within the Western Fold Belt of the Mt Isa Inlier. Structural geometries that gave rise to zones of compression during ENE-WSW oriented compression have the potential to host significant Cu resources. The exploration strategy currently in use through out the Mt Gordon Fault Zone has traditionally focussed on sites were structural geometries potentially gave rise to dilational fault jogs created during deformation. This research provides new insights into the structural controls on Cu mineralisation throughout the Mt Gordon Fault Zone, and by extrapolation the Western Fold Belt of the Mt Isa Inlier. In consideration of the constraints

placed on Cu mineralisation developed as result of this research it is proposed that the exploration targeting criteria be widened. These criteria should now include targets where structural geometries have the potential to create zones of E-W compression and/or N-S extension.

In addition, this work demonstrates that metamorphogenic Cu ore deposits can be hosted in rocks other than meta-carbonates. Other geological features that should be given consideration when exploration targeting include: 1) the potential for crustal scale faults to be connected to metamorphic fluid reservoirs (anticlinal structures within the Eastern Creek Volcanics) to enable for channelised metamorphic fluid flow; and 2) faults that are hosted in reduced units (McNamara Group) that have the potential to generate a methane bearing fluid during deep circulation of surface (meteoric) waters.

9.7.b Deposit Scale Targeting

The Mammoth deposit has experienced supergene modification and leaching down to depths 1,400 m. This is interpreted as the result of Cu mineralisation developed in silicate host rocks will undergo leaching to significant depths, due to the lack of carbonates in the ore and alteration assemblage to buffer supergene acid production.

Cobalt and Ni and to a lesser extent CaO and P_2O_5 appear to halo the hypogene ore zones at Mammoth. Within distal ore equivalent structures that have not been modified by meteoric and/or supergene processes the trace elements Zn, Ni and Co are significantly enriched relative to the ore zone. The concentrations of Cu, Bi, Pb, As and Fe increases towards mineralisation and therefore can be used as a geochemical vector for Mammoth style mineralisation. Within ore equivalent horizons leached through supergene and/or meteoric (near surface or at surface) processes the trace elements Cu, Pb, Zn, Ni, Bi, Sb, and As remain enriched relative to host rocks. This suit of trace elements can be used to identify Mammoth style mineralisation in surface or near surface leached structures (Fig. 7.13).

The LA ICPMS investigation into the sulfide mineral geochemistry of the Mammoth deposit demonstrated that the Bi content of bornite increases with depth, providing a possible vector for exploration programs; focused on near mine resource definition and extension

The occurrence of hypogene chalcocite has been confirmed as a result of this investigation. Therefore, exploration programs targeting chalcocite ore bodies are not limited to near surface regions and additional deep chalcocite resources may exist.

9.8 CONCLUSIONS

Geological, isotopic, paragenetic, geochemical and structural data suggest the Mammoth Cu deposit formed synchronous with regional deformation when channelised flow of hot saline-oxidised Cu enriched metamorphically derived fluid was focussed along the Esperanza, Mammoth and Mammoth Extended Faults where it mixed with a methane bearing crustal fluid of meteoric origin. The Mammoth deposit meets the majority of criteria for it to be included in the metamorphogenic Cu classification of deposits. Its inclusion in this class requires the classification to be broadened to represent the significantly different mechanisms for formation. The relatively chemically inert quartzite that hosts the Mammoth deposit precludes the interaction of the host rock as a mechanism to force the deposition of Cu via pH neutralisation. In conclusion, the Mammoth deposit provides evidence that metamorphogenic Cu deposits can be hosted in host rocks other than meta-carbonates.

CHAPTER 10

CONCLUSIONS

This study of the geology and genesis of the Mammoth Cu deposit has led to the following conclusions:

- The Mammoth deposit (16.8 Mt @ 3.4% Cu) is hosted in breccias and veins, which appear to be fault controlled and the Cu mineralisation is interpreted as occurring 260 to 150Ma after deposition of the host rocks during regional deformation (1590 to 1500 Ma; Isan Orogeny).

- Mineralisation is hosted within the Palaeoproterozoic Whitworth Quartzite of the Myally Subgroup.

- The Mammoth deposit formed during E-W transpression localised at the intersection of the Mammoth and Portal Faults during periods of high fluid pressure (P_f), subsequent to slip episodes, when the principle stresses were sub-equal ($\sigma_3 \cong \sigma_2 \leq \sigma_1$).

- Dilation was achieved when fluid pressure (P_f) exceeded the tensile strength (T) of the host rock as indicated: 1) by the irregular development of syn-deformational quartz-Cu sulfide extensional veins; and 2) by the regular development of syn-deformational quartz-Cu sulfide extensional veins along bedding planes when $\sigma_1 \cong \sigma_3$.

- The Mammoth deposit has 6 major ore lenes that extend over 1,100 metres vertically and have a strike extent of 100 to 300 m and widths from 10 to 75m.

- Within these lenses Cu mineralisation is hosted in veins and breccias adjacent to the intersection of the Mammoth and Portal Faults.

- Textural variations were used to categorise the brecciation and fracturing of the Whitworth Quartzite during mineralisation event. The grade of Cu mineralisation in these units is variable, but is high around zones of intense brittle deformation in the breccia units reflecting zones of enhanced permeability.

- Wall rock alteration, replacement and cementation of the breccia units by the hypogene mineral assemblage took place after and/or during the fragmentation.

- Hypogene Cu mineralisation consists of chalcopyrite, bornite and chalcocite. Supergene chalcocite (± covellite) has variably overprinted and enriched the hypogene assemblage.

- Hypogene and supergene chalcocite within the deposit are texturally, paragenetically and geochemically distinct.

- A four stage paragenetic sequence has been defined across the Mammoth ore zones: Stage I) hypogene pyrite and quartz; Stage II) hypogene chalcopyrite, bornite, chalcocite and carrollite (trace) + chlorite, illite and quartz; Stage III) supergene hematite, chalcocite, covellite and wittichenite, and Stage IV) supergene kaolinite, chalcocite, covellite and wittichenite.

- Hypogene Cu sulfides are broadly zoned within the Mammoth ore zones from hangingwall to footwall and up dip. This zonation is: 1) Stage II hypogene chalcocite ± bornite; 2) Stage II bornite ± hypogene chalcocite and 3) Stage II chalcopyrite ± bornite.

- The development of a new analytical technique to obtain high quality sub-ppm quantitative data from the in situ microanalysis of sulfide minerals using laser ablation (LA) ICP-MS analysis.

- Laser ablation (LA) ICP-MS analysis of both supergene and hypogene chalcocite were analysed demonstrated that Stage III supergene

chalcocite is enriched in Bi and depleted in both Ag, Co, Sb, and As compared to Stage II hypogene chalcocite.

- Laser ablation (LA) ICP-MS analysis of pyrite, chalcopyrite, bornite demonstrated that Stage I pyrite has elevated contents of As, Co, Ni, Sb, and Pb compared to Stage II chalcopyrite, bornite and chalcocite. Bornite is anomalously enriched in Bi compared to the other sulfides minerals

- The processes of meteoric and supergene alteration have led to complex geochemical dispersion patterns overprinting geochemical patterns developed during hypogene mineralisation.

- Whole-rock geochemistry analysis across the deposit revealed a distinct metal zonation. Elevated Co, Ni, CaO and P_2O_5 contents form a narrow halo (≅ 2 to 5m) around the hypogene ore zones at Mammoth. Along the ore equivalent structural horizon Zn, Co, and Ni are enriched distal (100 to 200m) to the ore zones. In contrast, Cu, Bi, As and Fe, initially at or below detection, all increase with proximity to the ore zones.

- Mineralised structures that have undergone supergene modification also have a similar suite of trace elements (Cu, Pb, Zn, Ni, Bi, Sb, and As). Their level of enrichment is significantly lower than their un-oxidised equivalent but more enriched than the enclosing host rocks. These suites of trace elements form potential vectors to differentiate mineralised and un-mineralised structures and can be used to identify Mammoth style mineralisation in surface or near surface leached structures.

- Lead isotopic ratios from Mammoth ore samples lie along a growth curve that originates from the Eastern Creek Volcanics, indicating that the Eastern Creek Volcanics were the source of Pb, and by inference Cu, contained in the Mammoth deposit.

- The $\delta^{34}S$ values of Stage I pyrite (- 15 to - 7 ‰; mean = – 12 ‰) and Stage II Cu and Cu-Fe sulfides (– 19 to – 1 ‰; mean = - 8 ‰) supports the conclusion that the Eastern Creek Volcanics were the source of metals and sulfur as they represent the only probable source of light sulfur in the Western Fold Belt.

- The calculated $\delta^{18}O$ and δD fluid composition in equilibrium with Stage I quartz and Stage II chlorite yielded a range of – 10 to - 2 ‰ $\delta^{18}O$ and – 2 to + 11 ‰ $\delta^{18}O$ and – 41 to – 56 ‰ δD respectively. These values suggest the fluid had two end members: 1) dominantly meteoric fluid and 2) fluid originating from metamorphic processes.

- Geological, isotopic, paragenetic, geochemical and structural data suggest the Mammoth Cu deposit formed synchronous with regional deformation when channelised flow of hot saline-oxidised Cu-enriched fluid generated by metamorphic devolatilisation, leached Cu and S from the Eastern Creek Volcanics, and was focussed along the Esperanza, Mammoth and Mammoth Extended Faults. Upon reaching the Whitworth Quartzite, a build up of fluid pressure combined with the existing regional stress field, create the appropriate conditions for brittle failure, and subsequent sites of Cu precipitation, in the quartzite. The hot metal and sulfur-bearing fluid mixed with a deep circulating methane-bearing hydrothermal fluid originally of meteoric origin. Changes in the physicochemical conditions upon this mixing destabilise the metal chlorine complexes resulting in sulfide precipitation.

- All of the above attributes broaden the classification of this style of metamorphogenic Cu deposit. Most notable of which is that the Mammoth deposit provides evidence this style of metamorphogenic Cu deposits can be hosted in host rocks other than meta-carbonates.

- The new model for the genesis of the Mammoth deposit has illuminated a series of criteria for the exploration of similar resources in the Western Fold Belt; including the world class Mt Isa Cu deposit.

The exploration strategy currently in use throughout the Mt Gordon Fault zone has traditionally focussed on sites where structural geometries potentially gave rise to dilatational fault zones during deformation. This research provides evidence that structural geometries that had the potential to create zones of E-W compression and/or N-S extension should now be included in exploration targeting.

REFERENCES

Ancey, M., Bastenaire, F., & Tixier, R, 1979, Application of statistical methods in microanalysis, *in* F. Maurice, L. M., and R. Tixier, ed., Microanalysis and scanning electron microscopy: Orsay, Les Editions de Physique, p. 319-343.

Anderson, J. A., 1982, Characteristics of leached capping and techniques of appraisal, *in* Titley, S. R., ed., Advances in geology of porphyry copper deposits; southwestern North America.: Tucson, AZ, United States, Univ. Ariz. Press, p. 275-295.

Andrew, A. S., Heinrich, C. A., Wilkins, R. W. T., and Patterson, D. J., 1989, Sulphur systematics of opper ore formation at Mount Isa, Australia: Economic Geology, v. 84, p. 1614-1626.

Anonymous, 1994, A Regional Structural Overview of the Mammoth Copper Deposit Gunpowder, Queensland: Confidential Company Report., ERA-MAPTEC Australia, p. 37.

Askew, R. L., 1992, Structural Setting of E. P. 8297 M, Gunpowder, Qld., & Implications for Further Work: Melbourne, Victorian Institute of Earth and Planetary Sciences, Monash University, p. 30.

Bayliss, P., 1975, Nomeclature of the trioctrahedral chlorites: The Canadian Mineralogist, v. 13, p. 178-180.

Bell, T. H., 1983, Thrusting and duplex formation at Mount Isa, Queensland, Australia: Nature (London), v. 304, p. 493-497.

Bell, T. H., 1991, The role of thrusting in the structural development of the Mount Isa Mine and its relevance to exploration in the surrounding region: Economic Geology, v. 86, p. 1602-1625.

Bell, T. H., and Hickey, K. A., 1998, Multiple deformations with successive subvertical and subhorizontal axial planes in the Mount Isa region; their impact on geometric development and significance for mineralization and exploration: Economic Geology, v. 93, p. 1369-1389.

Bell, T. H., Perkins, W. G., and Swager, C. P., 1988, Structural controls on development and localization of syntectonic copper mineralization at Mount Isa, Queensland: Economic Geology, v. 83, p. 69-85.

Berndt, M. E., Allen, D. E., and Seyfried, W. E., 1996, Reduction of CO2 during serpentinization of olivine at 300 degrees C and 500 bar.: Geology, v. 24, p. 351-354.

Bigeleisen, J., 1952, The effects of isotopic substituion on rates of chemical reactions.: Journal of Physical Chemistry, v. 56, p. 823-824.

Black, L. P., Carr, G. R., and Sun, S. S., 1997, Applied isotope geochronology and geochemistry, *in* Bain, J. H. C., and Draper, J. J., eds., North Queensland geology. AGSO Bulletin: Canberra, A.C.T., Australia, Australian Geological Survey Organisation, p. 429-447.

Blainey, G., 1965, Mines in the spinifex: Singapore, Angus and Robertson, 256 p.

Blake, D. H., 1987, Geology of the Mount Isa inlier and environs, Queensland and Northern Territory: Australian Bureau of Mineral Resources (BMR) Bulletin, v. 225, p. 83.

Blake, D. H., Etheridge, M. A., Page, R. W., Stewart, A. J., Williams, P. R., and Wyborn, L. A. I., 1990, Mount Isa Inlier; regional geology and mineralisation, *in* Hughes, F. E., ed., Geology of the mineral deposits of Australia and Papua New Guinea., 14. Monograph Series - Australasian Institute of Mining and Metallurgy: Melbourne, Victoria, Australia, Australasian Institute of Mining and Metallurgy, p. 915-925.

Blake, D. H., and Stewart, A. J., 1992, Stratigraphic and tectonic framework, Mount Isa Inlier: Australian Bureau of Mineral Resources (BMR) Bulletin, v. 243, p. 1-11.

Blanchard, R., 1968, Interpetation of Leached Outcrops: Reno, Navada Bureau of Mines, p. 196.

Briese, M., 1998, Supergene Cu ore and Regoltih Genesis, Esperanza Mine.: Unpub. Honours thesis, University of Queensland, 93 p.

Broadbent, G. C., Myers, R. E., and Wright, J. V., 1998, Geology and origin of shale-hosted Zn-Pb-Ag mineralization at the Century Deposit, Northwest Queensland, Australia: Economic Geology, v. 93, p. 1264-1294.

Brooks, J. H., 1957, Copper mining in the Cloncurry Mineral Field, Geological Survey Queensland, p. 7.

Brooks, J. H., 1962, Mammoth Copper Mine, Calton Hills-Mount Isa Mineral Field: Queensland Government Mining Journal, p. 376-379.

Canmet, 1994, Catalogue of Certified Reference Materials., CANMET.

Carr, G., 2001, User friendly isotope technologies in mineral exploration: Northern Australian Proterozoic basins, 2: Melbourne, AMIRA, p. 127.

Clayton, R. N., and Mayeda, T. K., 1963, The use of bromine penta-fluide in the extraction of oxygen form oxide and silicates for isotopic analysis.: Geochem. Cosmochim. Acta, v. 27, p. 43-52.

Colley, C., 1999, .

Connors, K., 1997, Regional Fault History of the Waggaboonya Area: Confiedential Company Report., Etheridge Henley Williams, p. 34.

Connors, K. A., and Page, R. W., 1995, Relationships between magmatism, metamorphism and deformation in the western Moutn Isa Inlier, Australia.: Precambrian Research, v. 71, p. 131-153.

Cox, S. F., 1995, Faulting processes at high fluid pressures: An example of fault-valve behaviour from the Wattle Gully Fault, Victoria, Australia.: Journal of Geophysical Research, v. 100, p. 12,841-12,860.

Davidson, G. J., and Dixon, G. H., 1992, Two sulphur isotope provinces deduced from ores in the Mount Isa eastern succession, Australia.: Mineralium Deposita, v. 27, p. 30-41.

Davidson, G. J., and Large, R. R., 1998, Proterozoic copper-gold deposits: AGSO Journal of Australian Geology and Geophysics, v. 17, p. 105-113.

Davidson, G. J., Large, R. R., Kary, G. L., and Osborne, R., 1989, The deformed iron-formation-hosted Starra and Trough Tank Au-Cu mineralization; a new association from the Proterozoic eastern succession of Mount Isa, Australia, *in* Keays, R. R., Ramsay, W. R. H., and Groves, D. I., eds., The geology of gold deposits; the perspective in 1988., 6. Ichnos: Chur, Switzerland, Harwood Academic Publishers, p. 135-150.

Derrick, G. M., Wilson, I. H., and Hill, R. M., 1976, Revision of stratigraphic nomenclature in the Precambrian of northwestern Queensland, II; Haslingden Group.: Queensland Government Mining Journal, v. 77, p. 300-306.

Dove, P. M., and Rimstidt, J. D., 1994, Silica-Water Interactions, *in* Heaney, P. J., Prewitt, C. T., and Gibbs, G. V., eds., Silica: Physical behaviour, geochemistry and materials applications, 29. Reviews in Mineralogy: Washington D.C., Mineralogical Society of America, p. 259-308.

Etheridge, M., and Wall, V. J., 1994, Tectonic and structural evolution of the Australian Proterozoic, *in* Freeman, M. J., ed., Geoscience Australia; 1994 and beyond., 37. Abstracts - Geological Society of Australia: Sydney, N.S.W., Australia, Geological Society of Australia, p. 102-103.

Etheridge, M. A., Rutland, R. W. R., and Wyborn, L. A. I., 1987, Orogenesis and tectonic process in the early to middle Proterozoic of northern Australia, *in* Kroener, A., ed., Proterozoic lithospheric evolution., 17. Geodynamics Series: Washington, DC, United States, American Geophysical Union, p. 131-147.

Forrestal, P. J., Pearson, P. J., Coughlin, T. B., and Schubert, C. J., 1998, Tick Hill gold deposit, *in* Berkman, D. A., and Mackenzie, D. H., eds., Geology of Australian and Papua New Guinean mineral deposits., 22. Monograph Series - Australasian Institute of Mining and Metallurgy: Melbourne, Victoria, Australia, Australasian Institute of Mining and Metallurgy, p. 699-706.

Giggenbach, W. F., Stewart, M. K., Sano, Y., Goguel, R. L., and Lyon, G. L., 1993, Isotopic waters and gases from the east coast accretionary prisim, New Zealand, International Atomic Energy Agency TECDOC.

Griffin, W. L., Ashley, P. M., Ryan, C. G., Sie, S. H., and Suter, G. F., 1991, Pyrite geochemistry in the North Arm epithermal Ag-Au deposit, Queensland, Australia; a proton-microprobe study: The Canadian Mineralogist, v. 29, p. 185-198.

Hannan, K. W., Golding, S. D., Herbert, H. K., and Krouse, H. R., 1993, Contrasting alteration assemblages in metabasites from Mount Isa, Queensland; implications for copper ore genesis.: Economic Geology, v. 88, p. 1135-1175.

Hedenquist, J. W., Izawa, E., Arribas, A., and White, N. C., 1996, Epithermal gold deposits: Styles, characteristics, and exploration: Tokyo, Komiyama Printing Co. Ltd., 16 p.

Heinrich, C. A., Andrew, A. S., and Knill, M. D., 2000, Regional metamorphism and ore formation; evidence from stable isotopes and other fluid tracers., *in* Spry, P. G., Marshall, B., and Volkes, F. M., eds., Reviews in Economic Geology, 11: Socorro, Society of Economic Geologists, p. 97-117.

Heinrich, C. A., Andrew, A. S., and Wilkins, R. W. T., 1989, A fluid inclusion and stable isotope study for synmetamorphic copper ore formation at Mount Isa, Australia: Economic Geology, v. 84, p. 529-550.

Heinrich, C. A., Bain, J. H. C., Fardy, J. J., and Waring, C. L., 1993, Br/ Cl geochemistry of hydrothermal brines associated with Proterozoic metasediment-hosted copper mineralization at Mount Isa, northern Australia: Geochimica et Cosmochimica Acta, v. 57, p. 2991-3000.

Heinrich, C. A., Bain, J. H. C., Mernagh, T. P., Wyborn, L. A. I., Andrew, A. S., and Waring, C. L., 1995, Fluid and mass transfer during metabasalt alteration and copper mineralization at Mount Isa, Australia: Economic Geology, v. 90, p. 705-730.

Heinrich, C. A., and Etheridge, M. A., 1989, Hydrology and water-rock reaction during regional metamorphic ore formation; Mount Isa example (Australia), *in* Anonymous, ed., 28th international geological congress; abstracts., 2. International Geological Congress, Abstracts--Congres Geologique Internationale, Resumes. 28, Vol: [location varies], International, [International Geological Congress], p. 2.47.

Hespe, A. M., 1999, .

Hinman, M., 1996, Constraints, timing and processes of stratiform base metal minerlaisation at the HYC Ag-Pb-Zn deposit, McArthur River: MIC'96, Townsville, 1996, Conference Exteneded Abstracts: James Cook University Economic Geology Research Unit Contribution 55, p. 56-59.

Honman, C. S., 1938, The Mount Oxide Area: Canberra, Aerial, Geological and Geophysical Survey of Northern Australia, p. 7.

Hunt, T. S., 1873, The geognastic history of the metals.: Transactions of the American Institute of Mining Engineers, v. 1, p. 331-342.

Huston, D., 1998, The hydrothermal environment: AGSO Journal of Australian Geology and Geophysics, v. 17, p. 15-30.

Huston, D. L., Sie, S. H., Suter, G. F., Cooke, D. R., and Both, R. A., 1995, Trace elements in sulfide minerals from eastern Australian volcanic-hosted massive sulfide deposits; Part I, Proton microprobe analyses of pyrite, chalcopyrite, and sphalerite, and Part II, Selenium levels in pyrite; comparison with delta (super 34) S values and implications for the source of sulfur in volcanogenic hydrothermal systems: Economic Geology, v. 90, p. 1167-1196.

Hutton, L. J., and Wilson, I. H., 1985, Mammoth Mines Region, Queensland. 1:100 000 Gelogical Map Commentary: Canberra, Geological Survey of Queensland, p. 26.

Jackson, S. E., Longerich, H. P., Dunning, G. R., and Freyer, B. J., 1992, The application of laser-ablation microprobe; inductively coupled plasma-mass spectrometry (LAM-ICP-MS) to in situ trace-element determinations in minerals: The Canadian Mineralogist, v. 30, p. 1049-1064.

Kaplan, I. R., Smith, J. W., and Ruth, E., 1970, Carbon and sulfur concentrations and isotopic composition in Apollo 11 lunar samples. Geochim.: Cosmochim. Acta Supplement, v. 1, p. 1317-1329.

Koons, P. O., and Craw, D., 1991, Evolution of fluid driving forces and composition within collisional orogens.: Geophysical Research Letters, v. 24, p. 631-636.

Laing, W. P., 1998, Structural-metasomatic environment of the East Mt Isa Block base-metal-gold province, *in* Pollard, P. J., ed., Geological framework and mineralisation in the Mt Isa Eastern Succession, Northwest Queensland., 45. Australian Journal of Earth Sciences: Melbourne, Victoria, Australia, Blackwell, p. 413-428.

Large, R. R., Bull, S. W., Cooke, D. R., and McGoldrick, P. J., 1998, A genetic model for the H.Y.C. Deposit, Australia; based on regional sedimentology, geochemistry, and sulfide-sediment relationships: Economic Geology, v. 93, p. 1345-1368.

Loftus, H. G., and Solomon, M., 1967, Cobalt, nickel and selenium in sulphides as indicators of ore genesis: Mineralium Deposita, v. 2, p. 228-242.

Longerich, H. P., Wilton, D. H. C., and Fryer, B. J., 1992, Isotopic and elemental analysis of uraninite concentrates using inductively coupled plasma-mass spectrometry (ICP-MS): Journal of Geochemical Exploration, v. 43, p. 111-125.

Machette, M. N., Personius, S. F., Nelson, A. R., Schwartz, D. P., and Lund, W. R., 1991, The Wasatch fault zone, Utah; segmentation and history of Holocene earthquakes, *in* Hancock, P. L., Yeats, R. S., and Sanderson, D. J., eds., Characteristics of active faults., 13. Journal of Structural Geology: Oxford-New York, International, Pergamon, p. 137-149.

McArthur, G., 1998, .

McCaig, 1988, Deep fluid circulation in fault zones.: Geology, v. 16, p. 867-870.

McClay, K. R., 2000, Structural Geology Workshop, 1: Hobart, CODES University of Tasmaina, p. 218.

Mitchell, J. W., and Moore, G. P., 1975, The Mammoth copper deposit, *in* Knights, C. L., ed., Economic Geology of Australia and Papua New Guinea, 1: Melbourne, Australasean Institue of Miningand Metallurgy, p. 383-389.

Murowchick, J. B., and Barnes, H. l., 1986, Marcasite preciptation from hydrothermal solutuions: Geochim. Cosmochim. Acta, v. 50, p. 2615-2630.

Norman, M. D., Pearson, N. J., Sharma, A., and Griffin, W. L., 1996, Laser microprobe ICPMS; a robust and cost effective microbeam technique for in situ quantitative trace element analysis, *in* Anonymous, ed., AGU 1996 fall meeting., 77. Eos, Transactions, American Geophysical Union: Washington, DC, United States, American Geophysical Union, p. 787.

O'Dea, M. G., Lister, G., MacCready, T., Betts, P. G., Oliver, N. H. S., Pound, K. S., Huang, W., and Valenta, R. K., 1997, Geodynamic evolution of the Proterozoic Mount Isa terrain, *in* Burg, J. P., and Ford, M., eds., Orogeny through time., 121. Geological Society Special Publications: London, United Kingdom, Geological Society of London, p. 99-122.

O'Dea, M. G., and Lister, G. S., 1996, Extensional geometries within the Leichhardt River Fault Trough of the Mount Isa Terrain, NW Queensland, Australia, *in* Kennard, J. M., ed., Geoscience for the community; 13th Australian geological convention., 41. Abstracts - Geological Society of Australia: Sydney, N.S.W., Australia, Geological Society of Australia, p. 322.

O'Dea, M. G., Lister, G. S., Betts, P. G., and Pound, K. S., 1997, A shortened intraplate rift system in the Proterozoic Mount Isa Terrane, NW Queensland, Australia: Tectonics, v. 16, p. 425-441.

Ohmoto, H., 1986, Stable isotope geochemistry of ore deposits, *in* Valley, J. W., Taylor, H. P., Jr., and O, N. J. R., eds., Stable isotopes in high temperature geological processes., 16. Reviews in Mineralogy: Washington, DC, United States, Mineralogical Society of America, p. 491-559.

Ohmoto, H., and Goldhaber, M., 1997, Surfur and Carbon Isotopes., *in* Barnes, H. L., ed., Geochemistry of hydrothermal ore deposits.: New York, NY, United States, John Wiley & Sons, p. 517-611.

Ohmoto, H., and Rye, R. O., 1979, Isotopes of sulfur and carbon, *in* Barnes, H. L., ed., Geochemisrty of the Hydrothermal Environment: New York, Wiley, p. 509-567.

Oliver, J., 1986, Fluids expelled tectonically from orogenic belts; their role in hydrocarbon migration and other geologic phenomena.: Geology, v. 14, p. 99-102.

Oliver, N. H. S., 1995, Hydrothermal history of the Mary Kathleen fold belt, Mt Isa Block, Queensland, *in* Oliver, N. H. S., Cartwright, I., and Rubenach, M. J., eds., Mid- to lower-crustal metamorphism and fluid-rock interaction, with reference to the Mt. Isa Inlier., 42. Australian Journal of Earth Sciences: Melbourne, Victoria, Australia, Blackwell, p. 267-279.

Oliver, N. H. S., Rubenach, M. J., and Valenta, R. K., 1998, Precambrian metamorphism, fluid flow, and metallogeny of Australia: AGSO Journal of Australian Geology and Geophysics, v. 17, p. 31-53.

Page, R. W., 1983, Timing of superposed volcanism in the Proterozoic Mount Isa Inlier, Australia: Precambrian Research, v. 21, p. 223-245.

Page, R. W., and Bell, T. H., 1986, Isotopic and structural responses of granite to successive deformation and metamorphism: Journal of Geology, v. 94, p. 365-379.

Page, R. W., and Carr, G. R., 1994, U-Pb zircon and Pb isotope studies in relation to Proterozoic sediment-hosted lead-zinc-silver deposits in northern Australia, *in* Lanphere, M. A., Dalrymple, G. B., and Turrin, B. D., eds., Abstracts of the Eighth international conference on Geochronology, cosmochronology, and isotope geology.

U. S. Geological Survey Circular: Reston, VA, United States, U. S. Geological Survey, p. 240.

Page, R. W., and Sweet, I. P., 1998, Geochronology of basin phases in the western Mt Isa Inlier, and correlation with the McArthur Basin, *in* McNaughton, N. J., Campbell, I. H., and Groves, D. I:, eds., Application of radiogenic isotopes to the study of Australian ore deposits., 45. Australian Journal of Earth Sciences: Melbourne, Victoria, Australia, Blackwell, p. 219-232.

Painter, M. G. M., Golding, S. D., Hannan, K. W., and Neudert, M. K., 1999, Sedimentologic, petrographic, and sulfur isotope constraints on fine-grained pyrite formation at Mount Isa Mine and environs, Northwest Queensland, Australia.: Economic Geology, v. 94, p. 883-912.

Perkins, C., Heinrich, C. A., and I, W. L. A., 1999, 40Ar/ 39Ar geochronology of copper mineralization and regional alteration, Mount Isa, Australia.: Economic Geology, v. 94, p. 23-36.

Perkins, W., 1984, Mount Isa silica dolomite and copper orebodies; the result of a syntectonic hydrothermal alteration system.: Economic Geology, v. 79, p. 601-637.

Philpots, A. R., 1990, Principles of igneous and metamorphic petrology: New Jersey, Prentice Hall.

Plumb, K. A., Ahmad, M., and Wygralak, A. S., 1990, Mid-Proterozoic basins of the North Australian and Papua New Guinea, *in* Hughes, F. E., ed., Geology of the mineral deposits of Australia and Papua New Guinea, 14: Melbounre, Australia Institute of Mining and Metallurgy, p. 881-902.

Powell, C. M., Oliver, N. H. S., Li, Z. X., Martin, D. M., and Ronaszeki, J., 1999, Synorogenic hydrothermal origin for giant Hamersley iron oxide ore bodies: Geology (Boulder), v. 27, p. 175-178.

Ramdohr, P., 1980, The ore minerals and their intergrowths. 2 ed: Oxford, United Kingdom, Pergamon Press, 1205 p.

Ramsay, J. G., and Huber, M. I., 1987, The techniques of modern structural geology; Volume 2; Folds and fractures: London, Academic Press, 462 p.

Richardson, S., 2000, E Lens Oriented Core Measurements, Western Metals Corperation, p. 13.

Richardson, S. M., and Moy, A. D., 1998, Gunpowder Copper Deposits, *in* Berkman, D. A., and Mackenzie, D. H., eds., Geology of Australian and Papua New Guinean Mineral deposits: Melbourne, The Australian Institute of Mining and Metallugy, p. 743-752.

Ridley, W. I., and Lichte, F. E., 1998, Major, trace, and ultratrace element analysis by laser ablation ICP-MS, *in* McKibben, M. A., Shanks, W. C., III, and Ridley, W. I., eds., Applications of microanalytical techniques to understanding mineralizing processes., 7. Reviews in Economic Geology: Socorro, NM, United States, Society of Economic Geologists, p. 199-215.

Rimstidt, J. D., 1997, Gangue Mineral Transport and Deposition, *in* Barnes, H. L., ed., Geochemistry of hydrothermal ore deposits.: New York, NY, United States, John Wiley & Sons, p. 487-515.

Robinson, B. W., and Kusakabe, M., 1975, Quantative preparation of sulphur dioxide, for 34S/32S analyses, from sulphides by combustion with cuprous oxide: Analytical Chemistry, v. 47, p. 1179-1181.

Rubenach, M. J., and Barker, A. J., 1998, Metamorphic and metasomatic evolution of the Snake Creek Anticline, Eastern Succession, Mt Isa Inlier, *in* Pollard, P. J., ed., Geological framework and mineralisation in the Mt Isa Eastern Succession, Northwest Queensland., 45. Australian Journal of Earth Sciences: Melbourne, Victoria, Australia, Blackwell, p. 363-372.

Scott, K. M., 1986, Sulphide geochemistry and wall rock alteration as a guide to mineralization, Mammoth area, NW Queensland, Australia: Journal of Geochemical Exploration, v. 25, p. 283-308.

Scott, K. M., 1989, Dolomite compositions as a guide to epigenetic copper mineralization, Mount Isa Inlier, NW Queensland: Mineralium Deposita, v. 24, p. 29-33.

Scott, K. M., Smith, J. W., Sun, S. S., and Taylor, G. F., 1985, Proterozoic copper deposits in NW Queensland, Australia; sulfur isotopic data: Mineralium Deposita, v. 20, p. 116-126.

Scott, K. M., and Taylor, G. F., 1977, Geochemistry of the Mammoth copper deposit, Northwest Queensland, Australia: Journal of Geochemical Exploration, v. 8, p. 153-168.

Scott, K. M., and Taylor, G. F., 1982, Eastern Creek Volcanics as the source of copper at the Mammoth Mine, Northwest Queensland: BMR Journal of Australian Geology and Geophysics, v. 7, p. 93-98.

Scott, R., and Berry, R., 2001, Structural data from axially orientated drill core: In Prep.

Seward, T. M., and Barnes, H. L., 1997, Metal transport by hydrothermal fluids, *in* Barnes, H. L., ed., Geochemistry of Hydrothermal Ore Deposits, 1: New York, John Wiley and Sons, p. 435-486.

Shepherd, S. R. L., 1946, Some mines on the Cloncurry Field: Queensland Goverment Mining Journal, v. 47, p. 48-49.

Sheppard, S. M. F., Nielsen, R. L., and Taylor, H. P. J., 1969, Oxygen and hydrogen isotope ratios of clay minerals from porphyry copper deposits.: Economic Geology, v. 64, p. 755-777.

Sillitoe, R., 1997, Cooments on geological models forthe Gunpowder copper deposits, Queensland, Australia, Aberfoyle Resources Limited, p. 11.

Simoneit, B. R. T., 2000, Alteration and migration process of organic matter in hydrothermal systems and implications for metallogenesis, *in* Glikson, M., and Mastalerz, M., eds., Oreganic Matter and Mineralisation: London, Kluwer Academic Publishers, p. 13-37.

Solomon, M., and Groves, D. I., 1994, The Geology and Origin of Australia's Mineral Deposits: Oxford, Oxford Science Publications, 951 p.

Southgate, P. N., Scott, D. L., Sami, T. T., Domagala, J., Jackson, M. J., James, N. P., and Kyser, T. K., 2000, Basin shape and sediment architecture in the Gun Supersequence; a strike-slip model for Pb-Zn-Ag ore genesis at Mt Isa: Carpentaria-Mt. Isa Belt; basement framework, chronostratigraphy and geodynamic evolution of Proterozoic successions.

Stewart, A. J., 1992, The role of thrusting in the structural development of the Mount Isa Mine and its relevance to exploration in the surrounding region; discussion: Economic Geology, v. 87, p. 1659-1664.

Sturchio, N. C., Arehart, G. B., Sultan, M., Sano, Y., AboKamar, Y., and Sayed, M., 1996, Composition and origin of thermal waters in the Gulf of Suez area, Egypt.: Applied Geochemistry, v. 11, p. 471-479.

Sun, S.-s., Carr, G. R., and Page, R., 1996, A continued effort to improve Pb isotope model ages.: AGSO Research Newsletter, p. 13-15.

Sun, S.-s., Page, R., and Carr, G. R., 1994, Lead-isotope-based stratigraphic correlations and ages of Proterozioc sediment-hosted Pb-Zn deposits in the Mount Isa Inlier: AGSO Research Newsletter, p. 1-2.

Swager, C. P., 1983, Cleavage and syntectonic vein development by pressure solution in the very low grade dolomitic Urquhart Shale, Mount Isa, *in* Leitch, E. C., and Shepherd, J., eds., Bermagui '84; International conference on multiple deformation and foliation development., 9. Newsletter of the Specialist Group in Tectonics and Structural Geology, Geological Society of Australia Incorporated: Sydney, N.S.W., Australia, Geological Society of Australia, Specialist Group in Tectonics & Structural Geology, p. 148.

Taylor, G. F., and Scott, K. M., 1976, The Geochemistry of ironstones and core samples from the Mount Kelly area, northwest Queensland., CSIRO.

Taylor, H. P., Jr., 1979, Oxygen and hydrogen isotope relationships in hydrothermal mineral deposits., *in* Barnes, H. L., ed., Geochemistry of hydrothermal ore deposits.: New York, NY, United States, John Wiley & Sons, p. 236-277.

Taylor, H. P., Jr., 1997, Oxygen and hydrogen isotope relationships in hydrothermal mineral deposits., *in* Barnes, H. L., ed., Geochemistry of hydrothermal ore deposits.: New York, NY, United States, John Wiley & Sons, p. 229-302.

Thompson, A. B., 1997, Flow and Focussing of Metamorphic Fluids, *in* Jamtveit, B., and Yardley, B. W. D., eds., Fluid Flow and Transport in Rocks: London, Chapman and Hall, p. 297-314.

Vaasjoki, M., 1980, Lead isotope determinations from the Mammoth Copper deposit, North-West Queensland., CSIRO.

Vaasjoki, M., and Gulson, B. L., 1979, The analytical methods used in the lead isotope assesment of gossans., CSIRO IER.

Valenta, R., 1994, Syntectonic discordant copper mineralization in the Hilton Mine, Mount Isa.: Economic Geology, v. 89, p. 1031-1052.

van Dijk, P. M., 1991, Regional syndeformational copper mineralization in the western Mount Isa Block, Australia: Economic Geology, v. 86, p. 278-301.

Vaughan, D. J., and Craig, J. R., 1978, Mineral chemistry of metal sulfides: Cambridge, United Kingdom, Cambr. Univ. Press, 493 p.

Viets, J. G., Leach, D. L., Lichte, F. E., Hopkins, R. T., Gent, C. A., and Powell, J. W., 1996, Paragenetic and minor- and trace-element studies of mississippi valley-type ore deposits of the Silesian-Cracow district, Poland, *in* Gorecka, E., and Leach, D. L., eds., Carbonate-hosted zinc-lead deposits in the Silesian-Cracow area, Poland., 154. Prace Panstwowego Instytutu Geologicznego (1988): Warsaw, Poland, Wydawnictwa Geologiczne, p. 51-71.

Waring, C. L., 1990, Genesis of the Mount Isa Cu ore system: Unpub. PhD thesis, Monash University, 409 p.

Waring, C. L., Andrew, A. S., and Ewers, G. R., 1998, Use of O, C, and S stable isotope in regional mineral exploration: AGSO Journal of Australian Geology and Geophysics, v. 17, p. 301-313.

Waring, C. L., Heinrich, C. A., and Wall, V. J., 1998, Proterozoic metamorphic copper deposits: AGSO Journal of Australian Geology and Geophysics, v. 17, p. 239-246.

Wickham, S. M., Peters, M. T., Fricke, H. C., and O'Neil, J. R., 1993, Identification of magmatic and meteoric fluid sources and upward- and downward-moving infiltrations fronts in a metamorphic core complex: Geology, v. 21, p. 81-84.

Williams, P. J., 1998, An Introduction to the Metallogeny of the McArthur River-Mount Isa-Cloncurry Minerlas Province: Economic Geology, v. 93, p. 1120-1131.

Williams, P. J., and Heinemann, M., 1993, Maramungee: A Proterozoic Zn skarn in the Cloncurry district, Mount Isa inlier, Queensland, Australia: Economic Geology, v. 93, p. 1180-1189.

Williams, P. R., 1999, Targeting, Mount Gordon Fault Zone: Confidential Company Report: West Perth, SRK Consulting, p. 9-20.

Wilson, I. H., Derick, G. M., and Perkin, D. J., 1985, Eastern Creek Volcanics: their geochemistry and possible role in copper mineralisation at Mount Isa, Queensland: BMR Journal of Australian Geology and Geophysics, v. 9, p. 317-328.

Woodhead, J. D., Volker, F., and McCulloch, M. T., 1995, Routine Lead Isotope Determinations Using a Lead-207-Lead-204 Double Spike: a Long-term Assessment of Analytical Precision and Accuracy: Analyst, v. 120, p. 35.

Wyborn, L. A. I., 1987, The petrology and geochemistry of alteration assemblages in the Eastern Creek Volcanics, as a guide to copper and uranium mobility associated with regional metamorphism and deformation, Mount Isa, Queensland., *in* Pharaoh, T. C., Beckinsale, R. D., and Rickard, D. T., eds., In: Geochemistry and mineralization of Proterozoic volcanic suites., 33: London, Geological Society of London, p. 425-434.

Wyborn, L. A. I., and Page, R. W., 1983, The Proterozoic Kalkadoon and Ewen batholiths, Mount Isa Inlier, Queensland; source, chemistry, age, and metamorphism: BMR Journal of Australian Geology and Geophysics, v. 8, p. 53-69.

Yapp, C. J., 1990, Oxygen isotopes in iron (III) oxides: 1, Mineral-water Fractionation factors: Chemical Geology, v. 85, p. 329-335.

Yardley, B. W. D., 1989, An introduction to metamorphic petrology.: New York, John Wiley & Sons, 248 p.

Yardley, B. W. D., 1997, The Evolotion of Fluids Through the Metamorphic Cycle, *in* Jamtveit, B., and Yardley, B. W. D., eds., Fluid Flow and Transport in Rocks: London, Chapman and Hall, p. 99-121.

APPENDIX 1

RELOGGED DIAMOND DRILL HOLES

Section ID	Focus	Hole ID's
28375mE	2 lens mineralisation	UD770, UD772, UD773, UD774
28315mE	2 lens mineralisation	UD713, UD766, UD767, UD768
20660mN	Lower D lens mineralisation	UD739, UD740, UD741, UD744, UD746, UD748
20660mN (oblique section)	Upper D lens mineralisation	UD717, UD715, UD718
20800mN	B & C lens mineralisation	UD710, UD711
21040mN	Northern extents of B & C lenses	UD730, UD731, UD732, UD733, UD735
E Lens oblique	E Lens	SD254, SD255, SD255A, SD255B, UD765
Miscellaneous holes	4720 mRl and infill	UD734, UD716, UD748, UD746, UD744, UD706, UD707, UD767, UD676, UD574, UD679, UD627, UD726, UD737, UD762, UD619, UD628, UD644, UD651, UD708, UD642, UD611.

Sample of drill core re-logging UD774. The remainder of drill core logged are stored in the University of Tasmanians Geology dept. archives

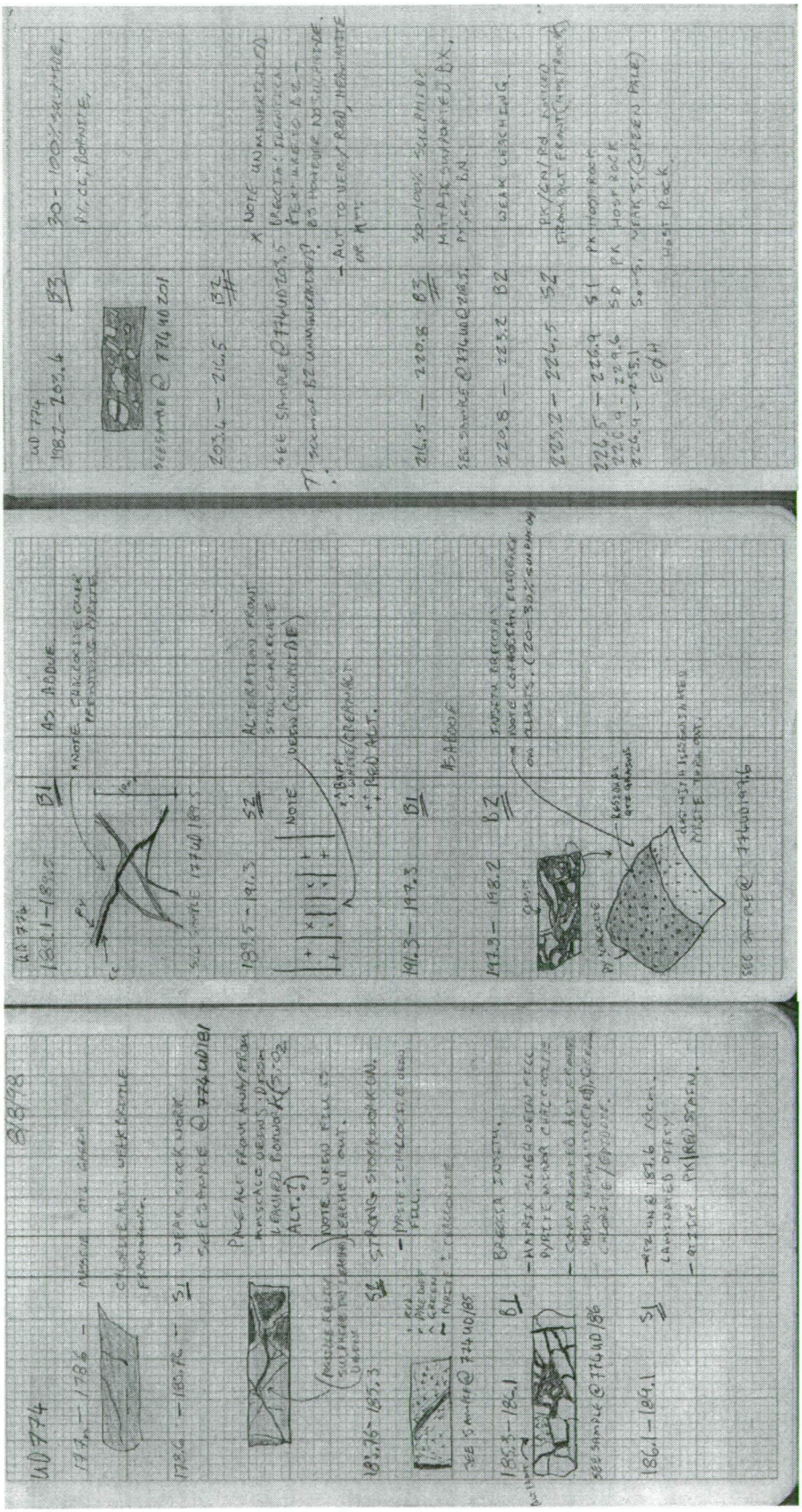

APPENDIX 2

LASER ABLATION (LA) ICPMS DATA

Sample ID (Lab Reference Number)		S ppm	Fe ppm	Co ppm	Ni ppm	Cu ppm	Zn ppm	As ppm	Mo ppm	Ag ppm	Sn ppm	Sb ppm	Pb ppm	Bi ppm	Peak	Thesis Sample ID & Sulfide phase analysed
		1885	82.09	0.15	0.51	1.0	2.05	1.08	1.54	0.20	0.23	0.21	0.25	0.03		Run detection limit
std-1	01	245700	428925.00	137.72	5823.47	563.6	102916.61	262.10	9.39	28.97	28.49	196.80	17569.59	5.85	47.9	stdgl-1
oc27d02	02	200900	<176.477	<0.263	<1.319	847369.8	<5.793	<2.333	<3.645	437.41	0.69	<0.455	1.41	21.99	19.6	255a-990.9cc
oc27d03	03	200900	7723.26	0.56	<1.333	877820.6	<5.766	6.44	21.34	421.51	0.71	2.07	6.85	35.48	23.9	255a-990.9cc
oc27d04	04	200900	780.77	0.33	<0.994	876474.6	<3.823	4.04	8.82	418.82	0.66	<0.440	2.96	23.76	30.5	255a-990.9cc
oc27d05	05	200900	362.81	<0.273	<1.222	926854.4	<5.747	6.58	<3.453	433.83	0.56	<0.484	0.84	23.10	44.6	255a-990.9cc
oc27d06	06	258700	118676.78	<0.193	<0.772	724714.7	<3.357	1.90	<3.415	122.83	0.67	0.62	11.88	757.95	50.1	255a-990.9bn
std-2	07	245700	408357.54	129.46	5473.43	526.7	99108.82	245.52	10.61	27.47	25.17	181.23	16561.68	7.76	33.7	stdgl-1
oc27d08	08	258700	118821.34	0.58	1.02	710670.8	<4.381	8.95	2.77	110.60	0.67	0.33	7.78	771.47	46.8	255a-990.9bn
oc27d09	09	525800	568005.85	7.58	5.07	11856.3	3.13	35176.36	4.26	8.73	0.57	85.81	304.75	14.88	30.5	255a-990.9bn
oc27d10	10	525800	553566.68	10.90	12.20	146.5	3.65	32666.25	3.76	1.00	0.27	1.16	8.44	2.80	19.6	255a-979.6py
oc27d11	11	525800	555446.97	164.32	61.12	8384.0	6.39	61432.81	6.59	22.61	0.45	113.29	33.32	102.83	31.6	255a-979.6py
oc27d12	12	258700	108588.23	<0.194	<0.695	653587.4	<3.543	3.08	<2.352	82.32	0.62	1.56	10.38	652.30	43.5	255a-979.6bn
oc27d13	13	258700	126249.82	<0.182	4.01	703455.4	<3.305	39.80	<2.856	77.73	0.70	0.90	6.71	632.34	40.3	255a-979.6py
std-3	14	245700	390238.15	124.90	5223.61	522.1	98255.20	240.37	10.09	28.51	22.99	180.39	16187.75	6.45	13.1	stdgl-1
oc27d15	15	258700	108756.19	0.20	<0.839	593354.9	<2.891	2.01	5.07	104.68	0.43	<0.291	0.94	392.11	39.2	255a-958.8bn
oc27d16	16	525800	523840.55	43.40	28.46	14634.6	4.69	46327.36	4.36	17.46	<0.288	171.07	167.05	30.04	30.5	255a-958.8py
oc27d17	17	525800	580624.45	<0.177	2.24	46.3	4.70	42155.49	2.28	1.27	<0.234	58.81	668.51	<0.042	17.4	255a-958.8py
oc27d18	18	258700	98058.76	<0.221	<0.893	577223.1	<3.309	24.00	<2.221	97.77	<25.191	<0.307	<0.427	439.24	42.5	255a-958.8bn
oc27d19	19	258700	127947.54	2.04	0.98	690125.8	<2.746	3.29	50.71	65.68	0.63	1.03	23.54	910.56	37.0	255a-1016.8bn
std-4	20	415700	736433.56	236.74	10125.33	946.6	176200.24	446.69	19.26	47.26	51.82	331.49	29913.76	11.03	28.3	stdgl-1

Abbreviations for sulfide phase analysed: cc = chalcocite; bn = bornite; py and vpy = veined pyrite; dpy = disseminated pyrite; cpy = chalcopyrite

Sample ID (Lab Reference Number)		S ppm	Fe ppm	Co ppm	Ni ppm	Cu ppm	Zn ppm	As ppm	Mo ppm	Ag ppm	Sn ppm	Sb ppm	Pb ppm	Bi ppm	Peak	Thesis Sample ID & Sulfide phase analysed
		1463	61.98	0.11	0.43	0.8	1.94	0.78	1.13	0.18	0.17	0.17	0.19	0.03		Run detection limit
std-1	01	237530	415700.00	133.52	5632.72	536.3	99789.17	243.77	5.20	26.60	24.83	187.26	16585.17	6.27	40.3	stdgl-1
oc27a02	02	258793	106000.00	<0.179	<0.559	617689.4	17.99	2.84	3.49	7.80	0.97	0.44	10.96	912.87	44.6	768-175.1bn
oc27a03	03	242395	106000.00	<0.168	<0.433	643723.7	<4.216	2.29	<1.974	6.55	0.65	<0.214	12.04	942.14	34.8	768-175.1bn
oc27a04	04	4619662	<2810.792	21.70	<18.086	15885371.2	310.87	<27.079	<42.767	375.74	21.21	<6.871	78.51	753.77	19.6	768-175.1cc
oc27a05	05	609588	700.00	1.84	4.39	2142751.4	39.25	5.78	<4.894	52.31	3.05	<0.858	7.11	99.73	38.1	768-175.1cc
oc27a06	06	466782	465600.00	80.91	25.70	9172.6	9.06	91.19	<1.010	2.42	0.18	13.25	874.63	89.79	45.7	768-175.1py
std-2	07	259670	415700.00	133.20	5656.70	557.3	102864.70	266.81	15.36	29.93	28.32	189.68	17089.19	6.93	41.4	stdgl-1
oc27a08	08	476784	465600.00	78.84	13.11	3536.7	4.81	28294.98	3.49	3.50	0.94	139.89	977.70	56.75	23.9	768-175.1py
oc27a09	09	494912	465600.00	15.90	27.59	210.7	9.04	38260.42	3.66	17.86	1.10	363.48	769.72	14.05	19.6	768-202.0py
oc27a10	10	451548	465600.00	81.85	95.06	466.5	5.97	25811.51	5.16	16.38	1.49	130.77	847.18	95.65	46.8	768-202.0py
oc27a11	11	279263	106000.00	2.93	1.19	791076.4	3.28	26.08	<2.084	9.64	1.04	<0.342	6.75	962.02	27.2	768-202.7abn
oc27a12	12	197841	106000.00	17.91	5.49	639242.2	<2.646	54.86	<1.781	4.19	0.47	0.42	4.98	663.09	38.1	768-202.7abn
oc27a13	13	448953	465600.00	76.94	12.18	8139.3	3.95	20625.49	6.97	12.48	0.71	269.51	783.50	108.62	38.1	768-202.7apy
std-3	14	224201	415700.00	136.71	5718.63	545.6	99739.51	244.50	9.82	28.56	29.16	187.11	16629.65	6.40	42.5	stdgl-1
oc27a15	15	486508	465600.00	67.03	7.87	10544.7	19.55	21275.95	6.06	41.30	5.27	175.48	644.93	86.07	51.2	768-202.7apy
oc27a16	16	48958	700.00	0.11	<0.187	180351.3	2.23	1.74	<0.525	6.28	0.24	<0.081	1.78	22.45	35.9	768-202.7acc
oc27a17	17	1865124	<1229.998	<2.281	<7.949	7790237.0	<33.466	26.25	<23.849	254.83	6.06	3.89	<3.686	241.67	20.7	768-202.7acc
oc27a18	18	308565	106000.00	<0.266	<0.964	694265.2	<4.301	2.34	<3.486	5.31	0.56	<0.477	0.78	762.47	37.0	768-211.6bn
oc27a19	19	363949	106000.00	<0.304	<1.225	706329.2	<4.156	<2.184	<3.268	6.98	0.59	<0.526	3.84	913.54	41.4	768-211.6bn
std-4	20	261894	415700.00	128.52	5494.48	532.5	102156.00	257.09	11.21	27.79	24.96	190.32	17664.23	6.95	14.2	stdgl-1
		1019	44.82	0.12	0.45	0.6	1.76	0.16	1.37	0.15	0.14	0.27	0.07	0.01		
std-1	01	251757	415700.00	132.26	5574.29	539.8	99766.38	346.95	11.59	28.76	27.39	187.15	17323.14	6.88	57.7	stdgl-1
std-2	02	239577	415700.00	133.74	5677.78	546.2	101110.51	196.60	9.27	27.68	26.26	190.02	16678.50	6.41	45.7	stdgl-1
0c29e03	03	216664	106000.00	<0.217	<0.775	596499.8	3.72	0.56	<2.464	75.69	1.14	0.67	5.57	1185.29	42.5	255b-1061.4bn
0c29e04	04	193736	106000.00	<0.259	<1.049	621713.0	<3.256	0.87	<3.423	66.49	0.69	<0.593	0.86	964.67	20.7	sd255b-1061.4bn
0c29e05	05	390250	465600.00	<0.144	2.88	23.5	2.41	9941.66	4.69	<0.182	0.38	38.90	109.07	<0.016	17.4	255b-1061.4py
0c29e06	06	376011	465600.00	1.49	34.48	238.4	5.62	15911.88	15.34	3.65	0.43	132.04	4.63	0.21	42.5	255b-1061.4py
0c29e07	07	230754	415700.00	131.38	5573.65	525.7	99040.74	65.64	7.25	28.86	26.80	183.23	17114.93	6.82	53.3	stdgl-1
0c29e08	08	339752	465600.00	4.66	12.88	1106.1	56.88	3921.94	4.07	1.71	0.29	310.75	68.22	6.44	26.1	255b-1062.1py
0c29e09	09	395023	465600.00	0.17	3.33	7.7	5.46	6871.46	4.20	0.33	0.74	310.16	960.32	0.04	23.9	255b-1062.1py

Abbreviations for sulfide phase analysed: cc = chalcocite; bn = bornite; py and vpy = veined pyrite; dpy = disseminated pyrite; cpy = chalcopyrite

Sample ID (Lab Reference Number)		S ppm	Fe ppm	Co ppm	Ni ppm	Cu ppm	Zn ppm	As ppm	Mo ppm	Ag ppm	Sn ppm	Sb ppm	Pb ppm	Bi ppm	Peak	Thesis Sample ID & Sulfide phase analysed
0c29e10	10	380979	465600.00	9.05	4.98	304.1	3.00	3497.79	10.22	0.66	0.46	202.90	425.11	3.40	31.6	255b-1062.1py
0c29e11	11	421717	465600.00	45.75	9.36	7683.7	3.01	11441.71	30.23	6.59	0.27	879.95	883.46	55.06	39.2	765-386.1py
0c29e12	12	440389	465600.00	22.06	2.14	2391.1	<2.542	10147.02	17.59	2.49	0.30	510.87	94.94	22.60	37.0	765-386.1py
0c29e13	13	463070	465600.00	22.10	4.08	3395.4	2.58	9815.38	25.28	2.33	0.50	863.09	800.90	14.08	44.6	765-386.1py
std-3	14	236629	415700.00	133.73	5525.34	539.6	102696.04	665.29	12.20	30.75	29.19	198.63	18723.01	7.16	30.5	stdgl-1
0c29e15	15	316300	292500.00	<0.218	<0.959	358702.3	<3.496	<0.374	4.48	0.53	0.93	<0.587	1.15	2.18	34.8	765-386.1cpy
0c29e16	16	215784	106000.00	<0.204	<0.765	611840.4	<3.227	1.64	<2.185	29.74	0.71	1.59	17.36	482.28	46.8	765-386.1bn
0c29e17	17	207577	106000.00	<0.148	<0.602	622189.4	2.42	<0.208	<2.176	29.86	0.61	<0.306	5.63	472.09	46.8	765-386.1bn
0c29e18	18	336059	292500.00	<0.238	<1.024	349022.7	<2.733	0.29	<2.669	0.97	0.98	1.10	2.53	6.49	33.7	765-386.1cpy
0c29e19	19	331840	292500.00	<0.194	<0.970	347507.7	<3.315	0.66	3.37	2.68	1.85	6.11	11.26	34.38	37.0	765-386.1cpy
std-4	20	238754	415700.00	132.69	5691.51	540.9	100404.99	23.07	8.32	26.47	25.48	181.18	15719.33	6.23	44.6	stdgl-1
		1418	52.63	0.13	0.53	0.7	2.01	0.80	1.41	0.17	0.16	0.32	0.08	0.02		Run detection limit
std-1	01	224644	415700.00	133.87	5683.32	544.6	98508.30	245.98	7.94	27.61	27.20	187.39	16530.83	6.14	42.5	stdgl-1
0c29f02	02	373773	292500.00	0.95	<2.648	368872.4	<9.531	157.04	<6.326	28.96	6.57	135.55	276.16	17.32	29.4	784-184.7cpy
0c29f03	03	630770	465600.00	<0.533	<1.925	10.1	<7.294	3002.04	<6.095	0.68	0.57	11.93	22.08	0.29	31.6	784-184.7py
0c29f04	04	600483	465600.00	236.65	63.90	5.1	<3.469	1245.68	<2.460	<0.291	0.43	<0.500	2.70	0.06	21.8	784-184.7py
0c29f05	05	569051	465600.00	33.30	147.96	13.5	<2.808	1051.42	<2.335	<0.272	1.85	2.08	5.94	0.13	13.1	784-184.7py
0c29f06	06	580409	465600.00	867.22	92.87	169.0	11.09	14162.67	<2.752	3.29	0.22	60.05	69.18	3.20	20.7	784-185.6py
0c29f07	07	480235	465600.00	107.42	23.63	37.9	3.01	4285.15	25.88	0.60	0.42	645.65	54.06	1.85	47.9	784-185.6py
std-2	08	289131	415700.00	131.80	5506.20	531.6	99686.86	262.22	11.40	29.04	24.88	189.70	17431.12	7.21	51.2	stdgl-1
0c29f09	09	416862	292500.00	0.38	<0.928	377121.5	<3.619	4.94	6.87	1.69	1.03	1.33	2.32	15.24	46.8	255d-1018.4cpy
0c29f10	10	367219	292500.00	1.07	<0.704	334361.6	<2.732	19.63	<2.314	1.30	1.67	0.92	2.22	7.14	50.1	255d-1018.4cpy
0c29f11	11	462873	465600.00	12.24	5.27	1573.0	10.48	3174.55	1.19	1.13	0.29	54.81	1822.93	11.37	43.5	255d-1018.4py
0c29f12	12	480961	465600.00	4.26	36.97	251.0	11.14	43770.60	11.83	2.63	0.27	419.77	6481.86	39.18	20.7	255d-1018.4py
std-3	13	244409	415700.00	132.91	5627.81	542.1	101726.48	252.62	10.46	28.18	26.85	188.62	16970.33	6.61	43.5	stdgl-1
std-4	14	247010	415700.00	133.09	5624.19	543.9	101873.38	253.38	10.40	28.26	26.79	188.56	17029.66	6.67	42.5	stdgl-1
		52	3.04	0.00	0.01	0.0	0.11	0.03	0.01	0.00	0.01	0.00	0.01	0.00		Run detection limit
std-1	01	249176	415700.00	136.71	5714.05	567.8	100923.51	260.26	19.22	28.00	25.98	188.44	15771.34	6.57	56.60	std
oc25a02	02	732757	700.00	2.51	<1.313	2615611.0	16.77	<1.865	<0.545	108.58	2.66	1.86	135.03	855.38	44.63	766-89.5cc

Abbreviations for sulfide phase analysed: cc = chalcocite; bn = bornite; py and vpy = veined pyrite; dpy = disseminated pyrite; cpy = chalcopyrite

Sample ID (Lab Reference Number)		S ppm	Fe ppm	Co ppm	Ni ppm	Cu ppm	Zn ppm	As ppm	Mo ppm	Ag ppm	Sn ppm	Sb ppm	Pb ppm	Bi ppm	Peak	Thesis Sample ID & Sulfide phase analysed
oc25a03	03	428559	700.00	2.59	1.97	1383456.2	6.84	<0.877	<0.222	64.55	0.85	3.21	184.99	1182.53	42.45	766-89.5cc
oc25a04	04	86930	700.00	0.21	<0.145	311455.9	<1.382	<0.176	<0.054	12.30	0.20	0.30	8.49	65.82	44.63	766-89.5cc
oc25a05	05	19067	700.00	0.28	<0.032	60856.3	0.39	0.31	0.02	3.17	0.06	0.42	8.16	50.98	43.54	766-89.5cc
std-2	06	237886	415700.00	129.26	5547.69	502.0	99236.00	245.02	1.78	27.70	26.82	185.61	17486.85	6.21	67.49	std
oc25a07	07	364093	700.00	0.91	2.64	1330159.4	27.59	<1.106	<0.215	61.76	0.88	0.90	6.51	26.44	40.27	766-186.5cc
oc25a08	08	1327744	700.00	<0.636	10.75	4545133.7	29.55	5.47	<0.797	261.16	3.28	4.61	19.21	89.40	38.10	766-186.5cc
oc25a09	09	421425	700.00	1.61	1.24	1471509.1	29.35	<0.975	2.53	70.29	1.40	0.34	5.50	33.59	27.21	766-186.5cc
oc25a10	10	1015569	700.00	<0.660	5.26	3868054.2	53.63	<2.479	<0.695	162.92	2.31	<0.671	4.90	55.55	46.81	766-186.5cc
std-3	11	248706	415700.00	130.28	5613.92	530.2	98912.37	247.80	2.17	28.63	29.90	188.65	17170.56	5.76	53.34	std
oc25a12	12	492483	465600.00	101.05	60.61	76964.9	<5.475	25222.20	1.51	47.00	0.57	441.06	1169.82	179.79	43.54	766-186.5py
oc25a13	13	523256	465600.00	75.01	44.70	204324.8	9.70	17915.08	0.74	41.96	<0.530	257.11	1061.25	185.46	44.63	766-186.5py
oc25a14	14	467654	465600.00	115.63	65.00	156854.6	21.96	12024.16	<0.364	29.10	<0.496	71.50	560.71	175.60	48.98	766-186.5py
oc25a15	15	372593	292500.00	0.57	<0.361	309090.0	6.81	681.43	0.28	48.80	0.67	708.11	225.70	37.73	29.39	766-230.1cpy
std-4	16	246984	415700.00	135.75	5628.12	571.2	104542.69	258.92	18.71	28.51	24.60	191.53	17455.66	7.86	57.69	std
oc25a17	17	380944	292500.00	0.62	<0.257	326569.7	6.82	380.25	0.25	54.46	0.59	792.41	210.65	44.52	52.25	766-230.1cpy
oc25a18	18	324174	292500.00	13.40	1.54	323189.8	22.86	18838.71	7.46	21.84	2.07	351.58	93.49	72.16	51.16	766-230.1cpy
oc25a19	19	4728	700.00	40.00	0.01	5180.9	26.94	4005.32	0.25	0.97	0.01	126.94	0.35	0.05	42.45	766-230.1cc
oc25a20	20	6210	700.00	50.66	0.00	6455.5	143.22	4814.09	0.34	1.12	0.01	234.16	0.52	0.07	45.72	766-230.1cc
		699	40.54	0.06	0.18	0.6	1.49	0.35	0.09	0.05	0.10	0.06	0.10	0.03		Run detection limit
std-1	01	245700	409900.47	134.85	5635.50	560.0	99761.78	256.71	19.07	27.59	25.60	185.78	15531.35	6.48	56.60	std
oc25a02	02	200900	191.87	0.69	<0.370	717447.8	4.60	<0.525	<0.154	29.76	0.73	0.51	36.99	234.56	44.63	766-89.5cc
oc25a03	03	200900	327.98	1.22	0.92	648951.0	<3.226	<0.420	<0.106	30.26	0.40	1.50	86.68	554.94	42.45	766-89.5cc
oc25a04	04	200900	1616.62	0.49	<0.341	720359.3	<3.252	<0.414	<0.127	28.43	0.45	0.70	19.62	152.40	44.63	766-89.5cc
oc25a05	05	200900	7369.38	2.92	<0.342	641798.1	4.15	3.31	0.16	33.36	0.59	4.37	85.96	538.42	43.54	766-89.5cc
std-2	06	245700	428943.05	133.41	5724.70	519.0	102419.01	252.93	1.87	28.61	27.70	191.67	18068.47	6.43	67.49	std
oc25a07	07	200900	385.85	0.50	1.46	734724.3	15.21	<0.613	<0.119	34.08	0.48	0.50	3.60	14.64	40.27	766-186.5cc
oc25a08	08	200900	105.80	<0.096	1.63	688456.4	4.47	0.83	<0.121	39.53	0.50	0.70	2.91	13.57	38.10	766-186.5cc
oc25a09	09	200900	333.35	0.77	0.59	702239.0	13.98	<0.463	1.23	33.52	0.67	0.16	2.62	16.07	27.21	766-186.5cc
oc25a10	10	200900	138.33	<0.129	1.04	765967.0	10.60	<0.486	<0.136	32.24	0.46	<0.132	0.97	11.03	46.81	766-186.5cc
std-3	11	245700	410295.07	128.61	5540.82	524.3	97642.61	244.67	2.18	28.30	29.54	186.35	16976.44	5.71	53.34	std
oc25a12	12	525800	496699.45	107.82	64.66	82243.9	<5.745	26916.05	1.63	50.20	0.61	470.88	1249.86	192.54	43.54	766-186.5py

Abbreviations for sulfide phase analysed: cc = chalcocite; bn = bornite; py and vpy = veined pyrite; dpy = disseminated pyrite; cpy = chalcopyrite

Sample ID (Lab Reference Number)		S ppm	Fe ppm	Co ppm	Ni ppm	Cu ppm	Zn ppm	As ppm	Mo ppm	Ag ppm	Sn ppm	Sb ppm	Pb ppm	Bi ppm	Peak	Thesis Sample ID & Sulfide phase analysed
oc25a13	13	525800	467564.96	75.34	44.89	205474.7	9.75	17996.12	0.75	42.18	<0.521	258.36	1067.07	186.86	44.63	766-186.5py
oc25a14	14	525800	523263.61	129.98	73.04	176466.7	24.68	13516.79	<0.399	32.72	<0.543	80.39	630.72	197.87	48.98	766-186.5py
oc25a15	15	258700	203050.65	0.40	0.25	214705.1	4.73	473.14	0.19	33.89	0.47	491.68	156.75	26.24	29.39	766-230.1cpy
std-4	16	245700	413576.67	135.08	5599.42	568.4	104030.08	257.64	18.70	28.37	24.45	190.56	17365.93	7.83	57.69	std
oc25a17	17	258700	198719.77	0.42	<0.168	221783.1	4.64	258.36	0.17	36.98	0.40	538.20	143.02	30.24	52.25	766-230.1cpy
oc25a18	18	258700	233604.84	10.70	1.23	257862.6	18.26	15045.58	5.95	17.43	1.65	280.62	74.57	57.56	51.16	766-230.1cpy
oc25a19	19	200900	29782.04	1701.91	0.22	220062.0	1146.64	170396.2 1	10.67	41.37	0.61	5395.82	15.01	2.32	42.45	766-230.1cc
oc25a20	20	200900	22684.25	1641.81	0.12	208700.8	4642.59	155979.7 3	11.06	36.34	0.43	7578.13	16.84	2.19	45.72	766-230.1cc
		65	3.89	0.01	0.02	0.0	0.13	0.06	0.05	0.00	0.01	0.01	0.01	0.00		Run detection limit
std-1	01	258243	415700.00	132.91	5579.28	408.2	92513.85	269.07	11.21	28.60	25.01	197.33	16718.47	6.61	64.22	stdgl-1
oc25b02	02	3979	700.00	48.39	0.01	4578.2	75.71	2614.70	3.31	1.95	0.01	307.22	0.80	0.12	60.96	766-230.1cc
oc25b03	03	418721	292500.00	11.51	<0.273	293167.2	4.18	836.49	4.01	59.01	0.56	739.99	219.81	44.54	54.42	766-230.1cpy
oc25b04	04	58765	700.00	6.28	0.79	190063.7	3.07	27.73	0.24	61.57	0.16	5.32	3.09	11.82	53.34	713-160.1cc
oc25b05	05	184298	700.00	12.22	0.55	564124.0	18.08	240.04	1.50	165.70	0.34	28.78	4.87	18.76	50.07	713-160.1cc
std-2	06	226298	415700.00	131.15	5523.09	708.5	108217.45	237.62	9.63	28.34	28.69	177.98	17071.38	6.73	64.22	stdgl-1
oc25b07	07	760390	700.00	11.96	2.29	2376144.8	73.52	82.87	<3.513	582.18	0.97	7.70	20.46	78.95	32.66	713-160.1cc
oc25b08	08	122310	700.00	7.05	0.94	403053.8	27.14	42.10	3.78	111.88	0.29	5.99	7.30	20.82	54.42	713-160.1cc
oc25b09	09	99797	700.00	3.27	0.64	318477.6	5.62	14.60	4.76	68.46	0.36	2.39	1.98	10.02	39.19	713-160.1cc
oc25b10	10	214126	106000.00	<0.126	0.74	437439.8	6.85	18.24	<0.670	32.26	0.33	2.30	0.85	607.27	47.89	713-160.1bn
std-3	11	233409	415700.00	132.76	5510.90	513.6	98177.41	252.70	8.97	27.87	25.52	190.32	17208.74	6.63	47.89	stdgl-1
oc25b12	12	198735	106000.00	0.47	2.46	485007.8	2.76	11.02	<0.730	29.52	1.14	0.15	2.39	531.93	54.42	713-160.1bn
oc25b13	13	188350	106000.00	<0.150	0.49	542073.0	9.87	9.79	<0.590	37.07	0.34	0.68	0.65	634.43	34.83	713-160.1bn
oc25b14	14	2556870	<1085.402	<1.784	<4.078	10674615.2	55.90	211.52	<9.961	3563.64	3.18	<1.348	8.52	197.98	32.65	713-178.6cc
oc25b15	15	2708675	<1808.255	<2.218	10.18	11917259.3	<69.371	151.96	<11.490	3218.38	8.01	<2.319	9.78	229.93	19.59	713-178.6cc
std-4	16	264382	415700.00	135.10	5876.50	548.0	105070.17	252.55	11.91	28.06	28.07	188.82	16994.16	6.59	44.63	stdgl-1
oc25b17	17	630152	700.00	<0.463	<1.243	2692889.5	10.42	61.08	<2.962	856.38	1.42	27.76	3.93	57.29	35.92	713-178.6cc
oc25b18	18	210490	106000.00	0.22	<0.480	532288.9	<3.704	29.64	<0.718	59.38	0.81	0.64	1.54	518.27	27.21	713-178.6bn
oc25b19	19	206491	106000.00	<0.150	<0.407	529861.3	<2.719	6.46	<0.758	79.07	0.51	<0.142	0.47	514.46	19.59	713-178.6bn
oc25b20	20	395266	525800.00	52.37	85.41	5136.4	19.91	11766.71	6.06	4.76	1.10	195.34	575.83	3.64	44.63	713-178.6py

Abbreviations for sulfide phase analysed: cc = chalcocite; bn = bornite; py and vpy = veined pyrite; dpy = disseminated pyrite; cpy = chalcopyrite

Sample ID (Lab Reference Number)		S ppm	Fe ppm	Co ppm	Ni ppm	Cu ppm	Zn ppm	As ppm	Mo ppm	Ag ppm	Sn ppm	Sb ppm	Pb ppm	Bi ppm	Peak	Thesis Sample ID & Sulfide phase analysed
		769	46.32	0.07	0.20	0.6	1.51	0.67	0.59	0.05	0.10	0.06	0.07	0.02		Run detection limit
std-1	01	245700	394841.63	126.20	5293.86	383.4	87922.99	256.37	10.68	27.19	23.68	187.81	15863.26	6.28	64.22	stdgl-1
oc25b02	02	200900	35243.93	2436.82	0.26	227852.5	3802.01	132024.5 6	167.52	98.46	0.61	15501.88	40.14	6.15	60.96	766-230.1cc
oc25b03	03	339800	236510.13	9.31	<0.229	234279.5	3.38	678.13	3.26	47.72	0.45	599.69	177.67	36.00	54.42	766-230.1cpy
oc25b04	04	200900	2382.48	21.40	2.69	639295.6	10.44	94.61	0.83	209.47	0.56	18.14	10.53	40.19	53.34	713-160.1cc
oc25b05	05	200900	759.14	13.27	0.60	604658.0	19.57	260.86	1.64	179.58	0.37	31.29	5.28	20.33	50.07	713-160.1cc
std-2	06	245700	448749.55	141.78	5978.84	756.1	116651.64	256.98	10.46	30.56	30.94	192.58	18434.79	7.26	64.22	stdgl-1
oc25b07	07	200900	183.79	3.15	0.60	617009.0	19.28	21.79	<0.931	152.67	0.25	2.03	5.37	20.71	32.66	713-160.1cc
oc25b08	08	200900	1142.15	11.52	1.53	650773.4	44.25	68.79	6.21	182.30	0.47	9.80	11.92	33.93	54.42	713-160.1cc
oc25b09	09	200900	1399.39	6.54	1.27	630505.0	11.23	29.22	9.60	136.65	0.71	4.79	3.96	20.01	39.19	713-160.1cc
oc25b10	10	258700	127152.99	<0.149	0.90	520134.3	8.22	21.91	<0.794	38.64	0.40	2.77	1.01	727.58	47.89	713-160.1bn
std-3	11	245700	434432.13	139.02	5784.36	532.6	102644.61	264.27	9.46	29.08	26.70	199.22	17996.57	6.92	47.89	stdgl-1
oc25b12	12	258700	136989.25	0.61	3.19	622854.5	3.57	14.25	<0.920	38.09	1.48	0.20	3.09	686.68	54.42	713-160.1bn
oc25b13	13	258700	144559.17	<0.198	0.68	735762.2	13.48	13.36	<0.778	50.48	0.47	0.93	0.88	864.32	34.83	713-160.1bn
oc25b14	14	200900	<81.330	<0.134	<0.306	830521.3	4.37	16.51	<0.746	277.77	0.25	<0.101	0.66	15.43	32.65	713-178.6cc
oc25b15	15	200900	<127.007	<0.156	0.75	877321.8	<4.872	11.20	<0.807	236.94	0.59	<0.163	0.72	16.93	19.59	713-178.6cc
std-4	16	245700	383952.07	124.94	5447.51	506.9	97316.86	233.20	11.13	25.90	26.03	174.39	15695.78	6.08	44.63	stdgl-1
oc25b17	17	200900	221.91	<0.138	<0.370	857163.1	3.31	19.36	<0.882	271.49	0.45	8.80	1.24	18.16	35.92	713-178.6cc
oc25b18	18	258700	129627.32	0.28	<0.548	655475.7	<4.222	36.23	<0.818	72.66	0.99	0.78	1.89	633.75	27.21	713-178.6bn
oc25b19	19	258700	132234.44	<0.173	<0.470	667755.8	<3.138	8.05	<0.875	98.75	0.64	<0.164	0.58	641.93	19.59	713-178.6bn
oc25b20	20	525800	697038.53	69.41	113.38	6903.3	26.53	15585.08	8.14	6.33	1.47	258.42	762.28	4.83	44.63	713-178.6py
		357	16.56	0.03	0.09	0.2	0.38	0.24	0.32	0.03	0.04	0.04	0.05	0.01		Run detection limit
std-1	01	250574	415700.00	132.53	5717.55	554.1	101183.65	239.94	11.64	27.58	25.90	186.61	16971.46	7.12	50.07	std
oc26a02	02	376668	465600.00	49.07	16.54	39226.0	47.52	17788.11	32.45	19.77	0.50	804.52	88.50	64.30	23.95	713-178.6py
oc26a03	03	368515	465600.00	32.78	34.47	20792.6	<2.212	24015.86	36.31	11.11	<0.196	1236.87	82.44	23.48	20.68	713-178.6py
oc26a04	04	353677	465600.00	<0.055	15.88	153.1	7.57	30118.19	<0.623	7.36	0.35	145.11	3140.71	0.05	50.07	713-205.5py
oc26a05	05	389264	465600.00	93.10	59.67	18125.4	6.54	37082.38	1.94	5.38	0.27	56.56	1700.79	89.27	37.01	713-205.5py
std-2	06	244799	415700.00	133.33	5534.75	530.5	97499.64	265.03	9.31	29.27	27.55	192.32	17285.39	6.30	42.45	stdgl-1
oc26a07	07	352707	465600.00	1.36	4.26	162.3	7.37	49526.15	2.72	6.12	0.25	64.86	1651.02	0.78	28.30	713-205.5py
oc26a08	08	255424	106000.00	<0.237	<0.831	604116.2	<2.305	2.57	<2.144	3.47	0.90	<0.193	1.73	708.52	41.36	713-205.5bn

Abbreviations for sulfide phase analysed: cc = chalcocite; bn = bornite; py and vpy = veined pyrite; dpy = disseminated pyrite; cpy = chalcopyrite

Sample ID (Lab Reference Number)		S	Fe	Co	Ni	Cu	Zn	As	Mo	Ag	Sn	Sb	Pb	Bi	Peak	Thesis Sample ID & Sulfide phase analysed
		ppm	ppm	ppm	ppm	ppm	ppm	ppm	ppm	ppm	ppm	ppm	ppm	ppm		
oc26a09	09	230812	106000.00	<0.156	<0.409	563360.8	<1.830	14.70	10.21	3.05	0.94	<0.199	1.21	653.02	40.27	713-205.5bn
oc26a10	10	1049074	700.00	<0.863	<3.224	4180247.9	16.47	17.89	<10.278	81.70	3.91	<0.934	2.50	153.31	38.10	713-205.5cc
std-3	11	240611	415700.00	135.54	5798.92	545.5	105216.09	259.14	10.21	28.14	27.28	185.42	16415.54	6.30	50.07	stdgl-1
oc26a12	12	247054	700.00	9.61	11.88	964732.3	14.36	4.44	<2.188	24.36	5.66	0.60	25.37	150.60	40.27	713-205.5cc
oc26a13	13	207974	700.00	0.77	<0.846	879451.2	6.62	3.10	<2.721	35.16	1.91	0.91	18.66	85.36	5.44	713-205.5cc
oc26a14	14	315490	700.00	1.30	9.52	1147746.1	14.10	3.98	4.28	35.35	2.16	0.70	34.08	184.26	20.68	713-205.5cc
oc26a15	15	3952	700.00	0.75	0.64	12333.1	0.07	43.35	0.15	0.36	0.06	0.93	2.38	2.60	42.45	713-205.5cc
std-4	16	246649	415700.00	130.61	5452.76	541.9	99591.93	247.85	10.55	27.89	26.55	190.03	17329.56	6.84	43.54	stdgl-1
oc26a17	17	396499	465600.00	16.59	6.92	1555.4	<1.595	20050.74	7.71	1.33	0.64	22.91	116.18	12.41	35.92	713-226.3py
oc26a18	18	435485	465600.00	15.66	10.62	3469.4	3.52	43232.28	10.21	1.32	0.52	151.81	282.32	19.70	45.72	713-226.3py
oc26a19	19	424427	465600.00	<0.084	0.86	5.5	4.51	46417.97	8.01	0.35	0.45	200.24	906.20	<0.033	47.89	713226.3py
oc26a20	20	433537	465600.00	8.68	5.96	14.9	5.55	33136.41	15.11	0.53	0.42	279.50	720.81	0.69	21.77	713-226.3py
		1280	59.42	0.10	0.32	0.7	1.37	0.87	1.13	0.12	0.13	0.14	0.18	0.03		Run detection limit
std-1	01	245700	407462.63	129.89	5606.34	543.4	99030.32	234.91	11.44	27.01	25.36	182.86	16633.29	6.99	50.07	std
oc26a02	02	525800	649564.17	68.45	23.08	54746.7	66.34	24788.48	45.38	27.57	0.70	1122.25	123.48	89.86	23.95	713-178.6py
oc26a03	03	525800	663819.13	46.73	49.16	29654.6	<3.068	34202.76	51.89	15.84	<0.272	1763.44	117.57	33.54	20.68	713-178.6py
oc26a04	04	525800	691572.06	<0.079	23.59	227.4	11.25	44688.75	<0.904	10.94	0.52	215.57	4667.18	0.08	50.07	713-205.5py
oc26a05	05	525800	628281.73	125.62	80.54	24463.8	8.83	49989.18	2.62	7.26	0.36	76.34	2296.41	120.72	37.01	713-205.5py
std-2	06	245700	416783.43	133.66	5550.41	532.0	97742.62	265.47	9.35	29.36	27.60	192.87	17342.38	6.33	42.45	stdgl-1
oc26a07	07	525800	693327.47	2.03	6.34	241.6	10.98	73685.24	4.07	9.12	0.37	96.61	2460.40	1.16	28.30	713-205.5py
oc26a08	08	258700	107240.83	<0.238	<0.835	611243.7	<2.316	2.59	<2.155	3.51	0.91	<0.194	1.75	718.28	41.36	713-205.5bn
oc26a09	09	258700	118680.24	<0.175	<0.457	630790.8	<2.043	16.45	11.45	3.42	1.05	<0.222	1.35	732.54	40.27	713-205.5bn
oc26a10	10	200900	133.92	<0.165	<0.618	799751.0	3.15	3.42	<1.969	15.64	0.75	<0.179	0.48	29.38	38.10	713-205.5cc
std-3	11	245700	424109.90	138.26	5916.69	556.6	107308.41	264.24	10.43	28.73	27.82	189.23	16759.31	6.43	50.07	stdgl-1
oc26a12	12	200900	568.79	7.81	9.66	783906.4	11.66	3.61	<1.795	19.80	4.60	0.49	20.62	122.53	40.27	713-205.5cc
oc26a13	13	200900	675.79	0.74	<0.828	849030.6	6.39	2.99	<2.663	33.96	1.84	0.88	18.02	82.49	5.44	713-205.5cc
oc26a14	14	200900	445.58	0.83	6.06	730585.5	8.97	2.53	2.72	22.50	1.38	0.44	21.70	117.37	20.68	713-205.5cc
oc26a15	15	200900	35579.02	38.11	32.59	626850.6	3.73	2203.05	7.68	18.07	3.03	47.48	120.94	132.14	42.45	713-205.5cc
std-4	16	245700	414159.27	130.12	5432.19	539.9	99225.48	246.94	10.51	27.78	26.45	189.32	17263.88	6.81	43.54	stdgl-1
oc26a17	17	525800	617715.76	22.01	9.18	2063.6	<2.180	26605.87	10.23	1.76	0.85	30.39	154.08	16.45	35.92	713-226.3py
oc26a18	18	525800	562610.94	18.92	12.83	4192.4	4.26	52255.92	12.32	1.59	0.63	183.38	340.93	23.78	45.72	713-226.3py

Abbreviations for sulfide phase analysed: cc = chalcocite; bn = bornite; py and vpy = veined pyrite; dpy = disseminated pyrite; cpy = chalcopyrite

Sample ID (Lab Reference Number)		S	Fe	Co	Ni	Cu	Zn	As	Mo	Ag	Sn	Sb	Pb	Bi	Peak	Thesis Sample ID & Sulfide phase analysed
		ppm	ppm	ppm	ppm	ppm	ppm	ppm	ppm	ppm	ppm	ppm	ppm	ppm		
oc26a19	19	525800	577490.24	<0.108	1.06	6.8	5.60	57598.79	9.92	0.43	0.56	248.24	1122.93	<0.043	47.89	713226.3py
oc26a20	20	525800	565591.40	10.54	7.24	18.1	6.75	40276.98	18.32	0.64	0.52	339.28	874.50	0.84	21.77	713-226.3py
		1286	57.39	0.09	0.31	0.6	1.49	0.75	1.06	0.11	0.12	0.11	0.12	0.03		Run detection limit
std-1	01	252763	415700.00	134.27	5724.52	558.8	100998.65	261.60	8.77	28.11	27.58	189.78	16942.26	6.90	43.54	stdgl-1
oc26b02	02	225052	106000.00	<0.162	<0.409	591038.7	<2.279	3.58	<1.755	9.55	0.82	0.41	8.70	158.67	45.72	713-231.9bn
oc26b03	03	221466	106000.00	<0.122	<0.336	571216.0	<1.718	3.10	2.32	11.60	0.68	0.54	7.20	138.53	31.57	713-231.9bn
oc26b04	04	236171	106000.00	<0.143	<0.486	619964.6	<2.392	2.93	<1.611	5.12	0.76	<0.176	2.39	159.40	44.63	713-231.9bn
oc26b05	05	247352	106000.00	<0.185	<0.696	628043.5	3.05	2.66	<2.598	5.40	0.74	<0.276	0.54	309.57	46.81	713-231.9bn
oc26b06	06	403567	465600.00	32.57	10.79	2349.5	21.31	4887.30	15.34	4.05	0.25	9.93	23.38	7.71	44.63	713-231.9py
std-2	07	237040	415700.00	131.80	5523.03	526.9	100724.99	252.90	12.58	28.90	26.36	188.23	16902.04	6.38	45.72	stdgl-1
oc26b08	08	429976	465600.00	61.05	87.43	4854.4	5.79	5117.30	<0.815	2.28	0.22	26.49	489.33	46.42	47.89	713-231.9py
oc26b09	09	408605	465600.00	62.95	34.01	3943.9	2.98	3637.51	6.06	1.56	0.30	34.98	789.00	30.17	23.95	713-231.9py
oc26b10	10	378080	292500.00	0.47	<0.565	352284.3	6.55	6.81	<2.015	0.32	2.55	1.69	2.24	21.53	42.45	768-84cpy
oc26b11	11	384053	292500.00	6.47	2.03	362847.7	<3.311	21.47	<1.941	0.34	5.85	1.52	1.71	12.68	50.07	768-84cpy
oc26b12	12	359546	292500.00	6.48	0.98	348870.5	<3.658	18.95	<1.909	<0.288	6.53	1.03	0.46	4.93	44.63	768-84cpy
oc26b13	13	395761	465600.00	2.32	43.95	105.9	5.23	3067.73	<0.869	1.38	0.21	19.91	411.65	24.78	46.81	768-84py
std-3	14	244744	415700.00	132.79	5601.08	534.5	99399.78	242.53	11.14	27.79	26.39	185.69	16753.41	6.46	52.25	stdgl-1
oc26b15	15	431903	465600.00	<0.066	0.57	3.3	6.95	636.97	1.16	<0.080	0.30	0.78	73.39	<0.020	51.16	768-84py
oc26b16	16	402516	465600.00	<0.100	11.16	34.1	4.39	2844.64	<0.894	0.56	0.25	5.49	76.20	0.22	19.59	768-84py
oc26b17	17	877380	700.00	14.23	<1.744	2442285.4	11.47	19.68	<5.358	41.84	4.39	<0.552	1.48	35.58	32.66	768-116.5cc
oc26b18	18	798842	700.00	8.68	2.38	2289956.5	<6.884	19.76	<5.183	27.89	4.56	<0.535	0.87	38.00	22.86	768-116.5cc
oc26b19	19	3209765	<1628.673	16.26	5.56	8017909.8	<28.172	78.80	<20.807	145.73	12.36	<2.802	3.57	168.57	27.21	768-116.5cc
std-4	20	248274	415700.00	133.15	5655.44	551.8	103344.11	254.20	9.22	28.06	26.94	190.66	17395.43	6.82	44.63	stdgl-1
		1221	54.47	0.09	0.30	0.6	1.41	0.71	1.00	0.10	0.11	0.10	0.11	0.03		Run detection limit
std-1	01	245700	403765.09	130.45	5562.94	543.2	98219.87	254.39	8.49	27.31	26.81	184.37	16453.29	6.71	43.54	stdgl-1
oc26b02	02	258700	121752.65	<0.188	<0.475	679414.4	<2.648	4.11	<2.040	10.97	0.94	0.47	9.99	182.44	45.72	713-231.9bn
oc26b03	03	258700	123724.76	<0.144	<0.397	667242.6	<2.026	3.63	2.69	13.54	0.80	0.64	8.40	161.86	31.57	713-231.9bn
oc26b04	04	258700	116022.84	<0.158	<0.537	679083.7	<2.642	3.20	<1.779	5.60	0.83	<0.194	2.62	174.65	44.63	713-231.9
oc26b05	05	258700	110779.72	<0.195	<0.733	656823.7	3.19	2.78	<2.736	5.64	0.77	<0.290	0.56	323.83	46.81	713-231.9bn

Abbreviations for sulfide phase analysed: cc = chalcocite; bn = bornite; py and vpy = veined pyrite; dpy = disseminated pyrite; cpy = chalcopyrite

Sample ID (Lab Reference Number)		S ppm	Fe ppm	Co ppm	Ni ppm	Cu ppm	Zn ppm	As ppm	Mo ppm	Ag ppm	Sn ppm	Sb ppm	Pb ppm	Bi ppm	Peak	Thesis Sample ID & Sulfide phase analysed
oc26b06	06	525800	606177.10	42.41	14.05	3060.9	27.75	6364.45	19.88	5.27	0.33	12.92	30.44	10.05	44.63	713-231.9py
std-2	07	245700	430580.30	136.54	5722.87	546.1	104359.46	261.98	12.97	29.92	27.31	194.98	17510.05	6.61	45.72	stdgl-1
oc26b08	08	525800	568972.28	74.62	106.88	5935.8	7.08	6253.37	<0.999	2.79	0.27	32.37	598.09	56.77	47.89	713-231.9py
oc26b09	09	525800	598748.48	80.97	43.74	5074.7	3.83	4677.21	7.77	2.00	0.39	44.99	1014.87	38.83	23.95	713-231.9py
oc26b10	10	339800	262721.23	0.42	<0.508	316587.8	5.88	6.12	<1.811	0.29	2.29	1.52	2.02	19.36	42.45	768-84cpy
oc26b11	11	339800	258644.97	5.72	1.80	321010.3	<2.926	18.98	<1.715	0.30	5.18	1.34	1.51	11.22	50.07	768-84cpy
oc26b12	12	339800	276285.60	6.12	0.92	329683.8	<3.448	17.90	<1.799	<0.271	6.17	0.97	0.44	4.66	44.63	768-84cpy
oc26b13	13	525800	618276.56	3.08	58.38	140.7	6.95	4072.33	<1.150	1.84	0.28	26.44	546.81	32.92	46.81	768-84py
std-3	14	245700	417135.34	133.26	5621.58	536.6	99755.07	243.29	11.14	27.87	26.48	186.34	16816.67	6.49	52.25	stdgl-1
oc26b15	15	525800	566595.55	<0.080	0.70	4.0	8.46	774.88	1.41	<0.097	0.37	0.95	89.34	<0.024	51.16	768-84py
oc26b16	16	525800	607995.20	<0.130	14.58	44.5	5.73	3713.55	<1.159	0.73	0.32	7.17	99.53	0.29	19.59	768-84py
oc26b17	17	200900	160.24	3.26	<0.396	559222.1	2.63	4.50	<1.215	9.58	1.00	<0.125	0.34	8.15	32.66	768-116.5cc
oc26b18	18	200900	176.00	2.18	0.60	575907.9	<1.713	4.97	<1.290	7.01	1.15	<0.133	0.22	9.56	22.86	768-116.5cc
oc26b19	19	200900	<100.733	1.02	0.35	501864.5	<1.742	4.93	<1.287	9.12	0.77	<0.173	0.22	10.55	27.21	768-116.5cc
std-4	20	245700	411353.72	131.76	5596.56	546.1	102281.00	251.56	9.12	27.77	26.66	188.69	17217.98	6.75	44.63	stdgl-1
		1373	60.65	0.10	0.31	1.6	1.56	1.00	1.11	0.11	0.14	0.12	0.15	0.03		Run detection limit
std-1	01	255047	415700.00	134.80	5725.21	556.8	98086.26	255.40	9.60	30.11	27.25	191.82	17723.03	6.88	43.54	stdgl-1
oc26c02	02	280008	106000.00	0.33	0.46	631061.8	3.59	4.51	<2.023	2.72	0.79	<0.162	0.47	471.24	39.19	768-116.5bn
oc26c03	03	289880	106000.00	0.42	<0.411	624690.0	3.44	8.54	<1.671	2.69	1.53	<0.193	1.25	435.00	47.89	768-116.5bn
oc26c04	04	1181590	106000.00	18.92	1.85	2667798.2	14.87	57.24	<6.590	62.44	16.19	1.98	16.99	709.39	47.89	768-116.5bn
oc26c05	05	455040	465600.00	75.55	20.51	2867.4	4.06	56603.12	7.38	3.63	0.48	341.84	1962.44	84.92	44.63	768-116.5py
oc26c06	06	455899	465600.00	318.14	51.30	10082.1	11.97	62779.33	15.91	10.16	1.13	742.58	2866.52	289.53	44.63	768-116.5py
std-2	07	234713	415700.00	130.71	5479.81	519.6	101392.37	238.97	11.06	25.46	26.76	185.33	16352.73	6.36	29.39	stdgl-1
oc26c08	08	423363	465600.00	209.68	58.55	7592.0	7.62	60506.21	19.25	8.99	0.42	881.43	3141.81	180.95	45.72	768-116.5py
oc26c09	09	455925	465600.00	8.95	27.62	2312.2	3.12	60207.40	6.22	2.19	0.52	389.46	19.08	15.84	22.86	768-162.2py
oc26c10	10	461640	465600.00	124.10	135.32	8792.1	3.49	66232.34	11.88	9.56	0.58	1135.97	378.24	183.44	41.36	768-162.2py
oc26c11	11	459075	465600.00	9.94	55.25	679.3	1.75	61503.52	10.03	2.97	0.52	480.01	24.27	29.81	34.83	768-162.2py
oc26c12	12	192449	106000.00	<0.132	<0.465	558753.9	<2.307	<2.714	<1.430	3.02	0.22	<0.497	0.63	564.21	21.77	768-162.2bn
oc26c13	13	234077	106000.00	0.39	0.36	584212.5	<2.174	10.26	<1.080	3.64	1.25	0.18	0.90	779.38	54.42	768-162.2bn
std-3	14	248421	415700.00	133.39	5536.60	527.6	98350.03	259.17	10.78	28.24	25.74	183.32	16792.86	6.56	51.16	stdgl-1
oc26c15	15	57632	700.00	<0.234	<0.467	199997.6	<2.759	2.75	<2.147	7.12	0.29	<0.228	1.37	31.92	25.04	768-162.2cc

Abbreviations for sulfide phase analysed: cc = chalcocite; bn = bornite; py and vpy = veined pyrite; dpy = disseminated pyrite; cpy = chalcopyrite

Sample ID (Lab Reference Number)		S	Fe	Co	Ni	Cu	Zn	As	Mo	Ag	Sn	Sb	Pb	Bi	Peak	Thesis Sample ID & Sulfide phase analysed
		ppm	ppm	ppm	ppm	ppm	ppm	ppm	ppm	ppm	ppm	ppm	ppm	ppm		
oc26c16	16	625663	<754.826	<1.145	<3.116	2211992.4	16.00	<274.724	<8.162	47.49	1.68	<0.923	2.69	103.45	29.39	768-162.2cc
oc26c17	17	444677	700.00	1.71	7.00	1337434.4	<6.578	48.06	<5.164	76.30	5.75	<4.061	3.31	85.09	17.42	768-162.2cc
oc26c18	18	240480	106000.00	<0.198	<0.668	579684.3	<2.763	2.28	<2.340	4.69	0.94	<0.235	3.31	614.56	25.04	768-163.1bn
oc26c19	19	249741	106000.00	<0.185	<0.634	698711.4	<3.560	2.93	<2.170	6.72	1.07	<0.180	11.92	743.69	19.59	768-163.1bn
std-4	20	244689	415700.00	133.11	5761.46	567.6	106418.84	257.63	10.27	29.08	27.53	193.89	17127.50	6.76	34.83	stdgl-1
		1423	62.84	0.11	0.33	1.6	1.62	1.03	1.15	0.12	0.14	0.12	0.15	0.04		Run detection limit
std-1	01	245700	399900.06	129.74	5511.03	536.1	94392.36	245.70	9.20	29.03	26.24	184.65	17077.77	6.63	43.54	stdgl-1
oc26c02	02	258700	97799.16	0.30	<0.431	582760.9	3.31	4.17	<1.891	2.51	0.73	<0.152	0.43	435.35	39.19	768-116.5bn
oc26c03	03	258700	94472.96	0.37	<0.370	557271.4	3.07	7.61	<1.506	2.40	1.37	<0.174	1.12	388.19	47.89	768-116.5bn
oc26c04	04	258700	23178.19	4.14	0.40	583893.6	3.25	12.52	<1.455	13.69	3.54	0.43	3.72	155.31	47.89	768-116.5bn
oc26c05	05	525800	537341.32	87.23	23.69	3312.4	4.68	65378.12	8.49	4.20	0.56	394.71	2267.60	98.12	44.63	768-116.5py
oc26c06	06	525800	536359.18	366.64	59.13	11625.2	13.79	72387.72	18.29	11.73	1.31	855.83	3305.89	333.90	44.63	768-116.5py
std-2	07	245700	434675.63	136.73	5733.27	543.8	106015.20	250.13	11.54	26.68	27.98	193.87	17116.78	6.66	29.39	stdgl-1
oc26c08	08	525800	577651.99	260.24	72.68	9427.5	9.46	75148.91	23.85	11.18	0.52	1093.98	3901.55	224.72	45.72	768-116.5py
oc26c09	09	525800	536432.03	10.31	31.84	2666.2	3.59	69444.01	7.16	2.53	0.60	448.86	22.01	18.27	22.86	768-162.2py
oc26c10	10	525800	529829.84	141.27	154.06	10013.1	3.97	75453.40	13.50	10.90	0.66	1293.06	430.74	208.92	41.36	768-162.2py
oc26c11	11	525800	532830.98	11.38	63.25	777.9	2.00	70461.57	11.46	3.41	0.59	549.46	27.79	34.14	34.83	768-162.2py
oc26c12	12	258700	142384.42	<0.177	<0.624	751053.9	<3.093	<3.639	<1.917	4.07	0.30	<0.667	0.84	758.37	21.77	768-162.2bn
oc26c13	13	258700	117072.52	0.43	0.40	645623.8	<2.393	11.34	<1.189	4.02	1.38	0.20	0.99	861.29	54.42	768-162.2bn
std-3	14	245700	410910.32	131.89	5474.46	521.7	97219.32	256.41	10.65	27.94	25.44	181.23	16605.90	6.48	51.16	stdgl-1
oc26c15	15	200900	2438.98	<0.809	<1.615	697127.4	<9.552	9.60	<7.433	24.84	1.02	<0.791	4.77	111.26	25.04	768-162.2cc
oc26c16	16	200900	<240.382	<0.365	<0.992	710208.7	5.14	<87.489	<2.599	15.25	0.54	<0.294	0.86	33.21	29.39	768-162.2cc
oc26c17	17	200900	316.16	0.77	3.16	604175.5	<2.943	21.72	<2.311	34.48	2.60	<1.817	1.49	38.44	17.42	768-162.2cc
oc26c18	18	258700	114010.79	<0.210	<0.710	623524.9	<2.940	2.45	<2.490	5.04	1.01	<0.250	3.56	661.07	25.04	768-163.1bn
oc26c19	19	258700	109795.24	<0.189	<0.648	723664.4	<3.642	3.03	<2.220	6.96	1.11	<0.184	12.35	770.31	19.59	768-163.1bn
std-4	20	245700	417436.51	133.66	5784.78	569.8	106843.37	258.66	10.32	29.19	27.64	194.68	17198.05	6.79	34.83	stdgl-1
		1418	52.63	0.13	0.53	0.7	2.01	0.80	1.41	0.17	0.16	0.32	0.08	0.02		Run detection limit
std-1	01	224644	415700.00	133.87	5683.32	544.6	98508.30	245.98	7.94	27.61	27.20	187.39	16530.83	6.14	42.5	stdgl-1
0c29f02	02	373773	292500.00	0.95	<2.648	368872.4	<9.531	157.04	<6.326	28.96	6.57	135.55	276.16	17.32	29.4	784-184.7cpy

Abbreviations for sulfide phase analysed: cc = chalcocite; bn = bornite; py and vpy = veined pyrite; dpy = disseminated pyrite; cpy = chalcopyrite

Sample ID (Lab Reference Number)		S ppm	Fe ppm	Co ppm	Ni ppm	Cu ppm	Zn ppm	As ppm	Mo ppm	Ag ppm	Sn ppm	Sb ppm	Pb ppm	Bi ppm	Peak	Thesis Sample ID & Sulfide phase analysed
0c29f03	03	630770	465600.00	<0.533	<1.925	10.1	<7.294	3002.04	<6.095	0.68	0.57	11.93	22.08	0.29	31.6	784-184.7py
0c29f04	04	600483	465600.00	236.65	63.90	5.1	<3.469	1245.68	<2.460	<0.291	0.43	<0.500	2.70	0.06	21.8	784-184.7py
0c29f05	05	569051	465600.00	33.30	147.96	13.5	<2.808	1051.42	<2.335	<0.272	1.85	2.08	5.94	0.13	13.1	784-184.7py
0c29f06	06	580409	465600.00	867.22	92.87	169.0	11.09	14162.67	<2.752	3.29	0.22	60.05	69.18	3.20	20.7	784-185.6py
0c29f07	07	480235	465600.00	107.42	23.63	37.9	3.01	4285.15	25.88	0.60	0.42	645.65	54.06	1.85	47.9	784-185.6py
std-2	08	289131	415700.00	131.80	5506.20	531.6	99686.86	262.22	11.40	29.04	24.88	189.70	17431.12	7.21	51.2	stdgl-1
0c29f09	09	416862	292500.00	0.38	<0.928	377121.5	<3.619	4.94	6.87	1.69	1.03	1.33	2.32	15.24	46.8	255d-1018.4cpy
0c29f10	10	367219	292500.00	1.07	<0.704	334361.6	<2.732	19.63	<2.314	1.30	1.67	0.92	2.22	7.14	50.1	255d-1018.4cpy
0c29f11	11	462873	465600.00	12.24	5.27	1573.0	10.48	3174.55	1.19	1.13	0.29	54.81	1822.93	11.37	43.5	255d-1018.4py
0c29f12	12	480961	465600.00	4.26	36.97	251.0	11.14	43770.60	11.83	2.63	0.27	419.77	6481.86	39.18	20.7	255d-1018.4py
std-3	13	244409	415700.00	132.91	5627.81	542.1	101726.48	252.62	10.46	28.18	26.85	188.62	16970.33	6.61	43.5	stdgl-1
std-4	14	247010	415700.00	133.09	5624.19	543.9	101873.38	253.38	10.40	28.26	26.79	188.56	17029.66	6.67	42.5	stdgl-1
		1759	79.18	0.14	0.39	0.9	2.01	1.46	1.35	0.15	0.17	0.18	0.20	0.05		Run detection limit
std-1	01	245700	417018.54	132.71	5730.29	558.7	99467.02	261.01	10.81	31.58	27.17	192.34	17744.79	7.17	34.83	stdgl-1
oc26d02	02	258700	105193.36	<0.248	<0.706	650632.8	<3.536	2.60	2.84	6.38	0.69	<0.226	10.68	799.72	19.59	768-163.1bn
oc26d03	03	525800	478737.83	93.83	40.10	6813.0	22.07	61731.97	7.58	4.57	1.94	709.85	625.08	129.85	23.95	768-163.1py
oc26d04	04	525800	499909.85	416.32	428.82	6809.4	2.64	57594.87	80.52	11.55	0.60	764.01	1917.75	134.45	31.57	768-163.1py
oc26d05	05	525800	503581.28	331.63	261.17	10582.5	8.96	54820.87	61.38	9.42	0.40	663.04	1204.82	119.03	29.39	768-163.1py
oc26d06	06	200900	1022.31	<0.303	<0.799	674673.9	<5.806	<85.135	<2.554	17.09	1.05	0.35	1.55	37.88	22.86	768-163.1cc
std-2	07	245700	412922.68	133.58	5557.95	548.8	102152.75	251.15	8.82	25.02	25.88	184.65	16684.41	6.26	64.22	stdgl-1
oc26d08	08	200900	247.28	<0.143	0.42	779592.1	6.06	6.85	<1.800	31.44	1.98	<0.184	3.14	29.93	47.89	768-163.1cc
oc26d09	09	200900	474.66	<0.252	<0.821	869144.1	<2.704	29.05	10.75	25.84	1.07	<0.333	3.20	39.79	23.95	768-163.1cc
oc26d10	10	525800	566232.04	6.96	53.02	266.6	4.53	62271.63	19.66	3.84	1.09	671.10	766.09	3.57	17.42	768-170.1py
oc26d11	11	525800	512478.52	23.47	47.06	96.9	4.41	39398.41	24.44	86.85	0.69	630.99	2174.45	1.98	13.06	768-170.1py
oc26d12	12	525800	533230.01	57.76	67.70	769.3	<2.509	57383.17	17.22	15.54	1.33	423.73	1237.93	51.85	11.97	768-170.1py
oc26d13	13	258700	82356.52	<0.718	<2.049	500370.6	54.21	<8.132	<6.428	5.10	<0.875	<1.259	13.16	980.39	22.86	768-175.1bn
std-3	14	245700	415845.72	132.97	5622.26	540.6	101625.66	252.34	10.54	28.20	26.88	188.61	16952.94	6.62	46.81	stdgl-1
std-4	15	245700	415554.39	133.03	5629.75	545.4	101974.94	253.67	10.32	28.24	26.76	188.57	17047.32	6.66	46.81	stdgl-1
		1530	64.86	0.12	0.45	0.8	2.03	0.82	1.18	0.19	0.17	0.18	0.20	0.03		Run detection limit

Abbreviations for sulfide phase analysed: cc = chalcocite; bn = bornite; py and vpy = veined pyrite; dpy = disseminated pyrite; cpy = chalcopyrite

Sample ID (Lab Reference Number)		S	Fe	Co	Ni	Cu	Zn	As	Mo	Ag	Sn	Sb	Pb	Bi	Peak	Thesis Sample ID & Sulfide phase analysed
		ppm	ppm	ppm	ppm	ppm	ppm	ppm	ppm	ppm	ppm	ppm	ppm	ppm		
std-1	01	245700	429706.46	138.01	5822.07	554.5	102869.76	252.22	5.47	27.55	25.74	193.61	17160.04	6.50	40.3	stdgl-1
oc27a02	02	258700	105830.05	<0.173	<0.540	616953.8	17.96	2.84	3.54	7.80	0.97	0.44	10.95	912.94	44.6	768-175.1bn
oc27a03	03	258700	112930.16	<0.174	<0.448	686177.4	<4.364	2.44	<2.044	6.99	0.69	<0.221	12.84	1005.32	34.8	768-175.1bn
oc27a04	04	200900	<119.100	0.94	<0.766	689706.3	13.49	<1.147	<1.812	16.33	0.92	<0.291	3.41	32.76	19.6	768-175.1cc
oc27a05	05	200900	230.08	0.60	1.44	704778.8	12.91	1.90	<1.578	17.22	1.00	<0.277	2.34	32.83	38.1	768-175.1cc
oc27a06	06	525800	522858.32	90.83	28.86	10308.2	10.18	102.61	<1.118	2.73	0.21	14.88	982.40	100.98	45.7	768-175.1py
std-2	07	245700	391992.74	125.55	5333.68	526.0	97092.88	252.14	14.64	28.25	26.68	178.90	16117.43	6.54	41.4	stdgl-1
oc27a08	08	525800	511558.04	86.58	14.40	3888.6	5.30	31158.82	3.87	3.85	1.03	153.74	1074.40	62.45	23.9	768-175.1py
oc27a09	09	525800	492693.45	16.82	29.19	223.2	9.57	40581.45	3.91	18.92	1.16	384.74	814.69	14.89	19.6	768-202.0py
oc27a10	10	525800	539893.83	94.84	110.20	541.3	6.93	30000.77	6.04	19.00	1.73	151.68	982.66	111.08	46.8	768-202.0py
oc27a11	11	258700	97767.25	2.70	1.10	730027.3	3.03	24.11	<1.942	8.90	0.96	<0.319	6.23	888.71	27.2	768-202.7abn
oc27a12	12	258700	137986.78	23.30	7.15	832487.9	<3.496	71.58	<2.353	5.45	0.61	0.55	6.49	864.63	38.1	768-202.7abn
oc27a13	13	525800	542810.35	89.61	14.19	9491.6	4.61	24099.30	8.18	14.55	0.83	314.32	914.09	126.87	38.1	768-202.7apy
std-3	14	245700	453467.50	148.95	6234.08	595.2	108920.55	267.28	10.78	31.16	31.70	204.19	18157.47	7.00	42.5	stdgl-1
oc27a15	15	525800	500894.25	72.01	8.46	11342.9	21.06	22933.79	6.56	44.42	5.65	188.86	694.63	92.79	51.2	768-202.7apy
oc27a16	16	200900	2859.40	0.44	<0.790	736469.7	9.12	7.12	<2.220	25.64	0.96	<0.343	7.28	91.89	35.9	768-202.7acc
oc27a17	17	200900	<137.071	<0.254	<0.886	834909.4	<3.729	2.82	<2.658	27.31	0.65	0.42	<0.411	25.98	20.7	768-202.7acc
oc27a18	18	258700	88487.66	<0.232	<0.840	579071.9	<3.748	<1.972	<3.038	4.43	0.47	<0.416	0.65	638.20	37.0	768-211.6bn
oc27a19	19	258700	75035.75	<0.226	<0.910	499423.6	<3.086	<1.622	<2.426	4.94	0.41	<0.390	2.73	648.55	41.4	768-211.6bn
std-4	20	245700	388477.46	119.84	5126.37	496.9	95463.99	240.44	10.52	25.94	23.22	177.96	16553.56	6.51	14.2	stdgl-1
		2261	95.85	0.18	0.65	1.4	2.80	1.25	1.60	0.28	0.24	0.28	0.36	0.04		Run detection limit
std-1	01	253630	415700.00	130.23	5570.13	539.9	97630.66	255.99	8.29	27.14	25.60	194.32	17628.37	6.85	13.1	stdgl-1
oc27b02	02	514214	465600.00	16.02	36.14	3240.2	12.47	7547.89	7.10	1.82	<0.218	32.11	335.77	20.57	16.3	768-211.6py
oc27b03	03	489517	465600.00	0.18	17.02	27.7	6.25	7012.47	6.04	1.91	0.32	31.33	553.70	0.08	33.7	768-211.6py
oc27b04	04	860351	<802.129	3.87	<6.484	4713897.0	<24.181	<12.065	<16.623	68.65	6.25	<2.548	<3.645	105.75	17.4	768-211.6cc
oc27b05	05	1817529	<1845.840	6.74	<10.390	9304603.1	<39.043	<21.372	<31.986	135.75	11.12	<3.713	15.31	315.97	39.2	768-211.6cc
oc27b06	06	1448242	<1503.106	<2.786	<9.854	7194602.4	<33.111	<16.408	<25.720	125.07	8.16	<3.506	<4.457	190.91	27.2	768-211.6py
std-2	07	236925	415700.00	134.41	5603.62	533.9	101096.96	242.44	13.01	28.81	27.48	181.75	16299.61	6.40	28.3	stdgl-1
oc27b08	08	493439	700.00	<0.792	<2.801	2490699.3	<11.788	<6.012	<8.144	44.51	1.80	<1.313	<1.880	51.94	26.1	768-208.9acc
oc27b09	09	1413680	<1216.706	3.63	<9.544	7207069.7	<33.107	<15.538	56.99	127.11	5.38	<3.747	4.37	204.31	25.0	768-208.9acc
oc27b10	10	264612	106000.00	<0.190	<0.680	757175.9	<3.064	<1.348	<2.147	6.92	1.20	0.35	3.30	756.03	27.2	768-208.9abn

Abbreviations for sulfide phase analysed: cc = chalcocite; bn = bornite; py and vpy = veined pyrite; dpy = disseminated pyrite; cpy = chalcopyrite

Sample ID (Lab Reference Number)		S	Fe	Co	Ni	Cu	Zn	As	Mo	Ag	Sn	Sb	Pb	Bi	Peak	Thesis Sample ID & Sulfide phase analysed
		ppm	ppm	ppm	ppm	ppm	ppm	ppm	ppm	ppm	ppm	ppm	ppm	ppm		
oc27b11	11	242733	106000.00	<0.207	<0.986	644209.8	<6.347	1.96	2.91	4.82	0.87	<0.497	<0.805	762.30	45.7	768-208.9abn
oc27b12	12	462654	465600.00	39.13	29.61	9945.3	9.51	11544.27	2.42	4.13	0.36	31.99	849.39	40.69	22.9	768-208.9apy
oc27b13	13	436546	465600.00	20.01	23.40	3225.6	7.57	15024.64	<1.518	2.82	<0.179	2.72	165.06	20.42	39.2	768-208.9apy
std-3	14	244995	415700.00	133.14	5659.76	538.6	101594.89	255.13	13.32	27.85	27.55	184.56	16541.47	6.47	32.7	stdgl-1
oc27b15	15	332334	292500.00	0.47	<0.937	377710.3	<5.759	3.56	2.72	<0.397	7.35	0.74	<0.753	3.50	46.8	768-189.8cpy
oc27b16	16	355860	292500.00	0.70	<0.907	363051.4	<3.241	5.00	<2.458	0.88	4.59	1.41	2.63	8.30	43.5	768-189.8cpy
oc27b17	17	361848	292500.00	0.30	<1.151	360222.6	<2.568	5.43	<2.909	1.00	4.83	1.92	1.66	8.57	49.0	768-189.8cpy
oc27b18	18	478078	465600.00	99.95	172.24	146.2	3.04	38556.18	29.62	46.80	1.85	296.25	1305.96	7.34	19.6	768-189.8py
oc27b19	19	484195	465600.00	102.24	77.35	2039.2	9.43	21400.87	9.16	7.11	1.75	74.39	2556.33	87.22	50.1	768-189.8py
std-4	20	247272	415700.00	134.15	5667.44	558.8	103845.71	258.06	7.03	29.04	26.62	193.72	17530.62	6.85	53.3	stdgl-1
		2005	84.98	0.16	0.58	1.3	2.48	1.11	1.42	0.25	0.21	0.25	0.32	0.04		Run detection limit
std-1	01	245700	402283.13	125.93	5388.24	522.3	94472.43	247.78	7.97	26.23	24.74	188.23	17079.65	6.64	13.1	stdgl-1
oc27b02	02	525800	475616.10	16.36	36.91	3309.2	12.73	7712.68	7.21	1.86	<0.224	32.84	343.39	21.03	16.3	768-211.6py
oc27b03	03	525800	499634.78	0.20	18.26	29.7	6.71	7527.95	6.44	2.05	0.34	33.65	594.83	0.08	33.7	768-211.6py
oc27b04	04	200900	<188.516	0.90	<1.524	1099684.5	<5.683	<2.836	<3.907	16.00	1.46	<0.599	<0.857	24.69	17.4	768-211.6cc
oc27b05	05	200900	<205.202	0.74	<1.155	1027615.1	<4.340	<2.376	<3.556	14.98	1.23	<0.413	1.69	34.93	39.2	768-211.6cc
oc27b06	06	200900	<209.559	<0.388	<1.374	997302.5	<4.616	<2.288	<3.586	17.32	1.13	<0.489	<0.621	26.48	27.2	768-211.6cc
std-2	07	245700	430768.65	139.24	5806.25	553.3	104754.82	251.37	13.40	29.83	28.45	188.49	16906.01	6.63	28.3	stdgl-1
oc27b08	08	200900	284.80	<0.324	<1.144	1013528.7	<4.817	<2.457	<3.328	18.10	0.73	<0.536	<0.768	21.15	26.1	768-208.9acc
oc27b09	09	200900	<173.405	0.51	<1.360	1023752.7	<4.718	<2.214	8.05	18.04	0.76	<0.534	0.62	29.04	25.0	768-208.9acc
oc27b10	10	258700	103569.41	<0.186	<0.666	739995.2	<3.002	<1.320	<2.103	6.76	1.18	0.34	3.23	739.21	27.2	768-208.9abn
oc27b11	11	258700	112910.87	<0.221	<1.052	686395.6	<6.774	2.08	3.09	5.13	0.93	<0.530	<0.859	812.52	45.7	768-208.9abn
oc27b12	12	525800	528886.37	44.44	33.64	11300.4	10.80	13120.74	2.74	4.70	0.41	36.36	965.48	46.25	22.9	768-208.9apy
oc27b13	13	525800	560548.40	24.09	28.17	3884.6	9.12	18098.20	<1.828	3.40	<0.215	3.28	198.84	24.60	39.2	768-208.9apy
std-3	14	245700	416737.06	133.47	5674.31	540.1	101865.27	255.90	13.30	27.92	27.61	185.11	16591.87	6.49	32.7	stdgl-1
oc27b15	15	339800	298974.91	0.48	<0.957	386187.9	<5.880	3.64	2.77	<0.406	7.51	0.75	<0.769	3.58	46.8	768-189.8cpy
oc27b16	16	339800	279225.93	0.66	<0.864	346677.1	<3.088	4.77	<2.342	0.84	4.38	1.34	2.51	7.93	43.5	768-189.8cpy
oc27b17	17	339800	274622.35	0.28	<1.078	338299.6	<2.405	5.10	<2.725	0.94	4.53	1.80	1.56	8.05	49.0	768-189.8cpy
oc27b18	18	525800	512004.11	109.92	189.42	160.8	3.35	42410.44	32.48	51.47	2.04	325.86	1436.56	8.08	19.6	768-189.8py
oc27b19	19	525800	505567.90	111.02	83.99	2214.8	10.24	23242.50	9.93	7.73	1.90	80.80	2776.46	94.73	50.1	768-189.8cpy
std-4	20	245700	413051.96	133.31	5631.63	555.3	103198.47	256.44	6.98	28.86	26.45	192.51	17422.11	6.80	53.3	stdgl-1

Abbreviations for sulfide phase analysed: cc = chalcocite; bn = bornite; py and vpy = veined pyrite; dpy = disseminated pyrite; cpy = chalcopyrite

Sample ID (Lab Reference Number)		S ppm	Fe ppm	Co ppm	Ni ppm	Cu ppm	Zn ppm	As ppm	Mo ppm	Ag ppm	Sn ppm	Sb ppm	Pb ppm	Bi ppm	Peak	Thesis Sample ID & Sulfide phase analysed
		138	6.13	0.01	0.04	0.1	0.16	0.08	0.13	0.02	0.01	0.02	0.02	0.00		Run detection limit
std-1	01	237070	415700.00	134.12	5658.80	548.1	98504.71	253.92	10.82	24.75	25.71	185.07	16824.75	6.28	39.19	stdgl-1
oc27c02	02	184942	106000.00	0.40	<0.677	524870.6	6.34	1.85	10.63	45.81	0.86	0.37	13.16	605.67	29.39	255a-1016.8bn
oc27c03	03	1530820	<1126.585	11.49	<6.726	7076813.5	<22.822	33.11	188.18	2655.80	3.40	<2.801	62.12	286.24	21.77	255a-1016.8cc
oc27c04	04	2568166	<2148.247	<3.719	<10.288	11202609.3	<43.494	<25.929	<45.608	3741.79	7.50	<4.282	28.38	393.09	23.95	255a-1016.8cc
oc27c05	05	594	700.00	<0.002	<0.005	3865.6	<0.026	0.05	0.07	0.40	0.01	0.00	0.05	5.69	13.06	255a-1016.8cc
oc27c06	06	5912	700.00	<0.010	<0.031	30108.9	<0.136	<0.061	<0.158	8.14	0.02	<0.018	0.60	5.95	8.71	255a-1016.8cc
std-2	07	254813	415700.00	133.52	5702.23	547.4	104043.58	256.53	10.89	33.00	29.61	194.17	17340.28	7.13	17.42	stdgl-1
oc27c08	08	327009	700.00	<0.512	<1.236	1453293.1	<5.614	<3.293	8.94	589.06	0.71	<0.659	<0.723	40.44	21.77	255b-1039cc
oc27c09	09	381665	700.00	<0.671	<2.213	2297641.8	<8.974	<4.074	18.61	898.39	1.67	<0.864	4.70	71.49	22.86	255b-1039cc
oc27c10	10	199410	106000.00	1.61	<0.557	641949.9	18.16	5.13	<2.318	78.36	2.33	<0.253	0.85	732.13	40.28	255b-1039bn
oc27c11	11	184618	106000.00	<0.209	<0.619	608823.7	<2.379	<1.370	12.57	81.79	0.35	<0.294	3.01	658.85	32.66	255b-1039bn
oc27c12	12	398811	465600.00	0.84	7.08	153.8	5.15	25905.24	14.40	2.95	<0.159	1119.24	656.86	1.18	10.89	255b-1039py
oc27c13	13	452302	465600.00	28.51	12.86	14849.3	6.94	24379.11	16.75	11.18	0.67	1130.25	1137.76	54.50	28.30	255b-1039py
std-3	14	232417	415700.00	130.52	5570.20	532.6	100200.40	250.39	10.24	27.99	26.24	188.23	16748.29	6.45	28.30	stdgl-1
oc27c15	15	306668	292500.00	459.39	170.58	353442.5	2.22	987.75	41.61	6.08	0.87	13.13	12.67	20.18	43.54	255b-901.4cpy
oc27c16	16	295933	292500.00	158.15	54.62	362731.0	<2.624	582.53	5.11	4.93	0.99	9.63	10.57	13.94	47.89	255b-901.4cpy
oc27c17	17	311329	292500.00	<0.225	0.69	370448.2	6.51	2.86	<3.061	0.85	0.83	1.27	2.63	2.37	45.72	255b-901.4cpy
oc27c18	18	518188	465600.00	4363.64	2573.54	22365.7	<4.659	22079.07	3.38	13.32	1.70	342.36	557.69	73.68	30.48	255b-901.4py
oc27c19	19	407758	465600.00	105.49	40.96	15241.4	5.54	12019.01	5.65	13.09	45.91	708.61	1235.35	54.91	28.30	255b-901.4
std-4	20	258547	415700.00	133.81	5567.52	543.5	101844.81	250.99	9.49	27.18	25.56	186.88	17087.50	6.70	29.39	stdgl-1
		2035	90.61	0.17	0.58	1.2	2.31	1.16	1.87	0.23	0.20	0.24	0.29	0.04		Run detection limit
std-1	01	245700	430324.86	138.79	5856.26	567.2	101966.20	262.80	11.19	25.73	26.65	191.70	17422.28	6.51	39.19	stdgl-1
oc27c02	02	258700	148087.26	0.56	<0.942	733001.1	8.86	2.59	14.82	64.25	1.20	0.51	18.40	847.70	29.39	255a-1016.8bn
oc27c03	03	200900	<147.237	1.51	<0.879	927185.6	<2.983	4.34	24.62	349.40	0.45	<0.366	8.14	37.58	21.77	255a-1016.8cc
oc27c04	04	200900	<167.417	<0.290	<0.802	874842.4	<3.390	<2.021	<3.554	293.33	0.59	<0.334	2.22	30.76	23.95	255a-1016.8cc
oc27c05	05	200900	236372.90	<0.557	<1.784	1305011.9	<8.911	17.34	22.36	134.07	1.98	1.07	16.40	1926.11	13.06	255a-1016.8cc
oc27c06	06	200900	23749.47	<0.353	<1.044	1021317.2	<4.618	<2.077	<5.349	277.08	0.71	<0.601	20.21	202.03	8.71	255a-1016.8cc
std-2	07	245700	400156.02	128.51	5487.60	526.8	100174.48	246.89	10.47	31.85	28.52	186.97	16697.82	6.88	17.42	stdgl-1

Abbreviations for sulfide phase analysed: cc = chalcocite; bn = bornite; py and vpy = veined pyrite; dpy = disseminated pyrite; cpy = chalcopyrite

Sample ID (Lab Reference Number)		S	Fe	Co	Ni	Cu	Zn	As	Mo	Ag	Sn	Sb	Pb	Bi	Peak	Thesis Sample ID & Sulfide phase analysed
		ppm	ppm	ppm	ppm	ppm	ppm	ppm	ppm	ppm	ppm	ppm	ppm	ppm		
oc27c08	08	200900	429.29	<0.314	<0.758	891124.6	<3.441	<2.019	5.47	362.11	0.43	<0.404	<0.443	24.84	21.77	255b-1039cc
oc27c09	09	200900	367.78	<0.352	<1.163	1207033.3	<4.715	<2.140	9.75	472.99	0.88	<0.454	2.47	37.62	22.86	255b-1039cc
oc27c10	10	258700	137250.05	2.08	<0.721	831121.8	23.52	6.64	<3.002	101.64	3.02	<0.327	1.11	949.23	40.28	255b-1039bn
oc27c11	11	258700	148234.35	<0.293	<0.867	851333.8	<3.330	<1.918	17.53	114.53	0.49	<0.411	4.21	922.50	32.66	255b-1039bn
oc27c12	12	525800	612563.15	1.11	9.31	202.3	6.78	34073.84	18.89	3.89	<0.210	1472.57	864.48	1.55	10.89	255b-1039py
oc27c13	13	525800	540074.70	33.07	14.91	17223.6	8.05	28271.16	19.37	12.98	0.78	1311.00	1320.18	63.29	28.30	255b-1039py
std-3	14	245700	438459.64	137.69	5872.82	561.8	105698.81	264.02	10.77	29.53	27.65	198.52	17670.78	6.81	28.30	stdgl-1
oc27c15	15	339800	323339.10	507.91	188.48	390693.7	2.45	1091.54	45.83	6.72	0.96	14.51	14.00	22.33	43.54	255b-901.4cpy
oc27c16	16	339800	335041.59	181.19	62.53	415474.3	<3.015	667.02	5.84	5.65	1.13	11.02	12.11	15.98	47.89	255b-901.4cpy
oc27c17	17	339800	318446.69	<0.246	0.75	403297.0	7.09	3.11	<3.345	0.92	0.90	1.38	2.87	2.58	45.72	255b-901.4cpy
oc27c18	18	525800	471214.60	4417.27	2603.10	22634.7	<4.735	22335.50	3.40	13.46	1.72	346.35	564.56	74.61	30.48	255b-901.4py
oc27c19	19	525800	598781.61	135.70	52.65	19600.3	7.13	15449.47	7.23	16.81	58.89	910.85	1589.07	70.65	28.30	255b-901.4
std-4	20	245700	393956.94	126.84	5272.75	515.1	96510.27	237.73	8.94	25.69	24.15	177.00	16197.07	6.36	29.39	stdgl-1
		1342	58.44	0.10	0.37	0.7	1.46	0.77	1.10	0.15	0.17	0.15	0.18	0.02		Run detection limit
std-1	01	237886	415700.00	133.49	5644.50	546.3	99618.27	254.06	9.06	28.07	27.64	190.82	17029.23	5.64	47.9	stdgl-1
oc27d02	02	1683760	<1448.333	<2.158	<10.824	7111389.4	<47.546	<19.151	<29.916	3669.04	5.84	<3.737	11.87	183.65	19.6	255a-990.9cc
oc27d03	03	18183	700.00	0.05	<0.119	79562.4	<0.513	0.58	1.92	38.18	0.06	0.19	0.62	3.20	23.9	255a-990.9cc
oc27d04	04	179831	700.00	0.29	<0.877	785732.2	<3.372	3.62	7.86	375.16	0.59	<0.388	2.65	21.22	30.5	255a-990.9cc
oc27d05	05	386935	700.00	<0.520	<2.326	1787918.3	<10.939	12.69	<6.574	836.06	1.09	<0.922	1.63	44.39	44.6	255a-990.9cc
oc27d06	06	230628	106000.00	<0.171	<0.682	647118.8	<2.967	1.70	<3.019	109.56	0.60	0.56	10.61	674.62	50.1	255a-990.9bn
std-2	07	249612	415700.00	131.78	5572.08	536.0	100859.08	249.86	10.74	27.92	25.66	184.44	16853.72	7.87	33.7	stdgl-1
oc27d08	08	230294	106000.00	0.51	0.91	633707.0	<3.890	7.98	2.46	98.49	0.60	0.29	6.94	686.14	46.8	255a-990.9bn
oc27d09	09	430048	465600.00	6.21	4.16	9713.8	2.56	28823.81	3.47	7.14	0.47	70.31	249.70	12.16	30.5	255a-990.9py
oc27d10	10	441234	465600.00	9.16	10.26	123.2	3.07	27464.55	3.15	0.84	0.23	0.98	7.09	2.35	19.6	255a-979.6py
oc27d11	11	439717	465600.00	137.73	51.24	7023.5	5.35	51474.85	5.50	18.91	0.37	94.92	27.92	85.97	31.6	255a-979.6py
oc27d12	12	251934	106000.00	<0.191	<0.683	637587.3	<3.483	3.01	<2.313	80.17	0.61	1.52	10.13	635.15	43.5	255a-979.6bn
oc27d13	13	216686	106000.00	<0.154	3.37	590213.6	<2.803	33.40	<2.422	65.10	0.59	0.75	5.63	529.60	40.3	255a-979.6py
std-3	14	261105	415700.00	133.05	5566.18	555.8	104581.16	255.95	10.72	30.30	24.56	192.06	17235.86	6.85	13.1	stdgl-1
oc27d15	15	251545	106000.00	<0.201	<0.831	577888.0	<2.864	1.96	4.93	101.77	0.42	<0.288	0.91	381.22	39.2	255a-958.8bn
oc27d16	16	466249	465600.00	38.58	25.31	12997.7	4.17	41163.34	3.87	15.48	<0.261	151.97	148.41	26.63	30.5	255a-958.8py
oc27d17	17	420674	465600.00	<0.145	1.80	37.1	3.76	33794.88	1.83	1.02	<0.192	47.13	535.86	<0.034	17.4	255a-958.8py

Abbreviations for sulfide phase analysed: cc = chalcocite; bn = bornite; py and vpy = veined pyrite; dpy = disseminated pyrite; cpy = chalcopyrite

Sample ID (Lab Reference Number)		S	Fe	Co	Ni	Cu	Zn	As	Mo	Ag	Sn	Sb	Pb	Bi	Peak	Thesis Sample ID & Sulfide phase analysed
		ppm	ppm	ppm	ppm	ppm	ppm	ppm	ppm	ppm	ppm	ppm	ppm	ppm		
oc27d18	18	279032	106000.00	<0.245	<0.990	623499.8	<3.669	25.94	<2.462	105.42	<27.928	<0.340	<0.473	473.48	42.5	255a-958.8bn
oc27d19	19	213869	106000.00	1.69	0.81	571322.1	<2.340	2.72	42.09	54.28	0.52	0.85	19.50	752.11	37.0	255a-1016.8bn
std-4	20	234181	415700.00	133.67	5720.36	533.9	99351.76	252.13	10.91	26.61	29.39	187.06	16881.29	6.21	28.3	stdgl-1
		1742	78.46	0.14	0.39	0.9	1.99	1.45	1.34	0.15	0.17	0.17	0.20	0.05		Run detection limit
std-1	01	244922	415700.00	132.29	5712.50	557.0	99190.91	260.22	10.77	31.50	27.08	191.74	17691.43	7.15	34.83	stdgl-1
oc26d02	02	260681	106000.00	<0.251	<0.715	655651.1	<3.578	2.62	2.86	6.43	0.70	<0.228	10.76	806.01	19.59	768-163.1bn
oc26d03	03	511363	465600.00	91.26	39.00	6625.8	21.47	60038.50	7.37	4.44	1.88	690.40	607.95	126.30	23.95	768-163.1py
oc26d04	04	489704	465600.00	387.73	399.39	6341.5	2.46	53640.27	75.04	10.76	0.56	711.60	1786.11	125.23	31.57	768-163.1py
oc26d05	05	486132	465600.00	306.60	241.47	9783.0	8.28	50682.72	56.79	8.71	0.37	613.05	1113.90	110.05	29.39	768-163.1py
oc26d06	06	137558	700.00	<0.208	<0.548	461884.0	<3.981	<58.373	<1.751	11.71	0.72	0.24	1.06	25.94	22.86	768-163.1cc
std-2	07	247346	415700.00	134.47	5595.15	552.3	102829.77	252.81	8.89	25.19	26.06	185.89	16794.92	6.30	64.22	stdgl-1
oc26d08	08	568695	700.00	<0.405	1.19	2206387.3	17.16	19.38	<5.094	89.02	5.61	<0.522	8.90	84.72	47.89	768-163.1cc
oc26d09	09	296266	700.00	<0.371	<1.210	1281465.3	<3.985	42.84	15.86	38.11	1.58	<0.490	4.72	58.68	23.95	768-163.1cc
oc26d10	10	432344	465600.00	5.72	43.59	219.2	3.73	51198.14	16.17	3.16	0.90	551.83	629.87	2.93	17.42	768-170.1py
oc26d11	11	477694	465600.00	21.33	42.75	88.0	4.00	35790.44	22.22	78.91	0.63	573.27	1975.33	1.80	13.06	768-170.1py
oc26d12	12	459106	465600.00	50.44	59.11	671.6	<2.184	50100.64	15.04	13.57	1.16	369.99	1080.82	45.27	11.97	768-170.1py
oc26d13	13	332966	106000.00	<0.921	<2.628	643954.2	69.77	<10.429	<8.244	6.57	<1.122	<1.614	16.94	1261.79	22.86	768-175.1bn
std-3	14	245613	415700.00	132.92	5620.25	540.4	101588.33	252.24	10.54	28.19	26.87	188.54	16946.62	6.62	46.81	stdgl-1
std-4	15	245787	415700.00	133.08	5631.76	545.6	102012.55	253.76	10.33	28.25	26.77	188.64	17053.72	6.66	46.81	stdgl-1

Abbreviations for sulfide phase analysed: cc = chalcocite; bn = bornite; py and vpy = veined pyrite; dpy = disseminated pyrite; cpy = chalcopyrite

Sample ID (Lab Reference Number)		S	Fe	Co	Ni	Cu	Zn	As	Mo	Ag	Sn	Sb	Tl	Pb	Bi	Peak	Thesis Sample ID & Sulfide phase analysed
			ppm	ppm	ppm	ppm	ppm	ppm	ppm	ppm	ppm	ppm	ppm	ppm	ppm		
fb28c03	03	275755	106000	<0.523	<1.962	478182.20	<13.686	<2.857	<4.582	55.84	0.97	<0.845	<0.473	1.38	768.19	31	255c-1123-bn
fb28c04	04	275442	106000	4.00	7.19	541373.25	<12.858	9.65	<5.133	59.54	2.16	4.90	<0.442	14.91	858.71	29	255c-1123-bn
fb28c05	05	430702	465600	20.38	3.06	6905.02	<4.260	34385.93	21.41	2.53	0.40	104.93	578.63	505.46	13.61	38	255c-1123-dpy
fb28c06	06	410553	465600	34.71	1.44	5336.42	<3.455	47776.97	36.93	5.28	<0.374	178.65	1688.57	1319.62	19.97	36	255c-1123-dpy
fb28c07	07	410335	465600	10.56	23.69	2583.51	5.77	8731.09	37.82	3.32	0.57	845.42	1742.88	9.98	7.37	21	255c-1123-vnpy
fb28c08	08	414668	465600	117.02	35.27	4341.04	8.57	8436.09	25.46	5.70	<0.342	678.79	1719.85	38.03	16.22	36	255c-1123-vnpy
fb28c09	09	257679	106000	<0.433	1.32	504375.18	<11.329	<2.105	<3.098	63.07	1.02	6.77	4.14	7.47	501.02	39	255d-1000-bn
fb28c10	10	343552	106000	<0.604	<2.615	673661.80	<13.452	<2.786	<3.732	92.65	1.69	<0.888	<0.454	<0.675	612.35	31	255d-1000-bn
fb28c11	11	398176	465600	56.49	17.18	12016.74	5.26	32998.82	7.04	7.14	1.01	270.16	272.80	1159.52	40.82	20	255d-1000-vnpy
fb28c12	12	455461	465600	11.20	13.72	365.62	<5.034	61.01	2.73	0.28	<0.590	58.19	<0.153	7.77	4.06	13	255d-1000-vnpy
fb28a03	03	429266	465600	70.79	52.73	6969.46	<9.026	16065.82	9.58	5.78	0.66	346.12	50.10	476.91	60.50	20	255_981_vnpy
fb28a04	04	443616	465600	59.47	31.33	15601.96	<11.489	7314.10	4.63	5.12	1.69	135.95	86.54	1062.10	96.23	33	255_981_dpy
fb28a05	05	417169	465600	62.74	22.27	13740.74	10.11	11579.14	2.49	6.98	1.04	114.20	61.20	693.98	68.69	26	255-981-dpy
fb28a06	06	468949	465600	97.23	96.92	41168.85	18.17	12572.04	8.59	10.57	2.52	122.18	37.29	296.25	97.81	18	255-981-dpy
fb28a07	07	445131	465600	362.53	177.42	38559.60	<9.333	24645.59	83.27	23.07	1.85	336.71	385.63	594.25	183.24	33	255-981-dpy
fb28a08	08	415055	465600	200.68	351.56	7870.94	<9.660	10847.25	24.94	5.84	<0.647	138.45	221.12	238.11	55.55	23	255-981-dpy
fb28a09	09	484695	465600	6.39	26.97	84.97	<8.967	20009.11	8.23	1.98	<0.479	897.80	159.46	1817.26	5.88	29	255-981-vpy
fb28a10	10	448538	465600	134.48	309.55	3314.00	<8.887	27326.70	97.41	4.96	0.74	675.56	260.98	1242.04	30.13	18	255-981-dpy
fb28a11	11	474014	465600	102.47	75.95	11807.20	<10.349	13742.40	14.90	6.21	1.17	571.05	106.97	1064.20	84.01	21	255-981-dpy
fb28a12	12	428867	465600	106.23	81.24	10627.76	<9.259	20438.78	43.00	5.56	0.60	668.03	154.75	848.54	70.60	41	255-981-dpy
fb28a13	13	453266	465600	109.11	146.75	3257.08	<6.629	24522.98	93.81	4.82	0.70	560.44	113.71	863.65	31.98	28	255-981-dpy
fb28a14	14	477166	465600	170.43	187.92	11499.37	<7.940	26577.47	74.14	6.53	1.24	832.18	252.67	1348.96	88.36	34	255-981-dpy
fb28a15	15	405080	465600	0.23	1.58	18.22	7.20	47793.87	144.85	<0.196	0.95	267.13	2051.99	26.71	0.15	21	255-981-vnpy
fb28a16	16	438467	465600	<0.205	1.84	4.03	<7.695	56477.01	150.20	<0.169	0.90	315.90	1951.38	47.55	<0.034	13	255-981-vpy
fb28a17	17	222451	106000	<0.496	<1.859	542117.29	<12.489	<2.925	<4.371	87.00	<1.040	<0.755	<0.288	0.69	1388.57	34	255-981-vnbn
fb28a18	18	251966	106000	<0.496	<1.702	473679.08	<17.107	<3.163	<6.182	84.25	<1.211	<0.938	<0.423	0.91	1473.04	36	255-981-vnbn
fb28b03	03	466167	465600	304.34	79.51	10681.41	5.93	27930.00	33.00	11.94	0.56	1032.90	303.23	1748.77	102.60	28	754-251-dpy
fb28b04	04	452703	465600	153.23	111.92	8722.39	<4.739	23325.83	23.53	7.94	0.35	652.57	181.63	1088.44	58.40	31	754-251-dpy
fb28b05	05	457924	465600	881.45	259.19	19830.38	6.03	24101.85	174.38	40.78	1.07	683.89	184.67	1406.87	254.85	29	754-251-dpy
fb28b06	06	440389	465600	248.63	387.86	10487.51	9.50	5136.47	93.03	9.95	0.63	1290.96	543.94	386.39	72.19	36	754-251-dpy

Abbreviations for sulfide phase analysed: cc = chalcocite; bn = bornite; py and vpy = veined pyrite; dpy = disseminated pyrite; cpy = chalcopyrite

Sample ID (Lab Reference Number)		S	Fe	Co	Ni	Cu	Zn	As	Mo	Ag	Sn	Sb	Tl	Pb	Bi	Peak	Thesis Sample ID & Sulfide phase analysed
			ppm	ppm	ppm	ppm	ppm	ppm	ppm	ppm	ppm	ppm	ppm	ppm	ppm		
fb28b07	07	414588	465600	480.11	422.55	3988.71	<7.781	15028.21	17.84	25.44	0.75	287.63	179.26	1197.25	70.12	16	754-251-dpy
fb28b08	08	436415	465600	166.74	76.48	13571.73	<5.224	14884.03	9.98	7.43	<0.577	239.96	63.48	720.15	52.23	33	255-1009-dpy
fb28b09	09	426729	465600	826.15	542.12	30125.04	12.95	24458.22	313.51	31.50	2.70	318.56	123.11	1321.77	104.96	26	255-1009-dpy
fb28b10	10	294301	106000	<0.687	<2.207	586282.17	<20.532	<3.693	<5.167	28.49	<1.289	<1.289	<0.430	<0.749	777.07	39	255-1009-bn
fb28b11	11	245500	106000	<0.882	<2.110	504676.88	<15.447	<3.984	<6.322	36.00	1.82	<1.095	<0.489	<0.790	680.86	31	255-1009-bn
fb28b12	12	256235	106000	<0.742	<2.137	581335.01	<18.117	<2.585	<5.196	91.74	<1.406	<1.314	<0.404	0.87	369.95	33	255c-1001-bn
fb28b13	13	260336	106000	<0.428	<1.451	530800.95	<16.378	<2.533	<6.327	101.60	<1.817	<1.070	<0.425	6.10	348.43	33	255c1001-bn
fb28b14	14	387518	465600	126.37	122.81	3780.96	<4.846	30463.04	191.42	8.48	0.98	176.66	400.47	659.92	63.85	16	255c-1093-dpy
fb28b15	15	426160	465600	75.19	29.18	6047.57	<4.788	14483.67	17.20	4.79	0.44	657.30	190.10	905.67	14.49	23	255c-1093-dpy
fb28b16	16	437971	465600	307.09	76.77	32958.53	<5.226	15528.47	96.82	16.48	0.88	409.99	153.85	796.06	106.45	24	255c1093-dpy
fb28b17	17	400638	465600	76.77	40.29	3716.93	<5.242	8608.58	39.57	5.11	0.73	239.52	246.16	531.85	19.95	20	255c-1093-dpy
fb28b18	18	396569	465600	41.78	30.22	7310.03	<6.424	5217.67	18.98	3.02	0.65	121.42	193.46	278.69	23.25	23	255c1093-dpy
		2796	185	0.19	0.76	0.92	6.84	0.92	1.58	0.16	0.41	0.28	0.13	0.19	0.05		Run detection limit
std-1	01	244907	415700	128.82	5399.06	519.07	97632.58	237.87	9.24	28.01	26.00	184.78	1.10	16369.39	6.46	33	stdgl-1
std-2	02	236034	415700	131.52	5613.43	543.83	101634.84	257.39	11.04	27.23	26.49	184.36	1.25	16905.87	6.54	38	stdgl-1
fb28a03	03	429266	465600	70.79	52.73	6969.46	<9.026	16065.82	9.58	5.78	0.66	346.12	50.10	476.91	60.50	20	255_981_vnpy
fb28a04	04	443616	465600	59.47	31.33	15601.96	<11.489	7314.10	4.63	5.12	1.69	135.95	86.54	1062.10	96.23	33	255_981_dpy
fb28a05	05	417169	465600	62.74	22.27	13740.74	10.11	11579.14	2.49	6.98	1.04	114.20	61.20	693.98	68.69	26	255-981-dpy
fb28a06	06	468949	465600	97.23	96.92	41168.85	18.17	12572.04	8.59	10.57	2.52	122.18	37.29	296.25	97.81	18	255-981-dpy
fb28a07	07	445131	465600	362.53	177.42	38559.60	<9.333	24645.59	83.27	23.07	1.85	336.71	385.63	594.25	183.24	33	255-981-dpy
fb28a08	08	415055	465600	200.68	351.56	7870.94	<9.660	10847.25	24.94	5.84	<0.647	138.45	221.12	238.11	55.55	23	255-981-dpy
fb28a09	09	484695	465600	6.39	26.97	84.97	<8.967	20009.11	8.23	1.98	<0.479	897.80	159.46	1817.26	5.88	29	255-981-vpy
fb28a10	10	448538	465600	134.48	309.55	3314.00	<8.887	27326.70	97.41	4.96	0.74	675.56	260.98	1242.04	30.13	18	255-981-dpy
fb28a11	11	474014	465600	102.47	75.95	11807.20	<10.349	13742.40	14.90	6.21	1.17	571.05	106.97	1064.20	84.01	21	255-981-dpy
fb28a12	12	428867	465600	106.23	81.24	10627.76	<9.259	20438.78	43.00	5.56	0.60	668.03	154.75	848.54	70.60	41	255-981-dpy
fb28a13	13	453266	465600	109.11	146.75	3257.08	<6.629	24522.98	93.81	4.82	0.70	560.44	113.71	863.65	31.98	28	255-981-dpy
fb28a14	14	477166	465600	170.43	187.92	11499.37	<7.940	26577.47	74.14	6.53	1.24	832.18	252.67	1348.96	88.36	34	255-981-dpy
fb28a15	15	405080	465600	0.23	1.58	18.22	7.20	47793.87	144.85	<0.196	0.95	267.13	2051.99	26.71	0.15	21	255-981-vnpy
fb28a16	16	438467	465600	<0.205	1.84	4.03	<7.695	56477.01	150.20	<0.169	0.90	315.90	1951.38	47.55	<0.034	13	255-981-vpy
fb28a17	17	222451	106000	<0.496	<1.859	542117.29	<12.489	<2.925	<4.371	87.00	<1.040	<0.755	<0.288	0.69	1388.57	34	255-981-vnbn
fb28a18	18	251966	106000	<0.496	<1.702	473679.08	<17.107	<3.163	<6.182	84.25	<1.211	<0.938	<0.423	0.91	1473.04	36	255-981-vnbn

Abbreviations for sulfide phase analysed: cc = chalcocite; bn = bornite; py and vpy = veined pyrite; dpy = disseminated pyrite; cpy = chalcopyrite

Sample ID (Lab Reference Number)		S	Fe	Co	Ni	Cu	Zn	As	Mo	Ag	Sn	Sb	Tl	Pb	Bi	Peak	Thesis Sample ID & Sulfide phase analysed
			ppm	ppm	ppm	ppm	ppm	ppm	ppm	ppm	ppm	ppm	ppm	ppm	ppm		
std-3	19	241567	415700	128.26	5330.72	522.51	100452.76	263.21	<10.526	27.43	28.36	187.76	<1.195	17082.31	6.49	39	stdgl-1
std-4	20	239369	415700	132.08	5681.85	540.39	98809.57	231.95	14.58	27.81	24.15	181.38	1.39	16194.57	6.51	39	stdtgl-1
																	Run detection
		3106	205	0.21	0.69	1.21	5.33	1.02	1.81	0.20	0.42	0.36	0.14	0.22	0.06		limit
std-1	01	240460	415700	128.34	5343.28	524.22	100716.78	263.97	<12.053	27.49	28.25	187.96	<1.134	17041.67	6.48	39	stdgl-1
std-2	02	240475	415700	132.00	5668.53	538.62	98550.59	231.30	15.86	27.74	24.24	181.18	1.40	16233.14	6.52	39	stdgl-1
fb28b03	03	466167	465600	304.34	79.51	10681.41	5.93	27930.00	33.00	11.94	0.56	1032.90	303.23	1748.77	102.60	28	754-251-dpy
fb28b04	04	452703	465600	153.23	111.92	8722.39	<4.739	23325.83	23.53	7.94	0.35	652.57	181.63	1088.44	58.40	31	754-251-dpy
fb28b05	05	457924	465600	881.45	259.19	19830.38	6.03	24101.85	174.38	40.78	1.07	683.89	184.67	1406.87	254.85	29	754-251-dpy
fb28b06	06	440389	465600	248.63	387.86	10487.51	9.50	5136.47	93.03	9.95	0.63	1290.96	543.94	386.39	72.19	36	754-251-dpy
fb28b07	07	414588	465600	480.11	422.55	3988.71	<7.781	15028.21	17.84	25.44	0.75	287.63	179.26	1197.25	70.12	16	754-251-dpy
fb28b08	08	436415	465600	166.74	76.48	13571.73	<5.224	14884.03	9.98	7.43	<0.577	239.96	63.48	720.15	52.23	33	255-1009-dpy
fb28b09	09	426729	465600	826.15	542.12	30125.04	12.95	24458.22	313.51	31.50	2.70	318.56	123.11	1321.77	104.96	26	255-1009-dpy
fb28b10	10	294301	106000	<0.687	<2.207	586282.17	<20.532	<3.693	<5.167	28.49	<1.289	<1.289	<0.430	<0.749	777.07	39	255-1009-bn
fb28b11	11	245500	106000	<0.882	<2.110	504676.88	<15.447	<3.984	<6.322	36.00	1.82	<1.095	<0.489	<0.790	680.86	31	255-1009-bn
fb28b12	12	256235	106000	<0.742	<2.137	581335.01	<18.117	<2.585	<5.196	91.74	<1.406	<1.314	<0.404	0.87	369.95	33	255c-1001-bn
fb28b13	13	260336	106000	<0.428	<1.451	530800.95	<16.378	<2.533	<6.327	101.60	<1.817	<1.070	<0.425	6.10	348.43	33	255c1001-bn
fb28b14	14	387518	465600	126.37	122.81	3780.96	<4.846	30463.04	191.42	8.48	0.98	176.66	400.47	659.92	63.85	16	255c-1093-dpy
fb28b15	15	426160	465600	75.19	29.18	6047.57	<4.788	14483.67	17.20	4.79	0.44	657.30	190.10	905.67	14.49	23	255c-1093-dpy
fb28b16	16	437971	465600	307.09	76.77	32958.53	<5.226	15528.47	96.82	16.48	0.88	409.99	153.85	796.06	106.45	24	255c1093-dpy
fb28b17	17	400638	465600	76.77	40.29	3716.93	<5.242	8608.58	39.57	5.11	0.73	239.52	246.16	531.85	19.95	20	255c-1093-dpy
fb28b18	18	396569	465600	41.78	30.22	7310.03	<6.424	5217.67	18.98	3.02	0.65	121.42	193.46	278.69	23.25	23	255c1093-dpy
std-3	19	234758	415700	129.45	5482.22	518.60	96106.38	236.83	11.02	27.25	25.17	188.33	1.19	16264.53	6.12	29	stdgl-1
std-4	20	246189	415700	130.88	5530.06	544.23	103146.62	258.36	9.42	27.99	27.33	180.82	1.16	17012.40	6.88	31	stdgl-1
																	Run detection
		2730	172	0.18	0.61	1.21	4.03	0.86	1.44	0.16	0.36	0.30	0.13	0.21	0.04		limit
std-1	01	234237	415700	129.27	5444.58	513.41	94789.73	234.16	10.31	27.08	25.06	186.96	1.19	16163.68	6.08	29	stdgl-1
std-2	02	246731	415700	131.07	5568.09	549.62	104515.44	261.18	9.68	28.16	27.44	182.17	1.16	17115.63	6.92	29	stdgl-1
fb28c03	03	275755	106000	<0.523	<1.962	478182.20	<13.686	<2.857	<4.582	55.84	0.97	<0.845	<0.473	1.38	768.19	31	255c-1123-bn
fb28c04	04	275442	106000	4.00	7.19	541373.25	<12.858	9.65	<5.133	59.54	2.16	4.90	<0.442	14.91	858.71	29	255c-1123-bn
fb28c05	05	430702	465600	20.38	3.06	6905.02	<4.260	34385.93	21.41	2.53	0.40	104.93	578.63	505.46	13.61	38	255c-1123-dpy

Abbreviations for sulfide phase analysed: cc = chalcocite; bn = bornite; py and vpy = veined pyrite; dpy = disseminated pyrite; cpy = chalcopyrite

Sample ID (Lab Reference Number)		S	Fe	Co	Ni	Cu	Zn	As	Mo	Ag	Sn	Sb	Tl	Pb	Bi	Peak	Thesis Sample ID & Sulfide phase analysed
			ppm	ppm	ppm	ppm	ppm	ppm	ppm	ppm	ppm	ppm	ppm	ppm	ppm		
fb28c06	06	410553	465600	34.71	1.44	5336.42	<3.455	47776.97	36.93	5.28	<0.374	178.65	1688.57	1319.62	19.97	36	255c-1123-dpy
fb28c07	07	410335	465600	10.56	23.69	2583.51	5.77	8731.09	37.82	3.32	0.57	845.42	1742.88	9.98	7.37	21	255c-1123-vnpy
fb28c08	08	414668	465600	117.02	35.27	4341.04	8.57	8436.09	25.46	5.70	<0.342	678.79	1719.85	38.03	16.22	36	255c-1123-vnpy
fb28c09	09	257679	106000	<0.433	1.32	504375.18	<11.329	<2.105	<3.098	63.07	1.02	6.77	4.14	7.47	501.02	39	255d-1000-bn
fb28c10	10	343552	106000	<0.604	<2.615	673661.80	<13.452	<2.786	<3.732	92.65	1.69	<0.888	<0.454	<0.675	612.35	31	255d-1000-bn
fb28c11	11	398176	465600	56.49	17.18	12016.74	5.26	32998.82	7.04	7.14	1.01	270.16	272.80	1159.52	40.82	20	255d-1000-vnpy
fb28c12	12	455461	465600	11.20	13.72	365.62	<5.034	61.01	2.73	0.28	<0.590	58.19	<0.153	7.77	4.06	13	255d-1000-vnpy
std-3	13	240104	415700	130.32	5467.33	526.73	101139.93	251.05	7.84	27.33	25.14	183.39	1.17	16986.05	6.64	44	stdgl-1
std-4	14	240833	415700	130.01	5545.24	536.18	98109.57	244.15	12.57	27.91	27.36	185.77	1.18	16287.09	6.36	49	stgl-1
reference1																	
STDGL-1		245700	424746	133.000	5626.00	543.00	101800.00	253.00	10.43	28.22	26.82	188.59	1.200	17000	6.640		
reference2																	
RTS-4		359000	567000	186.000	7940.00	280.00	158.00	207.00						60.000	3.300		
reference3																	
CZN-1		302000	109300			1440.00	447400.00	260.00		93.00	65.00	520.00		74500	27.000		
standard average		240476	415700	130.2	5506.31	531.48	99638.67	247.63	10.10	27.62	26.25	184.57	1.2	16638.1	6.5		
standard std. dev.		5109	0	0.7	59.62	15.28	4158.81	11.38	1.95	0.50	1.33	2.18	0.0	482.1	0.4		
standard rsd		0	0	0.6%	0.01	0.03	0.04	0.05	0.19	0.02	0.05	0.01	0.9%	2.9%	5.6%		
average/cert		1	1	0.979	0.98	0.98	0.98	0.98	0.97	0.98	0.98	0.98	0.979	0.979	0.979		
avg abnd norm cps/ppm		6	73	81	68.56	66.19	29.80	9.92	86.17	91.17	149.31	42.09	124	153	144		
i.s. norm drift Fe 57		1	1	0.99	0.94	0.90	0.90	0.90	0.99	0.95	0.99	0.92	0.86	0.91	0.92		
sigma ratio		5	2	1.8	1.80	1.79	1.88	1.89	1.73	1.72	1.76	1.66	1.8	1.8	1.8		

Abbreviations for sulfide phase analysed: cc = chalcocite; bn = bornite; py and vpy = veined pyrite; dpy = disseminated pyrite; cpy = chalcopyrite

APPENDIX 3

WHOLE-ROCK GEOCHEMICAL DATA (XRF; MAJORS AND TRACES); TRACE ELEMENT GEOCHEMICAL COMPANY DATA (IPOES)

Sample Location	Sample ID	SiO_2 (wt %)	TiO_2 (wt %)	Al_2O_3 (wt %)	Fe_2O_3 (wt %)	MnO (wt %)	MgO (wt %)	CaO (wt %)	Na_2O (wt %)	K_2O (wt %)	P_2O_5 (wt %)	BaO (wt %)	Loss inc. S (wt %)	Total (wt %)
E Lens	SD254995.7	56.92	0.54	17.96	5.30	0.00	3.96	0.56	<0.05	12.24	0.42	N/A	3.18	101.34
E Lens	SD2541012.5	25.50	0.26	7.46	30.21	0.12	2.19	2.94	0.20	5.64	0.32	N/A	19.12	100.39
E Lens	SD2541042.5	51.16	0.28	8.57	14.51	0.10	2.03	3.12	0.18	6.82	0.14	N/A	11.24	99.50
E Lens	SD2541051.3	22.48	0.14	3.95	35.30	0.04	0.64	0.88	0.34	2.90	0.12	N/A	18.90	100.08
E Lens	SD2541134.9	31.32	0.18	5.52	33.49	0.06	4.15	0.20	<0.05	0.74	0.18	N/A	17.55	99.00
E Lens	SD2541140.4	70.44	0.14	4.73	11.06	0.04	3.08	0.10	0.05	1.04	0.08	N/A	5.72	99.99
E Lens	SD2541155.8	34.82	0.08	4.53	28.82	0.00	0.26	0.02	0.16	1.42	0.06	N/A	13.40	99.03
E Lens	SD255955.5	68.18	0.20	7.90	12.16	0.24	6.48	0.28	<0.05	0.14	0.22	N/A	3.77	99.67
E Lens	SD255970.5	67.98	0.18	9.45	8.62	0.26	8.54	0.14	0.05	0.08	0.10	N/A	4.42	99.94
E Lens	SD255981	55.38	0.16	4.59	19.16	0.02	0.38	0.02	0.30	0.90	0.06	N/A	15.92	99.62
E Lens	SD255988.5	40.14	0.16	3.92	31.42	0.02	0.42	0.02	0.09	0.72	0.06	N/A	20.06	99.39
E Lens	SD255997.5	65.60	0.24	5.22	17.71	0.02	0.50	0.12	0.09	1.18	0.12	N/A	8.40	99.90
E Lens	SD2551009.5	25.46	0.10	2.31	37.85	0.00	0.20		0.11	0.62	0.06	N/A	26.14	99.51
E Lens	SD2551017	75.90	0.06	2.90	13.73	0.02	0.32	0.04	0.07	0.50	0.02	N/A	6.04	100.85
E Lens	SD2551020	66.64	0.06	2.07	15.58	0.00	0.10	<0.01	<0.05	0.56	0.04	N/A	12.00	99.83
E Lens	SD2551027.5	65.22	0.06	3.12	15.46	0.00	0.18	<0.01	0.05	0.80	0.02	N/A	11.96	100.07
E Lens	SD2551035	57.58	0.06	2.23	23.96	0.00	0.20	<0.01	0.05	0.50	0.02	N/A	8.94	99.74
E Lens	SD2551041	78.34	0.08	3.64	14.25	0.00	0.87	0.02	<0.05	0.70	0.02	N/A	1.32	100.47
E Lens	SD2551050	54.96	0.08	2.67	3.70	0.02	0.14	0.02	0.13	0.36	0.06	N/A	2.09	99.52
E Lens	UD754226.1	36.72	0.32	9.76	25.59	0.00	0.74	0.06	0.18	2.12	0.10	N/A	5.78	100.15
E Lens	UD754243.5	57.98	0.12	5.44	19.24	0.02	0.34	0.16	0.07	2.10	0.14	N/A	9.74	99.69
E Lens	UD754251.8	40.42	0.18	6.57	28.98	0.00	0.38	0.30	0.15	2.48	0.30	N/A	15.58	99.14

Sample Location	Sample ID	SiO_2 (wt %)	TiO_2 (wt %)	Al_2O_3 (wt %)	Fe_2O_3 (wt %)	MnO (wt %)	MgO (wt %)	CaO (wt %)	Na_2O (wt %)	K_2O (wt %)	P_2O_5 (wt %)	BaO (wt %)	Loss inc. S (wt %)	Total (wt %)
E Lens	UD754284.7	38.12	0.10	5.14	35.66	0.02	0.58	0.08	0.65	1.72	0.10	N/A	7.72	99.72
E Lens	UD754299.6	75.94	0.08	4.77	9.93	0.02	2.54	0.14	0.07	1.28	0.12	N/A	2.06	100.48
4720 B&C Lens	UD64252.5	78.96	0.15	4.78	4.65	0.24	6.00	1.24	<0.05	0.00	0.86	0.00	2.97	99.88
4721 B&C Lens	UD64255.5	87.93	0.07	2.40	4.10	0.09	2.68	0.10	<0.05	0.01	0.01	0.27	1.89	100.72
4722 B&C Lens	UD642100.5	67.26	0.31	12.41	4.30	0.06	5.48	0.24	<0.05	0.91	0.15	0.01	6.13	99.18
4723 B&C Lens	UD642105	63.13	0.44	14.22	5.26	0.28	5.83	0.23	0.06	5.12	0.17	0.04	4.49	99.64
4724 B&C Lens	UD642109.5	62.98	0.42	13.89	4.94	0.07	5.23	0.34	0.13	6.87	0.28	0.19	3.82	99.48
4725 B&C Lens	UD642114	70.07	0.35	12.10	3.17	0.05	2.84	0.18	0.09	7.54	0.15	0.19	2.47	99.47
4726 B&C Lens	UD642118.5	73.56	0.33	10.94	2.90	0.02	1.43	0.17	0.06	7.46	0.15	0.13	2.18	99.79
4727 B&C Lens	UD642123	77.51	0.26	8.79	2.70	0.06	1.91	0.50	0.08	5.77	0.38	0.06	1.84	100.06
4728 B&C Lens	UD642124.5	77.58	0.30	8.94	2.10	0.03	1.31	0.08	0.07	5.77	0.10	1.21	2.30	99.99
4729 B&C Lens	UD71773.5	53.81	0.26	7.98	24.70	0.07	3.96	0.10	<0.05	0.77	0.06	0.01	4.60	99.57
4730 B&C Lens	UD71776.5	76.52	0.23	7.22	5.82	0.02	4.55	0.04	<0.05	0.31	0.02	0.00	3.64	99.27
4731 B&C Lens	UD71778	57.68	0.34	10.33	10.31	0.06	11.81	0.53	<0.05	1.49	0.35	0.01	5.95	99.08
4732 B&C Lens	UD71781	50.17	0.42	12.96	9.19	0.06	15.93	0.61	<0.05	2.21	0.41	0.02	7.61	99.74
4733 B&C Lens	UD73228	93.90	0.05	1.73	1.71	0.06	1.93	0.01	<0.05	0.02	0.01	0.00	0.99	100.42
4734 B&C Lens	UD73231	92.58	0.04	1.37	1.46	0.10	1.94	0.64	<0.05	0.01	0.01	0.00	1.48	99.69
4735 B&C Lens	UD73241.5	93.57	0.07	1.97	1.59	0.04	1.83	0.03	<0.05	0.06	0.01	0.00	1.03	100.24
4736 B&C Lens	UD73244.5	93.30	0.07	1.91	2.04	0.01	0.70	0.03	<0.05	0.84	0.01	0.01	0.78	100.31
4737 B&C Lens	UD73246	91.22	0.08	2.25	3.16	0.01	0.83	0.01	<0.05	0.56	0.01	0.01	1.36	100.42
4738 B&C Lens	UD73250.5	90.19	0.08	2.28	2.88	0.04	1.20	0.01	<0.05	0.49	0.01	0.01	1.72	99.96
4739 B&C Lens	UD73258	85.70	0.06	1.31	6.51	0.01	0.44	<0.01	<0.05	0.46	0.01	0.00	4.60	100.25
4740 B&C Lens	UD73261	79.65	0.07	2.31	8.02	0.01	0.94	0.01	<0.05	0.43	0.01	0.01	5.72	98.99
4741 B&C Lens	UD73267	92.07	0.07	1.84	2.61	0.02	1.24	0.01	<0.05	0.18	0.01	0.00	1.15	100.30
4742 B&C Lens	UD73271.5	95.58	0.06	1.78	1.06	0.01	0.53	<0.01	<0.05	0.75	0.01	0.01	0.52	100.46
4743 B&C Lens	UD73279	79.64	0.24	7.70	2.78	0.03	3.55	0.09	<0.05	0.58	0.06	0.01	3.29	99.13
4744 B&C Lens	UD73283.5	82.72	0.23	7.67	1.32	0.03	1.49	0.09	<0.05	4.28	0.08	0.04	1.31	99.94

Sample Location	Sample ID	SiO_2 (wt %)	TiO_2 (wt %)	Al_2O_3 (wt %)	Fe_2O_3 (wt %)	MnO (wt %)	MgO (wt %)	CaO (wt %)	Na_2O (wt %)	K_2O (wt %)	P_2O_5 (wt %)	BaO (wt %)	Loss inc. S (wt %)	Total (wt %)
4745 B&C Lens	UD73285	90.02	0.12	4.35	1.19	0.02	0.69	0.06	<0.05	3.17	0.06	0.03	0.55	100.30
4746 B&C Lens	UD73288.5	82.55	0.21	6.77	2.34	0.04	3.10	0.04	<0.05	2.61	0.03	0.02	2.36	100.19
4747 B&C Lens	UD73299	77.19	0.30	10.06	2.02	0.01	1.29	0.07	0.07	7.23	0.07	0.05	1.53	100.06
4748 B&C Lens	UD732103.5	80.70	0.20	7.45	2.52	0.02	2.14	0.10	<0.05	4.67	0.09	0.04	1.81	99.95
4749 B&C Lens	UD732120	67.77	0.32	9.54	1.69	0.11	3.09	3.92	0.05	6.90	0.12	0.05	6.02	99.67
4750 B&C Lens	UD73413.5	90.33	0.10	4.95	0.82	0.01	1.44	0.08	<0.05	0.81	0.03	0.01	1.84	100.89
4751 B&C Lens	UD73416.5	88.40	0.11	5.76	0.69	<0.01	0.77	0.12	<0.05	1.40	0.04	0.01	2.03	100.37
4752 B&C Lens	UD734127.5	91.71	0.07	2.09	2.69	<0.01	0.34	0.01	<0.05	1.10	0.02	0.01	1.60	99.94
4753 B&C Lens	UD734132	46.43	0.14	4.73	21.93	0.01	1.83	0.09	<0.05	0.48	0.03	0.01	17.81	98.28
4754 B&C Lens	UD734135	25.12	0.06	2.02	34.74	<0.01	0.88	0.02	<0.05	0.28	0.02	0.00	29.00	99.60
4755 B&C Lens	UD734136.5	58.38	0.16	5.20	15.64	0.02	1.69	0.03	0.06	0.85	0.03	0.00	13.58	98.72
4756 B&C Lens	UD734138	85.70	0.11	3.59	4.55	0.02	1.27	0.03	<0.05	1.02	0.02	0.01	3.41	100.40
4757 B&C Lens	UD734139.5	80.96	0.11	3.50	7.66	0.01	1.17	0.02	<0.05	0.81	0.02	0.01	5.50	100.47
4758 B&C Lens	UD734141	38.30	0.06	2.48	22.22	<0.01	0.86	0.02	<0.05	0.32	0.00	0.00	19.52	99.37
4759 B&C Lens	UD734144	50.01	0.09	2.73	20.18	0.01	1.07	0.03	<0.05	0.35	0.02	0.00	17.81	97.91
4760 B&C Lens	UD736124.5	59.14	0.36	11.46	2.71	0.14	3.46	5.07	0.07	8.39	0.37	0.06	7.92	99.38
D Lens	UD739124.5	91.29	0.06	3.20	2.16	0.02	1.57	0.03	<0.05	0.63	0.03	N/A	1.19	100.20
D Lens	UD739127.5	82.89	0.15	6.50	3.82	0.05	3.48	0.15	<0.05	0.75	0.11	N/A	2.80	100.73
D Lens	UD739130.5	90.11	0.09	3.86	2.18	0.02	2.02	0.04	<0.05	0.35	0.03	N/A	1.65	100.39
D Lens	UD739157.5	63.91	0.32	10.35	9.44	0.13	8.15	0.24	<0.05	0.54	0.15	N/A	6.18	99.60
D Lens	UD739160.5	53.83	0.34	10.86	16.00	0.19	9.63	0.58	0.08	0.85	0.35	N/A	7.37	100.27
D Lens	UD739163.5	72.57	0.35	8.81	6.24	0.10	6.21	0.19	<0.05	1.21	0.13	N/A	4.03	99.91
D Lens	UD744108	66.43	0.09	4.29	20.71	0.07	5.31	0.08	<0.05	0.04	0.02	N/A	3.18	100.38
D Lens	UD744115.5	81.79	0.07	3.35	6.39	<0.01	0.19	0.01	<0.05	0.53	0.01	N/A	3.48	99.35
D Lens	UD744118.5	79.73	0.09	2.69	7.99	0.01	0.19	0.01	<0.05	0.48	0.01	N/A	5.53	98.82
D Lens	UD744127.5	85.67	0.06	2.60	7.11	<0.01	0.17	0.01	<0.05	0.65	0.01	N/A	2.59	99.63
D Lens	UD744144	68.95	0.06	2.69	15.21	<0.01	0.34	0.02	<0.05	0.70	0.01	N/A	8.96	98.90

Sample Location	Sample ID	SiO_2 (wt %)	TiO_2 (wt %)	Al_2O_3 (wt %)	Fe_2O_3 (wt %)	MnO (wt %)	MgO (wt %)	CaO (wt %)	Na_2O (wt %)	K_2O (wt %)	P_2O_5 (wt %)	BaO (wt %)	Loss inc. S (wt %)	Total (wt %)
D Lens	UD744151.5	44.98	0.04	2.40	31.03	<0.01	0.24	<0.01	<0.05	0.74	<0.01	N/A	14.80	99.90
D Lens	UD744153	67.28	0.06	2.83	16.32	<0.01	0.41	0.01	<0.05	0.78	0.02	N/A	8.10	98.48
D Lens	UD744157.5	72.76	0.09	3.39	17.54	0.02	2.13	0.02	<0.05	0.39	0.01	N/A	1.69	99.47
D Lens	UD744168	81.03	0.15	6.60	3.75	0.03	3.10	0.23	<0.05	3.52	0.17	N/A	1.47	100.10
D Lens	UD744180	72.19	0.24	9.42	7.08	0.02	2.90	0.31	<0.05	4.32	0.22	N/A	1.92	100.30
D Lens	UD746111	78.01	0.07	2.91	13.11	0.03	3.25	0.03	<0.05	0.14	0.01	N/A	1.93	100.47
D Lens	UD746123	86.63	0.09	3.26	4.67	<0.01	0.23	0.02	<0.05	0.66	0.01	N/A	1.91	100.14
D Lens	UD746133.5	73.07	0.06	2.65	11.85	<0.01	0.10	0.01	<0.05	0.48	0.01	N/A	8.87	99.33
D Lens	UD746135	73.96	0.09	3.31	10.65	<0.01	0.12	<0.01	<0.05	0.51	0.01	N/A	8.43	99.29
D Lens	UD746144	70.93	0.08	2.65	15.98	0.01	0.46	0.01	<0.05	0.33	0.01	N/A	4.76	99.84
D Lens	UD746153	83.41	0.11	4.03	6.71	0.01	1.15	0.05	<0.05	0.67	0.02	N/A	2.30	100.08
D Lens	UD746159	62.62	0.08	2.46	15.98	0.01	0.46	0.02	0.08	0.40	0.02	N/A	8.07	98.77
D Lens	UD746169.5	69.70	0.08	3.31	23.07	0.01	0.91	0.06	<0.05	0.43	0.04	N/A	1.32	100.55
D Lens	UD746190.5	62.47	0.25	6.64	12.91	<0.01	0.33	0.19	<0.05	2.84	0.14	N/A	9.26	97.83
D Lens	UD746196.5	56.67	0.21	6.36	15.27	<0.01	0.23	0.29	<0.05	4.38	0.22	N/A	9.26	97.41
D Lens	UD746198	60.73	0.16	5.40	15.23	<0.01	0.14	0.08	<0.05	4.06	0.08	N/A	10.24	98.48
D Lens	UD746201	49.61	0.27	8.91	16.01	<0.01	0.29	0.16	0.13	6.53	0.13	N/A	11.65	97.42
D Lens	UD746207	44.83	0.34	10.20	16.35	<0.01	0.43	0.18	0.09	6.01	0.15	N/A	12.58	97.48
D Lens	UD746210	51.50	0.18	6.48	19.73	<0.01	0.36	0.12	<0.05	2.94	0.08	N/A	12.74	99.46
D Lens	UD746211.5	29.60	0.08	3.28	35.48	<0.01	0.24	0.10	<0.05	1.32	0.08	N/A	22.22	98.83
D Lens	UD746214.5	49.47	0.35	10.33	17.72	<0.01	0.58	0.26	<0.05	4.11	0.19	N/A	11.93	97.62
D Lens	UD746220.5	43.74	0.20	6.82	22.68	<0.01	0.22	0.18	<0.05	4.78	0.14	N/A	15.48	98.93
D Lens	UD746223.5	59.38	0.17	5.69	16.17	<0.01	0.27	0.10	<0.05	3.78	0.09	N/A	10.95	98.70
D Lens	UD746229.5	39.56	0.14	4.44	28.19	<0.01	0.22	0.68	<0.05	2.76	0.48	N/A	19.00	98.31
D Lens	UD746232.5	62.83	0.13	4.61	15.61	<0.01	0.25	0.12	<0.05	2.99	0.10	N/A	10.27	98.43
D Lens	UD746234	44.48	0.17	6.07	23.12	<0.01	0.34	0.08	0.09	3.74	0.07	N/A	17.05	97.62
D Lens	UD746237	69.40	0.23	7.54	9.01	<0.01	0.49	0.10	<0.05	4.44	0.08	N/A	6.74	99.43

Sample Location	Sample ID	SiO_2 (wt %)	TiO_2 (wt %)	Al_2O_3 (wt %)	Fe_2O_3 (wt %)	MnO (wt %)	MgO (wt %)	CaO (wt %)	Na_2O (wt %)	K_2O (wt %)	P_2O_5 (wt %)	BaO (wt %)	Loss inc. S (wt %)	Total (wt %)
D Lens	UD746244.5	78.33	0.31	8.68	3.80	0.01	1.05	0.12	0.08	5.57	0.09	N/A	2.07	100.21
D Lens	UD746264	69.77	0.33	12.14	3.99	0.04	3.72	0.24	0.06	6.42	0.19	N/A	2.97	100.23
2 Lens	767UD163.80	61.32	0.65	16.64	5.40	0.07	6.44	0.05	0.08	3.32	0.05	N/A	5.38	99.41
2 Lens	767UD186.50	88.08	0.07	3.78	3.20	0.03	2.27	0.03	<0.05	0.07	0.02	N/A	2.26	99.92
2 Lens	767UD217.00	94.68	0.03	1.89	1.18	0.02	1.25	0.00	<0.05	0.07	0.01	N/A	1.05	100.19
2 Lens	767UD230.10	87.57	0.05	2.19	4.83	0.07	2.01	0.57	<0.05	0.04	0.42	N/A	2.10	99.85
2 Lens	767UD241.20	82.49	0.10	6.42	3.46	0.05	4.07	0.07	<0.05	0.18	0.05	N/A	3.21	100.11
2 Lens	767UD246.50	86.05	0.07	4.61	3.31	0.05	3.33	0.02	<0.05	0.04	0.01	N/A	2.58	100.10
2 Lens	767UD249.00	83.19	0.07	3.23	9.86	0.04	1.90	0.01	<0.05	0.13	0.01	N/A	1.67	100.15
2 Lens	767UD253.80	60.28	0.11	2.99	25.90	0.13	2.05	0.13	<0.05	0.04	0.05	N/A	7.83	99.55
2 Lens	767UD261.40	91.64	0.04	2.24	3.04	0.02	1.06	0.02	<0.05	0.10	<0.01	N/A	1.65	99.82
2 Lens	767UD264.70	82.97	0.11	7.40	2.84	0.01	3.39	0.05	<0.05	0.19	0.01	N/A	3.17	100.15
2 Lens	767UD281.90	79.72	0.05	2.72	10.20	0.02	1.10	1.01	<0.05	0.13	0.71	N/A	4.26	99.95
2 Lens	767UD288.20	89.58	0.15	4.48	1.45	0.01	1.72	0.07	<0.05	0.38	0.05	N/A	2.12	100.02
2 Lens	767UD305.80	88.97	0.08	4.11	2.38	0.01	1.69	0.02	<0.05	0.16	0.01	N/A	2.40	99.84
2 Lens	768UD125.80	76.15	0.41	10.32	2.60	0.05	2.75	0.17	0.06	4.15	0.14	N/A	2.29	99.11
2 Lens	768UD139.50	82.91	0.10	5.30	6.98	0.01	0.58	0.12	0.05	1.23	0.12	N/A	2.52	99.95
2 Lens	768UD146.10	59.03	0.06	2.33	27.00	0.14	2.55	0.27	0.05	0.01	0.07	N/A	8.21	99.85
2 Lens	768UD152.00	71.31	0.07	3.70	17.49	0.02	1.09	0.07	<0.05	0.30	0.02	N/A	4.00	99.63
2 Lens	768UD156.00	73.98	0.08	4.31	10.73	<0.01	0.34	0.02	<0.05	0.90	0.01	N/A	6.58	99.49
2 Lens	768UD157.50	57.64	0.19	7.03	17.62	<0.01	0.55	0.03	<0.05	1.72	0.03	N/A	11.02	98.81
2 Lens	768UD160.50	37.61	0.07	3.22	32.53	<0.01	0.24	0.01	<0.05	0.73	0.04	N/A	18.64	97.84
2 Lens	768UD161.50	19.25	0.04	1.14	42.54	0.01	0.20	0.10	<0.05	0.28	0.05	N/A	25.41	98.16
2 Lens	768UD162.20	85.38	0.12	5.51	2.90	<0.01	0.77	0.05	<0.05	0.58	0.03	N/A	3.46	99.44
2 Lens	768UD163.10	19.64	0.20	3.80	38.39	<0.01	0.44	0.06	0.12	1.08	0.09	N/A	21.75	97.43
2 Lens	768UD166.10	71.04	0.08	4.06	12.65	<0.01	0.20	0.03	<0.05	1.05	0.03	N/A	7.90	99.40
2 Lens	768UD167.00	86.96	0.11	5.05	1.87	<0.01	0.20	0.06	<0.05	3.50	0.05	N/A	1.29	100.31

Sample Location	Sample ID	SiO_2 (wt %)	TiO_2 (wt %)	Al_2O_3 (wt %)	Fe_2O_3 (wt %)	MnO (wt %)	MgO (wt %)	CaO (wt %)	Na_2O (wt %)	K_2O (wt %)	P_2O_5 (wt %)	BaO (wt %)	Loss inc. S (wt %)	Total (wt %)
2 Lens	768UD170.50	82.98	0.11	4.23	5.47	<0.01	0.15	0.02	<0.05	2.58	0.02	N/A	3.38	100.10
2 Lens	768UD175.10	52.01	0.18	6.28	19.62	<0.01	0.41	0.03	<0.05	2.75	0.05	N/A	11.63	98.70
2 Lens	768UD184.10	58.07	0.20	6.73	17.30	<0.01	0.30	0.03	<0.05	3.60	0.07	N/A	9.79	98.81
2 Lens	768UD193.00	69.88	0.09	3.99	13.21	<0.01	0.19	0.02	<0.05	1.82	0.04	N/A	7.72	98.89
2 Lens	768UD202.00	91.75	0.07	3.78	0.96	0.01	0.74	0.02	<0.05	0.41	0.01	N/A	1.59	99.60
2 Lens	768UD239.10	88.02	0.12	5.76	0.61	0.00	0.11	0.03	0.13	4.92	0.03	N/A	0.24	99.97
2 Lens	768098145.50	79.16	0.05	2.53	11.34	0.10	2.42	0.15	<0.05	0.16	0.06	N/A	3.90	99.97
2 Lens	768102151.50	68.25	0.11	4.40	15.83	0.01	0.78	0.08	<0.05	0.69	0.03	N/A	4.23	99.50
2 Lens	768105156.00	72.70	0.08	4.28	9.97	0.01	0.37	0.03	<0.05	0.67	0.01	N/A	8.10	99.37
2 Lens	768106157.50	71.04	0.09	5.18	10.66	<0.01	0.43	0.02	<0.05	0.83	0.02	N/A	9.46	99.45
2 Lens	768108160.50	29.58	0.07	2.59	30.79	<0.01	0.23	0.04	<0.05	0.57	0.04	N/A	25.72	98.78
2 Lens	768109162.00	53.95	0.14	4.91	17.59	<0.01	0.68	0.05	<0.05	0.86	0.05	N/A	15.20	98.64
2 Lens	768111165.00	80.46	0.08	4.39	6.36	<0.01	0.34	0.04	<0.05	1.70	0.03	N/A	5.16	99.67
2 Lens	768112166.50	69.59	0.21	7.43	8.90	<0.01	0.36	0.07	<0.05	3.60	0.06	N/A	7.41	99.01
2 Lens	768114169.50	77.87	0.11	4.92	6.91	0.01	0.21	0.03	<0.05	2.44	0.03	N/A	5.62	99.24
2 Lens	768117174.00	58.78	0.12	5.48	16.44	<0.01	0.25	0.03	<0.05	2.43	0.04	N/A	12.39	98.55
2 Lens Surface	20774.5mN5.50	94.59	0.07	3.21	0.47	0.02	0.03	0.01	0.05	0.04	0.04	N/A	1.49	5.43
2 Lens Surface	20782mN13.00	94.61	0.07	3.22	0.78	0.01	0.02	0.01	0.05	0.15	0.01	N/A	1.17	5.49
2 Lens Surface	20799mN30.00	95.36	0.09	2.74	0.49	0.01	0.02	0.01	0.06	0.06	0.07	N/A	0.58	4.132
2 Lens Surface	20800mN31.00	90.87	0.11	2.23	4.24	0.03	0.13	0.04	0.05	0.04	0.05	N/A	1.52	8.44
2 Lens Surface	20800.5mN31.50	56.22	0.11	2.17	37.07	0.01	0.09	0.01	0.05	0.05	0.13	N/A	1.2	40.89
2 Lens Surface	20801mN32.00	93.20	0.09	3.62	1.46	0.01	0.07	0.01	0.06	0.23	0.02	N/A	1.26	6.83
2 Lens Surface	20804mN35.00	94.84	0.05	2.42	1.25	0.01	0.08	0.01	0.11	0.43	0.02	N/A	0.75	5.13
2 Lens Surface	20808mN39.00	95.64	0.05	2.83	0.38	0.03	0.02	0.01	0.05	1.34	0.02	N/A	0.95	5.68
2 Lens Surface	20817mN48.00	91.40	0.08	3.87	0.66	0.01	0.04	0.01	0.05	2.48	0.02	N/A	1.77	8.99
2 Lens Surface	20818mN49.00	95.24	0.07	2.86	0.36	0.01	0.03	0.01	0.05	1.03	0.02	N/A	3.42	7.86
4720 B&C Lens	UD61148.1	75.11	0.34	9.39	4.40	0.10	5.09	0.20	<0.05	0.52	0.13	N/A	4.27	99.58

Sample Location	Sample ID	SiO_2 (wt %)	TiO_2 (wt %)	Al_2O_3 (wt %)	Fe_2O_3 (wt %)	MnO (wt %)	MgO (wt %)	CaO (wt %)	Na_2O (wt %)	K_2O (wt %)	P_2O_5 (wt %)	BaO (wt %)	Loss inc. S (wt %)	Total (wt %)
4720 B&C Lens	UD61166.9	47.89	0.13	4.69	25.39	0.01	1.11	0.10	<0.05	0.81	0.06	N/A	15.80	98.85
4720 B&C Lens	UD642132	74.41	0.28	9.52	3.47	0.02	1.20	0.17	0.07	6.69	0.15	N/A	2.38	99.32
4720 B&C Lens	UD642189	68.79	0.27	10.16	5.33	0.02	0.72	0.92	0.06	8.43	0.22	N/A	3.45	99.14
4720 B&C Lens	UD65186.5	88.61	0.08	3.44	3.06	0.11	3.34	0.04	<0.05	0.04	0.02	N/A	1.63	100.39
4720 B&C Lens	UD651103	84.18	0.06	3.19	6.58	0.11	2.39	0.09	<0.05	0.03	0.05	N/A	1.72	99.53
4720 B&C Lens	UD651152.5	56.87	0.33	9.88	11.99	0.03	2.31	0.26	<0.05	4.53	0.20	N/A	10.89	98.62
4720 B&C Lens	UD651169	69.18	0.41	12.40	4.08	0.01	1.38	0.21	0.11	8.90	0.18	N/A	2.35	99.49
4720 B&C Lens	UD67614.6	91.30	0.11	3.49	0.28	0.01	1.27	0.08	<0.05	0.36	0.04	N/A	1.66	99.57
4720 B&C Lens	UD67621.1	88.55	0.05	4.27	0.70	0.06	3.24	0.09	<0.05	0.16	0.05	N/A	2.43	99.62
4720 B&C Lens	UD67636.2	68.88	0.06	3.14	2.04	<0.01	2.10	0.02	0.64	0.18	0.02	N/A	2.68	99.11
4720 B&C Lens	UD67650.3	76.00	0.06	1.80	6.69	<0.01	0.38	<0.01	0.06	0.74	<0.01	N/A	3.44	98.86
4720 B&C Lens	UD67673.4	80.50	0.22	8.78	2.74	0.02	1.26	0.04	<0.05	2.02	0.01	N/A	2.90	99.32
4720 B&C Lens	UD676110.5	67.45	0.52	14.62	2.11	<0.01	0.84	0.17	0.14	11.38	0.15	N/A	2.40	99.83
4720 B&C Lens	UD70887.2	25.32	0.32	19.57	22.52	0.57	17.57	1.44	<0.05	0.05	0.11	N/A	12.05	99.57
4720 B&C Lens	UD708126.1	60.08	0.09	3.38	18.32	0.03	0.91	0.02	<0.05	0.63	0.01	N/A	10.37	98.70
4720 B&C Lens	UD71722.1	88.45	0.07	2.19	2.63	0.11	2.40	1.20	<0.05	0.05	0.87	N/A	1.74	99.73
4720 B&C Lens	UD71744.2	80.86	0.06	2.15	7.99	0.04	0.91	0.01	<0.05	0.18	0.02	N/A	4.18	98.75
4720 B&C Lens	UD71750.6	81.13	0.04	1.68	8.80	0.03	0.73	<0.01	<0.05	0.21	0.01	N/A	4.71	98.55
4720 B&C Lens	UD71755	41.34	0.04	1.30	32.35	0.03	0.88	0.01	<0.05	0.03	0.01	N/A	16.05	99.35
4720 B&C Lens	UD71775	54.50	0.28	8.02	21.62	0.02	3.02	0.11	<0.05	0.83	0.08	N/A	5.00	99.15
4720 B&C Lens	UD71785	63.11	0.32	10.67	6.71	0.04	9.88	0.36	0.07	3.59	0.24	N/A	4.88	99.94
4720 B&C Lens	UD73214.2	90.73	0.04	2.24	1.61	0.07	3.09	0.05	<0.05	<0.01	0.03	N/A	1.81	99.69
4720 B&C Lens	UD73225.3	78.82	0.09	5.77	2.78	0.30	7.05	0.38	<0.05	<0.01	0.27	N/A	4.11	99.58
4720 B&C Lens	UD73238.6	91.76	0.07	1.84	1.08	0.02	1.67	0.04	<0.05	<0.01	0.03	N/A	1.30	99.48
4720 B&C Lens	UD73253.9	76.89	0.05	1.47	10.44	<0.01	0.46	0.01	<0.05	0.45	0.01	N/A	6.49	99.29
4720 B&C Lens	UD73275.3	96.22	0.04	1.17	0.48	<0.01	0.08	0.01	<0.05	0.86	0.01	N/A	0.43	99.45
4720 B&C Lens	UD73293	71.93	0.36	11.51	2.87	0.04	3.39	0.10	0.06	6.41	0.09	N/A	3.02	99.81

Sample Location	Sample ID	SiO_2 (wt %)	TiO_2 (wt %)	Al_2O_3 (wt %)	Fe_2O_3 (wt %)	MnO (wt %)	MgO (wt %)	CaO (wt %)	Na_2O (wt %)	K_2O (wt %)	P_2O_5 (wt %)	BaO (wt %)	Loss inc. S (wt %)	Total (wt %)
4720 B&C Lens	UD76036	87.71	0.05	3.05	2.99	0.12	3.66	0.02	<0.05	<0.01	0.01	N/A	2.10	99.71
4720 B&C Lens	UD76049.3	88.95	0.06	2.58	3.47	0.07	2.43	0.03	<0.05	<0.01	0.01	N/A	2.18	99.80
4720 B&C Lens	UD76061.5	94.99	0.07	2.36	0.35	<0.01	0.33	0.03	<0.05	0.55	0.01	N/A	0.86	99.56

Sample Location	Sample ID	Y (ppm)	Rb (ppm)	Tl (ppm)	Pb (ppm)	Zn (ppm)	Cu (ppm)	Bi (ppm)	As (ppm)	Ni (ppm)	Se (ppm)	Co (ppm)	Ga (ppm)	S (ppm)	Sb (ppm)	Sn (ppm)	Zr (ppm)	Sr (ppm)	Ba (ppm)	Sc (ppm)	V (ppm)	Ag (ppm)	Mo (ppm)
E Lens	SD254995.7	18.70	212.30	2.68	10.10	64.10	1759.10	4.30	69.00	61.70	N/A	124.98	17.40	1.14	5.20	N/A	113.00	35.00	680.00	N/A	117.80	N/A	<1
E Lens	SD2541012.5	13.60	125.80	139.13	547.40	81.80	42200.00	102.70	7400.00	207.50	N/A	364.07	12.10	22.32	154.30	N/A	72.80	22.00	332.00	N/A	64.80	N/A	36.50
E Lens	SD2541042.5	12.60	152.90	133.12	237.00	45.90	4800.00	13.90	4800.00	83.80	N/A	125.74	12.10	10.98	65.30	N/A	112.40	38.00	418.00	N/A	60.90	N/A	10.30
E Lens	SD2541051.3	6.00	77.10	169.10	406.60	38.90	107200.00	200.90	6600.00	500.30	N/A	570.40	8.30	28.78	115.20	N/A	73.70	5.00	203.00	N/A	38.00	N/A	142.60
E Lens	SD2541134.9	15.83	30.13	428.45	142.93	358.77	35800.00	89.10	7400.00	192.43	N/A	163.65	12.60	24.66	166.35	N/A	78.45	<2	54.50	N/A	67.10	N/A	38.40
E Lens	SD2541140.4	17.90	30.90	46.26	35.20	351.00	25200.00	8.00	2385.00	53.10	N/A	59.06	6.60	6.92	20.12	N/A	70.54	3.00	62.00	N/A	60.50	N/A	4.60
E Lens	SD2541155.8	3.50	48.80	83.99	260.30	38.50	118000.00	142.10	4400.00	337.80	N/A	295.91	7.00	23.82	76.00	N/A	53.00	2.00	88.00	N/A	33.80	N/A	119.90
E Lens	SD255955.5	12.90	5.00	<2	9.60	58.00	666.50	27.10	136.20	52.50	N/A	88.28	8.90	0.04	10.60	N/A	142.40	7.00	191.00	N/A	75.10	N/A	2.80
E Lens	SD255970.5	17.50	2.90	<2	4.10	57.60	774.00	4.60	36.60	96.30	N/A	222.34	9.40	0.10	7.90	N/A	185.80	6.00	25.00	N/A	91.00	N/A	4.20
E Lens	SD255981	4.90	26.00	86.42	141.50	12.00	16400.00	77.60	4400.00	104.00	N/A	103.90	6.00	14.72	48.80	N/A	107.60	13.00	124.00	N/A	53.00	N/A	6.40
E Lens	SD255988.5	3.50	22.30	69.76	238.50	28.40	13000.00	100.50	4800.00	235.30	N/A	171.11	4.50	21.42	102.20	N/A	114.30	13.00	461.00	N/A	46.00	N/A	7.50
E Lens	SD255997.5	8.40	34.60	27.56	96.90	16.60	3400.00	29.10	1820.20	89.00	N/A	86.33	6.40	9.50	57.50	N/A	221.60	10.00	163.00	N/A	56.90	N/A	4.60
E Lens	SD2551009.5	2.80	20.00	197.68	404.40	25.10	41000.00	98.00	10000.00	131.60	N/A	222.90	3.00	29.86	120.50	N/A	86.60	<2	84.00	N/A	29.90	N/A	21.50
E Lens	SD2551017	3.60	13.20	48.14	66.80	14.00	8000.00	18.30	1705.60	105.70	N/A	60.59	2.40	5.18	22.80	N/A	59.40	5.00	43.00	N/A	63.90	N/A	3.30
E Lens	SD2551020	3.10	14.30	153.83	183.50	9.00	16600.00	38.40	4600.00	49.90	N/A	86.71	2.40	12.54	55.90	N/A	69.30	2.00	34.00	N/A	16.80	N/A	12.10
E Lens	SD2551027.5	2.20	21.20	186.95	156.70	10.10	18200.00	58.10	6000.00	48.20	N/A	89.63	3.90	11.62	53.10	N/A	61.70	<2	50.00	N/A	27.20	N/A	11.30
E Lens	SD2551035	2.20	15.60	89.25	156.50	11.20	46800.00	108.20	2200.80	69.10	N/A	57.16	2.70	10.18	43.20	N/A	78.50	<2	49.00	N/A	49.70	N/A	4.40
E Lens	SD2551041	3.40	21.10	3.16	29.50	14.30	9800.00	26.50	73.20	42.40	N/A	47.69	4.00	0.38	21.70	N/A	51.20	8.00	61.00	N/A	53.80	N/A	1.60
E Lens	SD2551050	2.60	9.00	<2	21.70		281600.00	150.20	273.50	21.40	N/A	21.35	<1	8.04	18.60	N/A	74.50	5.00	23.00	N/A	13.80	N/A	3.50
E Lens	UD754226.1	9.00	79.90	21.23	110.40	20.10	149600.00	321.30	884.50	57.30	N/A	33.40	13.90	9.34	42.10	N/A	87.00	28.00	1430.00	N/A	63.60	N/A	4.40
E Lens	UD754243.5	8.50	51.90	67.74	217.10	29.20	30000.00	62.90	3800.00	84.40	N/A	119.07	7.40	14.40	81.50	N/A	87.60	5.00	136.00	N/A	26.50	N/A	5.40
E Lens	UD754251.8	23.70	68.30	62.13	209.50	34.60	25400.00	89.30	4000.00	173.40	N/A	221.50	11.10	23.16	152.00	N/A	102.40	24.00	228.00	N/A	50.60	N/A	15.20
E Lens	UD754284.7	13.10	53.20	51.99	139.20	44.70	76800.00	83.50	1520.10	181.30	N/A	131.96	6.60	12.48	97.10	N/A	83.10	7.00	190.00	N/A	104.60	N/A	14.70
E Lens	UD754299.6	14.90	28.10	<2	7.00	40.30	28200.00	38.00	42.40	76.20	N/A	89.81	4.40	1.40	7.90	N/A	79.70	8.00	105.00	N/A	104.00	N/A	2.30
4720 B&C Lens	UD64252.5	13.50	<1.5	<1.5	4.02	118.32	90.38	24.00	38.70	276.80	N/A	767.25	5.40	<0.01	<2	N/A	212.37	2.97	13.00	N/A	64.51	N/A	0.90

Sample Location	Sample ID	Y (ppm)	Rb (ppm)	Tl (ppm)	Pb (ppm)	Zn (ppm)	Cu (ppm)	Bi (ppm)	As (ppm)	Ni (ppm)	Se (ppm)	Co (ppm)	Ga (ppm)	S (ppm)	Sb (ppm)	Sn (ppm)	Zr (ppm)	Sr (ppm)	Ba (ppm)	Sc (ppm)	V (ppm)	Ag (ppm)	Mo (ppm)
4721 B&C Lens	UD64255.5	11.00	<1.5	<1.5	36.45	41.51	9400.00	14.00	118.50	164.10	N/A	286.34	<1	0.46	8.80	N/A	82.91	1.98	2958.00	N/A	44.37	N/A	6.90
4722 B&C Lens	UD642100.5	29.90	33.15	2.13	16.38	63.24	15100.00	10.70	219.00	37.00	N/A	96.13	18.40	2.03	4.20	N/A	172.38	51.48	63.00	N/A	77.52	N/A	3.00
4723 B&C Lens	UD642105	20.90	99.55	<1.5	16.02	77.52	1699.98	3.00	123.20	32.70	N/A	110.89	14.80	1.19	3.30	N/A	154.06	25.74	400.00	N/A	77.43	N/A	<1
4724 B&C Lens	UD642109.5	23.80	133.31	2.24	18.67	37.03	1619.38	3.70	177.00	44.50	N/A	137.03	17.10	1.14	5.90	N/A	218.64	31.68	1746.00	N/A	87.12	N/A	1.60
4725 B&C Lens	UD642114	23.10	144.53	2.25	18.17	30.29	1552.10	5.60	143.30	32.70	N/A	51.97	14.50	0.96	5.20	N/A	142.39	20.79	1671.00	N/A	83.32	N/A	1.70
4726 B&C Lens	UD642118.5	14.90	140.35	7.69	20.12	19.28	3300.00	7.30	295.30	31.20	N/A	39.76	11.40	1.37	6.30	N/A	138.38	18.81	1170.00	N/A	59.38	N/A	2.20
4727 B&C Lens	UD642123	24.40	108.73	2.11	18.51	26.01	1065.58	4.20	166.60	25.50	N/A	33.71	8.10	0.90	5.20	N/A	122.11	28.71	544.00	N/A	52.25	N/A	1.70
4728 B&C Lens	UD642124.5	14.00	120.97	<1.5	11.73	18.46	1191.74	<2	107.10	21.90	N/A	25.29	5.30	1.09	3.60	N/A	220.50	86.13	12100.00	N/A	63.18	N/A	1.20
4729 B&C Lens	UD71773.5	12.70	19.89	5.93	54.89	37.33	25400.00	93.40	446.70	108.30	N/A	152.06	9.00	2.55	58.10	N/A	184.83	23.76	69.00	N/A	83.79	N/A	9.80
4730 B&C Lens	UD71776.5	10.90	10.20	<1.5	12.14	11.63	7100.00	19.30	27.30	71.70	N/A	76.90	8.30	0.27	8.00	N/A	136.22	7.92	32.00	N/A	55.48	N/A	18.80
4731 B&C Lens	UD71778	16.40	39.78	<1.5	10.76	28.46	1173.12	12.50	79.80	79.60	N/A	123.96	11.40	0.05	23.90	N/A	153.17	6.93	123.00	N/A	79.52	N/A	5.20
4732 B&C Lens	UD71781	17.80	57.94	<1.5	15.01	33.05	1142.34	24.60	124.40	69.70	N/A	83.90	14.50	0.01	35.50	N/A	164.74	9.90	161.00	N/A	78.19	N/A	3.40
4733 B&C Lens	UD73228	9.20	1.22	<1.5	1.91	28.66	138.74	<2	24.20	46.80	N/A	91.31	1.50	0.06	<2	N/A	57.53	2.97	11.00	N/A	10.17	N/A	3.60
4734 B&C Lens	UD73231	1.60	0.61	<1.5	<1.5	21.83	295.78	3.40	44.00	32.40	N/A	64.72	1.10	0.03	<2	N/A	41.36	5.94	9.00	N/A	13.68	N/A	3.30
4735 B&C Lens	UD73241.5	2.60	1.94	<1.5	<1.5	20.20	231.30	<2	17.30	17.20	N/A	46.00	2.10	0.01	<2	N/A	92.32	<2	11.00	N/A	12.45	N/A	2.90
4736 B&C Lens	UD73244.5	3.40	21.01	<1.5	6.51	4.08	4800.00	2.50	49.60	14.60	N/A	15.17	1.90	0.47	4.50	N/A	185.61	5.94	81.00	N/A	11.02	N/A	2.80
4737 B&C Lens	UD73246	4.00	14.99	4.26	15.47	6.32	7200.00	6.40	132.80	20.20	N/A	20.31	1.40	1.14	5.20	N/A	204.62	3.96	57.00	N/A	10.93	N/A	3.10
4738 B&C Lens	UD73250.5	3.20	12.85	11.13	12.70	12.85	8200.00	5.60	149.70	23.10	N/A	39.15	1.70	1.41	2.60	N/A	119.85	3.96	75.00	N/A	12.64	N/A	3.10
4739 B&C Lens	UD73258	2.90	11.63	41.21	40.45	6.02	7700.00	7.50	1193.40	39.60	N/A	62.56	1.30	4.61	15.70	N/A	83.69	1.98	42.00	N/A	7.70	N/A	4.50
4740 B&C Lens	UD73261	3.60	10.51	69.93	34.47	11.73	13300.00	12.30	967.20	65.80	N/A	55.68	2.00	5.70	10.20	N/A	92.71	<2	52.00	N/A	10.26	N/A	3.70
4741 B&C	UD73267	4.00	4.49	3.82	5.83	16.83	8700.00	5.70	77.00	70.60	N/A	58.87	1.40	0.56	3.20	N/A	87.42	2.97	25.00	N/A	11.21	N/A	2.80

Sample Location	Sample ID	Y (ppm)	Rb (ppm)	Tl (ppm)	Pb (ppm)	Zn (ppm)	Cu (ppm)	Bi (ppm)	As (ppm)	Ni (ppm)	Se (ppm)	Co (ppm)	Ga (ppm)	S (ppm)	Sb (ppm)	Sn (ppm)	Zr (ppm)	Sr (ppm)	Ba (ppm)	Sc (ppm)	V (ppm)	Ag (ppm)	Mo (ppm)
Lens																							
4742 B&C Lens	UD73271.5	2.40	19.99	<1.5	4.08	7.04	825.76	<2	26.20	18.10	N/A	14.00	1.30	0.23	2.10	N/A	66.35	1.98	65.00	N/A	5.70	N/A	3.30
4743 B&C Lens	UD73279	8.60	21.11	<1.5	8.26	25.81	9100.00	16.00	195.60	118.30	N/A	123.40	9.80	0.60	4.80	N/A	152.29	5.94	47.00	N/A	39.05	N/A	2.50
4744 B&C Lens	UD73283.5	9.70	85.27	<1.5	3.82	16.52	5500.00	2.30	13.60	16.70	N/A	51.74	7.90	0.36	<2	N/A	118.58	11.88	320.00	N/A	30.88	N/A	1.90
4745 B&C Lens	UD73285	9.20	63.14	<1.5	5.00	7.96	155.79	<2	74.50	15.00	N/A	34.87	3.40	0.24	<2	N/A	80.07	4.95	231.00	N/A	17.77	N/A	2.90
4746 B&C Lens	UD73288.5	7.10	68.65	2.41	11.33	30.60	582.71	3.50	167.30	38.50	N/A	47.94	8.40	0.73	3.90	N/A	161.60	11.88	180.00	N/A	40.66	N/A	3.10
4747 B&C Lens	UD73299	13.90	136.58	1.71	12.22	17.14	784.89	2.30	175.20	69.90	N/A	74.70	9.60	0.86	2.50	N/A	124.75	14.85	476.00	N/A	47.69	N/A	2.10
4748 B&C Lens	UD732103.5	15.40	92.62	3.65	18.66	38.56	1064.13	3.50	221.60	324.60	N/A	105.86	7.30	0.85	3.50	N/A	145.92	11.88	353.00	N/A	32.78	N/A	3.00
4749 B&C Lens	UD732120	20.30	155.04	1.85	7.08	46.00	372.53	<2	133.30	90.60	N/A	103.00	12.70	0.23	3.20	N/A	141.12	63.36	449.00	N/A	57.57	N/A	1.90
4750 B&C Lens	UD73413.5	4.40	21.01	<1.5	1.77	15.91	3800.00	<2	14.80	17.20	N/A	24.76	4.50	0.22	<2	N/A	89.38	1.98	55.00	N/A	14.82	N/A	2.90
4751 B&C Lens	UD73416.5	4.10	34.17	1.73	<1.5	6.83	8300.00	1.80	16.90	9.80	N/A	7.73	5.30	0.40	<2	N/A	72.72	2.97	78.00	N/A	20.43	N/A	3.10
4752 B&C Lens	UD734127.5	2.60	23.46	8.26	20.61	5.92	1641.22	4.00	193.60	15.00	N/A	25.67	1.60	1.60	4.50	N/A	109.07	5.94	88.00	N/A	8.17	N/A	4.20
4753 B&C Lens	UD734132	9.10	13.77	133.20	129.76	37.94	35600.00	48.50	2200.00	243.10	N/A	201.49	5.30	17.00	25.60	N/A	278.71	2.97	46.00	N/A	14.35	N/A	7.10
4754 B&C Lens	UD734135	3.90	8.16	378.88	280.65	29.27	53800.00	62.30	4200.00	245.50	N/A	218.19	2.70	29.30	52.40	N/A	128.28	<2	36.00	N/A	10.26	N/A	12.40
4755 B&C Lens	UD734136.5	7.60	24.48	162.23	106.94	36.72	21700.00	34.60	1951.60	188.70	N/A	210.99	6.90	12.19	22.80	N/A	102.12	<2	33.00	N/A	24.70	N/A	4.80
4756 B&C Lens	UD734138	5.00	21.22	13.61	29.90	17.44	5100.00	3.00	243.20	42.40	N/A	68.86	2.00	2.74	5.80	N/A	170.81	6.93	76.00	N/A	8.17	N/A	2.80
4757 B&C Lens	UD734139.5	4.60	18.36	35.95	44.68	21.52	4800.00	6.70	652.40	45.00	N/A	61.15	2.80	5.38	8.30	N/A	160.43	6.93	59.00	N/A	7.60	N/A	4.60
4758 B&C Lens	UD734141	4.40	9.59	269.98	114.65	26.32	121600.00	93.40	2400.00	203.00	N/A	148.27	3.40	20.66	32.10	N/A	127.11	<2	40.00	N/A	12.35	N/A	9.80
4759 B&C Lens	UD734144	3.20	11.83	389.10	145.94	29.68	40500.00	66.10	3500.00	572.40	N/A	752.00	3.30	15.91	32.90	N/A	93.39	<2	29.00	N/A	15.39	N/A	10.50
4760 B&C Lens	UD736124.5	27.80	186.25	3.16	19.57	43.86	854.05	2.10	506.70	373.90	N/A	554.02	13.50	0.93	5.50	N/A	149.45	99.99	517.00	N/A	64.70	N/A	2.60
D Lens	UD739124.5	5.77	14.31	<1	2.60	11.80	149.80	<2	19.10	20.10	N/A	32.39	2.49	0.01	<2	N/A	63.27	6.86	55.00	N/A	14.36	N/A	3.20

Sample Location	Sample ID	Y (ppm)	Rb (ppm)	Tl (ppm)	Pb (ppm)	Zn (ppm)	Cu (ppm)	Bi (ppm)	As (ppm)	Ni (ppm)	Se (ppm)	Co (ppm)	Ga (ppm)	S (ppm)	Sb (ppm)	Sn (ppm)	Zr (ppm)	Sr (ppm)	Ba (ppm)	Sc (ppm)	V (ppm)	Ag (ppm)	Mo (ppm)
D Lens	UD739127.5	18.95	21.01	<1	3.00	25.60	238.70	<2	25.10	34.60	N/A	69.25	5.89	0.01	5.50	N/A	80.06	11.76	71.00	N/A	31.91	N/A	2.00
D Lens	UD739130.5	4.84	10.35	<1	2.00	13.60	264.60	<2	23.90	20.00	N/A	38.22	3.24	0.01	<2	N/A	87.09	7.84	35.00	N/A	17.27	N/A	4.20
D Lens	UD739157.5	16.89	19.18	1.46	6.00	63.40	1431.20	9.60	97.30	91.70	N/A	148.56	10.87	0.02	12.50	N/A	248.90	25.48	56.00	N/A	83.42	N/A	1.70
D Lens	UD739160.5	19.47	34.92	<1	12.10	116.30	1426.40	7.40	94.50	187.80	N/A	203.67	15.11	0.01	30.60	N/A	162.75	21.56	95.00	N/A	106.51	N/A	2.10
D Lens	UD739163.5	19.98	52.58	<1	2.80	47.40	468.80	<2	78.70	42.40	N/A	103.53	12.45	0.01	9.10	N/A	177.29	12.74	89.00	N/A	62.47	N/A	2.70
D Lens	UD744108	10.61	2.13	1.07	34.30	35.40	1101.50	27.10	131.90	103.80	N/A	159.68	5.15	0.02	30.40	N/A	91.09	4.90	53.00	N/A	49.76	N/A	5.00
D Lens	UD744115.5	3.30	12.79	23.67	58.20	3.50	27200.00	22.60	813.80	31.70	N/A	35.05	2.66	3.63	11.70	N/A	92.73	2.94	133.00	N/A	10.38	N/A	6.30
D Lens	UD744118.5	3.91	10.66	67.42	98.20	3.60	13900.00	13.20	2300.00	27.60	N/A	32.91	2.32	5.14	11.80	N/A	229.03	3.92	42.00	N/A	11.35	N/A	4.60
D Lens	UD744127.5	3.40	14.21	6.69	32.50	3.50	5400.00	9.60	569.70	18.50	N/A	25.74	1.58	2.62	10.90	N/A	81.17	6.86	181.00	N/A	21.63	N/A	5.20
D Lens	UD744144	4.74	15.73	172.27	181.30	6.20	10500.00	34.50	4200.00	54.30	N/A	54.40	2.74	9.46	60.40	N/A	123.72	1.96	40.00	N/A	32.11	N/A	5.50
D Lens	UD744151.5	8.34	19.39	100.10	169.10	9.50	40200.00	97.90	4200.00	64.20	N/A	56.46	2.24	14.78	67.20	N/A	60.37	3.92	83.00	N/A	120.57	N/A	7.00
D Lens	UD744153	4.12	17.46	60.53	113.10	5.60	18000.00	42.00	2700.00	56.40	N/A	42.45	1.99	8.60	33.70	N/A	62.17	5.88	56.00	N/A	30.56	N/A	4.70
D Lens	UD744157.5	7.21	8.22	<1	22.70	12.00	11300.00	21.40	68.30	50.90	N/A	48.76	1.49	0.48	21.20	N/A	115.24	0.98	66.00	N/A	59.17	N/A	3.70
D Lens	UD744168	11.74	65.57	<1	8.60	30.70	369.60	5.70	26.70	29.80	N/A	35.79	5.40	0.02	9.80	N/A	101.09	9.80	341.00	N/A	31.23	N/A	3.10
D Lens	UD744180	15.04	100.49	<1	5.90	44.80	13400.00	8.00	11.10	67.20	N/A	48.53	11.62	0.42	6.00	N/A	103.45	9.80	313.00	N/A	85.26	N/A	2.80
D Lens	UD746111	4.33	3.96	<1	36.40	15.50	7800.00	78.00	52.20	43.00	N/A	67.70	2.41	0.26	25.10	N/A	68.39	<2	44.00	N/A	39.77	N/A	4.60
D Lens	UD746123	4.02	14.11	17.07	17.50	2.30	20800.00	12.80	393.00	24.10	N/A	18.03	2.32	2.33	3.20	N/A	110.13	8.82	64.00	N/A	15.52	N/A	4.30
D Lens	UD746133.5	3.30	10.35	107.28	72.70	3.00	12800.00	19.20	4100.00	39.70	N/A	50.14	2.74	8.41	18.90	N/A	74.54	3.92	40.00	N/A	13.39	N/A	7.40
D Lens	UD746135	2.58	11.57	90.40	65.10	3.90	12500.00	20.30	4200.00	52.80	N/A	65.66	4.07	7.37	17.70	N/A	113.38	1.96	41.00	N/A	15.71	N/A	6.80
D Lens	UD746144	4.84	8.53	52.48	63.60	11.20	34200.00	32.90	2200.00	188.60	N/A	68.87	3.24	5.12	32.60	N/A	99.10	7.84	94.00	N/A	73.91	N/A	6.10
D Lens	UD746153	4.64	16.85	13.48	24.50	7.00	12300.00	16.60	555.40	34.70	N/A	33.32	2.74	1.97	8.30	N/A	111.95	4.90	53.00	N/A	34.92	N/A	3.90
D Lens	UD746159	4.43	11.88	184.98	112.90	12.30	62100.00	60.30	5200.00	70.20	N/A	47.23	1.83	10.35	54.60	N/A	114.23	<2	95.00	N/A	26.38	N/A	5.90
D Lens	UD746169.5	4.53	11.37	0.10	39.40	15.30	12700.00	22.10	154.10	68.50	N/A	37.76	3.40	0.54	38.90	N/A	89.14	6.86	62.00	N/A	92.73	N/A	5.50
D Lens	UD746190.5	9.68	79.47	18.33	115.10	28.00	19500.00	15.40	2300.00	64.70	N/A	80.27	9.38	10.00	31.80	N/A	146.32	14.70	639.00	N/A	45.98	N/A	5.90
D Lens	UD746196.5	6.70	104.85	40.74	96.80	15.40	32100.00	<2	3300.00	83.40	N/A	137.36	10.38	11.65	83.60	N/A	96.58	18.62	354.00	N/A	58.98	N/A	10.90
D Lens	UD746198	4.53	96.43	37.35	120.40	11.10	14800.00	<2	3300.00	65.70	N/A	135.11	7.30	11.95	81.00	N/A	86.96	12.74	332.00	N/A	43.36	N/A	10.50
D Lens	UD746201	7.11	141.69	38.02	150.80	19.50	25600.00	<2	3400.00	121.60	N/A	198.12	13.20	12.70	87.40	N/A	101.01	10.78	530.00	N/A	54.90	N/A	13.80

Appendix 3 Whole-Rock Geochemical Data (XRF; Majors and Traces); Trace Element Geochemical Company Data (IPOES)

Sample Location	Sample ID	Y (ppm)	Rb (ppm)	Tl (ppm)	Pb (ppm)	Zn (ppm)	Cu (ppm)	Bi (ppm)	As (ppm)	Ni (ppm)	Se (ppm)	Co (ppm)	Ga (ppm)	S (ppm)	Sb (ppm)	Sn (ppm)	Zr (ppm)	Sr (ppm)	Ba (ppm)	Sc (ppm)	V (ppm)	Ag (ppm)	Mo (ppm)
D Lens	UD746207	11.54	142.91	51.41	155.80	26.10	46600.00	5.00	3200.00	412.30	N/A	741.50	14.69	11.85	48.50	N/A	117.42	9.80	415.00	N/A	63.63	N/A	8.20
D Lens	UD746210	7.42	77.24	88.66	159.20	27.00	36200.00	2.50	5200.00	868.10	N/A	1610.53	10.04	15.77	57.60	N/A	82.43	4.90	218.00	N/A	46.08	N/A	11.10
D Lens	UD746211.5	5.56	39.08	587.14	440.60	33.70	40400.00	7.30	9000.00	545.60	N/A	829.25	7.89	28.33	99.30	N/A	44.34	<3	124.00	N/A	29.68	N/A	18.30
D Lens	UD746214.5	27.71	110.33	58.69	187.20	45.20	11000.00	7.50	8500.00	1722.90	N/A	3088.28	15.27	12.74	68.60	N/A	137.99	9.80	173.00	N/A	66.64	N/A	8.90
D Lens	UD746220.5	9.89	112.36	92.44	170.80	20.80	29800.00	19.70	6200.00	401.00	N/A	1147.65	9.96	18.84	131.00	N/A	82.91	11.76	449.00	N/A	52.57	N/A	17.80
D Lens	UD746223.5	14.42	97.74	54.51	136.60	18.20	11900.00	16.10	4000.00	86.00	N/A	248.26	10.54	12.00	86.60	N/A	102.34	14.70	409.00	N/A	49.86	N/A	10.10
D Lens	UD746229.5	12.36	69.53	114.36	259.40	24.00	14800.00	33.40	6400.00	138.80	N/A	261.35	4.57	23.06	114.40	N/A	73.26	40.18	2386.00	N/A	32.20	N/A	11.10
D Lens	UD746232.5	7.11	76.43	96.22	165.60	14.30	7800.00	20.40	3600.00	85.10	N/A	166.99	6.14	11.66	49.00	N/A	114.01	11.76	349.00	N/A	32.30	N/A	8.10
D Lens	UD746234	6.80	93.58	83.71	272.60	17.60	13200.00	32.10	4900.00	135.80	N/A	216.57	8.88	17.82	76.20	N/A	175.72	12.74	416.00	N/A	35.31	N/A	13.30
D Lens	UD746237	8.55	106.07	50.15	91.80	16.80	9200.00	16.30	1595.80	55.60	N/A	96.50	10.54	6.33	34.50	N/A	167.01	16.66	415.00	N/A	49.57	N/A	7.70
D Lens	UD746244.5	11.23	124.13	5.63	20.30	24.40	459.60	3.60	307.10	21.20	N/A	40.14	10.71	1.31	6.10	N/A	177.41	21.56	613.00	N/A	64.12	N/A	3.30
D Lens	UD746264	21.84	145.45	4.17	12.60	74.80	2700.00	2.50	129.50	24.20	N/A	41.16	14.86	0.93	<2	N/A	196.70	21.56	412.00	N/A	65.09	N/A	1.90
2 Lens	767UD163.80	16.50	139.38	2.75	2.50	48.76	115.68	<2	13.40	86.30	<1	101.20	24.20	<0.01	4.70	6.50	169.00	62.00	207.00	14.60	81.20	<20	N/A
2 Lens	767UD186.50	5.25	2.17	<1	7.85	40.05	789.89	2.34	11.60	39.00	<1	140.00	3.80	0.01	4.50	<1.5	86.10	11.00	17.00	<2	37.30	<20	N/A
2 Lens	767UD217.00	4.30	2.12	<1	<1.5	14.93	63.58	1.98	102.90	23.10	<1	83.70	1.90	<0.01	2.40	<1.5	29.60	6.00	11.00	<2	13.80	<20	N/A
2 Lens	767UD230.10	15.70	0.91	<1	3.70	25.91	83.73	<2	6.10	30.20	<1	84.90	1.50	<0.01	2.30	<1.5	154.10	3.00	12.00	<2	28.80	<20	N/A
2 Lens	767UD241.20	6.40	6.67	1.02	2.20	45.89	122.88	<2	11.70	38.80	<1	101.90	6.10	<0.01	2.80	<1.5	165.40	15.00	24.00	<2	26.80	<20	N/A
2 Lens	767UD246.50	4.90	1.01	<1	1.60	40.35	261.84	3.43	2.30	51.10	<1	112.70	4.00	<0.01	1.90	<1.5	106.20	3.00	11.00	<2	22.40	<20	N/A
2 Lens	767UD249.00	5.40	3.54	<1	13.80	25.42	270.50	20.18	21.10	38.60	<1	69.00	2.00	0.01	18.50	<1.5	115.60	5.00	19.00	<2	172.10	<20	N/A
2 Lens	767UD253.80	8.50	1.72	<1	35.90	60.92	233.23	16.95	59.50	138.40	<1	124.50	4.60	<0.01	41.30	<1.5	100.30	3.00	36.00	<2	170.60	<20	N/A
2 Lens	767UD261.40	3.50	3.23	<1	7.60	14.44	50.53	2.50	18.10	10.40	<1	37.50	1.60	0.05	2.20	1.50	101.40	18.00	20.00	<2	36.30	<20	N/A
2 Lens	767UD264.70	5.30	7.68	<1	0.90	35.90	49.17	<2	12.80	24.60	<1	82.60	6.60	0.02	10.20	<1.5	82.20	25.00	20.00	<2	48.80	<20	N/A
2 Lens	767UD281.90	12.10	3.33	<1	9.90	17.70	79.45	5.20	61.70	12.80	<1	56.10	2.50	0.01	<2	<1.5	170.90	17.00	19.00	<2	33.40	<20	N/A
2 Lens	767UD288.20	7.50	10.20	<1	<1.5	23.04	106.70	<2	6.70	18.30	<1	96.50	4.80	0.02	3.10	<1.5	81.50	6.00	9.00	<2	24.90	<20	N/A
2 Lens	767UD305.80	4.20	4.75	<1	1.70	20.97	48.23	<2	5.50	13.70	<1	73.70	4.20	<0.01	4.00	4.90	204.70	12.00	400.00	7.90	59.50	<20	N/A
2 Lens	768UD125.80	17.90	124.13	<1	3.20	20.67	149.19	<2	27.20	12.30	<1	30.80	13.10	<0.01	8.30	2.30	103.10	353.00	32.00	<2	46.50	<20	N/A
2 Lens	768UD139.50	20.80	18.58	<1	12.10	4.75	79.34	7.59	138.00	16.60	<1	20.20	4.60	0.01	48.10	<1.5	52.80	3.00	53.00	<2	43.60	<20	N/A

Sample Location	Sample ID	Y (ppm)	Rb (ppm)	Tl (ppm)	Pb (ppm)	Zn (ppm)	Cu (ppm)	Bi (ppm)	As (ppm)	Ni (ppm)	Se (ppm)	Co (ppm)	Ga (ppm)	S (ppm)	Sb (ppm)	Sn (ppm)	Zr (ppm)	Sr (ppm)	Ba (ppm)	Sc (ppm)	V (ppm)	Ag (ppm)	Mo (ppm)
2 Lens	768UD146.10	4.40	1.11	<1	85.50	54.89	552.28	21.11	419.20	45.10	<1	97.70	2.80	<0.01	17.80	<1.5	75.10	15.00	31.00	<2	83.10	<20	N/A
2 Lens	768UD152.00	4.80	6.26	<1	24.90	12.26	12500.00	22.15	22.60	50.70	1.30	41.70	3.20	0.33	35.10	<1.5	49.60	8.00	34.00	<2	14.40	<20	N/A
2 Lens	768UD156.00	3.10	19.80	34.99	172.00	6.73	17200.00	26.52	2500.00	59.80	<1	57.50	4.50	8.09	56.30	2.50	79.80	34.00	79.00	<2	72.40	<20	N/A
2 Lens	768UD157.50	4.90	51.41	163.91	235.80	10.88	14600.00	58.86	7500.00	129.20	<1	122.30	13.50	14.39	67.50	<1.5	48.70	22.00	43.00	<2	21.70	<20	N/A
2 Lens	768UD160.50	3.20	24.54	184.82	415.60	16.22	27900.00	91.42	8200.00	132.10	<1	161.60	7.10	25.17	379.50	2.60	24.80	9.00	33.00	<2	12.10	<20	N/A
2 Lens	768UD161.50	1.40	12.12	1185.55	717.70	36.00	40700.00	163.90	26400.00	159.10	<1	231.00	3.20	33.06	11.10	<1.5	74.80	120.00	30.00	<2	28.30	<20	N/A
2 Lens	768UD162.20	10.00	14.14	26.62	23.30	7.02	3800.00	7.18	1006.10	52.90	<1	54.70	5.10	2.04	139.50	2.20	41.60	67.00	86.00	<2	64.50	<20	N/A
2 Lens	768UD163.10	4.30	50.00	436.76	413.10	19.98	73800.00	185.43	17100.00	191.20	<1	189.30	11.30	30.73	23.10	<1.5	67.00	49.00	62.00	<2	18.50	<20	N/A
2 Lens	768UD166.10	15.40	24.34	78.13	125.40	7.81	14700.00	33.18	3400.00	64.30	<1	72.70	3.80	9.81	5.00	1.70	122.50	76.00	261.00	<2	18.30	<20	N/A
2 Lens	768UD167.00	6.20	76.86	4.08	20.90	3.36	9400.00	15.08	284.80	16.00	<1	61.20	3.60	1.35	15.60	2.00	160.00	32.00	182.00	<2	17.10	<20	N/A
2 Lens	768UD170.50	5.60	56.46	26.62	61.80	6.53	7300.00	16.33	1600.00	25.70	<1	38.90	4.00	4.22	30.60	3.80	74.30	110.00	224.00	<2	35.70	<20	N/A
2 Lens	768UD175.10	5.70	77.67	98.23	179.80	9.20	39500.00	77.90	5200.00	72.80	<1	125.40	8.40	15.27	21.30	2.90	77.70	166.00	457.00	<2	51.20	<20	N/A
2 Lens	768UD184.10	7.10	105.55	80.89	252.70	11.08	16800.00	63.54	4000.00	59.50	<1	120.00	11.30	13.04	40.70	2.10	70.30	84.00	161.00	<2	21.60	<20	N/A
2 Lens	768UD193.00	4.30	46.86	63.55	105.70	4.55	11400.00	24.34	3300.00	45.40	<1	71.40	5.30	10.45	<2	<1.5	62.20	23.00	25.00	<2	11.30	<20	N/A
2 Lens	768UD202.00	3.30	9.90	<1	6.60	6.82	1900.00	2.08	110.90	18.90	<1	38.40	2.50	0.28	<2	1.80	152.40	20.00	434.00	<2	8.60	<20	N/A
2 Lens	768UD239.10	6.50	105.14	<1	3.70	1.68	24.85	<2	13.80	4.60	<1	<2	3.70	<0.01	3.00	<1.5	62.60	11.00	16.00	<2	19.40	<20	N/A
2 Lens	768098145.50	4.30	3.43	<1	31.80	40.75	473.14	9.67	280.00	44.00	<1	184.60	2.70	<0.01	17.50	<1.5	50.70	8.00	30.00	<2	27.60	<20	N/A
2 Lens	768102151.50	7.20	13.13	<1	26.50	10.68	40500.00	34.32	94.70	35.60	<1	25.30	4.30	1.25	11.30	2.30	121.90	25.00	38.00	<2	61.70	<20	N/A
2 Lens	768105156.00	4.00	14.54	50.90	84.90	5.24	22000.00	28.50	2600.00	43.40	<1	45.90	3.60	6.58	20.10	<1.5	60.50	9.00	30.00	<2	19.90	<20	N/A
2 Lens	768106157.50	3.70	18.79	80.89	115.00	6.92	9000.00	27.46	3900.00	71.00	<1	69.70	5.60	7.76	33.60	<1.5	80.00	16.00	35.00	<2	19.20	<20	N/A
2 Lens	768108160.50	3.40	20.71	442.68	444.90	20.57	54600.00	131.66	15100.00	150.70	<1	180.30	5.10	22.31	137.20	<1.5	38.40	28.00	48.00	<2	19.00	<20	N/A
2 Lens	768109162.00	6.30	29.09	152.69	184.30	15.53	33200.00	61.15	6900.00	109.30	<1	121.70	8.50	14.14	48.60	<1.5	72.40	119.00	61.00	<2	44.00	<20	N/A
2 Lens	768111165.00	9.70	39.09	43.55	71.60	4.35	6500.00	15.91	1900.00	30.90	<1	44.90	4.00	4.84	14.30	<1.5	80.80	62.00	114.00	<2	16.60	<20	N/A
2 Lens	768112166.50	6.80	91.41	54.16	82.50	7.22	7700.00	27.77	2700.00	42.10	<1	63.10	10.00	6.85	21.10	1.60	99.00	110.00	269.00	<2	46.00	<20	N/A
2 Lens	768114169.50	6.00	55.05	30.29	71.30	5.34	5800.00	15.18	2400.00	24.40	<1	34.70	5.70	5.34	19.10	2.00	156.70	41.00	171.00	<2	19.30	<20	N/A
2 Lens	768117174.00	4.50	65.65	74.66	146.90	8.80	14200.00	35.98	5300.00	50.30	<1	74.40	7.50	13.19	38.30	<1.5	66.10	76.00	190.00	<2	27.50	<20	N/A
2 Lens	20774.5mN5.50	4.80	1.58	1.50	6.86	0.80	14.57	2.00	11.12	6.00	N/A	N/A	2.60	4.00	2.00	N/A	103.84	39.60	236.00	N/A	5.92	N/A	1.60

Sample Location	Sample ID	Y (ppm)	Rb (ppm)	Tl (ppm)	Pb (ppm)	Zn (ppm)	Cu (ppm)	Bi (ppm)	As (ppm)	Ni (ppm)	Se (ppm)	Co (ppm)	Ga (ppm)	S (ppm)	Sb (ppm)	Sn (ppm)	Zr (ppm)	Sr (ppm)	Ba (ppm)	Sc (ppm)	V (ppm)	Ag (ppm)	Mo (ppm)
Surface																							
2 Lens Surface	20782mN 13.00	2.60	2.87	1.50	5.71	1.00	15.49	2.00	12.38	5.80	N/A	N/A	2.00	2.30	2.20	N/A	98.87	20.79	102.00	N/A	13.19	N/A	1.65
2 Lens Surface	20799mN 30.00	4.00	1.49	1.50	77.85	1.00	40.01	2.00	28.08	7.10	N/A	N/A	1.70	4.60	8.10	N/A	149.89	312.84	223.50	N/A	8.58	N/A	1.45
2 Lens Surface	20800mN 31.00	5.40	1.39	1.50	82.13	1.00	561.32	19.30	937.17	3.90	N/A	N/A	1.50	4.00	51.60	N/A	149.66	95.04	209.00	N/A	22.50	N/A	2.35
2 Lens Surface	20800.5mN 31.50	5.30	1.68	1.50	462.50	15.80	949.46	50.60	2828.18	21.50	N/A	N/A	4.20	18.60	123.50	N/A	188.90	404.91	367.00	N/A	13.58	N/A	9.75
2 Lens Surface	20801mN 32.00	4.80	5.05	1.50	6.65	0.80	27.60	2.00	33.15	5.30	N/A	N/A	2.20	4.70	3.60	N/A	127.79	42.57	49.00	N/A	12.17	N/A	1.40
2 Lens Surface	20804mN 35.00	3.70	10.40	1.50	4.68	0.70	30.57	2.00	10.34	4.30	N/A	N/A	1.50	4.00	2.00	N/A	71.57	18.81	71.00	N/A	11.45	N/A	1.00
2 Lens Surface	20808mN 39.00	3.00	28.51	1.50	2.82	1.00	11.08	2.00	3.12	4.90	N/A	N/A	1.80	3.10	2.00	N/A	40.38	12.87	204.00	N/A	4.07	N/A	1.00
2 Lens Surface	20817mN 48.00	6.70	51.18	1.50	3.83	1.00	14.26	2.00	10.04	5.70	N/A	N/A	2.40	2.50	2.00	N/A	128.26	24.75	301.00	N/A	8.34	N/A	1.10
2 Lens Surface	20818mN 49.00	5.10	24.95	1.50	4.09	1.00	17.85	2.00	5.17	5.40	N/A	N/A	1.70	2.20	2.00	N/A	99.27	18.81	171.00	N/A	8.73	N/A	1.45
4720 B&C Lens	UD61148.1	9.80	16.60	0.99	6.65	73.82	243.30	<2	16.46	107.70	N/A	N/A	8.60	0.03	3.80	N/A	137.31	3.00	39.00	N/A	70.80	N/A	<1
4720 B&C Lens	UD61166.9	5.40	26.80	93.10	262.67	20.52	22773.66	39.20	4583.04	135.30	N/A	N/A	5.70	20.58	41.20	N/A	52.88	30.00	53.00	N/A	33.00	N/A	6.80
4720 B&C Lens	UD642132	13.70	122.30	4.13	24.38	24.70	7698.80	6.10	341.50	50.30	N/A	56.48	9.30	1.60	5.80	N/A	117.55	20.00	525.00	N/A	51.30	N/A	3.30
4720 B&C Lens	UD642189	29.90	173.90	10.61	56.16	32.97	6179.30	13.80	632.34	44.40	N/A	49.60	12.10	3.04	17.00	N/A	166.17	25.00	505.00	N/A	62.10	N/A	2.10
4720 B&C Lens	UD65186.5	4.80	1.20	<1	1.71	45.51	139.80	<2	7.00	60.80	N/A	163.15	2.90	<0.01	<2	N/A	102.60	1.00	9.00	N/A	24.40	N/A	1.50
4720 B&C Lens	UD651103	21.30	1.40	<1	4.82	27.27	9015.70	11.50	17.49	79.80	N/A	101.68	2.60	0.31	<2	N/A	104.80	1.00	13.00	N/A	54.10	N/A	11.90
4720 B&C Lens	UD651152.5	22.20	101.00	37.96	111.20	67.55	10500.00	36.00	2369.50	158.50	N/A	300.29	14.10	7.09	44.30	N/A	119.85	20.00	305.00	N/A	98.30	N/A	11.90
4720 B&C Lens	UD651169	20.70	166.10	4.15	26.21	37.62	2228.60	8.20	335.03	48.10	N/A	59.79	14.90	1.50	17.30	N/A	157.14	17.00	548.00	N/A	81.80	N/A	1.60
4720 B&C Lens	UD67614.6	11.50	7.20	1.27	2.73	23.85	7800.10	<2	26.55	1.40	N/A	N/A	3.60	0.25	<2	N/A	100.81	2.00	20.00	N/A	9.00	N/A	<1
4720 B&C Lens	UD67621.1	4.20	4.00	<1	<1.5	242.06	47.80	<2	13.65	8.40	N/A	N/A	4.40	<0.01	<2	N/A	60.41	5.00	17.00	N/A	10.90	N/A	<1
4720 B&C Lens	UD67636.2	4.50	3.40	10.17	26.73	1113.59	154600.00	49.10	174.85	23.40	N/A	N/A	3.10	5.02	3.70	N/A	157.61	3.00	23.00	N/A	13.10	N/A	1.40

Appendix 3 Whole-Rock Geochemical Data (XRF; Majors and Traces); Trace Element Geochemical Company Data (IPOES)

Sample Location	Sample ID	Y (ppm)	Rb (ppm)	Tl (ppm)	Pb (ppm)	Zn (ppm)	Cu (ppm)	Bi (ppm)	As (ppm)	Ni (ppm)	Se (ppm)	Co (ppm)	Ga (ppm)	S (ppm)	Sb (ppm)	Sn (ppm)	Zr (ppm)	Sr (ppm)	Ba (ppm)	Sc (ppm)	V (ppm)	Ag (ppm)	Mo (ppm)
4720 B&C Lens	UD67650.3	2.40	9.70	26.77	69.13	7.13	77400.00	40.30	1030.44	25.90	N/A	N/A	1.10	6.22	12.60	N/A	47.52	7.00	23.00	N/A	22.40	N/A	2.10
4720 B&C Lens	UD67673.4	7.90	45.90	2.11	9.95	21.00	6584.50	4.90	63.10	99.20	N/A	N/A	8.40	0.77	1.50	N/A	120.33	11.00	113.00	N/A	31.40	N/A	<1
4720 B&C Lens	UD676110.5	17.00	223.30	5.13	13.75	15.96	330.20	4.60	293.03	14.00	N/A	N/A	17.80	0.71	6.80	N/A	175.16	23.00	729.00	N/A	79.90	N/A	<1
4720 B&C Lens	UD70887.2	18.20	3.20	<1	17.17	277.12	386.90	9.10	37.57	299.70	N/A	N/A	21.70	0.01	13.60	N/A	346.11	5.00	50.00	N/A	136.20	N/A	1.10
4720 B&C Lens	UD708126.1	4.20	15.30	180.09	220.75	15.87	38951.14	73.30	6551.05	81.30	N/A	N/A	4.90	14.33	76.90	N/A	73.30	<1	36.00	N/A	14.30	N/A	17.00
4720 B&C Lens	UD71722.1	13.10	2.10	1.66	4.11	30.97	118.00	0.40	115.86	18.40	N/A	N/A	2.70	0.03	3.60	N/A	81.61	2.00	11.00	N/A	28.80	N/A	<1
4720 B&C Lens	UD71744.2	5.00	5.20	142.77	68.32	12.07	18740.50	25.40	2928.20	39.00	N/A	N/A	2.50	5.12	16.60	N/A	77.31	3.00	16.00	N/A	24.40	N/A	3.00
4720 B&C Lens	UD71750.6	4.10	5.40	144.66	102.12	12.35	9623.50	19.80	4137.12	28.90	N/A	N/A	<1	6.05	27.20	N/A	47.31	2.00	14.00	N/A	7.20	N/A	4.70
4720 B&C Lens	UD71755	4.90	2.10	151.52	184.92	19.48	58373.11	95.10	3442.11	54.80	N/A	N/A	<1	24.07	28.40	N/A	53.30	<1	17.00	N/A	15.60	N/A	4.30
4720 B&C Lens	UD71775	24.60	25.00	15.38	70.00	18.91	45281.10	137.30	549.16	145.00	N/A	N/A	10.50	3.58	49.40	N/A	124.84	15.00	80.00	N/A	123.80	N/A	12.00
4720 B&C Lens	UD71785	16.80	74.40	<1	11.86	26.13	467.40	32.10	91.81	58.20	N/A	61.80	11.00	0.01	19.00	N/A	186.23	12.00	277.00	N/A	74.80	N/A	7.50
4720 B&C Lens	UD73214.2	3.00	<1	1.86	<1.5	45.13	45.10	<2	41.46	84.00	N/A	N/A	3.50	<0.01	<2	N/A	63.44	14.00	6.00	N/A	13.10	N/A	<1
4720 B&C Lens	UD73225.3	12.40	<1	0.92	3.52	98.23	113.60	<2	93.72	145.30	N/A	N/A	7.60	0.02	<2	N/A	103.96	22.00	19.00	N/A	18.20	N/A	<1
4720 B&C Lens	UD73238.6	3.90	<1	1.96	1.51	20.33	13371.60	2.70	16.00	24.10	N/A	N/A	1.70	0.37	<2	N/A	109.30	1.00	10.00	N/A	22.90	N/A	<1
4720 B&C Lens	UD73253.9	2.40	11.90	55.99	116.25	38.19	24123.00	21.80	1370.40	55.20	N/A	N/A	1.20	9.06	13.30	N/A	47.01	4.00	40.00	N/A	5.30	N/A	3.50
4720 B&C Lens	UD73275.3	2.30	21.90	5.17	6.19	3.14	1020.10	<2	82.00	4.00	N/A	N/A	<1	0.31	<2	N/A	67.51	3.00	66.00	N/A	2.30	N/A	<1
4720 B&C Lens	UD73293	14.60	142.20	1.34	20.57	36.86	170.10	2.20	208.06	93.40	N/A	N/A	17.70	1.10	4.80	N/A	112.34	17.00	442.00	N/A	60.80	N/A	<2
4720 B&C Lens	UD76036	2.60	<1	<1	3.02	45.32	44.70	<2	67.00	71.80	N/A	N/A	3.40	0.01	<2	N/A	86.52	8.00	13.00	N/A	14.70	N/A	2.40
4720 B&C Lens	UD76049.3	2.60	<1	<1	1.92	41.23	137.10	2.10	64.76	68.50	N/A	N/A	3.40	0.01	<2	N/A	60.65	59.00	13.00	N/A	20.50	N/A	<1
4720 B&C Lens	UD76061.5	2.70	8.80	1.43	<1.5	3.61	379.10	<2	16.28	10.90	N/A	N/A	2.00	0.01	<2	N/A	80.12	7.00	28.00	N/A	4.80	N/A	<1

Sample Location	Drill Hole ID	Down Hole From Depth	Ag (ppm)	As (ppm)	Bi (ppm)	Co (ppm)	Cu (ppm)	Fe (wt%)	Mn (ppm)	Mo (ppm)	Ni (ppm)	Pb (ppm)	Sb (ppm)	Zn (ppm)
E Lens	SD255B	828.5	0.70	81.00	0.00	15.00	1310.00	4.30	425.00	0.00	12.00	0.00	0.00	26.00
E Lens	SD255B	830.0	0.50	38.00	0.00	8.00	1340.00	4.25	480.00	0.00	6.00	0.00	0.00	24.00
E Lens	SD255B	831.5	0.70	64.00	0.00	11.00	775.00	4.10	435.00	0.00	8.00	0.00	0.00	44.00
E Lens	SD255B	833.0	0.50	79.00	0.00	16.00	725.00	4.10	485.00	0.00	10.00	0.00	0.00	51.00
E Lens	SD255B	834.5	0.70	124.00	0.00	29.00	540.00	4.20	410.00	0.00	17.00	0.00	0.00	49.00
E Lens	SD255B	836.0	0.80	148.00	0.00	26.00	780.00	4.60	490.00	0.00	15.00	0.00	5.00	44.00
E Lens	SD255B	837.5	0.60	96.00	16.00	34.00	1290.00	6.50	855.00	0.00	19.00	0.00	0.00	34.00
E Lens	SD255B	839.0	0.70	223.00	16.00	67.00	935.00	6.80	580.00	0.00	31.00	6.00	7.00	48.00
E Lens	SD255B	840.5	0.80	124.00	0.00	52.00	1100.00	4.30	450.00	0.00	28.00	9.00	0.00	64.00
E Lens	SD255B	842.0	0.60	109.00	0.00	30.00	1550.00	3.25	390.00	0.00	18.00	6.00	0.00	65.00
E Lens	SD255B	843.5	1.00	181.00	16.00	94.00	2520.00	6.15	505.00	0.00	45.00	6.00	0.00	47.00
E Lens	SD255B	845.0	1.00	141.00	0.00	67.00	4570.00	4.35	340.00	0.00	35.00	6.00	0.00	40.00
E Lens	SD255B	846.5	0.90	120.00	0.00	68.00	3470.00	4.70	470.00	0.00	31.00	6.00	0.00	48.00
E Lens	SD255B	848.0	0.90	94.00	0.00	70.00	3050.00	3.90	500.00	0.00	24.00	0.00	0.00	51.00
E Lens	SD255B	849.5	1.80	102.00	12.00	111.00	14100.00	5.25	565.00	0.00	48.00	5.00	0.00	77.00
E Lens	SD255B	851.0	1.10	107.00	0.00	203.00	7080.00	5.70	420.00	0.00	99.00	0.00	0.00	91.00
E Lens	SD255B	852.5	0.70	129.00	0.00	81.00	4040.00	3.55	385.00	0.00	34.00	7.00	0.00	150.00
E Lens	SD255B	854.0	1.40	110.00	20.00	137.00	10300.00	5.15	395.00	0.00	68.00	0.00	0.00	131.00
E Lens	SD255B	855.3	0.40	82.00	15.00	190.00	2710.00	6.90	240.00	0.00	86.00	0.00	0.00	92.00
E Lens	SD255B	856.8	0.00	54.00	0.00	169.00	305.00	5.30	150.00	0.00	78.00	0.00	0.00	82.00
E Lens	SD255B	858.3	0.30	53.00	12.00	164.00	275.00	5.75	235.00	0.00	78.00	0.00	0.00	92.00
E Lens	SD255B	859.8	0.70	51.00	0.00	193.00	3570.00	4.15	175.00	0.00	115.00	0.00	0.00	83.00
E Lens	SD255B	861.3	1.20	60.00	24.00	300.00	10000.00	4.65	200.00	0.00	172.00	0.00	0.00	81.00
E Lens	SD255B	862.8	0.50	55.00	0.00	345.00	1570.00	5.85	170.00	0.00	167.00	0.00	0.00	93.00
E Lens	SD255B	864.3	0.30	37.00	0.00	260.00	835.00	3.45	95.00	0.00	112.00	0.00	0.00	78.00
E Lens	SD255B	865.8	0.80	52.00	0.00	158.00	3320.00	4.15	140.00	0.00	74.00	0.00	0.00	63.00
E Lens	SD255B	867.3	1.00	54.00	0.00	191.00	2800.00	4.85	80.00	0.00	97.00	0.00	0.00	72.00
E Lens	SD255B	868.8	0.30	42.00	10.00	287.00	1390.00	5.30	120.00	0.00	157.00	0.00	2.00	139.00
E Lens	SD255B	870.3	0.00	40.00	0.00	182.00	78.00	4.95	120.00	0.00	67.00	0.00	0.00	157.00

Sample Location	Drill Hole ID	Down Hole From Depth	Ag (ppm)	As (ppm)	Bi (ppm)	Co (ppm)	Cu (ppm)	Fe (wt%)	Mn (ppm)	Mo (ppm)	Ni (ppm)	Pb (ppm)	Sb (ppm)	Zn (ppm)
E Lens	SD255B	871.8	0.40	30.00	0.00	143.00	160.00	5.80	135.00	0.00	44.00	0.00	0.00	118.00
E Lens	SD255B	873.3	0.30	39.00	0.00	169.00	715.00	5.45	130.00	0.00	76.00	0.00	0.00	126.00
E Lens	SD255B	874.8	0.00	37.00	0.00	158.00	54.00	5.30	120.00	0.00	49.00	0.00	0.00	133.00
E Lens	SD255B	876.3	1.00	90.00	30.00	111.00	3130.00	3.40	75.00	0.00	53.00	0.00	15.00	92.00
E Lens	SD255B	877.8	1.20	135.00	23.00	96.00	2420.00	3.85	60.00	3.00	43.00	0.00	3.00	64.00
E Lens	SD255B	879.3	0.90	179.00	14.00	93.00	1360.00	4.60	65.00	0.00	40.00	0.00	3.00	63.00
E Lens	SD255B	880.8	1.40	282.00	35.00	128.00	6340.00	6.30	70.00	0.00	59.00	11.00	0.00	67.00
E Lens	SD255B	882.3	1.90	633.00	36.00	153.00	5570.00	5.70	0.00	0.00	82.00	37.00	15.00	45.00
E Lens	SD255B	883.8	0.70	318.00	0.00	93.00	2190.00	2.95	0.00	0.00	49.00	20.00	5.00	26.00
E Lens	SD255B	885.3	0.40	179.00	0.00	93.00	1210.00	3.75	0.00	0.00	41.00	14.00	3.00	25.00
E Lens	SD255B	886.8	1.00	456.00	0.00	99.00	2190.00	4.25	0.00	0.00	38.00	25.00	9.00	26.00
E Lens	SD255B	888.3	1.80	628.00	20.00	102.00	2660.00	4.15	0.00	0.00	56.00	34.00	12.00	27.00
E Lens	SD255B	889.8	1.50	681.00	0.00	131.00	2090.00	3.95	0.00	0.00	75.00	28.00	18.00	24.00
E Lens	SD255B	891.3	2.30	860.00	0.00	178.00	3590.00	5.65	0.00	0.00	73.00	38.00	20.00	35.00
E Lens	SD255B	892.8	0.60	257.00	0.00	106.00	850.00	3.15	0.00	0.00	26.00	15.00	5.00	47.00
E Lens	SD255B	894.3	1.10	363.00	0.00	106.00	1440.00	4.10	0.00	0.00	30.00	20.00	8.00	43.00
E Lens	SD255B	896.3	6.20	2810.00	45.00	217.00	17200.00	17.30	0.00	7.00	91.00	117.00	80.00	51.00
E Lens	SD255B	897.8	3.70	2400.00	17.00	530.00	7990.00	11.80	0.00	3.00	295.00	78.00	42.00	53.00
E Lens	SD255B	899.3	4.80	2680.00	18.00	739.00	9150.00	11.30	0.00	3.00	426.00	82.00	46.00	52.00
E Lens	SD255B	900.3	11.10	4860.00	49.00	1120.00	31500.00	22.30	0.00	7.00	610.00	167.00	119.00	49.00
E Lens	SD255B	901.5	3.60	2160.00	14.00	466.00	8020.00	9.80	0.00	4.00	285.00	67.00	46.00	51.00
E Lens	SD255B	903.0	6.70	2450.00	23.00	342.00	12300.00	12.90	0.00	5.00	159.00	104.00	62.00	69.00
E Lens	SD255B	904.5	2.30	1205.00	0.00	184.00	3960.00	10.10	0.00	0.00	91.00	49.00	24.00	65.00
E Lens	SD255B	906.0	2.80	1655.00	0.00	248.00	5630.00	9.95	0.00	2.00	147.00	65.00	35.00	57.00
E Lens	SD255B	907.5	2.60	1565.00	0.00	142.00	5200.00	8.75	0.00	3.00	52.00	71.00	38.00	47.00
E Lens	SD255B	909.0	1.30	484.00	0.00	88.00	1960.00	4.65	0.00	0.00	26.00	23.00	8.00	40.00
E Lens	SD255B	910.5	0.80	366.00	0.00	95.00	915.00	5.15	0.00	0.00	25.00	15.00	4.00	45.00
E Lens	SD255B	912.0	3.20	1980.00	0.00	141.00	7150.00	12.80	0.00	0.00	46.00	91.00	37.00	60.00
E Lens	SD255B	913.5	2.60	1100.00	0.00	119.00	5640.00	7.20	0.00	0.00	40.00	58.00	12.00	64.00
E Lens	SD255B	915.0	1.60	450.00	0.00	125.00	2780.00	5.50	0.00	0.00	43.00	25.00	0.00	80.00

Sample Location	Drill Hole ID	Down Hole From Depth	Ag (ppm)	As (ppm)	Bi (ppm)	Co (ppm)	Cu (ppm)	Fe (wt%)	Mn (ppm)	Mo (ppm)	Ni (ppm)	Pb (ppm)	Sb (ppm)	Zn (ppm)
E Lens	SD255B	916.5	1.30	352.00	0.00	85.00	1770.00	4.20	0.00	0.00	32.00	21.00	0.00	45.00
E Lens	SD255B	918.0	1.60	451.00	0.00	104.00	2280.00	6.15	0.00	0.00	52.00	27.00	0.00	64.00
E Lens	SD255B	919.5	2.80	939.00	0.00	108.00	5560.00	7.05	0.00	0.00	56.00	60.00	3.00	57.00
E Lens	SD255B	921.0	4.40	2310.00	0.00	113.00	8070.00	10.30	0.00	2.00	54.00	138.00	23.00	60.00
E Lens	SD255B	922.5	3.20	2030.00	0.00	101.00	5150.00	7.65	0.00	0.00	43.00	122.00	19.00	69.00
E Lens	SD255B	924.0	2.70	1535.00	0.00	83.00	3440.00	6.70	0.00	0.00	37.00	95.00	11.00	60.00
E Lens	SD255B	925.5	4.10	1720.00	0.00	123.00	7450.00	9.10	0.00	0.00	56.00	110.00	19.00	71.00
E Lens	SD255B	927.0	3.50	2090.00	0.00	127.00	5360.00	8.15	0.00	0.00	49.00	128.00	7.00	92.00
E Lens	SD255B	928.5	2.80	971.00	0.00	108.00	3140.00	5.05	0.00	0.00	49.00	58.00	2.00	69.00
E Lens	SD255B	930.0	3.60	2010.00	0.00	130.00	5500.00	7.75	0.00	0.00	62.00	105.00	9.00	56.00
E Lens	SD255B	931.5	5.70	2920.00	0.00	150.00	12600.00	10.90	0.00	2.00	104.00	135.00	20.00	52.00
E Lens	SD255B	933.0	10.40	4890.00	0.00	203.00	17800.00	16.60	0.00	6.00	103.00	227.00	53.00	54.00
E Lens	SD255B	933.8	2.70	401.00	0.00	113.00	39000.00	4.40	0.00	4.00	64.00	28.00	0.00	30.00
E Lens	SD255B	935.3	1.60	519.00	0.00	91.00	3910.00	4.95	0.00	2.00	53.00	36.00	5.00	40.00
E Lens	SD255B	936.8	3.20	1765.00	0.00	95.00	4380.00	7.00	0.00	0.00	51.00	99.00	16.00	39.00
E Lens	SD255B	938.4	2.90	1655.00	0.00	116.00	4880.00	7.20	0.00	0.00	74.00	95.00	11.00	44.00
E Lens	SD255B	939.9	2.00	1185.00	0.00	98.00	2830.00	4.30	0.00	0.00	58.00	74.00	5.00	40.00
E Lens	SD255B	941.4	3.80	2100.00	0.00	143.00	6350.00	8.80	0.00	0.00	82.00	129.00	15.00	41.00
E Lens	SD255B	943.9	1.20	520.00	0.00	109.00	3140.00	4.70	0.00	0.00	60.00	41.00	0.00	38.00
E Lens	SD255B	945.5	1.80	1125.00	0.00	86.00	4110.00	5.10	0.00	0.00	54.00	58.00	10.00	24.00
E Lens	SD255B	947.0	0.60	247.00	0.00	104.00	2330.00	3.55	0.00	0.00	48.00	19.00	0.00	41.00
E Lens	SD255B	948.5	1.40	738.00	0.00	148.00	1720.00	5.80	0.00	0.00	44.00	41.00	0.00	64.00
E Lens	SD255B	950.0	0.90	314.00	0.00	103.00	1950.00	4.00	0.00	0.00	30.00	19.00	0.00	44.00
E Lens	SD255B	951.5	0.00	0.00	0.00	0.00	10.00	0.01	0.00	0.00	0.00	0.00	0.00	0.00
E Lens	SD255B	951.5	2.40	912.00	0.00	112.00	4720.00	5.10	0.00	0.00	45.00	43.00	0.00	40.00
E Lens	SD255B	953.0	2.40	1005.00	0.00	134.00	8400.00	6.45	0.00	0.00	90.00	55.00	3.00	42.00
E Lens	SD255B	954.5	1.50	546.00	0.00	119.00	3210.00	3.95	0.00	0.00	78.00	35.00	2.00	36.00
E Lens	SD255B	956.0	1.70	427.00	0.00	115.00	4850.00	4.35	0.00	0.00	46.00	31.00	0.00	42.00
E Lens	SD255B	957.5	1.40	497.00	0.00	101.00	4010.00	4.95	0.00	0.00	40.00	36.00	4.00	39.00
E Lens	SD255B	959.0	2.40	1280.00	0.00	116.00	8220.00	7.50	0.00	0.00	52.00	66.00	7.00	48.00

Sample Location	Drill Hole ID	Down Hole From Depth	Ag (ppm)	As (ppm)	Bi (ppm)	Co (ppm)	Cu (ppm)	Fe (wt%)	Mn (ppm)	Mo (ppm)	Ni (ppm)	Pb (ppm)	Sb (ppm)	Zn (ppm)
E Lens	SD255B	960.5	1.60	1000.00	0.00	118.00	3890.00	7.55	0.00	0.00	48.00	45.00	0.00	53.00
E Lens	SD255B	962.0	1.70	561.00	0.00	116.00	5780.00	7.45	0.00	0.00	72.00	45.00	0.00	52.00
E Lens	SD255B	963.5	1.90	734.00	0.00	76.00	5130.00	8.15	0.00	0.00	67.00	68.00	10.00	30.00
E Lens	SD255B	964.8	14.40	3130.00	55.00	126.00	69000.00	22.90	0.00	6.00	105.00	252.00	46.00	47.00
E Lens	SD255B	966.0	1.20	210.00	0.00	72.00	4400.00	3.65	0.00	0.00	54.00	28.00	0.00	26.00
E Lens	SD255B	967.5	1.10	244.00	0.00	73.00	3040.00	2.90	0.00	0.00	37.00	14.00	7.00	29.00
E Lens	SD255B	969.0	1.80	791.00	0.00	65.00	4300.00	5.35	0.00	0.00	41.00	53.00	6.00	26.00
E Lens	SD255B	970.5	2.10	1120.00	0.00	103.00	4420.00	6.40	0.00	0.00	67.00	66.00	5.00	52.00
E Lens	SD255B	972.0	2.90	1685.00	0.00	96.00	5690.00	8.70	0.00	0.00	56.00	117.00	19.00	44.00
E Lens	SD255B	973.2	8.20	3710.00	47.00	169.00	17800.00	14.70	0.00	6.00	102.00	245.00	35.00	37.00
E Lens	SD255B	974.6	6.50	2240.00	18.00	96.00	20000.00	8.45	0.00	4.00	57.00	125.00	26.00	26.00
E Lens	SD255B	975.8	9.90	3700.00	66.00	156.00	47500.00	14.90	0.00	9.00	95.00	209.00	41.00	36.00
E Lens	SD255B	977.3	6.20	1805.00	17.00	96.00	25500.00	9.15	0.00	3.00	75.00	118.00	22.00	46.00
E Lens	SD255B	978.8	1.50	413.00	0.00	76.00	2900.00	4.20	0.00	0.00	49.00	25.00	3.00	39.00
E Lens	SD255B	980.3	3.60	1445.00	0.00	110.00	10900.00	8.30	0.00	0.00	63.00	88.00	12.00	47.00
E Lens	SD255B	981.8	2.30	501.00	0.00	117.00	6400.00	6.20	0.00	0.00	52.00	35.00	4.00	55.00
E Lens	SD255B	983.3	2.40	499.00	0.00	110.00	5140.00	5.75	0.00	0.00	50.00	32.00	0.00	54.00
E Lens	SD255B	984.8	2.70	823.00	0.00	67.00	7060.00	5.25	0.00	0.00	38.00	54.00	5.00	29.00
E Lens	SD255B	986.3	5.20	2450.00	37.00	109.00	31000.00	16.60	0.00	6.00	87.00	164.00	20.00	31.00
E Lens	SD255B	987.8	2.60	1300.00	12.00	114.00	5520.00	7.85	0.00	2.00	74.00	76.00	12.00	44.00
E Lens	SD255B	989.3	2.40	949.00	20.00	109.00	6720.00	8.95	0.00	0.00	78.00	55.00	7.00	45.00
E Lens	SD255B	990.8	2.10	695.00	10.00	88.00	5300.00	6.35	0.00	0.00	43.00	43.00	3.00	36.00
E Lens	SD255B	992.3	3.20	705.00	29.00	111.00	10800.00	9.30	0.00	0.00	58.00	63.00	7.00	45.00
E Lens	SD255B	993.8	3.10	981.00	34.00	110.00	11700.00	12.30	0.00	0.00	63.00	72.00	8.00	39.00
E Lens	SD255B	995.5	1.30	252.00	0.00	89.00	2490.00	5.40	0.00	0.00	37.00	23.00	0.00	33.00
E Lens	SD255B	997.0	1.10	204.00	0.00	137.00	1840.00	5.75	0.00	0.00	53.00	15.00	0.00	50.00
E Lens	SD255B	998.5	2.10	709.00	13.00	114.00	4700.00	6.25	0.00	0.00	81.00	36.00	0.00	34.00
E Lens	SD255B	1000.6	4.30	1605.00	72.00	122.00	13300.00	19.40	0.00	3.00	104.00	128.00	19.00	45.00
E Lens	SD255B	1001.6	2.60	1035.00	36.00	107.00	9060.00	8.75	0.00	0.00	66.00	61.00	8.00	35.00
E Lens	SD255B	1003.0	1.30	417.00	10.00	85.00	3880.00	6.70	0.00	0.00	43.00	46.00	2.00	33.00

Sample Location	Drill Hole ID	Down Hole From Depth	Ag (ppm)	As (ppm)	Bi (ppm)	Co (ppm)	Cu (ppm)	Fe (wt%)	Mn (ppm)	Mo (ppm)	Ni (ppm)	Pb (ppm)	Sb (ppm)	Zn (ppm)
E Lens	SD255B	1004.5	3.00	697.00	42.00	74.00	12600.00	14.80	0.00	2.00	47.00	48.00	15.00	31.00
E Lens	SD255B	1006.0	2.50	1045.00	30.00	84.00	8430.00	8.25	0.00	0.00	47.00	45.00	6.00	27.00
E Lens	SD255B	1007.5	1.90	376.00	10.00	102.00	4900.00	7.10	0.00	0.00	59.00	28.00	5.00	33.00
E Lens	SD255B	1009.0	2.30	433.00	29.00	95.00	8570.00	10.10	0.00	0.00	84.00	51.00	11.00	30.00
E Lens	SD255B	1010.5	2.60	477.00	38.00	123.00	11100.00	10.30	0.00	2.00	114.00	48.00	12.00	39.00
E Lens	SD255B	1012.0	1.10	79.00	0.00	177.00	5390.00	6.80	0.00	0.00	106.00	15.00	4.00	64.00
E Lens	SD255B	1013.5	1.50	184.00	0.00	129.00	3560.00	4.95	0.00	0.00	58.00	11.00	0.00	45.00
E Lens	SD255B	1014.8	5.80	1555.00	65.00	145.00	24000.00	15.10	0.00	5.00	44.00	109.00	21.00	29.00
E Lens	SD255B	1016.0	4.30	832.00	37.00	116.00	15000.00	7.70	0.00	3.00	45.00	45.00	14.00	25.00
E Lens	SD255B	1017.5	5.50	706.00	61.00	91.00	24500.00	9.35	0.00	3.00	48.00	56.00	13.00	24.00
E Lens	SD255B	1019.0	4.40	196.00	60.00	95.00	22000.00	11.80	0.00	3.00	73.00	33.00	11.00	34.00
E Lens	SD255B	1020.5	4.40	506.00	55.00	59.00	22000.00	7.95	0.00	0.00	25.00	31.00	11.00	20.00
E Lens	SD255B	1022.0	2.20	106.00	27.00	136.00	10100.00	6.35	0.00	0.00	65.00	27.00	7.00	33.00
E Lens	SD255B	1023.3	4.80	100.00	74.00	227.00	24000.00	16.40	0.00	0.00	144.00	67.00	15.00	64.00
E Lens	SD255B	1024.3	1.50	133.00	15.00	160.00	5890.00	5.25	0.00	0.00	64.00	13.00	0.00	46.00
E Lens	SD255B	1026.2	4.90	647.00	92.00	167.00	30000.00	12.50	0.00	3.00	91.00	65.00	9.00	40.00
E Lens	SD255B	1027.8	1.70	345.00	19.00	112.00	7430.00	5.40	0.00	0.00	68.00	22.00	0.00	29.00
E Lens	SD255B	1029.0	2.20	369.00	22.00	127.00	8730.00	4.50	0.00	0.00	80.00	21.00	0.00	32.00
E Lens	SD255B	1030.3	2.80	269.00	58.00	119.00	19400.00	13.30	0.00	0.00	83.00	46.00	6.00	32.00
E Lens	SD255B	1031.8	1.10	90.00	27.00	199.00	4500.00	17.80	0.00	0.00	113.00	54.00	8.00	67.00
E Lens	SD255B	1033.3	3.80	89.00	37.00	250.00	10800.00	15.60	0.00	0.00	110.00	45.00	4.00	63.00
E Lens	SD255B	1034.8	4.40	110.00	52.00	244.00	14600.00	20.10	0.00	0.00	139.00	68.00	10.00	64.00
E Lens	SD255B	1036.3	6.90	107.00	67.00	250.00	28500.00	24.50	0.00	2.00	161.00	80.00	14.00	70.00
E Lens	SD255B	1037.8	118.00	1705.00	480.00	96.00	369000.00	13.30	0.00	14.00	48.00	198.00	16.00	308.00
E Lens	SD255B	1039.4	3.60	82.00	17.00	270.00	10900.00	13.40	0.00	0.00	128.00	35.00	4.00	85.00
E Lens	SD255B	1041.0	0.60	69.00	0.00	314.00	1540.00	6.90	60.00	0.00	77.00	14.00	0.00	168.00
E Lens	SD255B	1042.7	11.70	99.00	83.00	290.00	45500.00	23.60	50.00	2.00	89.00	67.00	5.00	117.00
E Lens	SD255B	1044.0	1.80	78.00	0.00	270.00	23500.00	5.15	80.00	0.00	65.00	16.00	8.00	131.00
E Lens	SD255B	1045.5	1.60	55.00	0.00	140.00	3890.00	5.10	0.00	0.00	42.00	10.00	0.00	65.00
E Lens	SD255B	1047.0	2.30	77.00	16.00	163.00	5670.00	9.35	0.00	0.00	54.00	27.00	0.00	80.00

Sample Location	Drill Hole ID	Down Hole From Depth	Ag (ppm)	As (ppm)	Bi (ppm)	Co (ppm)	Cu (ppm)	Fe (wt%)	Mn (ppm)	Mo (ppm)	Ni (ppm)	Pb (ppm)	Sb (ppm)	Zn (ppm)
E Lens	SD255B	1048.5	1.80	48.00	11.00	178.00	3580.00	6.50	0.00	0.00	51.00	12.00	0.00	91.00
E Lens	SD255B	1050.0	2.60	53.00	19.00	151.00	8970.00	8.60	0.00	0.00	50.00	25.00	0.00	51.00
E Lens	SD255B	1051.5	1.50	55.00	0.00	251.00	3270.00	9.35	0.00	0.00	75.00	19.00	0.00	80.00
E Lens	SD255B	1053.0	4.40	94.00	30.00	315.00	14100.00	18.10	0.00	3.00	100.00	38.00	4.00	96.00
E Lens	SD255B	1054.5	5.00	90.00	32.00	251.00	14200.00	16.10	0.00	0.00	84.00	44.00	9.00	81.00
E Lens	SD255B	1056.0	4.80	70.00	23.00	242.00	11500.00	15.30	0.00	0.00	66.00	32.00	6.00	74.00
E Lens	SD255B	1057.5	2.00	68.00	15.00	326.00	6660.00	12.90	0.00	2.00	84.00	20.00	0.00	93.00
E Lens	SD255B	1059.0	2.30	322.00	35.00	181.00	16500.00	14.00	0.00	0.00	69.00	36.00	4.00	47.00
E Lens	SD255B	1060.5	5.70	1970.00	57.00	39.00	41500.00	6.45	0.00	0.00	16.00	80.00	10.00	7.00
E Lens	SD255B	1062.0	2.30	621.00	27.00	119.00	12900.00	10.30	0.00	2.00	51.00	47.00	8.00	32.00
E Lens	SD255B	1063.5	0.80	58.00	0.00	167.00	2650.00	6.90	0.00	0.00	57.00	22.00	0.00	45.00
E Lens	SD255B	1065.0	0.50	45.00	0.00	225.00	1710.00	7.70	0.00	0.00	101.00	19.00	0.00	61.00
E Lens	SD255B	1066.5	0.90	342.00	20.00	286.00	3530.00	19.00	0.00	0.00	114.00	62.00	12.00	93.00
E Lens	SD255B	1068.4	1.10	126.00	17.00	204.00	6020.00	10.60	0.00	0.00	52.00	29.00	4.00	60.00
E Lens	SD255B	1070.0	2.00	503.00	27.00	60.00	11100.00	7.85	0.00	0.00	13.00	34.00	6.00	24.00
E Lens	SD255B	1071.5	1.00	154.00	0.00	131.00	3280.00	7.25	0.00	0.00	42.00	25.00	4.00	47.00
E Lens	SD255B	1073.0	0.80	68.00	11.00	231.00	5200.00	12.10	0.00	0.00	52.00	30.00	5.00	77.00
E Lens	SD255B	1074.5	0.50	91.00	24.00	492.00	3720.00	19.90	0.00	3.00	112.00	57.00	4.00	142.00
E Lens	SD255B	1076.0	0.80	74.00	15.00	385.00	4010.00	14.10	0.00	0.00	81.00	42.00	14.00	93.00
E Lens	SD255B	1077.5	1.10	68.00	20.00	366.00	7120.00	14.20	0.00	0.00	79.00	42.00	10.00	92.00
E Lens	SD255B	1079.0	1.60	96.00	23.00	406.00	9790.00	13.60	0.00	0.00	74.00	36.00	6.00	103.00
E Lens	SD255B	1080.5	1.20	94.00	45.00	409.00	12300.00	20.00	0.00	0.00	99.00	62.00	11.00	102.00
E Lens	SD255B	1082.0	1.10	95.00	32.00	357.00	10700.00	14.10	0.00	0.00	131.00	40.00	5.00	103.00
E Lens	SD255B	1083.5	3.10	2370.00	31.00	75.00	19200.00	13.50	0.00	2.00	30.00	98.00	20.00	23.00
E Lens	SD255B	1085.0	6.20	3250.00	43.00	75.00	35000.00	18.70	0.00	4.00	29.00	107.00	38.00	14.00
E Lens	SD255B	1086.5	10.30	7290.00	70.00	127.00	47500.00	18.70	0.00	7.00	38.00	273.00	28.00	15.00
E Lens	SD255B	1088.0	6.40	5280.00	45.00	91.00	31000.00	16.30	0.00	5.00	33.00	186.00	24.00	19.00
E Lens	SD255B	1089.5	6.30	5850.00	51.00	80.00	28500.00	18.30	0.00	5.00	35.00	197.00	29.00	25.00
E Lens	SD255B	1091.0	19.10	4330.00	52.00	157.00	113000.00	24.40	0.00	7.00	36.00	330.00	83.00	59.00
E Lens	SD255B	1092.5	13.30	5190.00	60.00	100.00	97500.00	15.70	0.00	6.00	31.00	236.00	59.00	47.00

Sample Location	Drill Hole ID	Down Hole From Depth	Ag (ppm)	As (ppm)	Bi (ppm)	Co (ppm)	Cu (ppm)	Fe (wt%)	Mn (ppm)	Mo (ppm)	Ni (ppm)	Pb (ppm)	Sb (ppm)	Zn (ppm)
E Lens	SD255B	1094.0	1.90	180.00	30.00	103.00	15100.00	16.90	0.00	0.00	213.00	43.00	11.00	54.00
E Lens	SD255B	1095.5	7.50	4110.00	120.00	59.00	52000.00	17.30	0.00	3.00	34.00	163.00	29.00	23.00
E Lens	SD255B	1097.0	4.10	827.00	71.00	38.00	37500.00	24.50	0.00	2.00	30.00	62.00	24.00	30.00
E Lens	SD255B	1098.8	9.60	1875.00	160.00	42.00	78000.00	19.70	0.00	3.00	31.00	107.00	11.00	32.00
E Lens	SD255B	1100.9	0.80	206.00	27.00	180.00	2050.00	30.80	0.00	3.00	109.00	44.00	5.00	232.00
E Lens	SD255B	1102.5	0.00	192.00	30.00	174.00	1000.00	8.95	145.00	0.00	73.00	43.00	0.00	697.00
E Lens	SD255B	1104.0	0.20	168.00	21.00	64.00	1550.00	6.40	115.00	0.00	48.00	8.00	0.00	175.00
E Lens	SD255B	1105.5	0.00	134.00	17.00	56.00	2650.00	7.35	135.00	0.00	49.00	17.00	0.00	171.00
E Lens	SD255B	1107.0	0.70	84.00	0.00	20.00	1050.00	3.50	70.00	0.00	20.00	0.00	0.00	59.00
E Lens	SD255B	1108.5	0.40	81.00	0.00	19.00	1000.00	2.95	65.00	0.00	23.00	6.00	0.00	61.00

Sample Location	Drill Hole ID	Down Hole From Depth	Ag (ppm)	As (ppm)	Bi (ppm)	Co (ppm)	Cu (ppm)	Fe (wt%)	Mn (ppm)	Mo (ppm)	Ni (ppm)	Pb (ppm)	Sb (ppm)	Zn (ppm)
E Lens	SD255A	869.00	0.00	46.00	0.00	54.00	105.00	5.30	225.00	0.00	27.00	10.00	0.00	117.00
E Lens	SD255A	870.50	0.00	51.00	0.00	49.00	190.00	5.90	180.00	0.00	24.00	5.00	0.00	52.00
E Lens	SD255A	872.00	5.90	89.00	56.00	20.00	41500.00	4.00	60.00	0.00	13.00	23.00	0.00	21.00
E Lens	SD255A	873.50	3.80	51.00	43.00	22.00	33000.00	6.50	90.00	0.00	18.00	17.00	0.00	26.00
E Lens	SD255A	875.00	2.90	45.00	115.00	19.00	91000.00	6.40	85.00	0.00	10.00	32.00	0.00	26.00
E Lens	SD255A	875.70	0.90	25.00	0.00	30.00	1900.00	4.70	90.00	0.00	10.00	0.00	0.00	28.00
E Lens	SD255A	877.20	0.50	38.00	0.00	59.00	405.00	5.45	135.00	0.00	27.00	0.00	0.00	44.00
E Lens	SD255A	906.00	3.40	136.00	31.00	112.00	1280.00	23.40	110.00	0.00	80.00	40.00	6.00	83.00
E Lens	SD255A	907.50	0.90	61.00	0.00	52.00	8550.00	8.25	55.00	0.00	37.00	26.00	0.00	44.00
E Lens	SD255A	909.00	3.60	58.00	0.00	23.00	41500.00	6.25	0.00	0.00	25.00	28.00	0.00	24.00
E Lens	SD255A	910.50	0.50	46.00	0.00	34.00	3710.00	6.75	50.00	0.00	36.00	18.00	0.00	43.00
E Lens	SD255A	944.00	0.00	260.00	13.00	254.00	390.00	13.30	80.00	0.00	93.00	69.00	20.00	71.00
E Lens	SD255A	945.50	0.40	370.00	39.00	239.00	470.00	35.90	100.00	0.00	117.00	78.00	29.00	68.00
E Lens	SD255A	947.00	0.00	403.00	22.00	268.00	345.00	26.40	60.00	0.00	118.00	63.00	21.00	77.00
E Lens	SD255A	948.50	0.60	445.00	54.00	199.00	280.00	50.80	105.00	0.00	86.00	73.00	45.00	60.00
E Lens	SD255A	950.00	0.40	394.00	73.00	156.00	190.00	55.90	75.00	3.00	69.00	67.00	55.00	54.00
E Lens	SD255A	951.50	0.60	479.00	84.00	204.00	380.00	56.70	100.00	0.00	90.00	51.00	38.00	64.00
E Lens	SD255A	953.00	0.70	450.00	64.00	244.00	540.00	55.60	105.00	3.00	118.00	51.00	43.00	75.00
E Lens	SD255A	954.50	0.60	472.00	67.00	189.00	360.00	53.60	65.00	4.00	101.00	62.00	48.00	59.00
E Lens	SD255A	956.00	2.50	501.00	115.00	96.00	16000.00	52.50	0.00	0.00	59.00	45.00	57.00	36.00
E Lens	SD255A	957.50	20.30	3090.00	125.00	73.00	122000.00	21.90	0.00	2.00	44.00	150.00	39.00	26.00
E Lens	SD255A	959.00	20.80	6790.00	97.00	90.00	110000.00	28.70	0.00	4.00	37.00	217.00	100.00	30.00
E Lens	SD255A	960.50	7.30	2350.00	63.00	99.00	45500.00	22.20	0.00	0.00	71.00	95.00	38.00	21.00
E Lens	SD255A	962.00	3.00	680.00	34.00	115.00	17100.00	15.50	0.00	0.00	64.00	50.00	8.00	20.00
E Lens	SD255A	963.50	2.80	568.00	31.00	101.00	21500.00	10.80	0.00	0.00	45.00	40.00	5.00	15.00
E Lens	SD255A	965.00	4.80	1015.00	52.00	133.00	29000.00	12.50	0.00	0.00	82.00	80.00	12.00	22.00
E Lens	SD255A	966.50	3.60	516.00	62.00	143.00	29000.00	30.80	0.00	2.00	105.00	61.00	16.00	29.00
E Lens	SD255A	968.00	4.50	1775.00	60.00	140.00	31500.00	18.00	0.00	0.00	81.00	79.00	16.00	23.00
E Lens	SD255A	969.50	4.10	1915.00	46.00	113.00	23500.00	15.10	0.00	0.00	62.00	72.00	12.00	19.00

Sample Location	Drill Hole ID	Down Hole From Depth	Ag (ppm)	As (ppm)	Bi (ppm)	Co (ppm)	Cu (ppm)	Fe (wt%)	Mn (ppm)	Mo (ppm)	Ni (ppm)	Pb (ppm)	Sb (ppm)	Zn (ppm)
E Lens	SD255A	971.00	3.10	377.00	52.00	161.00	30500.00	17.00	0.00	0.00	100.00	45.00	7.00	24.00
E Lens	SD255A	972.50	7.00	9000.00	81.00	112.00	33000.00	29.10	0.00	4.00	63.00	233.00	71.00	25.00
E Lens	SD255A	974.00	5.50	6580.00	59.00	81.00	23000.00	18.10	0.00	4.00	50.00	162.00	45.00	18.00
E Lens	SD255A	975.50	6.40	8450.00	100.00	108.00	39500.00	22.10	0.00	4.00	61.00	209.00	57.00	22.00
E Lens	SD255A	977.00	2.90	3310.00	50.00	111.00	18700.00	12.70	0.00	0.00	139.00	75.00	14.00	17.00
E Lens	SD255A	978.50	5.00	4990.00	55.00	95.00	24500.00	17.70	0.00	4.00	94.00	119.00	26.00	19.00
E Lens	SD255A	980.00	7.70	6610.00	53.00	66.00	42000.00	18.00	0.00	5.00	32.00	172.00	47.00	14.00
E Lens	SD255A	981.50	7.10	6780.00	56.00	55.00	27000.00	16.50	0.00	3.00	26.00	138.00	32.00	18.00
E Lens	SD255A	983.00	9.80	1125.00	41.00	52.00	23500.00	16.20	0.00	0.00	41.00	51.00	13.00	19.00
E Lens	SD255A	984.50	6.30	211.00	16.00	86.00	13400.00	9.70	0.00	0.00	72.00	24.00	2.00	20.00
E Lens	SD255A	986.00	6.50	87.00	21.00	99.00	14500.00	11.20	0.00	0.00	70.00	25.00	0.00	24.00
E Lens	SD255A	987.50	15.10	2180.00	41.00	64.00	40000.00	11.20	0.00	0.00	30.00	86.00	16.00	13.00
E Lens	SD255A	989.00	26.10	5450.00	76.00	46.00	63500.00	15.80	0.00	3.00	24.00	198.00	38.00	21.00
E Lens	SD255A	990.50	26.00	1280.00	75.00	33.00	56500.00	6.40	0.00	0.00	15.00	67.00	11.00	11.00
E Lens	SD255A	992.00	3.60	226.00	44.00	163.00	6210.00	18.70	60.00	2.00	44.00	39.00	32.00	65.00
E Lens	SD255A	993.50	1.20	293.00	31.00	180.00	590.00	6.35	65.00	0.00	28.00	16.00	10.00	71.00
E Lens	SD255A	995.00	1.40	331.00	13.00	123.00	815.00	3.75	50.00	0.00	13.00	6.00	0.00	50.00
E Lens	SD255A	996.50	0.90	374.00	25.00	135.00	430.00	21.60	55.00	3.00	19.00	28.00	42.00	74.00
E Lens	SD255A	998.00	1.00	571.00	37.00	154.00	800.00	17.90	60.00	0.00	32.00	42.00	28.00	74.00
E Lens	SD255A	999.50	0.60	319.00	39.00	167.00	1010.00	14.80	80.00	4.00	25.00	46.00	4.00	79.00
E Lens	SD255A	1001.00	0.80	389.00	29.00	215.00	880.00	12.10	90.00	0.00	66.00	33.00	9.00	98.00
E Lens	SD255A	1002.50	0.60	468.00	27.00	193.00	640.00	6.25	70.00	0.00	37.00	17.00	0.00	85.00
E Lens	SD255A	1004.00	0.70	394.00	27.00	220.00	655.00	11.10	80.00	4.00	98.00	26.00	0.00	146.00
E Lens	SD255A	1005.50	0.80	247.00	11.00	102.00	435.00	6.35	0.00	7.00	38.00	12.00	0.00	57.00
E Lens	SD255A	1007.00	0.90	405.00	21.00	96.00	405.00	12.20	0.00	3.00	39.00	26.00	14.00	59.00
E Lens	SD255A	1008.50	0.80	170.00	0.00	92.00	305.00	4.70	0.00	0.00	44.00	10.00	0.00	55.00
E Lens	SD255A	1010.00	1.20	135.00	0.00	135.00	345.00	6.30	60.00	0.00	82.00	13.00	0.00	86.00
E Lens	SD255A	1011.50	0.90	185.00	24.00	112.00	310.00	15.80	0.00	4.00	90.00	21.00	8.00	58.00
E Lens	SD255A	1013.00	2.80	180.00	38.00	100.00	4000.00	17.00	0.00	5.00	75.00	19.00	15.00	37.00
E Lens	SD255A	1014.50	11.40	91.00	51.00	123.00	30000.00	16.40	0.00	0.00	99.00	23.00	3.00	36.00

Sample Location	Drill Hole ID	Down Hole From Depth	Ag (ppm)	As (ppm)	Bi (ppm)	Co (ppm)	Cu (ppm)	Fe (wt%)	Mn (ppm)	Mo (ppm)	Ni (ppm)	Pb (ppm)	Sb (ppm)	Zn (ppm)
E Lens	SD255A	1016.00	32.40	101.00	145.00	176.00	105000.00	21.80	0.00	7.00	199.00	53.00	4.00	55.00
E Lens	SD255A	1017.50	5.40	236.00	48.00	115.00	12800.00	30.30	0.00	5.00	127.00	32.00	22.00	46.00
E Lens	SD255A	1019.00	2.20	162.00	17.00	136.00	900.00	7.85	0.00	0.00	87.00	20.00	4.00	43.00
E Lens	SD255A	1020.50	3.10	131.00	18.00	62.00	745.00	12.00	0.00	0.00	41.00	28.00	7.00	27.00
E Lens	SD255A	1022.00	3.00	212.00	25.00	73.00	840.00	9.90	0.00	2.00	55.00	23.00	8.00	28.00
E Lens	SD255A	1023.50	1.20	575.00	14.00	207.00	635.00	13.30	0.00	0.00	62.00	20.00	8.00	36.00
E Lens	SD255A	1025.00	1.60	147.00	22.00	147.00	510.00	7.15	55.00	0.00	63.00	22.00	4.00	46.00
E Lens	SD255A	1026.50	0.60	158.00	29.00	233.00	995.00	15.50	90.00	0.00	111.00	32.00	9.00	77.00
E Lens	SD255A	1028.00	1.20	951.00	30.00	321.00	460.00	15.10	0.00	3.00	88.00	28.00	23.00	41.00
E Lens	SD255A	1029.50	0.90	160.00	31.00	200.00	875.00	13.30	95.00	0.00	131.00	35.00	11.00	90.00
E Lens	SD255A	1031.00	0.80	484.00	0.00	173.00	475.00	2.95	75.00	0.00	26.00	7.00	0.00	37.00
E Lens	SD255A	1032.50	1.70	2970.00	0.00	181.00	560.00	3.00	0.00	0.00	9.00	7.00	0.00	20.00
E Lens	SD255A	1034.00	0.60	295.00	28.00	107.00	775.00	6.95	145.00	0.00	60.00	13.00	0.00	92.00
E Lens	SD255A	1035.50	0.70	215.00	13.00	67.00	370.00	4.65	115.00	2.00	37.00	7.00	0.00	57.00
E Lens	SD255A	1037.00	0.90	172.00	11.00	59.00	575.00	5.10	110.00	0.00	34.00	8.00	2.00	54.00
E Lens	SD255A	1038.50	1.00	3390.00	37.00	124.00	540.00	3.70	125.00	0.00	36.00	7.00	0.00	49.00

Sample Location	Drill Hole ID	Down Hole From Depth	Ag (ppm)	As (ppm)	Bi (ppm)	Co (ppm)	Cu (ppm)	Fe (wt%)	Mn (ppm)	Mo (ppm)	Ni (ppm)	Pb (ppm)	Sb (ppm)	Zn (ppm)
E Lens	UD765	377.0	0.2	270	12	213	100	15	N/A	0	142	46	26	70
E Lens	UD765	378.5	0.9	133	19	169	200	11.5	N/A	0	90	29	19	47
E Lens	UD765	380.0	4.2	4570	170	123	35800	26.2	N/A	0	107	158	87	35
E Lens	UD765	381.5	4.2	4490	165	115	35800	33	N/A	0	101	155	80	30
E Lens	UD765	383.0	7.7	6560	68	96	41800	17.3	N/A	0	53	226	88	23
E Lens	UD765	384.5	8.1	7830	72	102	48800	17.2	N/A	0	67	310	76	23
E Lens	UD765	386.0	8.1	6540	77	94	61200	20.7	N/A	0	53	249	72	29
E Lens	UD765	387.5	7.4	9080	78	106	34500	19.4	N/A	0	71	344	79	21
E Lens	UD765	389.0	9.5	8630	96	99	62400	23.4	N/A	0	76	437	79	27
E Lens	UD765	390.5	7.3	5360	82	89	51200	21.2	N/A	0	48	329	71	24
E Lens	UD765	392.0	6.3	6720	76	95	28900	23.2	N/A	0	59	349	92	21
E Lens	UD765	393.5	5.9	6350	79	91	27600	21.2	N/A	0	44	315	84	23
E Lens	UD765	395.0	5.3	6790	68	99	21200	21.8	N/A	0	56	298	97	19
E Lens	UD765	396.5	6.6	5110	150	84	43000	35	N/A	0	43	245	87	27
E Lens	UD765	398.0	1.3	2610	54	138	6700	25.4	N/A	0	116	144	84	44
E Lens	UD765	399.5	0.4	1460	42	190	800	34	N/A	0	121	95	95	75